Development of Matrix-Assisted Laser Desorption/Ionization and Liquid Chromatography - Electrospray Ionization Based Mass Spectrometric Techniques for Characterizing and Quantifying Endogenous and Therapeutic Biomolecules

By
Bingming Chen

A dissertation submitted in partial fulfillment of
the requirements for the degree of

Doctor of Philosophy
(Pharmaceutical Sciences)

at the
UNIVERSITY OF WISCONSIN-MADISON
2017

Date of final oral examination: March 24th, 2017

The dissertation is examined by the following members of the Final Oral Committee:
Lingjun Li, Professor, School of Pharmacy and Department of Chemistry
Robert G. Thorne, Assistant Professor, School of Pharmacy
Paul C. Marker, Professor, School of Pharmacy
Hrissanthi Ikonomidou, Professor, Department of Neurology
Antony O. Stretton, Professor, Department of Zoology

Acknowledgements

I would like to first acknowledge my advisor Dr. Lingjun Li for her support and guidance throughout my academic development. Dr. Li has always been incredibly supportive towards my thesis projects, and giving me freedom to become an independent researcher. None of the work in this dissertation could be possible without her. It is my honor to work with Dr. Li in our lab with cutting-edge bioanalytical instrumentation and research. I will be forever grateful for this invaluable opportunity.

I would also like to thank my thesis committee members, Dr. Robert Thorne, Dr. Paul Marker, Dr. Hrissanthi Ikonomidou and Dr. Antony Stretton for providing valuable suggestions and insights at my preliminary exam and this dissertation. Moreover, I wish to give special thanks to Dr. Thorne and Dr. Ikonomidou, who are not only my committee members, but also my collaborators. I am very thankful for their guidance and patience explaining the biological significance to me and helping me understand results.

In additional to my committee members, I wish to thank other collaborators who I have been fortunate enough to work with on various exciting bioanalytical projects: Niyanta Kumar and Mohan Gautam from Thorne Lab, Dr. Ross Cheloha from Gellman Lab, Dr. Izabela Sibilska from Yin Lab and Dr. Mingshe Zhu from Bristol-Myers Squibb (now the founder of Sunrise Forum for Drug Metabolism). I would also like to thank my undergraduate research advisors and mentors, Dr. Amy Wong, Dr. John Yin, Dr. Timothy Yoshino, Dr. Zachary Pratt, Dr. Adam Swick, Dr. Musarat Ishaq, and Dr. Xiao-Jun Wu, who introduced me into the world of research and encouraged me to pursue the Ph.D. study.

It is my honor to work alongside with extremely talented mentors and colleagues in our lab during my graduate study. At the very beginning of my graduate study, Dr. Vivian Hui Ye mentored me and taught me everything on mass spectrometry imaging and neuropeptide study. Dr. Chris Lietz led me into the method development projects, which had later become my main research focus. Dr. Xuefei Zhong has been a valued mentor and friend, whom I worked together with on glycan quantification projects. Dr. Erin Gemperline and Dr. Chuanzi OuYang, who are experts on mass spectrometry imaging, shared inspiring discussions with me on related projects and instrumentations. Yu Feng, Qinying Yu, Zichuan Tian and Meng Xu have been wonderful to work with and contributed significantly for our joint projects. It has also been a valuable experience to work with Dr. Dustin Frost, Amanda Buchberger, Kellen DeLaney and Jill Johnson in our collaborative project. I would like to give special thanks to Amanda Buchberger for her help in editing and polishing this dissertation. In addition, I have benefited from day-to-day interaction and discussions with other colleagues: Dr. Chenxi Yang, Dr. Chenxi Jia, Dr. Zhidan Liang, Dr. Tyler Greer, Dr. Xueqin Pang, Qing Yu, Qinjingwen Cao, Yatao Shi and Xiaofang Zhong.

I wish to thank Dr. Cameron Scarlett and Molly Pellitteri-Hahn from the Analytical Instrumentation Center in School of Pharmacy, for providing their expertise and assistances in instrumentation and experimental design. Many studies in this dissertation would be impossible without their help and support.

I would also like to extend my thanks to the professors that I worked with as a teaching assistant: Dr. Steven Oakes, Dr. Arash Bashirullah, Dr. Richard Peterson, Dr. Warren Heideman, and Dr. Lara Collier. In addition, I would like to give special thanks to Ken Niemeyer, who is the

graduate program coordinator and has been extremely helpful in every stage of my graduate study.

I would like to extend my gratitude to the institutions that provide financial support throughout my graduate career, including Wisconsin Alumni Research Foundation, University of Wisconsin graduate school, Witiak travel award and David & Kato Perlman Wisconsin Distinguished Graduate Fellowship.

Finally, I could not have achieved any of this without the support of my family and friends, especially my parents, my aunt's family and Ruxiu. Their unconditional love and support help me overcome the difficulties in my life and make me become a better person. To them I dedicate this thesis.

Table of Contents

Acknowledgement		**i**
Table of Contents		**iv**
Abstract		**v**
Chapter 1	Introduction and Research Summary	**1**
Chapter 2	*In Situ* Characterization of Proteins Using Laserspray Ionization on a High-Performance MALDI-LTQ-Orbitrap Mass Spectrometer	**12**
Chapter 3	Matrix-Assisted Ionization Vacuum for Protein Detection, Fragmentation and PTM Analysis on a High Resolution Linear Ion Trap-Orbitrap Platform	**30**
Chapter 4	Coupling Matrix-Assisted Ionization with High Resolution Mass Spectrometer and Electron Transfer Dissociation for Characterizing Intact Proteins and Post-Translational Modifications	**55**
Chapter 5	High Throughput *In Situ* DDA Analysis of Neuropeptides by Coupling Novel Multiplex Mass Spectrometric Imaging with Gas Phase Fractionation	**85**
Chapter 6	A High Resolution Atmospheric Pressure Matrix-Assisted Laser Desorption/Ionization-Quadrupole-Orbitrap Platform Enables *In Situ* Analysis of Biomolecules by Multi-Modal Ionization and Acquisition	**127**
Chapter 7	MALDI-MS Profiling and Imaging of Intranasally Administered Oxytocin and Neuropeptide Analogs	**161**
Chapter 8	Probing Neuropeptidomic Changes Related to Autism Spectrum Disorders via Mass Spectrometric Imaging for the Wisconsin Initiative for Science Literacy	**177**
Chapter 9	Stability Analysis of Parathyroid Hormone (1-34) and its Bioactive Analog in Rat Kidney Homogenate by MALDI-MS and Multiplexed Parallel Reaction Monitoring LC-MS/MS Analysis	**185**
Chapter 10	Relative Quantification of Glycans Using Multiplexed Carbonyl-Reactive Tandem Mass Tags and Targeted Product Ion Triggered MultiNotch MS^3	**214**
Chapter 11	Mass Defect-based DiPyrO Tags for Multiplex N-glycan Characterization and Relative Quantification on a High-Resolution Mass Spectrometer	**245**
Chapter 12	Conclusions and Future Directions	**274**
Appendix I	Publications and Presentations	**280**
Appendix II	Challenges and Recent Advances in Mass Spectrometric Imaging of Neurotransmitters	**284**
Appendix III	LC-MS Differential Analysis for Fast and Sensitive Determination of Biotransformation of Therapeutic Proteins	**329**
Appendix IV	Identification of a Bioactive Analog of Parathyroid Hormone with Widely Distributed Backbone Modifications that Shows High Stability in Diverse Biological Contexts	**358**

Development of Matrix-Assisted Laser Desorption/Ionization and Liquid Chromatography - Electrospray Ionization Based Mass Spectrometric Techniques for Characterizing and Quantifying Endogenous and Therapeutic Biomolecules

Bingming Chen
Under the supervision of Professor Lingjun Li
University of Wisconsin-Madison

Abstract

Endogenous biomolecules, such as neuropeptides, proteins, and carbohydrates, play important roles in biological and physiological processes. Over the last two decades, therapeutic biomolecules, including peptides, glycoproteins and monoclonal antibodies, have become large and fast-growing segments of the pharmaceutical industry. However, analyzing biomolecules is challenging due to their large size, complex structure, and various modifications. *In situ* analysis of biomolecules is even more challenging due to the wide dynamic range and complex microenvironments on the tissue surface. In this dissertation, novel and improved matrix-assisted laser desorption/ionization (MALDI) and liquid chromatography (LC) – electrospray ionization (ESI) based mass spectrometric techniques were developed to characterize and quantify endogenous and therapeutic biomolecules. Specifically, this work developed new ionization techniques and mass spectrometry imaging workflows to determine the sequence and map the *in situ* distribution of biomolecules on high resolution-accurate mass instrument platforms. Moreover, absolute or relative quantification of biomolecules, such as therapeutic peptides or N-linked glycans, were achieved by cutting-edge quantification workflows.

In summary, this work not only improves current analytical methodology for characterizing biomolecules but also demonstrates its potential applications in the pharmaceutical industry and clinical settings.

Chapter 1
Introduction and Research Summary

Method Development Milestones

2013
Laserspray ionization

MALDI-Orbitrap

2014
Matrix-assisted ionization vacuum

MALDI-Orbitrap

2015
Matrix-assisted ionization

Orbitrap Elite (ESI)

2016
MALDI, LSI, MAI

AP/MALDI-QE HF

Applications

Autism Spectrum Disorders
biomarker discovery
MALDI/LSI MSI

Oxytocin intranasal delivery
MALDI MSI
LC-MS/MS

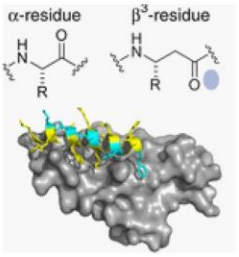

Parathyroid hormone analog
stability analysis
MALDI MS & LC-MS/MS

Introduction

In this dissertation, a multi-dimensional mass spectrometry (MS) platform, combining matrix-assisted laser desorption/ionization (MALDI) and liquid chromatography (LC) – electrospray ionization (ESI) techniques, was developed to characterize and quantify endogenous and therapeutic biomolecules. Novel ionization techniques, MS imaging workflows, and quantification strategies were developed and demonstrated in complex biological systems. This work not only improves current analytical methodology for characterizing biomolecules, but also demonstrates the potential applications in the pharmaceutical industry and clinical settings.

Chapter 1 is a general introduction with summaries of major findings of each project. **Chapters 2-4** seek to develop novel ionization techniques that are capable of producing multiply charged ions on high resolution-accurate mass (HRAM) instrument platforms.[1,2] **Chapter 5** shows the development of a method that couples novel multiplex MS imaging with gas phase fractionation to achieve *in situ* data dependent acquisition and biomolecule identification.[3] **Chapter 6** demonstrates high resolution MS imaging, both in mass and in space, on an atmospheric pressure MALDI-quadrupole-Orbitrap platform. **Chapters 7 and 8** describe two applications of MS imaging for mapping of either therapeutic or endogenous neuropeptides. **Chapters 9, 10 and 11** report on three quantification studies for measuring therapeutic peptides or N-glycans. **Chapter 12** concludes the dissertation and discusses future research directions. Additional information about the use of MS imaging for neurotransmitters,[4] LC-MS for biotransformation in antibodies, and designing backbone modified therapeutic peptides[5] can be found in **Appendices II, III and IV**.

Chapter 2 *In Situ* Characterization of Proteins Using Laserspray Ionization on a High-Performance MALDI-LTQ-Orbitrap Mass Spectrometer[1]

The MALDI-LTQ-Orbitrap XL mass spectrometer is a high-performance instrument capable of HRAM measurement. The maximum *m/z* of 4000 precludes the MALDI analysis of proteins without generating multiply charged ions. Herein, we present the study of HRAM laserspray ionization MS with MS/MS and MS imaging capabilities using 2-nitrophloroglucinol as matrix on the MALDI-LTQ-Orbitrap XL. The optimized conditions for multiply charged ion production have been determined and applied to tissue profiling and imaging. Biomolecules as large as 15 kDa have been detected with up to five positive charges at 100K mass resolution (at *m/z* 400). More importantly, MS/MS and protein identification on multiply charged precursor ions from both standards and tissue samples have been achieved for the first time with an intermediate-pressure source. The initial results reported in this study highlight potential utilities of laserspray ionization MS analysis for simultaneous *in situ* protein identification, visualization, and characterization from complex tissue samples on a commercially available HRAM MALDI system.

Chapter 3 Matrix-Assisted Ionization Vacuum for Protein Detection, Fragmentation and PTM Analysis on a High Resolution Linear Ion Trap-Orbitrap Platform[2]

Similar to laserspray ionization described in Chapter 2, matrix-assisted ionization vacuum (MAIV) is a novel ionization technique that generates multiply charged ions in vacuum. In contrast to laserspray ionization, MAIV does not require laser ablation or high voltage and can be achieved on both MALDI and ESI sources without instrument modification. Moreover, it tends to produce higher charge states compared to laserspray ionization. Herein, we adapt MAIV onto the MALDI-LTQ-Orbitrap XL platform for biomolecule analysis. As an attractive alternative to MALDI for in

solution and *in situ* analysis of biomolecules, MAIV coupled to a HRAM instrument has successfully expanded the mass detection range and improved the fragmentation efficiency due to the generation of multiply charged ions. Additionally, the softness of MAIV enables potential application of analysis of labile post-translational modification (PTM). In this study, proteins as large as 18.7 kDa were detected with up to 18 charges; intact peptides with labile PTM were well preserved during the ionization process; and peptides and proteins in complex tissue samples were detected and identified both in liquid extracts and *in situ*. Moreover, we demonstrated that this method facilitates MS/MS analysis with improved fragmentation efficiency compared to MALDI-MS/MS.

Chapter 4 Coupling Matrix-Assisted Ionization with High Resolution Mass Spectrometer and Electron Transfer Dissociation for Characterizing Intact Proteins and Post-Translational Modifications

In Chapter 3, a peptide with labile PTM was detected by full MS, but the PTM position could not be localized by the available fragmentation types on MALDI-LTQ-Orbitrap XL. To solve this problem, in Chapter 4, Matrix-assisted ionization (MAI) is a recently developed ionization technique that produces multiply charged ions on either ESI or MALDI platform without the need of high voltage or laser ablation. In this study, MAI has been coupled to a HRAM hybrid instrument, the Orbitrap Elite mass spectrometer, with electron transfer dissociation (ETD) module for high-throughput peptide and intact protein characterization. The softness of MAI process preserves labile PTM and allows fragmentation and localization by ETD. Moreover, MAI on ESI platform allows rapid sample analysis (~ 1 min/sample) due to the easiness of sample introduction. It significantly improves the throughput compared to ESI direct infusion and MAI on MALDI platform, which usually take more than 10 min/sample. Intact protein standards,

protein mixtures and neural tissue extracts have been characterized on this instrument platform with both full MS and MS/MS (CID, HCD and ETD) analyses. Furthermore, the performances of ESI, MALDI and MAI on both platforms have been tested to provide a systematic comparison among these techniques. We anticipate that the HRAM MAI-MS with ETD module will be widely applied in both bottom-up and top-down high throughput protein characterizations.

Chapter 5 High Throughput *in Situ* DDA Analysis of Neuropeptides by Coupling Novel Multiplex Mass Spectrometric Imaging with Gas Phase Fractionation[3]

Recent developments of hybrid MS instruments allow for the combination of different types of data acquisition by various mass analyzers into a single MS imaging acquisition, which reduces experimental time and sample consumption. In this chapter, using the well-characterized crustacean nervous system as a test-bed, we explore the utility of the HRAM MALDI Orbitrap platform for enhanced *in situ* characterization of the neuropeptidome with improved chemical information. Specifically, we report on a multiplex-MS imaging method, which combines HRAM MS imaging with data dependent acquisition (DDA) tandem MS analysis in a single experiment. This method enables simultaneous mapping of known neuropeptide distribution, sequence validation, and novel neuropeptide discovery in crustacean neuronal tissues. To enhance the dynamic range and efficiency of *in situ* DDA, we introduced a novel approach of fractionating full *m/z* range into several sub-mass ranges and embedding the setup using the multiplex-DDA-MS imaging scan events to generate pseudo fractionation before MS/MS scans. The division of entire *m/z* range into multiple segments of *m/z* sub-ranges for MS interrogation greatly decreased the complexity of the molecular species from tissue samples and the heterogeneity of the distribution and variation of intensities of *m/z* peaks. By carefully optimizing the experimental conditions, such as the dynamic exclusion, the multiplex-DDA-MS imaging approach demonstrates better

performance with broader precursor coverage, less biased MS/MS scans towards high abundance molecules, and improved quality of tandem mass spectra for low intensity molecular species.

Chapter 6 A High Resolution Atmospheric Pressure Matrix-Assisted Laser Desorption/Ionization-Quadrupole-Orbitrap Platform Enables *In Situ* Analysis of Biomolecules by Multi-Modal Ionization and Acquisition

Introduced in 2000, atmospheric pressure (AP) / MALDI has quickly attracted attention due to its ease of sample introduction and handling, interchangeability with ESI sources, and capability of analyzing volatile species. The AP/MALDI (ng) Ultra High Resolution (UHR) source, developed by MassTech Inc., is a next generation AP/MALDI source with fine laser spot < 10 µm and fast plate moving speed (4 mm/min, about 7 times faster than MALDI-LTQ-Orbitrap). In this chapter, the AP/MALDI(ng) UHR source was coupled to a Q Exactive HF mass spectrometer for high resolution *in situ* analysis by MALDI, laserspray ionization (LSI), and matrix assisted ionization (MAI) without any instrument modifications. LSI and MAI generated multiply charged ions, which expanded the mass detection range and improved fragmentation efficiency. Full MS, targeted MS/MS, DDA, and parallel reaction monitoring (PRM) acquisition modes were performed using standards, tissue exacts, and tissue sections to allow in-depth characterization of analytes. High resolution full MS and MS/MS images were obtained from crustacean and rat tissues with pixel size less than 30 µm. Overall, AP/MALDI-Q-Orbitrap is a fast scanning and versatile instrument that is capable of performing multiple types of ionization and acquisition modes without instrument modification. It could be an attractive alternative to other high resolution MALDI MS instruments.

Chapter 7 MALDI-MS Profiling and Imaging of Intranasally Administered Oxytocin and Neuropeptide Analogs

Over the last two decades, a number of studies have shown that oxytocin (OT) and arginine vasopressin (AVP) could affect social behavior. More than seventy on-going clinical trials are studying the treatment effects of OT and AVP for various diseases, including depression, autism, and social anxiety disorders. However, delivering peptides to the brain is challenging as the blood-brain barrier (BBB) blocks larger molecules from entering the brain via systemic circulation. Intranasal delivery is a non-invasive method to bypass the BBB and deliver biologics. In Chapter 7, we applied *in situ* MS profiling and imaging to study the distribution of intranasally delivered peptides, including OT, AVP, and their analogs, in the rat brain. Our findings coincided with previous autoradiographic studies, suggesting that the intranasally delivered peptide followed the olfactory and trigeminal pathways to the brain and further dispersed upon the brain entry point. Mapping the distribution of peptides by MS imaging provides a novel means to evaluate the efficacy of drug delivery.

Chapter 8 Probing Neuropeptidomic Changes Related to Autism Spectrum Disorders via Matrix-Assisted Laser Desorption/Ionization Mass Spectrometric Imaging

Autism spectrum disorders (ASD) are a group of neurodevelopmental disorders that have prevalence of 1 in 68 children. Despite its high prevalence, current diagnosis has been solely dependent on the patient's clinical phenotype with limited understanding of the disease's pathogenesis. Therefore, potential biomarkers can be essential for early identification of individuals at risk and potentially become novel therapeutic targets. MALDI MS imaging is a powerful tool to map the spatial distribution of a wide range of biomolecules simultaneously *in*

situ. It is particularly valuable in tissue biomarker discovery since both the identification and location of biomolecules could be achieved simultaneously. In Chapter 8, we developed a MALDI MS imaging approach to map the spatial distribution of neuropeptides in the brain tissue of a mouse model of ASD (*Fmr1* KO) compared to control animals. Results revealed differential expression patterns of multiple peptides in the brain sections of these animal models.

Chapter 9 Stability Analysis of Parathyroid Hormone (1-34) and its Bioactive Analog in Rat Kidney Homogenate by MALDI-MS and Multiplexed Parallel Reaction Monitoring LC-MS/MS Analysis

In Chapter 9, we established an analytical platform qualitatively and quantitatively monitor the stability and degradation of human parathyroid hormone (hPTH) 1-34 and its analog M-Cyc-9β. A high-throughput MALDI-MS method was developed to rapidly scan the degradation product at various time points, while a LC – MS/MS based multiplexed PRM method accurately quantified the peptide concentration at each time point. By applying this method, the degraded peptide fragments and peptide cleavage position were identified. The half-life of hPTH 1-34 was determined to be 1.9 min, and the half-life of back-bone modified analog M-Cyc-9β was determined to be 35.2 min. The MS-based analytical platform developed here can be widely applied to many biological applications and other polypeptide sequences, especially when bioassay-based readouts are not available.

Chapter 10 Relative Quantification of Glycans Using Multiplexed Carbonyl-Reactive Tandem Mass Tags and Targeted Product Ion Triggered MultiNotch MS^3

Glycosylation is one of the most important post-translational modifications and is involved in a variety of biological and physiological processes. Aberrant glycosylation is associated with

abnormal biological states, such as cancer progression and invasion. Therefore, proper quantification of glycans has significant biological value. The development of carbonyl-reactive tandem mass tags (AminoxyTMT) enables multiplexed quantification of glycans. However, the performance of collisionally activated dissociation (CAD) MS^2 based quantification of aminoxyTMT labeled glycans is not ideal due to the low reporter ion yield, especially for complex N-glycans. To circumvent this limitation, we implement a targeted product ion triggered MultiNotch MS^3 method for aminoxyTMT labeled N-glycans on the Orbitrap Fusion Lumos platform as detailed in this chapter. By systematically optimizing the parameters of the MultiNotch MS^3 method and comparing with MS^2 based and standard MS^3 based quantification approaches, the targeted product ion triggered MultiNotch MS^3 method offered the most precise and accurate measurements for both N-glycans released from single glycoprotein standards and glycoprotein mixtures.

Chapter 11 Mass Defect-based DiPyrO Tags for Multiplex N-glycan Characterization and Relative Quantification on a High-Resolution Mass Spectrometer

Despite its high biological relevance, the characterization and quantification of N-glycans are challenging. Relative quantifications are usually achieved by chemical tagging strategies, but MS^1 mass difference based quantification often suffers from increased spectral complexity while MS^2 isobaric tag based quantification suffers from poor fragmentation efficiency and low reporter ion yield. In Chapter 11, we developed a mass defect-based tag, dimethyl pyrimidinyl ornithine (DiPyrO), for multiplex N-glycan characterization and relative quantification. The DiPyrO tags rely on the small mDa mass differences between elemental isotopes. Each DiPyrO tag has the same nominal mass but different elemental compositions, which created a mass difference up to 45.3 mDa that can be separated by high resolution Fourier transform based mass spectrometers. The

DiPyrO tags were first introduced for protein analysis, but are also feasible for labeling freshly released glycosylamine. In this study, freshly released glycosylamine from glycoprotein standards and pancreatic cancer cell lysates were successfully labeled with DiPyrO tags. The labeled glycosylamines were characterized and quantified on both MALDI-LTQ-Orbitrap platform at 100,000 resolution (*m/z* 400) and the Fusion Lumos Orbitrap platform at 500,000 resolution (*m/z* 200) coupled with nanoflow hydrophilic interaction chromatography.

Chapter 12 Conclusions and Future Directions

The final chapter presents conclusions and future perspectives of several ongoing projects. It intends to recognize the limitation of current techniques and propose potential solutions or new directions in order to improve the analytical platforms or data collection strategies. In summary, this dissertation presents MALDI and LC-ESI based MS approaches for characterizing and quantifying endogenous and therapeutic biomolecules. It provides improved analytical platforms for biomolecule characterization as well as their wide-ranging applications in pharmaceutical industry and clinical studies.

References

[1] Chen, B., Lietz, C. B., and Li, L. (2014) In Situ Characterization of Proteins Using Laserspray Ionization on a High-Performance MALDI-LTQ-Orbitrap Mass Spectrometer, *J Am Soc Mass Spectr 25*, 2177-2180.

[2] Chen, B., Lietz, C. B., OuYang, C., Zhong, X., Xu, M., and Li, L. (2016) Matrix-assisted ionization vacuum for protein detection, fragmentation and PTM analysis on a high resolution linear ion trap-orbitrap platform, *Anal Chim Acta 916*, 52-59.

[3] OuYang, C., Chen, B., and Li, L. (2015) High Throughput In Situ DDA Analysis of Neuropeptides by Coupling Novel Multiplex Mass Spectrometric Imaging (MSI) with Gas-Phase Fractionation, *J Am Soc Mass Spectr 26*, 1992-2001.

[4] Gemperline, E., Chen, B., and Li, L. (2014) Challenges and recent advances in mass spectrometric imaging of neurotransmitters, *Bioanalysis 6*, 525-540.

[5] Cheloha, R. W. (2015) Exploration of alpha/beta-peptides as parathyroid hormone receptor ligands and recognition of alpha/beta-peptides by the immune system, In *Department of Chemistry*, p 454, University of Wisconsin-Madison, Madison, WI.

Chapter 2
In Situ Characterization of Proteins Using Laserspray Ionization on a High-Performance MALDI-LTQ-Orbitrap Mass Spectrometer

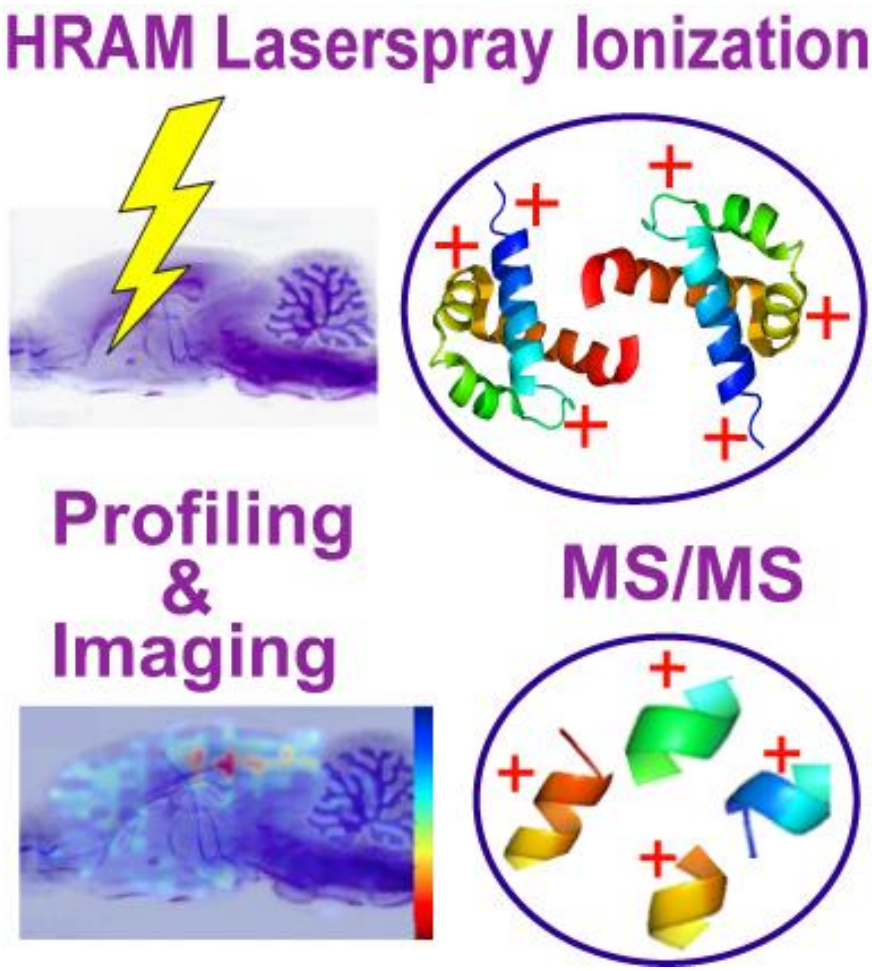

Adapted from **B.Chen,** C.B. Lietz, L. Li (2014). *In situ* Characterization of Multiply Charged Proteins Using a High-Performance MALDI-LTQ-Orbitrap Mass Spectrometer. *J. Am. Soc. Mass Spectrom.*, vol. 25 (12). *p. 2177-80.*

Author contribution: study was designed by B. Chen, C.B. Lietz and L. Li; experiment was performed by B. Chen; manuscript was written by B. Chen and edited by C.B. Lietz and L. Li.

Abstract

The MALDI-LTQ-Orbitrap XL mass spectrometer is a high-performance instrument capable of high resolution and accurate mass (**HRAM**). The maximum *m/z* of 4000 precludes the MALDI analysis of proteins without generating multiply charged ions. Herein, we present the study of HRAM laserspray ionization mass spectrometry (**MS**) with MS/MS and MS imaging capabilities using 2-nitrophloroglucinol (**2-NPG**) as matrix on MALDI-LTQ-Orbitrap XL. The optimized conditions for multiply charged ion production have been determined and applied to tissue profiling and imaging. Biomolecules as large as 15 kDa have been detected with up to five positive charges at 100K mass resolution (at *m/z* 400). More importantly, MS/MS and protein identification on multiply charged precursor ions from both standards and tissue samples have been achieved for the first time with an intermediate-pressure source. The initial results reported in this study highlight potential utilities of laserspray ionization MS analysis for simultaneous *in situ* protein identification, visualization and characterization from complex tissue samples on a commercially available HRAM MALDI system.

Introduction

Matrix-assisted laser desorption/ionization (**MALDI**)[1] is a soft ionization technique that predominantly generates singly charged ions from solid state analytes under vacuum, intermediate pressure[2], and atmospheric pressure (**AP**)[3]. The capability of ionizing solid-state analytes from surfaces makes MALDI mass spectrometry (**MS)** an ideal tool for biological tissue analysis. The development of MALDI MS imaging (**MSI**) to map molecular spatial distributions greatly diversified the utility of MALDI MS[4-6].

The limited mass range of high performance mass analyzers, inefficient fragmentation of singly charged ions, and difficulties in protein identification directly from tissue are three challenges facing MALDI analysis. MALDI is often coupled with a time-of-flight (**TOF**) mass analyzer, which theoretically has an unlimited mass range. However, the mass resolution and accuracy of TOF instruments are often limited, especially at high *m*/*z*. In contrast, the MALDI-LTQ-Orbitrap mass spectrometer combines the high mass accuracy (<3ppm with external calibration) and high resolution (>100k at *m/z* 400) of an orbitrap with the fast scan rates and MS/MS capabilities (collisional induced dissociation (**CID**)) of a linear ion trap[7]. The addition of a high-energy collision dissociation (**HCD**) cell provides significant flexibility to MS/MS experiments. However, the mass range for this instrument is limited to *m/z* 50-4000. Therefore, multiply charged ion generation is the only possibility for intact protein analysis directly from tissue.

Laserspray ionization (**LSI**) is a newer technique that utilizes laser ablation of a solid matrix/analyte mixture off a surface to produce multiply charged ions similar to those observed in electrospray ionization (**ESI**)[8]. It is a subset of the ionization techniques that produce multiply charged ions via matrix-assisted ionization (**MAI**)[9]. LSI was initially performed in transmission geometry, but has expanded to reflection geometry[10], intermediate-vacuum[11], and high-vacuum[12]. It has brought intact proteins larger than 60 kDa into the operational mass range of a linear ion-trap[13]. However, MAI-like multiply charged ions have not previously been reported on an LTQ-Orbitrap mass spectrometer with an intermediate-vacuum MALDI source. At lower source pressures, multiply charged ion generation with laser ablation becomes less straightforward and typically requires instrument-specific tuning parameters.

The goal of this study is to maximize multiply charged ion production for enhanced protein and peptide analysis on MALDI-LTQ-Orbitrap system. We use a common LSI matrix, 2-nitrophloroglucinol, first reported by Trimpin and coworkers[12]. For the first time, CID and HCD MS/MS analyses of multiply charged ions have been achieved, demonstrating the utility and application of multiply charged ions in high resolution MALDI MS for *in situ* protein identification, visualization and characterization.

Materials and methods

Reagents and sample preparation

All reagents and standards were used without additional purification. For peptide and protein analyses, bradykinin, insulin and lysozyme standards were prepared. For tissue analysis, animal experiments were conducted following institutional guidelines (UW-Madison IACUC). Rat brain tissue was embedded in gelatin, snap frozen, cryosectioned into 12 µm slices and thaw mounted onto micro slides. Further details can be found in the SI.

Optimization of multiply charged ion production

Parameters that were optimized for multiply charged ion profiling and imaging on rat brain included 2-NPG concentration (5, 10, 12.5, 15 and 20 mg/mL), formic acid percentage (0%, 0.025%, 0.1% and 1%), solvent composition (30% acetonitrile (**ACN**), 50% ACN, 70% ACN, 30% methanol, 50% methanol and 70% methanol) and laser energy (5, 10, 15, 20, 25µJ). The laser energy refers to the value indicated in the instrument control software, which is the energy at the laser head. The laser energy at the source is significantly lower, theoretically by a factor of 10 after the two neutral density filters. Fifteen consecutive 12 µm rat brain sections from the same rat brain were used for all optimization tests in order to minimize variability. For each matrix

combination, three spots of 0.5µL 2-NPG were applied onto the midbrain area of rat brain section. Different laser energies were used to analyze each matrix spot.

Multiply charged ion profiling and imaging

All MS experiments were performed on a MALDI-LTQ-Orbitrap XL (Thermo Scientific, Bremen, Germany) equipped with 60 Hz 337 nm N_2 laser. Full MS experiments for standards, tissue profiling and imaging were performed in FTMS mode under positive polarity with a mass range of 900-4000 (*m/z* 2000-4000 for lysozyme) and a mass resolution of 100,000 (at *m/z* 400). The step size for imaging experiments was set to be 300 µm. MS/MS experiments were performed by CID and HCD in both standards and tissue analyses. Collisional energy was optimized for each parent ion. Xcalibur (Thermo Scientific, Bremen, Germany) was used for spectrum processing. ImageQuest (Thermo Scientific, Bremen, Germany) and MSiReader[14] (NC State University, North Carolina, U.S.A) were used for MS image data processing. The mass window for each peak imaged was set to 10ppm.

Results and discussion

Optimization of laserspray ionization conditions for tissue sections

LSI conditions for generating multiply charged ions in the MALDI source were optimized on consecutive rat brain sections in order to account for the biological complexity. Each condition was evaluated by the largest molecule, highest charge state, and percentage of multiply charged peaks detected (Figure 1, Supplementary Figure S1). The production of multiply charged signals was most significantly affected by laser energy (Figure 1a and b) and solvent composition (Figure 1c and d). 25 µJ laser energy produced the highest abundance of multiply charged ions, with low abundance doubly charged ions being detected at 20µJ and 30µJ.

The largest molecule detected with 25μJ was 8564.67 Da. The dependence on laser energy is consistent with previously reported observations from intermediate- and high-vacuum LSI[11, 12]. For solvent composition, significantly more multiply charged ions were produced with 70% ACN compared to all other conditions (Figure 1c and d), as high organic solvent content tends to extract peptide and protein analytes better. Additionally, 70% ACN may facilitate the formation of loosely-packed crystals thought to give rise to high yields of multiply charged LSI ions[11]. The optimal 2-NPG concentration and formic acid composition was 12.5 mg/mL and 0.025%, respectively (Supplementary Figure S1).

HRAM analysis of peptide and protein standards with optimized conditions

Peptide and protein standards (bradykinin, insulin and lysozyme) were analyzed under the optimized conditions with 100K mass resolution (at *m/z* 400) (Figure 2).

With the optimized conditions, both singly and doubly charged ions were detected for bradykinin with 0.4ppm mass error (Figure 2a). MS/MS analyses were performed on the doubly charged bradykinin ion by CID and HCD. All b and y ions except b_1 were detected. To illustrate the difference in ion production from common MALDI matrices, peptide standards were also analyzed with 2,5-dihydroxybenzoic acid (**DHB**), α-cyano-4-hydroxycinnamic acid (**CHCA**), and sinapinic acid (**SA**) matrices. Doubly charged ions were only produced by DHB.

The masses of singly charged insulin and lysozyme exceed the detection range of the instrument. With the optimized LSI conditions developed in this study, multiply charged insulin and lysozyme ions were detected. 1.75μM insulin yielded +2 (R=48,807), +3 (R=60,945), and +4 (R=68,772) ions in the MS1 spectrum (Figure 2b). MS/MS spectra were achieved by HCD. For 15μM lysozyme, +4 (R=38,118) and +5 (R=30,735) charged ions were observed (Figure 2c).

Additional +4 charged ions were also observed near the main lysozyme peak due to the impurities from the standard. The largest detected ion has a molecular weight of 14930.86 Da.

In situ *protein characterization and visualization by full MS, MS/MS and MS imaging*

DHB was compared with 2-NPG for the ability to generate multiply charged ions on tissue using optimized LSI conditions. Only singly charged ions were observed on tissue sections prepared with DHB (Supplementary Figure 2). For 2-NPG, high resolution spectra with singly, doubly and triply charged ions were acquired (Figure 3a, Supplementary Figure S2b and c). Several peptides and proteins could be putatively identified by accurate mass matching with sub ppm mass error, such as myelin basic protein fragment 2-19, thymosin beta-4 and cytochrome c oxidase subunit 7c (Supplementary Figure 2c). MS imaging experiments were performed on rat brain tissue sections by applying 2-NPG using an airbrush. The distributions of doubly charged proteins (*m/z* 2482.264 and *m/z* 2868.456) were mapped in the MS imaging experiments (Figure 3a). However, due to the volatile nature of 2-NPG and the relatively slow acquisition rate of the instrument, the step size was compromised to be 300μm.

MS/MS was used to further confirm protein identity. Doubly charged ions at *m/z* of 2482.265 were fragmented and sequenced (Figure 3b). b and y ions were produced with high abundance and good sequence coverage. By manual *de novo* sequencing and in-house database searching, this protein was identified to be thymosin beta-4. The combination of HRAM full MS scan with CID MS/MS scan enabled confident protein identification. The ability to perform MS/MS also provides mechanistic insights into LSI[8] and MAI[9]. Previous intermediate-pressure and high vacuum LSI studies were unable to perform MS/MS, possibly due to ion liberation after

the instrument's isolation stage. Here, declustered multiply charged ions are formed before the ion trap enabling MS/MS fragmentation.

Conclusion

For the first time, multiply charged full MS, MS/MS and MSI analyses have been achieved on a commercially available, intermediate-vacuum, ultra high performance MALDI-LTQ-Orbitrap XL system. Molecules as large as 15 kDa have been detected with up to five positive charges at 100K mass resolution (at *m/z* 400). By expanding the mass range using multiply charged MALDI, MALDI-LTQ-Orbitrap provides an attractive platform that enables *in situ* analysis of both peptides and proteins in a single experiment.

Acknowledgement

The authors are thankful to Dr. Robert Thorne's laboratory for providing rat brain tissue samples and Dr. Sarah Trimpin for helpful suggestions. This work is supported in part by the National Institutes of Health grants (1R01DK071801, 1R56DK071801). We would like to acknowledge NIH shared instrument program for funding the instrument purchase (S10 RR029531). C.B.L. acknowledges an NIH-supported Chemistry Biology Interface Training Program Predoctoral Fellowship (grant number T32-GM008505) and an NSF Graduate Research Fellowship (DGE-1256259). L. Li acknowledges an H.I. Romnes Faculty Research Fellowship.

References

[1] Tanaka, K., Waki, H., Ido, Y., Akita, S., Yoshida, Y., Yoshida, T., and Matsuo, T. (1988) Protein and polymer analyses up to m/z 100 000 by laser ionization time-of-flight mass spectrometry, *Rapid Communications in Mass Spectrometry 2*, 151-153.

[2] Garrett, T. J., and Yost, R. A. (2006) Analysis of intact tissue by intermediate-pressure MALDI on a linear ion trap mass spectrometer, *Analytical chemistry 78*, 2465-2469.

[3] Cooks, R. G., Ouyang, Z., Takats, Z., and Wiseman, J. M. (2006) Detection Technologies. Ambient mass spectrometry, *Science 311*, 1566-1570.

[4] Ye, H., Gemperline, E., and Li, L. (2013) A vision for better health: mass spectrometry imaging for clinical diagnostics, *Clinica chimica acta; international journal of clinical chemistry 420*, 11-22.

[5] Stoeckli, M., Chaurand, P., Hallahan, D. E., and Caprioli, R. M. (2001) Imaging mass spectrometry: a new technology for the analysis of protein expression in mammalian tissues, *Nature medicine 7*, 493-496.

[6] Liu, J., and Ouyang, Z. (2013) Mass spectrometry imaging for biomedical applications, *Analytical and bioanalytical chemistry 405*, 5645-5653.

[7] Strupat, K., Kovtoun, V., Bui, H., Viner, R., Stafford, G., and Horning, S. (2009) MALDI Produced Ions Inspected with a Linear Ion Trap-Orbitrap Hybrid Mass Analyzer, *Journal of the American Society for Mass Spectrometry 20*, 1451-1463.

[8] Trimpin, S., Inutan, E. D., Herath, T. N., and McEwen, C. N. (2010) Laserspray ionization, a new atmospheric pressure MALDI method for producing highly charged gas-phase ions of peptides and proteins directly from solid solutions, *Molecular & cellular proteomics : MCP 9*, 362-367.

[9] Trimpin, S., and Inutan, E. D. (2013) Matrix assisted ionization in vacuum, a sensitive and widely applicable ionization method for mass spectrometry, *Journal of the American Society for Mass Spectrometry 24*, 722-732.

[10] Inutan, E. D., Richards, A. L., Wager-Miller, J., Mackie, K., McEwen, C. N., and Trimpin, S. (2011) Laserspray ionization, a new method for protein analysis directly from tissue at atmospheric pressure with ultrahigh mass resolution and electron transfer dissociation, *Molecular & cellular proteomics : MCP 10*, M110 000760.

[11] Inutan, E. D., Wang, B., and Trimpin, S. (2011) Commercial intermediate pressure MALDI ion mobility spectrometry mass spectrometer capable of producing highly charged laserspray ionization ions, *Analytical chemistry 83*, 678-684.

[12] Trimpin, S., Ren, Y., Wang, B., Lietz, C. B., Richards, A. L., Marshall, D. D., and Inutan, E. D. (2011) Extending the laserspray ionization concept to produce highly charged ions at high vacuum on a time-of-flight mass analyzer, *Analytical chemistry 83*, 5469-5475.

[13] Lietz, C. B., Richards, A. L., Ren, Y., and Trimpin, S. (2011) Inlet ionization: protein analyses from the solid state without the use of a voltage or a laser producing up to 67 charges on the 66 kDa BSA protein, *Rapid communications in mass spectrometry : RCM 25*, 3453-3456.

[14] Robichaud, G., Garrard, K. P., Barry, J. A., and Muddiman, D. C. (2013) MSiReader: an open-source interface to view and analyze high resolving power MS imaging files on Matlab platform, *Journal of the American Society for Mass Spectrometry 24*, 718-721.

Figure legends

Figure 1. Optimization of multiply charged MALDI MS. (a) Highest mass and highest charge state detected at different laser energies (5,10,15,20 and 25μJ), (b) Percentage of multiply charged ion produced among all peaks with S/N larger than 3 at different laser energies (5,10,15,20 and 25μJ). (c) Highest mass and highest charge state detected with different solvent compositions (30% ACN, 50% ACN, 70% ACN, 50% methanol and 70% methanol), (d) Percentage of multiply charged ion produced among all peaks with S/N larger than 3 with different solvent compositions. All measurements are in triplicates. The error bar represents the standard deviation at each condition. The best conditions are highlighted in yellow shading.

Figure 2. Peptide and protein standards analyzed under the optimized multiply charged MALDI condition. (a) Full MS and MS/MS analyses of 10μg/mL bradykinin peptide standard. MS/MS analysis of the doubly charged ion was performed by CID. (b) MS analysis of 10μg/mL insulin protein standard. (c) MS analysis of 214μg/mL lysozyme protein standard. Some other +4 charged ions, which were impurities, were also observed near the +4 lysozyme peak.

Figure 3. Multiply charged MALDI MS tissue profiling and imaging analysis. Full MS profiling, MS/MS and MS imaging analyses on rat brain tissue sections were performed with the optimized condition. (a) Full MS profiling and imaging analyses on rat brain tissue section. Multiply charged ions were detected. Spatial distributions of double charged signals at *m/z* 2482.264 and *m/z* 2868.456 were mapped by MS imaging. (b) CID MS/MS analysis at *m/z* 2482.265. This protein was identified to be thymosin beta-4 (*Rattus norvegicus*).

Figures

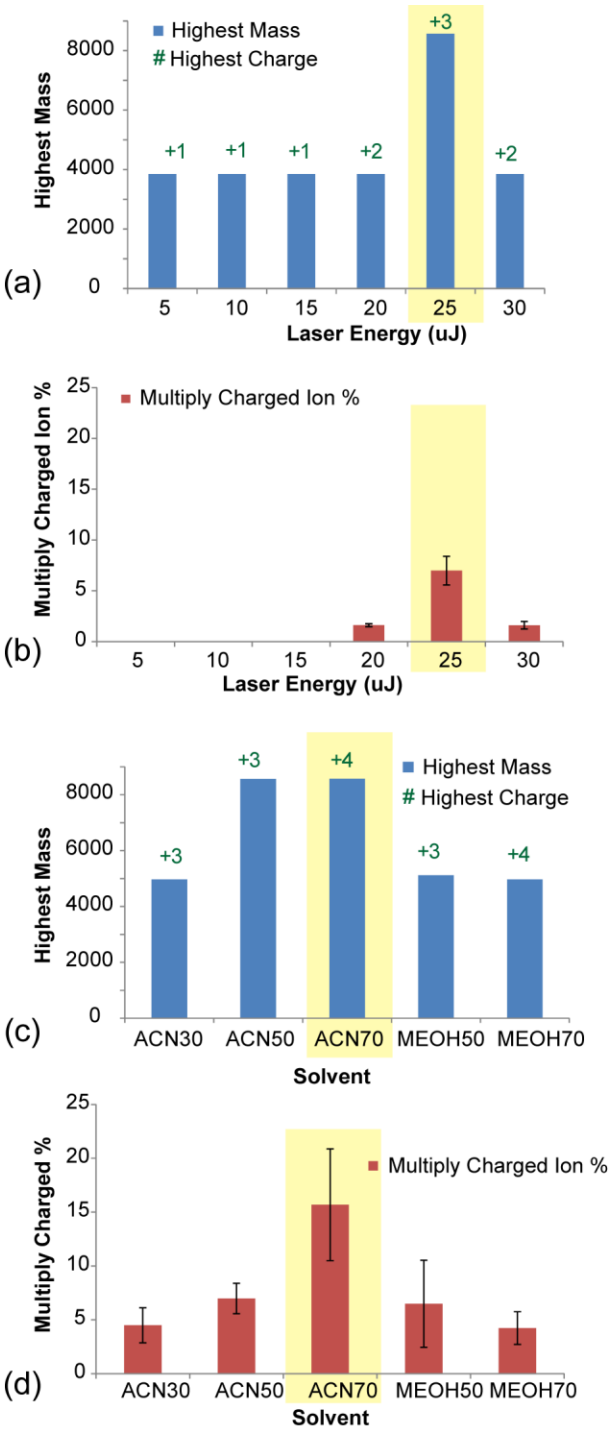

Figure 1

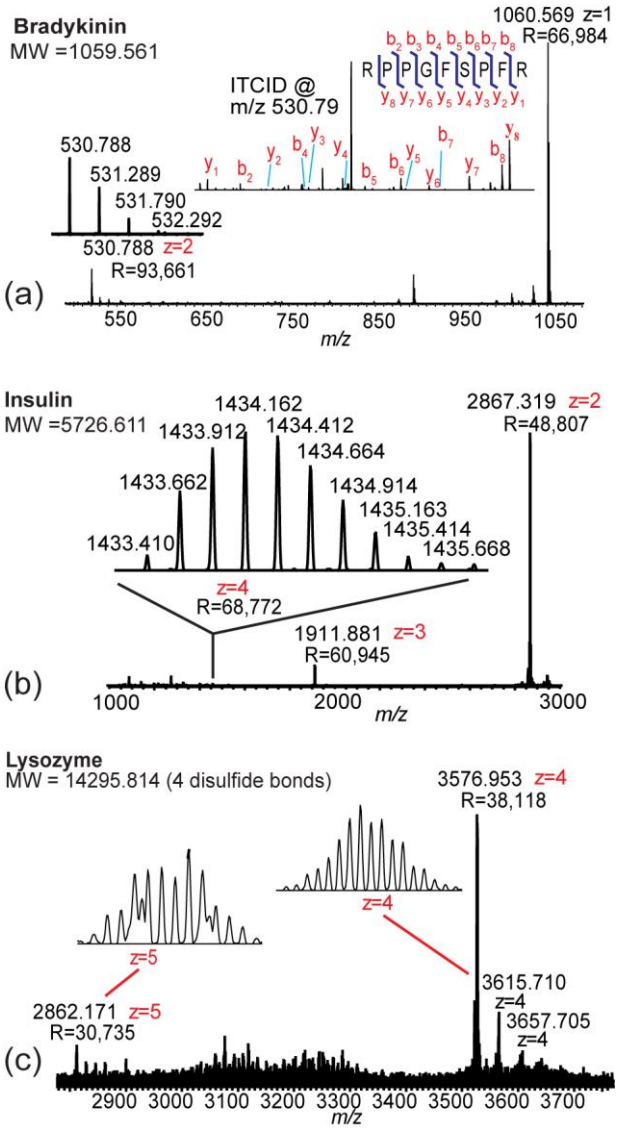
Bradykinin
MW =1059.561
1060.569 z=1
R=66,984
R P P G F S P F R
ITCID @
m/z 530.79
530.788
531.289
531.790
532.292
530.788 z=2
R=93,661
(a)
550
650
750
850
950
1050
m/z
Insulin
MW =5726.611
1434.162
1433.912
1434.412
1434.664
1433.662
1434.914
1435.163
1435.414
1433.410
1435.668
2867.319 z=2
R=48,807
z=4
R=68,772
1911.881 z=3
R=60,945
(b)
1000
2000
3000
m/z
Lysozyme
MW = 14295.814 (4 disulfide bonds)
3576.953 z=4
R=38,118
z=4
z=5
3615.710
z=4
2862.171 z=5
R=30,735
3657.705
z=4
(c)
2900 3000 3100 3200 3300 3400 3500 3600 3700
m/z

Figure 2

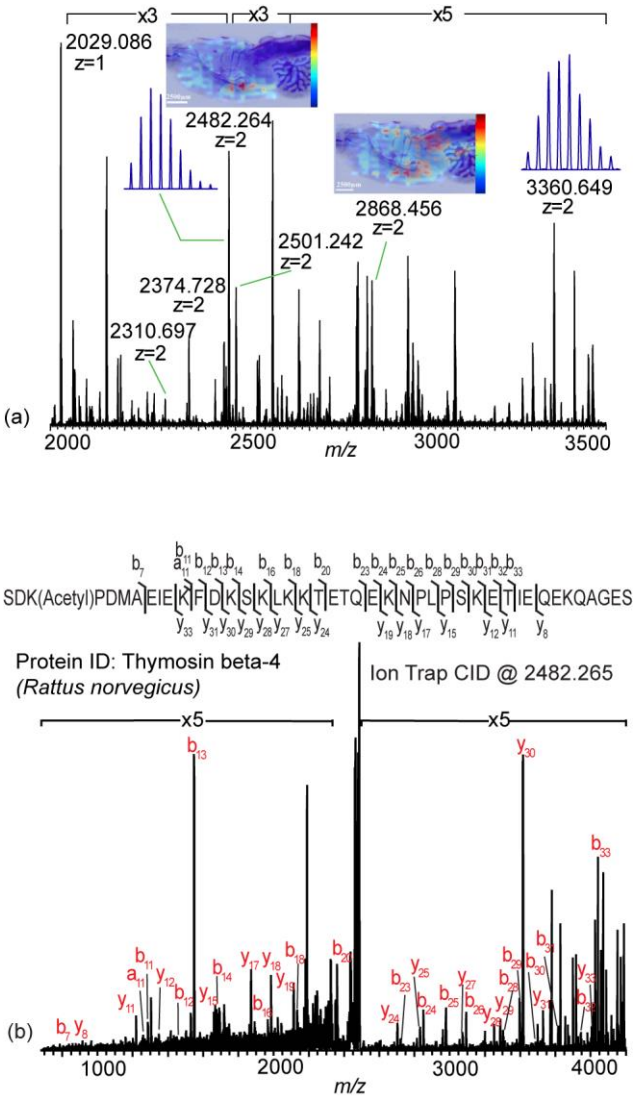
x3
x3
x5
2029.086
z=1
2482.264
z=2
2868.456
z=2
3360.649
z=2
2501.242
z=2
2374.728
z=2
2310.697
z=2
(a)
2000
2500
3000
3500
m/z
SDK(Acetyl)PDMAEIEKFDKSKLKKTETQEKNPLPSKETIEQEKQAGES
Protein ID: Thymosin beta-4
(Rattus norvegicus)
Ion Trap CID @ 2482.265
x5
x5
(b)
1000
2000
3000
4000
m/z

Figure 3

Supporting information

Experimental: reagents and sample preparation

All reagents and standards were used without additional purification. Acetonitrile (ACN), methanol and formic acid were purchased from Fisher Scientific (Pittsburgh, PA, USA). 2-nitrophloroglucinol (2-NPG) was purchased from Sigma Aldrich Inc. (St. Louis, MO, USA). Bovine insulin and lysozyme standards were purchased from Promega (Madison, WI, USA), and peptide standard (bradykinin) was purchased from American Peptide Company (Sunnyvale, CA, USA).

For analysis of standards, 0.5µL bradykinin (10µg/mL, dissolved in H_2O, 0.1% FA), substance P (10µg/mL, dissolved in H_2O, 0.1% FA), insulin (10µg/mL, 10µg/mL, dissolved in 1:1 ACN:H_2O, 0.1% FA) or lysozyme (214µg/mL, 10µg/mL, dissolved in 1:1 ACN:H_2O, 0.1% FA) standards was mixed with 0.5µL of 12.5µg/mL 2-NPG matrix (dissolved in 7:3 ACN:H_2O, 0.025%FA) on MALDI target plate. For substance P, 20mg/mL of α-cyano-4-hydroxycinnamic acid (dissolved in 1:1 ACN:H_2O, 0.1%FA), 150mg/mL 2,5-dihydroxybenzoic acid (dissolved in 1:1 MeOH: H_2O, 0.1%FA) and 20mg/mL sinapinic acid (dissolved in 1:1 ACN:H_2O, 0.1%FA) were also used as matrices to compare with 2-NPG. For tissue analysis, animal experiments were conducted following institutional guidelines (UW-Madison IACUC). Brains from female Sprague-Dawley rats were dissected, embedded in gelatin (100mg/mL in MilliQ water), snap frozen in dry ice, and stored at -80 ºC. The frozen brain was cryosectioned into 12 µm slices and thaw mounted onto micro slides (75x25x1mm). The slides with tissue were washed in 70% ethanol for 1 minute to remove lipid and dehydrated at room temperature for 30 minutes. 2-NPG matrix was spotted onto tissue surface by pipet for profiling purposes. For imaging, matrix was

applied by airbrush at a density of 5µL/mm^2: the airbrush was held at 20cm from the slide. Five coats of matrices were applied at medium flow rate with 30 sec drying time in between.

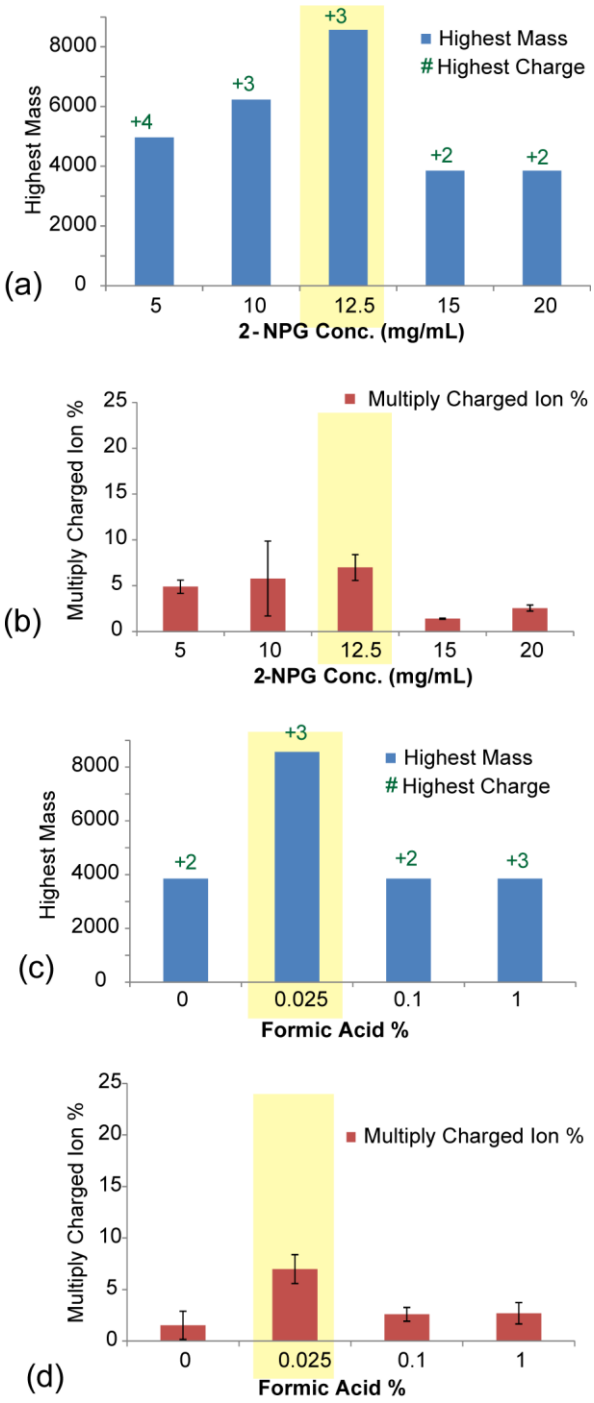

Supplementary Figure 1. Optimization of multiply charged MALDI MS. (**a**) Highest mass and highest charge state detected at different 2-NPG concentrations (5,10,12.5, 15, 20mg/mL), (**b**) Percentage of multiply charged ion produced among all peaks with S/N larger than 3 at different 2-NPG concentrations (5,10,12.5, 15, 20mg/mL). (**c**) Highest mass molecule and highest charge detected with different formic acid percentages (0%, 0.025%, 0.1%, 1%), (**d**) Percentage of multiply charged ion produced among all peaks with S/N larger than 3 with different formic acid percentages (0%, 0.025%, 0.1%, 1%). The best conditions are highlighted in yellow shading. Error bar represents the standard deviation of three replicates.

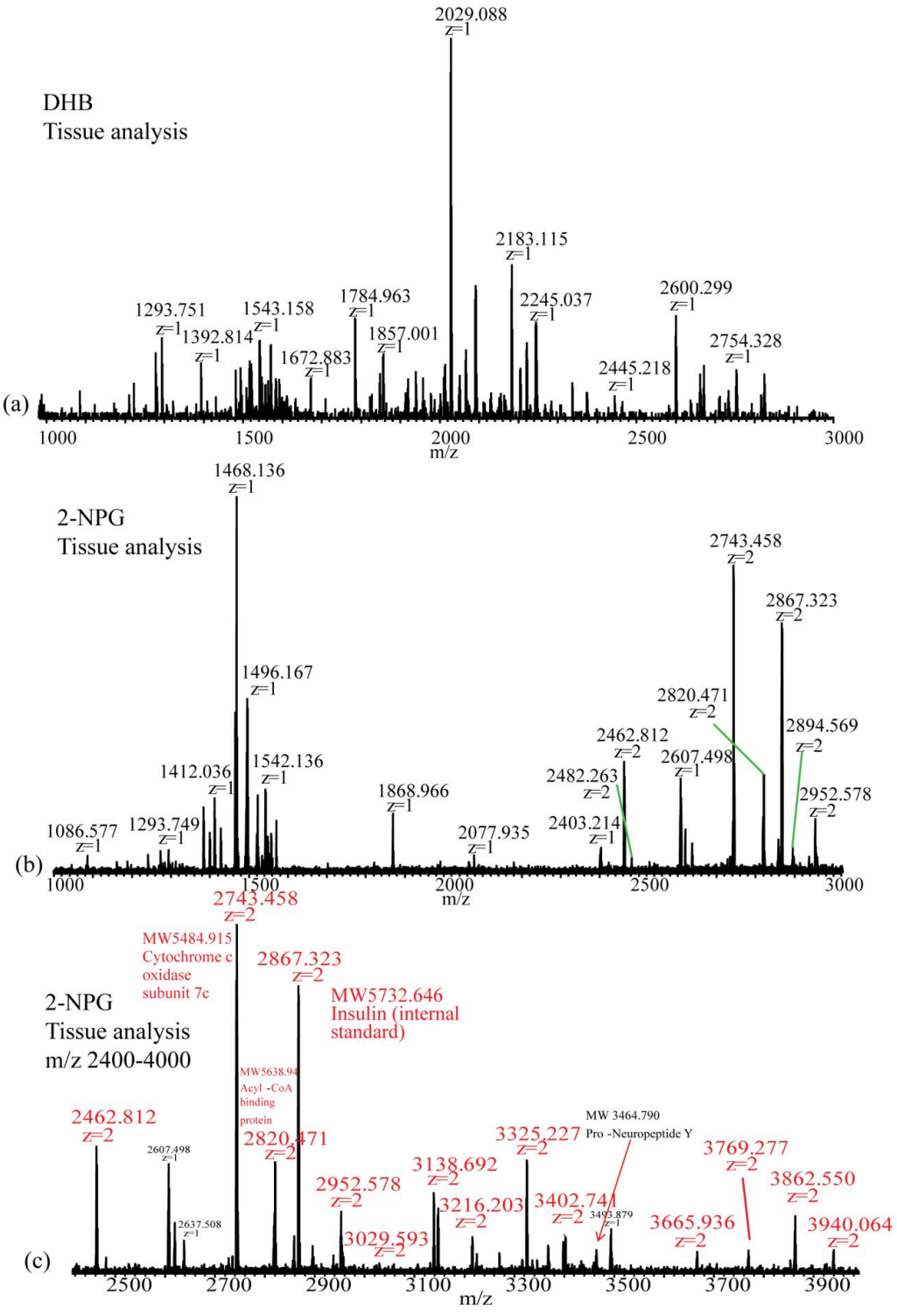

Supplementary Figure 2. Comparisons of DHB and 2-NPG's effects on tissue profiling. (a) DHB tissue profiling result. (b) 2-NPG tissue profiling result with *m/z* of 1000-3000. (c) 2-NPG tissue profiling result with *m/z* 2400-4000. Multiply charged ions were highlighted in red.

Chapter 3
Matrix-assisted Ionization Vacuum for Protein Detection, Fragmentation and PTM Analysis on a High Resolution Linear Ion Trap-Orbitrap Platform

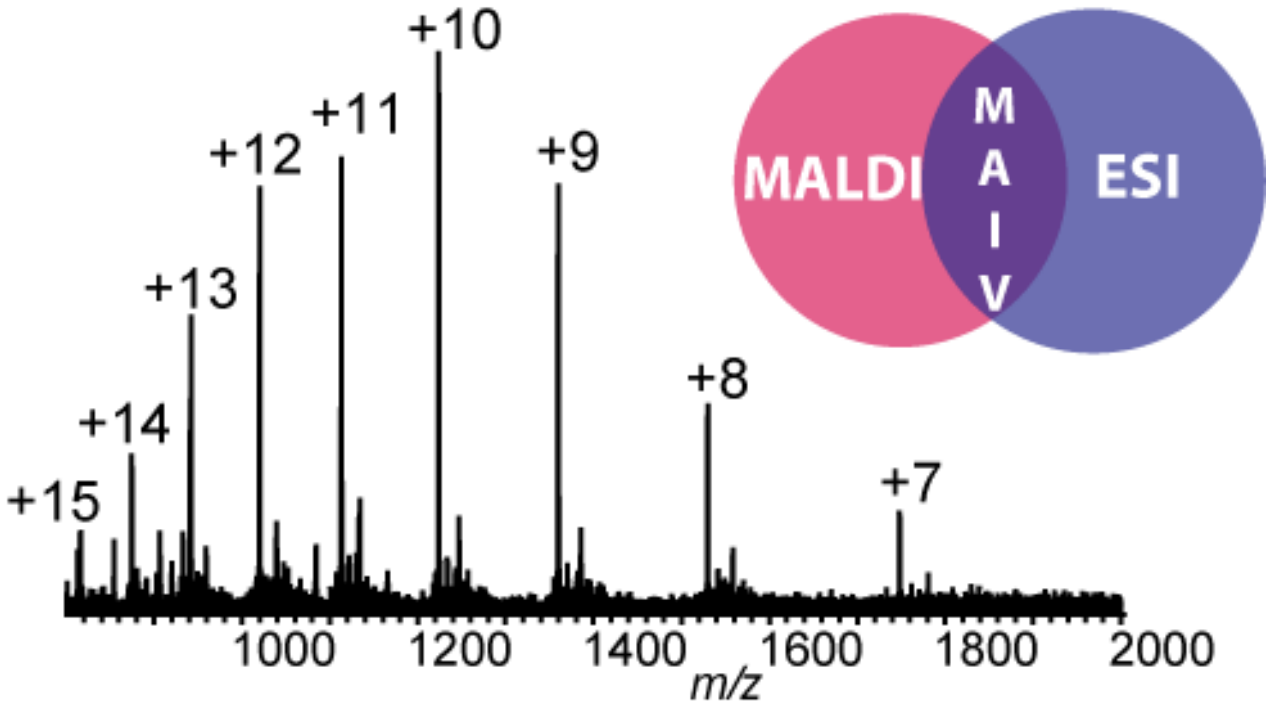

Adapted from **B.Chen**, C.B. Lietz, C.Ouyang, X. Zhong, M. Xu and L. Li (2016). Matrix-Assisted Ionization in Vaccum for Protein Detection, Fragmentation and PTM Analysis on a High Resolution Linear Ion Trap-Orbitrap Platform. *Analyt. Chim. Acta*., vol 916. p.52-59.

Author contribution: study was designed by B. Chen, C.B. Lietz, X. Zhong and L. Li; experiment was performed by B. Chen and C. Ouyang; data was analyzed by B. Chen and M. Xu; manuscript was written by B. Chen and edited by C.B. Lietz, X. Zhong and L. Li.

Abstract

Matrix-assisted ionization vacuum (MAIV) is a novel ionization technique that generates multiply charged ions in vacuum without the use of laser ablation or high voltage. MAIV can be achieved in intermediate-vacuum and high-vacuum matrix-assisted laser desorption/ionization (MALDI) sources and electrospray ionization (ESI) source without instrument modification. Herein, we adapt MAIV onto the MALDI-LTQ-Orbitrap XL platform for biomolecule analysis. As an attractive alternative to MALDI for in solution and *in situ* analysis of biomolecules, MAIV coupling to high resolution and accurate mass (HRAM) instrument has successfully expanded the mass detection range and improved the fragmentation efficiency due to the generation of multiply charged ions. Additionally, the softness of MAIV enables potential application in labile post-translational modification (PTM) analysis. In this study, proteins as large as 18.7 kDa were detected with up to 18 charges; intact peptides with labile PTM were well preserved during the ionization process and characterized MS/MS; peptides and proteins in complex tissue samples were detected and identified both in liquid extracts and *in situ*. Moreover, we demonstrated that this method facilitates MS/MS analysis with improved fragmentation efficiency compared to MALDI-MS/MS.

Keywords: Mass spectrometry, matrix-assisted ionization vacuum, high resolution and accurate mass, post-translational modification, multiply charged ions, protein analysis

Introduction

In the late 1980s, the development of MALDI [1] and ESI [2] revolutionized the field of mass spectrometry (MS) application in the analysis of large biomolecules.[3] MALDI utilizes laser desorption to produce mostly singly charged ions from a solid matrix, while ESI employs high voltage to produce multiply charged ions from solution. The capability of ionizing analytes directly from solid surface makes MALDI an ideal tool for *in situ* tissue analysis. However, as MALDI predominantly produces singly charged ions, a few challenges remain for MALDI analysis, especially for HRAM protein analysis. With the commonly used ion activation methods trap collisional induced dissociation (CID) and high collisional energy dislocation (HCD), the singly charged ions usually have lower fragmentation efficiencies compared with that of multiply charged ions, making the identification of analyte molecules difficult. Additionally, most current commercially available high-performance Orbitrap instruments cannot detect ions larger than *m/z* 10000. Moreover, in-source or post-source fragmentations of molecules are usually observed in MALDI process.[4, 5] On the other hand, although ESI overcome most problems mentioned above, it is impossible to preserve the spatial information on tissue sections using conventional ESI analysis since the analytes must be dissolved in a volatile solution.

In recent years, many approaches have been taken to address these problems. "Electron-free" MALDI was observed to produce higher percentage of multiply charged ions, when the number of electrons was limited in the plume.[6] Desorption electrospray ionization (DESI) ionizes analytes from surface by electrospray generated charged droplets and solvent ions.[7, 8] Matrix-assisted laser desorption electrospray ionization (MALDESI) generates ESI-like multiply charged ions with the assistance of matrix.[9, 10] Electrospray-assisted laser desorption ionization

(ELDI) is capable of ionizing peptides and proteins in solid materials by laser desorption and post-ionization electrospray without matrix.[11-15]

Laserspray ionization (LSI) and MAIV are relatively new ionization techniques that produce ESI-like multiply charged ions while also able to preserve spatial information on tissue sections. Unlike DESI, MALDESI or ELDI, LSI and MAIV can be readily achieved using commercially available MALDI sources without any instrumentation modification. These two ionization techniques were first introduced by the Trimpin lab and have been demonstrated on several MS platforms.[16-19] LSI utilizes volatile small molecule matrices with laser ablation to ionize analyte under atmosphere pressure (1.01 bar),[20] intermediate-vacuum (10^{-3} to 33 mbar) [18, 21] and high-vacuum (10^{-6} to 10^{-3} mbar) MALDI sources.[22] However, the involvement of laser in LSI could induce in-source or post-source fragmentations. In contrast, MAIV is a softer ionization method that generates multiply charged ions in a triboluminescence process, which does not involve either laser or high voltage application during the ionization process.[23] With the assistance of small volatile matrices, MAIV can generate highly charged ions from a wide variety of compounds.[24] The original MAIV study was performed on both LTQ and quadrupole time-of-flight instruments with low to medium mass resolution. It was also demonstrated on high resolution Fourier transform instruments for full MS analysis.[17, 19] However, to our knowledge, no study has been performed on a MALDI-Orbitrap platform, and MAIV-MS/MS data, especially for PTM analysis, is also limited in previous studies.

Many biological processes are regulated by PTM of peptides and proteins.[25] Understanding PTMs is essential for understanding the biological functions of various proteins and studying cell regulations. However, some labile PTMs, such as glycosylation, can be easily detached during ionization process, making them difficult to be analyzed by MS. Due to its

softness, we hypothesize that MAIV can reduce in-source and post-source fragmentation of biomolecules, especially peptides and proteins with labile PTMs.

The introduction of hybrid MALDI mass spectrometers has expanded the capability of MALDI MS analysis. The MALDI-LTQ-Orbitrap XL system (Thermo Fisher Scientific, Bremen, Germany) incorporates linear ion trap and orbitrap mass analyzers,[26] making HRAM analysis as well as MS^n by collisional induced dissociation (CID) and high-energy collision dissociation (HCD) possible on one platform. However, this instrument has a limited *m/z* range of 50-4000. With singly charged ions generated in the MALDI source, this instrument cannot analyze large molecules such as proteins, polysaccharides and polynucleotides.

The development of LSI[27, 28] and MAIV[29] prompted us to investigate the possibility of employing the MALDI-LTQ-Orbitrap XL as a HRAM platform for protein characterization. LSI has been adapted to MALDI-LTQ-Orbitrap XL hybrid system and the application has been expanded to *in situ* MS/MS analysis and *de novo* sequencing.[18] In this study, we adapted the recently developed MAIV technique to our hybrid MALDI-LTQ-Orbitrap XL system for peptide and protein analysis. Multiply charged ions were detected with this HRAM MS platform in the analysis of protein and peptide standards, tissue extracts and *in situ* tissue sections. Furthermore, MAIV-MS/MS analysis has been achieved in both standards and tissue protein extractions analysis. The fragmentation efficiency of multiply charged species has been greatly improved in comparison to that of the singly charged ions. We also demonstrated that MAIV-MS could be used for the analysis of labile PTMs on peptides because of the soft ionization nature of MAIV.

Materials and methods

Materials

Methanol (MeOH), ethanol (EtOH), acetonitrile (ACN), acetic acid (AA) and formic acid (FA) were purchased from Fisher Scientific (Pittsburgh, PA). 3-nitrobenzonitrile (3-NBN), α-cyano-4-hydroxycinnamic acid (CHCA), insulin (bovine), cytochrome C (bovine heart), lysozyme (chicken egg white) and myoglobin (equine heart) were purchased from Sigma Aldrich Inc. (St. Louis, MO). Peptide standard bradykinin was purchased from American Peptide Company (Sunnyvale, CA). Kinase domain of insulin receptor was purchased from AnaSpec (Fremont, CA) and glycosylated erythropoietin (EPO) 117-131 was purchased from Protea Biosciences Group, Inc. (Morgantown, WV). All standards and reagents were used without additional purification.

Sample preparation

Peptide and protein standard preparations. Peptide and protein stock solutions with concentration of 10 mg mL^{-1} were prepared by dissolving standards in water (0.1% FA). Standards with concentrations of 1 mg mL^{-1}, 100 µg mL^{-1}, 10 µg mL^{-1} and 1 µg mL^{-1} were prepared by serial dilutions in water (0.1% FA). Samples were stored at -20 °C until analysis.

Tissue analysis. Animal experiments were conducted following institutional guidelines (UW-Madison IACUC). Female Sprague-Dawley rats were anesthetized, perfused with chilled phosphate buffered saline, decapitated and removed brains. The brain tissues were either stored in Eppendorf tubes for protein extraction or embedded in gelatin solution (100 mg mL^{-1} in MilliQ water) for tissue sectioning. Tissue samples were snap frozen and stored in -80 °C until analysis.

A 3x volumes of chilled acidified MeOH solution (MeOH:H_2O:AA (v/v/v) 90 : 9: 1) was added to the brain tissue sample for neuropeptide extraction. The brain tissue was manually homogenized using a glass homogenizer and then centrifuged at 16,100 × g for 10 minutes. The supernatant was obtained and dried down in a speed vacuum concentrator and was reconstituted in water (0.1% FA) prior to desalting. A 10 µL C_{18} ZipTip (EMD Millipore, Darmstadt, Germany) was used for salt removal. The ZipTip was first conditioned with ACN and equilibrated with water (0.1% FA). After loading the tissue extract, the ZipTip was washed with water (0.1% FA) for 3 times and the sample was eluted with 10 µL of ACN:H_2O:FA (v/v/v) 49.95:49.95:0.1.The eluted peptide solution was then used for MS analysis.

Cryosectioned rat brain tissue was used for *in situ* biomolecule profiling. Gelatin embedded tissue was sectioned into 12 µm slices in a cryostat (Microm HM525, Thermo Scientific, Bremen, Germany), thaw mounted onto a glass slide (75x25x1mm) and stored in a desiccator at -80 °C until analysis.

MALDI-MS, MAIV-MS and MS/MS set up

CHCA matrix solution was prepared by dissolving 10 mg of CHCA in 1 mL solution of ACN:EtOH:H_2O:FA (v/v/v/v) 84:13:2.997:0.003. 3-NBN matrix solution was prepared as described by Inutan and Trimpin [23, 24]. Briefly, 10 mg of 3-NBN was dissolved in 50 µL acetonitrile, then mixed with 150 µL solution of ACN:H_2O:FA (v/v/v) 49.95:49.95:0.1. The matrix solution was made freshly before every experiment and kept at above 25 ℃ to avoid recrystallization. Other solvent combinations, including MeOH/water/FA and EtOH/water/FA, were also tested for optimization. For MALDI-MS analysis, 1 µL CHCA matrix was mixed with 1 µL analyte (standard or tissue extract) in an Eppendorf tube. The mixture was deposited on a stainless steel sample plate. For MAIV-MS analysis, 1.5 µL 3-NBN matrix was deposited on top

of 0.5 µL analyte directly on a stainless steel sample plate. Analyte and 3-NBN matrix could not be pre-mixed in an Eppendorf tube before depositing on the target plate, since 3-NBN crystallizes immediately upon mixing. One spot was prepared for each time of data acquisition. For *in situ* analysis, 1.5 µL matrix was spotted directly onto tissue sections.

The MALDI-LTQ-Orbitrap XL platform (Thermo Scientific, Bremen, Germany) was used for all data acquisitions. For all experiments, survey crystal positioning system (CPS) was used as the plate motion mode and 1 microscan was acquired per step. Laser energy of 10.5 µJ was used for all MALDI-MS analysis, and laser energy of 0.1 µJ (the minimum laser setting on the instrument in order to trigger data acquisition) was used for MAIV-MS. For full scan, FTMS mode was used with a resolving power of 100,000 at *m/z* of 400. Automatic gain control (AGC) was set at a target value of $1e^6$ and maximum laser shots of 80, indicating that a total ion count of $1e^6$ or 80 laser shots have to be reached for each microscan. Both HCD and CID were used to acquire MS/MS data. AGC target for MS/MS was set to be $1e^5$ and isolation window of 3 *m/z* was chosen for all parent ions. Normalized collisional energy was optimized for each parent ion. Database searching and *de novo* sequencing were performed by PEAKS 7 (Bioinformatics Solution Inc., ON, Canada) and verified manually.

Results and discussion

MAIV is a novel soft ionization technique that generates multiply charged ions from solid state samples without laser ablation or high voltage. Although a quantitative mechanism for MAIV has not yet been formulated, properties of the matrices used in these methods have offered clues. A recent review by McEwen and Larsen suggests two related matrix-dependent mechanisms. Matrices which produce greater ion yields at high temperatures, such as 2-nitrophloroglucinol and 2,5-dihydroxyacetophenone, may melt into liquid droplets within the

heated inlet and become ionized in the pressure gradient, thus leading to an ESI-like charged droplet event. More volatile matrices which produce greater ion yields at lower temperatures, such as 3-NBN, may form highly charged clusters from a crystal-shearing or triboluminescence process during sublimation [30, 31]. Due to the low energy ionization processes, it is a promising tool to analyze labile biomolecules without extensive in-source or post-source fragmentation. In this study, we have adapted MAIV to the HRAM MALDI-LTQ-Orbitrap XL platform for both extracted and *in situ* tissue analysis of peptides and proteins. Moreover, we have demonstrated improved HCD and CID fragmentation efficiency of MAIV produced multiply charged peptide ions.

Optimization of MAIV-MS conditions using peptide and protein standards

MAIV-MS Optimization. 3-NBN concentration, solvent composition and laser energy were optimized. Different 3-NBN concentrations (10, 50 and 100 mg mL^{-1}) were tested. Only 50 mg mL^{-1} 3-NBN allowed production of multiply charged ions under MAIV-MS condition. 100 mg mL^{-1} 3-NBN cannot be fully dissolved, whereas 10 mg mL^{-1} 3-NBN sublimates too rapidly in the intermediate vacuum source resulting in the absence of detectable signal. Different solvents, including ACN, MeOH, EtOH and water, were tested to dissolve 3-NBN. Only ACN is able to dissolve the 3-NBN powder. A small amount of water (less than 40% of total volume) could be added into the ACN dissolved 3-NBN solution without inducing recrystallization. Different laser energies (0.1, 5, 10, 15, 20, 25 and 30 μJ) were tested using 100 μg mL^{-1} insulin standard (0.1 μJ, which can be ignored, was the smallest laser energy value allowed to trigger data acquisition). Multiply charged ions were observed at every laser energy tested. Although the exact mechanism of MAIV is not fully understood yet, this observation suggests that the ionization process of MAIV does not involve laser, which allows a softer ionization compared to

MALDI. Based on these results, 50 mg mL^{-1} 3-NBN dissolved in ACN: H_2O:FA (v/v/v) 62.5:37.5:0.1 and 0.1 μJ laser energy were used for all subsequent MAIV-MS data acquisition.

Characterization of peptide and protein standards

250 μg mL^{-1} protein standards: insulin (Figure 1a), cytochrome C (Figure 1b), lysozyme (Figure 1c) and myoglobin (Figure 1d) were used to evaluate the HRAM MAIV-MS system for the generation of multiply charge ions. Most of the multiply charged ions appeared between *m/z* 700-2000. While most of the singly charged ions were observed below *m/z* of 700 and very small amount of ions were observed above *m/z* of 2000. For insulin, +3, +4 and +5 charged ions were detected with high mass accuracy (0.58 ppm in average) and high resolution (100,000 at *m/z* 400). Charge states +7 to +15 of cytochrome C and +8 to +12 of lysozyme were all detected and well resolved. Myoglobin (16952.30 Da) was the largest protein standard we tested using this platform and as many as 18 positive charges attached to the intact protein were observed. Isotopic peaks of +5 charged insulin, +14 charged cytochrome C, +13 charged lysozyme and +15 charged myoglobin were well resolved (Figure 1, zoomed in spectra) with the superior resolving power of the orbitrap.

To evaluate the sensitivity of HRAM MAIV-MS, serial dilutions of peptide and protein standards were tested. The lower limit of detection (LLOD) was determined by the lowest concentration where analyte ions could be detected. The LLODs of bradykinin, insulin, cytochrome C, lysozyme and myoglobin were determined as 250 ng mL^{-1} (236 nM), 250 ng mL^{-1} (43.6 nM), 2.50 μg mL^{-1} (202 nM), 2.50 μg mL^{-1} (175 nM) and 250 μg mL^{-1} (14.7 μM), respectively. The sensitivity for large proteins is limited on this platform as the detection of large proteins with Orbitrap is difficult. Modifications of instrument are required for extended mass range detection on Orbitrap [32].

MAIV-MS/MS by CID and HCD was also achieved using the LTQ-Orbitrap XL platform. To demonstrate the improved fragmentation efficiency on the multiply charged ions, bradykinin was chosen for MS/MS comparisons between +1 and +2 charged ions (Figure 2). HCD experiments were performed with MALDI produced +1 charged ion (Figure 2a), and MAIV produced +1 (Figure 2b) and +2 charged ions (Figure 2c) respectively. The fragmentation patterns of the +1 charged ions generated by MALDI and MAIV were similar: a few b and y ions were observed along with some a-type ions. Compared to +1 charged ions, +2 charged ions generated by MAIV showed significantly improved HCD fragmentation efficiency and almost all of the b and y ions were observed with the exception of b_7 ion.

As mentioned in introduction, we hypothesize that MAIV-MS can reduce in-source fragmentation of peptides and proteins with PTMs as MAIV does not require high energy (laser or high voltage) to ionize molecules. To test this hypothesis, phosphorylated kinase domain of insulin receptor and glycosylated EPO fragments were analyzed by MALDI-MS and MAIV-MS respectively (Figure 3). Under MALDI condition, in source fragmentation occurred to both phosphopeptide (Figure 3a) and glycopeptide (Figure 3b). Singly charged phosphopeptide ion was observed along with neutral loss fragment ions such as $[M\text{-}p+H]^+$, $[M\text{-}p\text{-}H_2O+H]^+$ and $[M\text{-}2p\text{-}H_2O+H]^+$ in MS^1 scan. For the glycosylated peptide, both intact glycosylated EPO ion and Y_0 ion (EPO losing the GalNAc) were observed in MS^1 scan. In contrast, under MAIV condition, doubly charged intact ions of both phosphopeptide and glycopeptide were observed as the base peak and very limited number of fragments were detected in MS^1 scan. Neutral loss fragment ions such as $[M\text{-}p+H]^+$ of the phosphopeptide and EPO Y_0 ions were detected but with much lower intensities compared to the base peaks (about 12% of the base peak). MAIV-MS/MS of the doubly charged glycosylated EPO ion was performed by both CID and HCD (Supplemental

Figure 1). The detected fragment ions were mostly b and y ions without the modification along with some ions having GalNAc preserved on the serine residue. The slow heating fragmentation techniques such as CID and HCD limit the comprehensive structure analysis by MS/MS as most of the labile PTM groups could be detached from the peptide backbone during the fragmentation process [33]. Coupling MAIV-MS to electron-transfer dissociation or electron-capture dissociation, which are advantageous to preserve labile PTM groups during the dissociation and thus facilitate pinpointing the modification site, will be explored for PTM analysis in future studies [34, 35].

MAIV-MS Analysis of Animal Brain Tissue

In addition to peptide and protein standards, analysis of complex samples in solution and *in situ* were also demonstrated using MAIV-MS. Neuropeptide and protein extracts from rat pituitary gland and rat brain were analyzed by MAIV-MS (Figure 4a-b). Highly charged ions were detected and protein species were identified based on accurate mass matching. It was observed that majority of the multiply charged ions were detected in the tissue extracts of both rat pituitary gland and entire brain (Table 1). Among the 861 mass spectral peaks (with signal to noise ratios greater than 3 and charge state assigned by Xcalibur) detected from rat pituitary gland extracts, only 11% of the peaks were singly charged. Majority of peaks (69%) had charge states between +2 to +4 and 20% peaks had charge states greater than four. Molecules as large as 14 kDa were detected with a charge state of 15. For the whole brain tissue extract, peaks with higher charge states were observed; a large portion of peaks (68%) had charge states greater than +4, 29% of the peaks were singly charged, and only 3% of the peaks were between +2 to +4.

MAIV-HCD-MS/MS analysis was performed with different charge states of a highly abundant endogenous neuropeptide SYSMEHFRWGKPV (N-term: diacetyl, C-term: amide) from the tissue extracts of a rat pituitary gland (Supplemental Figure 2). The HCD MS/MS

analyses of +2 and +3 charged ions showed highly abundant b and y ions, whereas the MS/MS of the +1 charged precursor ions produce barely detectable signals. As expected, the HCD fragmentation efficiency of the multiply charged ions was significantly improved compared to that of the singly charged ions.

Rat brain cryosections were used as the demonstration of *in situ* analysis by MAIV-MS (Figure 4c). A drop (1.5μL) of 3-NBN matrix was applied to the occipital cortex of a 12 μm rat brain section for profiling analysis. Singly charged neuropeptide (α-MSH), multiply charged protein (ubiquitin 6+) and several singly charged lipids (cardiolipin/CL) were detected from the tissue sections. In summary, MAIV-MS is suitable for the analyses of large molecules extracted from tissue as well as on tissue slices.

Challenges

As 3-NBN is a volatile matrix, it usually sublimates within 5 minutes in an intermediate vacuum MALDI source. MS imaging, which usually require much longer acquisition time, cannot be achieved by MAIV-MS at this stage. Moreover, detection of large proteins is still a problem with Orbitrap. The sensitivity of large protein (such as myoglobin) detection using MAIV-MS is mediocre, thus only the most abundant proteins in tissue could be detected. Slowing down the sublimation rate and enhancing the sensitivity/dynamic range for protein analysis remain to be addressed in order to make MAIV-MS a more useful and versatile analytical tool.

Conclusion

MAIV is a novel ionization technique that generates multiply charged ions during a triboluminescence process under vacuum without the use of high voltage or laser ablation. As an attractive alternative to MALDI for off-line and *in situ* analysis of biological samples, MAIV

coupling with HRAM instrument platforms such as LTQ-Orbitrap, has expanded the mass detection range of matrix-assisted ionization methods and improved the fragmentation efficiency because of the generation of multiply charged ions. In this study, we demonstrated the capability of HRAM MAIV-MS in detecting biomolecules as large as 18.7 kDa with 18 charge states in an orbitrap mass analyzer. MAIV-MS analysis of peptides and proteins were demonstrated with both extracts from rat brain and *in situ* tissue profiling. Compared to singly charged ions produced by conventional MALDI, MAIV generated multiply charged ions have been demonstrated to help improving the fragmentation efficiency for both peptide standards and endogenous peptides from complex tissue samples. Moreover, MAIV-MS can also be used as an alternative tool for labile PTM analysis due to the fact that neither laser ablation nor high voltage is involved in the ionization process, which decreases the chance of in source fragmentation.

Acknowledgements

The authors would like to acknowledge Dr. Sarah Trimpin's laboratory at Wayne State University for the inspiration of this work and Dr. Robert Thorne's laboratory at the University of Wisconsin-Madison for providing rat tissue samples. The instrument was purchased through funding support from NIH S10 RR029531. This work was supported by National Institutes of Health NIDDK R01DK071801. C.L. acknowledges an NIH-supported Chemistry Biology Interface Training Program Predoctoral Fellowship (grant number T32-GM008505) and an NSF Graduate Research Fellowship (DGE-1256259). LL acknowledges an H. I. Romnes Faculty Research Fellowship and a Vilas Distinguished Achievement Professorship with funding provided by the Wisconsin Alumni Research Foundation and University of Wisconsin-Madison School of Pharmacy.

References

[1] Tanaka, K., Waki, H., Ido, Y., Akita, S., Yoshida, Y., Yoshida, T., and Matsuo, T. (1988) Protein and polymer analyses up to m/z 100 000 by laser ionization time-of-flight mass spectrometry, *Rapid Commun. in Mass Spectrom. 2*, 151-153.

[2] Fenn, J. B., Mann, M., Meng, C. K., Wong, S. F., and Whitehouse, C. M. (1989) Electrospray ionization for mass spectrometry of large biomolecules, *Science 246*, 64-71.

[3] Yates, J. R. (2011) A century of mass spectrometry: from atoms to proteomes, *Nat. Methods 8*, 633-637.

[4] Chen, B., Zhong, X., Lietz, C., and Li, L. (2015) High resolution and accurate mass (HRAM) characterization of multiply charged proteins by newly developed ionization techniques on CE-LSI/MAIV-LTQ-Orbitrap platform, *Proceedings of the 63rd ASMS Conference on Mass Spectrometry and Allied Topics, St. Louis, MO, May 31-June 1*.

[5] Brown, R. S., Feng, J. H., and Reiber, D. C. (1997) Further studies of in-source fragmentation of peptides in matrix-assisted laser desorption-ionization, *Int J Mass Spectrom 169*, 1-18.

[6] Frankevich, V., Zhang, J., Dashtiev, M., and Zenobi, R. (2003) Production and fragmentation of multiply charged ions in 'electron-free' matrix-assisted laser desorption/ionization, *Rapid Commun. Mass Spectrom. 17*, 2343-2348.

[7] Takats, Z., Wiseman, J. M., Gologan, B., and Cooks, R. G. (2004) Mass spectrometry sampling under ambient conditions with desorption electrospray ionization, *Science 306*, 471-473.

[8] Cooks, R. G., Manicke, N. E., Dill, A. L., Ifa, D. R., Eberlin, L. S., Costa, A. B., Wang, H., Huang, G., and Ouyang, Z. (2011) New ionization methods and miniature mass spectrometers for biomedicine: DESI imaging for cancer diagnostics and paper spray ionization for therapeutic drug monitoring, *Faraday Discuss. 149*, 247-267; discussion 333-256.

[9] Sampson, J. S., Hawkridge, A. M., and Muddiman, D. C. (2006) Generation and detection of multiply-charged peptides and proteins by matrix-assisted laser desorption electrospray ionization (MALDESI) Fourier transform ion cyclotron resonance mass spectrometry, *J. Am. Soc. Mass Spectrom. 17*, 1712-1716.

[10] Robichaud, G., Barry, J. A., and Muddiman, D. C. (2014) IR-MALDESI Mass Spectrometry Imaging of Biological Tissue Sections Using Ice as a Matrix, *J. Am. Soc. Mass Spectrom. 25*, 319-328.

[11] Shiea, J., Huang, M. Z., Hsu, H. J., Lee, C. Y., Yuan, C. H., Beech, I., and Sunner, J. (2005) Electrospray-assisted laser desorption/ionization mass spectrometry for direct ambient analysis of solids, *Rapid Commun. Mass Spectrom. 19*, 3701-3704.

[12] Huang, M. Z., Hsu, H. J., Lee, J. Y., Jeng, J., and Shiea, J. (2006) Direct protein detection from biological media through electrospray-assisted laser desorption ionization/mass spectrometry, *J. Proteome Res. 5*, 1107-1116.

[13] Peng, I. X., Shiea, J., Ogorzalek Loo, R. R., and Loo, J. A. (2007) Electrospray-assisted laser desorption/ionization and tandem mass spectrometry of peptides and proteins, *Rapid Commun. Mass Spectrom. 21*, 2541-2546.

[14] Peng, I. X., Ogorzalek Loo, R. R., Shiea, J., and Loo, J. A. (2008) Reactive-electrospray-assisted laser desorption/ionization for characterization of peptides and proteins, *Anal. Chem. 80*, 6995-7003.

[15] Cho, Y. T., Huang, M. Z., Wu, S. Y., Hou, M. F., Li, J., and Shiea, J. (2014) Using electrospray laser desorption ionization mass spectrometry to rapidly examine the integrity of proteins stored in various solutions, *Analytical and bioanalytical chemistry 406*, 577-586.

[16] Nyadong, L., Inutan, E. D., Wang, X., Hendrickson, C. L., Trimpin, S., and Marshall, A. G. (2013) Laserspray and matrix-assisted ionization inlet coupled to high-field FT-ICR mass spectrometry for peptide and protein analysis, *J. Am. Soc. Mass Spectrom. 24*, 320-328.

[17] Chakrabarty, S., Pagnotti, V. S., Inutan, E. D., Trimpin, S., and McEwen, C. N. (2013) A new matrix assisted ionization method for the analysis of volatile and nonvolatile compounds by atmospheric probe mass spectrometry, *J. Am. Soc. Mass Spectrom. 24*, 1102-1107.

[18] Chen, B., Lietz, C. B., and Li, L. (2014) In Situ characterization of proteins using laserspray ionization on a high-performance MALDI-LTQ-Orbitrap mass spectrometer, *J. Am. Soc. Mass Spectrom. 25*, 2177-2180.

[19] Wang, B., Tisdale, E., Trimpin, S., and Wilkins, C. L. (2014) Matrix-assisted ionization vacuum for high-resolution Fourier transform ion cyclotron resonance mass spectrometers, *Anal. Chem. 86*, 6792-6796.

[20] Trimpin, S., Inutan, E. D., Herath, T. N., and McEwen, C. N. (2010) Laserspray ionization, a new atmospheric pressure MALDI method for producing highly charged gas-phase ions of peptides and proteins directly from solid solutions, *Molecular & cellular proteomics : MCP 9*, 362-367.

[21] Inutan, E. D., Wang, B., and Trimpin, S. (2011) Commercial intermediate pressure MALDI ion mobility spectrometry mass spectrometer capable of producing highly charged laserspray ionization ions, *Anal. Chem. 83*, 678-684.

[22] Trimpin, S., Ren, Y., Wang, B., Lietz, C. B., Richards, A. L., Marshall, D. D., and Inutan, E. D. (2011) Extending the laserspray ionization concept to produce highly charged ions at high vacuum on a time-of-flight mass analyzer, *Anal. Chem. 83*, 5469-5475.

[23] Trimpin, S., and Inutan, E. D. (2013) Matrix assisted ionization in vacuum, a sensitive and widely applicable ionization method for mass spectrometry, *J. Am. Soc. Mass Spectrom. 24*, 722-732.

[24] Inutan, E. D., and Trimpin, S. (2013) Matrix assisted ionization vacuum (MAIV), a new ionization method for biological materials analysis using mass spectrometry, *Mol. Cell. Proteom. 12*, 792-796.

[25] Witze, E. S., Old, W. M., Resing, K. A., and Ahn, N. G. (2007) Mapping protein post-translational modifications with mass spectrometry, *Nat. Methods 4*, 798-806.

[26] Strupat, K., Kovtoun, V., Bui, H., Viner, R., Stafford, G., and Horning, S. (2009) MALDI Produced Ions Inspected with a Linear Ion Trap-Orbitrap Hybrid Mass Analyzer, *J. Am. Soc. Mass Spectrom. 20*, 1451-1463.

[27] Trimpin, S., Inutan, E. D., Herath, T. N., and McEwen, C. N. (2010) Laserspray ionization, a new atmospheric pressure MALDI method for producing highly charged gas-phase ions of peptides and proteins directly from solid solutions, *Mol. Cell. Proteom. 9*, 362-367.

[28] Inutan, E. D., Richards, A. L., Wager-Miller, J., Mackie, K., McEwen, C. N., and Trimpin, S. (2011) Laserspray ionization, a new method for protein analysis directly from tissue at atmospheric pressure with ultrahigh mass resolution and electron transfer dissociation, *Molecular & cellular proteomics : MCP 10*, M110 000760.

[29] Inutan, E. D., and Trimpin, S. (2013) Matrix assisted ionization vacuum (MAIV), a new ionization method for biological materials analysis using mass spectrometry, *Molecular & cellular proteomics : MCP 12*, 792-796.

[30] McEwen, C. N., and Larsen, B. S. (2015) Fifty years of desorption ionization of nonvolatile compounds, *Int J Mass Spectrom 377*, 515-531.

[31] Woodall, D. W., Wang, B., Inutan, E. D., Narayan, S. B., and Trimpin, S. (2015) High-throughput characterization of small and large molecules using only a matrix and the vacuum of a mass spectrometer, *Analytical chemistry 87*, 4667-4674.

[32] Rose, R. J., Damoc, E., Denisov, E., Makarov, A., and Heck, A. J. (2012) High-sensitivity Orbitrap mass analysis of intact macromolecular assemblies, *Nature methods 9*, 1084-1086.

[33] Jones, A. W., and Cooper, H. J. (2011) Dissociation techniques in mass spectrometry-based proteomics, *Analyst 136*, 3419-3429.

[34] Zubarev, R. A., Kelleher, N. L., and McLafferty, F. W. (1998) Electron capture dissociation of multiply charged protein cations. A nonergodic process, *Journal of the American Chemical Society 120*, 3265-3266.

[35] Syka, J. E., Coon, J. J., Schroeder, M. J., Shabanowitz, J., and Hunt, D. F. (2004) Peptide and protein sequence analysis by electron transfer dissociation mass spectrometry, *Proceedings of the National Academy of Sciences of the United States of America 101*, 9528-9533.

Table 1. Summary of MAIV-MS tissue analysis results of tissue extracts from a rat pituitary gland and a whole rat brain.

Sample	Total Peaks*	Singly Charged Ion%	2-4 Charged Ion %	>4 Charged Ion %	Max. M.W. (Da)	Max. Charges
Pituitary Gland	861	11.27	68.64	20.09	14175	15
Whole Brain	223	29.15	3.14	67.71	15602	10

* Only peaks with signal to noise ratio greater than 3 and charge state assigned by Xcalibur were counted.

Figure legends

Figure 1. MAIV-MS analyses of protein standards: insulin, M.W. 5734.51 (a), cytochrome c, M.W. 12360.97 Da (b), lysozyme, M.W. 14295.81 Da (c) and myoglobin, M.W. 16952.30 Da (d).

Figure 2. Comparison of MALDI-HCD-MS/MS and MAIV-HCD-MS/MS using 10 μg mL^{-1} bradykinin. (a) HCD MS/MS spectrum of $[M+H]^+$ bradykinin ion (*m/z* 1060.57) produced by MALDI, normalized collisional energy was 40. (b) HCD MS/MS spectrum of $[M+H]^+$ bradykinin ion (*m/z* 1060.57) produced by MAIV, normalized collisional energy was 43. (c) HCD MS/MS spectrum of $[M+2H]^{2+}$ bradykinin ion (*m/z* 530.79) produced by MAIV, normalized collisional energy was 43.

Figure 3. MALDI-MS (a, b) and MAIV-MS (c, d) analysis of a phosphopeptide standard and a glycopeptide standard. Kinase domain of insulin receptor (a, c) and glycosylated erythropoietin (EPO) fragment 117-131 (b, d) were analyzed under MALDI-MS (a, b) and MAIV-MS (c, d) conditions respectively.

Figure 4. HRAM MAIV-MS analysis of different tissue samples: (a) neuropeptide and protein extracts from a rat pituitary gland; (b) neuropeptide and protein extracts from a whole rat brain; (c) *in situ* neuropeptide and protein profiling on the occipital lobe of rat brain cortex. Putative identifications of biomolecules were assigned by accurate mass matching.

Figures

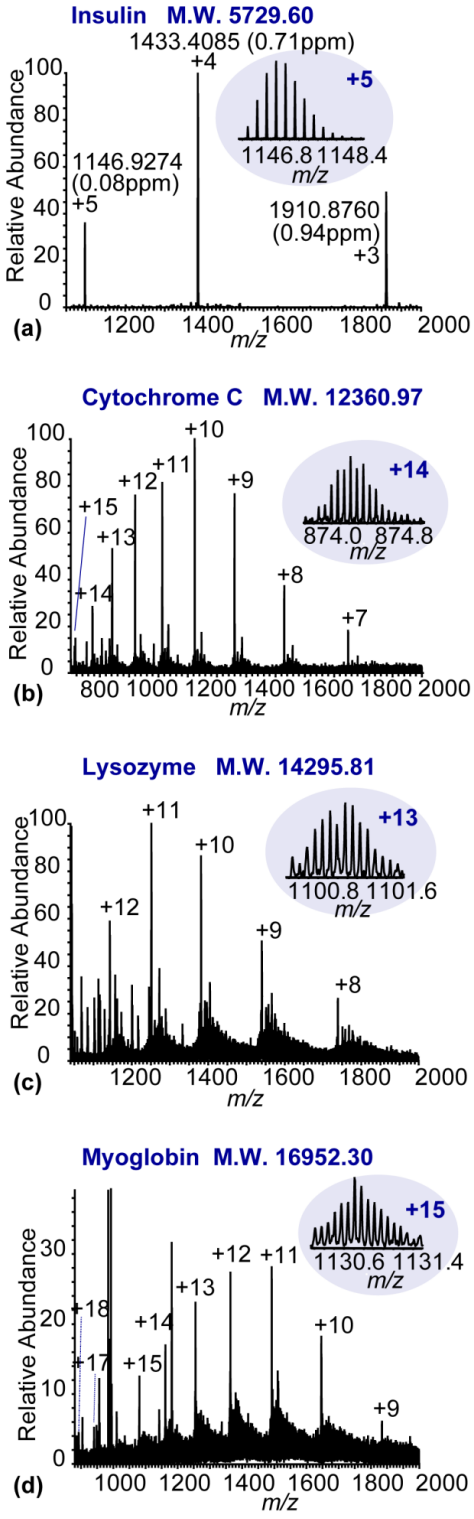

Figure 1

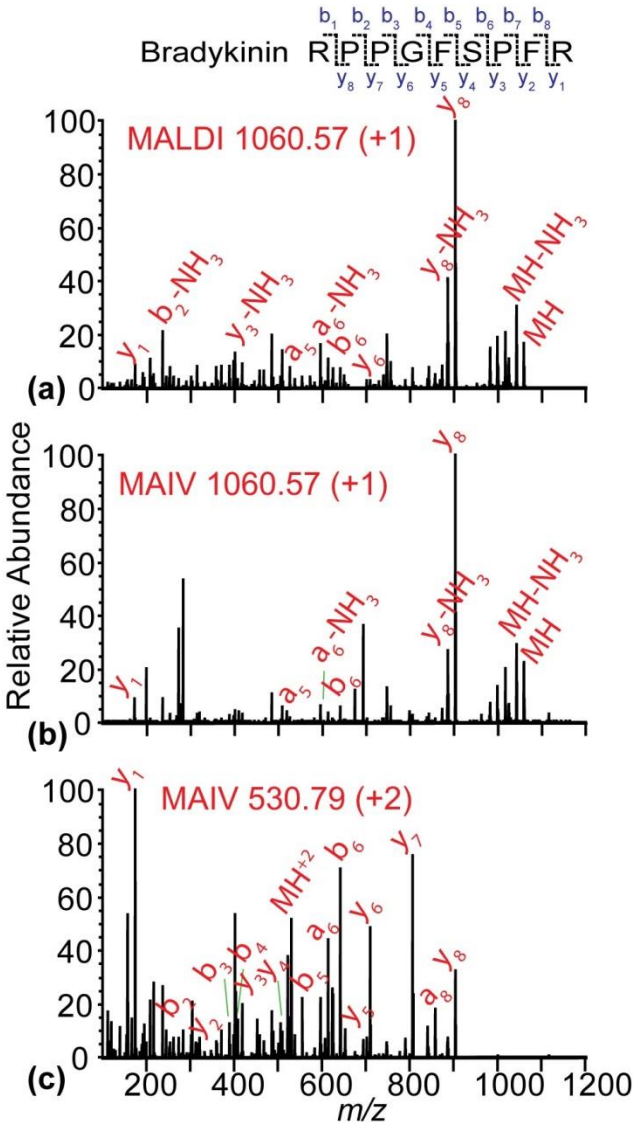
Bradykinin RPPGFSPFR
MALDI 1060.57 (+1)
MAIV 1060.57 (+1)
MAIV 530.79 (+2)
Relative Abundance
m/z
(a)
(b)
(c)

Figure 2

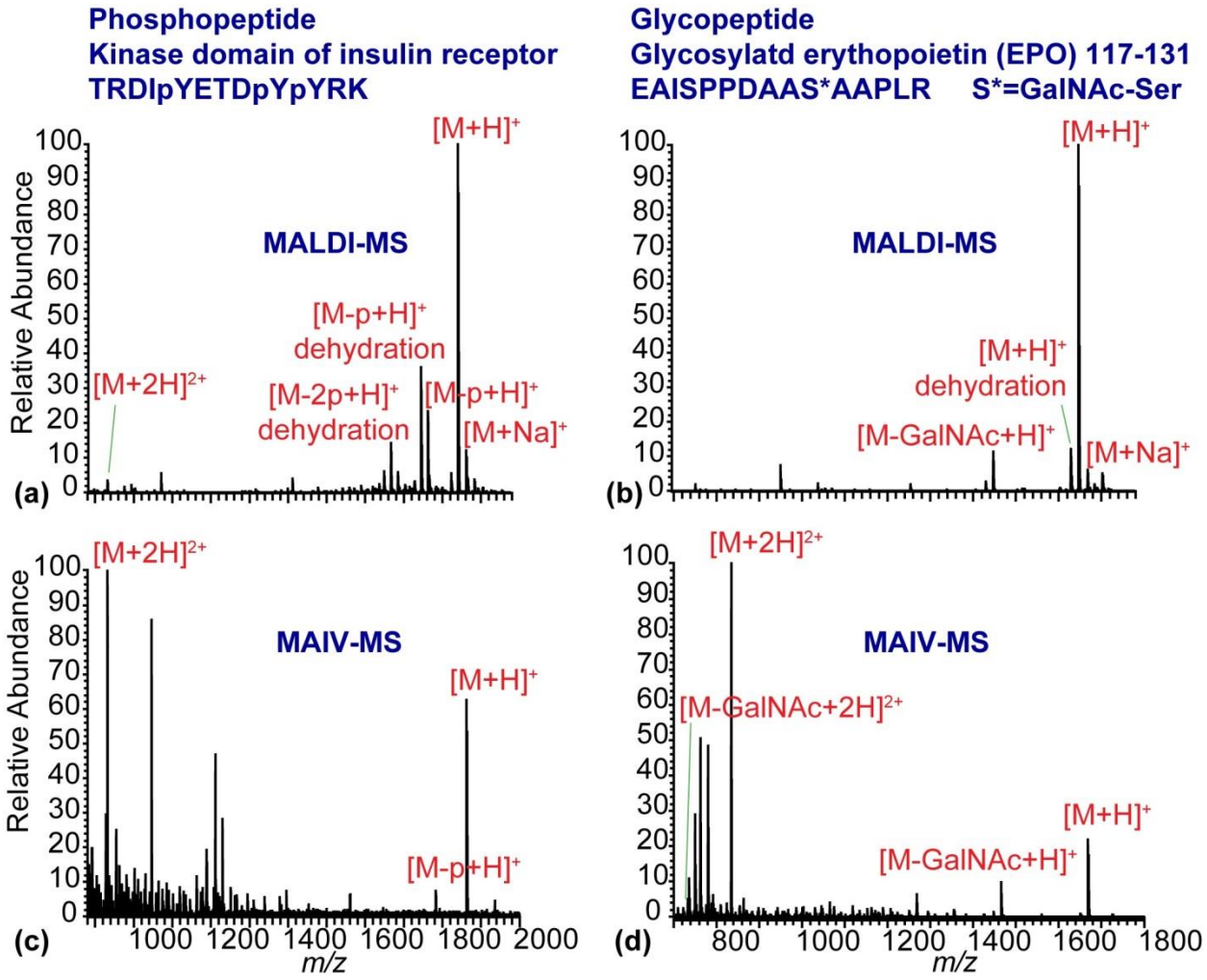
Phosphopeptide
Kinase domain of insulin receptor
TRDIpYETDpYpYRK
Glycopeptide
Glycosylatd erythopoietin (EPO) 117-131
EAISPPDAAS*AAPLR S*=GalNAc-Ser
MALDI-MS
MAIV-MS
Relative Abundance
m/z
[M+H]+
[M+2H]2+
[M-p+H]+ dehydration
[M-2p+H]+ dehydration
[M-p+H]+
[M+Na]+
[M-GalNAc+H]+
[M-GalNAc+2H]2+
(a)
(b)
(c)
(d)

Figure 3

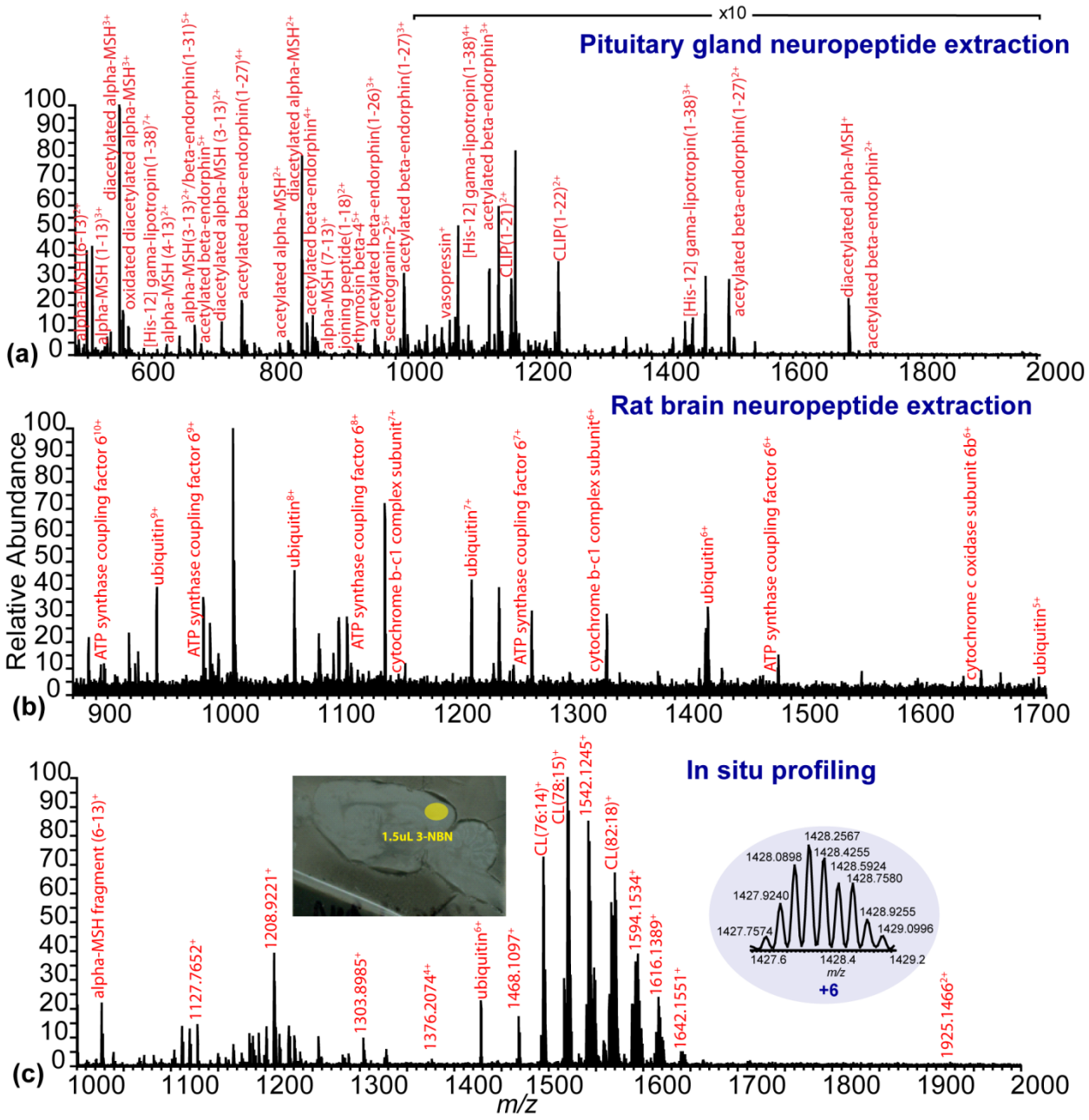
Pituitary gland neuropeptide extraction
x10
(a)
Rat brain neuropeptide extraction
Relative Abundance
(b)
In situ profiling
1.5uL 3-NBN
+6
m/z
(c)

Figure 4

Supporting Information

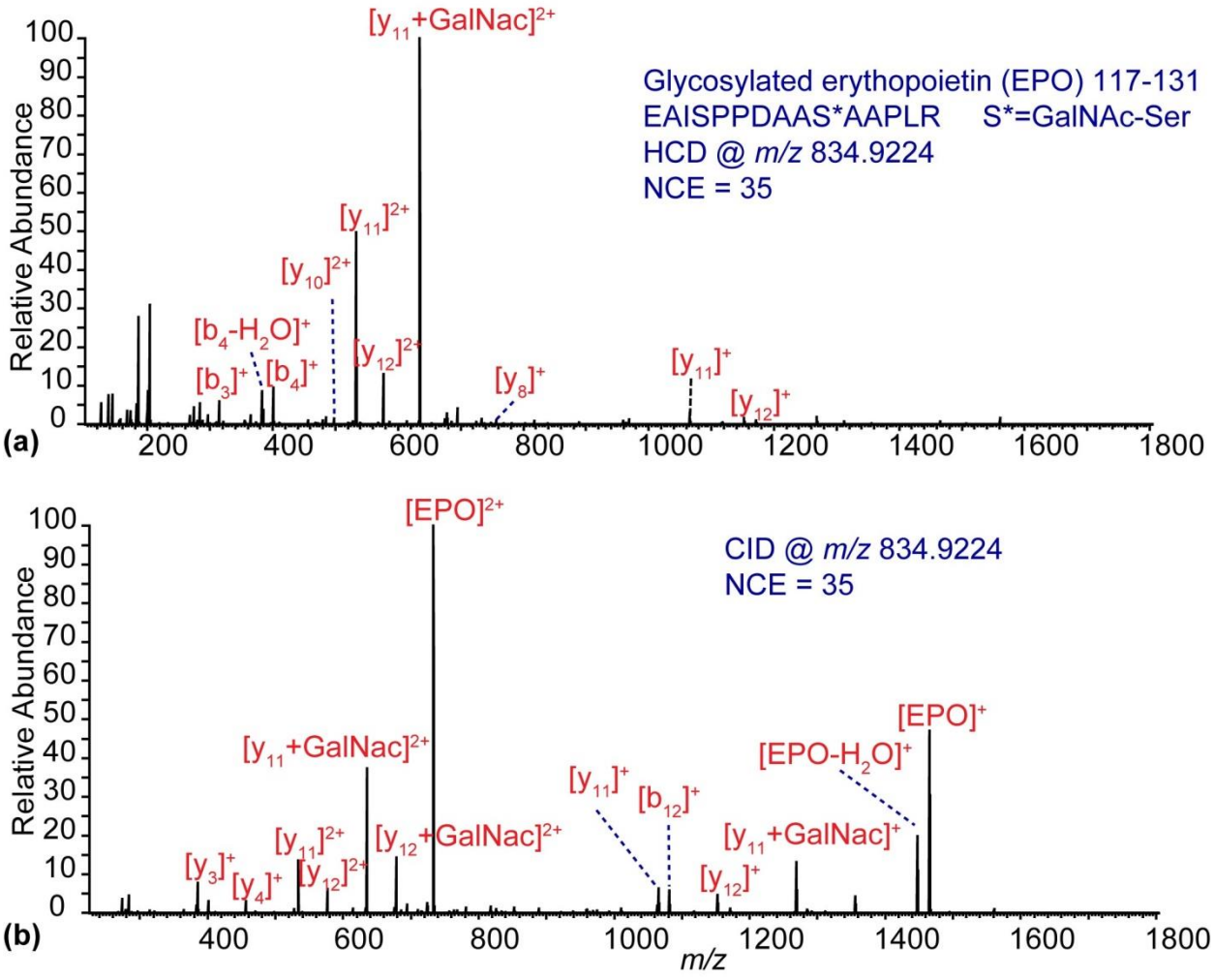

Supplemental Figure 1. HCD (a) and CID (b) MAIV-MS/MS analyses of $[M+2H]^{2+}$ ion (*m/z* 834.9224) glycosylated EPO standard. Normalized collision energy was 35.

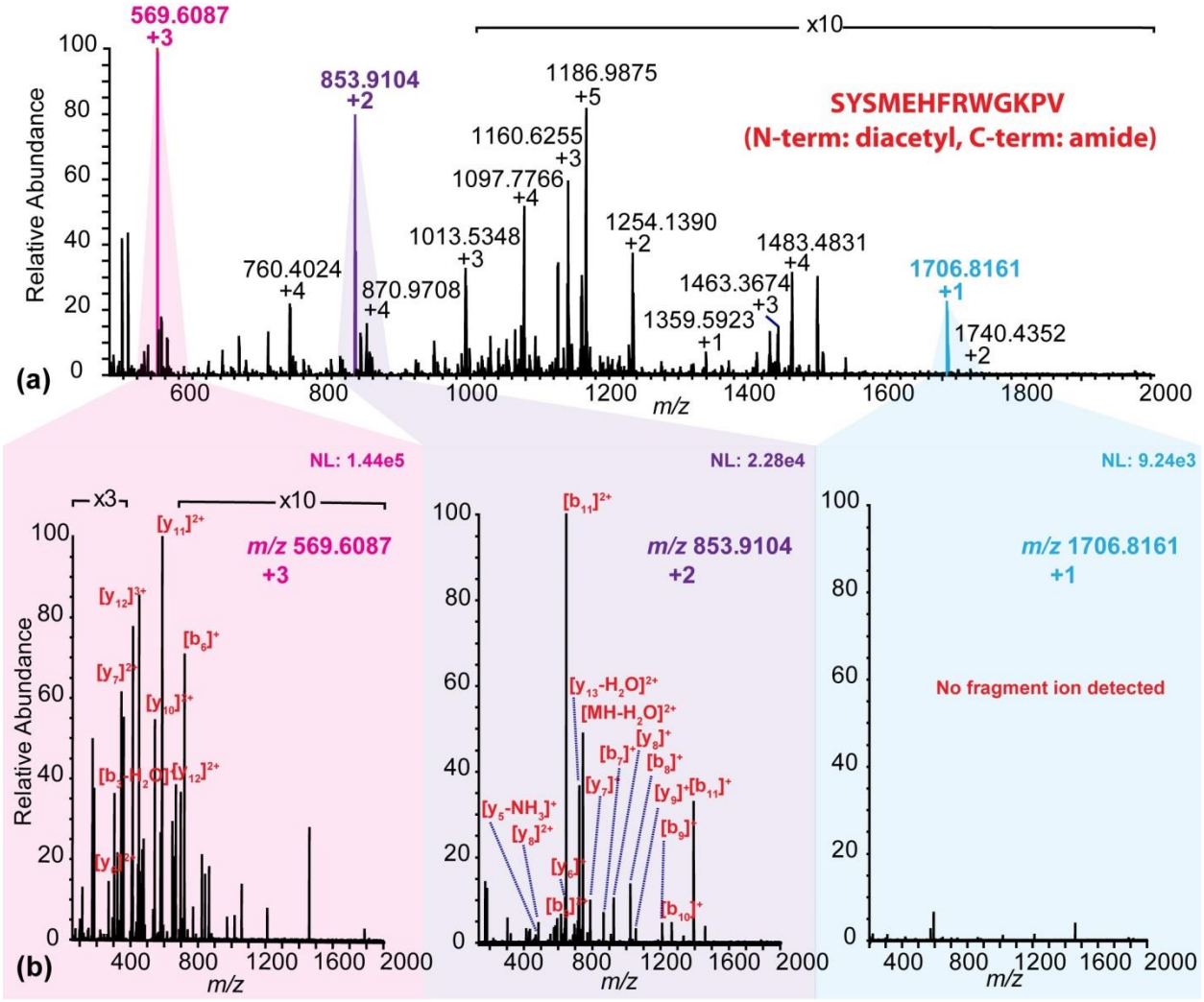

Supplemental Figure 2. MAIV-MS spectrum of neuropeptides and proteins extracted from rat pituitary gland (a). MAIV-HCD-MS/MS spectra of neuropeptide SYSMEHFRWGKPV (N-term: diacetyl, C-term: amide) ions with +3 charges (*m/z* 569.6087, left), +2 charges (*m/z* 853.9104, middle), +1 charge (*m/z* 1706.8161, right). Normalized collisional energy was 28.

Chapter 4
Coupling Matrix-Assisted Ionization with High Resolution Mass Spectrometer and Electron Transfer Dissociation for Characterizing Intact Proteins and Post-Translational Modifications

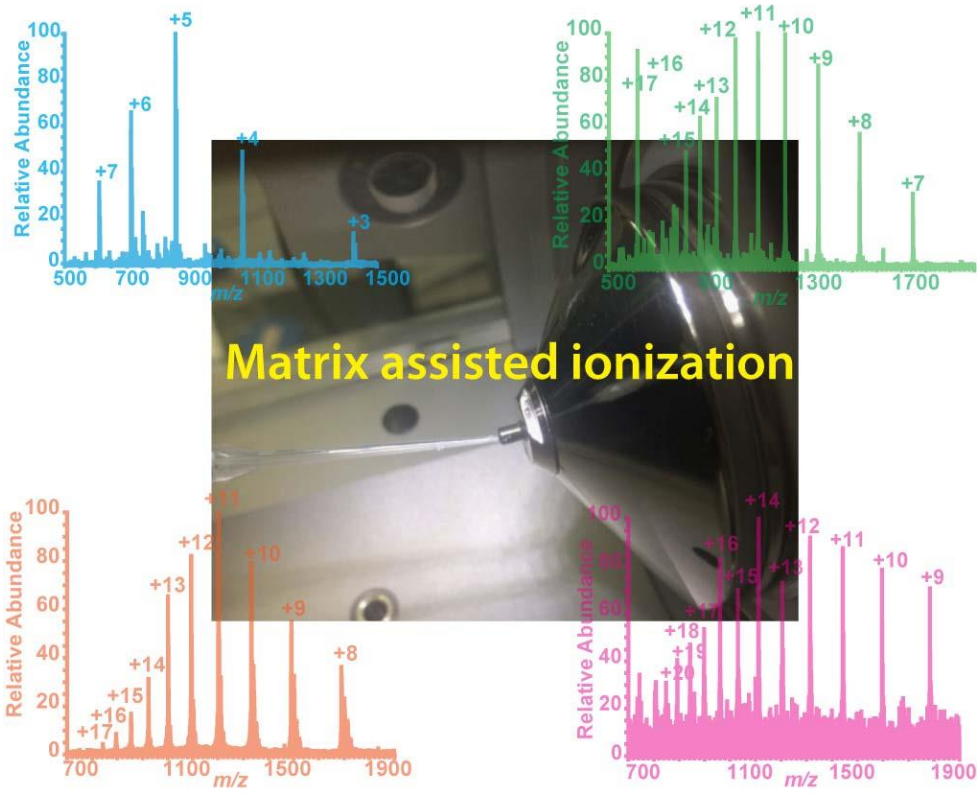

Adapted from **B.Chen**, C.B. Lietz, L. Li, Coupling Matrix-Assisted Ionization with High Resolution Mass Spectrometer and Electron Transfer Dissociation for Characterizing Intact Protein and Post-Translational Modifications. *To be submitted to Analytical and Bioanalytical Chemistry.*

Author contribution: study was designed by B. Chen, C.B. Lietz and L. Li; experiment was performed by B. Chen; manuscript was written by B. Chen and edited by C.B. Lietz and L. Li.

Abstract

Matrix-assisted ionization (MAI) is a recently developed ionization technique that produces multiply charged ions on either electrospray ionization (ESI) or matrix-assisted laser desorption/ionization (MALDI) platform without the need of high voltage or laser ablation. In this study, MAI has been coupled to a high resolution accurate mass (HRAM) hybrid instrument, the Orbitrap Elite mass spectrometer, with electron transfer dissociation (ETD) module for high-throughput peptide and intact protein characterization. The softness of MAI process preserves labile post-translational modifications (PTM) and allows fragmentation and localization by ETD. Moreover, MAI on ESI platform allows rapid sample analysis (~ 1 min/sample) due to the easiness of sample introduction. It significantly improves the throughput compared to ESI direct infusion and MAI on MALDI platform, which usually take more than 10 min/sample. Intact protein standards, protein mixtures and neural tissue extracts have been characterized on this instrument platform with both full MS and MS/MS (CID, HCD and ETD) analyses. Furthermore, the performances of ESI, MALDI and MAI on both platforms have been tested to provide a systematic comparison among these techniques. We anticipate that the HRAM MAI-MS with ETD module will be widely applied in both bottom-up and top-down high throughput protein characterizations.

Keywords: matrix-assisted ionization, post-translational modification, electron transfer dissociation, high resolution accurate mass

Introduction

Introduced in 2013 by Trimpin and Inutan [1,2], matrix-assisted ionization (MAI) is considered as a "magic" ionization that can produce multiply charged ions on either matrix-assisted laser desorption/ionization (MALDI) or electrospray ionization (ESI) platform (MAI (MALDI) or MAI (ESI)) without laser ablation or high voltage. The only requirements for the ionization process are the inherent vacuum of the instrument and a labile small molecule matrix, such as 3-nitrobenzonitrile (3-NBN). MAI has several advantages compared to conventional ionization techniques. Compared to MALDI, which predominantly generates singly charge ions, MAI produces multiply charged ions. Compared to ESI, MAI has higher throughput and less sample carryover or contamination [3]. Compared to laserspray ionization (LSI), which is also a novel ionization technique for generating multiply charged ions[4-6], MAI produces higher charge state ions without the requirement of laser ablation. Therefore, MAI efficiently improves the throughput and expands the mass detection range compared to MALDI and LSI on high resolution accurate mass (HRAM) mass analyzers, such as Orbitrap, which usually has an upper *m/z* limit of 4,000 or 6,000. In previous studies on MAI process, the influences of source temperature, matrix, solvent, sample introduction route were studied on various instruments. It was also applied on various samples, such as small molecules (drugs, pesticides, dyes), peptides, intact proteins as well as tissue extract and tissue sections, for quantitative and qualitative analyses[1, 2, 6-10]. A triboluminescence-based mechanism was proposed to explain the production of highly charged ions during the MAI process. The 3-NBN matrix produces strong dinitrogen discharge emission during the fracturing of crystal under vacuum and produced charged particles upon sublimation [2, 11].

Our previous study demonstrated the potential of MAI on analyzing peptides with labile PTMs on the MALDI-LTQ-Orbitrap XL platform to reduce in-source fragmentation [8]. During MALDI-MS acquisition, high intensities of dephosphorylated and deglycosylated peptides were observed with very low intensity of intact peptides. Under MAI condition, high intensities of intact peptides were observed, with only small amount of neutral loss ions. However, when we performed CID and HCD fragmentations on the intact peptide ions, the labile PTM groups were not preserved on fragment ions. We considered that the slow heating fragmentation techniques (CID and HCD) limit more comprehensive structural analysis on peptides with labile PTMs. In contrast, electron capture dissociation (ECD) [12] and electron transfer dissociation (ETD) [13], which produce c and z ions upon the reaction of a multiply protonated peptide with a low energy electron, can potentially preserve the labile PTM groups. Unlike ECD that is exclusive to Fourier transform ion cyclotron resonance (FTICR) instruments, ETD has been widely applied to commercially available quadrupole ion trap, linear 2D quadrupole ion trap and hybrid quadrupole time-of-flight (Q-TOF) and LTQ-Orbitrap instruments [14]. Therefore, we anticipated ETD could be used to better localize the PTM position on a LTQ-Orbitrap platform. The Orbitrap Elite mass spectrometer is a HRAM hybrid instrument with dual-pressure linear ion trap and Orbitrap mass analyzer, which enables superior resolution of up to 240,000 at *m/z* 400. Moreover, multiple fragmentation techniques, including CID, HCD and ETD, are available on this instrument, which offers versatility of structure elucidation [15].

Herein, we coupled MAI onto the HRAM Orbitrap Elite mass spectrometer with ETD module for high throughput peptide and protein analyses. In this study, we demonstrated the MAI-HRAM MS system using peptide and protein standards, protein mixture, tissue extract and protein digest for full MS and different types of MS/MS (CID, HCD and ETD). Moreover, the

performances of four ionization techniques MAI (ESI), MAI (MALDI), ESI and MALDI were compared. We anticipate that the HRAM MAI-MS with ETD module could be widely applied in both bottom-up and top-down high throughput protein characterizations.

Materials and Methods

Materials

All standards and reagents were used without additional purification. Acetonitrile (ACN), methanol (MeOH), ethanol (EtOH), formic acid (FA) acetic acid (AA), urea and ammonium bicarbonate and water were purchased from Fisher Scientific (Pittsburgh, PA). Iodoacetamide (IAA), 3-NBN, α-cyano-4-hydroxycinnamic acid (CHCA), cytochrome C (bovine heart), lysozyme (chicken egg white), alpha-casein (bovine milk), myoglobin (equine heart) and histone (calf thymus) were purchased from Sigma Aldrich (St. Louis, MO). Neuropeptide Y (human, rat) was purchased from American Peptide Company (Sunnyvale, CA, now Bachem, Torrance, CA). Phosphopeptide standard kit was purchased from AnaSpec (Fremont, CA). Glycosylated erythropoietin (EPO) 117-131 was purchased from Protea Biosciences Group, Inc (Morgantown, WV). Dithiothreitol (DTT) and sequencing grade modified trypsin were purchased from Promega (Madison, WI). The Ni-NTA magnetic agarose beads were purchased from QIAGEN (Valencia, CA).

Sample preparation

Peptide and protein stock solutions were prepared by dissolving standards in 50% ACN solution at 10 mg mL^{-1}. Serial dilutions of 1 mg mL^{-1}, 100 µg mL^{-1}, 10 µg mL^{-1} and 1 µg mL^{-1} standards were diluted from the stock solution with 50% ACN solution. Samples were stored in -20 °C until analysis.

Animal experiments were conducted following institutional guidelines (University of Wisconsin-Madison IACUC). Perfused brain tissue of female Sprague-Dawley rats were homogenized manually in acidified MeOH solution (MeOH:H_2O:AA (v/v/v) 90 : 9: 1) for peptide and protein extractions. The tissue was homogenized for approximately 5 min until no visible tissue chunk could be observed. The homogenized tissue was sonicated for 1 min followed by centrifugation (16,100 rcf, 10 min). The supernatant was transferred to a new micro-centrifuge tube and dried down in a speed vacuum concentrator. The tissue extract was reconstituted in water (with 0.1% FA) and cleaned up with C_{18} ZipTip (EMD Millipore Corporation, Darmstadt, Germany) according to manufacturer's instruction. The eluted fraction was dried down and reconstitute in 50% ACN for MS analysis.

MAI matrix, 3-NBN, was prepared as described by Inutan and Trimpin [1, 2]. Briefly, 50 µL ACN was added to 10 mg 3-NBN, the mixture was vortexed until 3-NBN was completely dissolved. A volume of 150 µL 50% ACN was then added to the mixture. The matrix solution was prepared freshly before each experiment. Before MS analysis, 1 µL analyte was mixed with 1 µL matrix solution on Parafilm (Bemis, Neenah, WI). One µL of the mixture was loaded onto a 10 µL gel loading pipette tip and waited until the mixture was crystalized before MS analysis. CHCA matrix, which was used in comparison MALDI experiment, was prepared by dissolving 10 mg of CHCA in 1 mL solution of ACN:EtOH:H_2O:FA (v/v/v/v) 84:13:2.997:0.003. The sample and matrix were premixed at a 1:1 ratio and 1 µL mixture was spotted onto MALDI plate.

Protein digestion and IMAC enrichment of phosphopeptides

One mg of alpha-casein standard was dissolved in 400 µL digestion solution (8M urea, 50 mM ammonium bicarbonate) to a final concentration of 2.5 mg/mL. The protein was reduced

with 10 mM DTT at room temperature for 1 hr and alkylated with 15 mM IAA in dark at room temperature for 1 hr. Extra DTT was added to the solution to make a final concentration of 20 mM in order to quench the alkylation reaction. Ammonium bicarbonate solution (2.2 mL 50 mM) was added to the sample in order to dilute urea (less than 1 M). Trypsin (20 µg) was reconstituted in 200 µL 50 mM ammonium bicarbonate and added to protein solution. The mixture was incubated in 37 °C water bath for 18 hours and dried down in a speed vacuum concentrator.

The digested peptide was reconstituted in 500 µL 0.1% FA/H_2O and desalted using a Sep-Pak C_{18} cartridge (Waters, Milford, MA) according to manufacturer's instruction. The samples were dried down in a speed vacuum concentrator and stored in freezer. Prior to immobilized metal affinity chromatography (IMAC) for phosphopeptide enrichment, 500 µL magnetic Ni-NTA magnetic agarose beads suspension was pipetted into a 2 mL tube. The beads were washed with 1 mL H_2O for 3 times and shaken in 1 mL EDTA (pH ~8) solution for 30 min. The beads were then washed with 1 mL H_2O for 5 more times and shaken in 1 mL 100 mM $FeCl_3$ for 30 min. The beads were then washed with 1 mL ACN:H_2O:TFA (v/v/v) 80:19.85:0.15 for 4 times. The sample was re-suspended in 1 mL ACN:H_2O:TFA (v/v/v) 80:19.85:0.15 and quantitatively transferred to the beads. The mixture was shaken for 30 min and the supernatant was saved as phosphopeptide depleted sample. The beads were washed again with 1 mL ACN:H_2O:TFA (v/v/v) 80:19.85:0.15 and the supernatant was combined with the phosphopeptide depleted sample. The phosphopeptides were eluted with 100 µL ACN:H_2O:NH_4OH (v/v/v) 50:49.3:0.7 twice (1 min vortex for each wash) and added to a tube which was pre-loaded with 50 µL of ACN:FA (v/v) 96:4. Both fractions were dried in a speed vacuum concentrator and stored in -80 °C until analysis [16].

Mass spectrometry

The Orbitrap Elite hybrid ion trap-Orbitrap mass spectrometer with NanoSpray Flex ion source (Thermo Scientific, Bremen, Germany) was used for data acquisition. The instrument was controlled with Tune Plus software (Thermo Scientific, Bremen, Germany). Spray voltage was set to be 0 kV and the capillary temperature was set to be 50 °C for all MAI acquisitions. *As MAI is a rapid sublimation process, the instrument parameters and file information (name and location) must be prepared before acquisition starts.* The gel loading tip with sample/matrix mixture was quickly approached to the inlet of ion transfer tube immediately after acquisition started. The acquisition was stopped after no visible analyte signal could be observed on the real time spectrum. Several acquisitions might be required to optimize instrument parameter. NanoESI data was acquired by direct infusing samples to the mass spectrometer at a rate of 0.3 µL/min. The spray voltage was set to be 1.9 kV and capillary temperature was 250 °C. All data on the Orbitrap Elite was acquired with resolution of 120,000 (*m/z* 400) with automatic gain control (AGC) target at 1e6 and maximum injection time at 300 ms. The normalized collision energies (NCE) of CID, HCD and the activation time for ETD were optimized for each sample and each charge state, which would be specified in the result. The resulting spectra were processed with XCalibur (Thermo Scientific, Bremen, Germany). The MS/MS spectra were compared with the theoretical mass list generated by MS-Product protein of ProteinProspector (UCSF Mass Spectrometry Facility, San Francisco, CA) and annotated manually.

In the comparison study, the MALDI and MAI (MALDI) spectra was acquired on MALDI-LTQ-Orbitrap XL mass spectrometer (Thermo Scientific, Bremen, Germany), which is also a hybrid ion-trap-Orbitrap mass spectrometer but with MALDI source. The instrument was controlled with Tune Plus software and the data was processed with Xcalibur software. The

MALDI-TOF full scan spectrum of histone mixture was acquired on UltrafleXtreme II MALDI TOF/TOF mass spectrometer (Bruker, Billerica, MA) with linear positive mode at *m/z* 3,000 – 30,000. Laser size was set at "4_large" and laser energy was set to be 80%. Ten thousand laser shots were accumulated. The resulting spectrum was processed with flexAnalysis to perform smooth and baseline subtraction.

Results and discussion

In this study, a HRAM MAI-MS platform was set up on the ESI-LTQ-Orbitrap (Orbitrap Elite) system with ETD module for high throughput top-down and bottom-up analyses of protein standards and mixtures. Detailed comparisons among four ionization techniques: MAI (ESI), MAI (MALDI), ESI and MALDI were performed for better understanding of their properties.

Instrument setup

The ESI-LTQ-Orbitrap (Orbitrap Elite) system was quickly switched to MAI-MS mode by simply remove the emitter tip holder on the Nanospray flex ion source (Figure 1). *The capillary temperature was set to be 50 °C and the voltage was set to be 0 kV.* If the system was used for ESI experiments before, an extra half-hour was required for the system to cool down. As the relationship between sublimation time, temperature and ion abundance were carefully examined and optimized in the study published by Woodall *et al.* [3], no further optimization was performed in this study. The capillary temperature of 50 °C was chosen as a good compromise of sensitivity and acquisition time. A 10 µL pipette with a gel loading pipette tip was used for sample introduction (Figure 1A). The matrix/analyte mixture (0.5 µL to 2 µL), which was crystalized on top of the pipette tip, was attached to the inlet of ion transfer tube for sample introduction (Figure 1 b&c). The matrix/analyte mixture was usually sublimated within 5 min (usually 30 sec) after attaching to the ion transfer tube. Due to the fast sublimation time of the

analyte, the instrument was prepared with all parameters entered and data acquisition turned on before sample introduction. The ion signal was monitored instantaneously on the Tune Plus software. The data acquisition was stopped after no ion signal could be observed.

HRAM MAI-MS full scan and MS/MS on standards and mixtures

HRAM MAI full MS analyses on the Orbitrap Elite platform were performed on both standards and mixtures. Neuropeptide Y, which is a mid-size peptide with molecular weight of 4269.08 Da, was detected with charge states from 3 to 7 (Figure 2a). The lower limit of detection (LLOD), which was determined by the lowest concentration detected with a signal to noise (S/N) ratio above 3, was tested to be 5 nM (5 fmol introduced). Intact protein standards, including cytochrome C (12360.97 Da, Figure 2b), lysozyme (14295.81, Figure 2c) and myoglobin (16952.30, Figure 2d) were also detected on the system with very spread out charge states. The LLODs of cytochrome C, lysozyme and myoglobin were determined to be 20.2 nM (20.2 fmol introduced), 75 pM (75 amol introduced) and 2.95 μM (2.95 pmol introduced) respectively. Myoglobin was by far the largest molecule detected on this instrument platform, which is consistent with the MAI study on MALDI-LTQ-Orbitrap system [8].

A comparison of MAI (ESI/Orbitrap Elite), MAI (MALDI-LTQ-Orbitrap), ESI (Orbitrap Elite) and MALDI (MALDI-LTQ-Orbitrap) ionizations was performed (Supplemental Figure 1). The sampling throughputs varied among these ionizations. The MAI (ESI) underwent a fast sublimation process and could achieve high-throughput analysis with approximately 1 min/sample. The MAI (MALDI) was also a fast sublimation process, but extended time periods were required for inserting and taking out plate as well as pumping down of the MALDI chamber. Therefore, it usually took approximately 10 min/sample on MAI (MALDI) system as

well as on MALDI system. Direct infusion based ESI analysis also required about 10 min/sample or even longer, as the fluid system needed to be flushed with solvent when switching samples to minimize sample carryover.

Lysozyme standard was used to compare the charge state, noise level and sensitivity of each ionization mode. MAI (ESI) produced the broadest charge state, from 8 to 17 (Supplemental Figure 1a); MAI (MALDI) and ESI produced the same charge states, from 8 to 12 (Supplemental Figure 1 b&c); no lysozyme ion could be detected by MALDI (Supplemental Figure 1d) as the molecular weight of lysozyme exceed the detection limit of the mass analyzer assuming only singly charged ion was produced. The MAI (MALDI) platform produced very high noise signal; MAI (ESI) produced less noise signal and the ESI had the least. The LLODs of MAI were determined to be 75 pM on the ESI/Orbitrap Elite platform and 175 nM on the MALDI-LTQ-Orbitrap platform. The significant differences of LLOD on these two platforms could be caused by the means of sample introduction and the differences in source pressure. On the ESI/Orbitrap Elite platform, the matrix/analyte mixture was directly attached to the inlet of the MS with no gap, allowing high transmission rate of the analyte into the instrument. Moreover, the matrix/analyte was stored at atmospheric pressure with a very slow sublimation rate before sample introduction, thus there was very little sample loss in the process. In contrast, on the MALDI-LTQ-Orbitrap system, the matrix/analyte was crystalized on the MALDI target plate, which was inserted into an intermediate vacuum chamber. Due to the gap between the MALDI target plate and the ion optics, there might be sample loss in this process. Moreover, when inserting the MALDI plate, the matrix/analyte was exposed to intermediate vacuum environment for a few minutes, which could stimulate the sublimation process before starting data acquisition.

Therefore, a significant difference in sensitivity between the MAI (ESI) and MAI (MALDI) platform was observed.

MAI-MS/MS analyses were performed using neuropeptide Y standard. Multiple fragmentation types, including CID, HCD and ETD, were compared and contrasted on the +6 charged neuropeptide precursor ion (Figure 3). The NCEs of CID and HCD as well as the activation time (ms) of ETD were optimized and labeled in the figure. The CID and HCD MS/MS spectra (Figure 3 a&b) revealed incomplete fragmentation. In contrast, the ETD MS/MS spectrum revealed nearly complete sequence coverage (Figure 3c). As annotated on the spectrum and on the sequence, most of the c and z ions were detected except for the ones next to a proline residue which could not be cleaved by ETD. From a mechanistic standpoint, the fragmentation of CID and HCD replies on randomized amide bond protonation, which is difficult to achieve for larger peptides as Arg residues tend to inhibit the random protonation. In contrast, the ETD process does not depend on amide bond protonation, which promotes random fragmentation along the peptide backbone and achieve high sequence coverage [13]. Therefore, the ETD module on the MAI-MS instrument platform significantly improved the sequence coverage of larger molecules, which made it applicable towards intact protein analysis.

The HRAM MAI-MS on the Orbitrap Elite system could also be used to analyze protein mixtures (Figure 4), such as histone mixture (Figure 4 a&b) and rat brain protein extract (Figure 4c). A full scan spectrum of histone mixture was acquired on the MALDI-TOF system with *m/z* 5,000-25,000 to show the relative abundance and mass of each histone molecule. In the MALDI-TOF spectrum, H_4 had the highest intensity, followed by H_{2a} and H_{2b}. A very small peak of H_3 was detected and no H_1 peak could be detected. Multiply charged histone molecules were detected on the MAI (ESI) platform: H_4 molecule was detected with charge states from 7 to 15;

H_{2a} was detected with charge state from 9 to 13 and H_{2b} was detected with charge states of 9 and 10. No H_1 and H_3 molecule was detected due to their low abundances. The same analyte was tested on the MAI (MALDI) platform, but no signal was detected (data not shown), presumably due to the lower sensitivity of the MAI (MALDI) platform. Rat brain protein extract was used as a complex sample to further test the MAI (ESI) system. Several high abundant proteins were detected in the mixture with various charge states, including thymosin beta-4 (a), ATP synthase-coupling factor (b), ubiquitin (c), Acyl-CoA binding protein (d), cytochrome C oxidase subunit 6b (e), mitochondria import inner membrane translocase (f), superoxidase dismutase [Cu-Zn] (g). The proteins were identified by accurate mass matching and a lot of multiply charged peaks in the spectrum were yet to be identified.

PTM analysis of glycopeptide and phosphopeptides

The characterization of labile PTMs, such as glycosylation and phosphorylation, has been a challenging field of MS research. The modification groups could be easily cleaved from the peptide backbone during the ionization or fragmentation process and become an unsolvable piece of puzzle for peptide mapping. Due to the softness of MAI, we anticipated that it could minimize in-source fragmentation. Our previous study demonstrated MAI's potential in analyzing labile PTM on the MALDI-LTQ-Orbitrap platform at full MS level: only a small peak corresponding to the doubly charged neutral loss ion was detected. However, the slow heating fragmentation techniques (CID and HCD) prevented us from further localizing the PTM groups on the peptide backbone, as most of them were cleaved first from the peptide backbone before breaking the peptide bonds [8].

This puzzle could be solved on the MAI-MS Orbitrap Elite platform with ETD module. A glycopeptide standard EPO (117-131) and a phosphopeptide standard UOM9 (phosphorylated PKC substrate) were tested on this system (Figure 5, Supplemental Figure 2 & 3). The HRAM MAI-MS full scan (Figure 5a) revealed most intact EPO peptides, with some singly and doubly charged neutral loss ions. No triply charged neutral loss ion was detected. The triply charged intact ion $[M+3H]^{3+}$ was selected for MS/MS analysis for structure elucidation and PTM localization. In the CID (Figure 5b) and HCD (Figure 5c) spectra, only a few b and y ions were detected and the GalNAc group was cleaved from most of the detected ions (except for y_7 and y_8 ions). The information acquired here was not sufficient to localize the GalNAc group. In contrast, all the theoretical c and z ions were detected in the ETD spectrum (Figure 5d) with the GalNAc group preserved, allowing accurate PTM localization. Similar trend was observed for phosphopeptide standard UOM9 (Supplemental Figure 2). Peptide with charge states from 2 to 5 were detected in the spectrum with no evident of neutral loss ion (Supplemental Figure 2a). Both CID and HCD had incomplete fragmentations with only a few b and y ions detected. In contrast to EPO, most of the phosphate groups were still preserved to the b and y ion after CID (Supplemental Figure 2b) and HCD (Supplemental Figure 2c) fragmentations, as the phosphate group is not as labile as the GalNAc group. In the ETD spectrum, all theoretical c and z ions were detected with phosphate group preserved, allowing accurately localizing the phosphorylation position (Supplemental Figure 2d).

A comparison among four ionization modes on analyzing the glycopeptide EPO was illustrated in Supplemental Figure 3. Neutral loss singly charged ion was detected in MAI (ESI), MAI (MALDI) and MALDI conditions. The neutral loss peaks became less intense with the charge state increased. The neutral loss peak was no long detectable for triply charged ion in

MAI (ESI) condition and for doubly charged ion in MAI (MALDI) condition. ESI had the best performance in preserving the GalNAc group, as neutral loss peaks could not be detected for any charge state.

To further test the potential of the HRAM MAI-MS system on bottom-up protein analysis, a phosphoprotein standard, alpha-casein, was enzymatically digested and IMAC enriched for phosphopeptide analysis (Figure 6). The phosphopeptide depleted fraction (Figure 6a) and the phosphopeptide enriched fraction (Figure 6b) were analyzed by MAI-MS. The peptides were identified and annotated by accurate mass matching. No phosphopeptide was detected in the phosphopeptide depleted fraction, while a lot of phosphopeptides were detected in the phosphopeptide enriched fraction.

Challenges

In this study, a HRAM MAI-MS platform was developed on the Orbitrap Elite system with ETD module for high throughput top-down and bottom-up analyses. Even though both full MS and MS/MS were successfully performed on this platform for both standards and complex tissue mixtures, several challenges remained. First of all, the matrix/analyte samples were usually sublimated within 5 min. This limited the researchers from performing long acquisitions, such as data dependent acquisitions or several parallel targeted MS/MS, which required pre-designed instrument methods. Secondly, although the MAI process does not require any high-energy process, such as high voltage and laser ablation, it still could not completely avoid in-source or post-source fragmentations for labile PTMs (Figure 5 and Supplemental Figure 3). We considered the strong dinitrogen discharge emission during the triboluminescent process could cause the dissociation of labile PTM groups during the MAI process. Thirdly, on-line coupling

MAI-MS with separation methods, such as capillary electrophoresis or liquid chromatography, could be challenging. This prevents the platform from performing in depth proteomics analysis from complex mixture. Lastly, comparing on MAI (MALDI), *in situ* tissue analysis on MAI (ESI) platform is challenging. Extending the sublimation time while preserving the performance of the MAI (ESI) platform will be the upcoming project.

Conclusion

A HRAM MAI-MS on the Orbitrap Elite platform was developed in this study. A volatile matrix, 3-NBN, was premixed with analyte and a gel loading pipette tip was used for sample introduction. The ionization process requires no voltage or laser and could be accomplished in a high throughput fashion (1 min/sample). Intact peptide, protein, protein mixture and tissue extract were analyzed on this system. Various dissociation types, including CID, HCD and ETD, were used for sequence elucidation. Labile PTM analyses of phosphopeptide and glycopeptide were achieved on this platform due to the softness of MAI and the coupling of ETD module. Compared to MAI (MALDI), the MAI (ESI) platform provides high sensitivity, better performance for protein mixture analysis and significantly higher throughput. Compared to direct infusion based ESI analysis on the same instrument, the MAI (ESI) platform has also significantly improved the throughput with reduced sample consumption and no worry of carrying over. Although challenges still exist, this instrument platform is a promising alternative to the conventional MALDI and ESI instrument platforms and could be beneficial for both bottom-up and top-down proteomics and biopharmaceutics analyses.

Acknowledgements

The authors would like to acknowledge Dr. Sarah Trimpin's laboratory at Wayne State University for the inspiration and Dr. Robert Thorne's laboratory at University of Wisconsin-

Madison for providing rat tissue samples. Dr. Xuefei Zhong, Dr. Xueqin Pang and Dr. Dustin Frost provided helpful discussion and assisted with instrument maintenance for this project. The instrument was purchased through the funding support from NIH S10 RR029531. This work was supported by NIH NIDDK R01DK071801 and NIMH 1R56MH110215. C.L. acknowledges an NIH-supported Chemistry Biology Interface Training Program Predoctoral Fellowship (grant number T32-GM008505) and an NSF Graduate Research Fellowship (DGE-1256259). L.L. acknowledges an H.I. Romnes Faculty Research Fellowship and a Vilas Distinguished Achievement Professorship with funding provided by the Wisconsin Alumni Research Foundation and University of Wisconsin-Madison School of Pharmacy.

References

[1] Trimpin, S., and Inutan, E. D. (2013) Matrix assisted ionization in vacuum, a sensitive and widely applicable ionization method for mass spectrometry, *J Am Soc Mass Spectrom 24*, 722-732.

[2] Inutan, E. D., and Trimpin, S. (2013) Matrix assisted ionization vacuum (MAIV), a new ionization method for biological materials analysis using mass spectrometry, *Mol. Cell. Proteomics 12*, 792-796.

[3] Woodall, D. W., Wang, B., Inutan, E. D., Narayan, S. B., and Trimpin, S. (2015) High-throughput characterization of small and large molecules using only a matrix and the vacuum of a mass spectrometer, *Anal Chem 87*, 4667-4674.

[4] Chen, B., Lietz, C. B., and Li, L. (2014) In Situ characterization of proteins using laserspray ionization on a high-performance MALDI-LTQ-Orbitrap mass spectrometer, *Journal of the American Society for Mass Spectrometry 25*, 2177-2180.

[5] Inutan, E. D., Richards, A. L., Wager-Miller, J., Mackie, K., McEwen, C. N., and Trimpin, S. (2011) Laserspray ionization, a new method for protein analysis directly from tissue at atmospheric pressure with ultrahigh mass resolution and electron transfer dissociation, *Mol. Cell. Proteomics 10*, M110 000760.

[6] Trimpin, S., Inutan, E. D., Herath, T. N., and McEwen, C. N. (2010) Laserspray ionization, a new atmospheric pressure MALDI method for producing highly charged gas-phase ions of peptides and proteins directly from solid solutions, *Mol. Cell. Proteomics 9*, 362-367.

[7] Devereaux, Z. J., Reynolds, C. A., Foley, C. D., Fischer, J. L., DeLeeuw, J. L., Wager-Miller, J., Narayan, S. B., Mackie, K., and Trimpin, S. (2016) Matrix-Assisted Ionization (MAI) on a Portable Mass Spectrometer: Analysis Directly from Biological and Synthetic Materials, *Anal Chem*.

[8] Chen, B., Lietz, C. B., OuYang, C., Zhong, X., Xu, M., and Li, L. (2016) Matrix-assisted ionization vacuum for protein detection, fragmentation and PTM analysis on a high resolution linear ion trap-orbitrap platform, *Analytica chimica acta 916*, 52-59.

[9] Wang, B., Tisdale, E., Trimpin, S., and Wilkins, C. L. (2014) Matrix-assisted ionization vacuum for high-resolution Fourier transform ion cyclotron resonance mass spectrometers, *Analytical chemistry 86*, 6792-6796.

[10] Chakrabarty, S., Pagnotti, V. S., Inutan, E. D., Trimpin, S., and McEwen, C. N. (2013) A new matrix assisted ionization method for the analysis of volatile and nonvolatile compounds by atmospheric probe mass spectrometry, *Journal of the American Society for Mass Spectrometry 24*, 1102-1107.

[11] Sweeting, L. M., Cashel, M. L., and Rosenblatt, M. M. (1992) Triboluminescence Spectra of Organic-Crystals Are Sensitive to Conditions of Acquisition, *J Lumin 52*, 281-291.

[12] Zubarev, R. A., Kelleher, N. L., and McLafferty, F. W. (1998) Electron capture dissociation of multiply charged protein cations. A nonergodic process, *Journal of the American Chemical Society 120*, 3265-3266.

[13] Syka, J. E., Coon, J. J., Schroeder, M. J., Shabanowitz, J., and Hunt, D. F. (2004) Peptide and protein sequence analysis by electron transfer dissociation mass spectrometry, *Proc Natl Acad Sci U S A 101*, 9528-9533.

[14] Kim, M. S., and Pandey, A. (2012) Electron transfer dissociation mass spectrometry in proteomics, *Proteomics 12*, 530-542.

[15] Michalski, A., Damoc, E., Lange, O., Denisov, E., Nolting, D., Muller, M., Viner, R., Schwartz, J., Remes, P., Belford, M., Dunyach, J. J., Cox, J., Horning, S., Mann, M., and Makarov, A. (2012) Ultra high resolution linear ion trap Orbitrap mass spectrometer (Orbitrap Elite) facilitates top down LC MS/MS and versatile peptide fragmentation modes, *Molecular & cellular proteomics : MCP 11*, O111 013698.

[16] Villen, J., and Gygi, S. P. (2008) The SCX/IMAC enrichment approach for global phosphorylation analysis by mass spectrometry, *Nature protocols 3*, 1630-1638.

Figure legends

Figure 1. **Instrument setup of MAI on Orbitrap-Elite platform with Nanospray flex ion source.** A 10 µL pipetted with a gel loading pipette tip was used for sample introduction. The gel loading tip was directly attached to the inlet of ion transfer tube which maximized sample transfer. a. Picture of the Nanospray flex ion source with pipette inserted for sample introduction. b. Zoom in image of gel loading pipette tip attached to the inlet of ion transfer tube. c. Picture of side camera showing the inlet of ion transfer tube.

Figure 2. HRAM full scan spectra of intact peptide and protein standards: 1.0 µM neuropeptide Y (a), 1.0 µM cytochrome C (b), 1.5 µM lysozyme (c) and 3.0 µM myoglobin (d). The molecular weight (M.W.) of each standard was shown in the figure. The *m/z* range of each spectra was chosen based on each sample in order to reveal all detected charge states.

Figure 3. MAI CID (a), HCD (b) and ETD (c) MS/MS spectra for +6 charged neuropeptide Y at *m/z* 712.86. The NCEs for CID and HCD as well as the reaction time for ETD were labeled in the figure. The sequence of neuropeptide Y was shown in each figure with the detected fragment ions labeled.

Figure 4. Full scan spectra of protein mixtures: MALDI-TOF spectrum of histone mixture, 10 mg/mL (a), HRAM MAI-Orbitrap spectrum of histone mixture, 1 mg/mL (b) and HRAM MAI-Orbitrap spectrum of rat brain protein extract. The masses of histone molecules (H1, H2a, H2b, H3 and H4) were listed in the figure. In the spectrum of rat brain extract, single letter code was used to annotate the spectrum. Each letter represents a single protein (identified by accurate mass matching): a: thymosin beta-4, b: ATP synthase-coupling factor, c: ubiquitin, d: Acyl-CoA binding protein, e: cytochrome C oxidase subunit 6b, f:

mitochondria import inner membrane translocase, g: superoxidase dismutase [Cu-Zn]. Usually, more than one charge states of one protein were observed in the spectrum.

Figure 5. MAI full MS (a), CID (b), HCD (c) and ETD (d) spectra of the glycopeptide EPO (117-131). The detected ion species on the full scan were annotated on the spectrum. The MS/MS analyses were all performed on the $[M+3H]^{3+}$ ions. NCEs or activation time were labeled on the figure. The detected fragments under each condition were annotated on the spectra and listed on the peptide sequence. The red letters represent the fragments with GalNAc group preserved, the blue letters represent the fragments with GalNAc group cleaved and the purple letters represent the fragments before GalNAc group.

Figure 6. HRAM MAI-MS detection of the tryptic digested alpha-casein after IMAC enrichment: (a) phosphopeptide-depleted fraction and (b) phosphopeptide enriched fraction. The spectra were annotated by accurate mass matching. The blue letters represent the peptide without phosphorylation and the red letters represent the peptide with phosphorylation.

Figures

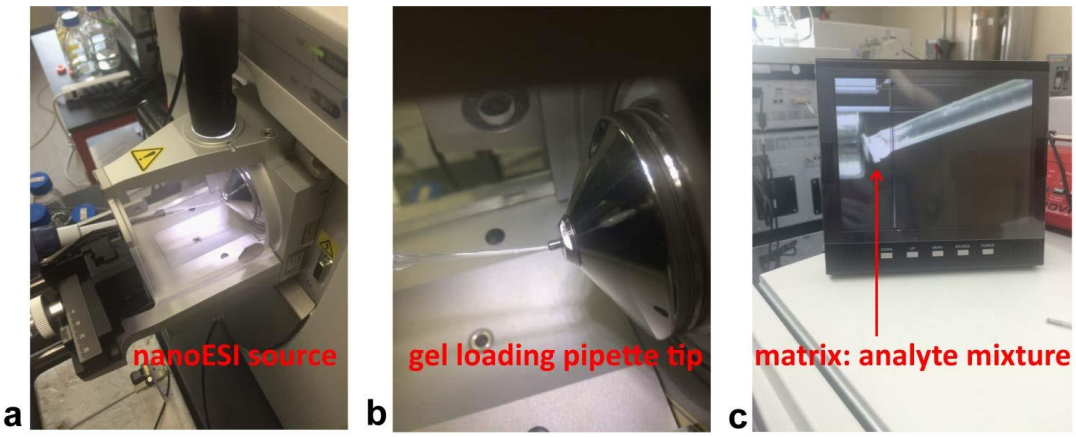

Figure 1

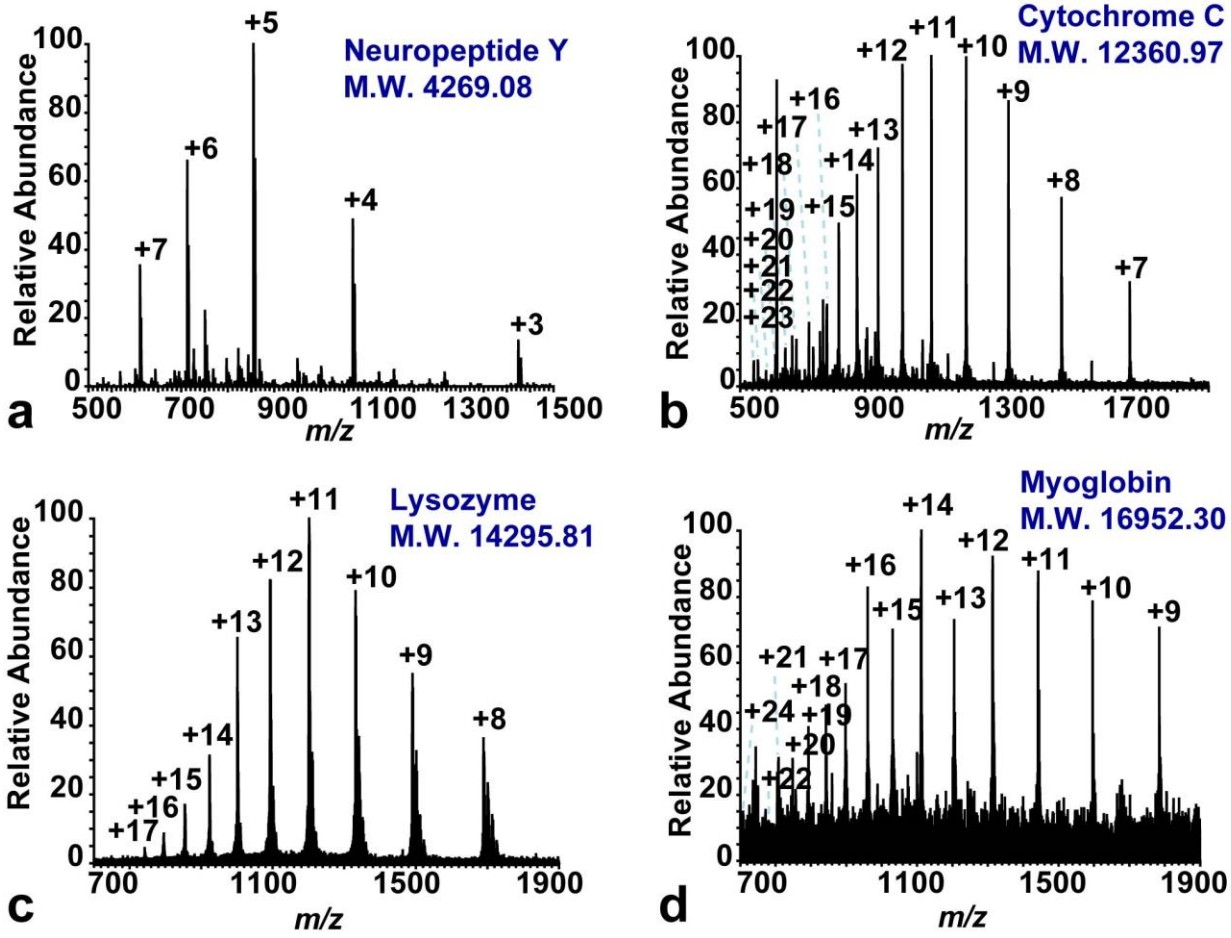
Neuropeptide Y
M.W. 4269.08
Cytochrome C
M.W. 12360.97
Lysozyme
M.W. 14295.81
Myoglobin
M.W. 16952.30
Relative Abundance
m/z
a
b
c
d

Figure 2

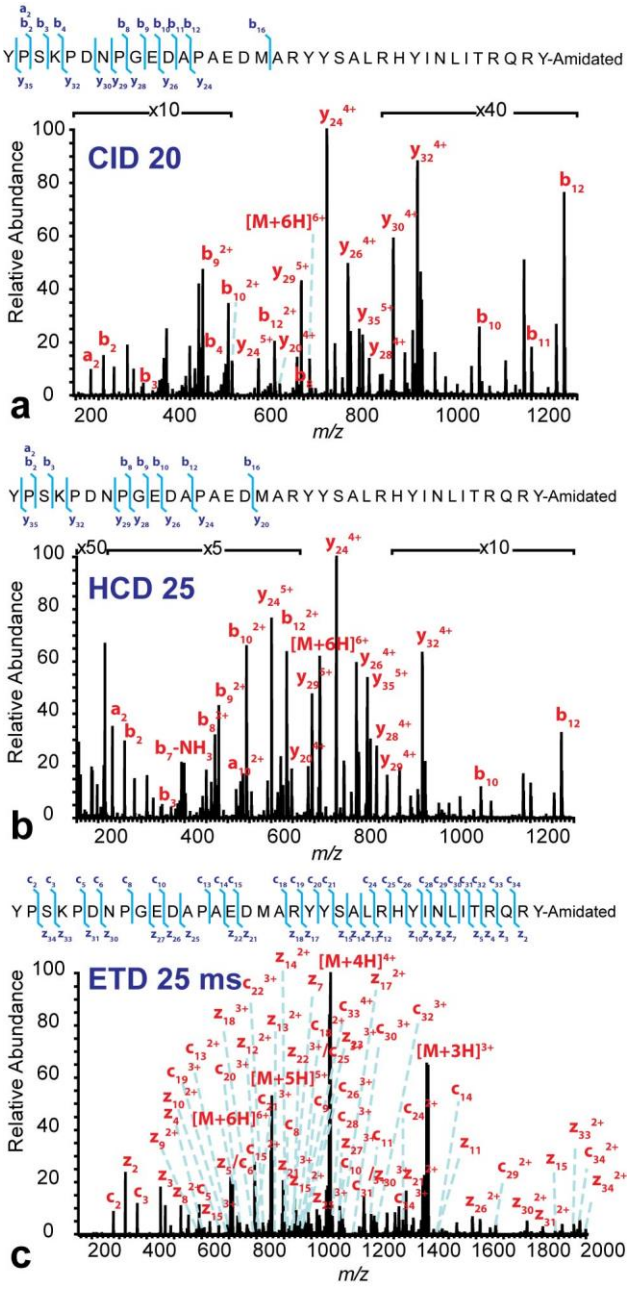
YPSKPDNPGEDAPAEDMARYYSALRHYINLITRQRY-Amidated
x10
x40
CID 20
Relative Abundance
m/z
a
YPSKPDNPGEDAPAEDMARYYSALRHYINLITRQRY-Amidated
x50
x5
x10
HCD 25
Relative Abundance
m/z
b
YPSKPDNPGEDAPAEDMARYYSALRHYINLITRQRY-Amidated
ETD 25 ms
[M+4H]4+
[M+3H]3+
[M+5H]5+
[M+6H]6+
Relative Abundance
m/z
c

Figure 3

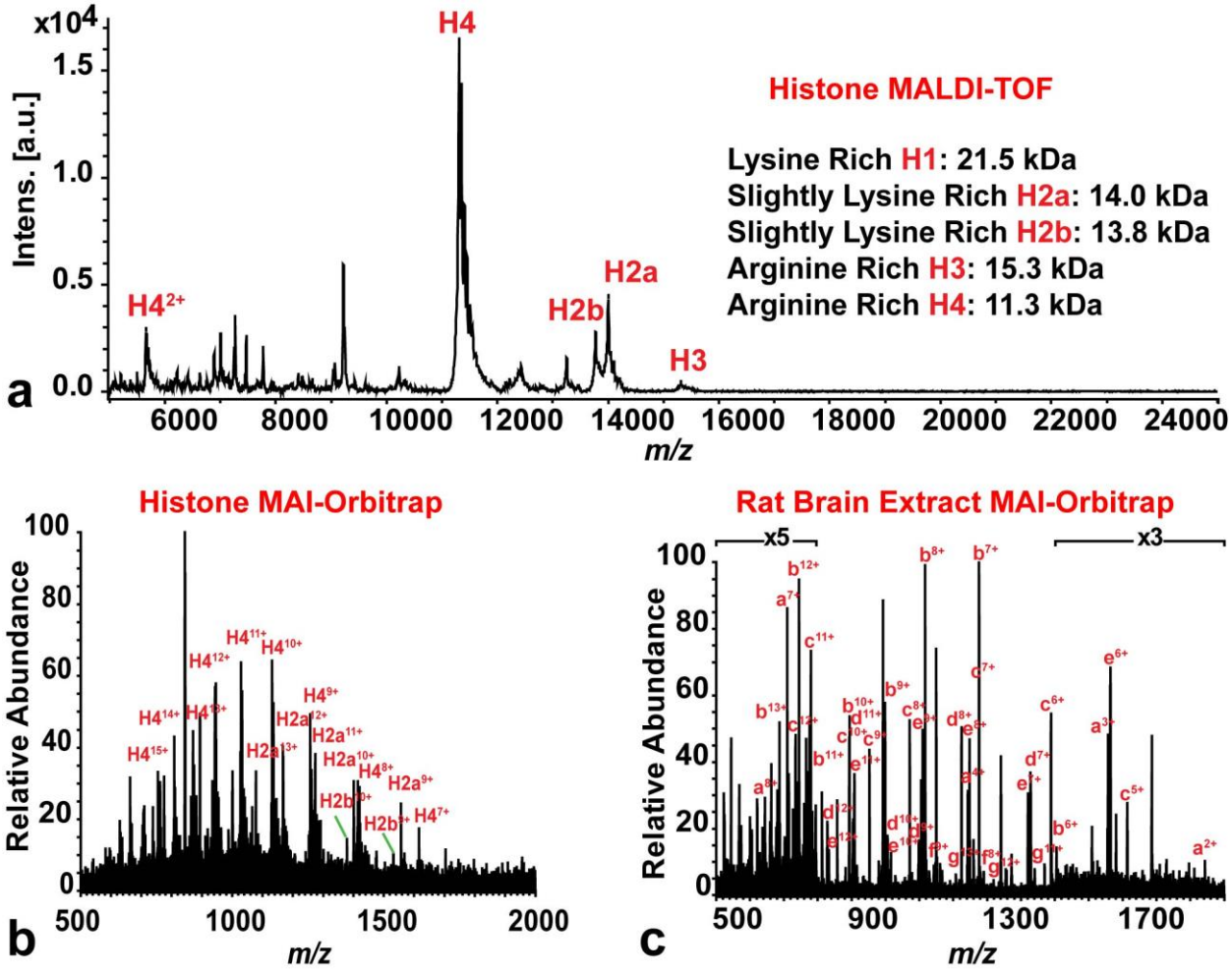
x10^4
Intens. [a.u.]
H4
H2a
H2b
H3
H4^2+
Histone MALDI-TOF
Lysine Rich H1: 21.5 kDa
Slightly Lysine Rich H2a: 14.0 kDa
Slightly Lysine Rich H2b: 13.8 kDa
Arginine Rich H3: 15.3 kDa
Arginine Rich H4: 11.3 kDa
m/z
a
Histone MAI-Orbitrap
Relative Abundance
m/z
b
Rat Brain Extract MAI-Orbitrap
x5
x3
Relative Abundance
m/z
c

Figure 4

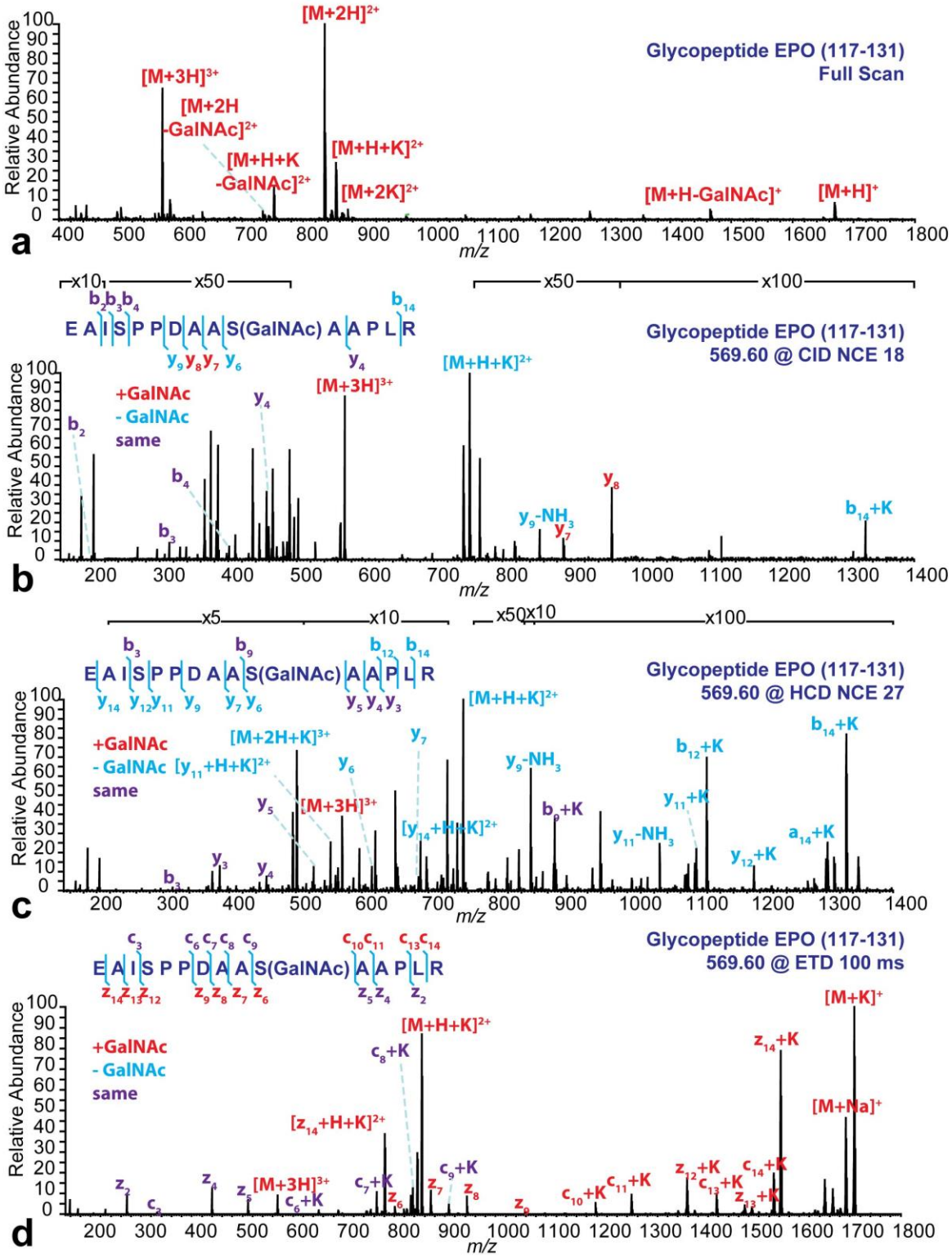
a
Glycopeptide EPO (117-131)
Full Scan
[M+2H]2+
[M+3H]3+
[M+2H -GalNAc]2+
[M+H+K -GalNAc]2+
[M+H+K]2+
[M+2K]2+
[M+H-GalNAc]+
[M+H]+
Relative Abundance
m/z
b
Glycopeptide EPO (117-131)
569.60 @ CID NCE 18
E A I S P P D A A S(GalNAc) A A P L R
+GalNAc
- GalNAc
same
[M+H+K]2+
[M+3H]3+
y9-NH3
b14+K
c
Glycopeptide EPO (117-131)
569.60 @ HCD NCE 27
[M+2H+K]3+
[y11+H+K]2+
[M+3H]3+
[y14+H+K]2+
y9-NH3
b9+K
y11-NH3
b14+K
a14+K
d
Glycopeptide EPO (117-131)
569.60 @ ETD 100 ms
[M+K]+
[M+H+K]2+
[z14+H+K]2+
[M+3H]3+
[M+Na]+

Figure 5

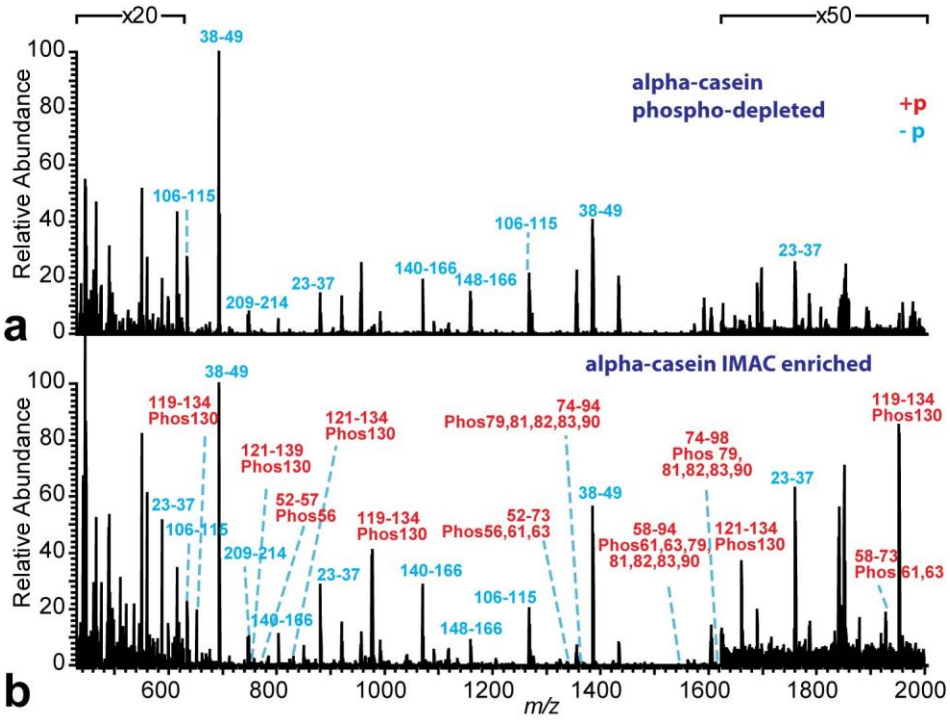
x20
x50
38-49
alpha-casein
phospho-depleted
+p
- p
Relative Abundance
106-115
106-115
38-49
23-37
140-166
148-166
209-214
23-37
a
alpha-casein IMAC enriched
38-49
119-134
Phos130
121-134
Phos130
74-94
Phos79,81,82,83,90
119-134
Phos130
121-139
Phos130
74-98
Phos 79,
81,82,83,90
23-37
38-49
23-37
52-57
Phos56
119-134
Phos130
52-73
Phos56,61,63
58-94
Phos61,63,79
81,82,83,90
121-134
Phos130
106-115
209-214
23-37
140-166
58-73
Phos61,63
106-115
140-166
148-166
b
600
800
1000
1200
1400
1600
1800
2000
m/z

Figure 6

Supporting information

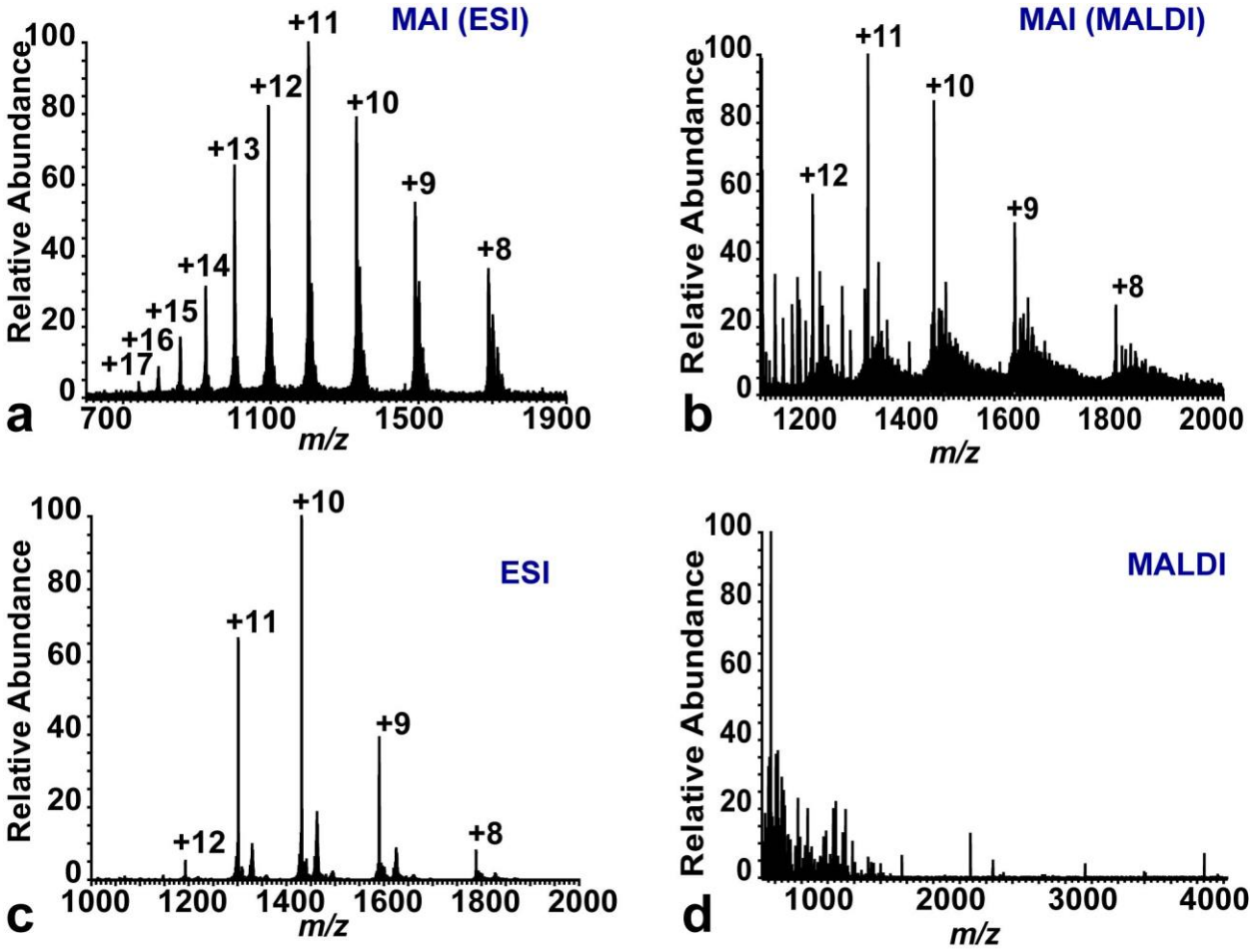

Supplemental Figure 1. Spectra comparison of lysozyme ionized by MAI (ESI) (a), MAI (MALDI) (b), ESI (c) and MALDI (d). The charge states were annotated on the spectra.

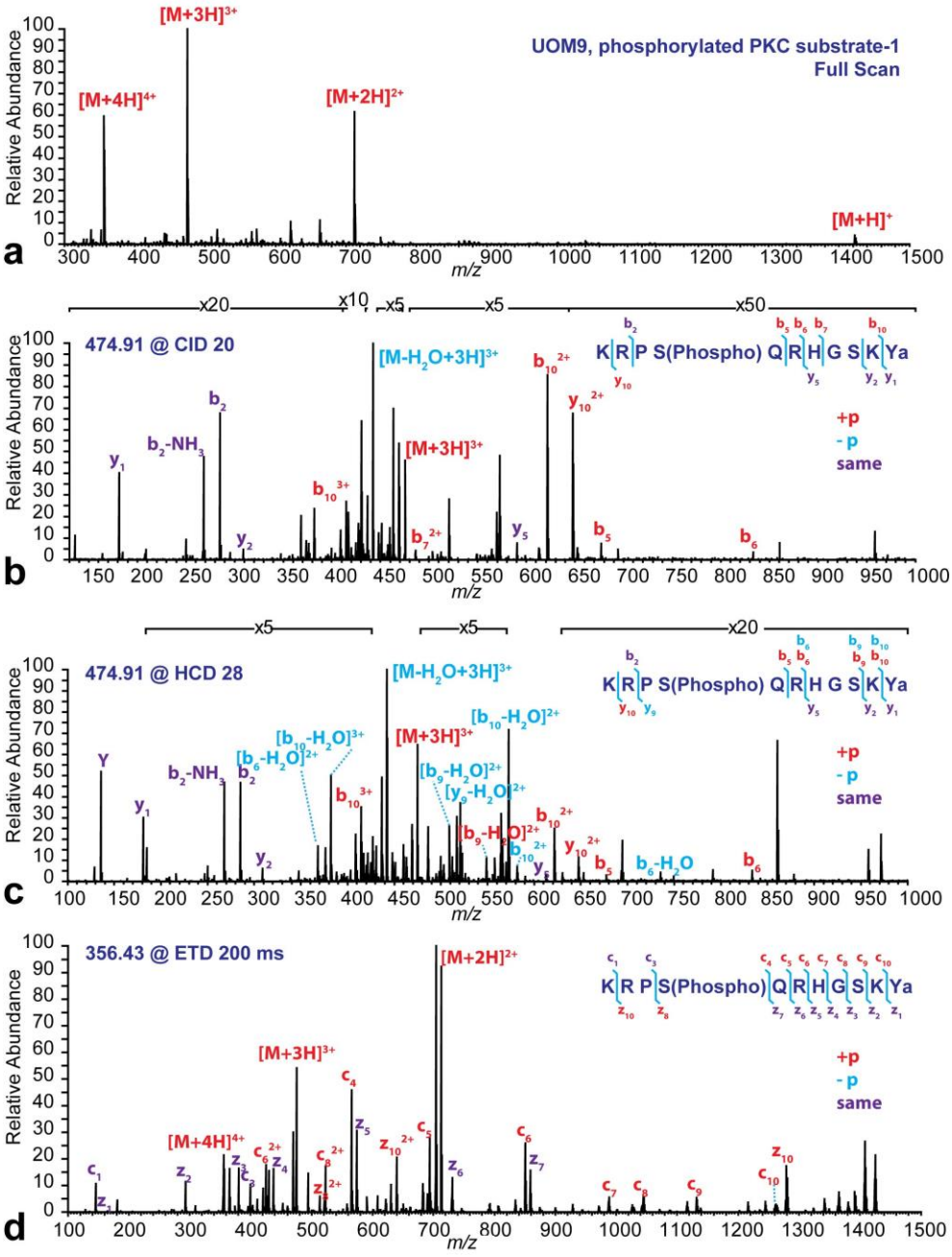

Supplemental Figure 2. MAI full MS (a), CID (b), HCD (c) and ETD (d) spectra of the phosphopeptide UOM9 (phosphorylated PKC substrate). The detected ion species on the full scan were annotated on the spectrum. NCEs or activation time were labeled on the figure. The detected fragments under each condition were annotated on the spectra and listed on the peptide sequence. The red letters represent the fragments with phosphate group preserved, the blue letters represent the fragments with phosphate group detached and the purple letters represent the fragments before phosphate group.

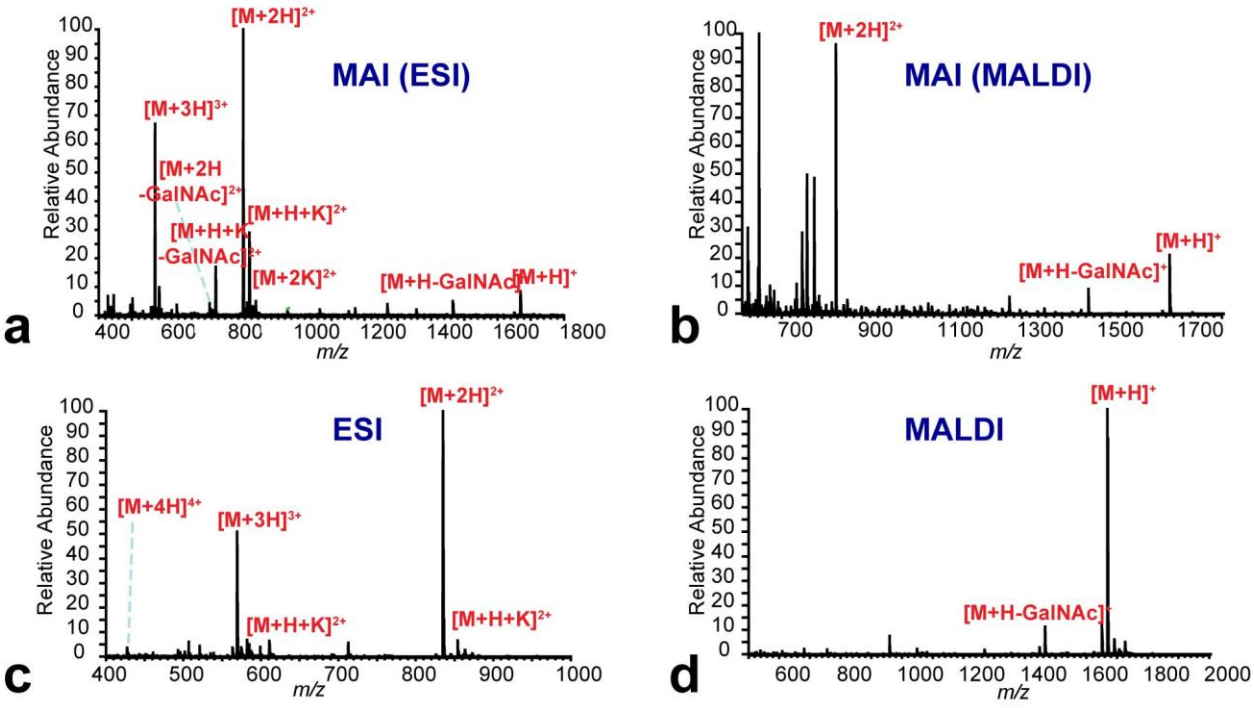

Supplemental Figure 3. Spectra comparison of glycopeptide EPO ionized by MAI (ESI) (a), MAI (MALDI) (b), ESI (c) and MALDI (d). The detected ion species were annotated on the spectra.

Chapter 5
High Throughput *in Situ* DDA Analysis of Neuropeptides by Coupling Novel Multiplex Mass Spectrometric Imaging with Gas Phase Fractionation

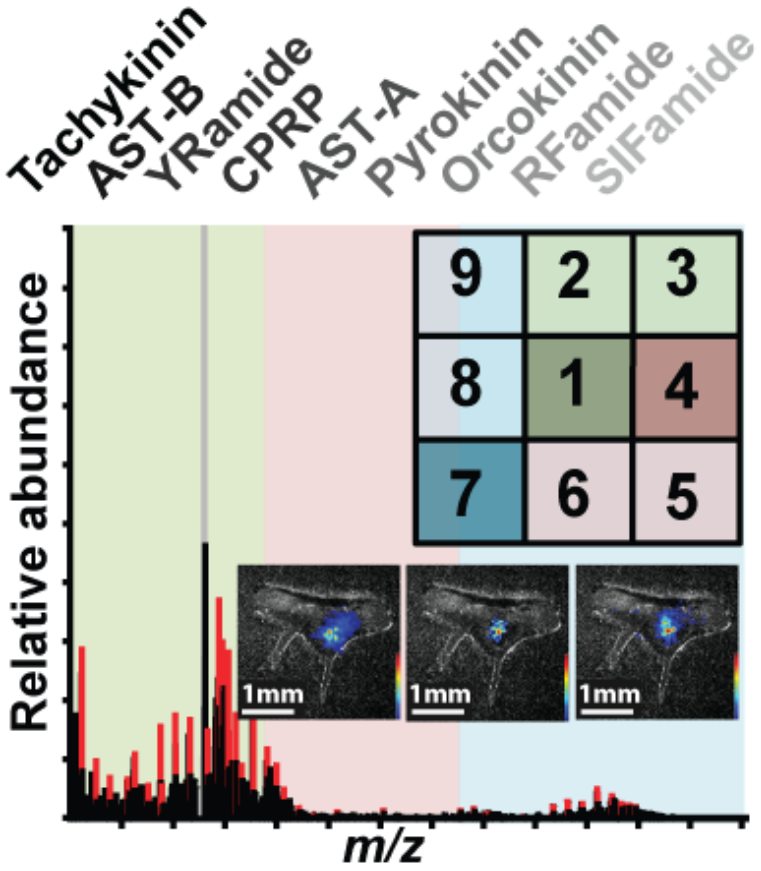

Adapted from **B. Chen**[#]**,** C. Ouyang[#] and L. Li (2015). High Throughput *In situ* DDA Analysis of Neuropeptides by Coupling Novel Multiplex Mass Spectrometric Imaging (MSI) with Gas-Phase Fractionation. *J. Am. Soc. Mass Spectrom.*, vol. 26 (12). p.1992-2001. Cover article ([#]Co-First authors)

Author contribution: study was designed by B. Chen, C. Ouyang and L. Li; experiment was performed by B. Chen and C. Ouyang; data was analyzed by B. Chen and C. Ouyang; manuscript was written by B. Chen, C. Ouyang and edited by L. Li.

Abstract

Matrix-assisted laser desorption/ionization (MALDI) mass spectrometric imaging (MSI) is a powerful tool to map the spatial distribution of biomolecules on tissue sections. Recent developments of hybrid MS instruments allow combination of different types of data acquisition by various mass analyzers into a single MSI analysis, which reduces experimental time and sample consumptions. Here, using the well-characterized crustacean nervous system as a test-bed, we explore the utility of high resolution and accurate mass (HRAM) MALDI Orbitrap platform for enhanced *in situ* characterization of the neuropeptidome with improved chemical information. Specifically, we report on a multiplex-MSI method, which combines HRAM MSI with data dependent acquisition (DDA) tandem MS analysis in a single experiment. This method enables simultaneous mapping of neuropeptide distribution, sequence validation and novel neuropeptide discovery in crustacean neuronal tissues. To enhance the dynamic range and efficiency of *in situ* DDA, we introduced a novel approach of fractionating full *m/z* range into several sub-mass ranges and embedding the setup using the multiplex-DDA-MSI scan events to generate pseudo fractionation before MS/MS scans. The division of entire *m/z* into multiple segments of *m/z* sub-ranges for MS interrogation greatly decreased the complexity of molecular species from tissue samples and the heterogeneity of the distribution and variation of intensities of *m/z* peaks. By carefully optimizing the experimental conditions such as the dynamic exclusion, the multiplex-DDA-MSI approach demonstrates better performance with broader precursor coverage, less biased MS/MS scans towards high abundance molecules and improved quality of tandem mass spectra for low intensity molecular species.

Key words: MALDI MS imaging, multiplex MS imaging, HRAM, neuropeptide, peptidomics, crustacean nervous system.

Introduction

Since its introduction in 1997, MALDI MSI has become one of the most powerful tools for mapping the spatial distributions of *in situ* biomolecules in tissue samples.[1] MALDI MSI experiment generates ion density maps of thousands of biomolecules by acquiring mass spectra based on a predefined Cartesian grid. It has been increasingly utilized to study proteins, peptides, lipids, and small molecules for neuroscience studies,[2-5] drug development and characterization,[6-10] biomarker discoveries,[11, 12] clinical diagnostics[13] and many other research areas. Moreover, novel ionization techniques have been developed for MSI to improved MSI performances, such as desorption electrospray ionization (DESI),[14-16] nanostructure initiator mass spectrometry (NIMS) [17, 18], matrix-assisted laser desorption electrospray ionization (MALDESI),[19] silver-assisted laser desorption ionization (LDI)[20] and laserspray ionization (LSI). [21, 22]

While MALDI MSI has undergone rapid development for nearly two decades, *in situ* biomolecule identification remains to be a major challenge in MALDI MSI studies. While putative identifications can be made by accurate mass matching, more confident identification relies on MS/MS fragmentation. *In situ* MS/MS experiments usually suffer from poor fragmentation efficiency caused by the low analyte abundance and complex biological context on the matrix coated tissue sections. Moreover, the limited fragmentation capability of most MALDI-TOF instruments prevents *in situ* MS/MS from achieving high efficiency and complete sequence coverage. In many tissue MSI studies, parallel LC-MS/MS experiments were performed using tissue homogenates for biomolecule identification.[11, 23]

The development of MALDI-LTQ-Orbitrap XL hybrid mass spectrometer has revolutionized MALDI-MS analysis by combining an HRAM orbitrap with a fast scanning linear ion trap. This instrument can perform both collisional induced dissociation (CID) in the linear ion

trap and high-energy collision dissociation (HCD) in the HCD cell, which provides flexibility to the MS/MS experiments.[24, 25] Furthermore, MALDI-LTQ-Orbitrap XL is capable of performing data-dependent acquisition (DDA) experiments to fragment top N ions after a full MS scan, which enables simultaneous high throughput distribution mapping and biomolecule identity verifying in complex samples. With the newly developed LSI and matrix assisted ionization vacuum (MAIV), MALDI-LTQ-Orbitrap XL can also be used in protein characterization and imaging.[21, 22, 26]

The MALDI-LTQ-Orbitrap XL is an ideal instrument for multiplex MSI, a concept first introduced by the Lee lab to reduce data acquisition time, increase throughput and improve chemical information in MSI experiments.[27] Depending on the goal of each experiment, different scan combinations can be used in a multiplex experiment. For example, orbitrap and ion trap scans can be combined to reduce instrument time and improve spatial resolution;[27] full MS and MS/MS scans can be combined to map biomolecule distribution while elucidating structures of targeted biomolecules;[28] positive and negative ion mode scans can be combined to provide more chemical information.[29] It has been proven that multiplex MSI is a powerful tool in small molecule and lipid studies.

Decapod crustaceans have been utilized as model organisms to elucidate the function of neuropeptides in various physiological processes.[30-34] Their central nervous system (CNS) and stomatogastric nervous system (STNS) have been extensively studied as expedient models for investigating the generation,[32] and modulation of rhythmic behavior[33] as well as regulatory roles of neuropeptides in food intake.[34] The neural circuits in their nervous system capable of producing motor patterns are extensively modulated by a collection of neuropeptides. The STNS is composed of several major neuronal ganglia, including the stomatogastric ganglion (STG), the paired commissural ganglia (CoG), the esophageal ganglion (OG) and other connecting nerves. The

crustacean brain connects with the STNS via inferior ventricular nerve while each of the paired circumesophageal commissures connects to a CoG.

Herein, we adapted the idea of multiplex MSI to study the neuropeptides in the crustacean nervous system by multiplex-DDA-MSI approach. The combination of full MS scan with DDA scans in one run allows high-throughput MSI analysis, which shortens the acquisition time by half in comparison to performing full MS and DDA analysis in two separate acquisitions. Moreover, a novel strategy of fractionating *m/z* range coupled with DDA method was developed to analyze complex tissue samples with pseudo mass fractionation on the MALDI-LTQ-Orbitrap XL platform.

Materials and methods

Materials

All reagents were used without additional purification. Methanol, acetic acid and formic acid (FA) were purchased from Fisher Scientific (Pittsburgh, PA). 2, 5-dihydroxybenzoic acid (DHB) was purchased from Acros Organics (Morris Plains, NJ). Microscope glass slides were purchased from VWR international, LLC (Radnor, PA). Physiological saline was composed of 440 mM NaCl, 26 mM $MgCl_2$, 13 mM $CaCl_2$, 11 mM KCl, 10 mM HEPES acid with pH value adjusted to 7.4 - 7.5. Distilled water mentioned in this work was Milli-Q water from a Millipore filtration system (Bedford, MA, USA).

Animal experiment

Animal experiments were operated following institutional guidelines (University of Wisconsin-Madison IACUC). Rock crabs, *Cancer irroratus*, of similar size were purchased from Ocean Resources Inc. (Sedgwick, ME, USA). Blue crabs, *Callinectes sapidus*, were purchased from local seafood market. Animals were maintained for at least a week in a flow-through artificial

seawater aquarium at ambient seawater temperature (12-13 ˚C) before use. Prior to dissection, animals were cold anesthetized by packing on ice for 20 minutes. Micro dissection was performed in chilled physiological saline. Supraesophageal ganglia (brain) and CoGs of crabs were harvested according to previously described dissection procedure [35].

MSI sample preparation

Tissue was embedded into gelatin solution (100 mg/mL in MilliQ water) and snap frozen on dry ice after dissection. The completely frozen tissue was sectioned into 12 µm slices on a cryostat (Thermo Scientific Microm HM 525) at -20 ˚C and thaw mounted onto a microscope glass slide (75x25x1 mm). The glass slide was dried in a desiccator at room temperature for 30 minutes before matrix application. DHB (50:50 methanol:water, vol:vol) was applied onto the tissue surface by a robotic TM sprayer (HTX Technologies, Carrboro, NC) for homogeneous matrix deposition. The nozzle temperature of the TM sprayer was set to be 80 ˚C with a moving velocity of 1000 mm/min. 10 passes of matrix was deposited with a flow rate of 0.25 mL/min and 30 seconds drying time between each pass. The slide was dried at room temperature after matrix application and stored in a desiccator in -80 ˚C until analysis.

MSI data acquisition

All MS experiments were performed on a MALDI-LTQ-Orbitrap XL mass spectrometer (Thermo Scientific, Bremen, Germany) equipped with 60 Hz 337 nm N_2 laser. Full scan mass resolution of 60,000 (at *m/z* 400), laser energy of 18 µJ and microscans of 4 were used for all analyses. MS/MS were performed in HCD mode with normalized collision energies of 45 and isolation window of 3 *m/z* (unless otherwise stated). Monoisotopic precursor selection was enabled. Different dynamic exclusion durations were tested and optimized. The multiplex MS imaging

method was set up in Xcalibur software (Thermo Scientific, Bremen, Germany) and the imaging position file was defined in TunePlus software (Thermo Scientific, Bremen, Germany).

4-step linear-DDA-MSI and multiplex-DDA-MSI on crab brain tissue sections. Two DDA-MSI experiments were performed to compare the influence of multiplexing on DDA-MSI of neuropeptide analysis using crustacean brain tissue sections. Four scan events were defined, with scan 1 as full MS scan and scans 2, 3 and 4 as data dependent MS/MS scans. A raster step size of 50 μm was used for linear-DDA-MSI and a raster step size of 100 μm with spiral step size of 50 μm was used for multiplex-DDA-MSI.

9-step targeted multiplex-MSI on CoG tissue sections. A 9-step multiplex-MSI experiment was performed on CoG tissue sections. Nine scan events were defined: scan 1 was a full MS scan and scans 2-9 were targeted MS/MS scans of highly abundant neuropeptides observed in full MS scans. The precursor ions used for targeted MS/MS in steps 2-9 were listed in Table 1. The targeted MS/MS spectra were acquired in the linear ion trap with CID fragmentation at normalized collisional energy of 35. A raster step size of 150 μm and spiral step size of 50 μm were used.

Step #	***m/z***	**Sequence**
1	Full scan	-
2	649.367	RYLPT
3	844.479	HL/IGSL/IYRamide
4	905.514	PSMRLRFamide

5	934.493	APSGFLGMRamide
6	1186.516	FDAFTTGFGHS
7	1198.549	NFDEIDRSGFamide
8	1204.559	TSWGKFQGSWamide+Na^+
9	1381.738	GYRKPPFNGSIFamide

Table 1. Precursor ion list for targeted multiplex-MSI on blue crab CoG tissue section.

9-step multiplex-DDA-MSI on brain tissue sections. Figure 1 illustrates the 9-step multiplex-DDA-MSI experimental set up on crab brain tissue section: each raster step of traditional MSI experiment is separated into 9 sub-steps or spiral steps. The number indicated the sequence of spiral plate movement. Steps 1, 4 and 7 were full MS scans at *m/z* ranges of 500-840, 840-1190 and 1190-1750, respectively. Steps 2/3, 5/6 and 8/9 were data dependent MS/MS scans of the top 2 most abundant ions detected in the previous full MS scans. The raster step size was 150 µm (i.e. step 1 to 1) and the spiral step size was 50 µm (i.e. step 1 to 2). The exact mass fractions for full MS scans and MS/MS scans could be varied for different tissue sections. The spatial distributions of biomolecules were assembled from each step 1, 4 or 7, while the identities of biomolecules were confirmed by MS/MS scans in steps 2/3, 5/6 or 8/9.

Data analysis

Xcalibur software was used for spectrum processing. MSiReader (North Carolina State University, NC)[36] and ImageQuest (Thermo Scientific, Bremen, Germany) were used for MS

image data processing. PEAKS DB (Bioinformatics Solution Inc, ON, Canada) was used for database searching.

Results and discussion

MALDI MSI is a powerful tool to study the distribution of *in situ* biomolecules in various tissue samples. With the development of multiplex MSI by the Lee lab [27], more chemical information can be acquired with reduced instrument time and less amount of samples. DDA analysis on the LC-ESI-MS platform is often more powerful in peptide and protein identification than on the MALDI-MSI platform primarily due to the separation provided by LC before ESI-MS and the inherent more efficient fragmentation generated by multiply charged ions. However, MALDI-MSI grants the opportunity to investigate the chemical information directly in tissue with much less sample tampering in comparison to liquid phase sample preparation needed for LC. In this study, we adapted the concept of multiplex MSI on the MALDI-LTQ-Orbitrap XL platform with the goal to generate enhanced chemical information with limited sample amount. Utilizing the neuronal tissues from crustacean as a biological model system, a superior multiplex-DDA-MSI methodology was developed. By combining full MS with DDA in one analysis, the acquisition time was shortened by half compared to performing full MS and DDA in two separate acquisitions, increasing the throughput of MSI analysis. In addition to traditional DDA experiments, we introduced an approach to fractionating the full *m/z* range into specific narrower sub-ranges and incorporating them into our multiplex-DDA-MSI setup. To achieve relatively even distribution of both peak number and peak intensity within each *m/z* sub-ranges, the original full MS scan was carefully tailored. Taking advantage of this pseudo fractionation strategy prior to DDA scans, we mimicked the separation process to make the precursor selection for MS/MS scans less biased and more efficient compared to the conventional DDA setup in MALDI-MSI.

Comparison between linear-DDA-MSI and multiplex-DDA-MSI. To compare the results from traditional DDA MSI (linear-DDA-MSI) with those from multiplex-DDA-MSI, two MSI experiments were performed with linear or multiplex-DDA-MSI on two consecutive crab brain tissue sections (Figure 2). Four scan events were set up with Step 1 as a full scan and Steps 2-4 as top 3 DDA scans for both experiments. A raster step size of 50 µm was used for linear-DDA-MSI (Figure 2a) and a raster step size of 100 µm with spiral step size of 50 µm was used for multiplex-DDA-MSI (Figure 2b). The distribution image of Total Ion Count (TIC) from MSI of linear-DDA-MSI (Figure 2c) appeared in a discontinued zigzag pattern, as only one out of four raster spots had the full MS scan information. In contrast, the TIC distribution image of multiplex-DDA-MSI (Figure 2d) displayed a continuous pattern with signals being distributed throughout the tissue, as the full MS scan information was available for every raster scan. In addition to the continuity of ion signals over the entire tissue, higher signal intensity on the olfactory and accessory lobes than the surrounding tissue also effectively demonstrated the variation of biomolecule abundances in different parts of the brain. The heterogeneous intensity distribution was not readily observed from the MSI image in the linear-DDA-MSI, as the isolated spots failed to produce signals representing the actual biomolecule concentrations in the remaining 3/4 of the tissue area where full scans were not acquired.

Furthermore, due to the heterogeneity of tissue surface, the neuropeptide species and abundance can be significantly different from spot to spot. For linear-DDA-MSI, the DDA scans were 50 µm (Step 2), 100 µm (Step 3), and 150 µm (Step 4) away from the full MS scan. The biochemical content in Step 3 or 4 may not be exactly the same as in Step 1 (full scan), which could lead to lower MS/MS quality of the DDA scans. In contrast, all DDA scans were 50 µm

away from the full MS scan in multiplex-DDA-MSI mode, which more accurately represents the chemical information of the full MS scan.

To further demonstrate the advantages and unique features of multiplex-DDA-MSI, comparisons of peptides (HL/IGSL/IYRamide, *m/z* 844.4788 and VSHNNFLRFamide, *m/z* 1132.6010) for linear- and multiplex-DDA MSI conditions are shown in Figure 2. As shown in Figure 2e and 2g, only a few discrete spots were observed in the linear-DDA-MSI for both peptides as a result of the limited amount of full MS raster spots; while continuous distributions of both peptide ions were observed in the multiplex-DDA-MSI (Figure 2f and 2h). The identity of the first peptide (*m/z* 844.4788*)* was assigned by both accurate mass matching and DDA MS/MS results, while the identity of the second peptide (*m/z* 1132.6010) was assigned by accurate mass matching only. No DDA MS/MS scan was acquired for the second peptide due to its low intensity in the full MS scans. Most of the precursor ions selected for MS/MS were from the lipid rich *m/z* range, where neuropeptides with lower intensity could not be selected. A fractionated mass range DDA method could significantly improve the precursor ion selection for lower intensity ions.

As shown, the traditional MSI is less compatible with DDA experiment because DDA scans sacrifice spatial resolutions for acquiring data dependent MS/MS scans. Nonetheless, multiplex-DDA-MSI acquires full MS scan in every raster position and simultaneously obtains data dependent MS/MS scans in subsequent spiral steps within the same raster step. This setup allows the image production of a more continuous distribution of neuropeptides on tissue surface while obtaining the MS/MS information to confirm the peptide sequences and identities.

The application of multiplex MSI for mapping neuropeptides in the CoG in blue crabs. To investigate the feasibility of applying the multiplex-MSI method to crustacean tissue, we

performed experiments using the CoG isolated from the blue crab *C. sapidus*, which is a pair of neuronal ganglia that connect the CNS to the STNS in crustacean. Although previous study showed the presence of various neuropeptides in the CoG [37], the amount of neuropeptides in this minute size cellular cluster (typically ~ 500 μm in diameter) is much lower than in other bigger tissues such as the brain or the pericardial organ. In an MSI experiment, a 12 μm-thick section only contains about 1/40 of a single CoG ganglion. Using a multiplex-MSI setup containing 9 spiral steps, a full MS spectrum was acquired followed by eight MS/MS scans in every raster step. Due to the low abundance of analytes in the CoG and the instrument configuration, shorter travelling distance to the ion trap than to the HCD cell [24] is advantageous in preserving more precursor ions, which produces better quality MS/MS spectra when using CID fragmentation.

As a result of the HRAM measurement in full MS scans, 41 neuropeptides were putatively identified by accurate mass matching to our crustacean neuropeptide database [38], among which 18 were identified in the CoG for the first time. As shown in Figure 3a, 38 of the 41 matches were highlighted in color coding with corresponding neuropeptide families in the zoom-in *m/z* range of 800-1600. However, due to the complex tissue context, signals from neuropeptides were masked by higher intensity peaks (such as lipids, protein fragments and matrix etc.) when multiplex-DDA-MSI were adopted to confirm their identities. In order to obtain high quality MS/MS information to confidently identify the neuropeptides, a target list was generated and built in steps 2 to 8 in the 9-step-multiplex-MSI experiment. Figures 3b-3e are representative MS/MS spectra and distribution patterns of neuropeptides (overlaid with optical image) from 4 different neuropeptide families: tachykinin (Figure 3b), orcomyotropin (Figure 3c), SIFamide (Figure 3d) and orcokinin (Figure 3e). The sequence-specific b- and y-ions along with some internal fragment ions were produced with high abundance enabling good sequence coverage.

Although we demonstrated that simultaneous identification and distribution mapping were accomplished using targeted multiplex-MSI setup, this targeted method was not efficient enough for complex samples with more chemical information to be validated. Data dependent acquisition in MSI is still of great importance. Therefore, we performed further method development with multiplex-DDA-MSI using more complex tissue samples.

Comparison between regular DDA and fractionated mass range DDA in multiplex-DDA-MSI. While the multiplex-DDA-MSI has improved the throughput of MSI experiment by acquiring distribution and identity of biomolecules in one analysis, it has some drawbacks. Most precursor ions selected for data dependent MS/MS scans were from the lipid rich mass ranges (*m/z* 500-840 and *m/z* 1400-1600). Very few neuropeptide ions were selected due to their relatively lower intensities compared to the abundant lipid ions. To circumvent this problem, a fraction mass DDA setup was developed to improve the multiplex-DDA-MSI method. The full mass range of *m/z* 500-1750 was divided into three fractions: *m/z* 500-840 (fraction 1), *m/z* 840-1190 (fraction 2) and *m/z* 1190-1750 (fraction 3). The *m*/z ranges of these fractions were determined by inspecting a profiling full MS scan and evenly dividing up the number of the analytes of interest into three fractions. Each fraction contained approximately 35-40 peaks for subsequent MS/MS analyses. In this more evenly fractionated mass-range DDA method, top 2 most abundant ions were selected for MS/MS within each mass range window. Since the dynamic exclusion for DDA is a global setting for all of the scan events, using similar number of target peaks to fractionate the full MS spectrum enabled an un-biased precursor selection across the entire *m/z* range. Fraction 1 was a complex mixture of matrix derived peaks, small neuropeptides and lipids while dominated by high abundance lipid species. The peak density and intensities in fraction 2 were much lower than in fraction 1. The rich neuropeptide information contained in fraction 2 was better separated from fraction 1 to achieve a

less biased DDA setting for these low intensity species. Fraction 3 was a mixture of lipids and larger neuropeptides which had relatively higher signal intensities than the ions in fraction 2.

Interestingly, the number of peaks having MS/MS acquired in fraction 2 was lower than our expectation. It was noted that the peak intensities in *m/z* 840-920 were significantly higher than the rest of the analytes in fraction 2, which could lead to more biased MS/MS events for high abundant species, leaving these low intensity peptide peaks not selected for MS/MS scans in this *m/z* sub-range. To further optimize the performance of this fractionated mass DDA method, the profiling spectrum was re-evaluated and divided into the following segments: *m/z* 500-920 (fraction 1), *m/z* 920-1430 (fraction 2) and *m/z* 1430-1750 (fraction 3). Although the number of peaks differs from region to region, the signal intensities of the peaks within each fraction were more comparable. To accommodate these unevenly fractionated sub mass ranges, differential DDA setup was implemented. Top 3 most abundant ions were selected for MS/MS experiments from fraction 1, top 2 most abundant ions were selected from fraction 2, and top 1 most abundant ion was selected from fraction 3.

Figure 4 compares these three multiplex-DDA-MSI methods (regular multiplex-DDA-MSI, evenly fractionated mass multiplex-DDA-MSI and unevenly fractionated mass multiplex-DDA-MSI) from the brain tissue of blue crab *C. sapidus*. The number of precursor ions selected within each mass fraction window was compared in Figure 4a. As expected, in a regular DDA method without mass fractionation, most precursor ions selected for MS/MS were from mass fraction 1. Only a few ions were selected for MS/MS in mass fraction 2 and fraction 3. For the evenly fractionated mass DDA method, similar numbers of precursor ions were selected in each mass fractions. Much fewer peaks were selected in the lipid rich fraction 1 and many more peaks were selected in the neuropeptide rich fraction 2 and fraction 3 than the regular DDA method. The

unevenly fractionated mass DDA method further improves the number of peaks selected for MS/MS in each mass region. Figure 4b and 4c compared the spectra of regular DDA (Figure 4b) and fractionated mass DDA (Figure 4c). The precursor ions selected for MS/MS were highlighted in red and the precursor ions excluded for MS/MS were in grey. Peaks in black were not chosen by the instrument to perform MS/MS scans. Most peaks in the lipid rich mass range were selected for MS/MS in the regular DDA method, while only a few peaks were selected in the neuropeptide rich region (zoomed in spectrum). In contrast, significantly more peaks in the neuropeptide rich mass range (zoomed in spectrum) were selected for MS/MS under the fractionated mass DDA condition, which provides more useful peptide sequence information and greater peptidome coverage compared to conventional DDA condition.

By accurate mass matching to the custom-built crustacean neuropeptide database, 120 neuropeptides were putatively identified. 89 of the matches displayed on-tissue distribution overlapping with the neuronal clusters in the brain, which improves the confidence of their identities. These results were consistent with both regular multiplex-DDA-MSI and the fractionated mass multiplex-DDA-MSI methods. However, only 10 neuropeptide identifications were confirmed by MS/MS data acquired using the regular spiral setup, presumably due to the biased precursor selection without pre-separation before DDA scans. In contrast, the combination of evenly and unevenly fractionated mass range multiplex-DDA-MSI methods allowed confident identification of 39 neuropeptides with excellent sequence coverage. Details on the identified peptide family, peptide name, sequence, *m/z*, ppm and specific multiplex-DDA-MSI method employed can be found in Table S1.

In addition to the on-tissue characterization of known neuropeptides, the fractionated *m/z* multiplex-DDA method also enabled the discovery of novel neuropeptides. One novel RFamide

was identified using the unevenly fractionated mass range setup, while not selected for MS/MS in other experiments. This RFamide has also been observed in our ongoing neuropeptidome characterization of *C. irroratus* using LC-ESI-MS/MS platform. As shown in Figure 5, this neuropeptide is more concentrated in the lateral antenna I neuropil and tegumentary neuropil, which are situated in the medial protocerebrum of the rock crab brain.

In summary, the unevenly fractionated mass multiplex-DDA-MSI method is most suitable for neuropeptide analysis in crustacean nervous system among the three multiplex-DDA-MSI methods. This improved performance is largely due to specific adjustment of the number of MS/MS scans according to the relative intensity and abundance of putative peptide peaks observed in a typical direct tissue MALDI mass spectrum. Therefore, the unevenly fractionated mass range multiplex-DDA-MSI method enables the acquisition of many more peptide sequences via tandem MS events while reducing the interference from other high abundance biomolecules. Moreover, because a greater number of low abundance molecular species could be selected for MS/MS analysis using this novel approach, it provides great opportunity to discover additional novel neuropeptides that have been overlooked in previous peptidomic analysis using the traditional DDA method.

Conclusion

For the first time, multiplex MSI was coupled with DDA to achieve simultaneous identification and distribution mapping of neuropeptides in crustacean neuronal tissues. As we demonstrated in this study, traditional MSI is not amenable to direct coupling with DDA as it sacrifices spatial resolution for acquiring data dependent MS/MS scans. In contrast, the multiplex-DDA-MSI method acquires full MS scan in every raster position while obtaining DDA scans in subsequent spiral steps surrounding the main full MS step. This setup allows a continuous full MS

acquisition while obtaining MS/MS information to confirm the peptide identities, which enhances the overall throughput of MSI analysis by reducing total acquisition time. Novel neuropeptides or other biomolecules can also be discovered by *de novo* sequencing from the MS/MS scans. Moreover, we introduced the concept of fractionating *m/z* range into multiple segments in multiplex-DDA-MSI acquisition to create *in situ* pseudo gas-phase fractionation of molecular species from a tissue sample before DDA analysis. This novel setup compensates to some degree for the lack of separation in MALDI-MSI based DDA experiments and significantly improves the efficiency and coverage of precursor selection and subsequent peptidome coverage. With multiplex-DDA-MSI, the spatial distributions of neuropeptides, lipids and protein fragments were mapped directly in the crustacean brain and CoG tissue sections while obtaining the structural information about these biomolecules. In total, 39 known neuropeptides were identified *in situ* from the blue crab *C. sapidus* brain tissue by the multiplex-DDA-MSI method, including a novel RFamide neuropeptide, which highlights its utility for large-scale *in situ* peptidomic analysis. In summary, the multiplex-DDA-MSI method with fractionating *m/z* range expands the capability and analytical performance of MALDI-MSI. It is capable of simultaneous distribution mapping, biomolecule identification, and novel molecule discovery. This novel platform has great potential to be widely applied to a variety of tissue types and target molecules. This work will benefit the research field of tissue imaging and stimulate future investigations of signaling biomolecules that may span a wide mass range and dynamic range.

Acknowledgements

The authors wish to thank Dr. Kerstin Strupat at Thermo Scientific for her technical support and helpful discussions. This work was supported by National Institutes of Health NIDDK R01DK071801. We would like to acknowledge NIH shared instrument program for funding the

instrument purchase under grant NIH S10 RR029531. L. Li acknowledges an H.I. Romnes Faculty Research Fellowship and the Vilas Distinguished Achievement Professorship from the Vilas Trust and School of Pharmacy at the University of Wisconsin-Madison.

References

[1] Caprioli, R. M., Farmer, T. B., and Gile, J. (1997) Molecular imaging of biological samples: localization of peptides and proteins using MALDI-TOF MS, *Anal. Chem. 69*, 4751-4760.

[2] Chen, R., Cape, S. S., Sturm, R. M., and Li, L. (2010) Mass spectrometric imaging of neuropeptides in decapod crustacean neuronal tissues, *Methods Mol. Biol. 656*, 451-463.

[3] Zimmerman, T. A., Rubakhin, S. S., and Sweedler, J. V. (2011) MALDI mass spectrometry imaging of neuronal cell cultures, *J. Am. Soc. Mass Spectrom. 22*, 828-836.

[4] Rubakhin, S. S., Ulanov, A., and Sweedler, J. V. (2015) Mass Spectrometry Imaging and GC-MS Profiling of the Mammalian Peripheral Sensory-Motor Circuit, *J. Am. Soc. Mass Spectrom. 26*, 958-966.

[5] Gemperline, E., Chen, B., and Li, L. (2014) Challenges and recent advances in mass spectrometric imaging of neurotransmitters, *Bioanalysis 6*, 525-540.

[6] Rubakhin, S. S., Jurchen, J. C., Monroe, E. B., and Sweedler, J. V. (2005) Imaging mass spectrometry: fundamentals and applications to drug discovery, *Drug Discov. Today 10*, 823-837.

[7] Nilsson, A., Goodwin, R. J., Shariatgorji, M., Vallianatou, T., Webborn, P. J., and Andren, P. E. (2015) Mass spectrometry imaging in drug development, *Anal. Chem. 87*, 1437-1455.

[8] Liu, X., Weaver, E. M., and Hummon, A. B. (2013) Evaluation of therapeutics in three-dimensional cell culture systems by MALDI imaging mass spectrometry, *Anal. Chem. 85*, 6295-6302.

[9] Li, H., and Hummon, A. B. (2011) Imaging mass spectrometry of three-dimensional cell culture systems, *Anal. Chem. 83*, 8794-8801.

[10] Ahlf Wheatcraft, D. R., Liu, X., and Hummon, A. B. (2014) Sample preparation strategies for mass spectrometry imaging of 3D cell culture models, *J. Vis. Exp.*

[11] Meistermann, H., Norris, J. L., Aerni, H. R., Cornett, D. S., Friedlein, A., Erskine, A. R., Augustin, A., De Vera Mudry, M. C., Ruepp, S., Suter, L., Langen, H., Caprioli, R. M., and Ducret, A. (2006) Biomarker discovery by imaging mass spectrometry: transthyretin is a biomarker for gentamicin-induced nephrotoxicity in rat, *Mol. Cell. Proteom. 5*, 1876-1886.

[12] Jiang, L., Chughtai, K., Purvine, S., Bhujwalla, Z. M., Raman, V., Pasa-Tolic, L., Heeren, R. M., and Glunde, K. (2015) MALDI-mass spectrometric imaging reveals hypoxia-driven lipids and proteins in a breast tumor model, *Anal. Chem.*

[13] Seeley, E. H., Washington, M. K., Caprioli, R. M., and M'Koma, A. E. (2013) Proteomic patterns of colonic mucosal tissues delineate Crohn's colitis and ulcerative colitis, *Proteomics Clin. Appl. 7*, 541-549.

[14] Takats, Z., Wiseman, J. M., Gologan, B., and Cooks, R. G. (2004) Mass spectrometry sampling under ambient conditions with desorption electrospray ionization, *Science 306,* 471-473.

[15] Eberlin, L. S., Liu, X. H., Ferreira, C. R., Santagata, S., Agar, N. Y. R., and Cooks, R. G. (2011) Desorption Electrospray Ionization then MALDI Mass Spectrometry Imaging of Lipid and Protein Distributions in Single Tissue Sections, *Anal. Chem. 83,* 8366-8371.

[16] Cooks, R. G., Manicke, N. E., Dill, A. L., Ifa, D. R., Eberlin, L. S., Costa, A. B., Wang, H., Huang, G., and Ouyang, Z. (2011) New ionization methods and miniature mass spectrometers for biomedicine: DESI imaging for cancer diagnostics and paper spray ionization for therapeutic drug monitoring, *Faraday Discuss. 149,* 247-267; discussion 333-256.

[17] Yanes, O., Woo, H. K., Northen, T. R., Oppenheimer, S. R., Shriver, L., Apon, J., Estrada, M. N., Potchoiba, M. J., Steenwyk, R., Manchester, M., and Siuzdak, G. (2009) Nanostructure initiator mass spectrometry: tissue imaging and direct biofluid analysis, *Anal. Chem. 81,* 2969-2975.

[18] Sturm, R. M., Greer, T., Chen, R. B., Hensen, B., and Li, L. J. (2013) Comparison of NIMS and MALDI platforms for neuropeptide and lipid mass spectrometric imaging in C. borealis brain tissue, *Anal. Methods 5,* 1623-1628.

[19] Robichaud, G., Barry, J. A., and Muddiman, D. C. (2014) IR-MALDESI Mass Spectrometry Imaging of Biological Tissue Sections Using Ice as a Matrix, *J. Am. Soc. Mass Spectrom. 25,* 319-328.

[20] Dufresne, M., Thomas, A., Breault-Turcot, J., Masson, J. F., and Chaurand, P. (2013) Silver-assisted laser desorption ionization for high spatial resolution imaging mass spectrometry of olefins from thin tissue sections, *Anal. Chem. 85,* 3318-3324.

[21] Trimpin, S., Inutan, E. D., Herath, T. N., and McEwen, C. N. (2010) Laserspray ionization, a new atmospheric pressure MALDI method for producing highly charged gas-phase ions of peptides and proteins directly from solid solutions, *Mol. Cell. Proteom. 9,* 362-367.

[22] Chen, B., Lietz, C. B., and Li, L. (2014) In Situ characterization of proteins using laserspray ionization on a high-performance MALDI-LTQ-Orbitrap mass spectrometer, *J. Am. Soc. Mass Spectrom. 25,* 2177-2180.

[23] Ye, H., Mandal, R., Catherman, A., Thomas, P. M., Kelleher, N. L., Ikonomidou, C., and Li, L. (2014) Top-down proteomics with mass spectrometry imaging: a pilot study towards discovery of biomarkers for neurodevelopmental disorders, *PloS one 9,* e92831.

[24] Strupat, K., Kovtoun, V., Bui, H., Viner, R., Stafford, G., and Horning, S. (2009) MALDI Produced Ions Inspected with a Linear Ion Trap-Orbitrap Hybrid Mass Analyzer, *J. Am. Soc. Mass Spectrom. 20,* 1451-1463.

[25] Makarov, A., Denisov, E., Kholomeev, A., Balschun, W., Lange, O., Strupat, K., and Horning, S. (2006) Performance evaluation of a hybrid linear ion trap/orbitrap mass spectrometer, *Anal. Chem. 78*, 2113-2120.

[26] Inutan, E. D., and Trimpin, S. (2013) Matrix assisted ionization vacuum (MAIV), a new ionization method for biological materials analysis using mass spectrometry, *Mol. Cell. Proteom. 12*, 792-796.

[27] Perdian, D. C., and Lee, Y. J. (2010) Imaging MS methodology for more chemical information in less data acquisition time utilizing a hybrid linear ion trap-orbitrap mass spectrometer, *Anal. Chem. 82*, 9393-9400.

[28] Yagnik, G. B., Korte, A. R., and Lee, Y. J. (2013) Multiplex mass spectrometry imaging for latent fingerprints, *Journal of mass spectrometry : JMS 48*, 100-104.

[29] Korte, A. R., and Lee, Y. J. (2013) Multiplex mass spectrometric imaging with polarity switching for concurrent acquisition of positive and negative ion images, *J. Am. Soc. Mass Spectrom. 24*, 949-955.

[30] Li, L., Kelley, W. P., Billimoria, C. P., Christie, A. E., Pulver, S. R., Sweedler, J. V., and Marder, E. (2003) Mass spectrometric investigation of the neuropeptide complement and release in the pericardial organs of the crab, Cancer borealis, *J. Neurochem. 87*, 642-656.

[31] DeKeyser, S. S., Kutz-Naber, K. K., Schmidt, J. J., Barrett-Wilt, G. A., and Li, L. (2007) Imaging mass spectrometry of neuropeptides in decapod crustacean neuronal tissues, *J. Proteome. Res. 6*, 1782-1791.

[32] Cape, S. S., Rehm, K. J., Ma, M., Marder, E., and Li, L. (2008) Mass spectral comparison of the neuropeptide complement of the stomatogastric ganglion and brain in the adult and embryonic lobster, Homarus americanus, *J. Neurochem. 105*, 690-702.

[33] OuYang, C., Liang, Z., and Li, L. (2014) Mass spectrometric analysis of spatio-temporal dynamics of crustacean neuropeptides, *Biochim. Biophys. Acta.*

[34] Chen, R., Hui, L., Cape, S. S., Wang, J., and Li, L. (2010) Comparative Neuropeptidomic Analysis of Food Intake via a Multi-faceted Mass Spectrometric Approach, *ACS Chem. Neurosci. 1*, 204-214.

[35] Kutz, K. K., Schmidt, J. J., and Li, L. (2004) In situ tissue analysis of neuropeptides by MALDI FTMS in-cell accumulation, *Anal. Chem. 76*, 5630-5640.

[36] Robichaud, G., Garrard, K. P., Barry, J. A., and Muddiman, D. C. (2013) MSiReader: an open-source interface to view and analyze high resolving power MS imaging files on Matlab platform, *J. Am. Soc. Mass Spectrom. 24*, 718-721.

[37] Ye, H., Hui, L., Kellersberger, K., and Li, L. (2012) Mapping of Neuropeptides in the Crustacean Stomatogastric Nervous System by Imaging Mass Spectrometry, *J. Am. Soc. Mass Spectrom.*

[38] Schmerberg, C. M. (2012) Functional neuropeptidomics in the decapod crustacean method development and application to behavioral neuroscience research, *Ph.D. Thesis of University of Wisconsin-Madison*.

Figure legends

Figure 1. Illustration of 9-step multiplex MSI experiment with DDA. The number indicated the sequence of spiral plate movement. A raster step size of 150 µm and a spiral step size of 50 µm were used. Steps 1, 4 and 7 were full MS scans at *m/z* ranges of 500-840, 840-1190 and 1190-1750 respectively. Steps 2/3, 5/6 and 8/9 were data dependent MS/MS scans of the top 2 most abundant ions detected in the previous full MS scans. The exact mass fractions for full MS scans can be varied for different experimental setup.

Figure 2. Comparisons between linear DDA MSI and spiral DDA MSI. (a, b) Illustrations of linear DDA MSI (a) and spiral DDA MSI (b), each with a step size of 50 µm. Step 1 was a full MS scan and steps 2, 3, 4 were data dependent MS/MS scans of the top 3 most abundant ions detected in step 1; (c, d) MSI result of total ion count (TIC) on CoG tissue sections for linear DDA MSI (c) and spiral DDA MSI (d); (e, f) neuropeptide (HL/IGSL/IYRamide) distribution at *m/z* 844.4788 ± 5ppm for linear DDA MSI (e) and spiral DDA MSI (f); (g, h) neuropeptide (VSHNNFLRFamide) distributions at *m/z* 1132.6010 ± 5ppm for linear DDA MSI (g) and spiral DDA MSI (h).

Figure 3. 9-step multiplex MSI results obtained from the CoG tissue of the blue crab *C. sapidus*. (a) Full MS spectrum of CoG neuropeptide profile with spatial resolution of 50 µm. The spectrum was zoomed in at *m/z* 800-1600 and averaged over 5 scans. Annotated peaks were color coded with corresponding neuropeptide families based on accurate mass matching. Six additional peaks were identified from *m/z* 1600-2000, which were not shown in the spectrum. (b-e) annotated MS/MS spectra and MSI distributions of APSGFLGMRa (b), FDAFTTGFGHS (c), GYRKPPFNGSIFa (d) and NFDEIDRSSFG (e).

Figure 4. Comparisons among regular spiral DDA, even fraction mass DDA and uneven fraction mass DDA from the brain tissue of blue crab *C. sapidus*. (a) Comparisons of numbers of precursor ions selected by DDA under different setup within *m/z* ranges of 500-840, 840-1190 and 1190-1750. (b, c) Precursor ions selected for DDA (highlighted in red) under regular spiral DDA condition (b) and fraction mass DDA condition (c).

Figure 5. MS/MS spectrum and on-tissue distribution image of the novel neuropeptide obtained using fractionated mass multiplex-DDA-MSI method from the brain tissue of blue crab *C. sapidus*. Neuropeptide sequence: DLRTPALRLRFamide (*m/z* 1356.8223).

Figures

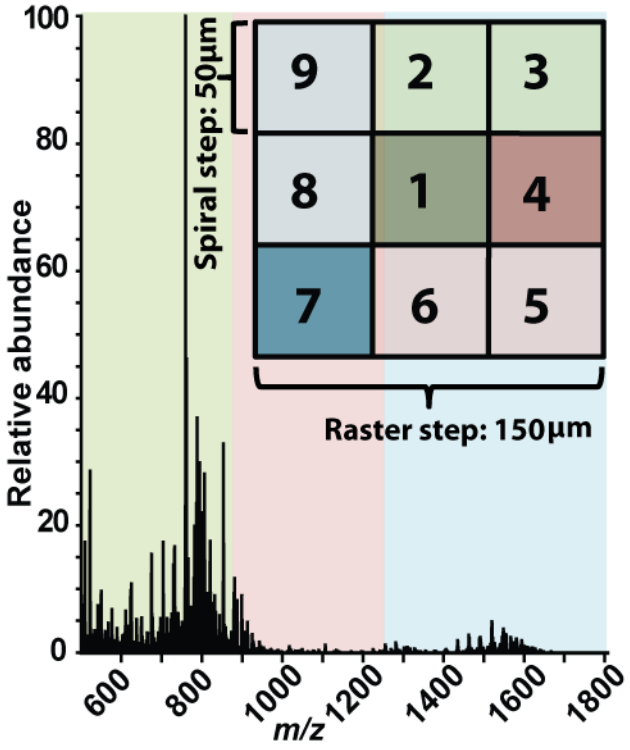

Figure 1

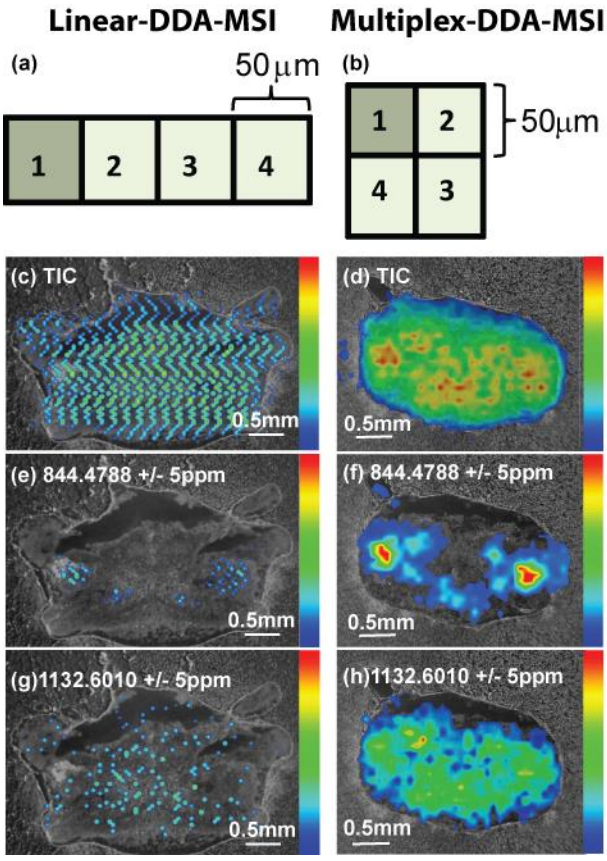
Linear-DDA-MSI
Multiplex-DDA-MSI
(a)
50μm
1
2
3
4
(b)
1
2
4
3
50μm
(c) TIC
0.5mm
(d) TIC
0.5mm
(e) 844.4788 +/- 5ppm
0.5mm
(f) 844.4788 +/- 5ppm
0.5mm
(g)1132.6010 +/- 5ppm
0.5mm
(h)1132.6010 +/- 5ppm
0.5mm

Figure 2

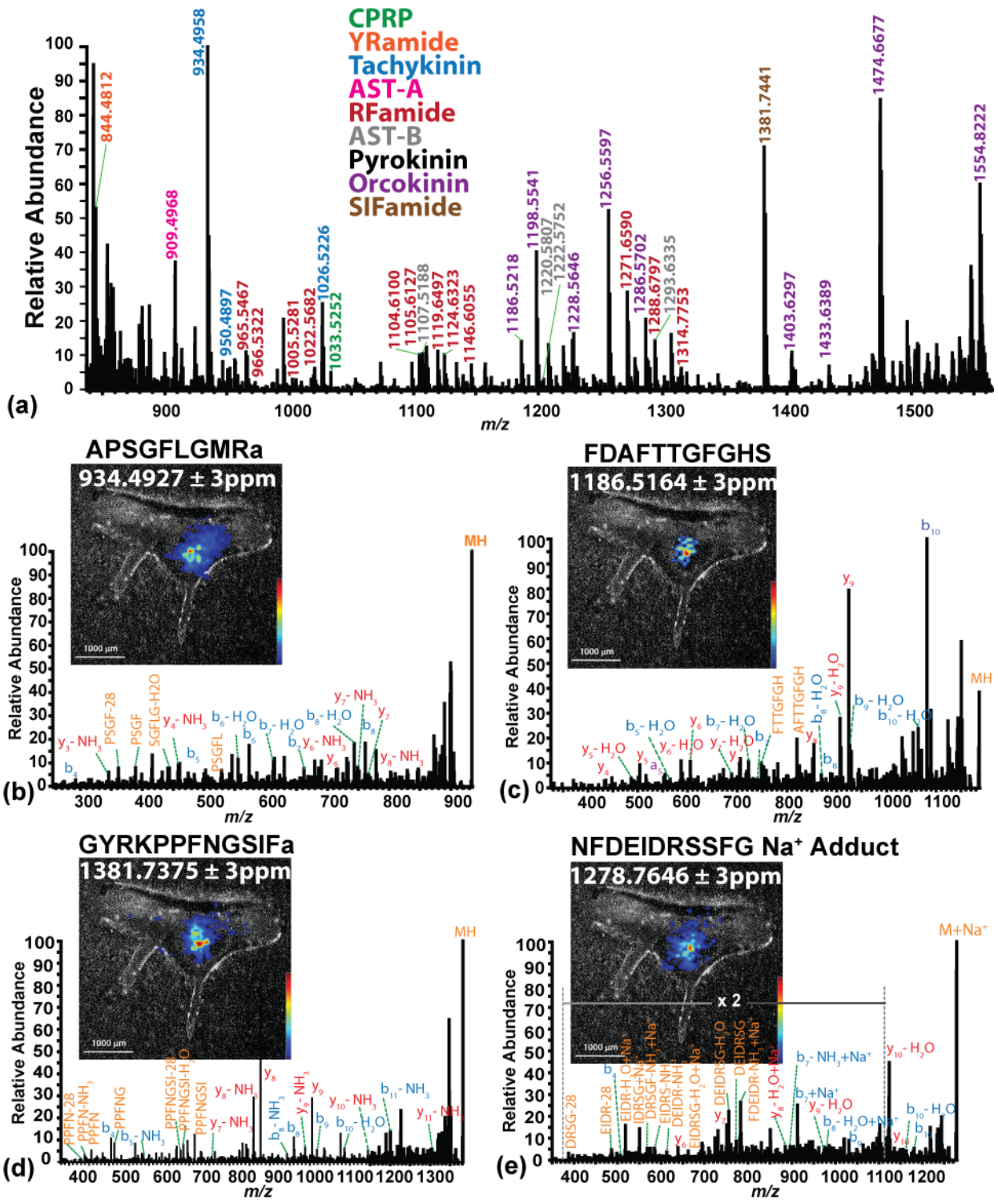
CPRP
YRamide
Tachykinin
AST-A
RFamide
AST-B
Pyrokinin
Orcokinin
SIFamide
Relative Abundance
m/z
(a)
APSGFLGMRa
934.4927 ± 3ppm
(b)
FDAFTTGFGHS
1186.5164 ± 3ppm
(c)
GYRKPPFNGSIFa
1381.7375 ± 3ppm
(d)
NFDEIDRSSFG Na⁺ Adduct
1278.7646 ± 3ppm
(e)

Figure 3

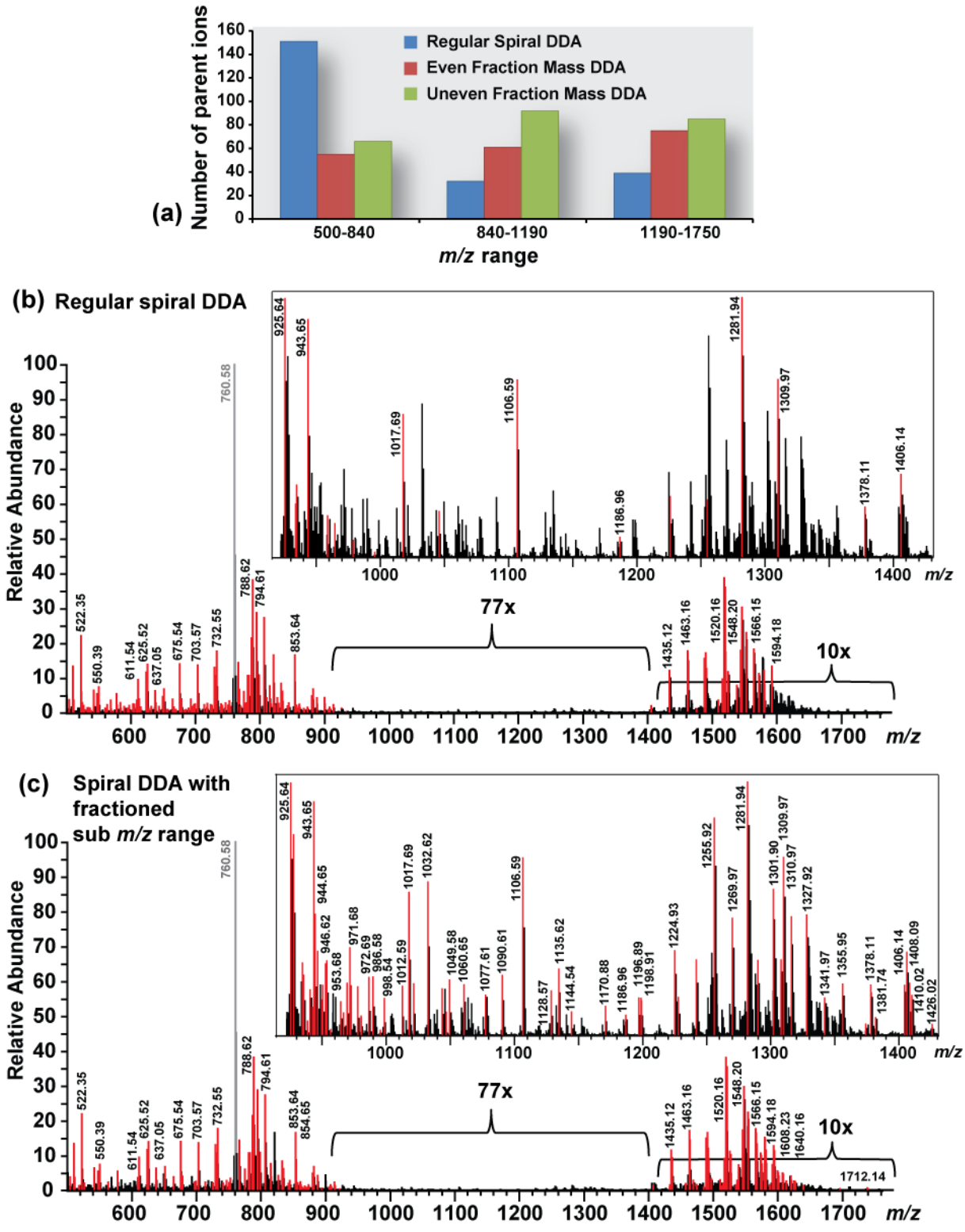
(a)
Number of parent ions
Regular Spiral DDA
Even Fraction Mass DDA
Uneven Fraction Mass DDA
500-840
840-1190
1190-1750
m/z range
(b) Regular spiral DDA
Relative Abundance
77x
10x
m/z
(c) Spiral DDA with fractioned sub m/z range
Relative Abundance
77x
10x
1712.14
m/z

Figure 4

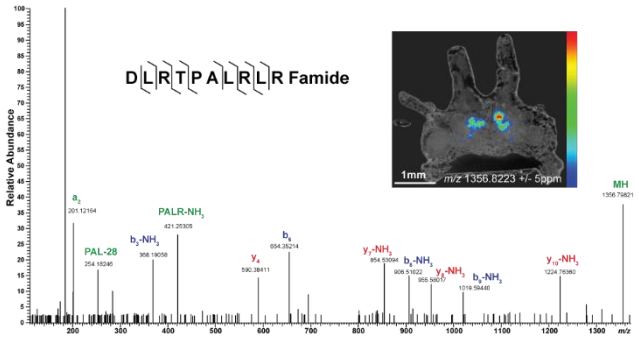
DLRTPALRLR Famide
1mm
m/z 1356.8223 +/- 5ppm
Relative Abundance
m/z
MH
1356.76821
PALR-NH3
421.25305
PAL-28
254.16246
b2-NH3
358.19058
a2
201.12164
b4
654.35214
y4
590.38411
y7-NH3
854.53094
b8-NH3
908.51622
y6-NH3
955.56077
b9-NH3
1019.59446
y10-NH3
1224.76360

Figure 5

Supporting information

Table S1 Details of neuropeptides identified on crab brain tissues by regular DDA, evenly fractionated DDA and unevenly fractionated DDA methods.

Family	Peptide name	Sequence	Theoretical *m/z*	Measured *m/z*	ppm	Regular DDA	Evenly fractionated	Unevenly fractionated	On tissue distribution
Others	[Leu]-enkephalin	YGGFL	556.2766	556.2721	8.07				
Allatostatin A-type	Penaeustatin 30	YDFGLamide	613.2980	613.2937	7.08				
Pyrokinin		FSPRLamide	618.3722	618.3746	3.90				*
Proctolin	Proctolin	RYLPT	649.3668	649.3649	2.86				*
Tachykinin	TRP	GFLGMRamide	679.3708	679.3692	2.33				*
RFamide		NFLRFamide	695.3988	695.3987	0.07	*			*
RFamide		GPFLRFamide	735.4301	735.4343	5.66				*
Kinins	pev-Kinin 3	PAFSPWGamide	760.3777	760.3687	11.88				
Tachykinin	CabTRP lb	SGFLGMRamide	766.4029	766.4017	1.57		*		*
Tachykinin		APSGFLGM	779.3756	779.3746	1.23				

Family	Peptide name	Sequence	Theoretical *m/z*	Measured *m/z*	ppm	Regular DDA	Evenly fractionated	Unevenly fractionated	On tissue distribution
Allatostatin A-type	Carcinustatin 8, Penaeustatin 6, Procastatin 17	AGPYAFGLamide	794.4196	794.4196	0.00	*	*		*
RFamide	pem-PYF1	RARPRFamide	801.4955	801.4909	5.63				*
RFamide		ASNNLRFamide	820.4424	820.4424	0		*		*
RYamide		FYANRYamide	832.4101	832.3941	19.14				
Unknown	Unknown	Unknown	N/A	836.4271	N/A				*
Allatostatin A-type	Penaeustatin 33	PSAYSFGLamide	840.4250	840.4318	8.10				*
Allatostatin A-type		AGLYSYGLamide	842.4407	842.4477	8.31			*	*
Others		HL/IGSL/IYRamide	844.4788	844.4788	0.00		*		*
Allatostatin A-type	Penaeustatin 31/Penaeustatin 7	AGHYSFGLamide/ SGHYAFGLamide	850.4206	850.4153	6.20		*	*	
Allatostatin A-type		GKPYAFGLamide	851.4774	851.4678	11.32				*
RFamide		RNFLRFamide	851.4999	851.5032	3.93				*

Family	Peptide name	Sequence	Theoretical *m/z*	Measured *m/z*	ppm	Regular DDA	Evenly fractionated	Unevenly fractionated	On tissue distribution
Allatostatin A-type	Penaeustatin 20	AGPYEFGLamide	852.4250	852.3993	30.15				
Allatostatin A-type		DGPYSFGLamide	854.4043	854.4070	3.10				*
Others		KPKTEKK	858.5407	858.5769	42.16				
Allatostatin A-type	Penaeustatin 22	AAPYEFGLamide	866.4407	866.4341	7.57				*
Allatostatin A-type	Procastatin 8	SGNYNFGLamide	870.4104	870.4062	4.78		*		
Allatostatin A-type	Penaeustatin 8	ANQYAFGLamide	882.4468	882.4421	5.31				
RYamide		L/IFVGGSRYamide	897.4941	897.4871	7.78			*	*
Allatostatin A-type	Lepidopteran peptide Lepidostatin I	AKSYNFGLamide	898.4781	898.4751	3.37				
Allatostatin A-type	AST-3	GGSLYSFGLamide	899.4621	899.4621	0.00		*		*
Allatostatin A-type	Procastatin 6	ADMYSFGLamide	902.4077	902.4092	1.71				
RFamide		PSMRLRFamide	905.5138	905.5132	0.64		*	*	*
Allatostatin A-type	Procastatin 13	PRVYGFGLamide	907.5148	907.5148	0.00		*		*
RFamide			908.5213	908.5213	0.00		*		*

Family	Peptide name	Sequence	Theoretical *m/z*	Measured *m/z*	ppm	Regular DDA	Evenly fractionated	Unevenly fractionated	On tissue distribution
Allatostatin A-type	Lepidopteran peptide cydiastatin 4, helicostatin 4	ARPYSFGLamide	909.4941	909.4899	4.65				*
Allatostatin A-type	Procastatin 5	PDLYSFGLamide	910.4669	910.4686	1.83			*	*
Allatostatin A-type	Penaeustatin 14	ANQYTFGLamide	912.4574	912.4512	6.76				
Tachykinin		APSGFLGMRamide-NH3-loss	917.4623	917.4644	2.32				
Allatostatin A-type		KLPYSFGLamide	923.5349	923.5388	4.24				*
Allatostatin A-type / Rfamide	Lepidopteran peptide cydiastatin 3,helicostatin 3	SRPYSFGLamide/ETNFLR Famide	925.4890	925.4890	0.00	*			*
Allatostatin A-type	Lepidopteran peptide helicostatin 7	ARSYNFGLamide	926.4843	926.4801	4.51				
RPCH	Panbo-RPCH	pELNFSPGWamide	930.4468	930.4426	4.52			*	*

Family	Peptide name	Sequence	Theoretical *m/z*	Measured *m/z*	ppm	Regular DDA	Evenly fractionated	Unevenly fractionated	On tissue distribution
Allatostatin A-type	Lepidopteran peptide cydiastatin 1	SPHYNFGLamide	933.4577	933.4601	2.53			*	
Tachykinin	CabTRP la	APSGFLGMRamide	934.4927	934.4939	1.20		*		*
Allatostatin A-type	Procastatin 11	PRNYAFGLamide	936.5050	936.5031	2.07				*
Allatostatin A-type		PRDYAFGLamide	937.4890	937.4904	1.41				*
Allatostatin A-type		TRPYSFGLamide	939.5047	939.5083	3.78				
Allatostatin A-type		QRAYSFGLamide	940.4999	940.4977	2.41				*
Allatostatin A-type	Penaeustatin 3	DRLYAFGLamide	953.5203	953.6206	105.20		*		*
RFamide		SRNYLRFamide	954.5268	954.5271	0.34				*
Allatostatin A-type	Procastatin 9	SRQYSFGLamide	956.4948	956.4966	1.83				*
Tachykinin	CabTRP II	TPSGFLGMRamide	964.5033	964.5043	1.03		*		*
RFamide	NF 1, PrcFaRP 2	NRNFLRFamide	965.5428	965.5446	1.84		*		*

Family	Peptide name	Sequence	Theoretical *m/z*	Measured *m/z*	ppm	Regular DDA	Evenly fractionated	Unevenly fractionated	On tissue distribution
RFamide	DF 2, Mar-FLP 1, PrcFaRP 5	DRNFLRFamide	966.5268	966.5284	1.60		*		*
CCAP	Lepidopteran peptide CAP2b	pELYAFPRVamide	975.5411	975.5368	4.44				*
TachykiniN		TPSGFLGM(O)Ramide	980.4982	980.4992	0.98		*		*
Allatostatin A-type		SKSPYSFGLamide	984.5149	984.5200	5.21				*
Unknown	Unknown	Unknown	N/A	986.4879	N/A		*		*
RFamide		SGRNFLRFamide	995.5534	995.5552	1.89		*		*
RFamide		GPRNFLRFamide	1,005.5741	1005.5688	5.31			*	*
RFamide		PKSNFLRFamide	1,007.5785	1007.5710	7.41				*
RFamide		APRNFLRFamide	1,019.5897	1019.5856	4.03				*
Allatostatin A-type		PADLYEFGLamide	1,023.5146	1023.5114	3.13				
RFamide	pem-FLP 1	GDRNFLRFamide	1,023.5483	1023.5510	2.68				*
Pyrokinin		TSFAFSPRLamide	1,024.5574	1024.5591	1.69				*

Family	Peptide name	Sequence	Theoretical *m/z*	Measured *m/z*	ppm	Regular DDA	Evenly fractionated	Unevenly fractionated	On tissue distribution
RYamide		SRFVGGSRYamide	1,027.5432	1027.5498	6.42				*
RFamide		LETNFLRFamide	1,038.5731	1038.5724	0.69				
Allatostatin A-type		SPRLTYFGLamide	1,052.5887	1052.5878	0.90				*
Orcokinin/Orcomyotropin-related		TPRDIANLYamide	1,061.5738	1061.5795	5.34				*
Orcokinin		NFDEIDRSA	1,066.4800	1066.4892	8.60				
RFamide		LFDDFLRFamide	1,071.5622	1071.5569	4.98				*
CCAP	CCAP precursor related peptide	DIGDLLEGKD	1,074.5313	1074.5330	1.57				
RFamide		LDRNFLRFamide	1,079.6109	1079.6085	2.26		*	*	*
RFamide	Mar-FLP 6	DGGRNFLRFamide	1,080.5697	1080.5665	3.04		*		*
Orcokinin		EIDRSGFGFA	1,098.5215	1098.5213	0.15				
Others		DLPKVDTALK	1,099.6358	1099.6416	5.24		*	*	

Family	Peptide name	Sequence	Theoretical *m/z*	Measured *m/z*	ppm	Regular DDA	Evenly fractionated	Unevenly fractionated	On tissue distribution
CPRP (CHH precursor-related peptide)	truncated Hoa CPRP-A (SN-16) 23-32, B&C 22-31	PLGFLSQDHS	1,100.5371	1100.5371	0.02				*
RFamide		GAHKNYLRFamide	1,104.6061	1104.6067	0.50				*
RFamide		LNPSNFLRFamide	1,106.6105	1106.6105	0.00	*			*
Allatostatin B-type	CbAST-B2	QWSSMRGAWamide	1,107.5153	1107.5164	1.03				
RFamide		SMPTLRLRFamide	1,119.6455	1119.6453	0.21		*	*	*
Allatostatin B-type		AGWSSM(O)RGAWamide	1,123.5102	1123.5097	0.45				
RFamide		TGNRNFLRFamide	1,123.6119	1123.6176	5.08		*		*
RFamide		GLSRNYLRFamide	1,124.6323	1124.6307	1.43			*	*
RFamide	Mar-FLP 8	VSHNNFLRFamide	1,132.6010	1132.6031	1.77	*			*
RFamide		DGNRNFLRFamide	1,137.5912	1137.5977	5.68				*

Family	Peptide name	Sequence	Theoretical *m/z*	Measured *m/z*	ppm	Regular DDA	Evenly fractionated	Unevenly fractionated	On tissue distribution
Orcokinin		FDEIDRSGFG	1,142.5113	1142.5156	3.80				
RFamide		GYSKNYLRFamide	1,146.6055	1146.6082	2.37		*		*
RFamide		LSPRNFLRFamide	1,148.6687	1148.6689	0.19				
RFamide	PrcFaRP 4	ALDRNFLRFamide	1,150.6480	1150.6464	1.43				*
RFamide		GYNRSFLRFamide	1,158.6167	1158.6187	1.70				*
RFamide		QYFMRLFRamide	1,159.6193	1159.6209	1.38				*
RFamide	NPY/PP peptide pem-PYF4	YSLRARPRFamide	1,164.6749	1164.6772	1.98				
RFamide	[ala1]-FaRP	AYNRSFLRFamide	1,172.6323	1172.6357	2.86				
RFamide		SENRNFLRFamide	1,181.6174	1181.6207	2.75				*
Orcomyotropin		FDAFTTGFGHS	1,186.5164	1186.5186	1.91		*	*	*
Cryptocyanin	cryptocyanin fragment CC1 20-28	YKIFEPLRE	1,194.6517	1194.6511	0.54				
Orcokinin		NFDEIDRSGFamide	1,198.5487	1198.5518	2.59				*

Family	Peptide name	Sequence	Theoretical *m/z*	Measured *m/z*	ppm	Regular DDA	Evenly fractionated	Unevenly fractionated	On tissue distribution
Orcomyotropin		FDAFTTGFGHN	1,213.5273	1213.5268	0.41				
RFamide	Mar-FLP 3	NYDKNFLRFamide	1,215.6269	1215.6207	5.12				*
Allatostatin B-type	CbAST-B6	GNWNKFQGSWamide	1,222.5752	1222.5749	0.25				*
RFamide	Mar-FLP 7	GYGDRNFLRFamide	1,243.6331	1243.6283	3.80				*
Orcokinin	Orcokinin[1-11]	NFDEIDRSGFG	1,256.5542	1256.5571	2.28			*	*
RFamide	pem-FLP 2	AYSNLNYLRFamide	1,259.6531	1259.6598	5.26				*
Allatostatin B-type	CbAST-B3	SGKWSNLRGAWamide	1,260.6596	1260.6613	1.32				*
RFamide	[glu2-leu3]-SchistoFLRFa	pQDLDHVFLRFamide	1,271.6531	1271.6570	3.07				*
Allatostatin B-type		LGNWSNLRGAWamide	1,272.6596	1272.6582	1.13				*

Family	Peptide name	Sequence	Theoretical *m/z*	Measured *m/z*	ppm	Regular DDA	Evenly fractionated	Unevenly fractionated	On tissue distribution
Orcokinin		NFDEIDRSSFG	1,286.5648	1286.5681	2.57			*	*
RFamide		QDLDHVFLRFamide	1,288.6797	1288.6832	2.73				*
Allatostatin B-type	CbAST-B8	STNWSSLRSAWamide	1,293.6335	1293.6369	2.67		*		*
RFamide	pem-FLP 6	DGRTPALRLRFamide	1,300.7597	1300.7565	2.42				*
CPRP (CHH precursor-related peptide)	truncated Hoa CPRP-B 11-23	KLLSSISPSSTPL	1,329.7624	1329.7606	1.35				
Allatostatin B-type		LGNWNKFQGSWamide	1,335.6593	1335.6526	5.00				
CPRP (CHH precursor-related peptide)	truncated Capr CPRP I 1-12	RSAQGMGKMEHL	1,344.6511	1344.6588	5.73				*
Corazonin	Corazonin	pQTFQYSRGWTNamide	1,369.6284	1369.6322	2.75				*

Family	Peptide name	Sequence	Theoretical *m/z*	Measured *m/z*	ppm	Regular DDA	Evenly fractionated	Unevenly fractionated	On tissue distribution
CPRP (CHH precursor-related peptide)	truncated Hoa CPRP-A20-32, B19-31	SSTPLGFLSQDHS	1,375.6488	1375.6536	3.51				*
SIFamide	pem-FLP 7	GYRKPPFNGSIFamide	1,381.7375	1381.7404	2.06		*	*	*
Orcokinin	Orcokinin[1-12]	NFDEIDRSGFGF	1,403.6226	1403.6238	0.83				*
Orcokinin	[Ala13]-orcokinin	NFDEIDRSGFGFA	1,474.6597	1474.6638	2.75	*	*	*	*
Orcokinin	[val13]-OrcoKinin	NFDEIDRSGFGFV	1,502.6910	1502.6960	3.27				*
Orcokinin	[Ser9-val13]-Orcokinin	NFDEIDRSSFGFV	1,532.7016	1532.7072	3.66				*
Orcokinin	[Ser9]-Orcokinin	NFDEIDRSSFGFN	1,547.6761	1547.6803	2.70	*	*	*	*
Allatostatin A-type	Penaeustatin 2	PDAEESNKRDRLYAFGL amide	1,979.9934	1979.8968	48.79	*			

Family	Peptide name	Sequence	Theoretical *m/z*	Measured *m/z*	ppm	Regular DDA	Evenly fractionated	Unevenly fractionated	On tissue distribution
Allatostatin A-type	Penaeustatin 26	NEVPDPETERNSYDFGL amide	1,980.8934	1980.8995	3.08	*			
CRPR	Truncated Hoa CPRP-B 11-32	KLLSSISPSSTPLGFLSQD HSV	2,300.2133	2300.1662	20.48	*			

Chapter 6
A High Resolution Atmospheric Pressure Matrix Assisted Laser Desorption/Ionization-Quadrupole-Orbitrap Platform Enables *In Situ* Analysis of Biomolecules by Multi-Modal Ionizations and Acquisitions

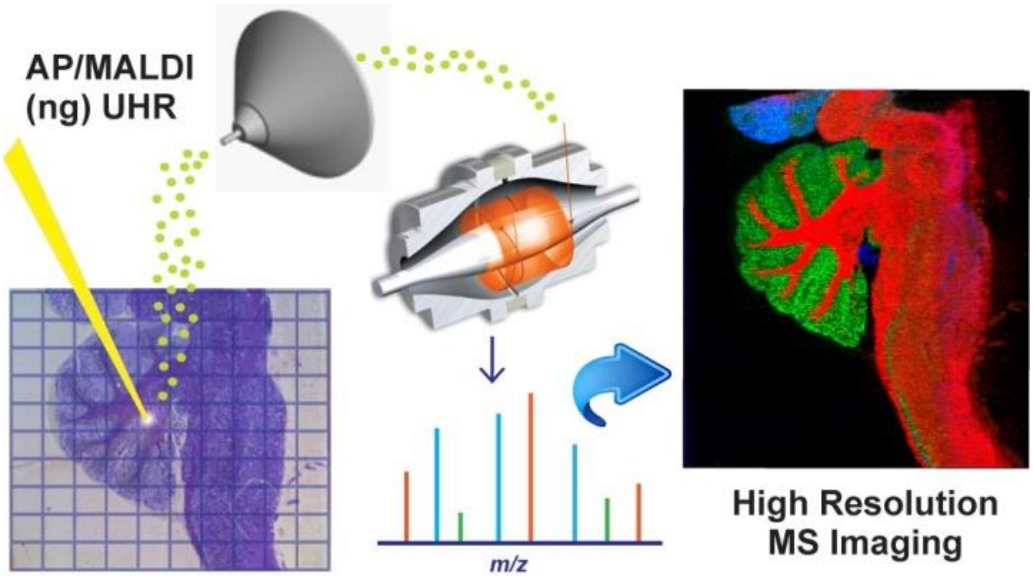

Adapted from **B. Chen**[#]**,** C. Ouyang[#], Z. Tian, M. Xu and L. Li, AP/MALDI (ng) UHR source coupled to Q Exactive HF mass spectrometer enables high resolution *in situ* analysis of biomolecules by multi-ionization and multi-acquisition modes. *To be submitted to Analyt. Chim. Acta*. ([#]Co-First authors)

Author contribution: study was designed by B. Chen, C. Ouyang and L. Li; experiment was performed by B. Chen and C. Ouyang; data was analyzed by B. Chen, C. Ouyang, Z. Tian and M. Xu; manuscript was written by B. Chen, C. Ouyang, and edited by L. Li.

Abstract

Introduced in 2000, Atmospheric pressure (AP)/ matrix assisted laser desorption/ ionization (MALDI) has quickly attracted attentions in mass spectrometry society due to its ease of sample introduction and handling, interchangeability with ESI sources and capability of analyzing volatile species. AP/MALDI (ng) Ultra High Resolution (UHR) source, developed by MassTech Inc., is a next generation AP/MALDI source with fine laser spot < 10 ppm and fast plate moving speed. In this study, AP/MALDI(ng) UHR source was coupled to a Q Exactive HF mass spectrometer for high resolution *in situ* analysis by MALDI, laserspray ionization (LSI) and matrix assisted ionization (MAI) without instrument modification. LSI and MAI generated multiply charged ions, which expanded the mass detection range and improved fragmentation efficiency. Full MS, targeted MS-MS, data dependent acquisition (DDA) and parallel reaction monitoring (PRM) acquisitions were performed on standards, tissue exacts and tissue sections for in depth deciphering of analytes. High resolution full MS and MS-MS images were achieved on crustacean and rat tissues with pixel size less than 30 µm. Overall, AP/MALDI-Q-Orbitrap a fast scanning instrument that is capable of performing multiple types of ionizations and multiple acquisition modes without instrument modification. It could be an attractive alternative to other high resolution MALDI instruments.

Keywords: Atmospheric pressure ionization, high resolution accurate mass, mass spectrometry imaging, matrix assisted laser desorption/ionization, laserspray ionization, neuropeptide.

Introduction

Mass spectrometry imaging (MSI) is a powerful analytical technique that allows mapping the spatial distributions of metabolites [1, 2], drugs [3], lipids[4], neuropeptides [5, 6] and proteins [7] on tissue sections by collecting mass spectra in a predefined raster. Since its first introduction in 1997 on a matrix assisted laser desorption ionization (MALDI) – time-of-flight (TOF) mass spectrometer [8], various ionization techniques have been employed for MSI analysis. These includes secondary ion mass spectrometry (SIMS) [9-12], desorption electrospray ionization (DESI) [13], matrix-assisted laser desorption electrospray ionization (MALDESI) [14], laser ablation electrospray ionization (LAESI) [15] and laser ablation/atmospheric pressure chemical ionization (LA/APCI) [16]. Among these ionizations, SIMS offers the highest spatial resolution, but it can only be used for small molecule analysis. On the other hand, MALDI, a soft ionization technique, is one of the most widely used ionization methods in MSI studies [1].

Developed in 2000, AP/ MALDI technique has become an alternative to traditional vacuum MALDI, due to its ease of sample introduction and sample handling at AP condition as well as the capability of analyzing volatile molecules [17]. Throughout the years, the AP/MALDI source geometry design [18] and ion transfer efficiency have been optimized [19] The sensitivity of AP/MALDI is considered to be comparable with vacuum MALDI [20]. A high-resolution scanning microprobe AP/MALDI source (AP-SMALDI, TransMIT GmbH, Giessen, Germany) was developed by the Spengler group and was used to analyze various biomolecules (metabolites, drug compounds, lipids, neuropeptides and tryptic digested peptides) in different samples ranging from single cell to pituitary gland [21-30].

AP/MALDI (ng) UHR (MassTech Inc., Columbia, MD) is an ultra-high spatial resolution, AP/MALDI source that is compatible with mass spectrometers of several vendors. With a

compact design, it can be easily interchanged with ESI source in minutes. The design and schematic of this source are shown in Figure 1. Briefly, it is equipped with a solid state 355 nm Nd:YAG laser with output frequency up to 10 kHz. Compared to a nitrogen laser, a solid state laser can generate many orders of magnitude more laser pulses during its lifetime, which is beneficial for MSI experiments. A 25-mm aspheric lens, which is positioned 75 mm to the MALDI target plate, can produce laser spot as small as 10 μm in a slightly elliptic shape. An optical system, which consists of a laser beam attenuator, a positive aspheric and negative lenses, focuses the laser beam at 60º incidence angle onto the MALDI target plate on the XY stages. The XY stages are driven by a step motor, with its control electronics located in the same housing and is directly connected to an MS front end. The distance between MALDI plate and the MS inlet capillary is approximately 2 mm. A CCD camera located inside the source can be used to monitor the sample on the MALDI target plate. The TARGET software (MassTech Inc., Columbia, MD) controls the laser energy, laser repetition rate and XY stages movement of the source. MSI experiments are performed using a constant speed raster mode, where the laser spot is driven along parallel raster lines. The width of the line is approximately equal to laser diameter, and the distance between each line is equal to the predefined pixel size. During MSI experiment, the XY coordinates of the laser spot and the acquisition time stamp are recorded into a XML file, which is then used along with the MS data file to generate ion images by ImageQuest software (Thermo Scientific, Bremen, Germany).

In recent years, novel ionizations have been reported to produce multiply charged ions on commercially available MALDI sources without instrument modification. These ionizations include laserspray ionization (LSI) [31-33], matrix assisted ionization (MAI) [34-37] and liquid AP/MALDI [38, 39]. By generating multiply charged ions, some limitations of high resolution

MALDI MS analyses can be overcome, such as the limited detection range of FTMS instruments with singly charged ion produced and the limited fragmentation efficiencies of singly charged ions.

In this study, the AP/MALDI (ng) UHR source is coupled to a Q Exactive HF hybrid quadrupole-Orbitrap mass spectrometer (QE HF). The QE HF is equipped with a segmented quadrupole and ultra-high-field Orbitrap mass analyzer with high mass resolution (240k at *m/z* 200) and high mass accuracy (< 3ppm) (Figure 1) [40].Compared to MALDI-LTQ-Orbitrap XL system, which is a commercially available high resolution vacuum MALDI instrument, the AP/MALDI-Q-Orbitrap system offers faster and customizable imaging speed, higher spatial and mass resolution and interchangeable with ESI source. Herein, we demonstrated the potential of the AP/MALDI-Q-Orbitrap platform in profiling and imaging diverse classes of biomolecules (metabolite, lipid, neuropeptides and small proteins) *in situ* by multiple types of ionization (MALDI, LSI and MAI) and multiple acquisition modes (Full MS, targeted MS-MS, DDA and PRM).

Materials and methods

Materials

Methanol (MeOH), ethanol (EtOH) acetonitrile (ACN), acetic acid (AA) and formic acid (FA) were purchased from Fisher Scientific (Pittsburgh, PA). α-cyano-4-hydroxycinnamic acid (CHCA), 2-nitrophloroglucinol (2-NPG) and 3-nitrobenzonitrile (3-NBN) were purchased from Sigma-Aldrich (St. Louis, MO). 2,5-dihydroxybenzoic acid (DHB) was purchased from Acros Organics (Morris Plains, NJ). Cresyl violet acetate working solution was purchased from Electron Microscope Sciences (Hatfield, PA). Microscope glass slides were purchased from VWR international, LLC (Radnor, PA). Conductive ITO coating glass slides were purchased

from Bruker (Billerica, MA). Physiological saline was composed of 440 mM NaCl, 26 mM $MgCl_2$, 13 mM $CaCl_2$, 11 mM KCl, 10 mM HEPES acid with pH value adjusted to 7.4 - 7.5. Bovine insulin standard was purchased from Promega (Madison, WI, USA). Peptide standards (bradykinin, neuropeptide Y, substance P, substance K, oxytocin, [Arg8] vasopressin, proctolin, corazonin, somatostatin (1-14), angiotensin I, alpha-MSHamide, alpha-MSH free acid, LH-RH (human), bactenecin (bovine), allatostatin I, II & III, crustacean cardioactive peptide (CCAP), FMRF, FMRFamide, FMRFamide-like peptide I & II (lobster), FMRF-like neuropeptide and FMRFamide related peptide) were purchased from American Peptide Company (Sunnyvale, CA, USA). Distilled water mentioned in this work was Milli-Q water from a Millipore filtration system (Bedford, MA). All reagents were used without additional purification.

Animal Experiment

Animal experiments were conducted following institutional guidelines (University of Wisconsin-Madison IACUC). Rock crabs (*Cancer irroratus*) of similar size were purchased from Ocean Resources Inc. (Sedgwick, ME). Crabs were maintained for at least a week at ambient seawater temperature (12-13 ˚C) in a flow-through artificial seawater aquarium before use. Prior to dissection, animals were cold anesthetized. Micro-dissection was performed in chilled physiological saline. Supraesophageal ganglia (brain) and pericardial organ (PO) of crab were harvested according to previously described dissection procedure [41]. Female Sprague-Dawley rats were anesthetized, perfused with chilled phosphate buffered saline, decapitated and removed brains. The brains were then cut along midline. Each hemisphere was embedded in gelatin (100 mg mL^{-1} in water) and snap frozen in dry ice for tissue MSI. These samples were stored at -80 ºC before analysis.

Sample preparation

Matrix

CHCA, DHB, 2-NPG and 3-NBN matrices were used in this study for MALDI, LSI and MAI analyses. 10 mg mL^{-1} CHCA (ACN:EtOH:H_2O:FA (v/v/v/v) 84:13:2.997:0.003), 150 mg mL^{-1} DHB (MeOH:H_2O:FA (v/v/v) 49.95:49.95:0.1), 12.5 mg mL^{-1} 2-NPG (ACN:H_2O:FA (v/v/v) 69.93:29.97:0.1) [33] and 50 mg mL^{-1} 3-NBN (ACN:H_2O (v/v/v) 62.46:37.46:0.08) [37] were used for standards and tissue extraction analysis. 5 mg mL^{-1} CHCA (ACN:H_2O:FA (v/v/v) 49.95:49.95:0.1) and 40 mg mL^{-1} DHB (MeOH:H_2O:FA (v/v/v) 49.95:49.95:0.1) were used for tissue MSI.

Standard

Serial dilutions of bradykinin, neuropeptide Y and insulin standards (10 µM, 1 µM, 100 nM and 10 nM) were dissolved and diluted in ACN:H_2O:FA (v/v/v) 49.95:49.95:0.1 solution. A master mix of standard peptides (substance P, substance K ,oxytocin, [Arg8] vasopressin, bradykinin, proctolin, corazonin, somatostatin (1-14), angiotensin I, alpha-MSHamide, alpha-MSH free acid, LH-RH (human), bactenecin (bovine), allatostatin I, II & III, CCAP, FMRF, FMRFamide, FMRFamide-like peptide I & II (lobster), FMRF-like neuropeptide and FMRFamide related peptide) were prepared by combining 0.2 µg of each peptide in 230 µL H_2O to achieve a final concentration of 0.87 µg mL^{-1} per peptide. 1 µL of the diluted standard solution was mixed with 1 µL matrix solution, and 0.3 µL of the mixture was deposited on the ABI Opti-TOF 192 stainless steel target plate (Applied Biosystems, Foster City, CA).

Tissue extraction

Crustacean and rat brain neuropeptides were extracted with chilled acidified MeOH (MeOH: H_2O:AA (v/v/v) 90:9:1) as described in previous literatures [42]. Briefly, tissues were homogenized manually with 3x volumes of acidified MeOH in a glass homogenizer, centrifuged at 16,100 $\times$ *g* for 10 minutes. The supernatant was dried in in a speed vacuum concentrator,

reconstituted in water with 0.1% FA. A 10 µL C_{18} ZipTip (EMD Millipore, Darmstadt, Germany) was used for desalting prior to MS analysis. 1 µL of the desalted tissue extract was then mixed 1 µL matrix and applied on MALDI target plate.

Tissue MSI

The gelatin embedded tissue was cryosectioned into 12 µm slices on a cryostat (Thermo Scientific Microm HM 525, Thermo Scientific, Kalamazoo, MI) at -20 ˚C and thaw mounted onto an ITO coated slide or a microscope glass slide. The slide was dried at room temperature for 30 minutes in a desiccator before matrix application. A robotic TM sprayer system (HTX Technologies, Carrobo, NC) was used for depositing DHB matrix (40 mg mL^{-1}). The nozzle temperature was set to 80 ˚C with a moving velocity of 600 or 800 mm min^{-1}. Four or eight passes of matrix were deposited at a flow rate of 0.2 mL min^{-1} and 30 seconds drying time between each pass. The sprayed slide was dried at room temperature for 30 minutes and stored in a desiccator in - 20 ˚C until analysis.

After MSI analysis, the tissue slides were washed in 70% EtOH solution for matrix removal, then stained in cresyl violet acetate working solution for 20 minutes. The optical images of tissue section were acquired by an Olympus SZX16 stereo microscope (Olympus, Center Valley, PA) with brightfield illumination.

Mass spectrometry

An AP/MALDI (ng) UHR Ion source (MassTech, Columbia, MD) was coupled with QE HF mass spectrometer for all data acquisition. Target-ng software (MassTech, Columbia, MD) was used to control the AP/MALDI source. Laser energy of 30% and repetition rate of 5000 Hz were used unless otherwise specified. The voltage applied onto the plate varies from 2 kV to 4 kV, depending on the type of plate. For profiling experiments, samples were premixed with matrix solutions and applied onto an ABI Opti-TOF 192 target plate (Applied Biosystems, Foster

City, CA). Spiral plate motion was used. For MSI experiments, constant speed raster motion was used. Plate velocity and spatial resolution were sample dependent and will be specific in the result section.

The mass spectrometer was operated at full MS, targeted MS-MS DDA and PRM modes with positive polarity in this study. Tune or Xcalibur (Thermo Scientific, Bremen, Germany) was used to control the mass spectrometer. Capillary temperature was set to 200 °C and S-lens RF level was 50%. During full scans, mass range of *m/z* 500-2000 was used with resolution of 30k unless otherwise specified. Automatic gain control (AGC) target of 1e6 with 200 ms maximum injection time was used. This AGC value allowed all scans to reach maximum injection time, which ensured consistent scan time at each pixel. During targeted MS-MS scans, precursor ions were fragmented by high-energy collision induced dissociation (HCD). An isolation window of 3 *m/z* was used. The normalized collisional energy (NCE) was optimized for each sample and will be specified in result section. During DDA analysis, top 5 ions were selected for MS-MS analysis with a dynamic exclusion of 10 seconds. During PRM acquisitions, a target list of 10 to 20 ions was used as inclusion list and HCD MS-MS scans were performed on these ions.

Data analysis

Xcalibur (Thermo Scientific, Bremen, Germany) was used to process spectra. ImageQuest (Thermo Scientific, Bremen, Germany) and MSiReader (NC State University, Raleigh, NC) [43] were used for image processing, including image normalization and ion image generations. METLIN metabolite database (Scripps Center for Metabolomics, La Jolla, CA), LIPID Metabolites and Pathways Strategy (LIPID MAPS, University of California-San Diego, La Jolla, CA), Sweden peptide database (SwePep, Uppsala University, Uppsala, Sweden) and the

Li Lab crustacean neuropeptide databases were used for accurate mass matching of metabolites, lipids and neuropeptides with 10 ppm tolerance.

Results and Discussion

The goal of this study is to demonstrate the potential of the AP/MALDI-Q-Orbitrap platform in analyzing diverse classes of biomolecules in solution and *in situ* by multiple types of ionization and acquisitions.

The instrument platform is illustrated in Figure 1, with a picture of the system (Figure 1a) and the schematics of AP/MALDI source (Figure 1b) and the QE HF (Figure 1c). Detailed specifications of the source and the mass spectrometers could be found in the introduction section. Herein, we will introduce the instrument platform in the following four aspects: parameter optimizations for the AP/MALDI-Q-Orbitrap platform; multiple types of ionizations for generating single and multiply charged ions; in depth analysis of complex mixtures by various acquisition modes; and *in situ* analysis with high resolutions in space and mass.

Optimization of operational and instrumental parameters (temperature, plate voltage, S-lens RF level, laser repetition rate and laser energy) on the AP/MALDI-Q-Orbitrap platform

According to Schneider *et al.,* AP/MALDI has similar performance compared to vacuum MALDI when the parameters are properly optimized on a QqLIT instrument [20]. Therefore, operational and instrumental parameters of the AP/MALDI source and QE HF, including laser repetition rate, laser energy, S-lens RF level, plate voltage and capillary temperature were carefully optimized (Figure S1). Neuropeptide standard mixtures were spotted on MALDI target plate for all optimization experiments. S-lens RF level (Figure S1c), spray voltage (Figure S1d) and capillary temperature (Figure S1e) played important roles in neuropeptide ionizations and detections, while laser repetition rate (Figure S1a) and laser energy (Figure S1b) did not affect

the signal intensity significantly. The optimized parameters for neuropeptide analysis were capillary temperature of 400 ºC, plate voltage of 4 kV and S-lens RF level of 80%. This setting was applied to general MALDI neuropeptide analysis, while fine tuning of these parameters were performed before each experiment, especially for different ionizations (MALDI, LSI and MAI) and different target analytes (small molecules, lipids and neuropeptides).

Multiple types of ionization (MALDI, LSI and MAI) on the AP/MALDI-Q-Orbitrap platform

LSI and MAI are two novel ionizations that can generate multiply charged ions without instrument modification. Both of them have been achieved on this instrument platform and demonstrated by bradykinin and neuropeptide Y (Figure 2). LSI generates multiply charged ions by laser ablation and 2-NPG matrix with an ESI-like mechanism [31, 33], while MAI ideally does not require laser ablation or high voltage. During MAI process, sample is co-crystalized with 3-NBN matrix, which is then ionized by a triboluminescence process with the assistant with the vacuum environment inside MS [44]. However, due to the longer distance between sample plate and MS inlet (2 mm) on this instrument platform, laser ablation and plate voltage were required under MAI condition for directing the sample to the MS inlet.

Singly charged bradykinin peak was observed under MALDI (Figure 2a), LSI (Figure 2b) and MAI (Figure 2c) conditions, while doubly charged bradykinin peaks could only be observed under LSI (Figure 2b) and MAI conditions (Figure 2c) due to their abilities to generate multiply charged ions. No neuropeptide Y related peak could be detected at MALDI condition when CHCA was used as matrix (Figure 2d), as CHCA matrix was not suitable for ionizing large molecules. Singly and double charged ions were detected at LSI condition (Figure 2e), with the intensity of doubly charged ion slightly higher than the intensity of singly charged ion. Neuropeptide Y peaks from +2 to +7 charged were detected under MAI condition (Figure 2f)

which is known to be able to generate multiply charged ions. All peaks were detected with low ppm mass errors.

MS-MS acquisitions were performed on bradykinin peaks under MALDI, LSI and MAI conditions to compare their fragmentation efficiencies. Similar fragmentation patterns were observed for the singly charged ion generated at MALDI (Figure 3a) and LSI (Figure 3b) conditions: larger fragment ions were detected at higher abundance, and vice versa. Improved fragmentation efficiencies were observed for the doubly charged ions at LSI (Figure 3c) and MAI conditions (Figure 3e). Singly and doubly charged fragment ions were observed with similar signal abundance throughout the entire *m/z* range. By generating multiply charged ions, the fragmentation efficiency of neuropeptide could be improved at this instrument platform. The singly charged ion at MAI (Figure 3d) was not fragmented very well due to the low abundances of their parent ions (Figure 2f).

Lower limit of detection tests were performed on serial dilutions of bradykinin standards (ACN:H_2O:FA (v/v/v) 49.95:49.95:0.1) at MALDI, LSI and MAI conditions. Both MALDI and LSI could constantly detect bradykinin at 1 ng μL^{-1}, while MAI could detect bradykinin at 100 pg μL^{-1}. However, MAI could not generate constant signal. At MAI condition, ion signals could be detected only at approximately 1 out of 100 scans with other 99 scans being noise (Figure S2). Moreover, both laser energy and high voltage were needed for sample introduction, thus, losing its advantages of being a spontaneous/low energy ionization process. We hypothesize that the low efficiency of MAI was caused by the longer distance between the plate and MS inlet (2 mm) and the system is at atmospheric pressure: at the MALDI-LTQ-Orbitrap XL system, the vacuum MALDI chamber could assist introducing samples to MS after the triboluminescence process [37]; at other instrument equipped with ESI sources, sample/matrix mixture is directly attached to the

inlet of the MS, which could then be introduced by vacuum in the MS. Due to MAI is not stable at this instrument platform, the rest of the study will only focus on MALDI and LSI.

Multi-acquisition modes (HRAM full MS, targeted MS-MS, DDA and PRM) for characterizing complex mixture on AP/MALDI-Q-Orbitrap platform

AP/MALDI-Q-Orbitrap platform is capable of analyzing mixtures, ranging from standard neuropeptide mixtures to complex tissue extracts in both full MS and MS-MS modes under MALDI and LSI conditions. Full MS and MS-MS analyses were performed on standard neuropeptide mixtures by DDA (Figure S3) and PRM (Figure S4) acquisition modes. For the DDA method, top 5 most intense ions were isolated and fragmented with a dynamic exclusion time of 10 seconds and NCE of 32. However, the fragmentation efficiency of each ion was limited. Only one or a few fragment ions could be detected for each parent ion. The reason for limited fragmentation efficiency could be that only a few scans were accumulated for each ion and a uniform collisional energy of 32 was applied for all ions. For the PRM method, an inclusion list was imported into the method for MS-MS acquisitions. The instrument switches between full MS and MS-MS acquisitions to fragment the ions in the inclusion list. The identity of each peak was assigned by accurate mass matching (Figure S4a) and verified by targeted MS-MS (Figure S4 b-i). Improved fragmentation efficiencies were observed with PRM acquisition due to more scans accumulated and customized NCE for each parent ion. The DDA method works better for unknown complex samples as it allows a better exploration of unknown species and no previous knowledge is needed to construct an inclusion list. However, the MS-MS spectra qualities for PRM much better than DDA, as same amount of MS-MS spectra are acquired and accumulated for every ion listed in the inclusion list. So PRM works better for MS-MS analyses of known sample mixtures.

Full MS and MS-MS acquisitions on neuropeptide mixtures were also performed on both crustacean and mammalian tissue extracts (Figure 4). Crustacean PO neuropeptide extracts were examined under MALDI condition (Figure 4 a&b). Thirty-seven neuropeptides were tentatively identified by accurate mass matching against the Li Lab crustacean neuropeptide database with mass tolerance of 10 ppm. The identifications of selected neuropeptide were further confirmed by targeted MS-MS with good sequence coverage (Figure S5). Pituitary gland neuropeptide extract was examined under LSI condition (Figure 4c). Neuropeptides, such as vasopressin, POMC fragments and CLIP fragments were identified by accurate mass matching in full MS. Selected peaks, such as *m/z* 1706.80 and *m/z* 1882.90, were also selected for targeted MS-MS. Their identities were verified to be POMC (124-136) and joining peptide by MS-MS.

High resolution MSI in mass and space for in situ tissue analysis

The fine laser spots and the customizable plate moving speed make the AP/MALDI-Q-Orbitrap platform a powerful tool for MSI studies. High resolution MSI acquisitions, both in space and in mass, have been achieved on this platform for small molecule, lipid and neuropeptide detection on crustacean and mammalian tissue sections.

A 12 µm rock crab brain section was imaged for neuropeptide detection with a spatial resolution of 30 µm. 117 peaks, which have distribution on the tissue area, were tentatively identified as crustacean neuropeptide by accurate mass matching. Selected neuropeptide MSI results were demonstrated in Figure 5. MS imaging of neuropeptide has always been challenging due to the low abundance and fast degradation of neuropeptide *in situ*. By successfully detecting and mapping the distribution of endogenous crustacean neuropeptide, this instrument platform has been proven to be sensitive enough for low abundance analyte detection. It can therefore be used in a variety of challenging studies ranging from neurosciences to clinical studies.

MSI acquisition on mammalian tissue section has also performed. A 12 μm rat cerebellum section was imaged with pixel size of 25 μm. The total acquisition time was 18 hours with a plate velocity of 4 mm min^{-1} to finish the entire section (10 mm x 10 mm). It will take MALDI-LTQ-Orbitrap XL 5.5 days to finish same amount of pixels with an average speed of 3 sec $pixel^{-1}$. The same amount of pixels. 1281 peaks were detected with S/N larger than 3. 267 peaks show distributions on tissue section. Selected ion images were presented in Figure 6. The laser burnt mark could be observed on the microscopic optical image of cresyl violet stained tissue after MSI acquisition. Each line was 25 μm apart and well separated from each other, suggesting the laser diameter is much smaller than 25 μm and higher spatial resolution MSI could be achieved. The tentative identifications of these biomolecules were assigned by accurate mass matching using METLIN database search. Biomolecules with distributions all over the tissue (Figure 6b), only in the center of cerebellum and brain stem (Figure 6c), at the peripheral area of the cerebellum (Figure 6d) and some unique patterns (Figure 6e) were observed.

MS-MS imaging was performed on the adjacent rat cerebellum tissue section with larger pixel size (lower spatial resolution) to verify the identification of the peak at *m/z* 760.58237 (Figure S6). Larger pixel size was selected to save instrument time as the spatial resolution is not crucial in MS-MS imaging. With a pixel size of 100 μm, it only took 1 hour to finish the MS-MS acquisition. Based on the MS-MS, a signature fragment ion of phosphatidylcholine at 184.0738 displayed the same distribution as its parent ion at 760.5824, which verify the classification of this ion.

Conclusion

AP/MALDI (ng) UHR source, developed by MassTech Inc., is a high resolution atmospheric pressure MALDI source, which is interchangeable with ESI source and has a laser

spot of less than 10 μm. In this study, this source was coupled to QE HF to achieve high resolution analysis in both space and mass. Multiple ionization modes, including MALDI, LSI and MAI have been successfully performed in this platform without instrument modification. By generating multiply charged ions under LSI and MAI conditions, the fragmentation efficiencies have been improved and the detection range of Orbitrap has been expanded. Full MS, targeted MS-MS, DDA and PRM acquisitions were achieved on standard neuropeptide mixtures and tissue sections. Due to the high mass accuracy of Orbitrap, biomolecules were identified based on accurate mass matching with extremely low ppm error. Identifies of selected ions were also verified by MS-MS analysis. High resolution full MS and MS-MS images were achieved on crustacean and rat tissues. Overall, the AP/MALDI-Q-Orbitrap is a powerful instrument platform that is capable of multi-ionization and multi-acquisitions for various samples. It could be an attractive alternative to other high resolution MALDI instruments.

Acknowledgements

The authors would like to acknowledge MassTech Inc. for providing the AP-MALDI (ng) UHR source, especially Dr. Vladimir M. Doroshenko, Dr. Victor V. Laiko and Dr. Eugene Moskovets for their generous technical supports. The authors would also like to thank Dr. Robert Thorne's laboratory at University of Wisconsin-Madison for providing rat tissue samples. This work was supported by the National Institutes of Health.

References

[1] Gemperline, E., Chen, B., and Li, L. (2014) Challenges and recent advances in mass spectrometric imaging of neurotransmitters, *Bioanalysis 6*, 525-540.

[2] Ye, H., Wang, J., Greer, T., Strupat, K., and Li, L. (2013) Visualizing neurotransmitters and metabolites in the central nervous system by high resolution and high accuracy mass spectrometric imaging, *ACS chemical neuroscience 4*, 1049-1056.

[3] Liu, X., and Hummon, A. B. (2015) Mass spectrometry imaging of therapeutics from animal models to three-dimensional cell cultures, *Analytical chemistry 87*, 9508-9519.

[4] Patterson, N. H., Doonan, R. J., Daskalopoulou, S. S., Dufresne, M., Lenglet, S., Montecucco, F., Thomas, A., and Chaurand, P. (2016) 3D imaging mass spectrometry of lipids in atherosclerotic plaques: Open-source methods for reconstruction and analysis, *Proteomics*.

[5] OuYang, C., Chen, B., and Li, L. (2015) High Throughput In Situ DDA Analysis of Neuropeptides by Coupling Novel Multiplex Mass Spectrometric Imaging (MSI) with Gas-Phase Fractionation, *Journal of the American Society for Mass Spectrometry 26*, 1992-2001.

[6] Ye, H., Hui, L., Kellersberger, K., and Li, L. (2012) Mapping of Neuropeptides in the Crustacean Stomatogastric Nervous System by Imaging Mass Spectrometry, *J. Am. Soc. Mass Spectrom.*

[7] Ye, H., Mandal, R., Catherman, A., Thomas, P. M., Kelleher, N. L., Ikonomidou, C., and Li, L. (2014) Top-Down Proteomics with Mass Spectrometry Imaging: A Pilot Study towards Discovery of Biomarkers for Neurodevelopmental Disorders, *PLoS One 9*, e92831.

[8] Caprioli, R. M., Farmer, T. B., and Gile, J. (1997) Molecular imaging of biological samples: localization of peptides and proteins using MALDI-TOF MS, *Anal. Chem. 69*, 4751-4760.

[9] Liebl, H. (1967) Ion Microprobe Mass Analyzer, *J Appl Phys 38*, 5277-&.

[10] Brown, A., and Vickerman, J. C. (1984) Static Sims, Fabms and Sims Imaging in Applied Surface-Analysis, *The Analyst 109*, 851-&.

[11] Cliff, B., Lockyer, N. P., Corlett, C., and Vickerman, J. C. (2003) Development of instrumentation for routine ToF-SIMS imaging analysis of biological material, *Appl Surf Sci 203*, 730-733.

[12] Lanni, E. J., Masyuko, R. N., Driscoll, C. M., Dunham, S. J. B., Shrout, J. D., Bohn, P. W., and Sweedler, J. V. (2014) Correlated Imaging with C-60-SIMS and Confocal Raman Microscopy: Visualization of Cell-Scale Molecular Distributions in Bacterial Biofilms, *Analytical chemistry 86*, 10885-10891.

[13] Wiseman, J. M., Ifa, D. R., Song, Q., and Cooks, R. G. (2006) Tissue imaging at atmospheric pressure using desorption electrospray ionization (DESI) mass spectrometry, *Angewandte Chemie 45*, 7188-7192.

[14] Sampson, J. S., Hawkridge, A. M., and Muddiman, D. C. (2006) Generation and detection of multiply-charged peptides and proteins by matrix-assisted laser desorption electrospray ionization (MALDESI) Fourier transform ion cyclotron resonance mass spectrometry, *Journal of the American Society for Mass Spectrometry 17*, 1712-1716.

[15] Nemes, P., and Vertes, A. (2010) Laser ablation electrospray ionization for atmospheric pressure molecular imaging mass spectrometry, *Methods in molecular biology 656*, 159-171.

[16] Lorenz, M., Ovchinnikova, O. S., Kertesz, V., and Van Berkel, G. J. (2013) Laser microdissection and atmospheric pressure chemical ionization mass spectrometry coupled for multimodal imaging, *Rapid communications in mass spectrometry : RCM 27*, 1429-1436.

[17] Laiko, V. V., Baldwin, M. A., and Burlingame, A. L. (2000) Atmospheric pressure matrix-assisted laser desorption/ionization mass spectrometry, *Analytical chemistry 72*, 652-657.

[18] Doroshenko, V. M., Laiko, V. V., Taranenko, N. I., Berkout, V. D., and Lee, H. S. (2002) Recent developments in atmospheric pressure MALDI mass spectrometry, *International journal of mass spectrometry 221*, 39-58.

[19] Tan, P. V., Laiko, V. V., and Doroshenko, V. M. (2004) Atmospheric pressure MALDI with pulsed dynamic focusing for high-efficiency transmission of ions into a mass spectrometer, *Analytical chemistry 76*, 2462-2469.

[20] Schneider, B. B., Lock, C., and Covey, T. R. (2005) AP and vacuum MALDI on a QqLIT instrument, *Journal of the American Society for Mass Spectrometry 16*, 176-182.

[21] Koestler, M., Kirsch, D., Hester, A., Leisner, A., Guenther, S., and Spengler, B. (2008) A high-resolution scanning microprobe matrix-assisted laser desorption/ionization ion source for imaging analysis on an ion trap/Fourier transform ion cyclotron resonance mass spectrometer, *Rapid communications in mass spectrometry : RCM 22*, 3275-3285.

[22] Guenther, S., Rompp, A., Kummer, W., and Spengler, B. (2011) AP-MALDI imaging of neuropeptides in mouse pituitary gland with 5 mu m spatial resolution and high mass accuracy, *International journal of mass spectrometry 305*, 228-237.

[23] Rompp, A., Guenther, S., Takats, Z., and Spengler, B. (2011) Mass spectrometry imaging with high resolution in mass and space (HR(2) MSI) for reliable investigation of drug compound distributions on the cellular level, *Analytical and bioanalytical chemistry 401*, 65-73.

[24] Schober, Y., Guenther, S., Spengler, B., and Rompp, A. (2012) Single cell matrix-assisted laser desorption/ionization mass spectrometry imaging, *Analytical chemistry 84*, 6293-6297.

[25] Schober, Y., Guenther, S., Spengler, B., and Rompp, A. (2012) High-resolution matrix-assisted laser desorption/ionization imaging of tryptic peptides from tissue, *Rapid communications in mass spectrometry : RCM 26*, 1141-1146.

[26] Berisha, A., Dold, S., Guenther, S., Desbenoit, N., Takats, Z., Spengler, B., and Rompp, A. (2014) A comprehensive high-resolution mass spectrometry approach for characterization of metabolites by combination of ambient ionization, chromatography and imaging methods, *Rapid communications in mass spectrometry : RCM 28*, 1779-1791.

[27] Bhandari, D. R., Shen, T., Rompp, A., Zorn, H., and Spengler, B. (2014) Analysis of cyathane-type diterpenoids from Cyathus striatus and Hericium erinaceus by high-resolution MALDI MS imaging, *Analytical and bioanalytical chemistry 406*, 695-704.

[28] Li, B., Bhandari, D. R., Janfelt, C., Rompp, A., and Spengler, B. (2014) Natural products in Glycyrrhiza glabra (licorice) rhizome imaged at the cellular level by atmospheric pressure matrix-assisted laser desorption/ionization tandem mass spectrometry imaging, *The Plant journal : for cell and molecular biology 80*, 161-171.

[29] Bhandari, D. R., Schott, M., Rompp, A., Vilcinskas, A., and Spengler, B. (2015) Metabolite localization by atmospheric pressure high-resolution scanning microprobe matrix-assisted laser desorption/ionization mass spectrometry imaging in whole-body sections and individual organs of the rove beetle Paederus riparius, *Analytical and bioanalytical chemistry 407*, 2189-2201.

[30] Khalil, S. M., Rompp, A., Pretzel, J., Becker, K., and Spengler, B. (2015) Phospholipid Topography of Whole-Body Sections of the Anopheles stephensi Mosquito, Characterized by High-Resolution Atmospheric-Pressure Scanning Microprobe Matrix-Assisted Laser Desorption/Ionization Mass Spectrometry Imaging, *Analytical chemistry 87*, 11309-11316.

[31] Trimpin, S., Inutan, E. D., Herath, T. N., and McEwen, C. N. (2010) Laserspray ionization, a new atmospheric pressure MALDI method for producing highly charged gas-phase ions of peptides and proteins directly from solid solutions, *Mol. Cell. Proteom. 9*, 362-367.

[32] Inutan, E. D., Wager-Miller, J., Mackie, K., and Trimpin, S. (2012) Laserspray ionization imaging of multiply charged ions using a commercial vacuum MALDI ion source, *Analytical chemistry 84*, 9079-9084.

[33] Chen, B., Lietz, C. B., and Li, L. (2014) In Situ characterization of proteins using laserspray ionization on a high-performance MALDI-LTQ-Orbitrap mass spectrometer, *J. Am. Soc. Mass Spectrom. 25*, 2177-2180.

[34] Li, J., Inutan, E. D., Wang, B., Lietz, C. B., Green, D. R., Manly, C. D., Richards, A. L., Marshall, D. D., Lingenfelter, S., Ren, Y., and Trimpin, S. (2012) Matrix assisted ionization: new aromatic and nonaromatic matrix compounds producing multiply charged lipid, peptide, and protein ions in the positive and negative mode observed directly from surfaces, *Journal of the American Society for Mass Spectrometry 23*, 1625-1643.

[35] Inutan, E. D., and Trimpin, S. (2013) Matrix assisted ionization vacuum (MAIV), a new ionization method for biological materials analysis using mass spectrometry, *Mol. Cell. Proteom. 12*, 792-796.

[36] Trimpin, S., and Inutan, E. D. (2013) Matrix assisted ionization in vacuum, a sensitive and widely applicable ionization method for mass spectrometry, *J. Am. Soc. Mass Spectrom. 24*, 722-732.

[37] Chen, B., Lietz, C. B., OuYang, C., Zhong, X., Xu, M., and Li, L. (2016) Matrix-assisted ionization vacuum for protein detection, fragmentation and PTM analysis on a high resolution linear ion trap-orbitrap platform, *Analytica Chimica Acta*.

[38] Cramer, R., Pirkl, A., Hillenkamp, F., and Dreisewerd, K. (2013) Liquid AP-UV-MALDI enables stable ion yields of multiply charged peptide and protein ions for sensitive analysis by mass spectrometry, *Angewandte Chemie 52*, 2364-2367.

[39] Ryumin, P., Brown, J., Morris, M., and Cramer, R. (2016) Investigation and optimization of parameters affecting the multiply charged ion yield in AP-MALDI MS, *Methods (San Diego, Calif.)*.

[40] Scheltema, R. A., Hauschild, J. P., Lange, O., Hornburg, D., Denisov, E., Damoc, E., Kuehn, A., Makarov, A., and Mann, M. (2014) The Q Exactive HF, a Benchtop Mass Spectrometer with a Pre-filter, High-performance Quadrupole and an Ultra-high-field Orbitrap Analyzer, *Mol Cell Proteomics 13*, 3698-3708.

[41] Schmerberg, C. M. (2012) Functional neuropeptidomics in the decapod crustacean method development and application to behavioral neuroscience research, In *Ph.D. Thesis of University of Wisconsin-Madison*, University of Wisconsin-Madison.

[42] Chen, R. B., Ma, M. M., Hui, L. M., Zhang, J., and Li, L. J. (2009) Measurement of Neuropeptides in Crustacean Hemolymph via MALDI Mass Spectrometry, *Journal of the American Society for Mass Spectrometry 20*, 708-718.

[43] Robichaud, G., Garrard, K. P., Barry, J. A., and Muddiman, D. C. (2013) MSiReader: An Open-Source Interface to View and Analyze High Resolving Power MS Imaging Files on Matlab Platform, *Journal of the American Society for Mass Spectrometry 24*, 718-721.

[44] Trimpin, S. (2015) "Magic" Ionization Mass Spectrometry, *Journal of the American Society for Mass Spectrometry*.

Figure legends:

Figure 1. The instrument platform of AP/MALDI (ng) UHR source coupled to a Q Exactive HF hybrid quadrupole-Orbitrap mass spectrometer. (a) A picture of the AP/MALDI (ng) UHR source attached to QE HF. (b) The schematic of AP/MALDI(ng) UHR source. (c) The schematic of QE HF, which is equipped with a segmented quadrupole and ultra-high-field Orbitrap mass analyzer.

Figure 2. Full MS comparisons of MALDI, LSI and MAI on bradykinin (1059 Da) (a, b & c) and neuropeptide Y (4269 Da) (d, e & f). Singly charged bradykinin peak was observed at MALDI (a), LSI (b) and MAI (c) conditions, while doubly charged bradykinin peak could only be observed at LSI (b) and MAI (c) conditions. No neuropeptide Y related peak could be detected at MALDI condition when CHCA was used as matrix (d). Singly and double charged ions were detected at LSI condition (e) and +2 to +7 charged neuropeptide Y peaks were detected under MAI condition (f). All peaks were detected with low ppm mass errors as labeled.

Figure 3. MS-MS comparisons of bradykinin ionized by MALDI, LSI and MAI. (a) MS-MS of singly charged bradykinin under MALDI condition at NCE 33. (b) MS-MS of singly charged bradykinin under LSI condition at NCE 33. (c) MS-MS of doubly charged bradykinin under LSI condition at NCE 32. (d) MS-MS of singly charged bradykinin under MAI condition at NCE 33. (e) MS-MS of doubly charged bradykinin under MAI condition at NCE 32. All MS-MS were acquired with isolation window of 2 *m/z* and resolution of 30,000 at *m/z* 200. Y-axis represents relative signal abundance.

Figure 4. Full MS and MS-MS analyses of crustacean PO and rat pituitary gland neuropeptide extractions. (a) MALDI full MS spectrum of Rock Crab PO neuropeptide extraction at low *m/z* region (*m/z* 620-1000). (b) MALDI full MS spectrum of Rock Crab PO neuropeptide extraction at normal *m/z* region (*m/z* 1000-2000). (c) LSI full MS and MS-MS

spectra of pituitary neuropeptide extraction. Neuropeptides were tentatively identified by accurate mass matching within 10 ppm of theoretical masses. Targeted MS-MS were performed on selected peaks to verify the identifications. NCEs were optimized for each ion.

Figure 5. High resolution MSI of crustacean brain tissue section with 30 µm pixel size. (a). Optical image of brain tissue section. (b-q) Selected ion images of crustacean neuropeptides in the following families: RFamide (b,e,f,i,j & q), tachykinin (c,l & n) and allatostatin A (d, g, h, k, m & p). Neuropeptide identifications were tentatively assigned by accurate mass matching against the Li Lab crustacean neuropeptide database with a mass tolerance of 10 ppm.

Figure 6. High resolution MSI of rat cerebellum section with 25 µm pixel size. (a) Microscopic optical image of cresyl violet stained rat cerebellum after MSI acquisition. The laser burnt mark could be observed on the zoomed in optical. The distance between each line is 25 µm. (b) Selected ion images that have distributions all around the tissue. (c) Selected ion images that have distribution only in the center of cerebellum. (d) Selected ion images that have distribution at the peripheral area of cerebellum. (e) Selected ion images that have special distribution. Identifications were tentatively assigned by database search with a mass tolerance of 10 ppm in METLIN. All MSIs were normalized to TIC and presented without smooth.

Figure

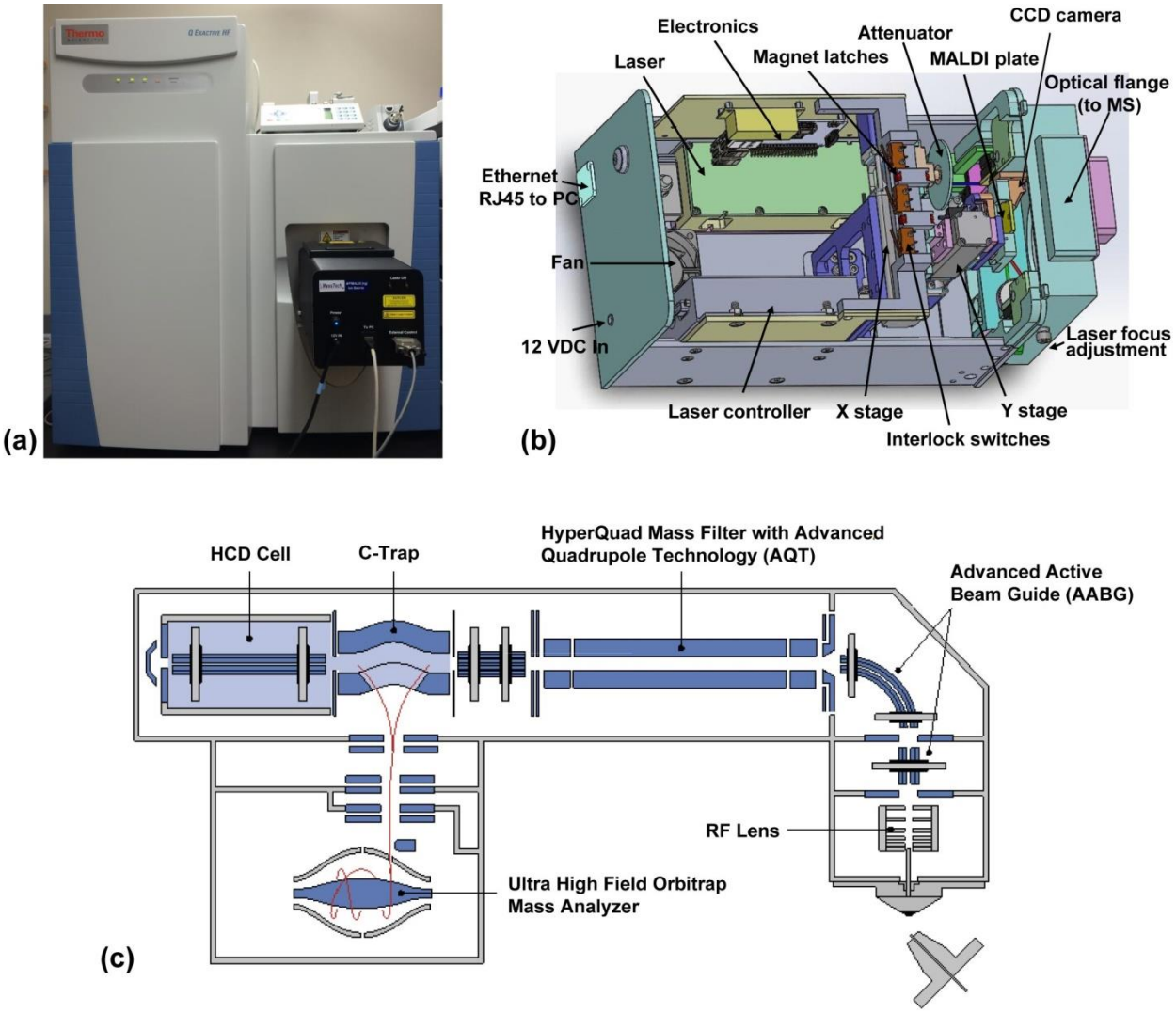

Figure 1

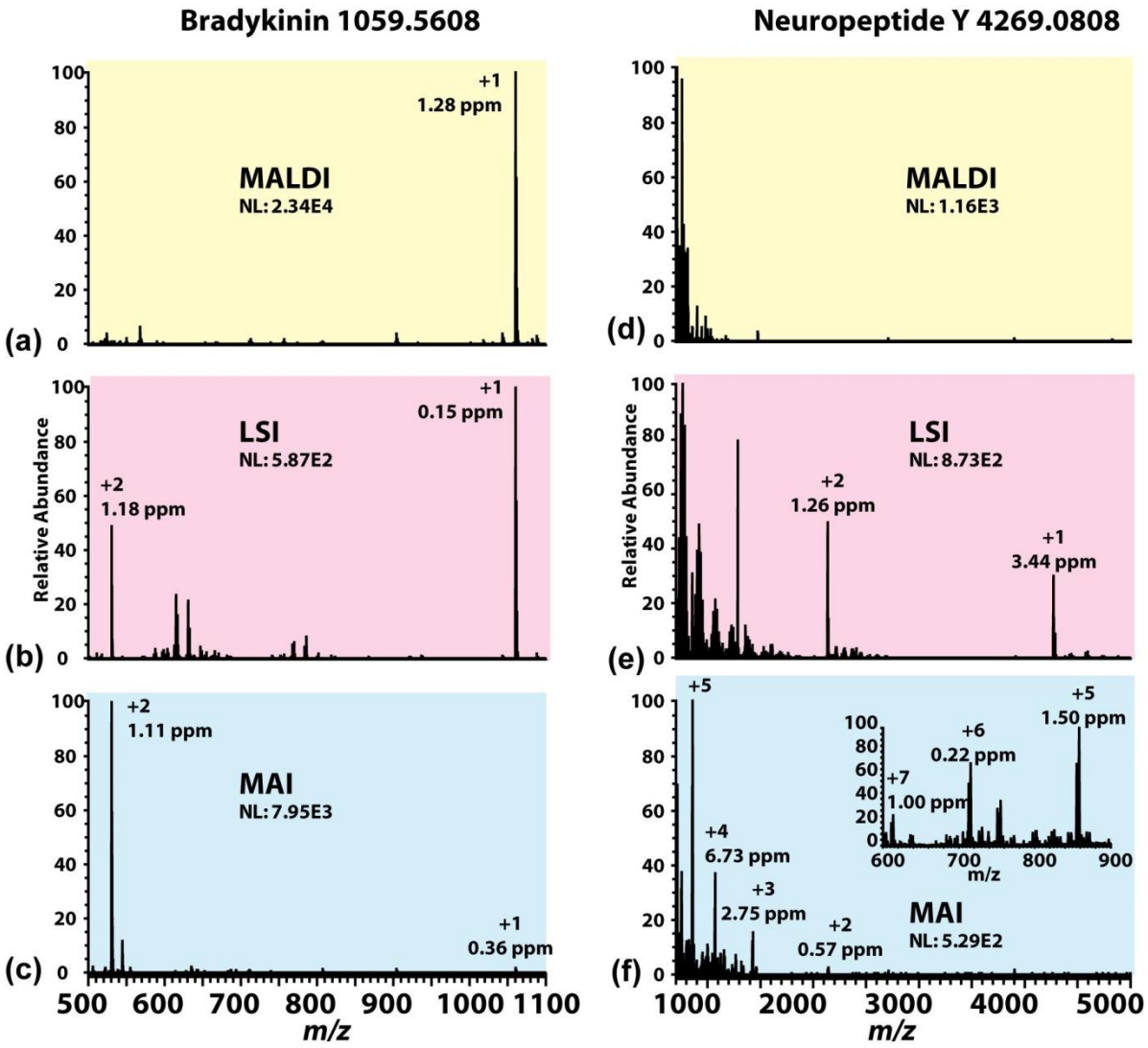
Bradykinin 1059.5608
Neuropeptide Y 4269.0808
MALDI
NL: 2.34E4
+1
1.28 ppm
(a)
MALDI
NL: 1.16E3
(d)
LSI
NL: 5.87E2
+1
0.15 ppm
+2
1.18 ppm
Relative Abundance
(b)
LSI
NL: 8.73E2
+2
1.26 ppm
+1
3.44 ppm
Relative Abundance
(e)
MAI
NL: 7.95E3
+2
1.11 ppm
+1
0.36 ppm
(c)
+5
+4
6.73 ppm
+3
2.75 ppm
+2
0.57 ppm
MAI
NL: 5.29E2
+5
1.50 ppm
+6
0.22 ppm
+7
1.00 ppm
(f)
m/z
m/z

Figure 2

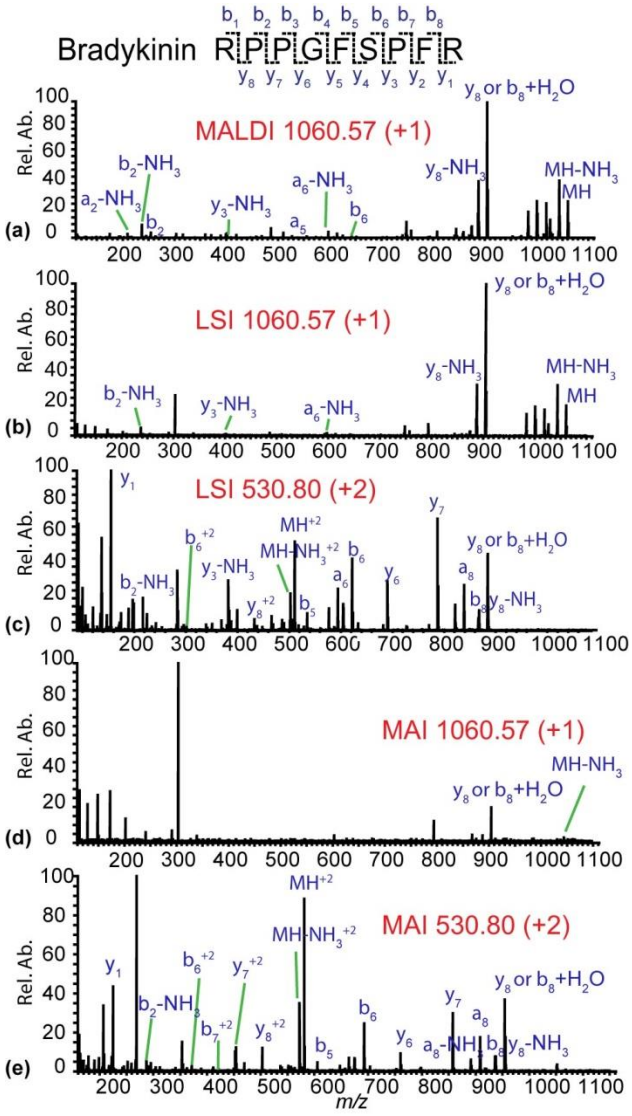
Bradykinin RPPGFSPFR
MALDI 1060.57 (+1)
LSI 1060.57 (+1)
LSI 530.80 (+2)
MAI 1060.57 (+1)
MAI 530.80 (+2)
Rel. Ab.
m/z
(a)
(b)
(c)
(d)
(e)

Figure 3

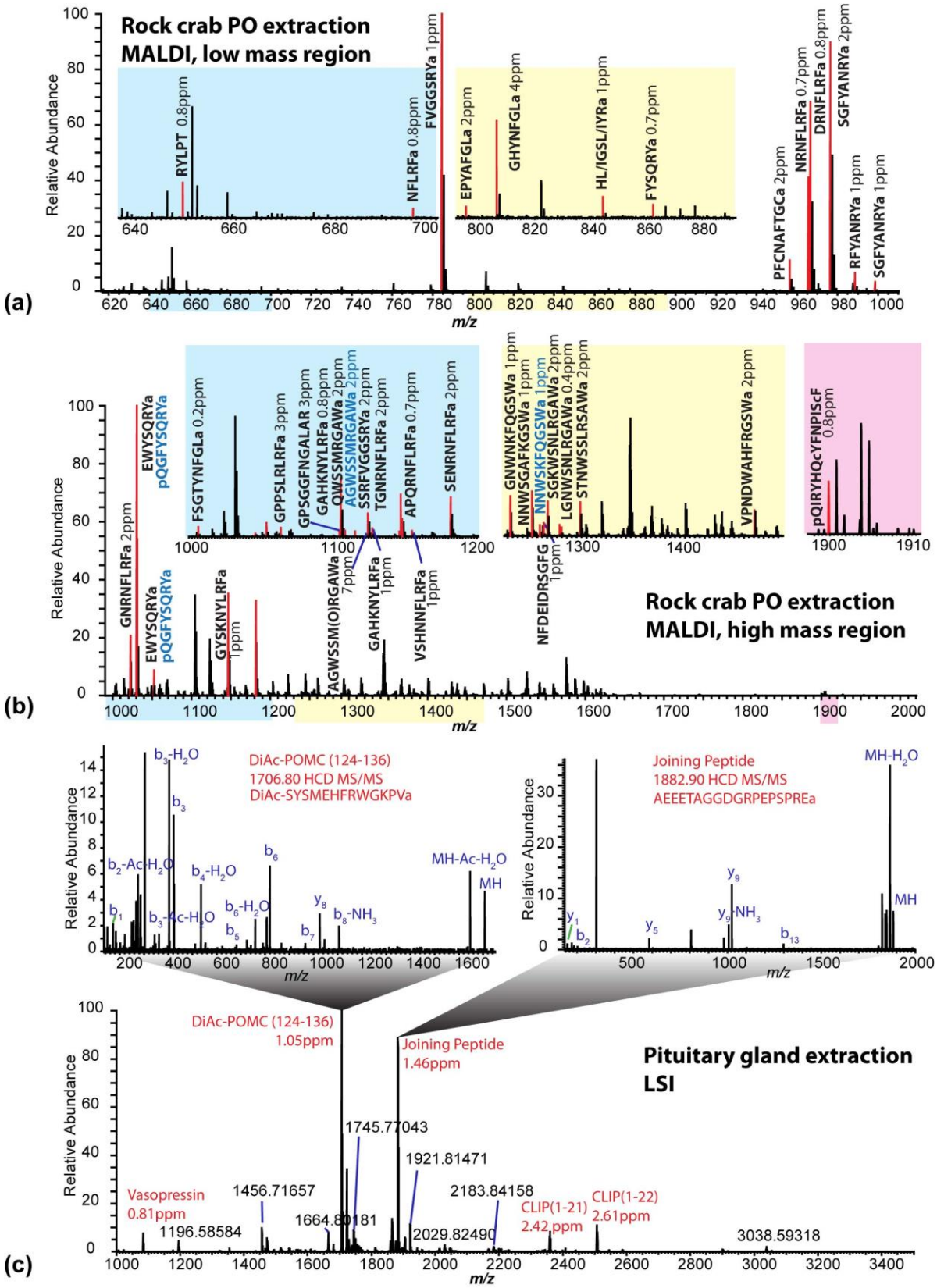
(a)
Rock crab PO extraction
MALDI, low mass region
Relative Abundance
m/z
RYLPT 0.8ppm
NFLRFa 0.8ppm
FVGGSRYa 1ppm
EPYAFGLa 2ppm
GHYNFGLa 4ppm
HL/IGSL/IYRa 1ppm
FYSQRYa 0.7ppm
PFCNAFTGCa 2ppm
NRNFLRFa 0.7ppm
DRNFLRFa 0.8ppm
SGFYANRYa 2ppm
RFYANRYa 1ppm
SGFYANRYa 1ppm
(b)
Rock crab PO extraction
MALDI, high mass region
Relative Abundance
m/z
FSGTYNFGLa 0.2ppm
GPPSLRLRFa 3ppm
GPSGGFNGALAR 3ppm
GAHKNYLRFa 0.8ppm
QWSSMRGAWa 2ppm
AGWSSMRGAWa 2ppm
SSRFVGGSRYa 2ppm
TGNRNFLRFa 2ppm
APQRNFLRFa 0.7ppm
SENRNFLRFa 2ppm
GNWNKFQGSWa 1ppm
NNWSGAFKGSWa 1ppm
NNWSKFQGSWa 1ppm
SGKWSNLRGAWa 2ppm
LGNWSNLRGAWa 0.4ppm
STNWSSLRSAWa 2ppm
VPNDWAHFRGSWa 2ppm
pQIRYHQcYFNPISCF 0.8ppm
EWYSQRYa
pQGFYSQRYa
GNRNFLRFa 2ppm
EWYSQRYa
pQGFYSQRYa
GYSKNYLRFa 1ppm
AGWSSM(O)RGAWa 7ppm
GAHKNYLRFa 1ppm
VSHNNFLRFa 1ppm
NFDEIDRSGFG 1ppm
(c)
DiAc-POMC (124-136)
1706.80 HCD MS/MS
DiAc-SYSMEHFRWGKPVa
Joining Peptide
1882.90 HCD MS/MS
AEEETAGGDGRPEPSPREa
Relative Abundance
m/z
DiAc-POMC (124-136)
1.05ppm
Joining Peptide
1.46ppm
Pituitary gland extraction
LSI
1745.77043
1921.81471
Vasopressin
0.81ppm
1456.71657
2183.84158
CLIP(1-21)
2.42ppm
CLIP(1-22)
2.61ppm
1196.58584
1664.80181
2029.82490
3038.59318

Figure 4

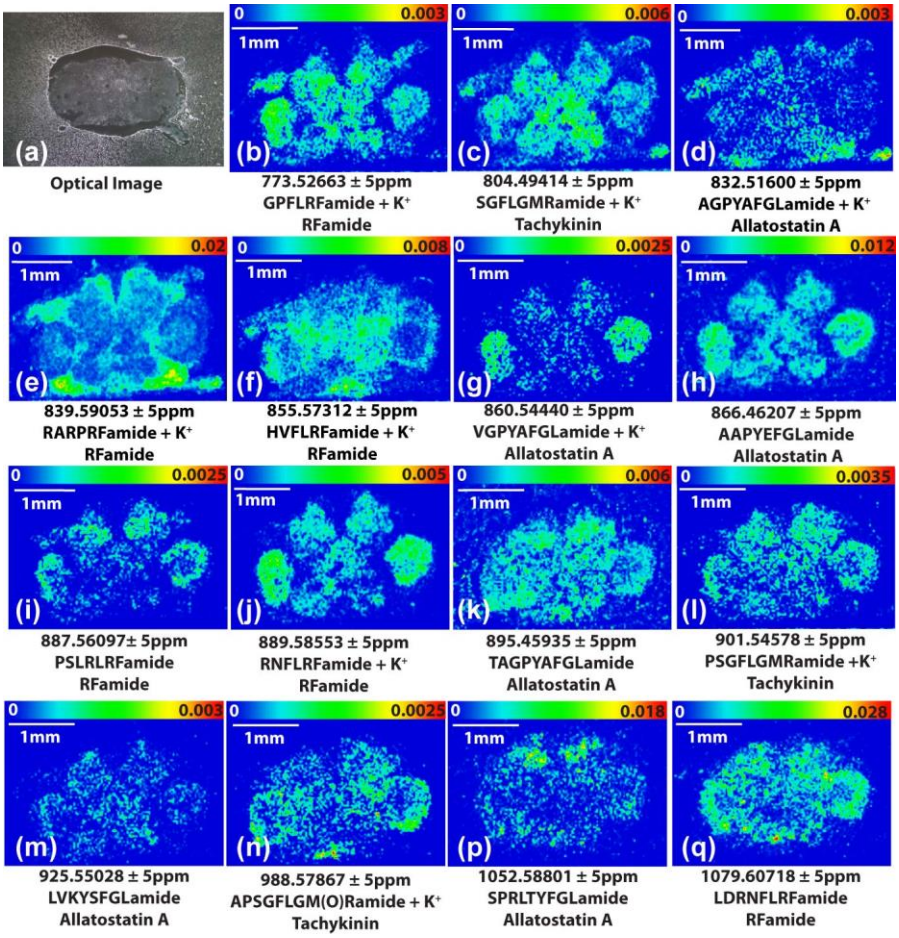
(a)
Optical Image
(b)
773.52663 ± 5ppm
GPFLRFamide + K+
RFamide
(c)
804.49414 ± 5ppm
SGFLGMRamide + K+
Tachykinin
(d)
832.51600 ± 5ppm
AGPYAFGLamide + K+
Allatostatin A
(e)
839.59053 ± 5ppm
RARPRFamide + K+
RFamide
(f)
855.57312 ± 5ppm
HVFLRFamide + K+
RFamide
(g)
860.54440 ± 5ppm
VGPYAFGLamide + K+
Allatostatin A
(h)
866.46207 ± 5ppm
AAPYEFGLamide
Allatostatin A
(i)
887.56097± 5ppm
PSLRLRFamide
RFamide
(j)
889.58553 ± 5ppm
RNFLRFamide + K+
RFamide
(k)
895.45935 ± 5ppm
TAGPYAFGLamide
Allatostatin A
(l)
901.54578 ± 5ppm
PSGFLGMRamide +K+
Tachykinin
(m)
925.55028 ± 5ppm
LVKYSFGLamide
Allatostatin A
(n)
988.57867 ± 5ppm
APSGFLGM(O)Ramide + K+
Tachykinin
(p)
1052.58801 ± 5ppm
SPRLTYFGLamide
Allatostatin A
(q)
1079.60718 ± 5ppm
LDRNFLRFamide
RFamide

Figure 5

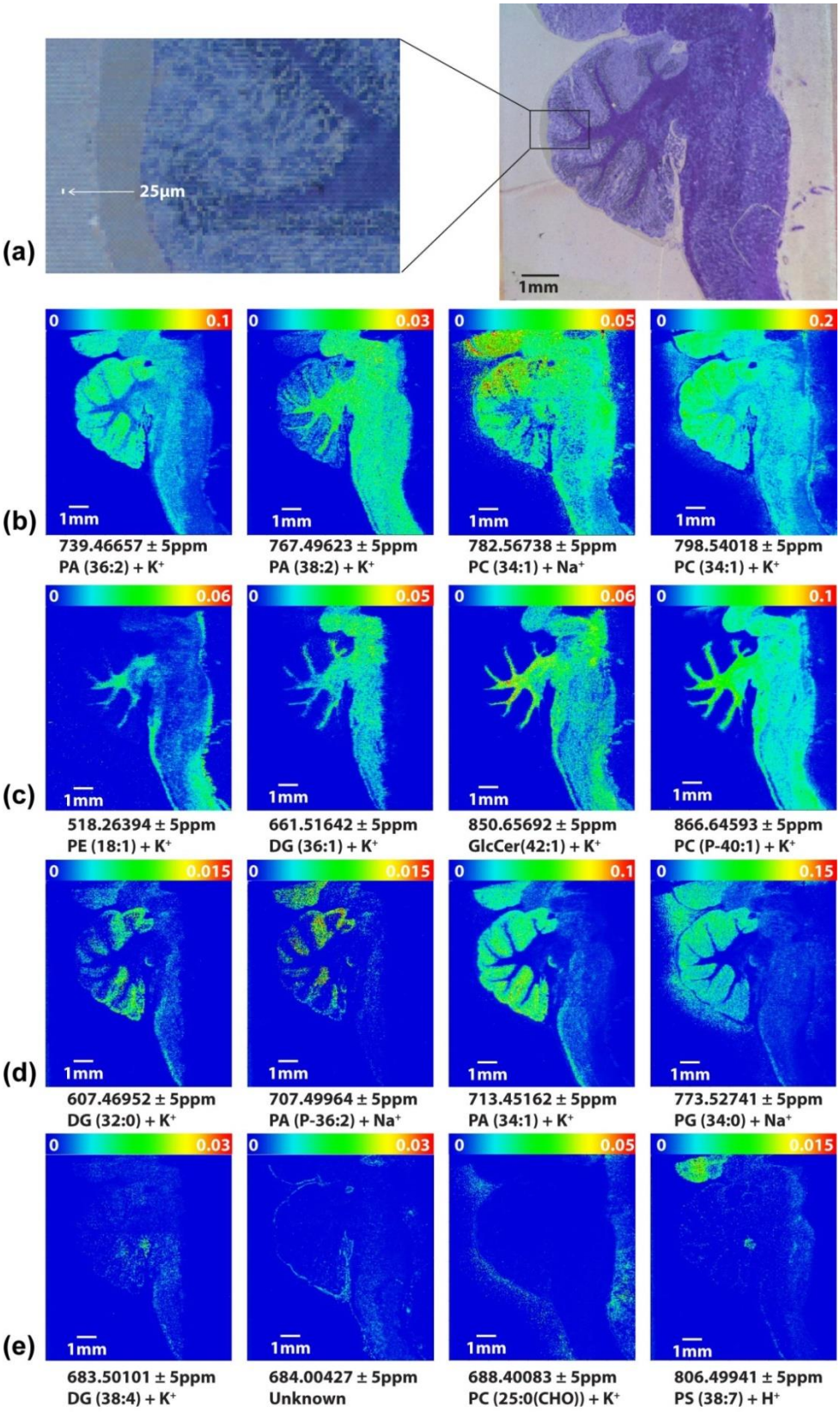
(a)
25µm
1mm
(b)
0
0.1
1mm
739.46657 ± 5ppm
PA (36:2) + K+
0
0.03
1mm
767.49623 ± 5ppm
PA (38:2) + K+
0
0.05
1mm
782.56738 ± 5ppm
PC (34:1) + Na+
0
0.2
1mm
798.54018 ± 5ppm
PC (34:1) + K+
(c)
0
0.06
1mm
518.26394 ± 5ppm
PE (18:1) + K+
0
0.05
1mm
661.51642 ± 5ppm
DG (36:1) + K+
0
0.06
1mm
850.65692 ± 5ppm
GlcCer(42:1) + K+
0
0.1
1mm
866.64593 ± 5ppm
PC (P-40:1) + K+
(d)
0
0.015
1mm
607.46952 ± 5ppm
DG (32:0) + K+
0
0.015
1mm
707.49964 ± 5ppm
PA (P-36:2) + Na+
0
0.1
1mm
713.45162 ± 5ppm
PA (34:1) + K+
0
0.15
1mm
773.52741 ± 5ppm
PG (34:0) + Na+
(e)
0
0.03
1mm
683.50101 ± 5ppm
DG (38:4) + K+
0
0.03
1mm
684.00427 ± 5ppm
Unknown
0
0.05
1mm
688.40083 ± 5ppm
PC (25:0(CHO)) + K+
0
0.015
1mm
806.49941 ± 5ppm
PS (38:7) + H+

Figure 6.

Supporting information

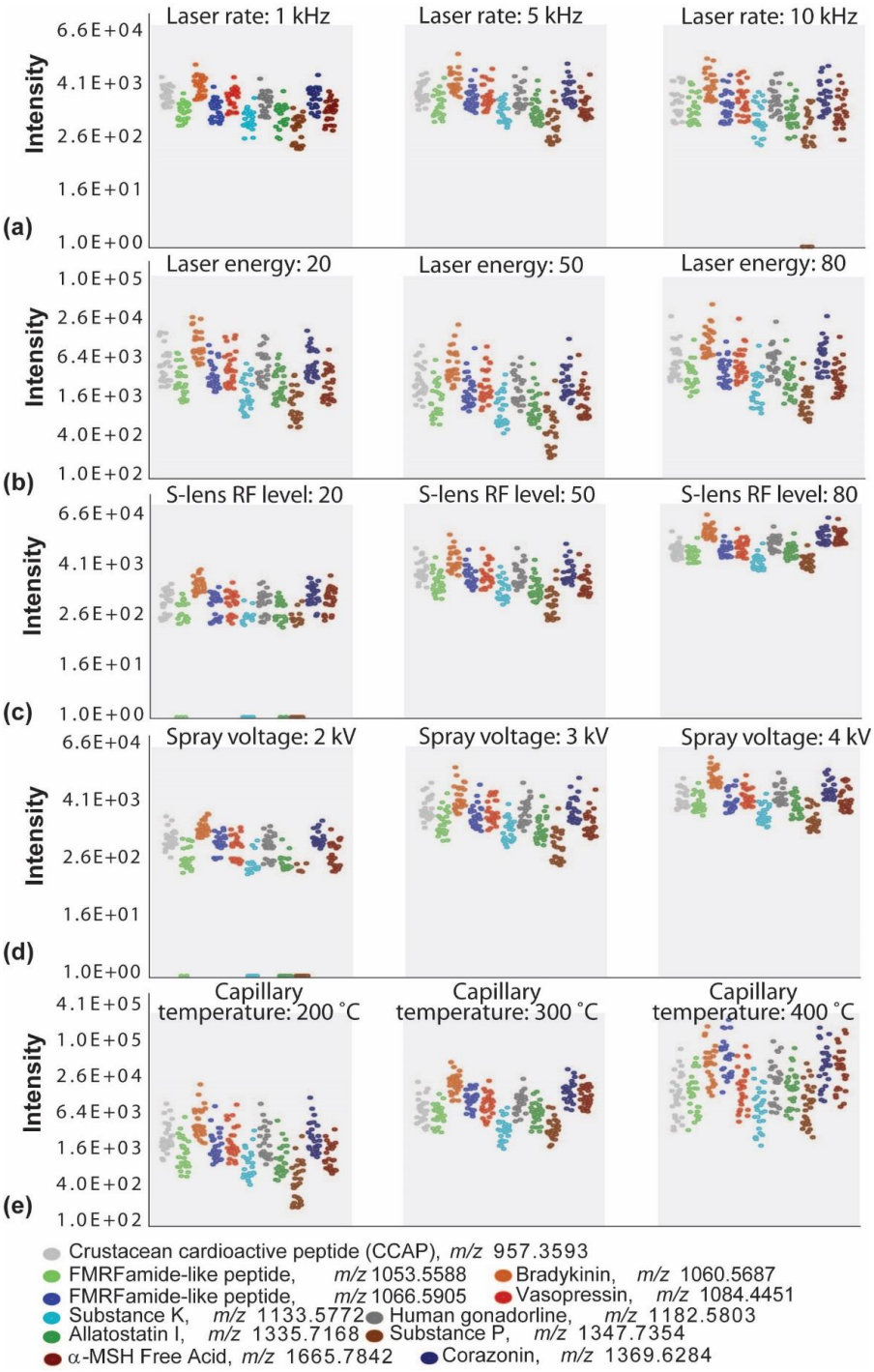

Supplemental Figure 1. AP/MALDI-Q-Orbitrap parameter optimization on neuropeptide standard mixtures. (a) Laser repetition rate comparison (1, 5, 10 kHz). (b) Laser energy comparison (20, 50, 80 %). (c) S-lens RF level comparison (20%, 50% and 80%). (d) Plate voltage comparison (2, 3 and 4 kV). (e) Capillary temperature comparison (200, 300 and 400 °C).

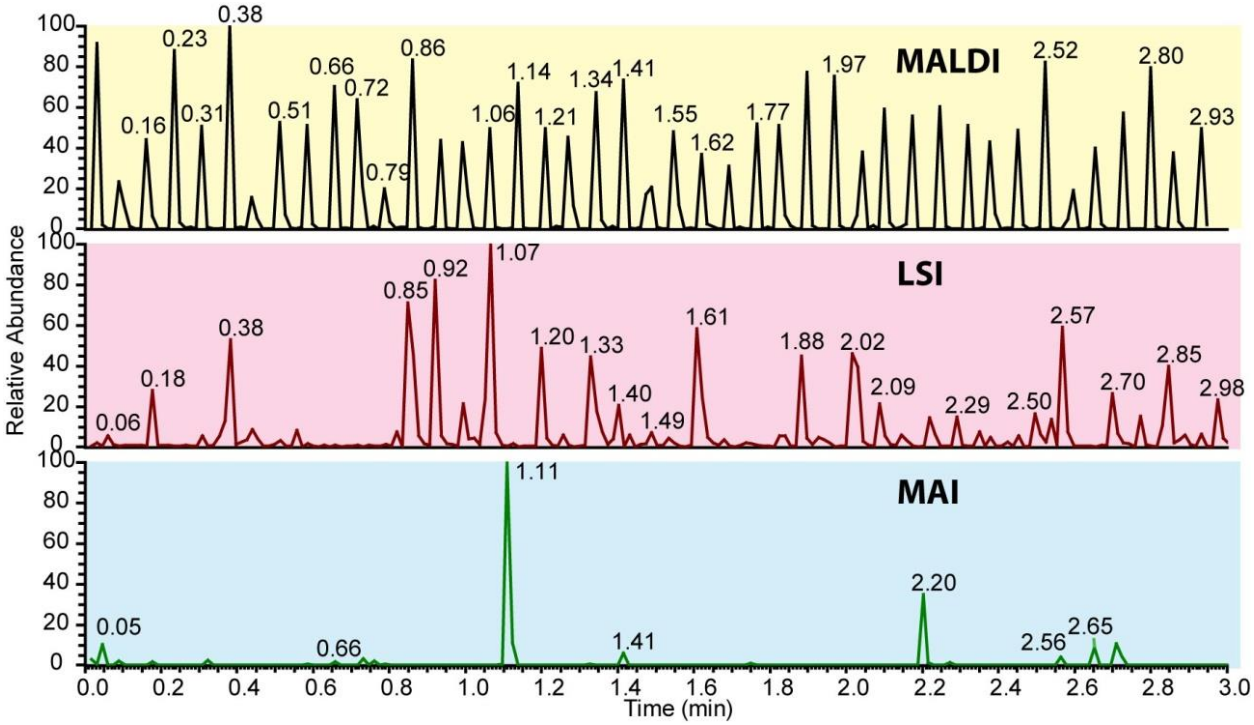

Supplemental Figure 2. Bradykinin full MS chromatograms of MALDI, LSI and MAI. 100 µg mL^{-1} bradykinin standards were used and data was acquired for 3 min under each ionization mode. Bradykinin could be ionized and generated constant signal at MALDI condition. Larger variance in signal intensity was observed at LSI condition. No constant signal could be generated at MAI condition.

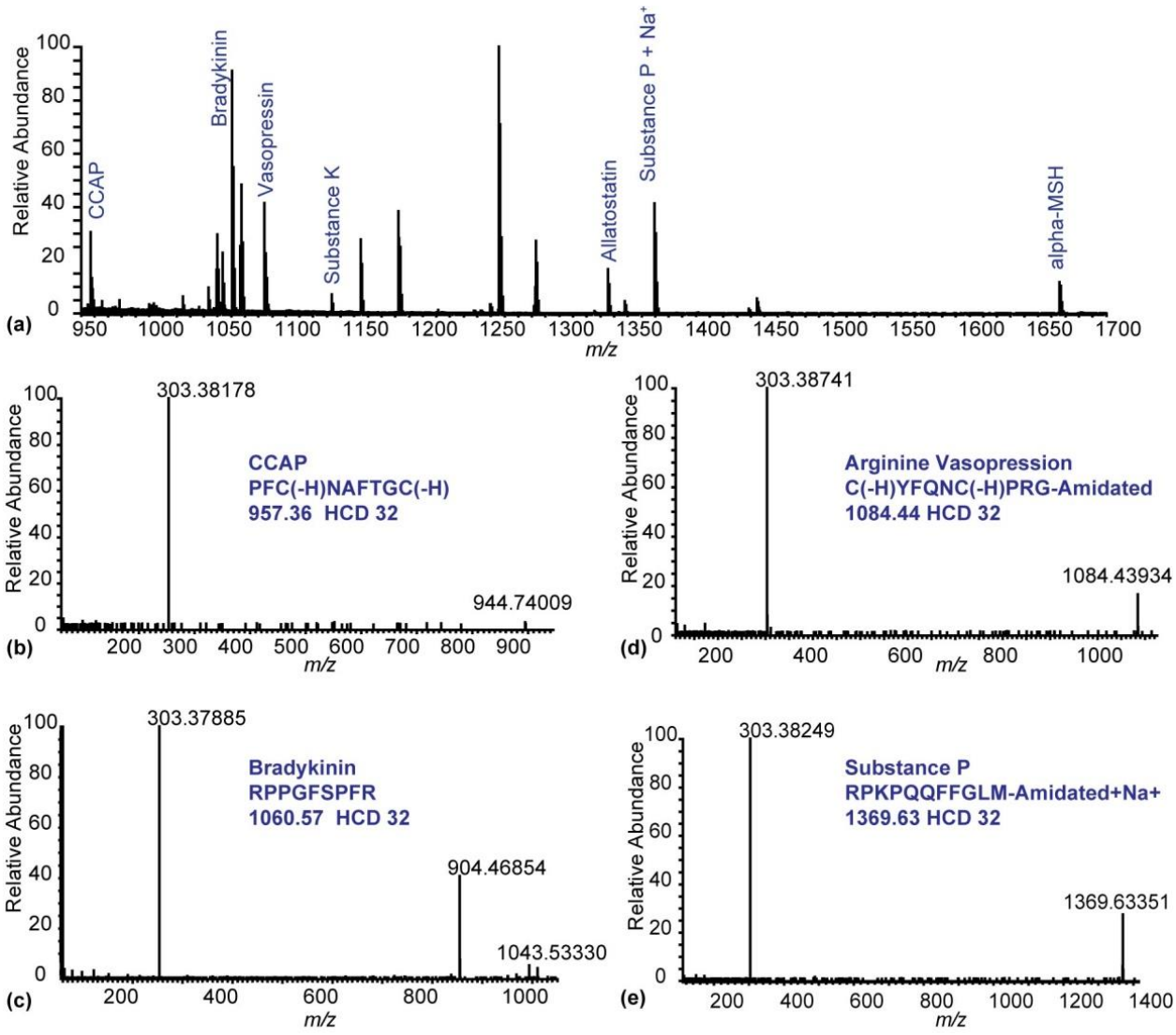

Supplemental Figure 3. DDA on neuropeptide standard mixtures. Mass window of 3 *m/z* and NCE of 32 were used for all peaks. (a) Full MS acquisition of the neuropeptide mixture, the identity of each peptide was assigned by accurate mass matching. (b-e) Annotated MS-MS spectra of selected ions: CCAP (b), bradykinin (c), arginine vasopressin (d) and substance P (e).

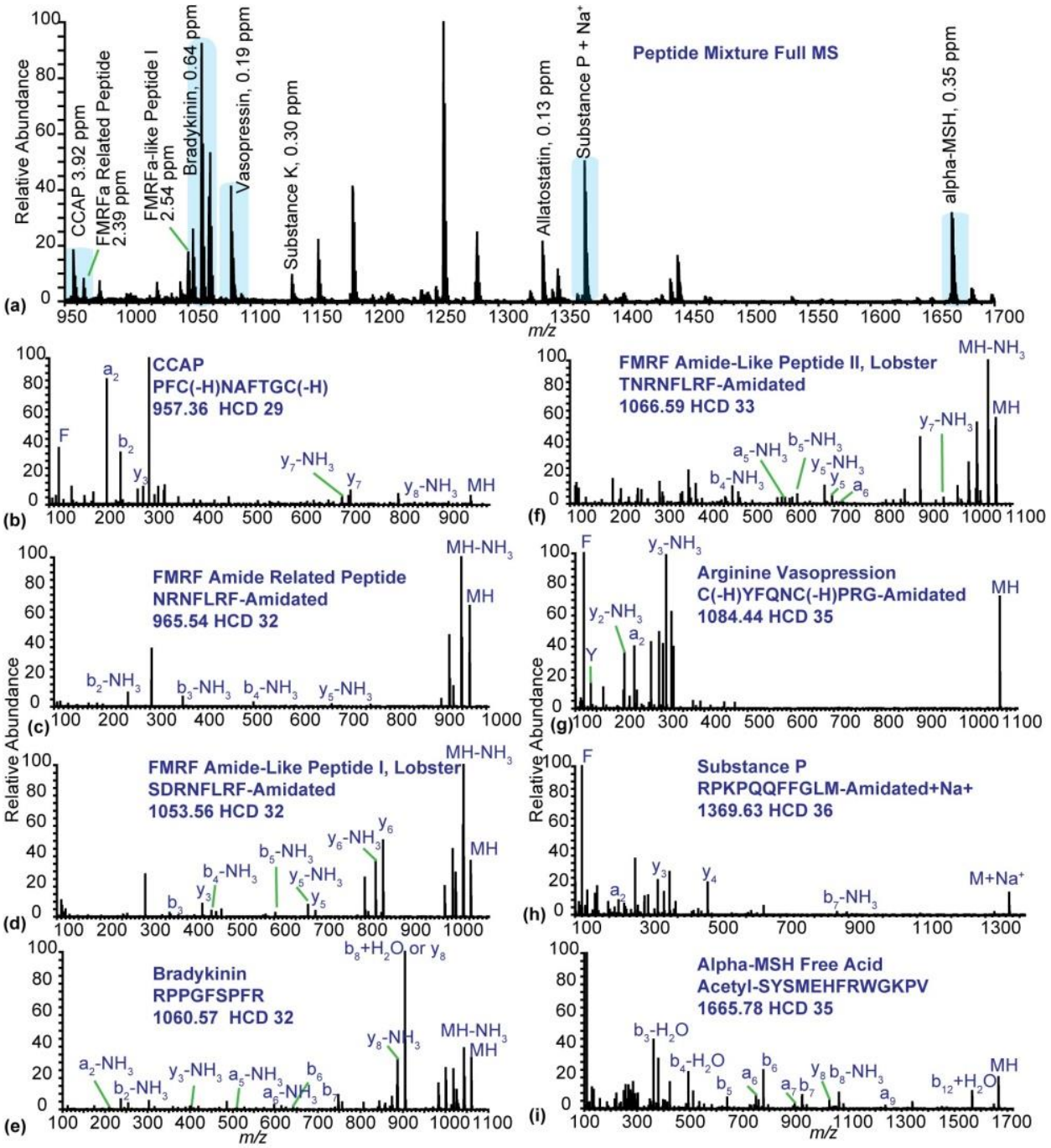

Supplemental Figure 4. PRM on neuropeptide standard mixtures. Mass window of 3 *m/z* was used for all peaks and the NCE were optimized for each ion. (a) Full MS acquisition of the neuropeptide mixture, the identity of each peptide was assigned by accurate mass matching. (b-i) Annotated MS-MS of selected ions in the inclusion list: CCAP, NCE 29 (b), FMRFamide related peptide, NCE 32 (c), FMRFamide-like peptide I, lobster, NCE 32 (d), bradykinin, NCE 32 (e), FMRFamide-like peptide II, lobster, NCE 33 (f), arginine vasopressin, NCE 35 (g), substance P, NCE 36 (h) and alpha-MSH free acid, NCE 35 (i).

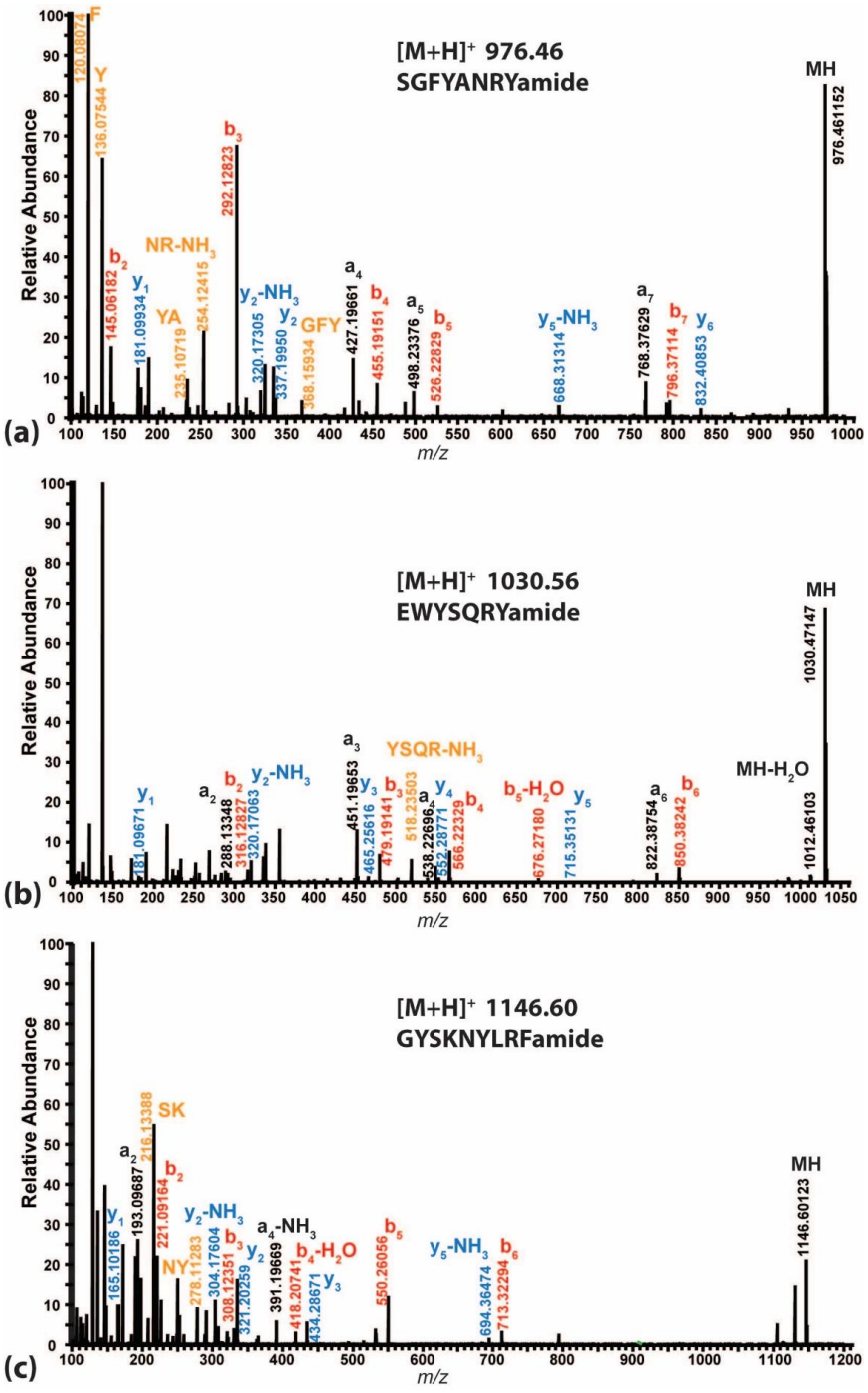

Supplemental Figure 5. Representative MS-MS spectra of Rock crab PO neuropeptide extraction. Selected peaks detected in the full MS scans were selected for targeted MS-MS scans to verify their identifications. (a) MS-MS spectrum of a RYamide at *m/z* 976.46. (b) MS-MS spectrum of a RYamide at *m/z* 1030.56. (c) MS-MS spectrum of a RFamide at *m/z* 1146.60.

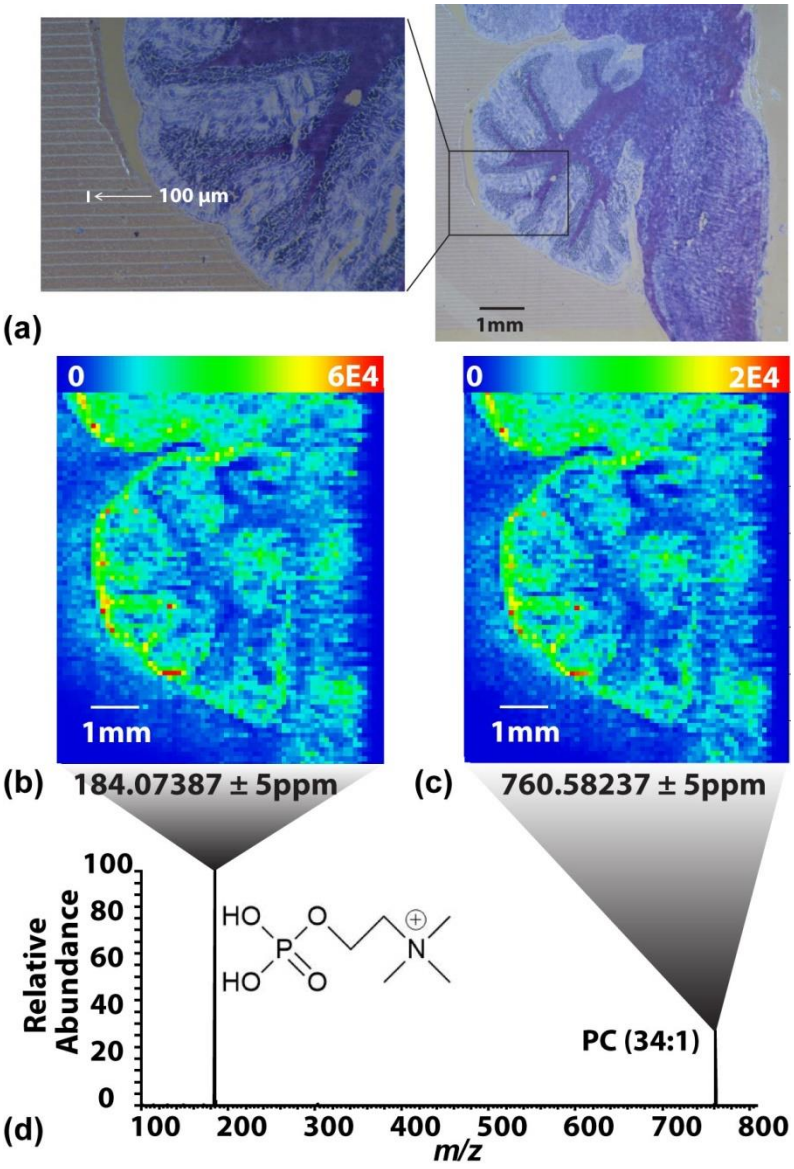

Supplemental Figure 6. MS-MS imaging of rat cerebellum with 100 µm pixel size. (a) Microscopic optical image of cresyl violet stained rat cerebellum after MSI acquisition. The laser burnt mark could be observed on the zoomed in optical image on the left. The distance between each line is 100 µm. (b) Fragment ion image at *m/z* 184.07. (c) Parent ion image at *m/z* 760.58, which was identified to be phosphatidylcholine (34:1). (d) MS-MS spectrum of *m/z* 760.58 with NCE 18 and mass window of 3 *m/z*.

Chapter 7
MALDI-MS Profiling and Imaging of Intranasally Administered Oxytocin and Neuropeptide Analogs

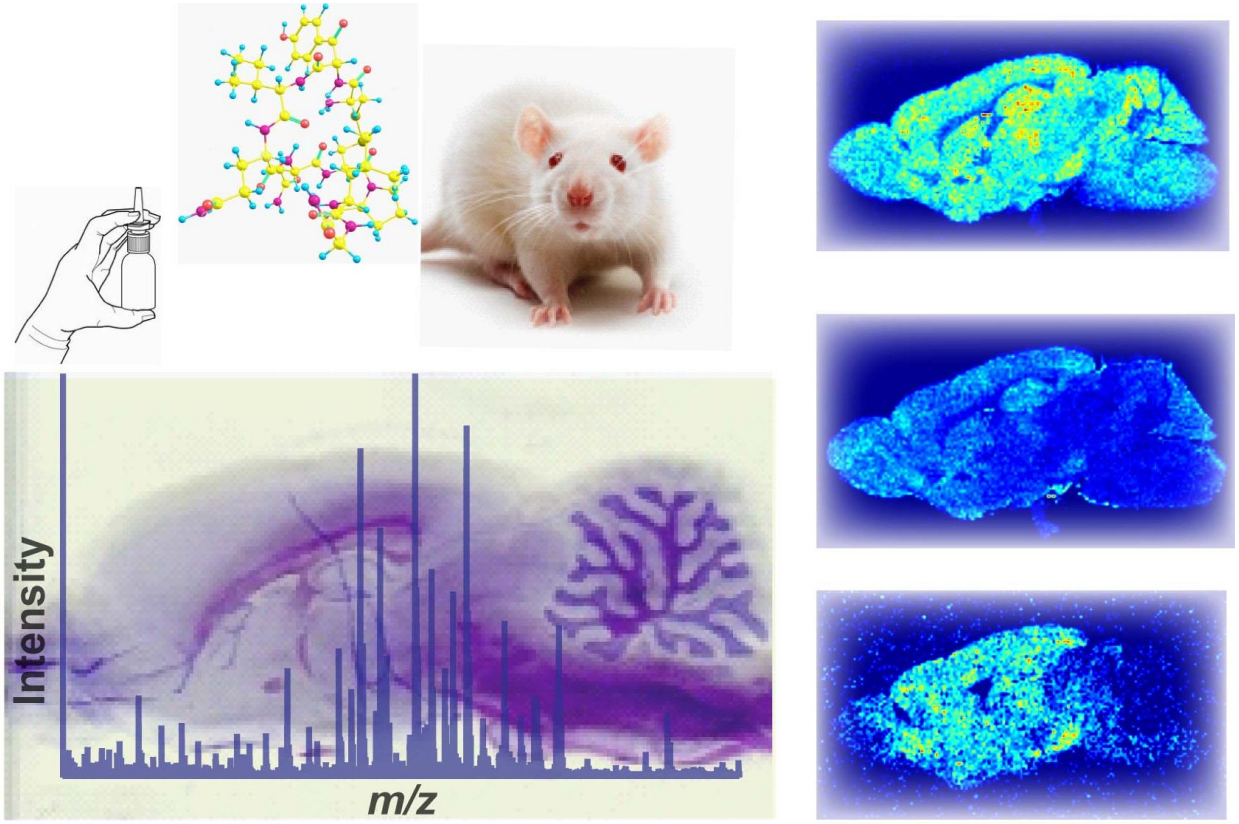

In collaboration with Niyanta Kumar, Mohan Gautam and Dr. Robert Thorne, School of Pharmacy, University of Wisconsin-Madison

Abstract

Over the last two decades, a number of studies have shown that oxytocin (OT) and arginine vasopressin (AVP) could affect social behavior. More than seventy on-going clinical trials are studying the treatment effect of OT and AVP for various diseases, including depression, autism and social anxiety disorders. However, delivering peptides to brain is challenging as the blood-brain barrier (BBB) blocks larger molecules from entering the brain via systemic circulation. Intranasal delivery is a non-invasive method to bypass the BBB and deliver biologics. In this study, we applied *in situ* MS profiling and imaging to study the distribution of intranasally delivered peptides, including OT, AVP, and their analogs, in rat brain. Our findings coincided with previous autoradiographic studies, suggesting that the intranasal delivered peptides followed the olfactory and trigeminal pathways to the brain and further dispersed upon the brain entry point. Mapping the distribution of peptide by MS imaging provides a novel means to evaluate the efficacy of drug delivery.

Introduction

Several animal and human studies have revealed the unique roles of oxytocin (OT) and arginine vasopressin (AVP) in social behavior over the last two decades.[1-5] OT has been shown to facilitate prosocial effects, such as stimulating approaching behaviors and inhibiting defensive behaviors,[5] while AVP has been shown to be associated with male-typical behaviors, such as aggression and courtship.[2] A study by Baumgartner *et al.* suggested that OT administration facilitated trusting behavior through a post-betrayal phase compared to control group. [1] It is considered that OT and AVP bind to receptors in the brain regions that regulate emotion and higher cognitive functions, including the orbitofrontal cortex, hippocampus, amygdala, brainstem nuclei and others.[4] Up till the beginning of this study (2013), over 70 clinical trials of OT and 3

clinical trials of AVP have been initiated to study their effects in the treatment of disorders, including autism, depression, and social anxiety disorder.[3]

OT and AVP are nona-peptides that have molecular weights above 1000 Da. Transporting these neuropeptides to the brain via the systemic circulation is limited by the blood-brain barrier (BBB). Only lipophilic small molecules and a limited range of ligands (via receptor mediated transport) can pass through the BBB.[6] Alternatively, intranasal delivery provides a non-invasive means to bypass the BBB. During intranasal delivery, the substance travels across nasal epithelia by paracellular transport, followed by rapid extracellular flow along olfactory and trigeminal nerve pathway after entry into the brain. Widespread distribution in the brain potentially occurs via flow within perivascular spaces.[7]

Mass spectrometry (MS) imaging is a powerful tool to investigate a broad range of biomolecules, ranging from metabolites to proteins, by collecting mass spectra in a predefined raster across tissue. It has several advantages compared to conventional imaging modalities, such as immunohistochemistry and autoradiography. MS imaging can analyze thousands of analytes in one run without prior knowledge. It also offers specificity by differentiating parent drugs/molecules from their metabolites.[8-11] A study by Liu *et al.* demonstrated the potential of using MS imaging to monitor drug transit through the BBB.[12] In this study, they validated heme as a marker for the lumen of blood vessels in brain and demonstrated 3 examples of drug transit.

To our knowledge, there are no available data reporting the spatial distribution of exogenously delivered neuropeptides in the brain tissue after intranasal administration. Herein, we applied MS imaging to characterize the spatial distribution of intranasally delivered OT and AVP analogs in rat brain tissues. As administering exogenous OT and AVP may induce the

release of endogenous peptides and interfere with the MS detection, synthetic OT and AVP analogs were used in order to differentiate from endogenous versions. Moreover, intranasally delivered saline alone was performed as control experiment to monitor non-specific signals in the brain.

Materials and methods

Materials

All materials were used without additional purification. Methanol, formic acid, acetic acid, and HPLC water were purchased from Fishier Scientific (Pittsburgh, PA). Matrix 2,5-dihydroxybenzoic acid (DHB) was purchased from Acros Organics (Morris Plains, NJ), and matrix α-cyano-4-hydroxycinnamic acid (CHCA) was purchased from Sigma Aldrich (St. Louis, MO). Distilled water (MilliQ) was treated with a Millipore filtration system (Bedford, MA). Neuropeptide standards, including OT and AVP, and their analogs, including [Asu 1,6] OT, [Thr4, Ile7] OT, [Ser4, Ile8] OT, and dDAVP, were purchased from American Peptide Company (Sunnyvale, CA, now part of Bachem, Torrance, CA).

Animal experiment and intranasal delivery

Animal care and use were in accordance with institutional guidelines (University of Wisconsin-Madison, IACUC). Female Sprague-Dawley rats (weighing 180-200 g) were used as a model system. The rat was anesthetized by intra-peritoneal administration of Urethane (0.6061 g/mL) with an initial dosage of 1.5 mg/kg, followed by a booster dosage of 0.3 mg/kg after 10 min. Next, surgery was performed to insert a cannula into the abdominal aorta, which was used to perform perfusion with phosphate buffer saline (PBS). The rat was then placed in a supine position and a gauze pad was placed under the dorsal neck to extend the head back towards the

supporting surface. This position allows the maximum residency time of exogenous substances on the olfactory epithelium.[13] Four drops (12 µL/drop) of a neuropeptide solution in 0.9% saline was administered over a span of 15 min, alternating the left and right nares at an interval of 5 min between drops. During the administration to the left naris, the right naris was closed and vice versa. This procedure allowed the rat to aspirate the peptide solution naturally. Various dosages (0 for control, 1 µg/kg, 1 mg/kg and 5 mg/kg) of neuropeptides were tested for optimization. To differentiate from the endogenous peptides, neuropeptide analogs of [Asu 1,6] OT, [Thr4, Ile7] OT, [Ser4, Ile8] OT, and dDAVP were delivered to the rat brain. At 20 min post administration of first drop, the animal was perfused with 50 mL of 10 mM PBS and decapitated with a guillotine. The brain was then quickly extracted from the skull, cut along midline, embedded in gelatin solution (100 mg/mL in MilliQ water) or stored in microcentrifuge tubes, and snap frozen on dry ice. Tissues from 10 histological brain areas (olfactory bulb, mid brain, cerebellum, spinal cord, brain stem, pituitary gland, amygdala, frontal pole, occipital pole, and hypothalamus) were collected and stored in microcentrifuge tubes for tissue extraction tests. A whole brain hemisphere was embedded for tissue MS profiling and imaging. The samples were stored in -80 ºC freezer until analysis.

Sample preparation

Three approaches were tested for detecting the intranasally delivered peptides (Figure 1): tissue extraction, tissue MS profiling, and tissue MS imaging. Tissues stored in microcentrifuge tubes were used for neuropeptide extraction. Neuropeptides were extracted by homogenization with a glass homogenizer and acidified methanol (90% methanol, 9% water and 1% acetic acid, approximately 3x of the tissue volume) as the buffer. The resulting mixture was centrifuged at 14,000 g for 10 min, and the supernatant was desalted with C_{18} ZipTip. The desalted solution

was mixed with DHB matrix (150 mg/mL in 50% methanol solution) at a 1:1 (v/v) ratio, and 1 µL of the mixture was spotted onto MALDI target plates. Prior to tissue profiling and imaging analysis, the tissue embedded in gelatin was cryosectioned into 12 µm sections at -20 ºC, thaw mounted onto glass slide, and dried in a desiccator at room temperature for 30 min. DHB matrix (1 µL/spot) was added to the tissue section by a micropipette for tissue profiling experiments. For MS imaging experiments, the matrix application methods were optimized (spraying method, matrix and detailed spraying parameter). For the selected methodology, diluted DHB (40 mg/mL) solution was sprayed to the tissue section by an automatic spraying system (TM Sprayer, HTX Technologies, Chapel Hill, NC). The optimized parameters sprayed 8 passes/layers of matrix at a nozzle moving speed of 600 mm/min, temperature of 80 ºC, and matrix flow rate of 0.3 mL/min.

Mass spectrometry

An UltrafleXtreme MALDI-TOF/TOF MS (Bruker, Billerica, MA) and a MALDI-LTQ-Orbitrap XL (Thermo Scientific, Bremen, Germany) were used for MALDI MS analysis. A standardized calibration mixture was used for external calibration of the instrument prior to MS acquisition. Both full MS and MS/MS were performed for accurate mass matching and structure elucidation, respectively. Spectra were collected with *m/z* range of 900-3000 at positive ion mode for full MS analysis. The collisional energy of higher-energy collisional dissociation (HCD) was optimized to achieve the best fragmentation. For imaging acquisition, a pixel size of 100 µm (x and y plane) was used for all tissue sections. All data on the MALDI-LTQ-Orbitrap XL were acquired in the Orbitrap with a mass resolution of 30,000 (*m/z* 400). MS data processing software flexAnalysis (Bruker) and Xcalibur (Thermo) were used for data analysis. MS imaging software such as flexImaging (Bruker), ImageQuest (Thermo), and MSiReader[14] (NC State

University, Raleigh, NC) were used for generating MS images for analyte of interest. A mass window of 10 ppm was used when generating the MS images.

Results and discussion

In this study, MS profiling and imaging approaches were applied to characterize the spatial distribution of intranasally administered OT, AVP, and their analogs in rat brain tissues. Prior to this study, there are no available data reporting the distribution of exogenously delivered neuropeptide in brain tissue after intranasal delivery. The neuropeptide dosage, sample preparation process, and instrument method were carefully optimized. In this study, both the exogenously administered neuropeptides and other endogenous neuropeptides were simultaneously monitored by MS profiling and imaging experiments.

Optimization

Due to the biological variability and relatively low delivery efficiencies of intranasal delivery,[7] various dosages of neuropeptides were tested for detection capability. Dosages of 0 (control), 1 µg/kg, 1 mg/kg, and 5 mg/kg were tested. No corresponding peptide signal could be detected at dosages of 0 or 1 µg/kg. Weak signal could be detected at dosage of 1 mg/kg. As a result, 5 mg/kg dosage was used to ensure detection.

Different matrix application approaches (airbrush vs. automatic sprayer) were compared to achieve the best detection of the molecules of interest. An airbrush is a portable device that can be used to manually spray matrix in a cost- and time-efficient manner. However, it is challenging to generate reproducible results, and the method is not transferable among researchers. Alternatively, a TM sprayer is an automatic spraying device that can generate homogeneous matrix layer, can be customized, and be easily reproduced by other researchers.

Therefore, the TM sprayer system was used for matrix deposition to generate reproducible results.

To further optimize the parameters on TM sprayer system, different flow rates (0.20, 0.25, 0.30 and 0.35 mL/min), nozzle moving velocities (400, 600, 800 and 950 mm/min) and passes (8, 12 and 16) were compared. The spraying parameters were evaluated by examining the homogeneity and length of spraying time. As MS imaging is a time-consuming process, only selected conditions with more homogenous matrix layer were tested for MS imaging. Tissue sections sprayed with a flow rate of 0.3 mL/min, nozzle velocity of 600 mm/min at 80 ºC, and 8 passes were observed to have the best result in MS imaging.

Detection of OT, AVP and analogs

Three MS approaches, tissue extraction, *in situ* profiling, and imaging, were used to detect exogenously administered peptide signals (Figure 1). The tissue extraction approach offered the best sensitivity, as the neuropeptides were extracted, desalted, and concentrated, but it did not reveal spatial information. During *in situ* MS profiling and imaging, both biomolecule detection and spatial information could be collected. In comparison to MS imaging, MS profiling offered better sensitivity due to better peptide extraction efficiency of matrix droplet compared to matrix layer. Although, MS imaging offered more detailed spatial information, as distribution map of each analyte could be generated from imaging experiment.

The detection of exogenously administered neuropeptides was summarized in Figure 2. The rat brain atlas (Figure 2A) demonstrates the major brain area, and the MS image (Figure 2B) is presented in the same orientation as the atlas. MS imaging of [Thr4, Gly7] OT shows widespread signal distribution across the brain tissue section (Figure 2B). Most signal was

observed in the olfactory bulb and brain stem, but [Thr4, Gly7] OT was also observed in cerebellum, cortex, and other areas. Exogenously delivered OT signal was also detected in the tissue extractions of olfactory bulb (Figure 2C) and trigeminal nerve (Figure 2D). The profiling and imaging matched observations from previous studies, suggesting that intranasal delivered peptides traveled along olfactory and trigeminal nerve pathways in nasal epithelium and reached olfactory bulb and brain stem. It further dispersed to other brain area upon initial brain entry.[7, 13, 15]

MS imaging of other neuropeptides

MS imaging allows visualization of thousands of molecules simultaneously. Besides the intranasally delivered peptides, the distributions of other neuropeptides were also monitored. Three representative neuropeptide distributions are shown in Figure 3: reticulon 1 (A), myelin basic protein 2-11 (B), and proenkephalin B 235-248 (C). Other biomolecule distributions can also be visualized if the accurate molecular weight is known and within the *m/z* range of the imaging experiment. Monitoring the change of a biomolecule's distribution and intensity before and after the intranasal delivery can be a potential future direction.

Conclusion

Over the last two decades, several studies have shown that OT and AVP could affect social behavior, and several on-going clinical trials are studying the treatment effect of OT and AVP for various diseases. However, delivering peptides to brain is challenging due to the existing of BBB. Intranasal delivery is a non-invasive method to bypass BBB and deliver biologics such as peptides and proteins. In this study, we applied *in situ* MS profiling and imaging to study the distribution of intranasally delivered peptides, including OT, AVP, and their

analogs, in rat brain tissues. Our findings coincided with previous autoradiographic studies, suggesting that the intranasal delivered peptide followed the olfactory and trigeminal pathways to the brain, and further dispersed upon the brain entry point. Future experiments will focus on studying the neuropeptidome changes on rat brain after intranasal delivery of peptides.

References

[1] Baumgartner, T., Heinrichs, M., Vonlanthen, A., Fischbacher, U., and Fehr, E. (2008) Oxytocin shapes the neural circuitry of trust and trust adaptation in humans, *Neuron 58*, 639-650.

[2] Lim, M. M., and Young, L. J. (2006) Neuropeptidergic regulation of affiliative behavior and social bonding in animals, *Hormones and behavior 50*, 506-517.

[3] Macdonald, K., and Feifel, D. (2013) Helping oxytocin deliver: considerations in the development of oxytocin-based therapeutics for brain disorders, *Frontiers in neuroscience 7*, 35.

[4] Macdonald, K., and Macdonald, T. M. (2010) The peptide that binds: a systematic review of oxytocin and its prosocial effects in humans, *Harvard review of psychiatry 18*, 1-21.

[5] Young, L. J. (2002) The neurobiology of social recognition, approach, and avoidance, *Biological psychiatry 51*, 18-26.

[6] Pardridge, W. M. (2002) Drug and gene delivery to the brain: the vascular route, *Neuron 36*, 555-558.

[7] Lochhead, J. J., and Thorne, R. G. (2012) Intranasal delivery of biologics to the central nervous system, *Advanced drug delivery reviews 64*, 614-628.

[8] Angel, P. M., and Caprioli, R. M. (2013) Matrix-assisted laser desorption ionization imaging mass spectrometry: in situ molecular mapping, *Biochemistry 52*, 3818-3828.

[9] Caprioli, R. M., Farmer, T. B., and Gile, J. (1997) Molecular imaging of biological samples: localization of peptides and proteins using MALDI-TOF MS, *Analytical chemistry 69*, 4751-4760.

[10] Gemperline, E., Chen, B., and Li, L. (2014) Challenges and recent advances in mass spectrometric imaging of neurotransmitters, *Bioanalysis 6*, 525-540.

[11] Gessel, M. M., Norris, J. L., and Caprioli, R. M. (2014) MALDI imaging mass spectrometry: spatial molecular analysis to enable a new age of discovery, *Journal of proteomics 107*, 71-82.

[12] Liu, X., Ide, J. L., Norton, I., Marchionni, M. A., Ebling, M. C., Wang, L. Y., Davis, E., Sauvageot, C. M., Kesari, S., Kellersberger, K. A., Easterling, M. L., Santagata, S., Stuart, D. D., Alberta, J., Agar, J. N., Stiles, C. D., and Agar, N. Y. (2013) Molecular imaging of drug transit through the blood-brain barrier with MALDI mass spectrometry imaging, *Scientific reports 3*, 2859.

[13] Thorne, R. G., Emory, C. R., Ala, T. A., and Frey, W. H., 2nd. (1995) Quantitative analysis of the olfactory pathway for drug delivery to the brain, *Brain research 692*, 278-282.

[14] Robichaud, G., Garrard, K. P., Barry, J. A., and Muddiman, D. C. (2013) MSiReader: an open-source interface to view and analyze high resolving power MS imaging files on Matlab platform, *J Am Soc Mass Spectrom 24*, 718-721.

[15] Thorne, R. G., Hanson, L. R., Ross, T. M., Tung, D., and Frey, W. H., 2nd. (2008) Delivery of interferon-beta to the monkey nervous system following intranasal administration, *Neuroscience 152*, 785-797.

Figure legends

Figure 1. Overall workflow. Therapeutic peptides were intranasally delivered to rat brain and the animal was sacrificed 20-30 min after peptide delivery. The brain tissues were used for 3 approaches: 1. Brain tissues were homogenized and the extracted peptides were applied on MALDI MS plate for target peptide detection; 2. Brain tissues were cryosectioned and a matrix droplet was applied onto the tissue section for MS detection; 3. Brain tissues were also cryosectioned and matrix was homogeneously applied onto the section for MALDI MS imaging.

Figure 2. MALDI MS imaging and profiling of OT and its analog on rat brain sections or homogenates after intranasal delivery. (A) Structure of rat brain. (B) Distribution of [Thr4, Gly7] OT on rat brain section. (C) OT signal detected in the olfactory bulb extract. (D) OT signal detected in trigeminal nerve extract.

Figure 3. MS images of endogenous neuropeptides detected on the same rat brain section: (A) Reticulon 1, (B) Myelin basic protein 2-11, (C) Proenkephalin B 235-248.

Figures

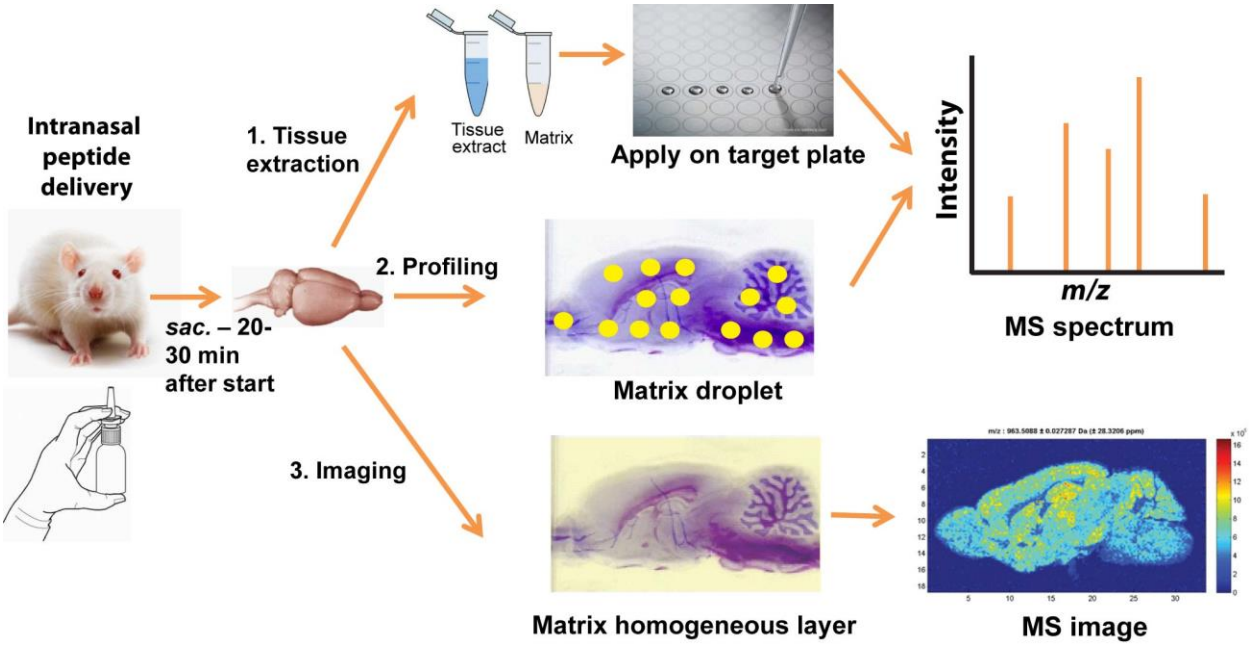

Figure 1

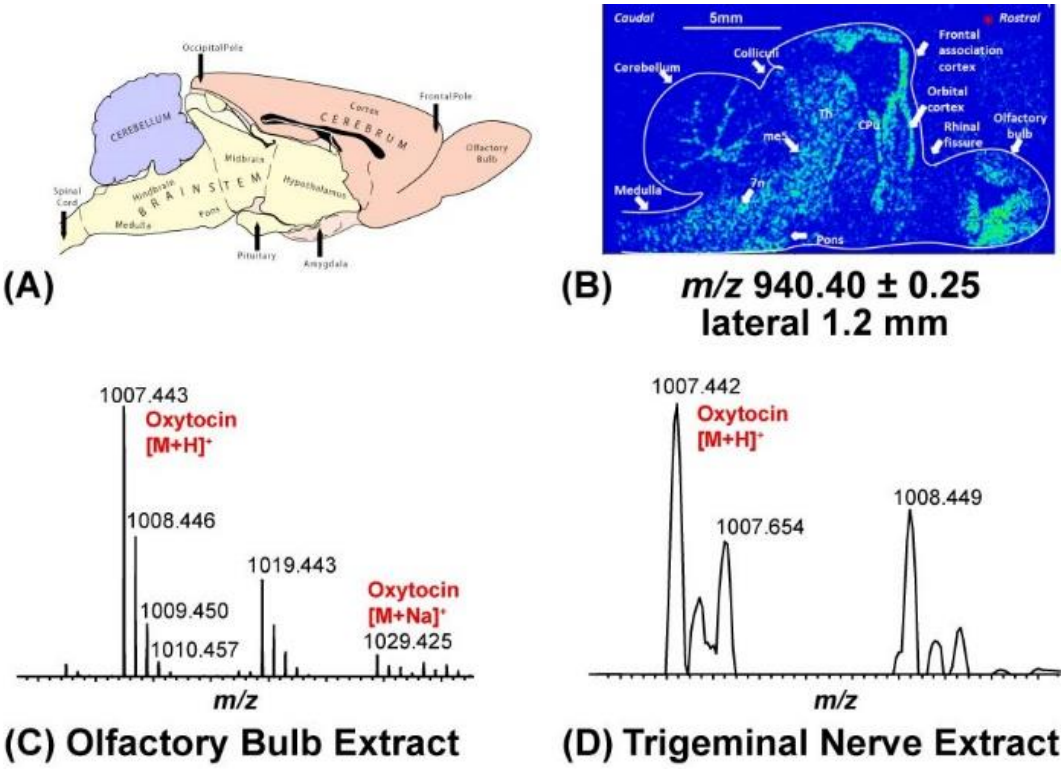
OccipitalPole
CEREBELLUM
Cortex
CEREBRUM
FrontalPole
Olfactory Bulb
Midbrain
BRAINSTEM
Hypothalamus
Spinal Cord
Hindbrain
Pons
Medulla
Pituitary
Amygdala
(A)
Caudal
5mm
Rostral
Cerebellum
Colliculi
Frontal association cortex
Orbital cortex
Rhinal fissure
Olfactory bulb
Th
CPu
me5
Medulla
Pons
(B)
m/z 940.40 ± 0.25
lateral 1.2 mm
1007.443
Oxytocin
[M+H]+
1008.446
1019.443
1009.450
1010.457
Oxytocin
[M+Na]+
1029.425
m/z
(C) Olfactory Bulb Extract
1007.442
Oxytocin
[M+H]+
1008.449
1007.654
m/z
(D) Trigeminal Nerve Extract

Figure 2

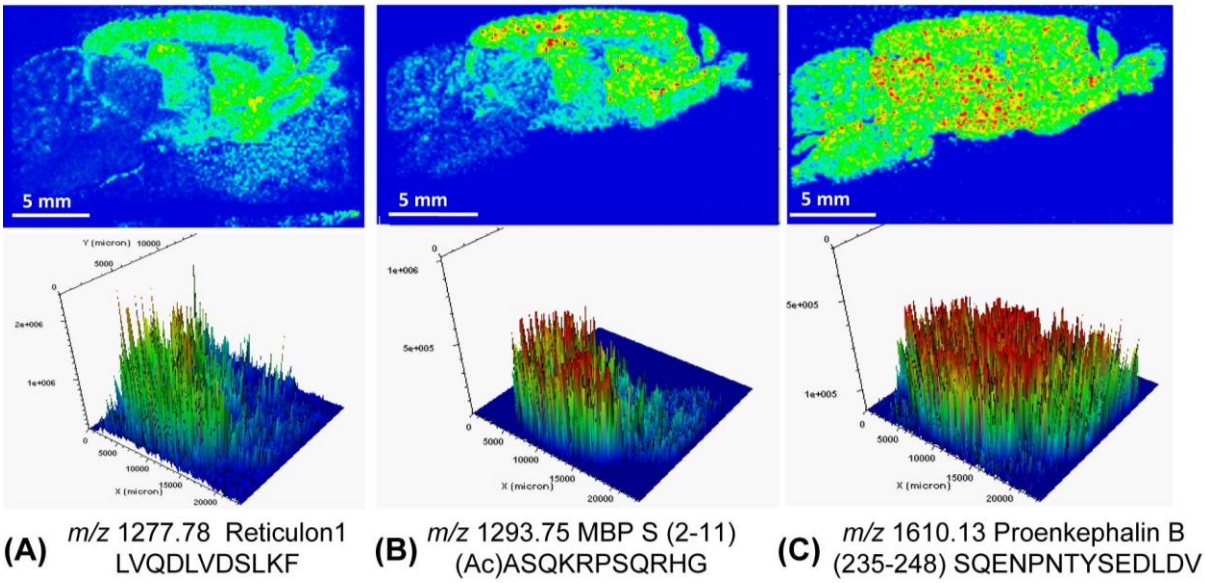
5 mm
5 mm
5 mm
Y (micron)
X (micron)
(A) m/z 1277.78 Reticulon1 LVQDLVDSLKF
(B) m/z 1293.75 MBP S (2-11) (Ac)ASQKRPSQRHG
(C) m/z 1610.13 Proenkephalin B (235-248) SQENPNTYSEDLDV

Figure 3

Chapter 8
Probing Neuropeptidomic Changes Related to Autism Spectrum Disorders via Mass Spectrometry Imaging For the Wisconsin Initiative for Science Literacy

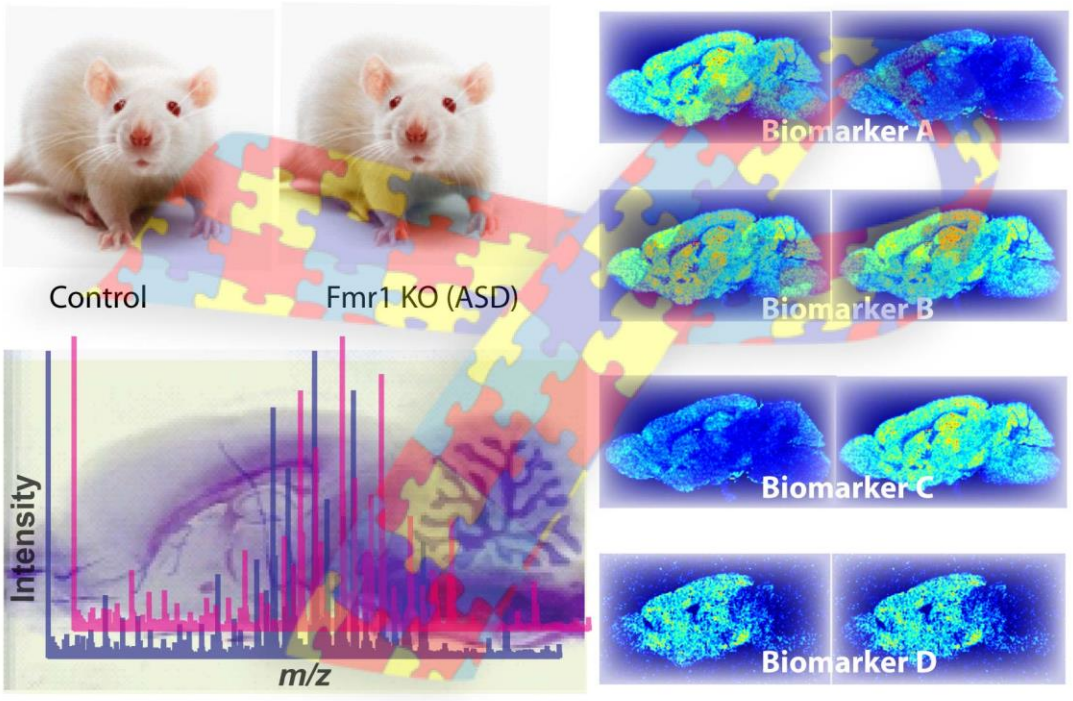

Author contribution: study was designed by B. Chen, H. Ikonomidou and L. Li; analytical experiment was performed by B. Chen; animal experiment was performed by H. Ikonomidou; data was analyzed by B. Chen; manuscript was written by B. Chen and edited by L. Li.

Abstract

Autism spectrum disorders (ASD) are a group of neurodevelopmental disorders that have prevalence of 1 in 68 children. Despite its high prevalence, doctors solely depend on behavioral tests for diagnosis, which could be biased and inaccurate. Up to today, we have no clue about the exact cause of ASD: we are not sure whether it is caused by a change in protein or a gene mutation. Therefore, we are interested in searching for molecules, which can serve as a target of ASD. We hope that the presence or absence of these target molecules can indicate whether a patient has ASD without performing behavioral testing. Furthermore, we hope to develop treatments that target these molecules and alleviate or cure ASD. These target molecules are called biomarkers. In order to look for potential biomarkers, we will use mass spectrometry (MS) imaging technique, which is a powerful tool to localize a wide range of biomolecules simultaneously on tissue. It is particularly valuable in tissue biomarker discovery as it not only tells us what the molecule is, but also where the molecule is located. In this study, we developed a MS imaging method to search for biomarkers in some lab mice with ASD and compared them with normal, healthy mice. Several molecules appear differently in brains of autistic and healthy mice. These molecules can be potential biomarkers for ASD after additional verification studies.

What is Autism Spectrum Disorders (ASD)?

ASD are common neurobehavioral disorders in children that impair the ability to interact and communicate. Patients with ASD tend to have reduced motor coordination and impaired intellectual level. However, some children with ASD can be very talented in a special area, such as math, art, music or visual skills. There are more than 200 thousand US cases each year, and they are more common among boys. Based on statistics from U.S. Centers of Disease Control and Prevention, 1 out of 42 boys and 1 out of 189 girls are diagnosed with ASD in the United States. Although the exact cause of ASD is not known, researchers consider that some

interference in the brain before or right after birth can lead to the disease. In most cases, toddlers start showing obvious symptoms or signs of ASD between 12 and 18 months, but in some cases, it can be as late as 2 years. The diagnosis of ASD is entirely based on behavioral tests in three categories: impairments in social interaction, impairment in communication and restricted, repetitive and stereotyped patterns of behavior. Studies find that early diagnosis and early intervention for children with ASD are highly effective ways to improve IQ, communication skill and social interaction. Although we now know that several genes are related to ASD, the exact cause of the disease is still unknown. Also, we do not have an effective treatment that targets a specific molecule to help alleviate or cure the symptoms. Therefore, we are very interested in looking for target molecules that play important roles in the development of ASD. We can then use them as a marker for diagnosis and drug targets. These molecules are called biomarkers, which will be introduced in the next section.

What is a biomarker?

A biomarker is a biomolecule that can be used for disease diagnosis or as a target for drug development. It could be any biomolecule, such as proteins, metabolites and lipids. Biomarker discovery usually goes through stages of discovery, verification and qualification (Figure 1). During the discovery stage, we compare a small number of samples (~10) to examine all possible molecules and pick out potential biomarker candidates. During the verification stage, we only examine the biomarker candidates which have been identified during the discovery stage. At this stage, we use a larger sample set (~100) and eliminate most of these candidates that do not meet the requirement. At the qualification stage, we use a very large sample set (~1000) to further confirm and validate the chosen biomarkers. After this final stage, a biomolecule officially becomes a biomarker for certain disease or biological state.

Our work here focuses on the discovery stage and we use mice models instead of human samples for all experiments. During the discovery stage, animal models can be used instead of human clinical samples, especially when human clinical samples are difficult to obtain due to technical or ethical difficulties. Using animal models allows better understanding of disease without adding risk of human harm. Here, we use a mouse model called "*Fmr1* KO" mouse to mimic ASD condition. The *Fmr1* KO mice displayed ASD-like symptoms, such as repetitive behavior, anxiety and impaired social behavior.

Figure 1. Three essential stages for biomarker discovery.

What is mass spectrometry (MS) and mass spectrometry imaging (MSI)

Mass spectrometry (MS) is a commonly used technique that measures the mass of biomolecules. A mass spectrometer is usually composed of four parts: ion source, mass analyzer, detector and computer (**Figure 2**). It offers speed and sensitivity to detect hundreds of molecules at once. To be more precise, a mass spectrometer measures the mass-to-charge ratio (*m/z*) of a molecule. Therefore, a molecule has to become positively or negatively charged, called ionization, before a mass spectrometer "sees" it. The ionization process happens in the ion source. The mass analyzer is then used to separate the mixture according to *m/z*, which is then detected in the detector. The signal is converted to a spectrum in the computer for us to further analyze the result. There are usually two types of MS analyses, which are full MS and tandem MS

fragmentation (**Figure 3**). During a full MS analysis, the mass spectrometer sees almost everything in our samples. This step gives us a basic idea about what molecules are present in our sample. During a tandem MS fragmentation analysis, some molecules that we are interested in are selected and shredded into pieces, allowing us to know the structure of the molecule.

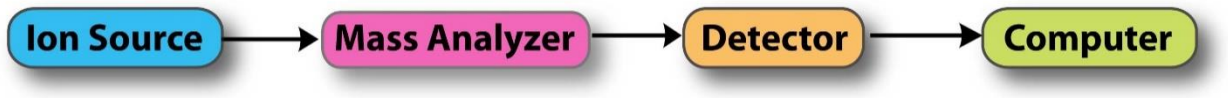

Figure 2. Main components of a mass spectrometer.

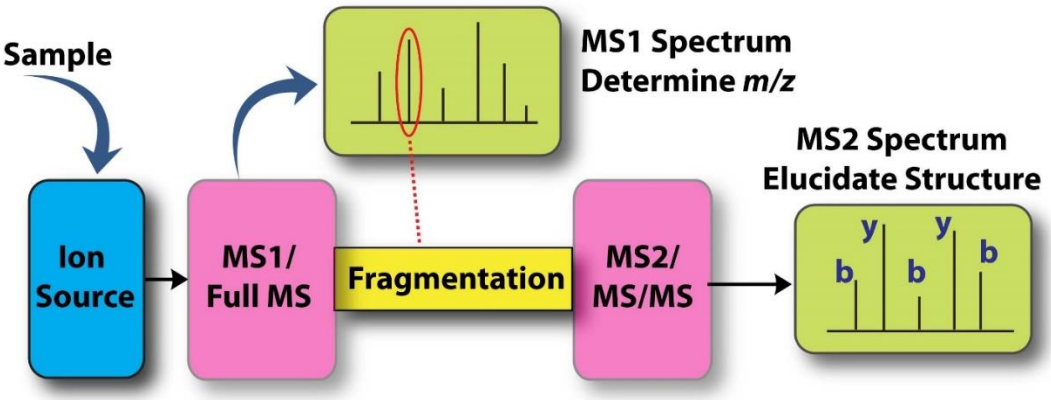

Figure 3. Full MS and tandem MS fragmentation illustration.

Now that we have learnt some concepts about MS, let's explore a very exciting area of study in MS: MS imaging. It is a powerful technique that not only gives me the mass of a molecule, but also a picture of its location on tissue. I put together a typical workflow of MS imaging in **Figure 4**. During the experiment, I slice tissues into very thin slices (12 micrometer, similar to the diameter of a human hair) in a freezer and lay the slices on a microscope slide. Then, I coat the slide with a homogenous layer of small molecule, called matrix, that helps the ionization process. The sample preparation process usually takes about 2 hours to finish. Then, I can load the slide into a mass spectrometer, choose the area of interest to analyze and start the automatic data acquisition. The resulting imaging data are analyzed by specialized software to

construct the distribution pictures. studies on MS imaging have grown rapidly in the last two decades (**Figure 5**). More than 700 papers are published each year on the topic of MS imaging.

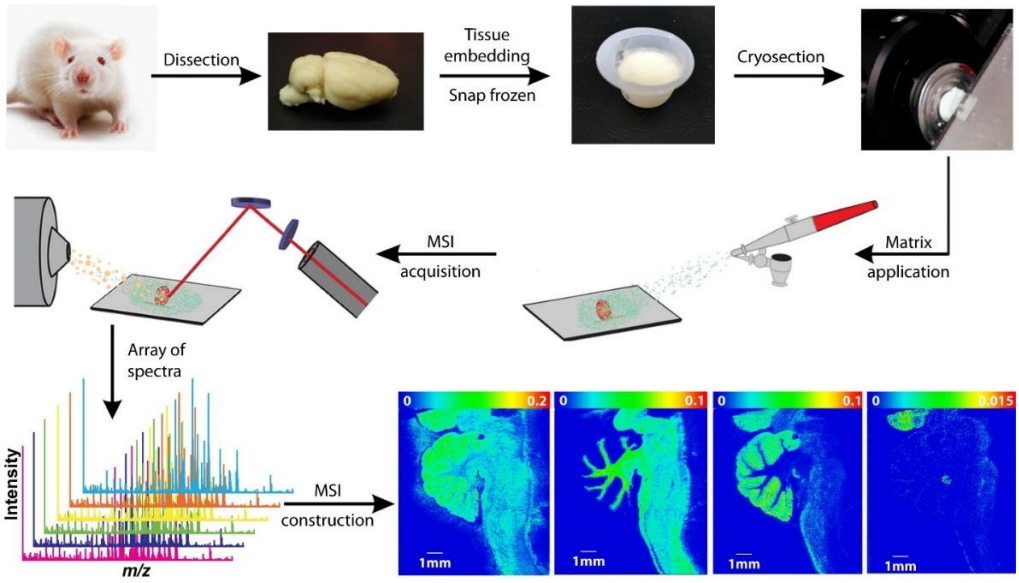

Figure 4. A typical workflow of MS imaging.

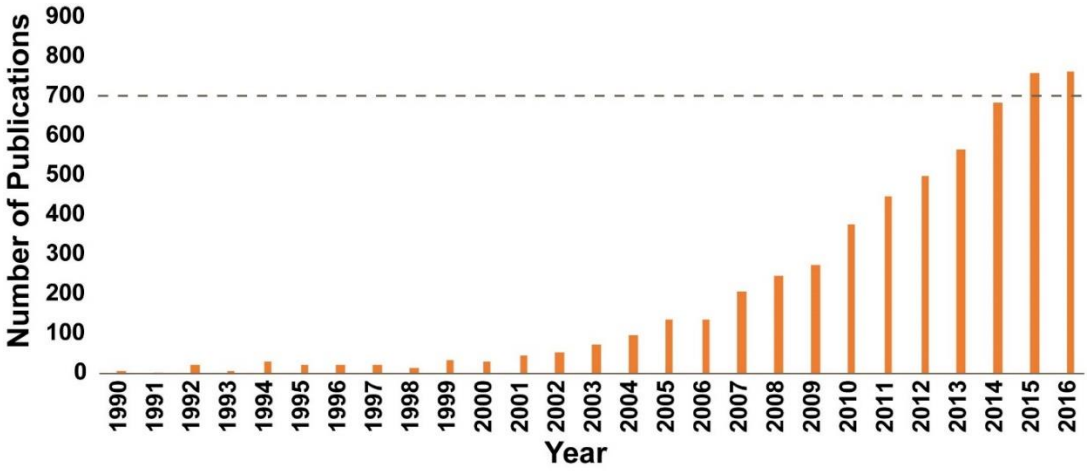

Figure 5. Number of publication MS imaging since 1990. Data were collected from PubMed search of "mass spectrometry imaging" or "imaging mass spectrometry" from 1990 to 2016.

Result of my research

In my study of ASD biomarkers, I used MS imaging to look at the neuropeptide distribution on brain sections of autistic mice (*Fmr1* KO) and compared with healthy/control mice. Neuropeptide is a small protein-like molecule, which helps neurons to communicate and

transfer signal. We are interested in studying neuropeptide as potential ASD biomarker, as it is involved in a variety of brain functions, including social behavior and learning. The neuropeptides that behave differently were listed as biomarker candidates. I detected hundreds of biomolecules on the brain tissue sections. Among them, ten neuropeptides revealed obviously different abundances between control and autistic mice brain sections. **Figure 6** shows three representative neuropeptide MS images. A fragment of neuroendorcrine protein 7B2 at *m/z* 1772.97 only shows up in the control brain section. In contrast, a fragment of secretogranin-2 and pro-opiomelanocortin only show up in the *Fmr1* KO brain section. These results were verified by three technical replicates. A more systematic approach with five biological replicates is currently under investigation.

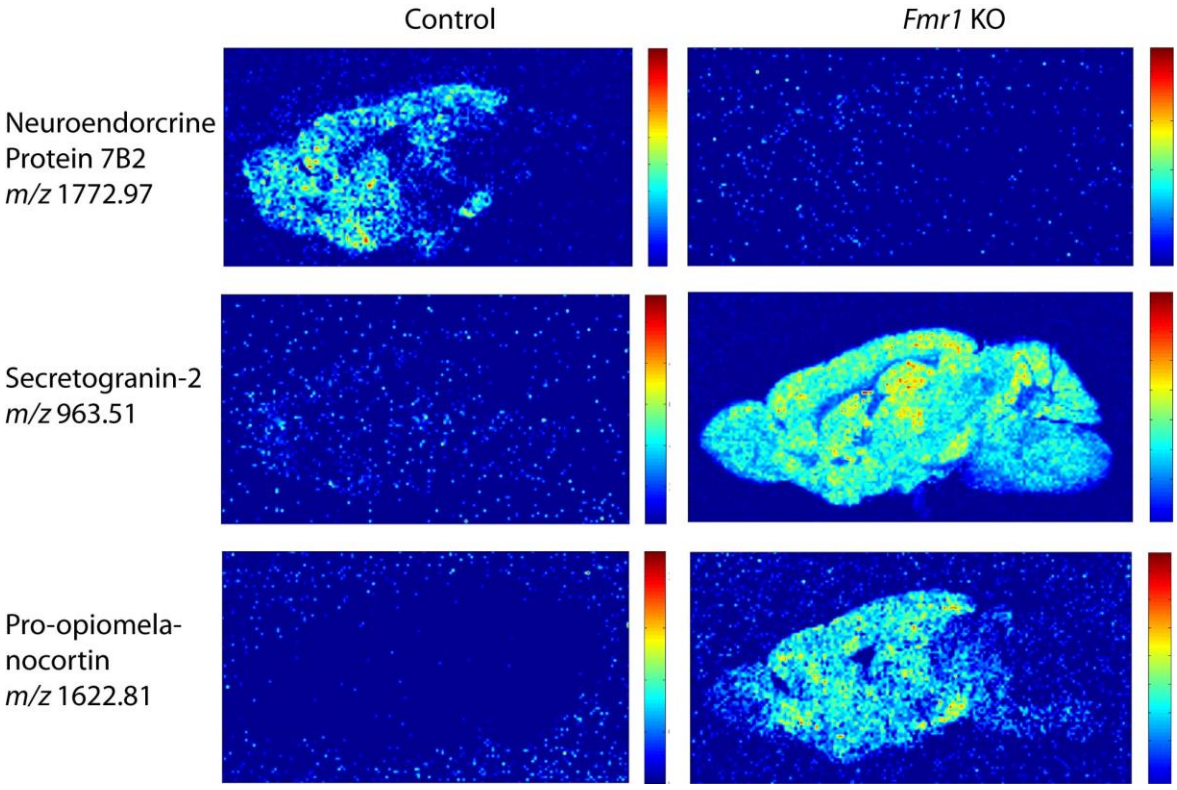

Figure 6. Selected neuropeptide MS images that show obvious differences between control and *Fmr1* KO mice brain sections.

Finally, I compiled a list of neuropeptides that show obvious differences between control

and *Fmr1* KO mice brain sections in the MS imaging experiment in **Table 1**. Overall, four neuropeptides show obviously higher abundance in control samples and six neuropeptides show obviously higher abundance in *Fmr1* KO sample.

Table 1. List of neuropeptides that reveal obvious differences between control and *Fmr1* KO mice brain sections in MS imaging experiment.

Intensity: control > *Fmr1* KO		
m/z	**Precursor name**	**Peptide name**
746.489	Neurotensin	N/A
1570.905	Proenkephalin-B	Dynorphin B
1772.973	Neuroendorcrine protein 7B2	N/A
1522.830	Orexin	N/A
Intensity: *Fmr1* KO > control		
866.433	Protachykinin-1	N/A
963.509	Secretogranin-2	N/A
984.530	Proenkephalin-A	N/A
1100.606	Proenkephalin-B	Beta-neoendorphin
1622.807	Pro-opiomelanocortin	N/A
2180.084	Secretogranin-1	N/A

The MS images provide a lot of useful information about these neuropeptides. The imaging result not only shows the presence or absence of certain neuropeptides between samples, but also provides distribution information. For example, some neuropeptides are located all over the brain, while others are in specific areas, such as the olfactory bulb or cerebellum. Based on this information, biologists can associate the neuropeptide distribution with brain areas and their functions in order to predict how the peptides might affect autistic symptom. This study will hopefully increase the understanding of ASD underlying mechanisms and identify putative biomarkers as diagnosis and therapeutic targets.

Chapter 9
Stability Analysis of Parathyroid Hormone (1-34) and Its Bioactive Analog M-Cyc-9β in Rat Kidney Homogenate by MALDI-MS and Multiplexed Parallel Reaction Monitoring LC-MS/MS

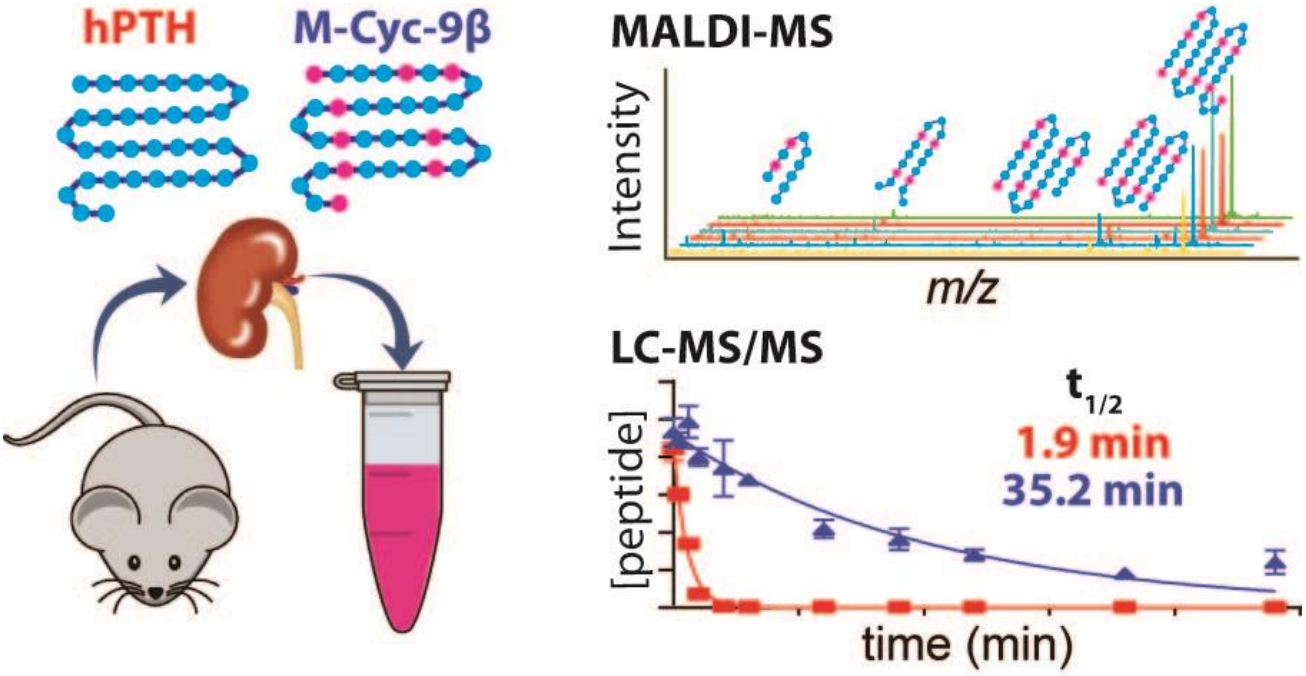

Adapted from: **B. Chen,** R. Cheloha, N. Kumar, M. Xu, J. Checco, S. Nelson, R. Thorne, S. Gellman and L. Li, Stability Analysis of Parathyroid Hormone (1-34) and Its Bioactive Analog in Rat Kidney Homogenate by MALDI-MS and Multiplexed Parallel Reaction Monitoring LC-MS/MS. *To be submitted to ACS Chem. Bio.*

Author contribution: study was designed by B. Chen, R. Cheloha, N. Kumar, R. Thorne, S. Gellman and L. Li; analytical experiment was performed by B. Chen; peptide was designed and synthesized by R. Cheloha; animal experiment was performed by N. Kumar; data analysis software was written by J. Checco and S. Nelson; data was analyzed by B. Chen, M. Xu and R. Cheloha; manuscript was written by B. Chen and edited by R. Cheloha, N. Kumar, J. Checco, R. Thorne, S. Gellman and L. Li. Study on peptide design and synthesis is included in Appendix IV.

Abstract

Human parathyroid hormone (hPTH) 1-34 is the active ingredient of the therapeutic teriparatide (Forteo), which is used to treat osteoporosis and hypoparathyroidism. hPTH (1-34) rapidly disappears from the bloodstream following injection and is degraded by proteases in several tissues. An analog of hPTH (1-34), M-Cyc-9β which contains β-amino acid residues distributed throughout the sequence, was developed to decrease susceptibility to degradation by proteases. In this study, an analytical platform was developed to qualitatively and quantitatively monitor the stability and degradation products of hPTH (1-34) and M-Cyc-9β. A high-throughput matrix-assisted laser desorption/ionization (MALDI) – mass spectrometry (MS) method was applied to rapidly scan and monitor the production of degradation products as a function of time. A liquid chromatography (LC) – MS/MS based multiplexed parallel reaction monitoring (PRM) method was used to accurately quantify the peptide concentration at each time point. Through application of these techniques the major sites of peptide bond cleavage in both peptides were identified. The half-lives of these peptides in kidney homogenate were determined to be 1.9 min for hPTH (1-34) and 35.2 min for M-Cyc-9β. This MS-based analytical platform can be applied to study the metabolism and stability of peptide drugs and analogs with non-natural building blocks, especially when bioassay-based readouts are not available. To our knowledge, this is the first example of using an MS-based peptidomics approach to characterize α→β backbone modified peptide. These findings provide novel insights into the molecular details of degradation of PTH by the kidney.

Introduction

Therapeutic biologics, including peptides, proteins, monoclonal antibodies (mAbs) and antibody drug conjugates, have come to represent a large and fast-growing segment of the pharmaceutical industry over the past two decades.[1-5] Peptides, in particular, comprise an expanding class of potential drug candidates.[6] Peptides offer advantages over full-size proteins, such as mAbs, that include reduced manufacturing costs and higher activity per unit mass. Peptides also possess benefits relative to small molecule drugs; namely, higher specificity for their targets, less accumulation in tissue, and non-toxic metabolites (mainly amino acids).[7] Therefore, metabolic studies are not routinely conducted (or reported) in the course of peptide development even though valuable information on cleavage sites and degradation rates could be obtained from such studies.[6] In addition, many peptides are rapidly degraded by proteases *in vivo*, further underscoring the value of characterizing peptide degradation profiles.[7]

Parathyroid hormone (PTH) is an 84-residue protein that plays important roles in the regulation of bone turnover and the maintenance of blood calcium and phosphate levels.[8] PTH (1-34) preserves the potency and efficacy of full-length PTH for activating signaling at the PTH receptor-1 (PTHR1), a B-family G protein-coupled receptor.[9] hPTH (1-34) is the active ingredient of the osteoporosis drug teriparatide (Forteo) and is also used for treating hypoparathyroidism. The half-life of hPTH (1-34) following injection in animals is less than 30 minutes;[10] thus, frequent injections are required for patients with osteoporosis or PTH deficiency.[11] However, continuous infusion of PTH causes a net loss in bone mass.[12] The optimal profile for PTHR1 activation, in the context of osteoporosis or hypoparathyroidism, is currently unknown. The development of stabilized analogs of PTH with prolonged durations of biological

activity may thus be useful in identifying improved approaches for treating osteoporosis or hypoparathyroidism.

Several recent studies suggest that the systematic replacement of a subset of α-amino acid residues with β residues in certain bioactive peptides can effectively enhance their stabilities in the presence of proteases.[13-17] One study using hPTH(1-34) showed that backbone α→β modifications improve the proteolytic stability and prolong the duration of biological activity of the resulting analogs.[17] Other studies have reported a modified-PTH (M-PTH) scaffold that contains five to six side chain modifications relative to the natural hPTH sequence.[18, 19] M-PTH analogs possess higher affinity for G-protein uncoupled PTHR1 (R^0 state) and induce stronger biological responses than corresponding PTH analogs.[18-20] M-Cyc-9β, which contains β-amino acid residues distributed throughout the sequence, was derived from the M-PTH scaffold and was validated as a bioactive analog of hPTH (1-34) by the cAMP bioassay and in mice.[21] The sequences and structures of hPTH (1-34), rat PTH (rPTH) (1-34) and M-Cyc-9β are shown in Figure 1. The structure of rPTH (1-34) is similar to hPTH (1-34), variation at only five positions. Previous work demonstrated that rPTH (1-34) serves as a good internal standard (IS) for LC-MS/MS analysis of hPTH (1-34).[22]

Filtration from the bloodstream by the kidney, followed by cellular uptake and proteolysis, represents a common mechanism for the elimination of medium-sized peptides, such as hPTH (1-34).[23] Moreover, PTHR1 is highly expressed in certain cell types in kidney tissue, highlighting the importance of the kidney for PTH function and metabolism.[24] Past work showed that various proteases in rat kidney homogenates rapidly hydrolyze hPTH (1-34) at multiple sites.[25] Therefore, our study sought to assess the stabilities of hPTH (1-34) and M-Cyc-9β in rat kidney homogenate to provide insight into the *in vivo* behavior of these peptides with reduced

workloads and animal numbers relative to conventional approaches used to study pharmacokinetics and metabolism.

Peptide activity and stability can be evaluated using biological assays or high performance liquid chromatography (HPLC)-based methods.[17] Cyclic adenosine monophosphate (cAMP) is a common marker used for evaluating the activation of PTHR1, and many other GPCRs, by ligands.[26] The cAMP bioassay described here measures the temporal progression of the loss of biological activity for solutions of PTH or analogues following exposure to degradative conditions, and is helpful in identifying more stable PTH derivatives. However, it is difficult to tell if the cAMP response is stimulated by the intact peptide or bioactive fragments produced by proteolysis. Moreover, the cAMP-based assay requires custom made reporter cell lines that are not available or not compatible with many ligand-receptor pairs and require the use of specialized reagents.[27] An HPLC-based method can be used to measure the amount of intact peptide at each time point based on the intensity of the signal corresponding to undegraded material. This method provides information that is complementary to the biological-based assay as only the level of the intact peptide is measured, which will not be confounded by the presence of proteolytic fragments that may alter bioactivity of intact peptide. However, without coupling to MS, this method is not suitable for monitoring samples in complex matrix backgrounds, such as tissue homogenates, due to the presence of diverse endogenous and interfering biomolecules found at high concentrations.

To circumvent the problems associated with bioassay and HPLC-based methods, MS-based methods were developed to assess PTH peptide stability in kidney tissue homogenates. MS-based peptidomics approaches have been used to study the proteolysis of endogenous bioactive peptides,[28-33] such as substance P,[30] peptide histidine isoleucine [29, 32] and calcitonin

gene-related peptide,[28, 29] using both MALDI-MS and LC-MS/MS. This study extends the scope of MS-based techniques to study stabilized peptides containing α→β backbone modifications. Herein, MALDI-MS was used to qualitatively monitor the change in the abundance of intact peptide as well as the fragments produced by its proteolytic degradation at each time point. MALDI is a soft ionization technique that can be used to ionize biomolecules without extensive ion source fragmentation. When coupled to time-of-flight (TOF) mass analyzer, MALDI-MS can be used to detect medium to large size biomolecules, such as peptide and proteins[34-36]. It is a rapid analytical technique that requires minimal sample preparation, thus it can be used to profile many samples in a short period. A LC-MS/MS based parallel reaction monitoring (PRM) method was used to quantify the concentration of the intact peptide at each time point. Developed in 2012, PRM gained its popularity on quantitative peptidomics and proteomics. By replacing the third quadrupole of a triple-quadrupole instrument with a high resolution accurate mass Orbitrap mass analyzer, PRM offers wider dynamic range and higher selectivity compared to selected reaction monitoring, which has been the "gold-standard" for targeted proteomics.[37]

The goal of this study was to develop an analytical platform to monitor the stability of hPTH (1-34) and its modified analog M-Cyc-9β in rat kidney homogenates by MALDI-MS and LC-MS/MS based PRM method. Monitoring peptide degradation by MALDI-MS provides dynamic snapshots of the degraded peptide profile at each time point, and a more complete understanding of the enzymatic degradation process through revealing the sites of proteolytic cleavage for each peptide. LC-MS/MS based PRM allows high-throughput absolute quantification of intact peptide while monitoring all fragment ions to ensure specificity.[37] Through the combination of these two methods, the degradation products of hPTH (1-34) and M-Cyc-9β were closely monitored at each time point and peptide concentrations were accurately

quantified. The extension of this MS-based peptidomics methodology to peptides containing α→β backbone substitutions, for the first time, highlights the utility of this approach for high-throughput analysis of peptide analogs containing non-natural building blocks.

Materials and methods

Chemicals and reagents

hPTH (1-34) and M-Cyc-9β were synthesized according to a previously reported method.[17, 21] The synthesized peptides were purified on reversed-phase HPLC. rPTH (1-34) was purchased from the American Peptide Company (Sunnyvale, CA). HPLC grade water, acetonitrile (ACN), methanol and formic acid (FA) were purchased from Fisher Scientific (Pittsburgh, PA). TFA was purchased from Sigma-Aldrich. 2, 5-dihydroxybenzoic acid (DHB) was purchased from Acros Organics (Morris Plains, NJ). All reagents were used without additional purification.

Rat kidney homogenate studies: Kidney preparation

All experimental protocols were approved by the Institutional Animal Care and Use Committee at the University of Wisconsin-Madison and performed in accordance with the National Institutes of Health Guide

for the Care and Use of Laboratory Animals (8th edition; 2011). Adult female Sprague-Dawley rats (180–200 g; Harlan/Envigo, Indianapolis, IN, USA) were housed individually or in groups of two at room temperature under a 12-h light/dark cycle. Food and water were provided ad libitum. Animals were anesthetized with 1.5 g/kg urethane administered via intraperitoneal injections to effect. Body temperature of anesthetized animals was maintained at 37 °C using a homeothermic blanket (Harvard Apparatus). Anesthetized rats were perfused transcardially with

50 mL cold 0.01 M PBS (pH 7.4) and then decapitated. Kidney tissues were harvested, washed with ice-cold saline solution and adhering tissues were trimmed off. Four mL of incubation buffer (50 mM Tris-HCl, pH 7.4) was added per gram of tissue, which was homogenized using a Teflon homogenizer. The homogenates were centrifuged at 2000 xg for 10 min at 4 °C and the supernatants were stored at -80 °C for future analysis. The homogenate samples were used for the stability assay within 8 days of tissue collection. Bicinchonic acid (BCA) assay was used to determine the total protein concentration in the tissue homogenates, which were then diluted to 2.5 mg protein/mL with incubation buffer.

Before analysis, rat kidney homogenates were thawed and incubated at 37 °C water bath to promote recovery of enzymatic activity. hPTH (1-34) and M-Cyc-9β were spiked in rat kidney homogenates at a final concentration of 50 µg/mL with 3 technical replicates. The homogenates were then incubated at 37 °C and samples were collected at 0, 1, 3, 5, 10, 15, 30, 45, 60, 90, 120 and 240 min. An equal volume of 1% TFA or a 3-fold excess (by volume) of ice-cold methanol were used to quench proteolytic activity. At each time point, 2 sets of samples were collected for MALDI-MS and LC-MS/MS analysis: for MALDI-MS analysis, 10 µL sample was collected into a tube preloaded with quenching solution; for LC-MS/MS analysis, 50 µL sample was collected into a tube preloaded with quenching solution and 5 µL of internal standard (IS, 10 µg/mL rPTH (1-34)). Another set of control samples were prepared by spiking analytes and IS into inactivated kidney homogenates. Calibration standards for LC-MS/MS analysis were prepared by dissolving peptide standards (0, 0.05, 0.1, 0.5, 1, 5, 10, 25, 50 and 75 µg/mL) into sample matrix (1:1 1% TFA in H_2O: kidney homogenate with 1 µg/mL rPTH). Blank sample was prepared by sample matrix only without analyte or IS. The resulting sample mixtures were centrifuged at 10,000 g at 4 °C for 10 min and the supernatant were dried in a SpeedVac.

MALDI-MS Analysis

UltrafleXtreme MALDI-TOF/TOF mass spectrometer (Bruker Daltonics, Bremen, Germany) were used for all MALDI-MS analysis. MALDI-MS sample was reconstituted in 10 µL 0.1% FA/H_2O solution. One µL DHB matrix (150 mg/mL in 49.95:49:95:0.1 (v/v/v) MeOH:H_2O:FA) was mixed with 1 µL sample and spotted onto MALDI 384 stainless steel ground target plate. Reflectron positive mode at *m/z* 700-5000 was used with 5000 laser shots and 80% laser energy for all MALDI-MS analysis. FlexAnalysis 3.4 (Bruker Daltonics, Bremen, Germany) was used for data analysis. Accurate mass matching was used to identify the degraded peptide fragment, with the assistance of Badger Amino Acid Finder, which is a publicly available software developed by the Gellman lab.

LC-MS/MS Analysis

All LC-MS/MS analyses were acquired on Dionex UltiMate 3000 UHPLC LC system coupled to Q Exactive quadrupole-Orbitrap mass spectrometer (Thermo Scientific, Bremen, Germany). A C_{18} column (Phenomenex Kinetex, 100 x 2.1 mm ID, 1.7 µm) was used for separating analytes. Mobile phase A was 0.1% FA/H_2O and mobile phase B was 0.1% FA/ACN. Before LC-MS/MS analysis, samples were reconstituted in 50 µL 0.1% FA/H_2O. Three injections with 3 µL/injection were performed for each sample. The following gradient was used for all analysis (time (min), mobile phase B%): (0, 15), (3.8, 50), (4, 98), (5.3, 98), (5.4, 15), (6, 15) with a flow rate of 0.30 mL/min and column temperature of 30 °C.

On the mass spectrometer, a multiplexed PRM method with two scan events were created, with scan event 1 as a full MS scan (*m/z* 133.4-2,000, R=70,000 at *m/z* 200) and scan event 2 as targeted MS^2 scan. During the targeted MS^2 scan, +5 charged analytes (hPTH (1-34), *m/z* 823.8367 or M-Cyc-9β, *m/z* 826.0801) and IS (*m/z* 812.0365) were co-fragmented at

normalized collisional energy (NCE) of 26 and +6 charged ions (hPTH (1-34), *m/z* 686.6984 or M-Cyc-9β, *m/z* 688.5679) and IS (*m/z* 676.8650) were co-fragmented at NCE of 20.

Data analysis for the LC-MS/MS data was performed on Xcalibur (Thermo Scientific, Bremen, Germany), Excel (Microsoft, Seattle, WA) and GraphPad Prism 6 (GraphPad Software Inc., La Jolla, CA). Peak area ratios of y_{32} ion for analyte to IS were calculated. A linear equation was established between concentration and peak area ratios based on calibration standard samples. The concentrations of unknown samples were then calculated based on this equation.

Method Validation

Linearity, accuracy, precision and sensitivity – A calibration curve was used to evaluate the linearity, accuracy and precision. Linearity was evaluated by the R^2 value of the calibration curve. Accuracy, the proximity between true and measured values, was determined by the percent RE ((actual amount – measured amount) / actual amount x 100). Precision, the repeatability or reproducibility of measurements, was measured by the percent CV (standard deviation of measurements / mean x 100). Both interday and intraday accuracies and precisions were evaluated. The sensitivity was evaluated by LLOQ, which was determined by the lowest concentration of analyte in sample matrix detected with peak area five times larger than the blank sample.

Specificity and matrix effect and recovery – In this study, the most prominent fragment ion (y_{32}) of the +6 charged parent ion was used for quantification. However, all fragment ions of +5 and +6 charged parent ions were monitored by PRM to ensure specificity. To determine the matrix effect, analyte (10 µg/mL) was dissolved in water and sample matrix. The matrix effect was calculated by [(the peak area of the analyte in post-extraction matrix/the peak area of analyte spiked in water)-1] x 100 (n=3). Recovery from the 1% TFA quenching method was evaluated

from the peak areas of 10 µg/mL pre-preparation spiked standards and the post-preparation spiked samples (n=3).

Results and discussion

The workflow of the MS-based analytical platform developed for these studies is shown in Figure 2. Briefly, rat kidney tissues were harvested and homogenized. PTH peptides were spiked in the diluted kidney homogenates under the following four conditions: hPTH only, M-Cyc-9β only, hPTH with 1% trifluoroacetic acid (TFA) and M-Cyc-9β with 1% TFA. TFA was included to eliminate protease activity in the homogenate samples. The mixtures were incubated at 37 °C and sampled at different time points up to 4 hours. MALDI-MS was used for degradation product detection and LC-MS/MS was used for absolute quantification of the intact peptides at each time point to determine half-life. Detailed protocols are included in the method section.

MALDI-MS analysis

MALDI-MS was used to evaluate the effectiveness of different additives used to terminate proteolytic activity and to characterize the production of degradation products produced by exposure of hPTH (1-34) and M-Cyc-9β at several time points. This methodology allowed for rapid evaluation of the degradation product profiles and rapid optimization of experimental conditions that were later applied in more complex LC-MS/MS experiments. The time required for sample preparation following exposure to homogenate and instrument analysis was less than 30 minutes.

Both ice-cold methanol and 1% TFA effectively quench proteolytic activity for kidney homogenates spiked with hPTH (1-34) and do not preclude detection of peptide by MS (Figure

3a, Figure 4a). However, only the 1% TFA quenching solution satisfied these requirements for samples spiked with M-Cyc-9β (Figure 3c): no M-Cyc-9β signal was detected in the samples treated with ice-cold methanol (Figure 4b). This loss of signal may result from the precipitation of M-Cyc-9β from solution following methanol addition. This result indicated that ice-cold methanol was not suitable for quenching the kidney homogenate in studies with M-Cyc-9β. Therefore, a solution of 1% TFA was used to quench enzymatic activity for all subsequent samples in this study.

MALDI-MS provided dynamic snapshots of the peptide degradation profiles at each time point (Figures 3b and 3d). For samples that contained hPTH (1-34) exposed to kidney homogenate, signal from intact hPTH (1-34) disappeared within 5 min, and signals generated corresponding to smaller peptide fragments emerged. The sequence of the fragments resulting from degradation were identified by accurate mass matching, and the identities of most of the major peaks were assigned, such as hPTH (17-34) and hPTH (19-34). After 30 min, no fragments above 1000 Da could be detected (Figure 3b). This dataset suggested that the hPTH (1-34) underwent a very rapid degradation in rat kidney homogenate. The degradation products detected match those reported by Liao *et al.*[25]: hPTH (1-33), hPTH (13-34), hPTH (17-34) and hPTH (19-34) were observed as major fragments.

In contrast, MALDI-MS analysis of M-Cyc-9β exposed to kidney homogenate demonstrated that M-Cyc-9β was much more stable than hPTH (1-34) (Figure 3d). Full length M-Cyc-9β could be detected at each time point throughout the 4-hour sampling period. Weak signals corresponding to degraded peptide fragments, such as M-Cyc-9β (1-32), appeared within first 10 min. Additional degraded peptide fragments were detected after 10 min, such as M-Cyc-9β (17-34), but with relatively weaker signals compared to the full-length peptide.

MALDI-MS is typically considered as a non-quantitative method, which could complicate conclusions made from this data regarding the rate of peptide degradation (Figure 3). The formation of "hot-spots" by MALDI matrix leads to sample inhomogeneity, thus causing poor sample-to-sample and spot-to-spot reproducibility.[34, 38-40] Data from MALDI-MS experiments was thus useful to rapidly characterize sample degradation profiles and provide a "snap-shot" of the degradation products, but could not be used to precisely quantify intact peptide levels. To circumvent this problem, a LC-MS/MS-based PRM method was developed and implemented to quantify the absolute amount of the intact peptide at each time point.

LC-MS/MS based PRM method validation

The linearity, precision, accuracy, sensitivity and matrix effect of optimized methods were characterized for both hPTH (1-34) and M-Cyc-9β in order to validate their application (Table 1). hPTH (1-34) and M-Cyc-9β calibration standards ranging from 0-75 µg/mL were used to establish the calibration curves. Linear fits with R^2 of 0.97 and 0.99 were obtained for hPTH (1-34) and M-Cyc-9β, respectively. Alternative linear fit equations were tested for both peptides. Equations yielding to the lowest percentage relative error (RE) relative to the calibration standards were used instead of those that provided the best R^2 to more accurately quantify peptide concentrations. Quality control (QC) standards were used to determine the interday and intraday precisions and accuracies. Both hPTH (1-34) and M-Cyc-9β had interday and intraday coefficient of variation (CV) less than 17%, which corresponded to good reproducibility/precision of measurements. The interday and intraday RE values of hPTH (1-34) and the interday RE value of M-Cyc-9β were all within 7%, which represented good accuracies. The intraday accuracy for M-Cyc-9β was 28%, which reflected a lower accuracy. The lower limit of quantitation (LLOQ) of hPTH (1-34) and M-Cyc-9β were both determined to be 10

ng/mL (corresponding to 30 pg loaded on column). The effect of rat kidney homogenate matrix on quantification results were evaluated at a concentration of 10 µg/mL. A slight enhancement of signal strength (0.82% ± 2.12%) was observed for hPTH (1-34) and modest suppression (21.02% ± 7.41%) was observed for M-Cyc-9β in the presence of kidney homogenate, relative to samples not exposed to homogenate. Recovery efficiencies for hPTH (1-34), M-Cyc-9β and IS after 1% TFA treatment, relative to samples prior to treatment, were calculated in 3 replicates. 70.19% ± 2.51% of hPTH (1-34), 86.43% ± 11.93% of M-Cyc-9β and 73.12% ± 1.09% of IS were recovered after treatment.

PTH stability and half-life in rat kidney homogenate

Medium-sized peptides are filtered from bloodstream and eliminated by kidney *in vivo*.[23] Therefore, it is important to characterize the stability of PTH peptides, and stabilized analogs, in kidney tissue. Representative extracted ion chromatograms and calibration curves of hPTH (1-34) and M-Cyc-9β from LC-MS/MS analyses are shown in Figure 5. The extracted ion chromatogram of hPTH (1-34) (Figure 5a) and M-Cyc-9β (Figure 5c) were both sharp Gaussian peaks, which eluted at 1.27 min and 1.28 min, respectively. The calibration curves of hPTH (1-34) (Figure 5b) and M-Cyc-9β (Figure 5d) had a R^2 values of 0.97 and 0.99, respectively, both representing good fits for the linear models. The absolute concentrations of hPTH (1-34) and M-Cyc-9β were calculated at each time point (Table 2 & Figure 6) for both the untreated rat kidney homogenate (Figure 6a) and 1% TFA treated rat kidney homogenate (Figure 6b). In the untreated rat kidney homogenates, the concentration of hPTH (1-34) decreased rapidly within 10 min, while the concentration of M-Cyc-9β decreased more slowly (Figure 6a). In the 1% TFA treated homogenates, the concentrations of both hPTH (1-34) and M-Cyc-9β stayed relatively constant, providing evidence for the effectiveness of 1% TFA in quenching enzymatic activities (Figure

6b). Non-linear regression curve fitting was performed using a one-phase exponential decay function for both hPTH (1-34) and M-Cyc-9β (Figure 6a). The half-life of hPTH (1-34) was calculated to be 1.9 min with R^2 of 0.99; and the half-life of M-Cyc-9β was calculated to be 35.2 min with R^2 of 0.95.

Data from complementary MALDI-MS and LC-MS/MS methods were also useful in efforts to cross-validate data and conclusions. While the MALDI-MS spectra revealed a weak signal for intact hPTH (1-34) at 5 min and a barely detectable signal 10 min, the calculated concentration from LC-MS/MS analysis also reported a similar trend (3.65 μg/mL at 5 min and 0.28 μg/mL at 10 min). For the M-Cyc-9β samples, the intact ion peak could be observed consistently at each time point and the calculated concentration from the LC-MS/MS also revealed similar results. Similar trends could also be observed among data for inactivated samples.

Conclusion

In this study, an analytical platform was developed to qualitatively and quantitatively monitor the stability and degradation products for peptide drug hPTH (1-34) and its modified analog M-Cyc-9β by MALDI-MS and LC-MS/MS. These data provided quantitative and molecular insight on how highly backbone-modified peptides may be processed following capture by the kidney. These findings represent the first insight into how backbone modified peptides, which comprise an valuable class of molecules for future biomedical application,[41] are processed by the kidney. This MS-based platform can be widely applied to the study of degradation products and stability of peptide drugs as well as other polypeptides in a variety of biological contexts, especially when bioassay-based readouts are not available.

Acknowledgements

This work was supported in part by a Wisconsin Alumni Research Foundation Discovery Challenge grant. The instrument was purchased through funding support from NIH shared instrument grant S10 RR029531. LL acknowledges a Vilas Distinguished Achievement Professorship with funding provided by the Wisconsin Alumni Research Foundation and a Janis Apinis Professorship provided by the University of Wisconsin-Madison School of Pharmacy. This work was also supported by a National Institute of Health grant GM-056414 (R01; S.H.G.). The authors would like to acknowledge the Analytical Instrumentation Center of the School of Pharmacy, University of Wisconsin-Madison, for instrumentation support. Additional support was provided through the University of Wisconsin-Madison Institute for Clinical and Translational Research and the Clinical and Translational Science Award program administered through the NIH National Center for Advancing Translational Sciences (NIH UL1TR000427 and KL2TR00428; RGT) and the University of Wisconsin-Madison School of Pharmacy (RGT). R.W.C and J.W.C. were supported in part through Biotechnology Training Grant from NIGMS (T32 GM008349).

References

[1] Hamuro, L. L., and Kishnani, N. S. (2012) Metabolism of biologics: biotherapeutic proteins, *Bioanalysis 4*, 189-195.

[2] Prueksaritanont, T., and Tang, C. Y. (2012) ADME of Biologics-What Have We Learned from Small Molecules?, *Aaps Journal 14*, 410-419.

[3] Vugmeyster, Y., Harrold, J., and Xu, X. (2012) Absorption, distribution, metabolism, and excretion (ADME) studies of biotherapeutics for autoimmune and inflammatory conditions, *The AAPS journal 14*, 714-727.

[4] Xu, X., and Vugmeyster, Y. (2012) Challenges and Opportunities in Absorption, Distribution, Metabolism, and Excretion Studies of Therapeutic Biologics, *Aaps Journal 14*, 781-791.

[5] Zhao, L., Ren, T. H., and Wang, D. D. (2012) Clinical pharmacology considerations in biologics development, *Acta pharmacologica Sinica 33*, 1339-1347.

[6] Cuyckens, F., Dillen, L., Cools, W., Bockx, M., Vereyken, L., de Vries, R., and Mortishire-Smith, R. J. (2012) Identifying metabolite ions of peptide drugs in the presence of an in vivo matrix background, *Bioanalysis 4*, 595-604.

[7] Vlieghe, P., Lisowski, V., Martinez, J., and Khrestchatisky, M. (2010) Synthetic therapeutic peptides: science and market, *Drug discovery today 15*, 40-56.

[8] Vilardaga, J. P., Romero, G., Friedman, P. A., and Gardella, T. J. (2011) Molecular basis of parathyroid hormone receptor signaling and trafficking: a family B GPCR paradigm, *Cell Mol Life Sci 68*, 1-13.

[9] Cheloha, R. W., Gellman, S. H., Vilardaga, J. P., and Gardella, T. J. (2015) PTH receptor-1 signalling-mechanistic insights and therapeutic prospects, *Nature reviews. Endocrinology 11*, 712-724.

[10] Serada, M., Sakurai-Tanikawa, A., Igarashi, M., Mitsugi, K., Takano, T., Shibusawa, K., and Kohira, T. (2012) The role of the liver and kidneys in the pharmacokinetics of subcutaneously administered teriparatide acetate in rats, *Xenobiotica 42*, 398-407.

[11] Winer, K. K., Ko, C. W., Reynolds, J. C., Dowdy, K., Keil, M., Peterson, D., Gerber, L. H., McGarvey, C., and Cutler, G. B., Jr. (2003) Long-term treatment of hypoparathyroidism: a randomized controlled study comparing parathyroid hormone-(1-34) versus calcitriol and calcium, *The Journal of clinical endocrinology and metabolism 88*, 4214-4220.

[12] Qin, L., Raggatt, L. J., and Partridge, N. C. (2004) Parathyroid hormone: a double-edged sword for bone metabolism, *Trends in endocrinology and metabolism: TEM 15*, 60-65.

[13] Johnson, L. M., and Gellman, S. H. (2013) alpha-Helix Mimicry with alpha/beta-Peptides, *Methods in Protein Design 523*, 407-429.

[14] Horne, W. S., Johnson, L. M., Ketas, T. J., Klasse, P. J., Lu, M., Moore, J. P., and Gellman, S. H. (2009) Structural and biological mimicry of protein surface recognition by

alpha/beta-peptide foldamers, *Proceedings of the National Academy of Sciences of the United States of America 106*, 14751-14756.

[15] Checco, J. W., Kreitler, D. F., Thomas, N. C., Belair, D. G., Rettko, N. J., Murphy, W. L., Forest, K. T., and Gellman, S. H. (2015) Targeting diverse protein-protein interaction interfaces with alpha/beta-peptides derived from the Z-domain scaffold, *Proceedings of the National Academy of Sciences of the United States of America 112*, 4552-4557.

[16] Johnson, L. M., Barrick, S., Hager, M. V., McFedries, A., Homan, E. A., Rabaglia, M. E., Keller, M. P., Attie, A. D., Saghatelian, A., Bisello, A., and Gellman, S. H. (2014) A potent alpha/beta-peptide analogue of GLP-1 with prolonged action in vivo, *Journal of the American Chemical Society 136*, 12848-12851.

[17] Cheloha, R. W., Maeda, A., Dean, T., Gardella, T. J., and Gellman, S. H. (2014) Backbone modification of a polypeptide drug alters duration of action in vivo, *Nat Biotechnol 32*, 653-655.

[18] Okazaki, M., Ferrandon, S., Vilardaga, J. P., Bouxsein, M. L., Potts, J. T., Jr., and Gardella, T. J. (2008) Prolonged signaling at the parathyroid hormone receptor by peptide ligands targeted to a specific receptor conformation, *Proceedings of the National Academy of Sciences of the United States of America 105*, 16525-16530.

[19] Shimizu, M., Potts, J. T., Jr., and Gardella, T. J. (2000) Minimization of parathyroid hormone. Novel amino-terminal parathyroid hormone fragments with enhanced potency in activating the type-1 parathyroid hormone receptor, *J Biol Chem 275*, 21836-21843.

[20] Shimizu, N., Guo, J., and Gardella, T. J. (2001) Parathyroid hormone (PTH)-(1-14) and -(1-11) analogs conformationally constrained by alpha-aminoisobutyric acid mediate full agonist responses via the juxtamembrane region of the PTH-1 receptor, *J Biol Chem 276*, 49003-49012.

[21] Cheloha, R. W. (2015) Exploration of alpha/beta-peptides as parathyroid hormone receptor ligands and recognition of alpha/beta-peptides by the immune system, In *Department of Chemistry*, p 454, University of Wisconsin-Madison, Madison, WI.

[22] MacNeill, R., Stromeyer, R., Urbanowicz, B., Acharya, V., and Moussallie, M. (2013) LC-MS/MS quantification of parathyroid hormone fragment 1-34 in human plasma, *Bioanalysis 5*, 415-422.

[23] Maack, T., Johnson, V., Kau, S. T., Figueiredo, J., and Sigulem, D. (1979) Renal filtration, transport, and metabolism of low-molecular-weight proteins: a review, *Kidney Int 16*, 251-270.

[24] Orloff, J. J., Ribaudo, A. E., McKee, R. L., Rosenblatt, M., and Stewart, A. F. (1992) A pharmacological comparison of parathyroid hormone receptors in human bone and kidney, *Endocrinology 131*, 1603-1611.

[25] Liao, S., Qie, J. K., Xue, M., Zhang, Z. Q., Liu, K. L., and Ruan, J. X. (2010) Metabolic stability of human parathyroid hormone peptide hPTH (1-34) in rat tissue homogenates: kinetics and products of proteolytic degradation, *Amino Acids 38*, 1595-1605.

[26] Gardella, T. J., and Vilardaga, J. P. (2015) International Union of Basic and Clinical Pharmacology. XCIII. The parathyroid hormone receptors--family B G protein-coupled receptors, *Pharmacological reviews 67*, 310-337.

[27] Binkowski, B. F., Butler, B. L., Stecha, P. F., Eggers, C. T., Otto, P., Zimmerman, K., Vidugiris, G., Wood, M. G., Encell, L. P., Fan, F., and Wood, K. V. (2011) A luminescent biosensor with increased dynamic range for intracellular cAMP, *ACS chemical biology 6*, 1193-1197.

[28] Kim, Y. G., Lone, A. M., Nolte, W. M., and Saghatelian, A. (2012) Peptidomics approach to elucidate the proteolytic regulation of bioactive peptides, *Proceedings of the National Academy of Sciences of the United States of America 109*, 8523-8527.

[29] Kim, Y. G., Lone, A. M., and Saghatelian, A. (2013) Analysis of the proteolysis of bioactive peptides using a peptidomics approach, *Nature protocols 8*, 1730-1742.

[30] Mitchell, A. J., Lone, A. M., Tinoco, A. D., and Saghatelian, A. (2013) Proteolysis controls endogenous substance P levels, *PloS one 8*, e68638.

[31] Tagore, D. M., Nolte, W. M., Neveu, J. M., Rangel, R., Guzman-Rojas, L., Pasqualini, R., Arap, W., Lane, W. S., and Saghatelian, A. (2009) Peptidase substrates via global peptide profiling, *Nature chemical biology 5*, 23-25.

[32] Tinoco, A. D., Kim, Y. G., Tagore, D. M., Wiwczar, J., Lane, W. S., Danial, N. N., and Saghatelian, A. (2011) A peptidomics strategy to elucidate the proteolytic pathways that inactivate peptide hormones, *Biochemistry 50*, 2213-2222.

[33] Tinoco, A. D., and Saghatelian, A. (2011) Investigating endogenous peptides and peptidases using peptidomics, *Biochemistry 50*, 7447-7461.

[34] Bucknall, M., Fung, K. Y., and Duncan, M. W. (2002) Practical quantitative biomedical applications of MALDI-TOF mass spectrometry, *Journal of the American Society for Mass Spectrometry 13*, 1015-1027.

[35] Chen, R., Hui, L., Sturm, R. M., and Li, L. (2009) Three dimensional mapping of neuropeptides and lipids in crustacean brain by mass spectral imaging, *Journal of the American Society for Mass Spectrometry 20*, 1068-1077.

[36] Ye, H., Mandal, R., Catherman, A., Thomas, P. M., Kelleher, N. L., Ikonomidou, C., and Li, L. (2014) Top-down proteomics with mass spectrometry imaging: a pilot study towards discovery of biomarkers for neurodevelopmental disorders, *PloS one 9*, e92831.

[37] Peterson, A. C., Russell, J. D., Bailey, D. J., Westphall, M. S., and Coon, J. J. (2012) Parallel reaction monitoring for high resolution and high mass accuracy quantitative, targeted proteomics, *Mol Cell Proteomics 11*, 1475-1488.

[38] Szajli, E., Feher, T., and Medzihradszky, K. F. (2008) Investigating the quantitative nature of MALDI-TOF MS, *Mol Cell Proteomics 7*, 2410-2418.

[39] Gutierrez, J. A., Dorocke, J. A., Knierman, M. D., Gelfanova, V., Higgs, R. E., Koh, N. L., and Hale, J. E. (2005) Quantitative determination of peptides using matrix-assisted laser desorption/ionization time-of-flight mass spectrometry, *Biotechniques Suppl*, 13-17.

[40] Tholey, A., and Heinzle, E. (2006) Ionic (liquid) matrices for matrix-assisted laser desorption/ionization mass spectrometry-applications and perspectives, *Anal Bioanal Chem 386*, 24-37.

[41] Horne, W. S. (2015) Foldamers: Biomimetic and built to order, *Nature chemistry 7*, 858-859.

Figure legends

Figure 1. Sequences of hPTH (1-34) (a), rPTH (1-34) (b) and M-Cyc-9β (c). The single letter code in black indicated naturally occurring amino acid residues; the single letter code in red indicated the site with α→β replacements. The structures of nonstandard amino acids (U, X, Z and ^{h}R) are listed at the bottom of the figure.

Figure 2. Workflow of PTH peptide stability analysis. Kidney tissues were harvested from female Sprague-Dawley rats and homogenized. The protein concentration of the resulting kidney homogenates was determined by BCA assay and the homogenate was diluted to 2.5 mg protein/mL. PTH peptides were spiked in kidney homogenates as the following four conditions: hPTH (1-34) only, M-Cyc-9β only, hPTH (1-34) with 1% TFA and M-Cyc-9β with 1% TFA. The mixtures were incubated at 37 °C water bath and sampled at the following 12 time points: 0, 1, 3, 5, 10, 15, 30, 45, 60, 90, 120 and 240 min. MALDI-MS was used for the measurement of degradation products and LC-MS/MS was used for absolute quantification of the peptides at each time point.

Figure 3. MALDI-MS spectra of PTH peptide stability analysis at different time points (0, 1, 3, 5, 10, 15, 30, 45, 60, 90, 120 and 240 min). (a) hPTH (1-34) spiked in inactivated rat kidney homogenate; **(b)** hPTH (1-34) spiked in regular rat kidney homogenate; **(c)** M-Cyc-9β spiked in inactivated rat kidney homogenate and **(d)** M-Cyc-9B spiked in regular rat kidney homogenate. 1% TFA was used to quench the enzymatic acitivity.

Figure 4. MALDI-MS spectra of hPTH (1-34) (a) and M-Cyc-9β (b) quenched with methanol. The spectra at 0 min were presented.

Figure 5. Representative chromatograms (a, b) and calibration curves (c, d) for hPTH (1-34) (a, c) and M-Cyc-9β (b, d). The chromatograms were obtained from 50 μg/mL calibration standards of hPTH (1-34) and M-Cyc-9β. The elution time for each peptide was labeled on the figure. Symbols and error bars on the calibration curve plots were mean ± SD.

Figure 6. Concentration-time plots for hPTH (1-34) and M-Cyc-9β spiked in rat kidney homogenate. (a) hPTH (1-34) and M-Cyc-9β were spiked into regular rat kidney homogenates without any pre-treatment. Non-linear regression curve fitting was performed using a single phase exponential decay model. For hPTH (1-34), half-life = 1.9 min, R^2 = 0.99; for M-Cyc-9β, half-life = 35.2 min, R^2 = 0.95. **(b)** hPTH (1-34) and M-Cyc-9β spiked in rat kidney homogenates pretreated with 1% TFA, which terminated enzymatic activity. The starting concentrations for hPTH (1-34) and M-Cyc-9β were both 50 μg/mL. Symbols and error bars are mean ± SD.

Figures

(a) hPTH (1-34)
SVSEI QLMHN LGKHL NSMER VEWLR KKLQD VHNF

(b)rPTH (1-34)
AVSEI QLMHN LGKHL ASVER MQWLR KKLQD VHNF

(c) M-Cyc-9β
XVUEX QXMHQ ^{h}RAKXL NSXRR VZWLR ZKLQX VHNX

Red residues are beta amino acids
^{h}R = homoarginine
X = ACPC (5 membered ring constrained beta)
Z = APC (5 membered ring constrained beta)

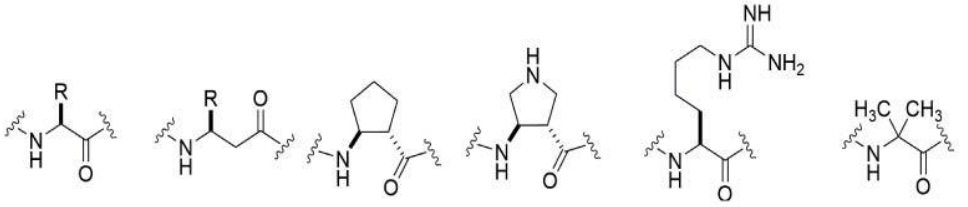

Figure 1

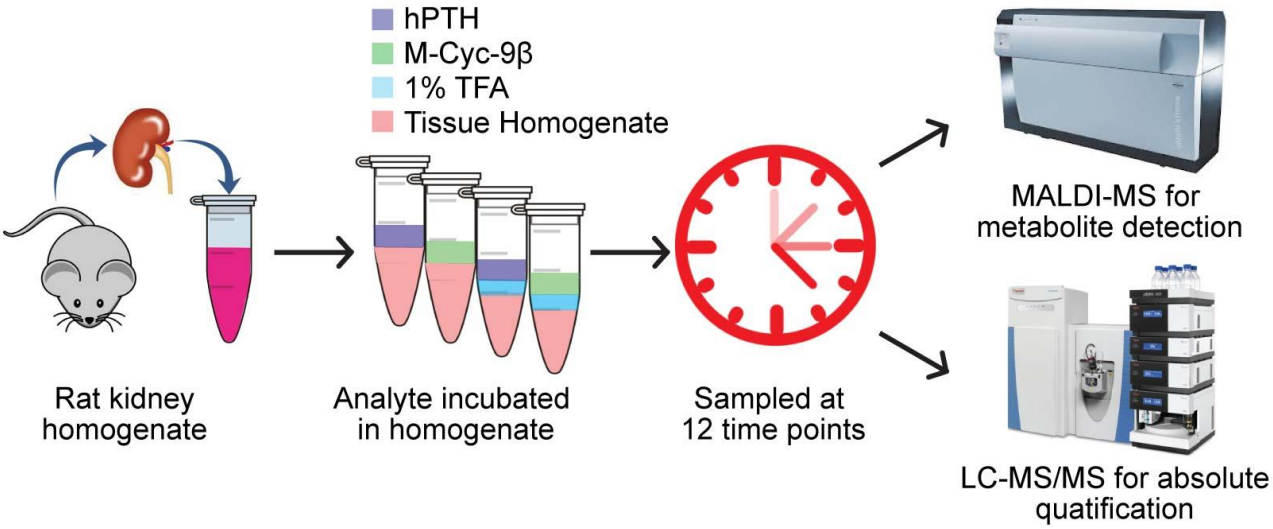
hPTH
M-Cyc-9β
1% TFA
Tissue Homogenate
Rat kidney homogenate
Analyte incubated in homogenate
Sampled at 12 time points
MALDI-MS for metabolite detection
LC-MS/MS for absolute quatification

Figure 2

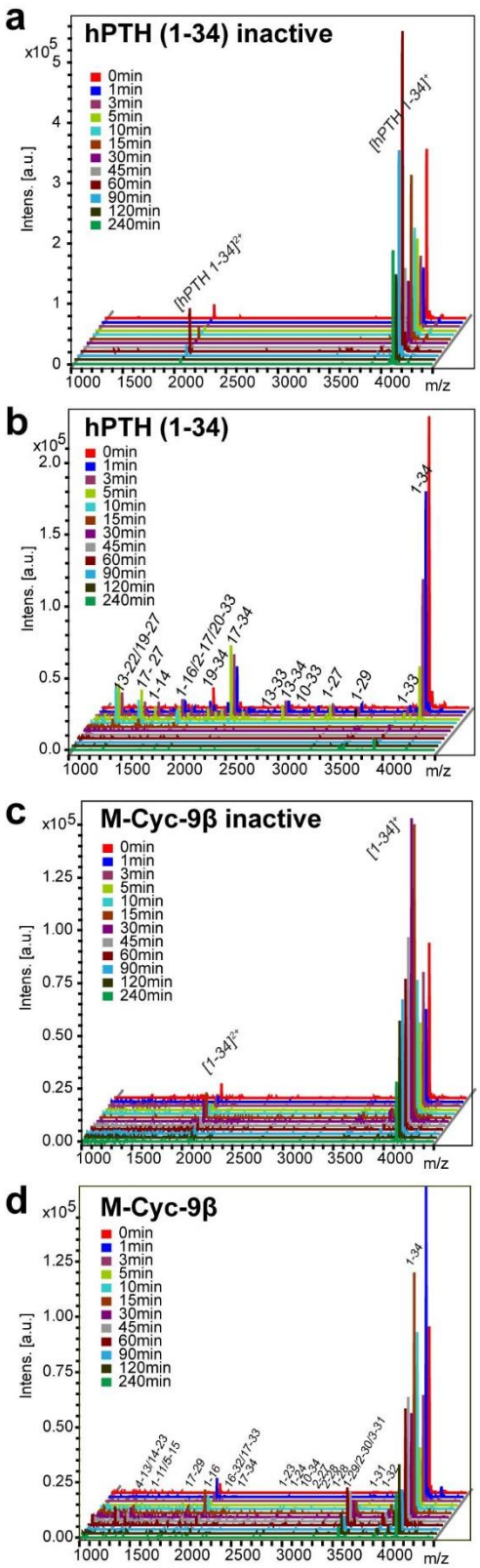
a
hPTH (1-34) inactive
x10^5
Intens. [a.u.]
0min
1min
3min
5min
10min
15min
30min
45min
60min
90min
120min
240min
[hPTH 1-34]2+
[hPTH 1-34]+
m/z
b
hPTH (1-34)
1-34
13-22/19-27
17-27
1-14
1-16/2-17/20-33
19-34
17-34
13-33
13-34
10-33
1-27
1-29
1-33
c
M-Cyc-9β inactive
[1-34]+
[1-34]2+
d
M-Cyc-9β
1-34
4-13/14-23
1-11/5-15
17-29
1-16
16-32/17-33
17-34
1-23
1-24
10-34
2-25/26
1-28
1-29/2-30/31-31
1-31
1-32

Figure 3

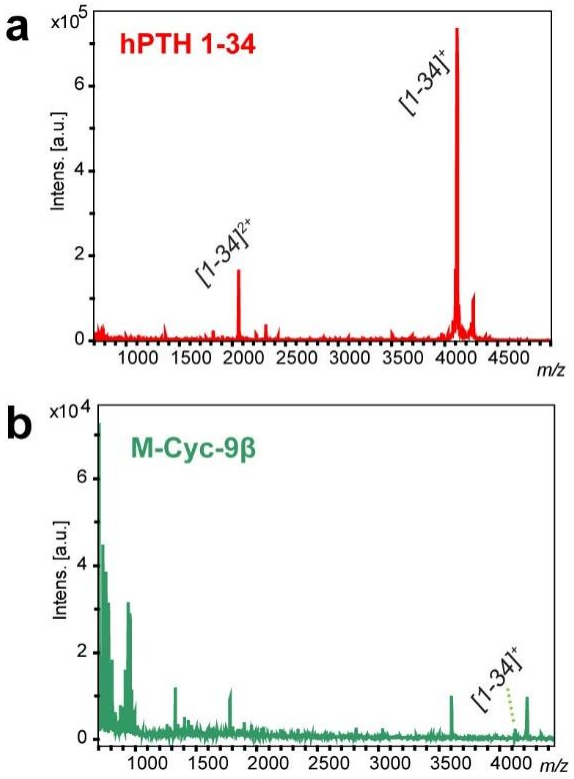
a
x10^5
hPTH 1-34
[1-34]3+
[1-34]2+
Intens. [a.u.]
0
2
4
6
1000 1500 2000 2500 3000 3500 4000 4500
m/z
b
x10^4
M-Cyc-9β
Intens. [a.u.]
0
2
4
6
[1-34]3+
1000 1500 2000 2500 3000 3500 4000
m/z

Figure 4

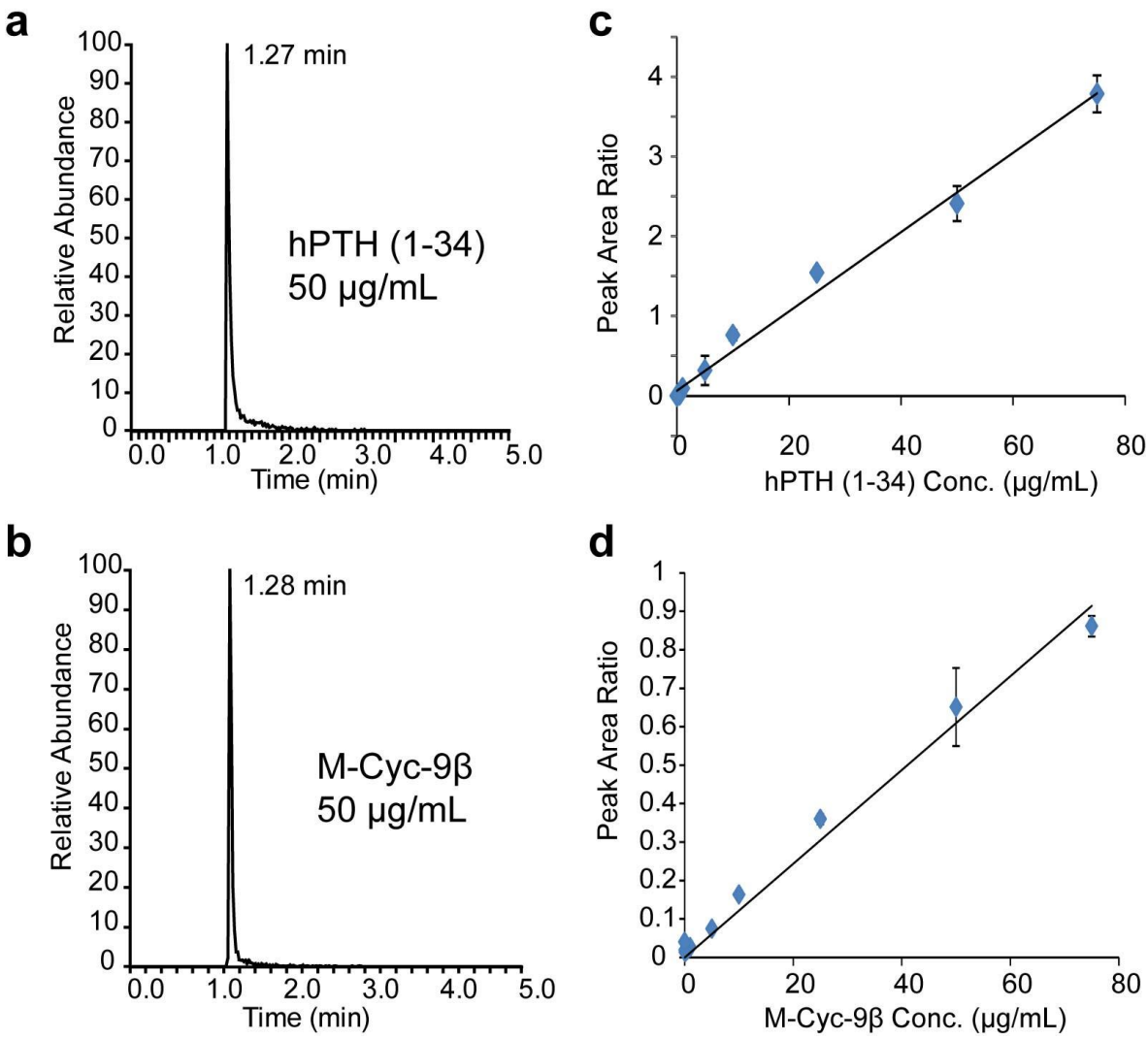
a
1.27 min
hPTH (1-34)
50 µg/mL
Relative Abundance
Time (min)
b
1.28 min
M-Cyc-9β
50 µg/mL
Relative Abundance
Time (min)
c
Peak Area Ratio
hPTH (1-34) Conc. (µg/mL)
d
Peak Area Ratio
M-Cyc-9β Conc. (µg/mL)

Figure 5

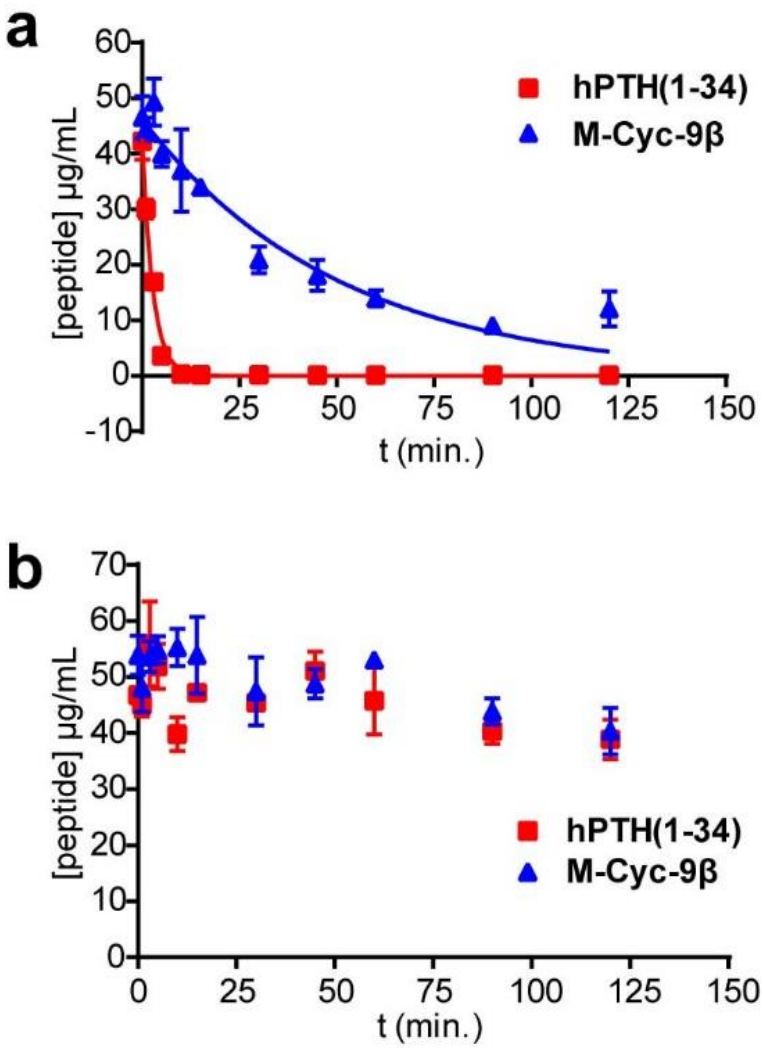
a
60
50
40
30
20
10
0
-10
[peptide] µg/mL
25
50
75
100
125
150
t (min.)
hPTH(1-34)
M-Cyc-9β
b
70
60
50
40
30
20
10
0
[peptide] µg/mL
0
25
50
75
100
125
150
t (min.)
hPTH(1-34)
M-Cyc-9β

Figure 6

Tables

Table 1. LC-MS/MS method validation result. R^2 of calibration curves, interday and intraday precisions (CV, %), accuracy (RE, %), LLOQ, recovery (%) and matrix effect (%) were listed for hPTH (1-34), M-Cyc-9β and IS. Values of recovery and matrix effect were represented by mean ± SD from 3 replicates. 50 μg/mL QC standards were used to calculate the precisions and accuracies.

		hPTH (1-34)	M-Cyc-9β	rPTH (1-34) (IS)
Linearity (R^2)		0.97	0.99	N/A
Precision (CV, %)	Interday	8.33	15.58	N/A
	Intraday	16.50	6.53	N/A
Accuracy (RE, %)	Interday	2.09	6.76	N/A
	Intraday	3.25	27.83	N/A
LLOQ		30.00 pg	30.00 pg	N/A
Recovery (%)		70.19 ± 2.51	86.43 ± 11.93	73.12 ± 1.09
Matrix effects (%)		0.82 ± 2.12	-21.02 ± 7.41	N/A

Table 2. Concentrations of hPTH (1-34) and M-Cyc-9β at each time point following spiked in rat kidney homogenates. Concentrations were represented by mean ± SD.

Time (min)	hPTH (1-34) Conc. (μg/mL)	hPTH (1-34) Inactive Conc. (μg/mL)	M-Cyc-9β Conc. (μg/mL)	M-Cyc-9β Inactive Conc. (μg/mL)
0	42.26 ± 3.28	46.75 ± 0.41	46.57 ± 3.82	53.86 ± 3.50
1	30.07 ± 1.71	45.01 ± 2.04	44.47 ± 2.06	48.07 ± 4.33
3	16.93 ± 0.58	55.93 ± 7.61	49.27 ± 4.28	53.63 ± 2.76
5	3.65 ± 0.10	51.87 ± 4.07	39.96 ± 2.28	54.81 ± 2.46
10	0.28 ± 0.04	39.84 ± 3.05	36.96 ± 7.41	55.30 ± 3.34
15	0.18 ± 0.06	47.22 ± 1.15	34.00 ± 0.35	53.88 ± 6.81
30	0.18 ± 0.01	45.40 ± 0.71	20.86 ± 2.39	47.47 ± 6.09
45	0.12 ± 0.03	51.06 ± 3.48	18.10 ± 2.81	48.78 ± 2.67
60	0.10 ± 0.02	45.78 ± 6.00	13.92 ± 1.49	53.03 ± 1.30
90	0.10 ± 0.01	40.36 ± 2.31	9.08 ± 1.00	43.85 ± 2.33
120	0.12 ± 0.18	38.88 ± 3.55	12.07 ± 3.15	40.33 ± 4.15

Chapter 10
Targeted MultiNotch MS^3 Approach for Relative Quantification of N-glycans Using Multiplexed Carbonyl-Reactive Isobaric Tags

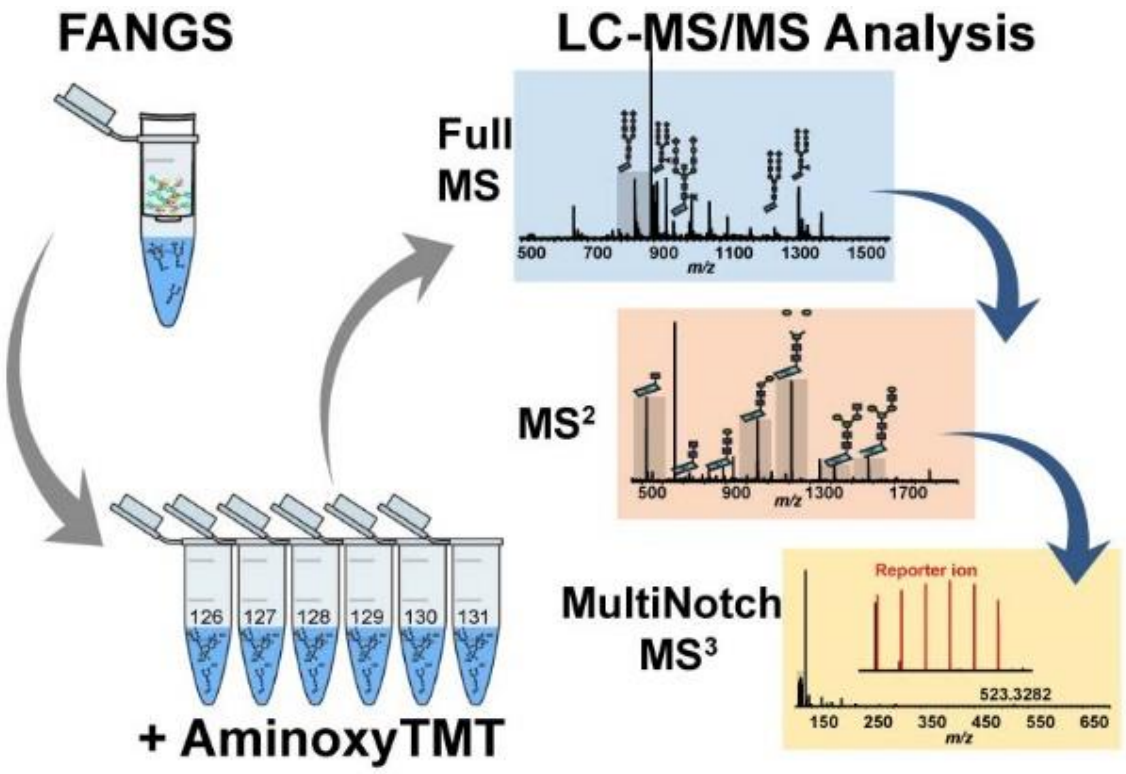

Adapted from **B. Chen**[#]**,** X. Zhong[#], Y. Feng, S. Snovida, M. Xu, J. Rogers and L. Li, Relative Quantification of N-Glycan Using Multiplex Carbonyl-Reactive Tandem Mass Tags and MultiNotch MS3. *To be submitted to Anal. Chem.* ([#]Co-First authors)

Author contribution: study was designed by B. Chen, X. Zhong, J. Rogers and L. Li; experiment was performed by B. Chen, X. Zhong, Y. Feng and S. Snovida; data was analyzed by B. Chen, M. Xu and Y. Feng; manuscript was written by B. Chen, X. Zhong and edited by Y. Feng and L. Li.

Abstract

The recently developed and commercially available carbonyl-reactive tandem mass tags (aminoxyTMT) enables multiplexed quantification of glycans through comparison of reporter ion intensity. However, challenge still exist for collision activated dissociation (CAD) MS/MS based quantification of aminoxyTMT due to the low reporter ion yield especially for glycans with labile structures. To circumvent this limitation, we utilized the unique structural features of N-glycan molecules, the common core sugar sequence $(HexNAc)_2(Man)_3$ and common m/z of Y_n ions generated from different type of precursors by MS/MS, and designed a Y_1 ion triggered, targeted MultiNotch MS^3 relative quantification approach based on aminoxyTMT labeling. This approach was implemented on a nanoHILIC-Tribrid quadrupole-ion trap-Orbitrap platform, which enables pre-screening of aminoxyTMT labeled N-glycan precursor ions by Y_1 ion fragment ion mass in HCD MS/MS scan, and co-isolation and co-fragmentation of multiple Y_n fragment ions that carry the isobaric tags from the inclusion list in MS/MS/MS scan. Through systematical optimization and evaluation using N-glycans released from several glycoprotein standards and human serum proteins, we demonstrated that the Y_1 ion triggered, targeted MultiNotch MS^3 approach offers improved accuracy, precision and sensitivity for relative quantification compared to traditional data-dependent MS^2 and Y_1 ion MS^3 quantification methods.

Keywords: aminoxyTMT, N-glycan, carbohydrate, MultiNotch MS^3, tandem mass tag, relative quantification

Introduction

Glycosylation of protein is one of the most important PTMs. It is involved in a variety of biological and physiological states. Alteration of glycosylation is associated with abnormal biological states, such as cancer progression and invasion. [1, 2] In glycobiology studies, it is observed that the significant change of glycans could be an indicator for the disease state. [3] Therefore, it is crucial to develop proper methods for relative glycan quantification.

Significant efforts have been made to develop analytical methods for relative quantification of glycans, especially for N-glycans, which is attached to an asparagine residue in proteins with sequons N-X-S or N-X-T (X can be any amino acid except for Pro). [1] Among different methods for glycan quantification, mass spectrometry based approaches become popular because of the large advancement of MS technologies. In general, glycan abundance in different biological samples can be quantified by label-free and chemical labeling approach by comparing MS signal intensities. The label-free approach compares relative peak intensity or spectral abundance between underivatized N-glycans. Alternatively, N-glycans can be derivatized with isotopic or isobaric labels and the intensity ratios between labels represent the relative abundance of individual N-glycans. [3] Several tags have been developed by various vendors and research groups, such as Isotopic Glycan Hydrazide Tags (INLIGHT, 2-plex isotopic tag) [4-6], isobaric aldehyde reactive tags (iARTs, 2-plex isobaric tag)[7], Quanternary Amine Containing Isobaric Tag for Glycan (QUANTITY, 4-plex isobaric tag)[8] and carbonyl-reactive tandem mass tag (aminoxyTMT, 6-plex isobaric tag). [9]

The development of aminoxyTMT enables high-throughput quantification of carbonyl containing compounds, including N-glycans. It is a set of isobaric tags with the same chemical structure but different isobaric distributions. The aminoxyTMT reagent reacts with the reducing

end of N-glycan to produce a stable oxime product. Each plex generates a unique reporter ion from 126 to 131 at the low mass region upon fragmentation.[9] However, the performance of CAD MS^2 based quantification is not ideal due to the low reporter ion yield from some categories of glycans, such as the complex type of N-glycans with core-fucosylation, and acidic N-glycans with labile residues.[9-11] As the Y_n ions are always observed to be abundant in the CAD MS/MS of most type of N-glycans, and they carry the intact aminoxyTMT tags, further isolation and fragmentation of Y_n ions can be employed for reporter ion intensity based quantification.

To improve the duty cycle of MS^3-based quantification method, MultiNotch MS^3 method was introduced recently for quantitative proteomics and implemented on a commercially available high resolution/accurate mass (HR/AM) instrument: Orbitrap Fusion Lumos.[12] In this approach, isolation waveforms with multiple frequency notches were used to co-isolate and co-fragment multiple MS^2 fragment ions. It was demonstrated that the interference from coeluting peptides was minimized and the quantification accuracy was enhanced.[12] Enlighten by this MultiNotch MS^3 quantification for TMT labeled peptides, we further extend this approach to relative quantification of aminoxyTMT labeled N-glycans. Specifically, a Y_1 product-ion triggered, targeted MultiNotch MS^3 approach, based on the unique structural features of N-glycans was developed for relative glycan quantification. As all N-glycans share the same conserved core, the signature Y_1 ions ($[HexNAc\text{-}aminoxyTMT+H]^+$ or $[HexNAcFuc\text{-}aminoxyTMT+H]^+$) generated by CAD cleavage can be used as selection criteria for amixoyTMT labeled precursor ions to trigger MultiNotch MS^3 scan event. Moreover, a target inclusion list including all conserved Y ions could be used for MultiNotch MS^3 to improve the specificity.

In this study, we systematically optimized and evaluated the nanoHILIC-MS parameters of targeted MultiNotch MS^3 method and compare with standard MS^3 and MS^2 methods for quantifying aminoxyTMT labeled N-glycans from glycoprotein standards and protein mixture.

Materials and methods

Materials and chemicals

All reagents were used without additional purification. Methanol (MeOH), acetonitrile (ACN), water, acetic acid (AA) and formic acid (FA) were purchased from Fisher Scientific (Pittsburgh, PA). Triethylammonium bicarbonate buffer (TEAB, 1.0 M) and Tris (2-carboxy-ethyl) phosphine hydrochloride (TCEP) were purchased from Sigma-Aldrich (St. Louis, MO). PNGase F was purchased from Promega (Madison, WI). AminoxyTMT reagents, bovine thyroglobulin (BTG), bovine lactoferrin (BLF), RNaseB and human serum protein mixture (HSP) were provided by Thermo Fisher Scientific (Rockford, IL). Oasis HLB 3cc (60 mg) extraction cartridges were purchased from Waters Corporation (Milford, MA). Microcon-30kDa centrifugal filters (30K MWCO) were purchased from Merck Millipore Ltd. (Darmstadt, Germany). PolyGLYCOPLEX A™ beads (3 µm) were purchased from PolyLC Inc. (Columbia, MD). Fused silica capillary tubing (inner Diameter 75 µm, outer diameter 375 µm) was purchased from Polymicro Technologies (Phoenix, AZ).

Filter-Aided-N-Glycan Separation (FANGS)

N-glycans were released from glycoproteins following the FANGS protocol [4] with slight modifications (Figure 1). Briefly, glycoprotein (2 µg/uL dissolved in 50 mM TEAB buffer) was mixed with 4 µL 0.5 M TCEP, heat-denatured and added to a 30K MWCO filter. Heat-denaturing was performed by alternating sample tube between 100 °C and room temperature water baths for 4 times, 15 seconds each. The mixture was then buffer exchanged with 200 µL

50 mM TEAB buffer for three times (centrifuged at 14,000 g for 20 min at 20 °C each time) and incubated with PNGaseF (1 µL PNGaseF/10 µg protein) for 18 hours at 37 °C. The released glycosyamines were separated from the de-glycosylated protein by centrifugation at 14,000 g for 20 min at 20 °C. The pH of the flow through solution was adjusted to 3 by adding 1% acetic acid solution and the mixture was vortexed at room temperature for 40 min. The resulting N-glycans were then evaporated to dryness under vacuum and stored in -20 °C (Figure 1).

AminoxyTMT labeling and cleaning up

AminoxyTMT labeling reaction was performed following the manufacturer's instruction (Thermo Scientific, Rockford, IL) with slight modification. Briefly, aminoxyTMT reagent was reconstituted in 200 µL 95% MeOH with 0.1% acetic acid and mixed with acidified N-glycans released from 10 to 30 µg glycoproteins standards (dissolved in 10 to 30 µL H_2O). The mixture was vortexed for 10 min at room temperature and evaporated to dryness under vacuum. The dried mixture was then reconstituted in 200 µL 95% MeOH, vortexed for 10 min at room temperature and evaporated to dryness under vacuum again. The excess labeling reagent was quenched by 100 µL 10% acetone and vortexed for 10 min at room temperature. All labeled products were quantitatively transferred, combined into a single tube, and evaporated to dryness under vacuum. An Oasis HLB 3cc cartridge was used for sample clean-up. The cartridge was conditioned by sequentially washing with 3 mL of 95% ACN, 1 mL of 50% ACN and 3 mL of 95% ACN. In the sample loading step, the labeled N-glycans were dissolved in 200 µL 50% ACN and added to a conditioned cartridge which was pre-loaded with 3 mL of 95% ACN. The loaded cartridge was washed twice with 3 mL 95% ACN and eluted with 2 mL of 50% ACN. The eluted sample was evaporated to dryness under vacuum and stored in -20 °C until LC-MS/MS analysis.

NanoHILIC column fabrication and LC conditions

A NanoHILIC column was self-fabricated with 3 µm PolyGLYCOPLEX A™ beads and 75 µm ID fused-silica capillary. A laser pulled fused silica capillary tubing end was etched with hydrogen fluoride for 3 min and washed with MeOH. A slurry of beads was prepared by adding 1:4 of isopropanol and methylene chloride and packed into the capillary with a pressure bomb until the desired length (30 to 40 cm) was reached. The packed column was then washed with MeOH and flushed with nitrogen.

A Dionex Ultimate 3000 nanoLC system was used for nanoHILIC separation. Mobile phase A was H_2O with 0.1% FA and mobile phase B was ACN with 0.1% FA. A flow rate of 0.30 or 0.45 µL/min was used. AminoxyTMT labeled N-glycans released from 1 to 2 µg glycoproteins were loaded onto the column. Different linear and stepped gradients were tested and the optimization results are specified in the result and discussion sections.

MS methods and parameters

Orbitrap Fusion Lumos Tribrid quadrupole-ion trap-Orbitrap mass spectrometer with NanoSpray Flex ion source (Thermo Scientific, Bremen, Germany) was used for data acquisition. The following parameters were used unless otherwise specified. The data was acquired by positive ion mode with spray voltage of 3 kV and ion transfer tube temperature of 300 °C. Full MS was acquired with *m/z* range of 500-1700 and detected in Orbitrap at resolution of 120K at *m/z* 200 with automatic gain control (AGC) target of 1E6, maximal injection time of 100 ms and 1 microscan. At MS^2 level, data dependent acquisition (DDA) was performed by collision-induced dissociation (CID) on the top 6 most intense ions with a dynamic exclusion period of 10 seconds and detected in the Orbitrap with resolution of 30K at *m/z* 200 (MS^2 workflow) or in the ion trap with rapid scans (MS^3 workflows). Two extra higher-energy collisional dissociation (HCD) scans were performed at different normalized collisional energies

(NCE) at low (NCE 30) and high (NCE 70) settings for the MS^2 workflow. For the MS^3 methods, the MS^3 scans were triggered by appearance of either of the two Y_1 ions, $[HexNAc\text{-}aminoxyTMT+H]^+$ (*m/z* 523.3289) and $[HexNAcFuc\text{-}aminoxyTMT+H]^+$ (*m/z* 669.3869) above the intensity threshold of 5% of base peak intensity in HCD MS/MS scan. HCD was used for MS^3 scans with NCE of 70 and detected by Orbitrap at a resolution of 120K at *m/z* 200. AGC target was 5E4 with maximum injection time of 100 ms. In the standard MS^3 method, only Y_1 ion (*m/z* of 523.3289) was isolated for MS^3 scan; in the MultiNotch MS^3 method, top six intense Y ions from an inclusion list including Y_1 ions (*m/z* 523.3289 & 669.3868), Y_2 ions (*m/z* 726.4084 & 872.4662), etc. were synchronously isolated in ion trap and fragmented by HCD.

Results and discussion

A Y_1 ion triggered, targeted MultiNotch MS^3 method was developed on a Tribrid quadrupole-ion trap-Orbitrap platform to improve the quantification precision and accuracy of aminoxyTMT labeled N-glycans. Quantification results from MultiNotch MS^3, data-dependent MS^2 and standard MS^3 quantification methods were compared.

Method setup and workflows

Three instrument methods were created in Xcalibur for comparison of MS^2-based and MS^3 based quantification performance (Figure 2). All methods started with HR/AM full scans followed by MS^2 scans in a data dependent manner. The MS^2 method combined HCD scans with low (NCE 30) and high (NCE 70) collisional energies (Figure 2A). Both MS^3 methods started with a HR/AM full scan followed by top 6 DDA scans by ion trap "rapid" scan mode. MS^3 scans are triggered by detection of Y_1 ion at *m/z* 523.3289 or 669.3868 in the MS^2 scan. Upon detection of the Y_1 ions, the standard MS^3 method would isolate the fragment the Y_1 ion for HR/AM MS^3 scans, while the MultiNotch MS^3 method would co-isolate several Y ions that

matched the pre-defined inclusion list and co-fragment them for HR/AM SPS MS^3 scans (Figure 2B and C). Otherwise, the instrument continues with the top 6 DDA MS/MS scan.

LC gradient optimization

Both LC and MS conditions were optimized to achieve the best quantification performance. Various LC gradients and flow rates were compared to optimize the separation of aminoxyTMT labeled N-glycans released from BTG (Figure S2), including a 60-min linear gradient of 90%-20% ACN at a flow rate of 300 nL/min (Figure S2A), same gradient with flow rate of 450 nL/min (Figure S2B), a 60-min linear gradient of 80%-20% ACN at flow rate of 450 nL/min (Figure S2C) and a stepped gradient of 75%-60% (0 – 18 min), 50% - 40% (19 – 33 min), 35% - 30% (34 – 48 min) (Figure S2D). The elution order of N-glycans mainly depend on the numbers of sialic acids residues presented. The stepped gradient improved the separation of N-glycans with the same number of sialic acids while shorten the time intervals between each group. Figure S3 demonstrated the elution sequence of some representative aminoxyTMT labeled N-glycans: the neutral N-glycans were eluted between 7 and 13 min (Figure S3A-C), followed by N-glycans with one sialic acid (23 to 24 min, Figure S3D-F) and N-glycans with two sialic acids (38 to 40 min, Figure S3G&H). The stepped gradient was used for all quantification acquisitions.

MS parameter optimization

The MS parameters for MultiNotch MS^3, standard MS^3, low and high MS^2 methods were optimized by directly infusing aminoxyTMT^{130} labeled N-glycans released from BTG, which consist of both high-mannose and complex N-glycans. S-lens RF levels (Figure S1A), NCEs at MS^2 (Figure S1B&C) and MS^3 levels (Figure S1D), AGC target values at each MS level, MS^2 ion trap scan speeds and isolation widths were optimized. Due to the fragile glycosidic bond, the S-lens RF level was optimized to maximize ion transmission while minimize fragmentation. The

intensities of the signature Y_1 ion peak at *m/z* 523.3289 and the most abundant parent ion peak ($[H_5N_2$-aminoxyTMT+2H+K$]^{3+}$) at *m/z* 525.5482 were monitored over 3 min at each RF level. The average signal intensities at each RF level were plotted in Figure S1 with error bars representing the standard deviation. At S-lens RF level of 30%, the parent ion intensity reached plateau while the fragment ion intensity was not at a significant level. Based on the results, this S-lens RF level was selected for all following experiments.

According to previous studies, MS^2 quantification of aminoxyTMT labeled N-glycans, especially acidic complex N-glycans suffered from low reporter ion yield due to the alternative fragmentation pathway. Here, the NCEs for each type of aminoxyTMT labeled N-glycans at MS^2 (CID & HCD) and MS^3 (HCD) levels were carefully optimized. At MS^2 level, a high mannose N-glycan ($[H_5N_2$-aminoxyTMT+2H$]^{2+}$) and a complex N-glycan ($[H_5N_2S_2F$-aminoxyTMT+3H$]^{3+}$) were selected to represent each class of N-glycans. The intensities of the parent ions and several fragment Y ions were monitored at different NCEs. For both N-glycan species, the fragment signals reached plateau while the parent ion signals were still preserved at NCE 30. NCE 30 was chosen as the optimum energy to preserve backbone fragment information and NCE 70 was chosen as the optimum energy to maximize reporter ion yield. To optimize the MS^3 NCE of HCD, a pseudo MS^3 method was set up: S-lens RF lens level was set to 100% to maximize fragmentation during ion transmission and the Y_1 ion at *m/z* 523.3289 was isolated and fragmented at MS^2 level. The reporter ion reached the highest intensity at NCE 70, which was chosen as the optimum energy for MS^3.

Representative spectra for MS^2 and MS^3 quantification methods

Representative spectra acquired by the three quantification methods were summarized in Figure 3. A HR/AM full scan was acquired in all three methods and the N-glycans corresponding

to each peak could be assigned by accurate mass matching (Figure 3A). For the MS^2 method, HCD MS^2 spectra of low and high NCEs were represented in Figure 3B and Figure 3C. At low NCE, the backbone fragments of the N-glycan were well preserved but the reporter ion yields were low; at high NCE, none of the backbone fragment was preserved, but the reporter ion yields were high and the ratios were much more accurate than the low energy ones. For both MS^3 methods, MS^2 scan was acquired in the ion trap using rapid scan mode (Figure 3 D&F). In the standard MS^3 run, the Y_1 ion was isolated and fragmented to generate the MS^3 spectrum shown in Figure 3E. In the MultiNotch MS^3 run, several Y ions were co-isolated and co-fragmented to generate the MultiNotch MS^3 spectrum shown in Figure 3G. The average reporter ion signal intensity acquired by the MultiNotch MS^3 method (8.75E5) was approximately nine times higher than standard MS^3 method (1.05E5). The spectra with zoomed in reporter ion region revealed very accurate reporter ion ratios for both MS^3 methods.

Quantification results of MS^2 and MS^3 methods

The scan statistics of N-glycans released from BTG and quantified by the both MS^3 quantification methods were summarized in Supplemental Figure 4. Approximately 15% of the MS^2 scans were selected for MS^3 scans in both workflows. This dataset suggested that a large percentage of peaks, which did not have the Y_1 ion detected, were filtered away by the system. These peaks could either be non-N-glycan peaks, or N-glycan peaks with poor fragmentation efficiency. With the irrelevant or low quality peaks filtered, the workflow could confidently select the N-glycan peaks for quantification and thus improve the quantification performance. The other two sets of columns represented the percentage of quantifiable scans by summarizing the number of scans with at least one reporter ion detected (middle columns) and with all reporter ion detected (right columns) within 10 ppm. With both criteria, the MultiNotch MS^3

method has approximately 15% to 20% more quantifiable scans compared to the standard MS^3 method.

The quantification results of 1:1:1:1:1:1 aminoxyTMT labeled N-glycans released from BTG by the 3 methods (with 4 quantification approaches) were summarized in Figure 4 as box-and-whisker plots for high mannose N-glycan H_5N_2 (Figure 4A) and complex N-glycan $H_5N_4S_2$ (Figure 4B). The average reporter ion intensities and the average ratios were labeled on each panel. The average, median, standard deviation and data points (N) were summarized in Supplementary Table 1. Quantification accuracy (systematic error), precision (statistical variability) and reporter ion yield (reporter ion intensity) were used to evaluate these methods. All four methods could accurately quantify the high-mannose N-glycans with small relative error. The MultiNotch MS^3 method and high-energy MS^2 method had small signal variance and could be used for precise measurements. The standard MS^3 method had slightly larger variance while the low energy MS^2 method had very large variance due to the low reporter ion intensities with the boxes and whiskers wide separated. In terms of reporter ion intensities, the MultiNotch MS^3 method had the highest signal intensity, followed by high energy MS^2. The reporter ion intensity of standard MS^3 method was one order of magnitude lower than the MultiNotch MS^3 method, while the low energy MS^2 method had the lowest signal intensity, which was two orders of magnitude lower than the MultiNotch MS^3 method. Both the MultiNotch MS^3 and the high energy MS^2 methods were suitable for accurately and precisely quantify the high mannose N-glycans.

More different trend was observed for the complex N-glycan $H_5N_4S_2$ (Figure 4B). The MultiNotch MS^3 method produced accurate and precise measurements (Supplemental Table 1, right panel) with the highest signal intensity (8.75E4). All other methods produced large

variances (Supplemental Table 1, right panel). The high energy MS^2 had signal intensity of 6.07E4, similar quantification accuracy as the MultiNotch MS^3 but with larger variance. Both standard MS^3 and low energy MS^2 methods have lower signal intensities and large signal variance: most of standard MS^3 data points were close to 1:1 ratio, with some scatter outliners, which resulted in small boxes but large whiskers. The data points for low energy MS^2 had both large boxes and whiskers, which represented large various throughout the whole dataset.

The quantification results of N-glycans differentially labeled with six-plex aminoxyTMT (1:2:3:4:5:6) were summarized in Figure S4 for both high mannose and complex/acidic N-glycans. Similar trends with 1:1:1:1:1:1 labeled N-glycans were observed. The targeted MultiNotch MS^3 method precisely and accurately measured the relative quantitation of both types of N-glycans. Both the standard MS^3 method and the low energy MS^2 method produced large signal variance and large quantification errors for both high-mannose and complex N-glycans. The high energy MS^2 method could be used to precisely measure the high mannose N-glycans with larger quantification errors; however, it did not perform well for the complex N-glycans. To conclude, the targeted MultiNotch MS^3 approach was most suitable for accurately and precisely measuring different types of N-glycans.

Quantification comparisons of MS^2 and MS^3 methods for complex mixture

To test the performance of the MultiNotch MS^3 method in complex mixture, N-glycans released from same amount of BTG and HSP were analyzed by nanoHILIC-MS with MultiNotch MS^3, standard MS^3 and MS^2 (high-low HCD). (Figure 5). The N-glycans of BTG were labeled with aminoxyTMT^{126}, aminoxyTMT^{128} and aminoxyTMT^{130}, while the N-glycans of HSP were labeled with aminoxyTMT^{127}, aminoxyTMT^{129} and aminoxyTMT ^{131}. The labeled N-glycans were then mixed for quantitative analysis. Figure 5A summarized the numbers of N-glycan

moieties which were putatively identified by full MS (accurate mass matching), fragmented by MS^2 and quantified by MS^3 (at least 3 reporter ions detected). Among the 3 methods (MultiNotch MS^3, standard MS^3 and MS^2), similar numbers of N-glycan moieties were identified by full MS and fragmented by MS^2. At MS^3 level, the MultiNotch MS^3 method quantified 35 N-glycan moieties with at least 3 reporter ions detected, while the standard MS^3 method quantified 26 of them. Co-isolating and co-fragmenting multiple Y ions in a targeted way during MultiNotch MS^3 runs improved the reporter ion yields, which made more N-glycans, especially the low abundance ones, became quantifiable.

Selected quantification results were shown in Figure 5B: the blue columns represented the inter-sample ratios of N-glycans (e.g. 126/127, 128/129, 130/131) and the orange columns represented the intra-sample ratios of N-glycans released from BTG (e.g. 129/127, 131/129?), which served as quality control and have a theoretical ratio of 1. Only N-glycans with all reporter ion intensities above 1000, relative error of the intra-sample less than 10% and t values from student's t-Test above 3 were shown in this figure. Various N-glycan categories, including high mannose, complex/neutral and complex/acidic N-glycans were quantified in the mixture. Most N-glycans detected in BTG tended to have higher concentrations than N-glycans from HSP, as they were from a purified glycoprotein rather than a protein mixture.

Box-whisker plots of the quantification of H_5N_4FS by four approaches were shown in Figure 5C. In these plots, the first, third and fifth columns were the inter-sample ratios, which represented the relative amounts of H_5N_4FS between HSP and BTG; the second and fourth columns were intra-sample ratios of H_5N_4FS from BTG, which were quality controls and have theoretical ratio of 1. The MultiNotch MS^3 revealed accurate and precise quantification results for the two quality control data points and the variations among the three inter-sample data were

small (Supplemental Table 2). Both the low energy MS^2 and standard MS^3 methods had large variances of the quality control ratios and the accuracies were complemented. Inter-sample ratios from these two method were not available due to the zero reporter ion counts of HSP N-glycan. High energy MS^2 reported non-zero values for the inter-sample ratios. However, the measured $\log_2$ ratios of the reporter ions were not as accurate or precise as the MultiNotch MS^3 method. It is the second-best method among these four methods. The ability of generating decent intensities of reporter ions is essential for precisely and accurately quantify analytes, especially for sample mixtures with a wide dynamic range.

The MultiNotch MS^3 method provided the most precise and accurate measurements followed by the high energy MS^2 method for N-glycans released from complex protein mixture. The low energy MS^2 and standard MS^3 approaches were not suitable for quantifying aminoxyTMT labeled N-glycans, predominantly due to the low reporter ion generation. Alternatively, the high-low MS^2 HCD MS/MS approach could be used for identification and quantification by summing up the two MS/MS scans with different NCEs.

Conclusions

A Y_1 ion triggered, targeted MultiNotch MS^3 method was developed to improve the quantification performance of aminoxyTMT labeled N-glycans released from glycoproteins and complex mixtures. By this approach, multiple Y ions were co-isolated and co-fragmented at MS^3 level, which resulted in significantly improved MS^3 spectral quality and reporter ion intensities. Meanwhile, N-glycan composition could be confirmed by MS^2 scans. This method significantly improves the quantification performance and has the potential to be widely applied in quantitative glycomics analysis.

Acknowledgements

The authors would like to thank Thermo Fisher Scientific (Rockford, IL) for providing the aminoxyTMT reagents and glycoprotein standards. The authors would also like to acknowledge Premier Biosoft (Palo Alto, CA) for providing the trail version of SimGlycan software and technical supports. This research was supported in part by the National Institutes of Health grants R21AG055377 and NIH R01 DK071801. The Orbitrap instruments were purchased through the support of an NIH shared instrument grant (NIH-NCRR S10RR029531) and Office of the Vice Chancellor for Research and Graduate Education at the University of Wisconsin-Madison.

References

[1] Alley, W. R., Mann, B. F., and Novotny, M. V. (2013) High-sensitivity Analytical Approaches for the Structural Characterization of Glycoproteins, *Chemical reviews 113*, 2668-2732.

[2] Alley, W. R., and Novotny, M. V. (2013) Structural Glycomic Analyses at High Sensitivity: A Decade of Progress, *Annu Rev Anal Chem 6*, 237-265.

[3] Moh, E. S., Thaysen-Andersen, M., and Packer, N. H. (2015) Relative versus absolute quantitation in disease glycomics, *Proteomics. Clinical applications 9*, 368-382.

[4] Hecht, E. S., McCord, J. P., and Muddiman, D. C. (2015) Definitive Screening Design Optimization of Mass Spectrometry Parameters for Sensitive Comparison of Filter and Solid Phase Extraction Purified, INLIGHT Plasma N-Glycans, *Analytical chemistry 87*, 7305-7312.

[5] Walker, S. H., Budhathoki-Uprety, J., Novak, B. M., and Muddiman, D. C. (2011) Stable-Isotope Labeled Hydrophobic Hydrazide Reagents for the Relative Quantification of N-Linked Glycans by Electrospray Ionization Mass Spectrometry, *Anal Chem 83*, 6738-6745.

[6] Walker, S. H., Taylor, A. D., and Muddiman, D. C. (2013) Individuality Normalization when Labeling with Isotopic Glycan Hydrazide Tags (INLIGHT): a novel glycan-relative quantification strategy, *Journal of the American Society for Mass Spectrometry 24*, 1376-1384.

[7] Yang, S., Yuan, W., Yang, W. M., Zhou, J. Y., Harlan, R., Edwards, J., Li, S. W., and Zhang, H. (2013) Glycan Analysis by Isobaric Aldehyde Reactive Tags and Mass Spectrometry, *Anal Chem 85*, 8188-8195.

[8] Yang, S., Wang, M., Chen, L., Yin, B., Song, G., Turko, I. V., Phinney, K. W., Betenbaugh, M. J., Zhang, H., and Li, S. (2015) QUANTITY: An Isobaric Tag for Quantitative Glycomics, *Scientific reports 5*, 17585.

[9] Hahne, H., Neubert, P., Kuhn, K., Etienne, C., Bomgarden, R., Rogers, J. C., and Kuster, B. (2012) Carbonyl-Reactive Tandem Mass Tags for the Proteome-Wide Quantification of N-Linked Glycans, *Anal Chem 84*, 3716-3724.

[10] Zhong, X., Chen, Z., Snovida, S., Liu, Y., Rogers, J. C., and Li, L. (2015) Capillary Electrophoresis-Electrospray Ionization-Mass Spectrometry for Quantitative Analysis of Glycans Labeled with Multiplex Carbonyl-Reactive Tandem Mass Tags, *Anal Chem 87*, 6527-6534.

[11] Zhou, S., Hu, Y., Veillon, L., Snovida, S. I., Rogers, J. C., Saba, J., and Mechref, Y. (2016) Quantitative LC-MS/MS Glycomic Analysis of Biological Samples Using AminoxyTMT, *Anal Chem 88*, 7515-7522.

[12] McAlister, G. C., Nusinow, D. P., Jedrychowski, M. P., Wuhr, M., Huttlin, E. L., Erickson, B. K., Rad, R., Haas, W., and Gygi, S. P. (2014) MultiNotch MS3 enables accurate, sensitive, and multiplexed detection of differential expression across cancer cell line proteomes, *Anal Chem 86*, 7150-7158.

Figure legends

Figure 1. General sample preparation and data acquisition workflow: N-glycans were released by FANGS, labeled with 6-plex aminoxyTMT, combined and cleaned up with Oasis HLB cartridge, and analyzed on LC-Tribrid quadrupole-ion trap-Orbitrap MS platform.

Figure 2. MS data acquisition decision trees of MS^2 (A), standard MS^3 (B) and MultiNotch MS^3 (C) quantification methods.

Figure 3. Representative spectra of HR/AM full MS (A), low energy HCD MS^2 (B), high energy HCD MS^2 (C), low energy CID MS^2 (D, F), standard MS^3 (E) and MultiNotch MS^3 (G) of triply charged complex N-glycan $H_5N_4S_2$. The spectra circled in each box represent one of the quantification methods: (B & C) for MS^2, (D & E) for standard MS^3 and (F & G) for MultiNotch MS^3. The highlighted peaks were isolated and fragmented in the next level MS analyses.

Figure 4. Representative box-and-whisker plots of 1:1:1:1:1:1 aminoxyTMT labeled N-glycans released from BTG: high mannose N-glycan H_5N_2 (A) and complex N-glycan $H_5N_4S_2$ (B), quantified by MultiNotch MS^3, standard MS^3, low energy MS^2 and high energy MS^2. The box represented the 25 and 75 percentiles, whiskers represented 5 and 95 percentiles and the crosses represented the 1 and 99 percentiles. The average reporter ion intensities and average calculated ratios were labeled on the figure. Data quantified by each approach was highlighted in the same color. The average, median, standard deviation and number of data points were summarized in Table S1.

Figure 5. Quantification results of N-glycans released from BTG and HSP. The N-glycans released from BTG were labeled with aminoxyTMT^{126}, aminoxyTMT^{128} and aminoxyTMT^{130}, while the N-glycans of HSP were labeled with aminoxyTMT^{127}, aminoxyTMT^{129} and

aminoxyTMT ^{131}. (A) Number of N-glycan moieties identified by full MS (orange), fragmented by MS^2 (blue), quantified by MS^3 with at least 3 reporter ions detected (yellow). (B) Selected quantified ratios of N-glycan moieties which were significantly different between BTG and HSP: columns in blue represented the averaged ratios of BTG/HSP and the columns in orange represented the average ratios of BTG between channel 126, 128 and 130. (Filter of 5B: all reporter ion intensity > 1000, relative error of BTG control ratio < 10%, t-value >3). (C). Box-and-whisker plots of $H_5N_4F_S$ quantified by MultiNotch MS^3, standard MS^3, low energy MS^2 and high energy MS^2. Supporting data (average, median, standard deviation and number of data points) were summarized in Table S2.

Figures

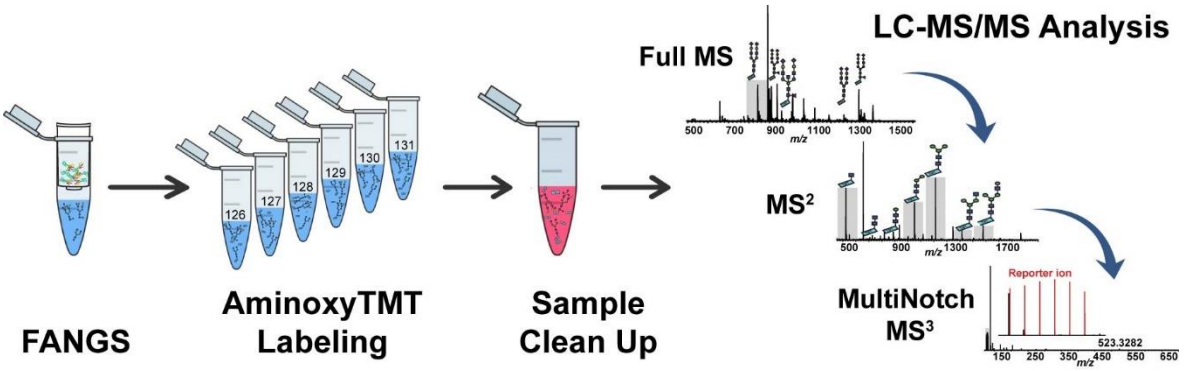

Figure 1

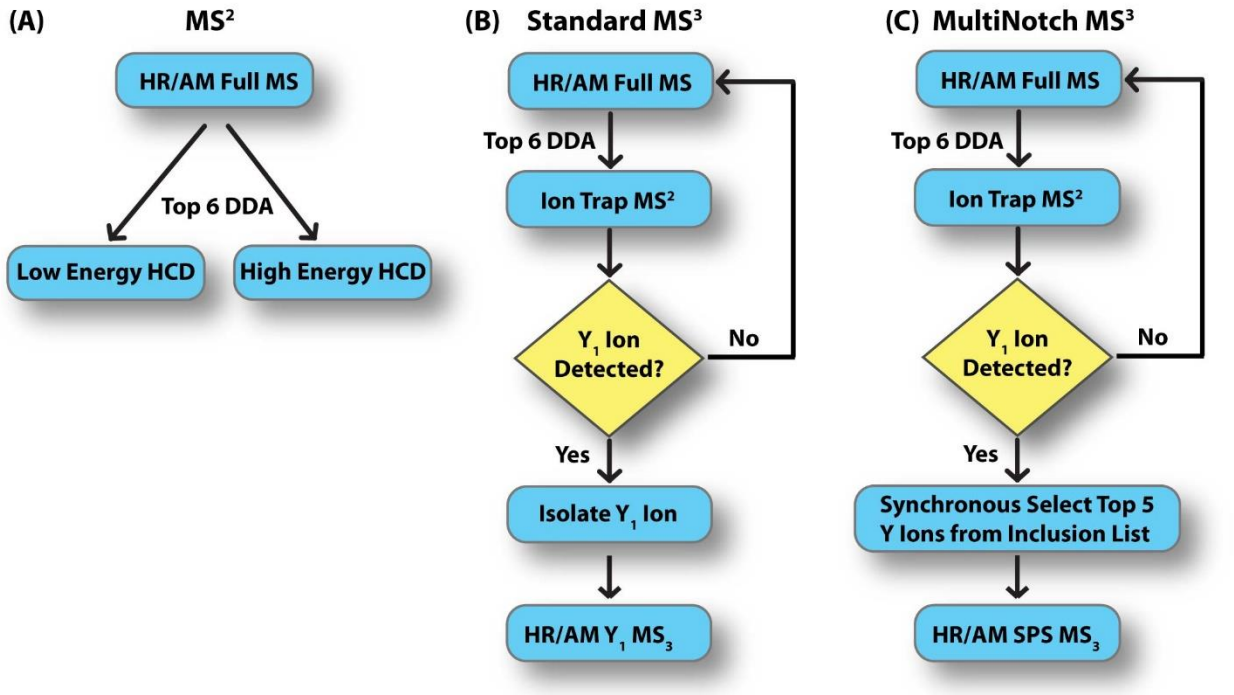
(A)
MS²
HR/AM Full MS
Top 6 DDA
Low Energy HCD
High Energy HCD
(B)
Standard MS³
HR/AM Full MS
Top 6 DDA
Ion Trap MS²
Y1 Ion Detected?
No
Yes
Isolate Y1 Ion
HR/AM Y1 MS3
(C)
MultiNotch MS³
HR/AM Full MS
Top 6 DDA
Ion Trap MS²
Y1 Ion Detected?
No
Yes
Synchronous Select Top 5 Y Ions from Inclusion List
HR/AM SPS MS3

Figure 2

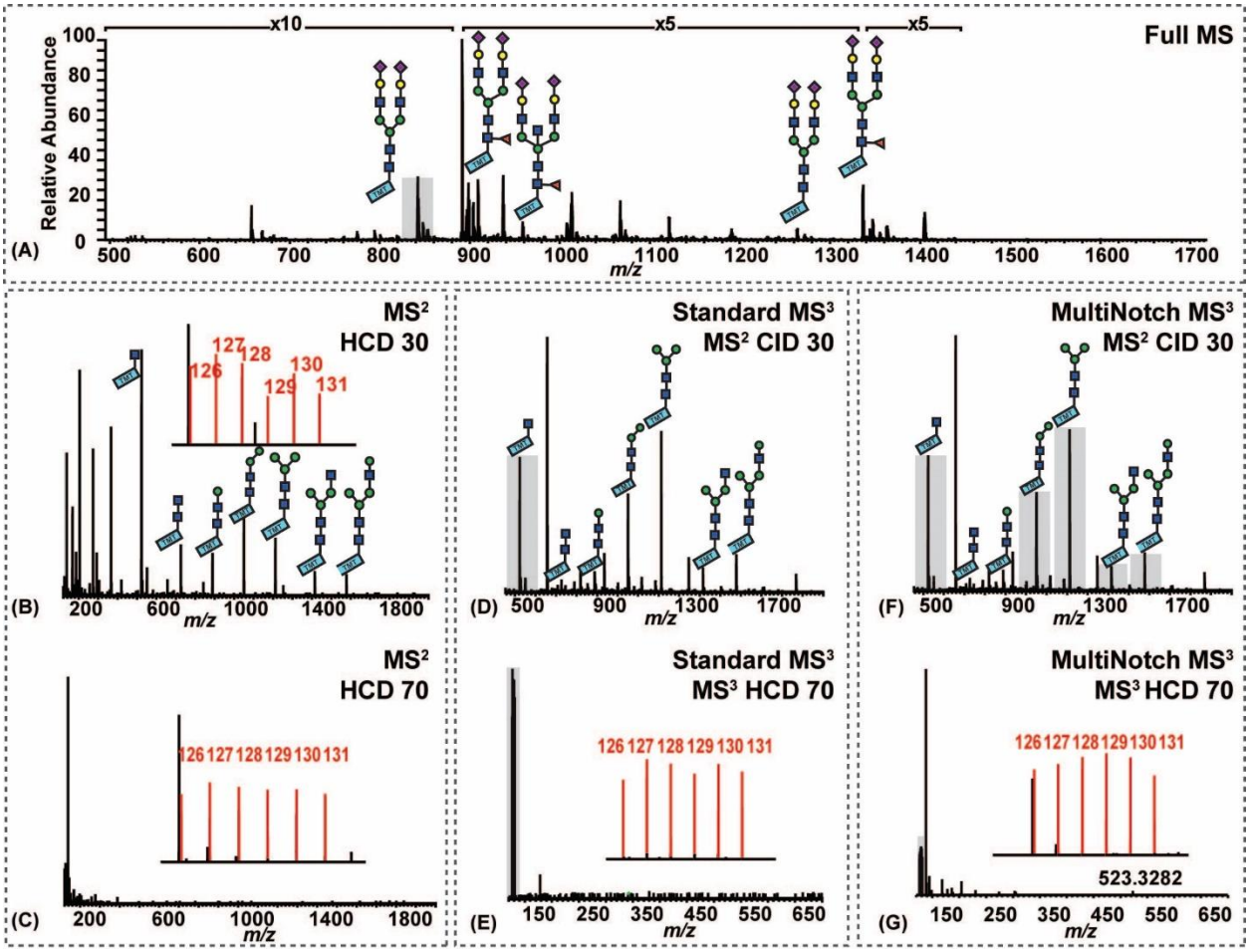
Full MS
x10
x5
x5
Relative Abundance
m/z
(A)
MS²
HCD 30
(B)
Standard MS³
MS² CID 30
(D)
MultiNotch MS³
MS² CID 30
(F)
MS²
HCD 70
(C)
Standard MS³
MS³ HCD 70
(E)
MultiNotch MS³
MS³ HCD 70
523.3282
(G)

Figure 3

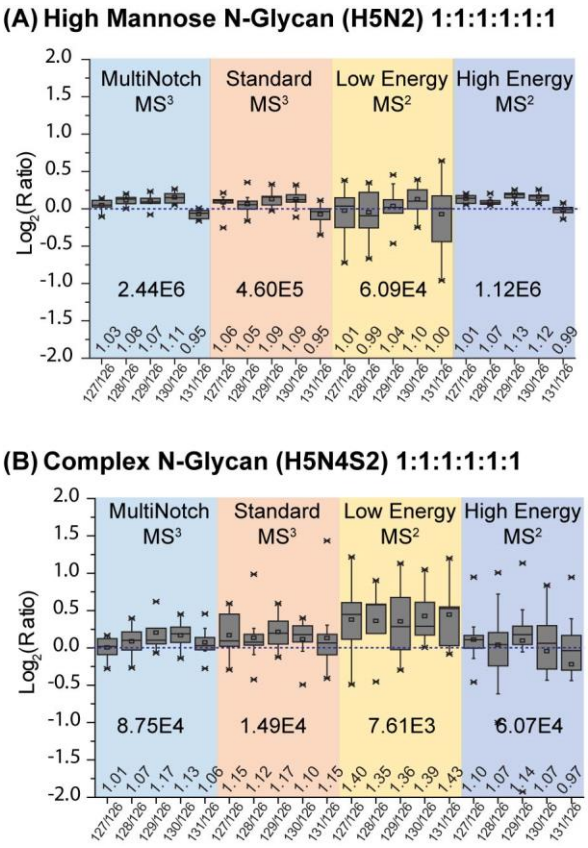
(A) High Mannose N-Glycan (H5N2) 1:1:1:1:1:1
MultiNotch MS3
Standard MS3
Low Energy MS2
High Energy MS2
Log2(Ratio)
2.44E6
4.60E5
6.09E4
1.12E6
(B) Complex N-Glycan (H5N4S2) 1:1:1:1:1:1
8.75E4
1.49E4
7.61E3
6.07E4

Figure 4

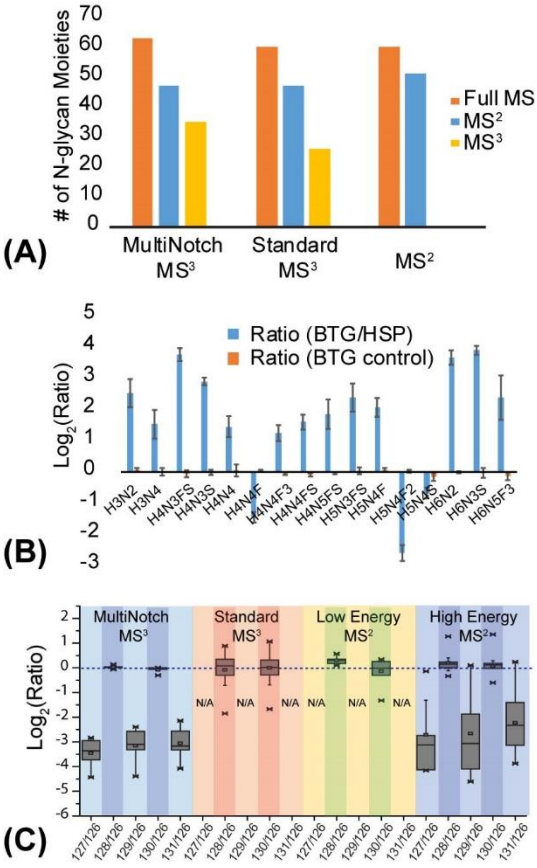
(A)
# of N-glycan Moieties
70
60
50
40
30
20
10
0
Full MS
MS2
MS3
MultiNotch MS3
Standard MS3
MS2
(B)
Log2(Ratio)
5
4
3
2
1
0
-1
-2
-3
Ratio (BTG/HSP)
Ratio (BTG control)
H3N2
H3N4
H4N3FS
H4N3S
H4N4
H4N4F
H4N4F3
H4N4FS
H4N5FS
H5N3FS
H5N4F
H5N4F2
H5N4S
H6N2
H6N3S
H6N5F3
(C)
Log2(Ratio)
MultiNotch MS3
Standard MS3
Low Energy MS2
High Energy MS2
N/A
127/126
128/126
129/126
130/126
131/126

Figure 5

Supporting information

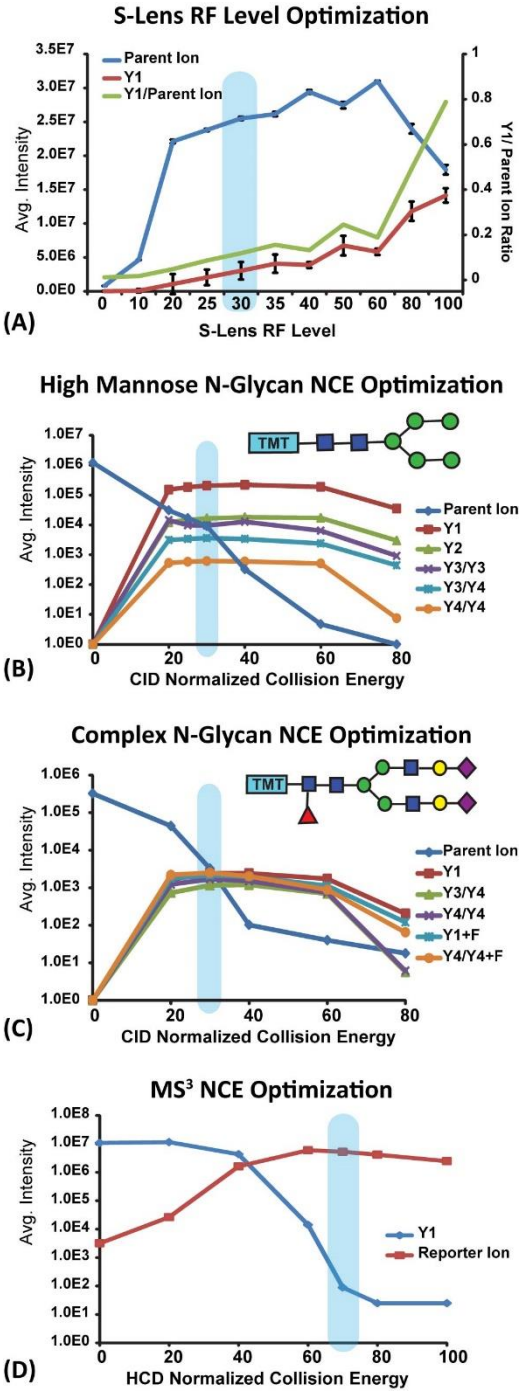

Supplemental Figure 1. Parameter optimization for MultiNotch MS^3: S-lens RF level (A), high mannose N-glycan (H_5N_2) CID NCE (B), complex N-glycan ($H_5N_4S_2F$) CID NCE (C) and MS^3 HCD NCE optimization by pseudo MS^3.

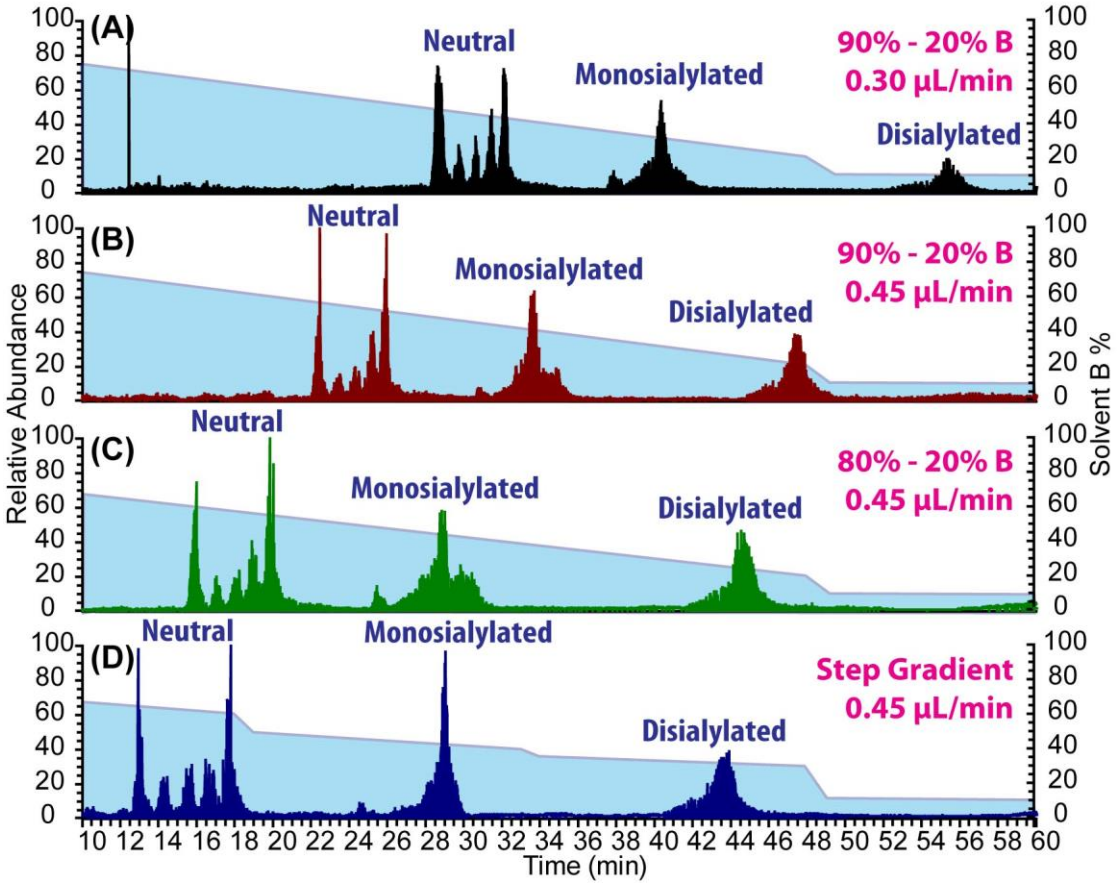

Supplemental Figure 2. Total ion counts of aminoxyTMT labeled N-glycans released from BTG eluted with 4 different gradients for HILIC gradient optimization: (A) linear gradient of 90% - 20% ACN with flow rate of 0.30 µL/min; (B) linear gradient of 90% - 20% ACN with flow rate of 0.45 µL/min; (C) linear gradient of 80% - 20% ACN with flow rate of 0.45 µL/min; (D) stepped gradient with flow rate of 0.45 µL/min.

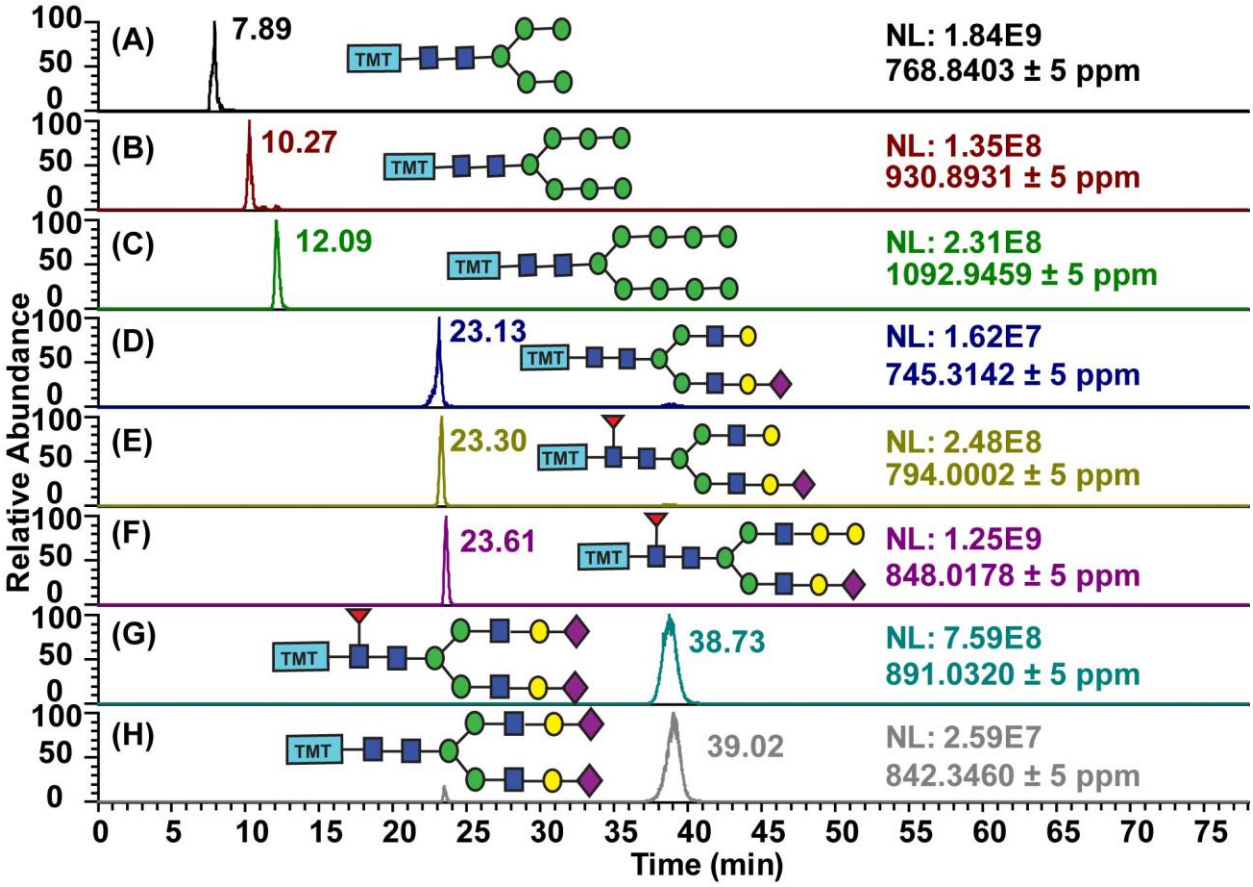

Supplemental Figure 3. Selected extracted ion chromatogram of the optimized HILIC gradient. Retention time (min), *m/z* and mass window, signal intensity and potential N-glycan structures were labeled.

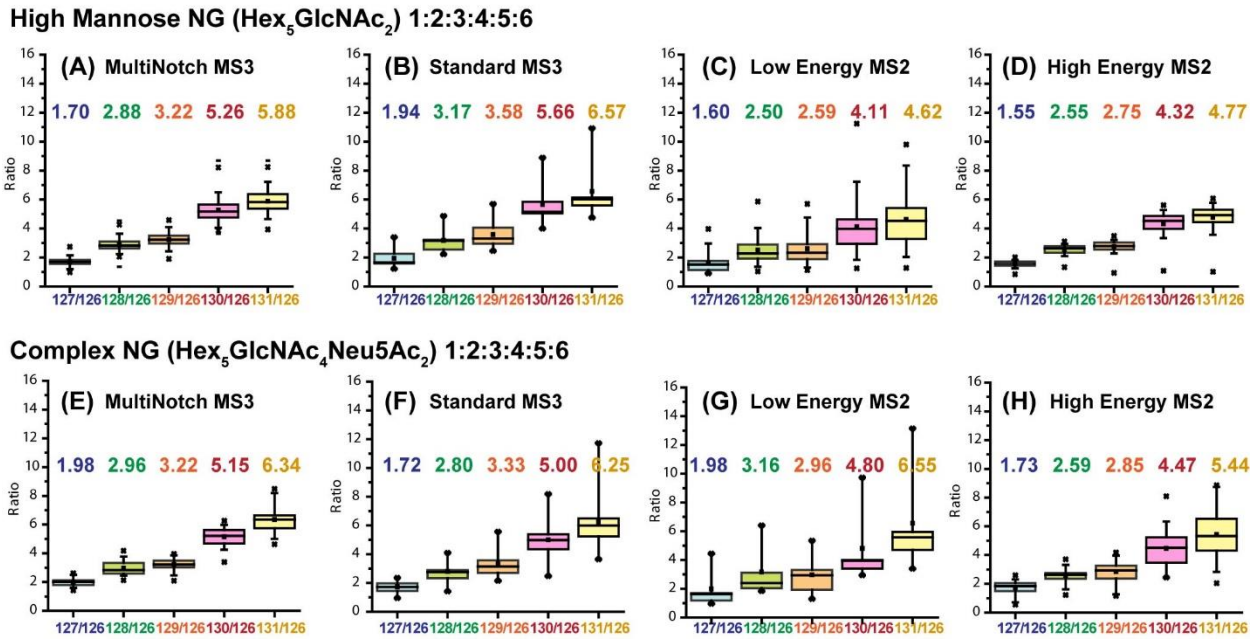

Supplemental Figure 4. Box-and-whisker plots of 1:2:3:4:5:6 aminoxyTMT labeled N-glycans released from BTG by MultiNotch MS^3 (A, E), standard MS^3 (B, F), low energy MS^2 (C, G) and high energy MS^2 (D, H) for high mannose N-glycans H5N2 and complex N-glycans H5N4S2. The average signal intensities and calculated ratios were labeled. The square represented the average, lines represented the 25, 50 and 75 percentiles, whiskers represented 5 and 95 percentiles and the crosses represented the 1 and 99 percentiles.

Supplemental Table 1. Quantification result of aminoxyTMT 1:1:1:1:1:1 labeled high mannose and complex N-glycans released from BTG by MultiNotch MS^3, standard MS^3, low energy MS^2 and high energy MS^2. – supporting data for figure 5

Method	Ratio	H5N2 1:1:1:1:1:1				H5N4S2 1:1:1:1:1:1			
		Average	Median	StDev	N	Average	Median	StDev	N
Multi-Notch MS^3	127/126	1.035	1.046	0.060	10	1.008	1.013	0.099	10
	128/126	1.081	1.101	0.047	10	1.071	1.077	0.136	10
	129/126	1.071	1.068	0.058	10	1.167	1.096	0.203	10
	130/126	1.114	1.115	0.058	10	1.130	1.156	0.137	10
	131/126	0.954	0.961	0.041	10	1.061	1.043	0.146	10
Standard MS^3	127/126	1.064	1.074	0.078	13	1.145	1.068	0.223	17
	128/126	1.047	1.040	0.091	13	1.119	1.055	0.254	17
	129/126	1.095	1.113	0.072	13	1.170	1.146	0.171	17
	130/126	1.094	1.087	0.085	13	1.097	1.132	0.158	17
	131/126	0.953	0.974	0.076	13	1.145	1.048	0.438	17
Low Energy MS^2	127/126	1.010	1.031	0.229	12	1.401	1.362	0.602	5
	128/126	0.988	0.948	0.201	12	1.347	1.492	0.430	5
	129/126	1.042	1.017	0.186	12	1.361	1.220	0.549	5
	130/126	1.101	1.075	0.140	12	1.389	1.223	0.425	5
	131/126	0.999	1.049	0.310	12	1.433	1.440	0.537	5
High Energy MS^2	127/126	1.099	1.104	0.040	12	1.103	1.083	0.252	24
	128/126	1.069	1.058	0.035	12	1.074	1.033	0.324	24
	129/126	1.134	1.148	0.039	12	1.141	1.154	0.383	24
	130/126	1.120	1.128	0.040	12	1.067	1.058	0.375	24
	131/126	0.990	0.995	0.045	12	0.972	0.980	0.356	24

Supplemental Table 2. Data summery of H5N4FS released from BTG and HSP and quantified by MultiNotch MS^3, standard MS^3, low energy MS^2 and high energy MS^2.

		Average	Median	StDev	N
Multi-Notch MS^3	127/126	0.098	0.097	0.039	5
	128/126	1.023	1.015	0.054	5
	129/126	0.125	0.117	0.057	5
	130/126	0.947	0.962	0.079	5
	131/126	0.133	0.111	0.066	5
Standard MS^3	127/126	0.021	0.000	0.103	1
	128/126	0.983	1.058	0.429	22
	129/126	0.003	0.000	0.010	2
	130/126	0.934	0.932	0.525	20
	131/126	0.006	0.000	0.027	1
Low Energy MS^2	127/126	0.000	0.000	0.000	0
	128/126	1.243	1.250	0.144	6
	129/126	0.000	0.000	0.000	0
	130/126	0.971	1.074	0.325	6
	131/126	0.000	0.000	0.000	0
High Energy MS^2	127/126	0.149	0.057	0.254	8
	128/126	1.201	1.110	0.413	13
	129/126	0.163	0.059	0.292	8
	130/126	1.118	1.090	0.472	13
	131/126	0.239	0.151	0.317	10

Chapter 11
Quantitative Glycomics Analysis by Mass Defect Based DiPyrO Tags and High Resolution Mass Spectrometry

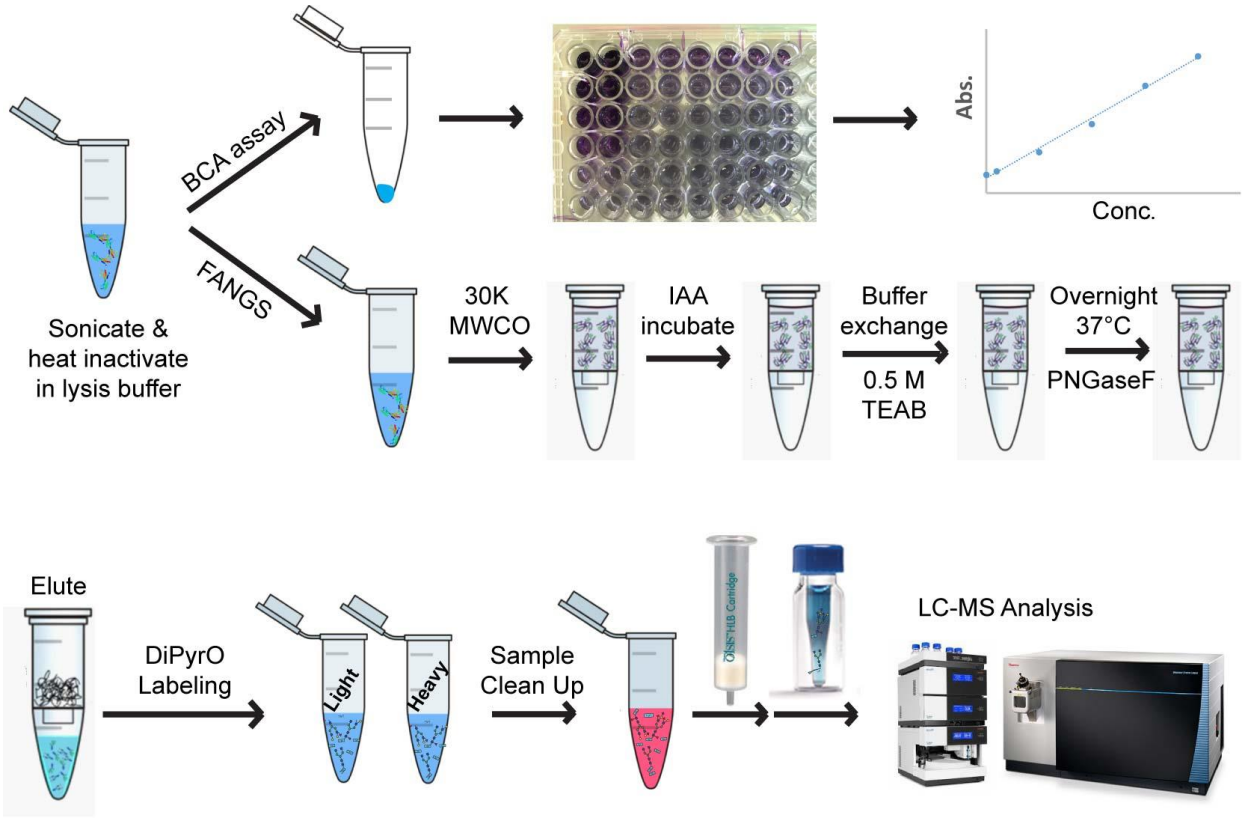

Contribution: Study was designed by B. Chen, X. Zhong, Y. Feng, J. Johnson and L. Li; analytical experiments were performed by B. Chen, Y. Feng and Q. Yu; DiPyrO design and synthesis was performed by D. Frost and A. Buchberger; PANC1 cells were provided by J. Johnson and data processing program was written by K. DeLaney.

Abstract

Glycan is an important class of macromolecule and is highly relevant to biological functions as well as disease states. N-linked glycans (N-glycans) are covalently attached to the asparagine residues on glycoproteins and can be enzymatically cleaved by PNGase F. Despite its high biological relevance, the characterization and quantification of N-glycans are challenging. Absolute quantification of N-glycans is extremely difficult due to the lack of corresponding N-glycan standards. Relative quantifications are usually achieved by chemical labeling strategies, but MS^1 mass difference-based quantification often suffers from increased spectral complexity while MS^2 isobaric tag based quantification suffers from poor fragmentation efficiency and low reporter ion yield. Herein, we developed a mass defect-based tag, dimethyl pyrimidinyl ornithine (DiPyrO), for multiplex N-glycan characterization and relative quantification. The DiPyrO tags rely on the small mDa mass differences between elemental isotopes. Each DiPyrO tag has the same nominal mass but different elemental compositions, which created a mass difference up to 45.3 mDa that can be separated by high resolution Fourier transform based mass spectrometers. The DiPyrO tags were first introduced for protein analysis, but are also feasible for labeling freshly released glycosylamine. In this study, freshly released glycosylamine from glycoprotein standards and pancreatic cancer cell lysates were successfully labeled with DiPyrO tags. The labeled glycosylamines were characterized and quantified on both MALDI-LTQ-Orbitrap platform with 100,000 resolution (*m/z* 400) and the Fusion Lumos Orbitrap platform with 500,000 resolution (*m/z* 200) coupled with a nanoflow hydrophilic interaction chromatography.

Introduction

Glycosylation is one of the most important post-translational modifications in protein. [1] Glycan moieties attached to glycoproteins play essential roles in many biological processes, such as cell-cell signaling and protein trafficking.[1-4] Changes in glycan profiles are associated with a variety of diseases, including cancer, cardiovascular diseases and neurodegenerative diseases.[5-9] Therefore, it is urgent for researchers to develop innovative bioanalytical platforms for qualitative and quantitative glycomics analysis, and to elucidate the roles of glycan in human diseases.

It is challenging for high-throughput quantitative analysis of glycans due to the high complexity of glycan structure, lack of glycan standards, and low ionization efficiency of glycan in mass spectrometry (MS) analysis. Developing a set of multiplex chemical labels could improve the throughput and ionization efficiency for quantitative glycomics.

Mass defect-based quantification is a newly developed concept that allows multiplexed quantification at MS^1-level without increasing spectral complexity inherent to mass difference-based quantification or precursor isolation interference inherent to MS^2-based quantification.[10] This approach relies on isotopic mass defect, which refers to small mDa mass difference between elemental isotopes that caused by differences in nuclear binding energy.[10, 11] Analytes are labeled with the same nominal mass tags but with different elemental composition, which leads to distinct masses differed by mere mDa. These isotopic mass defects can be differentiated at high resolution in MS^1 scans and used for quantification. The labeled ions are selected for fragmentation within the same MS^2 isolation window, multiplexing is achievable without increasing the duty cycle of the instrument. Moreover, since the quantification is performed at MS^1-level, precursor interference does not affect the accuracy of quantification.[12]

Mass defect-based multiplex dimethyl pyrimidinyl ornithine (DiPyrO) tags were designed in 2- (light and heavy version of 3-plex), 3-, 4-, 6-, 8-plex at minimal resolving powers of 120 K, 240 K, 480 K, 960 K and > 1M respectively, to maximize the multiplexing capability. The general structure of DiPyrO and multiplex isotopologues are shown in Figure 1. The DiPyrO labeling reagent consists of an amine-reactive triazine ester group and a dimethyl pyrimidinyl ornithine. Up to six stable isotopes were incorporated onto the tag in different configurations.[12] The N-glycosylamine released from glycoproteins can react with the triazine ester group on DiPyrO tag for relative quantification.

Alternation of N-linked glycans, such as increasing branching, sialylation and fucosylation, were frequently reported during cancer cell invasion and metastasis.[13, 14] In this study, comparative glycomics analysis of pancreatic cancer cell lysates from 2D and 3D cell cultures, were used as a model system for validating the quantitative performance of the DiPyrO tags for complex samples. The goal of this study is to develop an innovated bioanalytical platform for quantitative glycomics using multiplex mass defect-based DiPyrO tags. The glycan profiles of 2D and 3D cultured pancreatic cancer cells were compared by the developed quantification platform.

Materials and methods

Materials and reagents

Methanol (MeOH), acetonitrile (ACN), water, acetic acid (AA) and formic acid (FA) were purchased from Fisher Scientific (Pittsburgh, PA). Triethylammonium bicarbonate buffer (TEAB, 1.0 M), 4-(2-hydroxyethyl)-1-piperazineethanesulfonic acid (HEPES), Tris (2-carboxy-ethyl) phosphine hydrochloride (TCEP), dithiothreitol (DTT), iodoacetamide (IAA), *N*,*N*-dimethylformamide (DMF), 4-(4,6-dimethoxy-1,3,5-triazin-2-yl)-4-methylmorpholinium

tetrafluoroborate (DMTMM), *N*-methylmorpholine (NMM) were purchased from Sigma-Aldrich (St. Louis, MO). PNGase F was purchased from Promega (Madison, WI). Bovine thyroglobulin (BTG), bovine lactoferrin (BLF), RNaseB and human serum protein mixture (HSP) were provided by Thermo Fisher Scientific (Rockford, IL). Oasis HLB 3cc (60 mg) extraction cartridges were purchased from Waters Corporation (Milford, MA). Microcon-30kDa centrifugal filters (30K MWCO) were purchased from Merck Millipore Ltd. (Darmstadt, Germany). PolyGLYCOPLEX A^{TM} beads (3 µm) were purchased from PolyLC Inc. (Columbia, MD). Fused silica capillary tubing (inner Diameter 75 µm, outer diameter 375 µm) was purchased from Polymicro Technologies (Phoenix, AZ). All reagents were used without additional purification.

PANC1 cell lysate

PANC1 pancreatic ductal adenocarcinoma cells were cultured in 150 cm^2 culture flasks in an incubator containing 98% humidity and 5% CO_2. The cells were routinely maintained and used once 80% confluence was achieved. The cell culture media consisted of DMEM F-12 (ATCC), 10% Fetal Bovine Serum and 1% antibiotic- antimicotic solution (Thermo fisher) solution and was replaced every 2-3 days as needed. Once confluent, cells were washed once with 1X phosphate-buffered saline (PBS) without Ca^{2+} and Mg^{2+}, then trypsinized using a 2.5% trypsin EDTA solution. For 3D cell culture, cells were seeded on Microtissues agarose dishes at a cell density of 3.5E6 cells/microdish. The non-adhesive surface of agarose allowed cells to form spheroids in suspension. These spheroids were pelleted after 7 days of culture. Cell pellets were washed three times with PBS without Ca^{2+} and Mg^{2+}, flash frozen on dry ice and stored at -80 °C.

Cell pellet was re-suspended in lysis buffer (4% (w/v) sodium dodecyl sulfate (SDS), 100 mM Tris/HCl pH 7.6) at a 1:10 pellet/lysis buffer volume ratio. The mixture was briefly vortexed

at low speed and incubated at 95 °C for 5 min. The mixture was then placed on ice and sonicated with 20% amplitude (5 sec on and 5 sec on) until the mixture became clear. The lysate was centrifuged at 14,000 rcf for 10 min. A small portion of the supernatant was used for bicinchoninic acid (BCA) assay to determine the protein concentration and the rest supernatant was treated with the Filter-aided N-glycan Separation (FANGS) protocol for N-glycan release.

N-glycan releasing by FANGS

N-glycans of PANC1 cell lysate were released with the original FANGS protocol [15] with slight modification. Briefly, freshly prepared cell lysate was diluted with lysis buffer containing 0.2 M DTT and incubated at 95 °C for 5 min. The lysate was centrifuged at 14,000 rcf for 10 min and the supernatant was 10-fold diluted with urea solution (8 M in 100 mM Tris/HCl, pH 8.5). The solution was transferred to a 30 kDa molecular weight cut-off filter, 300 µL at a time and centrifuged at 14,000 rcf for 10 min until all liquid passed through the filter. The filter was washed with 250 µL urea solution and centrifuge at 14,000 rcf for 10 min. 250 µL of freshly prepared 40 mM IAA in urea solution was added to the filter, briefly vortex and incubated in dark at room temperature for 15 min, then centrifuged at 14,000 rcf for 10 min. The sample retained above the filter was washed with 250 µL 0.5 M TEAB buffer and centrifuge at 14,000 rcf, 20 min at four times.

N-glycans of glycoprotein standards and human serum protein mixtures were released with a simplified FANGS protocol [16] with slight modification. Briefly, glycoprotein (2 µg/µL dissolved in 50 mM TEAB buffer) was mixed with 4 µL 0.5M TCEP and added to a 30K MWCO filter. The protein was heat-denatured by alternating sample tube between 100 °C and room temperature water baths for 4 times, 15 seconds each. The mixture was then buffer exchanged with 200 µL 0.5 M TEAB buffer for three times (centrifuged at 14,000 g for 20 min).

The prepared cell lysates or protein standards were incubated with PNGase F (4 µL PNGase F in 96 µL 0.5 M TEAB per filter) and incubated at 37 °C overnight. The pH value of 7-8 was carefully controlled by using 0.5 M TEAB buffer during digestion in order to preserve the amino group for the subsequent labeling reaction. The released glycosylamines were separated from the de-glycosylated protein by centrifuging at 14,000 rcf for 20 min. The filter was washed with 100 µL 0.5 M TEAB buffer. Both fractions were combined and dried in SpeedVac.

N-glycan DiPyrO labeling and cleaning up

DiPyrO in anhydrous DMF was combined with DMTMM and NMM and vortexed at room temperature for 30 min for DiPyrO activation. The activated DiPyrO was mixed with released N-glycosylamine at a mass ratio of 1:25 (glycoprotein:DiPyrO) and vortexed at room temperature for 1 hr. The labeling reaction was quenched by addition of hydroxylamine to a concentration of 0.25%.

Oasis HLB 3cc cartridge was used to remove excess labels and purify the labeled N-glycans. The cartridge was conditioned by 3 mL of 95% ACN, 1 mL of 50% ACN and 3 mL of 95% ACN again. The crude reaction mixture was added to the conditioned cartridge which was pre-filled with 3 mL of 95% ACN for sample loading. Then the cartridge was washed twice with 3 mL of 95% ACN and the labeled N-glycans were eluted with 1 mL 50% ACN. The eluting fraction was dried in the SpeedVac, reconstituted in 30 µL 80% ACN and analyzed by LC-MS/MS immediately.

MALDI-MS analysis

MALDI-LTQ-Orbitrap XL (Thermo Scientific, Bremen, Germany) was used for all MALDI-MS analysis. A *m/z* range of 900-4000 was used with laser energy of 20 µJ. Orbitrap mass analyzer was used with a mass resolution of 30,000 at *m/z* 400. Sample was prepared by

premixing 1 µL of DiPyrO labeled N-glycan with 1 µL DHB matrix (2% N,N-dimethylaniline, 49% MeOH and 49% water). 1 µL of matrix/sample mixture was added to MALDI target plate.

LC-MS/MS analysis

A Dionex Ultimate 3000 nanoLC system was coupled to Orbitrap Fusion Lumos tribrid quadrupole-ion trap-Orbitrap mass spectrometer with NanoSpray Flex ion source (Thermo Scientific, Bremen, Germany) for all LC-MS/MS analysis. A self-fabricated nanoHILIC column (20 cm, 75 µm i.d.) was used for glycan separation. Mobile phase A was water with 0.1% FA and mobile phase B was ACN with 0.1% FA. The flow rate was set at 0.3 µL/min and injection volume was set to be 3 µL. The following gradient was used (time/min, % mobile phase B) unless otherwise specified: (0, 80), (20, 80), (80, 20), (80.1, 10), (90, 10), (90.1, 80), (110, 80).

The following MS parameters were used for all data acquisition unless otherwise noted. Data was acquired by positive ion mode with spray voltage of 3 kV, S-lens RF level of 30 and capillary temperature of 300 °C. Full MS scans were acquired at resolution of 500K (*m/z* 200) with *m/z* 300-1500. Maximum injection time of 100 ms, automatic gain control (AGC) target value of 2E5 and 1 microscan were used for full MS. Top 20 data dependent analysis was performed at MS^2 level with collision-induced dissociation (CID) at normalized collisional energy of 30 and detected in ion trap with rapid mode. First mass was fixed at *m/z* 110 and dynamic exclusion was set to be 15 sec.

N-glycan data analysis

The N-glycans were identified by accurate mass matching by an in-housed developed JAVA program. A peaklist was exported based on average spectrum and compared against a database including all possible combination of N-glycan unites (Hexose (H), HexNAc (N),

Fucose (F) and NeuAc (S)) with a mass window of 10 ppm. Peak area of chromatogram was used for quantification. Microsoft Excel was used for calculation and statistical analysis.

Results and discussion

A quantitative glycomics strategy was developed in this study using multiplex mass defect-based DiPyrO tags. The labeling condition, separation method and instrument parameter were carefully optimized in order to achieve the optimum quantification performance. This strategy was also applied to study complex biological systems by comparing the N-glycan profiles of 2D and 3D cultured pancreatic cancer cells. This study not only developed a quantification strategy for glycomics analysis, but also unlocked the potential of using various proteomics chemical tags for quantitative glycomics analysis.

Labeling chemistry

Various of chemical tags have been developed to label the reducing end of glycans using reductive amination. Some of the most commonly used labels include 2-aminobenzamide (2-AB), 2-aminobenzoic acid (2-AA) and 2-aminopyridine (PA).[17] These labels are widely used in high performance liquid chromatography (HPLC) with fluorescence detection or mass spectrometry analysis, but they lack multiplex capability for relative quantification. On the other hand, a large amount of multiplex chemical labels, such as tandem mass tags (TMT)[18], isobaric tags for relative and absolute quantification (iTRAQ)[19], our lab's own custom *N*,*N*-dimethyl leucine (DiLeu)[20-22] and DiPyrO[12], have been developed to label peptide N-termini and lysine side-chains in quantitative proteomics study. Adapting the multiplexed chemical labels in proteomics study for quantitative glycomics could be a time- and cost-efficient approach, but the structural difference between glycan and protein limits this application. Comparing to peptide, the steric of

glycosylamine decreased the labeling rate with chemical labels for glycans. However, this limit could be solved by increasing the mass ratio of chemical tags and glycans.

During PNGase F releasing of N-glycans, glycosylamine is produced at pH 7-8. While a deamination step in acidic pH is usually followed by the PNGase F digestion to produce N-glycan in conventional approaches, the primary amine in the glycosylamine makes it capable of reacting with proteomics chemical labels (Figure 2). In this study, glycosylamine released from glycoprotein was labeled with DiPyrO tags for relative quantification.

Optimization

The PNGase F digestion protocol, DiPyrO labeling condition and labeling ratios were carefully optimized. Both FANGS (10K vs 30K MWCO filters) and in-solution digestion were tested with HEPES or TEAB buffer. By evaluating the digestion process and result, the FANGS protocol with 30K MWCO filter using TEAB buffer was finalized, as the FANGS protocol allowed fast and convenient N-glycan separation and enrichment compared to the in-solution approach; 30K MWCO filter ensured all N-glycans to be collected and TEAB buffer produced cleaner MS spectra compared to HEPES buffer.

DiPyrO labeling condition for N-glycans was carefully optimized. N-glycans were labeled with or without aqueous buffer. The resulting labeling efficiency was evaluated by MALDI-MS using the following equation: *labeling efficiency = labeled peak intensity / (labeled peak intensity + unlabeled peak intensity) X 100%*. Although 30% aqueous buffer was used to dissolve peptides in proteomics analysis to achieve the optimum labeling efficiency, the existence of aqueous buffer in glycan labeling limited the labeling efficiency to approximately 50% (Figure 3). In contrast, the reaction in anhydrous condition could reach ~100% labeling efficiency. Therefore, anhydrous labeling condition was finalized for N-glycan labeling reaction.

The labeling mass ratio of glycoprotein:DiPyrO was tested. The glycoprotein mass was used due to the mass of released N-glycans was difficult to measure. Ratios of 1:5, 1:10 (data not shown), 1:25 and 1:50 (Figure 3) were tested and the labeling efficiency was evaluated. Both 1:25 and 1:50 could reach ~100% labeling efficiencies, except for some larger N-glycans such as H_4N_5 and H_3N_6. So 1:25 labeling ratio was finalized in order to achieve high labeling efficiency while save labeling reagent.

In order to maximize the separation of mass-defect peak pair while minimize ion coalescence (merging of two peaks due to saturated ion population in Orbitrap/space charge effect) [23], the mass resolution and AGC value were carefully optimized. Duplex DiPryO labeled N-glycan was tested at resolution of 15K, 30K, 60K, 120K, 240K and 500K (at *m/z* 200) (Supplemental Figure (SFigure) 1). At resolution of 15K, 30K and 60K, the peak pair could not be separated. At 120K and 240K, the peak pair could be separated but not resolved at baseline. At 500K, the peak pair could be separated and resolved at baseline. Therefore, a resolution of 500K was used for measuring the DiPyrO labeled N-glycans.

When too many ions accumulated in the Orbitrap, ion coalescence (merging of peaks) could be observed even very high resolution was used, due to the space charge effect.[23] The AGC values were carefully optimized in order to minimize ion coalescence (Supplemental Figure 2). Different AGC values (1e5, 2e5, 5e5 and 1e6) were tested at resolution of 500K (at *m/z* 200). No coalescence peak was observed at AGC values of 1e5 and 2e5 and the base peak was detected at similar intensity. At AGC of 5e5, peak coalescence started to occur and at AGC of 1e6, the two peaks completely merged into one. Therefore, AGC value of 2e5 was used to ensure enough ion count and limited ion coalescence.

Characterization of quantification performance

The quantification accuracy and dynamic range of the duplex DiPyrO tags were characterized by labeling the N-glycans released from BTG at various ratios (light:heavy 1:1, 1:2, 1:4, 1:8 and 1:16). The resulting measured ratio vs. theoretical ratio plot of selected N-glycans was summarized in Figure 4. Both measured and theoretical ratios were presented in $\log_2$ ratios. Good linearity, measured by R^2, was observed for each N-glycans: the R^2 values for high mannose N-glycans were all above 0.97, and for complex acidic N-glycans were slightly lower, but still above 0.93.

Representative MS spectra and LC chromatogram were shown in Figure 5 for duplex DiPyrO 1:2 labeled high mannose N-glycan H_5N_2 (Figure 5A&B) and acidic complex N-glycan H_5N_4FS (Figure 5 C&D). The peak intensities of monoisotopic peak pairs of both N-glycans were observed to be approximately 1:2. The peak area ratio of LC peaks was calculated to be 1:2.2 for H_5N_2 and 1:2.93 for H_5N_4FS.

Relative quantifications of N-glycans released from 2D and 3D PANC1 cell lysate

The ultimate goal of this study is to apply the quantification method onto complex biological system and to accurately and precisely quantify the N-glycan profile at various biological states. Therefore, PANC1 cell line was used as a model system to characterize the quantification performance of duplex DiPyrO. N-glycan profiles of 2D and 3D PANC1 cell culture were compared by labeling each condition with light or heavy DiPyrO. The workflow was summarized in Figure 6 and described in material and methods section. Briefly, the BCA assay was used to measure total protein concentration. The rest cell lysate was used for releasing

N-glycans by FANGS. The resulting N-glycans were labeled with DiPyrO, quenched, combined and cleaned up for MS analysis.

Prior to combining the N-glycans from 2D and 3D cell lysates for relative quantification, N-glycans released from each condition was separately labeled and run on the instrument as control experiments for charactering labeling efficiency, N-glycan types, LC retention time and MS signal intensities. Compared to glycoprotein standards, the N-glycan concentrations was much less in cell lysate. Therefore, instead of using glycoprotein:DiPyrO ratio of 1:25 as for glycoprotein standards, a ratio of 1:4 was tested instead. MALDI-MS was used to quickly examine the digestion or labeling efficiency without sample clean-up (SFigure 3) and LC-MS/MS was used to analyze each sample in depth (SFigure 4). MALDI-MS spectrum of crude digestion mixture revealed several N-glycan peaks, suggesting good digestion efficiency (SFigure 3A). Several DiPyrO labeled N-glycans from either 2D (SFigure 3B) or 3D (SFigure 3C) cell lysates were identified from the MALDI-MS spectra. However, mainly neutral N-glycans, which were higher in abundance and easier to detect, were detected in MALDI-MS spectrum. Few acidic N-glycans were detected, suggesting more in-depth LC-MS/MS analysis is required to separate mixture before MS detection. As shown in SFigure 4, much more DiPyrO labeled N-glycans were detected. The LC chromatogram (SFigure 4A) revealed both labeled and unlabeled N-glycan peaks, suggesting an incomplete labeling reaction and a higher glycoprotein:DiPyrO ratio is needed for labeling N-glycans from cell lysate. Between 10 to 20 min, mainly DiPyrO labeled neutral N-glycans were eluted (SFigure 4B). A total of 11 labeled neutral N-glycans were detected based on accurate mass matching. Between 30-40 min, mainly labeled N-glycans with 2 sialic acids were eluted (SFigure 4C). These are more hydrophilic

glycans, so they eluted at a lower ACN percentage. A total of 12 labeled N-glycans with 2 sialic acids were detected.

The N-glycan relative quantification result of PANC1 2D and 3D cell culture was summarized in Figure 7. The N-glycans released from 300 μg PANC1 2D cell lysate were labeled with light-DiPyrO and the N-glycans released from 300 μg PANC1 3D cell lysate were labeled with heavy-DiPyrO. The labeled N-glycans were quenched and combined prior to sample clean-up and LC-MS/MS analysis. Figure 7 represents the average spectrum between 20-25 min. Nine neutral labeled N-glycans were detected with either complex or high mannose compositions. The ratios, calculated from the peak area of extracted ion chromatogram, were labeled on the spectrum. The isotopologues of selected peaks were shown above the main spectrum. The peak pairs could be clearly observed on the zoom in spectra: the first peak in the peak pair represented the N-glycan released from PANC1 2D cell lysate and labeled with light-DiPyrO; the second peak represented the N-glycans from 3D cell lysate and labeled with heavy-DiPyrO. For each detected N-glycans, the ones released from 2D cell lysate were presented at higher abundance compared to the ones from 3D cell lysate. This result suggests that the N-glycosylation in PANC1 2D cell culture could generally be more abundant than in the 3D cell culture. A more systematic experiment with four biological replicates is currently underway in order to reach a more conclusive result.

Conclusion

In this study, an innovated strategy was developed for quantitative glycomics using multiplexed mass defect-based DiPyrO tags. The labeling condition, separation method and instrument parameters were carefully optimized to achieve the best quantification performance.

This strategy was applied onto complex biological system. The N-glycan profiles of 2D and 3D PANC1 cells were compared by duplex DiPyrO labeling. This strategy not only developed a quantification strategy for glycomics analysis, but also unlocked the potential of using proteomics chemical labels to study N-glycans.

Acknowledgements

This research was supported in part by the National Institutes of Health grant R21AG055377. The Orbitrap instruments were purchased through the support of an NIH shared instrument grant (NIH-NCRR S10RR029531) and Office of the Vice Chancellor for Research and Graduate Education at the University of Wisconsin-Madison.

References

[1] Varki, A. L., J.B. (2009) Biological Roles of Glycans, In *Essentials of Glycobiology* (Varki, A. C., R.D.; Esko J.D. et al., Ed.) 2nd ed., Cold Spring Harbor Laboratory Press, Cold Spring Harbor, NY.

[2] Moremen, K. W., Tiemeyer, M., and Nairn, A. V. (2012) Vertebrate protein glycosylation: diversity, synthesis and function, *Nature reviews. Molecular cell biology 13*, 448-462.

[3] Dwek, R. A. (1996) Glycobiology: Toward Understanding the Function of Sugars, *Chemical reviews 96*, 683-720.

[4] Defaus, S., Gupta, P., Andreu, D., and Gutierrez-Gallego, R. (2014) Mammalian protein glycosylation--structure versus function, *The Analyst 139*, 2944-2967.

[5] Alley, W. R., Mann, B. F., and Novotny, M. V. (2013) High-sensitivity Analytical Approaches for the Structural Characterization of Glycoproteins, *Chemical reviews 113*, 2668-2732.

[6] An, H. J., Kronewitter, S. R., de Leoz, M. L. A., and Lebrilla, C. B. (2009) Glycomics and disease markers, *Curr Opin Chem Biol 13*, 601-607.

[7] Arnold, J. N., Saldova, R., Hamid, U. M. A., and Rudd, P. M. (2008) Evaluation of the serum N-linked glycome for the diagnosis of cancer and chronic inflammation, *Proteomics 8*, 3284-3293.

[8] Jankovic, M. (2011) Glycans as Biomarkers: Status and Perspectives, *J Med Biochem 30*, 213-223.

[9] Taniguchi, N. (2008) Human Disease Glycomics/Proteome Initiative (HGPI), *Mol Cell Proteomics 7*, 626-627.

[10] Hebert, A. S., Merrill, A. E., Bailey, D. J., Still, A. J., Westphall, M. S., Strieter, E. R., Pagliarini, D. J., and Coon, J. J. (2013) Neutron-encoded mass signatures for multiplexed proteome quantification, *Nature methods 10*, 332-334.

[11] Merrill, A. E., Hebert, A. S., MacGilvray, M. E., Rose, C. M., Bailey, D. J., Bradley, J. C., Wood, W. W., El Masri, M., Westphall, M. S., Gasch, A. P., and Coon, J. J. (2014) NeuCode labels for relative protein quantification, *Mol Cell Proteomics 13*, 2503-2512.

[12] Frost, D. (2016) Development and Application of Novel Chemical Labels for Highly Multiplexed Quantitative Proteomics by Mass Spectrometry, In *School of Pharmacy*, University of Wisconsin-Madison, Madison, WI.

[13] Norton, P. A., Comunale, M. A., Krakover, J., Rodemich, L., Pirog, N., D'Amelio, A., Philip, R., Mehta, A. S., and Block, T. M. (2008) N-linked glycosylation of the liver cancer biomarker GP73, *Journal of cellular biochemistry 104*, 136-149.

[14] Zhao, J., Qiu, W. L., Simeone, D. M., and Lubman, D. M. (2007) N-linked glycosylation profiling of pancreatic cancer serum using capillary liquid phase separation coupled with mass spectrometric analysis, *J Proteome Res 6*, 1126-1138.

[15] Abdul Rahman, S., Bergstrom, E., Watson, C. J., Wilson, K. M., Ashford, D. A., Thomas, J. R., Ungar, D., and Thomas-Oates, J. E. (2014) Filter-aided N-glycan separation (FANGS): a convenient sample preparation method for mass spectrometric N-glycan profiling, *J Proteome Res 13*, 1167-1176.

[16] Hecht, E. S., McCord, J. P., and Muddiman, D. C. (2015) Definitive Screening Design Optimization of Mass Spectrometry Parameters for Sensitive Comparison of Filter and Solid Phase Extraction Purified, INLIGHT Plasma N-Glycans, *Analytical chemistry 87*, 7305-7312.

[17] Ruhaak, L. R., Zauner, G., Huhn, C., Bruggink, C., Deelder, A. M., and Wuhrer, M. (2010) Glycan labeling strategies and their use in identification and quantification, *Analytical and bioanalytical chemistry 397*, 3457-3481.

[18] Thompson, A., Schafer, J., Kuhn, K., Kienle, S., Schwarz, J., Schmidt, G., Neumann, T., Johnstone, R., Mohammed, A. K., and Hamon, C. (2003) Tandem mass tags: a novel quantification strategy for comparative analysis of complex protein mixtures by MS/MS, *Analytical chemistry 75*, 1895-1904.

[19] Ross, P. L., Huang, Y. N., Marchese, J. N., Williamson, B., Parker, K., Hattan, S., Khainovski, N., Pillai, S., Dey, S., Daniels, S., Purkayastha, S., Juhasz, P., Martin, S., Bartlet-Jones, M., He, F., Jacobson, A., and Pappin, D. J. (2004) Multiplexed protein quantitation in Saccharomyces cerevisiae using amine-reactive isobaric tagging reagents, *Mol Cell Proteomics 3*, 1154-1169.

[20] Xiang, F., Ye, H., Chen, R., Fu, Q., and Li, L. (2010) N,N-dimethyl leucines as novel isobaric tandem mass tags for quantitative proteomics and peptidomics, *Analytical chemistry 82*, 2817-2825.

[21] Frost, D. C., Greer, T., Xiang, F., Liang, Z., and Li, L. (2015) Development and characterization of novel 8-plex DiLeu isobaric labels for quantitative proteomics and peptidomics, *Rapid communications in mass spectrometry : RCM 29*, 1115-1124.

[22] Frost, D. C., Greer, T., and Li, L. (2015) High-resolution enabled 12-plex DiLeu isobaric tags for quantitative proteomics, *Analytical chemistry 87*, 1646-1654.

[23] Gorshkov, M. V., Fornelli, L., and Tsybin, Y. O. (2012) Observation of ion coalescence in Orbitrap Fourier transform mass spectrometry, *Rapid communications in mass spectrometry : RCM 26*, 1711-1717.

Figure legends

Figure 1. DiPyrO general structure and multiplex isotopologues. (A) The DiPyrO mass defect labeling reagent consists of a dimethyl pyrimidinyl ornithine and an amine-reactive triazine ester group. A total of six stable isotopes (^{13}C, ^{2}H, ^{15}N, ^{18}O) are incorporated onto the mass defect based tag in differing configurations to create (B) a 3-plex set, (C) a 4-plex set, (D) a 6-plex set, and (E) an 8-plex set with minimum mass defects of 20.95 mDa, 12.64 mDa, 8.31 mDa, and 5.84 mDa, respectively.

Figure 2. Chemistry of PNGase F digestion of N-glycans from glycopeptide followed by deamination.

Figure 3. Labeling efficiencies of 10 selected N-glycans at 4 different labeling conditions: 1:25 at 30% aqueous buffer (blue), 1:50 at 30% aqueous buffer (red), 1:25 anhydrate (green) and 1:50 anhydrate (purple).

Figure 4. Dynamic range test of duplex DiPyrO labeled N-glycans released from BTG. DiPyrO labeling ratios (light:heavy) of 1:1, 1:2, 1:4, 1:8 and 1:16 were tested. The result was plotted as measured ratios vs. theoretical ratios at $\log_2$ scale. Representative results from 8 N-glycans were shown with the linear equation and R^2 value.

Figure 5. Representative MS spectra and LC chromatogram of duplex DiPyrO light:heavy 1:2 labeled high mannose N-glycans H_5N_2 (A&B) and acidic complex N-glycan H_5N_4FS (C&D).

Figure 6. Workflow of FANGS from PANC1 cell lysate and duplex DiPyrO labeling.

Figure 7. Representative results of duplex DiPyrO labeled N-glycans from 2D and 3D cultured PANC1 cell lysates.

Figures

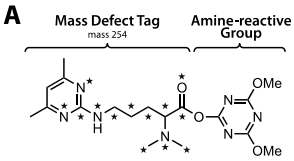

B 3-plex DiPyrO Reagents

DiPyrO label	Stable Isotopes	Isotope mass	Δ mDa
1	●●●●●	5.9924	0
2	●●●●●●	6.0133	20.95
3	●●●●●●	6.0377	24.33

C 4-plex DiPyrO Reagents

DiPyrO label	Stable Isotopes	Isotope mass	Δ mDa
1	●●●●●	5.9924	0
2	●●●●●	6.0050	12.64
3	●●●●●●	6.0201	15.11
4	●●●●●●	6.0377	17.53

D 6-plex DiPyrO Reagents

DiPyrO label	Stable Isotopes	Isotope mass	Δ mDa
1	●●●●●	5.9924	0
2	●●●●●●	6.0007	8.31
3	●●●●●	6.0109	10.17
4	●●●●●●	6.0201	9.26
5	●●●●●	6.0294	9.22
6	●●●●●●	6.0377	8.31

E 8-plex DiPyrO Reagents

DiPyrO label	Stable Isotopes	Isotope mass	Δ mDa
1	●●●●●	5.9924	0
2	●●●●●●	6.0007	8.31
3	●●●●●●	6.0075	6.80
4	●●●●●●	6.0133	5.84
5	●●●●●●	6.0201	6.80
6	●●●●●●	6.0260	5.84
7	●●●●●●	6.0318	5.84
8	●●●●●●	6.0377	5.84

● ^{13}C ● ^{2}H ● ^{15}N ● ^{18}O

Figure 1

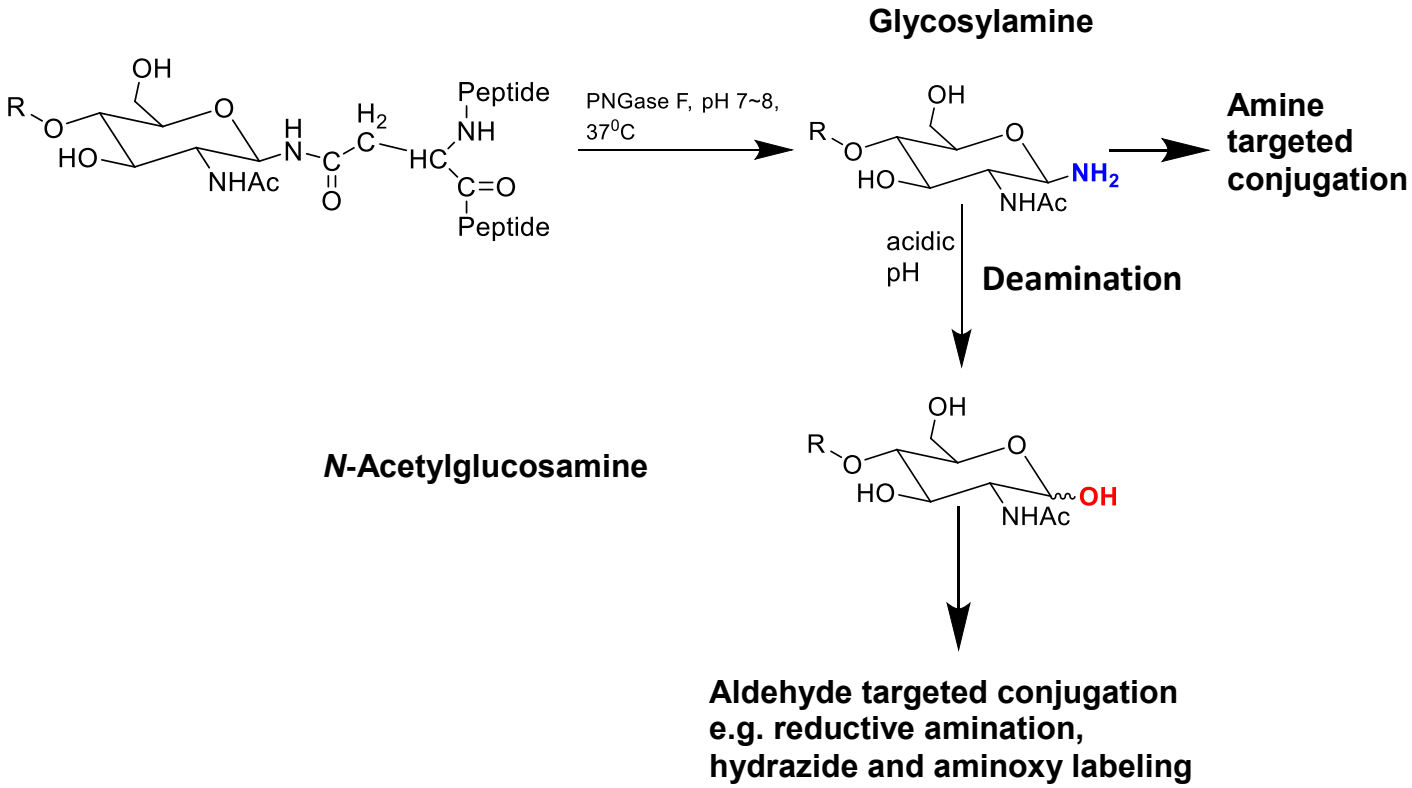
Glycosylamine
PNGase F, pH 7~8,
37^{0}C
Amine
targeted
conjugation
acidic
pH
Deamination
N-Acetylglucosamine
Aldehyde targeted conjugation
e.g. reductive amination,
hydrazide and aminoxy labeling

Figure 2

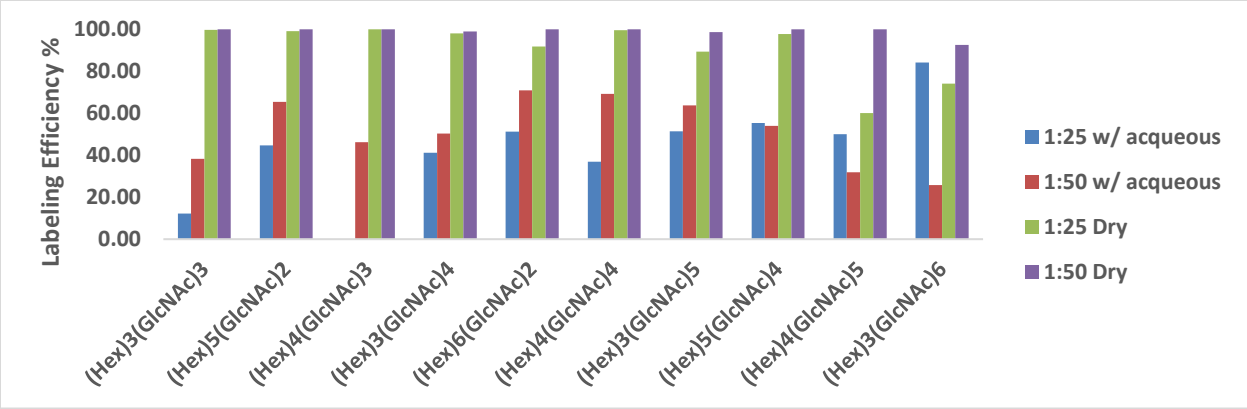
Labeling Efficiency %
100.00
80.00
60.00
40.00
20.00
0.00
(Hex)3(GlcNAc)3
(Hex)5(GlcNAc)2
(Hex)4(GlcNAc)3
(Hex)3(GlcNAc)4
(Hex)6(GlcNAc)2
(Hex)4(GlcNAc)4
(Hex)3(GlcNAc)5
(Hex)5(GlcNAc)4
(Hex)4(GlcNAc)5
(Hex)3(GlcNAc)6
1:25 w/ acqueous
1:50 w/ acqueous
1:25 Dry
1:50 Dry

Figure 3

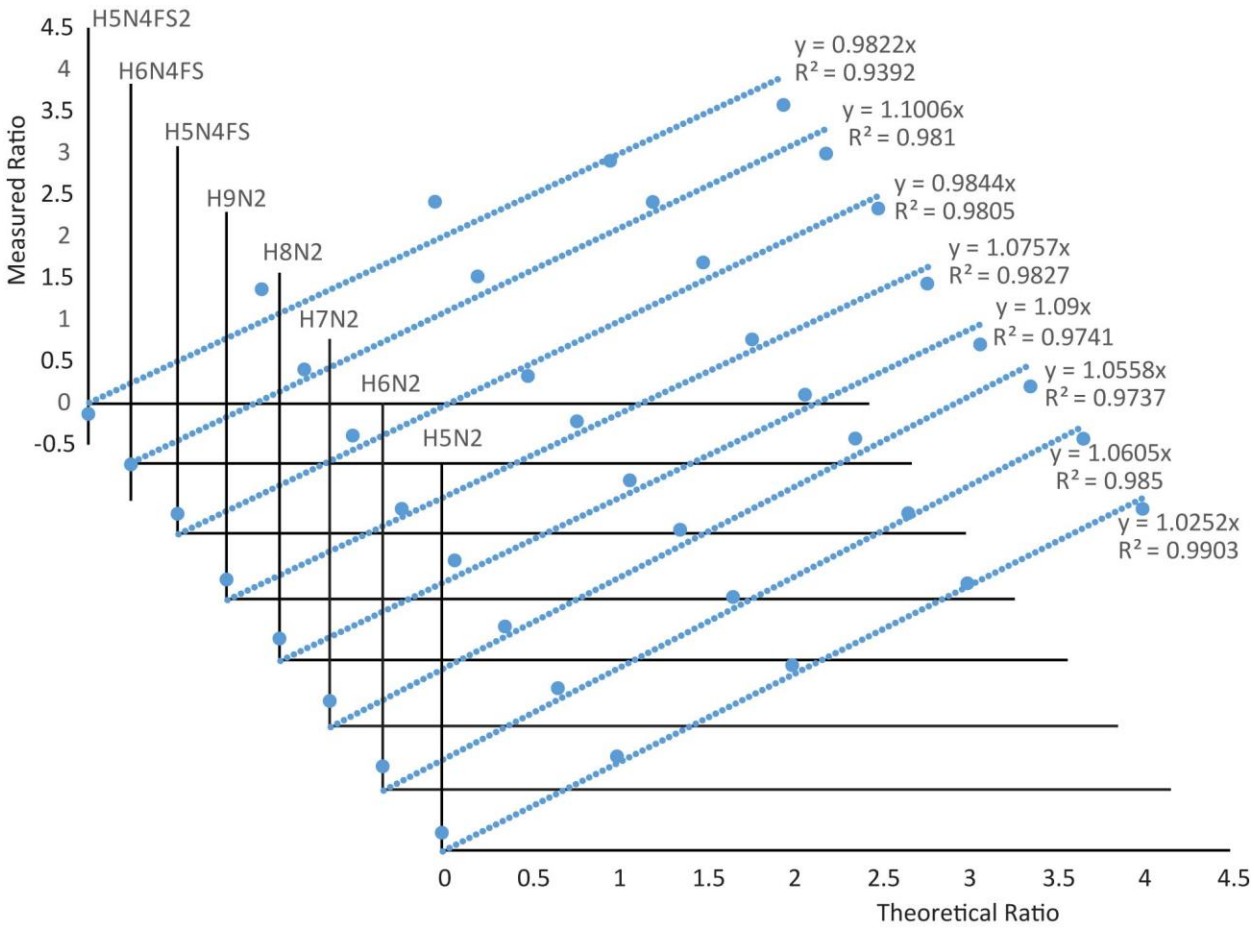
H5N4FS2
H6N4FS
H5N4FS
H9N2
H8N2
H7N2
H6N2
H5N2
y = 0.9822x
R² = 0.9392
y = 1.1006x
R² = 0.981
y = 0.9844x
R² = 0.9805
y = 1.0757x
R² = 0.9827
y = 1.09x
R² = 0.9741
y = 1.0558x
R² = 0.9737
y = 1.0605x
R² = 0.985
y = 1.0252x
R² = 0.9903
Measured Ratio
Theoretical Ratio
4.5
4
3.5
3
2.5
2
1.5
1
0.5
0
-0.5
0
0.5
1
1.5
2
2.5
3
3.5
4
4.5

Figure 4

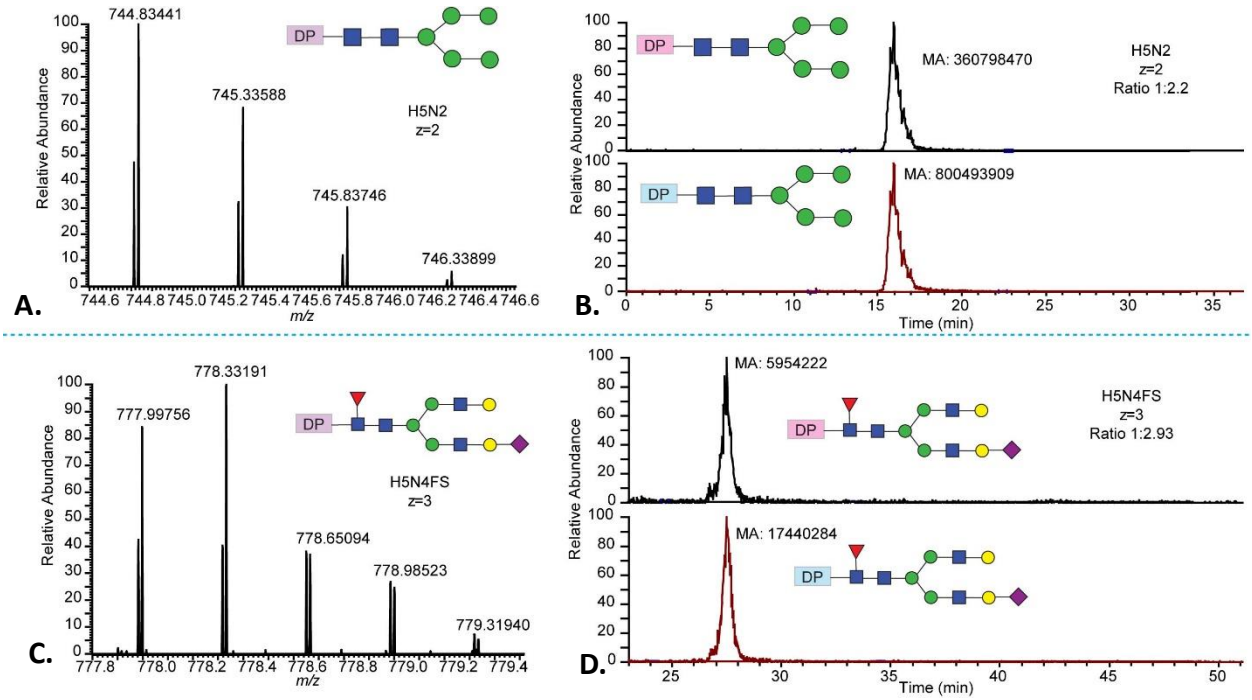
A.
744.83441
745.33588
745.83746
746.33899
H5N2
z=2
DP
Relative Abundance
m/z
B.
MA: 360798470
H5N2
z=2
Ratio 1:2.2
MA: 800493909
Time (min)
C.
778.33191
777.99756
778.65094
778.98523
779.31940
H5N4FS
z=3
D.
MA: 5954222
H5N4FS
z=3
Ratio 1:2.93
MA: 17440284

Figure 5

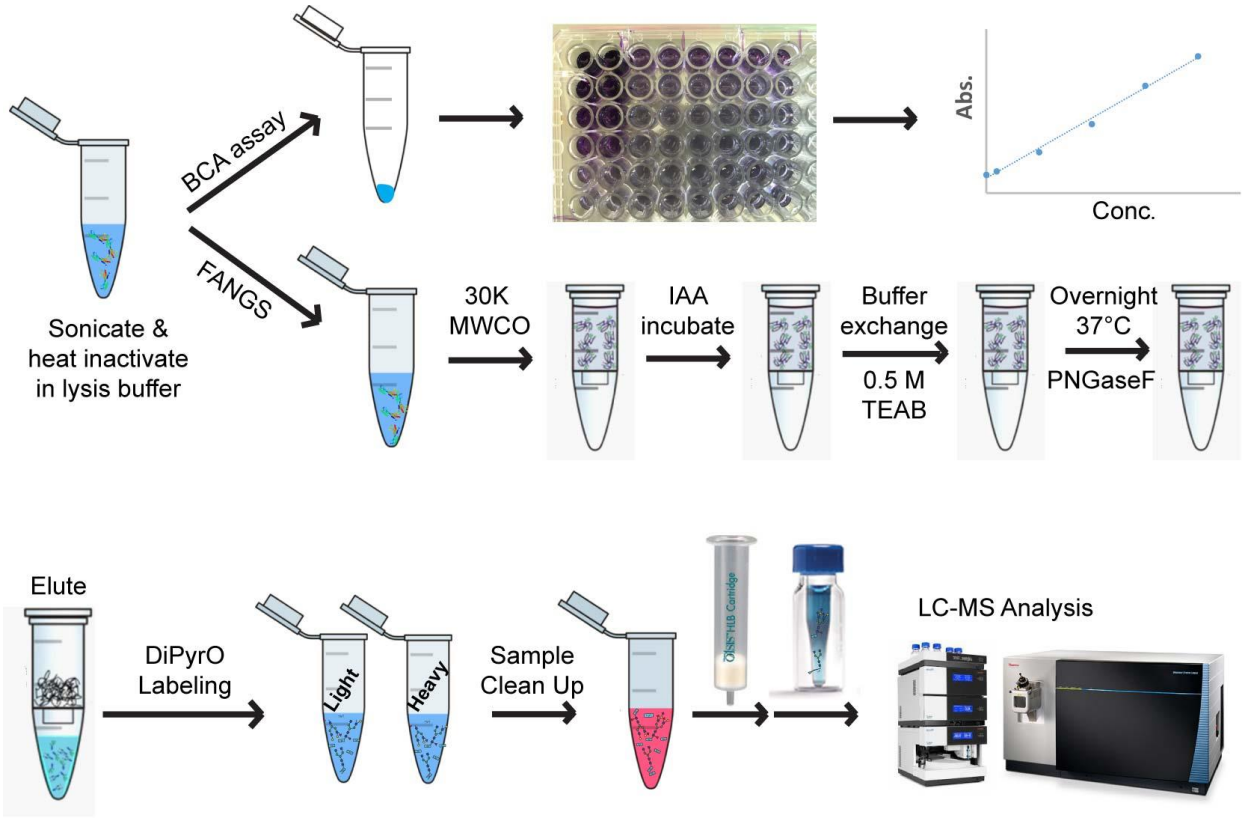
BCA assay
FANGS
Abs.
Conc.
Sonicate &
heat inactivate
in lysis buffer
30K
MWCO
IAA
incubate
Buffer
exchange
0.5 M
TEAB
Overnight
37°C
PNGaseF
Elute
DiPyrO
Labeling
Light
Heavy
Sample
Clean Up
LC-MS Analysis

Figure 6

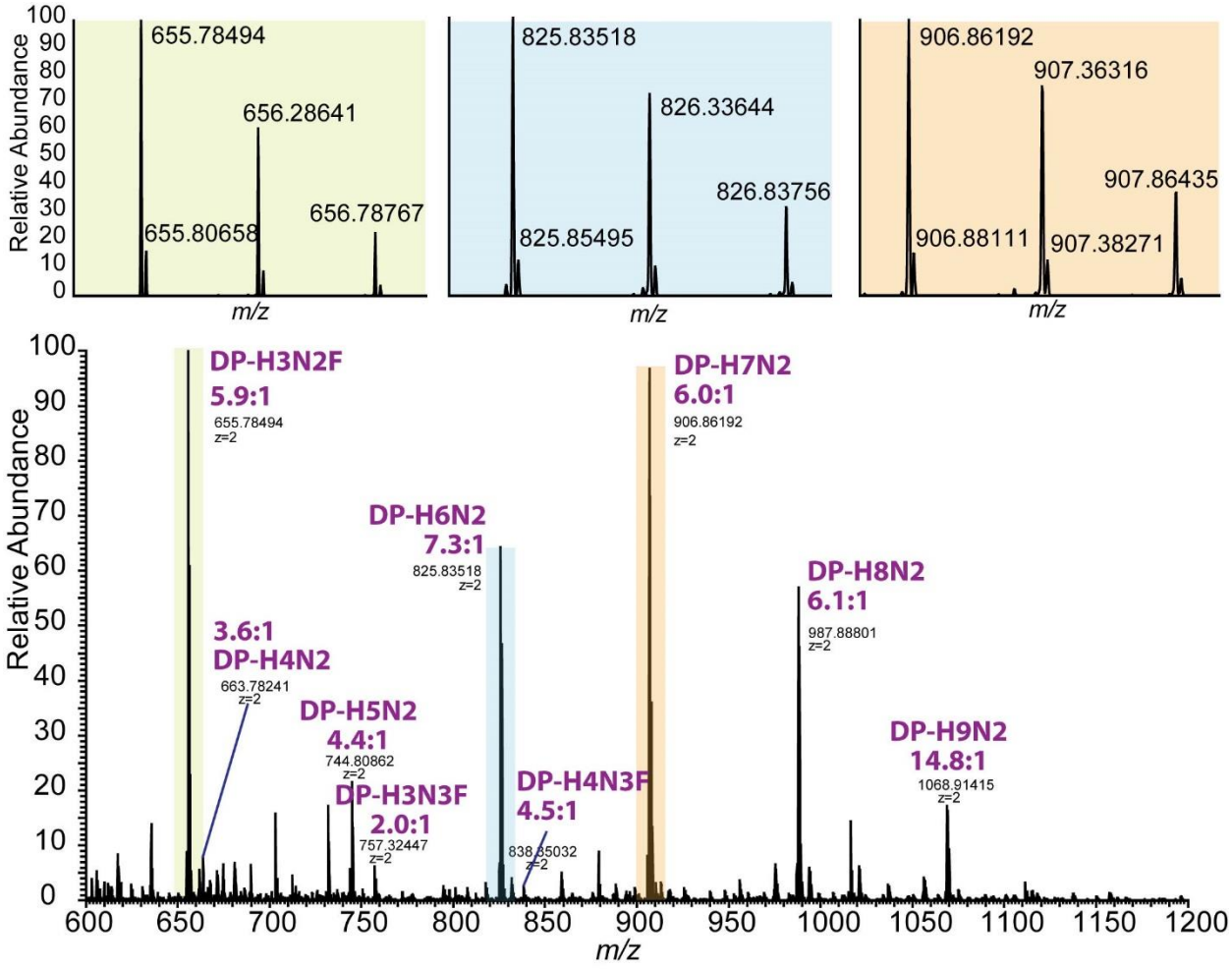
Relative Abundance
m/z
655.78494
656.28641
655.80658
656.78767
825.83518
826.33644
825.85495
826.83756
906.86192
907.36316
907.86435
906.88111
907.38271
DP-H3N2F
5.9:1
655.78494
z=2
DP-H7N2
6.0:1
906.86192
z=2
DP-H6N2
7.3:1
825.83518
z=2
DP-H8N2
6.1:1
987.88801
z=2
3.6:1
DP-H4N2
663.78241
z=2
DP-H5N2
4.4:1
744.80862
z=2
DP-H3N3F
2.0:1
757.32447
z=2
DP-H4N3F
4.5:1
838.85032
z=2
DP-H9N2
14.8:1
1068.91415
z=2

Figure 7

Supporting information

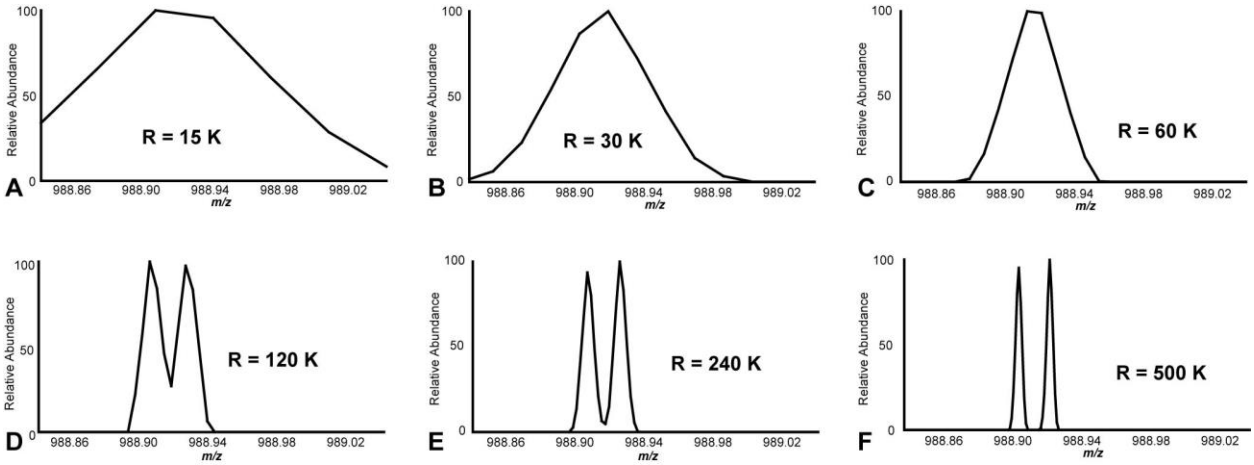

Supplemental Figure 1. Duplex DiPyrO labeled N-glycan $[H_3N_6+DiPyrO+2H]^{2+}$ at *m/z* 988.85 to 989.05 measured with different resolutions (15K, 30K, 60K, 120K, 240K and 500K).

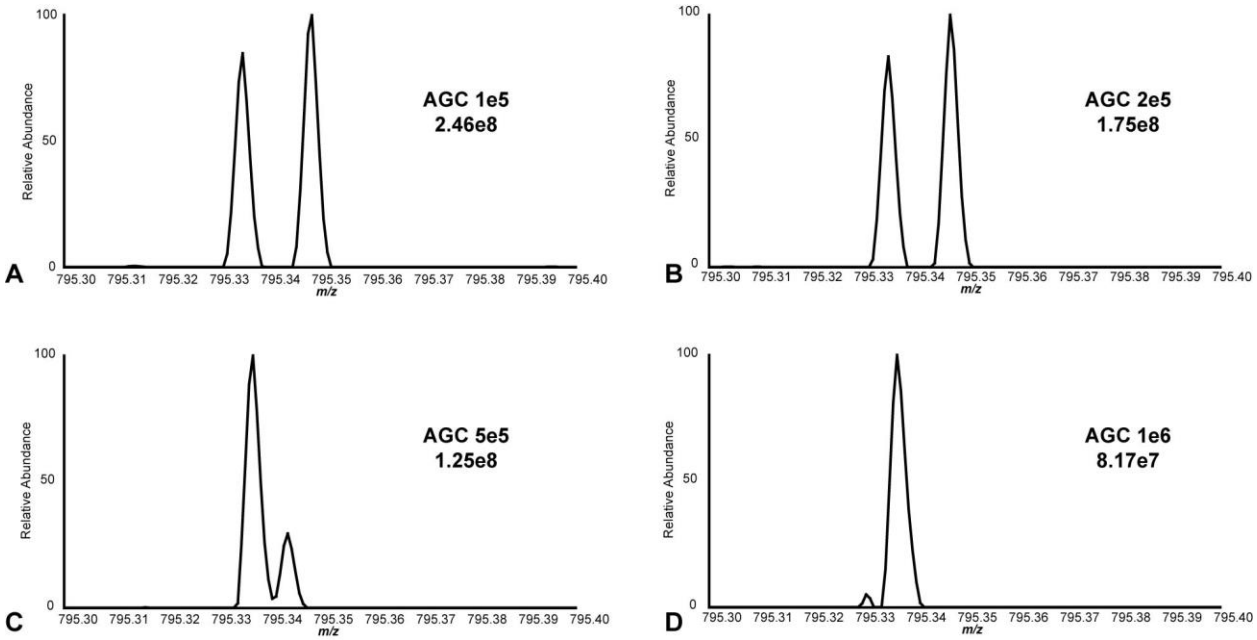

Supplemental Figure 2. Duplex DiPyrO labeled N-glycan at *m/z* 795.30 to 795.40 measured with different AGC values: 1e5 (A), 2e5 (B). 5e5 (C) and 1e6 (D). The signal intensity of base peak is labeled.

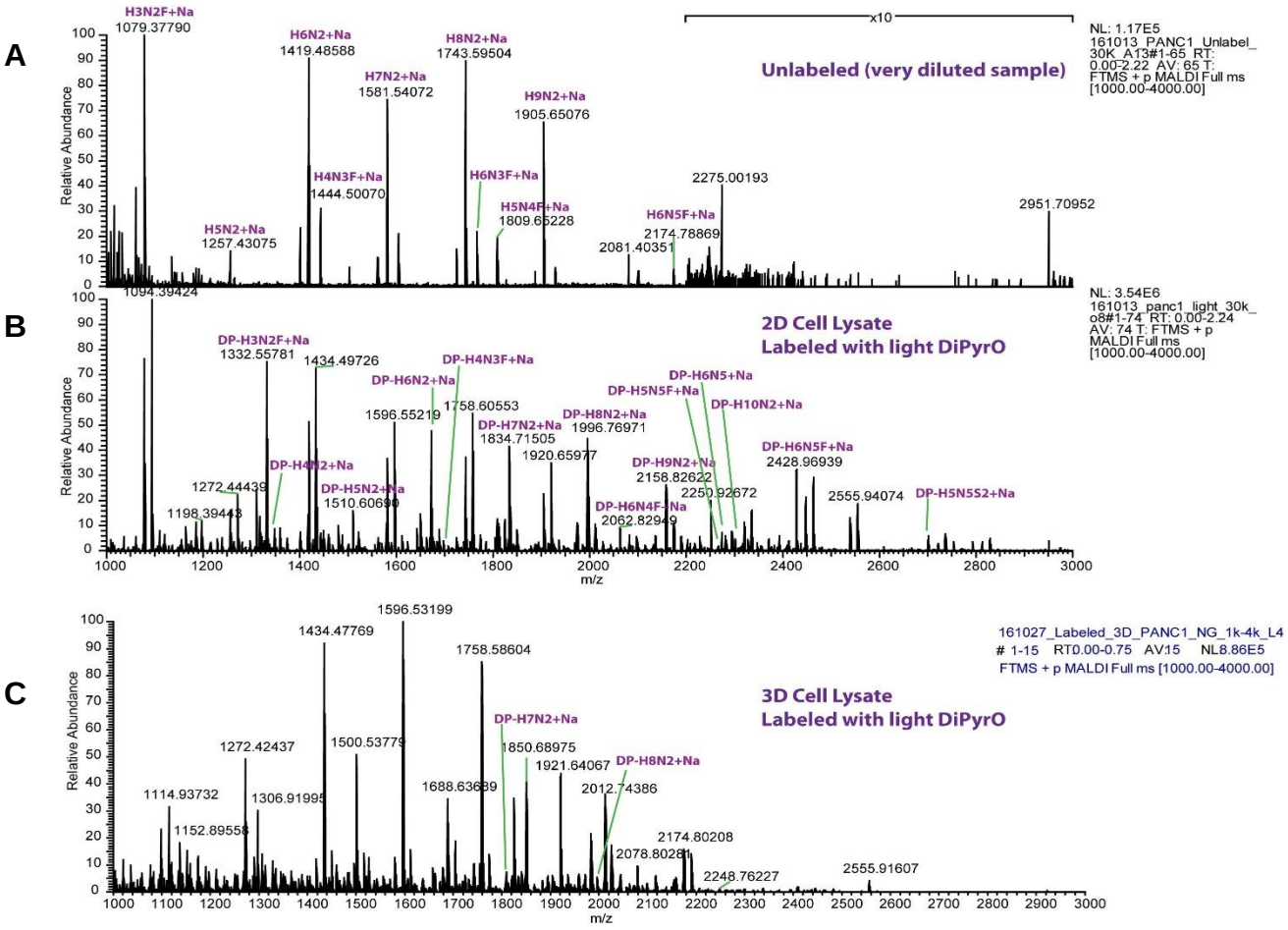

Supplemental Figure 3. MALDI-MS profiling of N-glycans released from PANC1 cell lysates: unlabeled N-glycan from 2D cell lysate (A), light DiPyrO labeled N-glycan from 2D cell lysate (B) and light DiPyrO labeled N-glycan from 3D cell lysate (C).

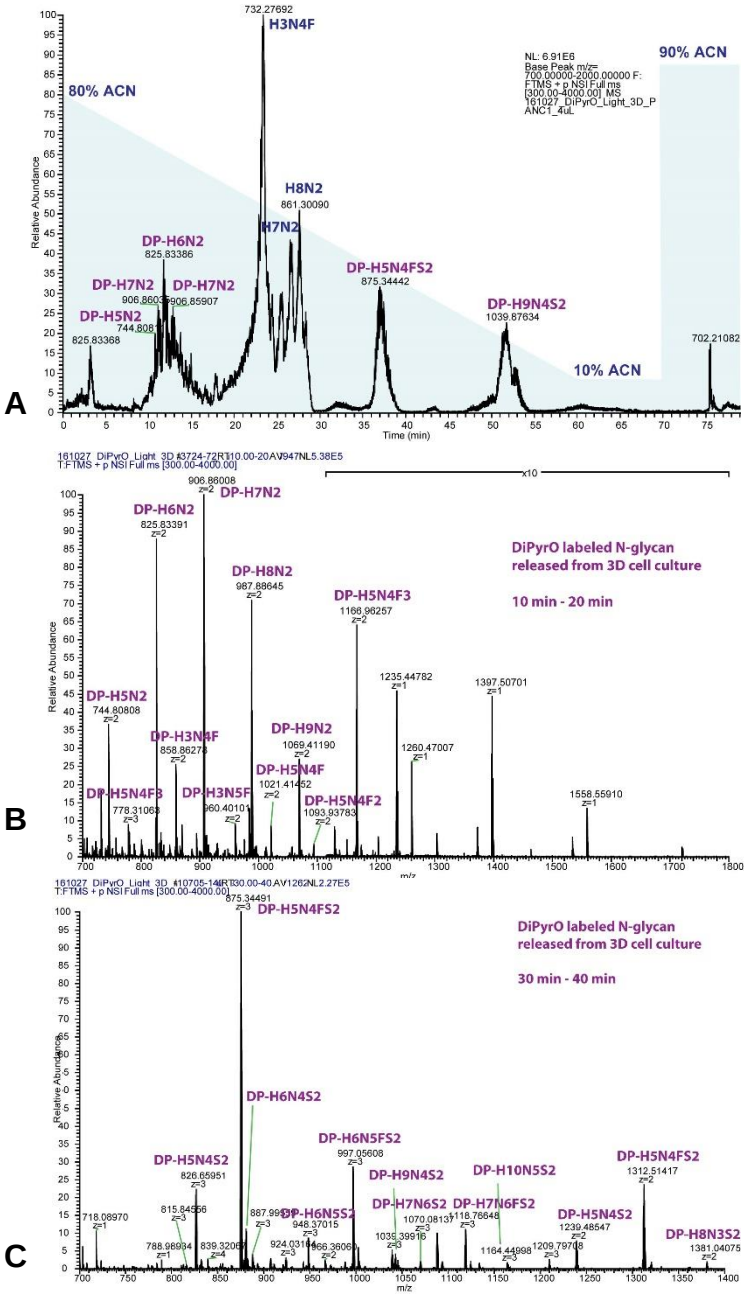

Supplemental Figure 4. LC-MS/MS analysis of light-DiPyrO labeled N-glycans released from 3D PANC1 cell lysate. (A). The LC chromatogram of base peaks in *m/z* range of 700-2000. The corresponding N-glycans were labeled (purple: DiPyrO labeled; dark blue: unlabeled). LC-gradient was overlapped in light blue shade with corresponding ACN percentage. (B). Averaged MS spectrum from 10 to 20 min. Mainly neutral N-glycans were observed. (C). Averaged MS spectrum from 30 to 40 min. Mainly acidic N-glycans with 2 sialic acids were observed.

Chapter 12
Conclusions and Future Directions

Method Development Milestones

2013
Laserspray ionization

MALDI-Orbitrap

2014
Matrix-assisted ionization vacuum

MALDI-Orbitrap

2015
Matrix-assisted ionization

Orbitrap Elite (ESI)

2016
MALDI, LSI, MAI

AP/MALDI-QE HF

Applications

Autism Spectrum Disorders
biomarker discovery
MALDI/LSI MSI

Oxytocin intranasal delivery
MALDI MSI
LC-MS/MS

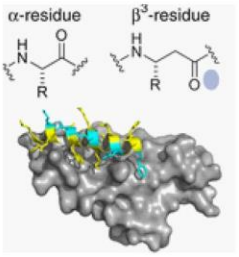

Parathyroid hormone analog
stability analysis
MALDI MS & LC-MS/MS

Conclusions

In this dissertation, matrix-assisted laser desorption/ionization (MALDI) and liquid chromatography (LC) – electrospray ionization (ESI) based mass spectrometry (MS) techniques were developed to characterize and quantify endogenous and therapeutic biomolecules. This work not only improves current analytical methodology for characterizing biomolecules but also demonstrates the potential applications in pharmaceutical industry and clinical settings.

High performance MS instruments offer superior resolution and mass accuracy. However, the *m/z* range of Fourier transform mass analyzers is usually limited. When these analyzers are coupled to a MALDI source, which predominantly produces singly charged ions, the mass detection range and the fragmentation efficiency are often inadequate for analysis of larger biomolecules. In Chapters 2-4, I focused on solving this problem by developing novel ionization techniques, including laserspray ionization (Chapter 2) and matrix-assisted ionization (Chapters 3 & 4), which produce multiply charged ions on both MALDI and ESI sources. Large peptides and proteins were detected with high mass accuracy at various charge states. The fragmentation efficiency on multiply charged ions was greatly improved compared to the singly charged ions produced by MALDI. By coupling to electron transfer dissociation, as demonstrated in Chapter 4, labile modifications on peptides could be preserved and localized, and large peptides could be fragmented with high sequence coverage. I was able to use these methods to analyze biomolecule standards, mixtures, tissue homogenates as well as tissue sections *in situ*.

Biomolecule identification of MS imaging experiment is challenging due to the lack of MS/MS information. In Chapter 5, we developed a method that couples multiplexed MS imaging with gas phase fractionation to achieve *in situ* data dependent acquisition and biomolecule

identification. The resulting MS imaging data could be subjected to database search directly for biomolecule identification and *de novo* sequencing. We used crustacean neural tissue as a model system to demonstrate this method. Thirty-nine known neuropeptides were identified *in situ* by database search and one novel RFamide neuropeptide was detected by *de novo* sequencing.

We utilized a high resolution atmospheric pressure MALDI mass spectrometer in Chapter 6 to detect biomolecules, including lipids, neuropeptides, and proteins, by multi-mode ionization and acquisition techniques. In this study, high resolution MS imaging was achieved both in mass (240K mass resolution at *m/z* 200) and in space (< 10 μm spatial resolution). Besides MALDI, we also performed laserspray ionization and matrix assisted ionization on this instrument platform to expand the mass detection range and improve fragmentation efficiency.

In Chapters 7 and 8, I demonstrated the applications of MS imaging in mammalian brain tissues. I studied the distribution of intranasally administered therapeutic peptides in rat brain tissue (Chapter 7). The exogenously administered peptides were detected in various brain regions, including olfactory bulb, brain stem, and trigeminal nerve, suggesting that the peptide followed the olfactory and trigeminal pathways to the brain as demonstrated in previous studies.[1-3] In Chapter 8, I aimed to use MS imaging for detecting potential neuropeptide and protein biomarkers of autism spectrum disorders (ASD) in the brain tissue of *Fmr1* knocked out mouse, which is a mouse model of fragile X syndrome. I found that several biomolecules, such as secretogranin-2 and beta-neoendorphin, exhibited different expression patterns between *Fmr1* knocked out mice and C57BL/6J control mice in terms of localization and concentration.

Finally, I developed several quantification strategies for biomolecules in Chapters 9-11. I monitored the stability and degradation products of a therapeutic peptide, human parathyroid

hormone (hPTH) 1-34, and its α→β backbone modified analog, M-Cyc-9β, by LC-MS/MS and MALDI-MS in Chapter 9. Through LC-MS/MS absolute quantification, the half-lives of these peptides were determined to be 1.9 min for hPTH (1-34) and 35.2 min for M-Cyc-9β. Through MALDI-MS, the major degradation products were monitored as a function of time. These findings provided novel insights into the molecular details of PTH degradation by kidney. In Chapters 10 and 11, I established two relative quantification strategies for N-glycans by isobaric aminoxyTMT (Chapter 10) and mass defect-based DiPyrO (Chapter 11) tags. Due to the low reporter ion yield at MS^2 level of the aminoxyTMT tags, I implemented a targeted Y_1 ion triggered MultiNotch MS^3 method to circumvent this problem. Significant improvements in quantification precision and accuracy were observed for the MultiNotch MS^3 method compared to the MS^2 method. Alternatively, I used the custom DiPyrO tag to perform relative quantification on N-glycans at MS^1 level in Chapter 11. This method also enabled accurate measurement of the N-glycan relative concentrations, even with large dynamic ranges.

Future directions

The development of laserspray ionization and matrix assisted ionization on high resolution accurate mass instruments in Chapters 2-4 could be applied on other instrument platforms, such as Orbitrap Fusion Lumos, for improvements on sensitivity, mass resolution, and alternative fragmentation strategies (EThcD, etc.). Moreover, introducing samples with robotic systems would greatly improve the throughput of matrix assisted ionization compared to manually introducing samples with pipette tips. A major drawback of these ionization techniques is the volatile nature of these matrices, which prevents us from performing long MS imaging acquisitions. Alternative strategies that slow down the matrix sublimation process could unlock the potential of MS imaging by these ionization methods, especially matrix assisted ionization.

Further work is currently ongoing for the multiplex MS imaging project described in Chapter 5. We are applying this method on more complex biological systems, such as mammalian tissues, to investigate its efficiency. Moreover, this method is being coupled with *in situ* enzymatic digestion for a bottom-up proteomic approach on tissue. The combination of CID and HCD scans are also being tested for improving sequence coverage. Other MS workflows, such as data independent acquisition, polarity switching, and parallel reaction monitoring, could also be implemented on the multiplexed MS imaging method.

The high-resolution AP/MALDI system described in Chapter 6 could be used to investigate many biological systems. As this system is capable of achieving ultrahigh spatial resolution (< 10 μm), it is interesting to see its performance on single cell MS imaging. The relatively lower sensitivity prevents it from detecting low abundance species on tissue; only lipid species and high abundant neuropeptides were detected. A new generation of low pressure (subAP) MALDI source with improved sensitivity will be tested at our laboratory in the near future.[4]

The ASD biomarker discovery project, described in Chapter 8, is still in progress. In this study, we focused on studying the localization and relative concentration of neuropeptides between *Fmr1* knock out and control mice. The potential neuropeptide biomarkers need to be validated by more quantitative approaches, such as LC-MS/MS based absolute quantification. Further investigation on potential protein biomarkers will be performed by combining *in situ* enzymatic digestion and laserspray/matrix assisted ionization techniques.

The N-glycan relative quantification projects, described in Chapters 10 and 11, could be further improved by designing new generation of chemical tags. The performance of aminoxyTMT isobaric tag, described in Chapter 10, is limited due to the low reporter ion yields. We are currently

designing and synthesizing a new customized 4-plex isobaric tag, which is derived from the N, N-dimethyl leucine (DiLeu) tag that our group developed for protein quantification. The weaker bond in DiLeu could improve the reporter ion yield while preserve the backbone fragments of N-glycans.

In summary, the studies presented in this dissertation has showcased a powerful bioanalytical platform combining MALDI- and LC-ESI-based MS techniques to characterize and quantify biomolecules. In this work, I not only developed novel ionization techniques, MS imaging workflow, and quantification strategies, but also applied them on complex biological systems to solve challenging problems. These methods can be transferred to other instrumentation platforms and biological systems to solve various problems. I anticipate that this dissertation can assist researchers in biochemistry, analytical chemistry, and pharmaceutical sciences to impact their future studies.

References

[1] Lochhead, J. J., and Thorne, R. G. (2012) Intranasal delivery of biologics to the central nervous system, *Advanced drug delivery reviews 64*, 614-628.

[2] Thorne, R. G., Hanson, L. R., Ross, T. M., Tung, D., and Frey, W. H., 2nd. (2008) Delivery of interferon-beta to the monkey nervous system following intranasal administration, *Neuroscience 152*, 785-797.

[3] Thorne, R. G., Pronk, G. J., Padmanabhan, V., and Frey, W. H., 2nd. (2004) Delivery of insulin-like growth factor-I to the rat brain and spinal cord along olfactory and trigeminal pathways following intranasal administration, *Neuroscience 127*, 481-496.

[4] Moskovets, E., Misharin, A., Laiko, V., and Doroshenko, V. (2016) A comparative study on the analytical utility of atmospheric and low-pressure MALDI sources for the mass spectrometric characterization of peptides, *Methods 104*, 21-32.

Appendix I
List of Publications and Presentations

Publications

1. **B. Chen[#],** C. Ouyang[#], Z. Tian, M. Xu and L. Li, AP/MALDI (ng) UHR Source Coupled to Q Exactive HF Mass Spectrometer Enables High Resolution *in Situ* Analysis of Biomolecules by Multi-Ionization and Multi-Acquisition Mode. *To be submitted to Analyt. Chim. Acta*. ([#]Co-First authors)

2. **B. Chen[#],** X. Zhong[#], Y. Feng, S. Snovida, M. Xu, J. Rogers and L. Li, Relative Quantification of N-Glycan Using Multiplex Carbonyl-Reactive Tandem Mass Tags and MultiNotch MS3. *To be submitted to Anal. Chem.* ([#]Co-First authors)

3. **B. Chen[#]**, M. Yao[#], W. Zhao, J. Mehl, L. Li and M. Zhu, Liquid Chromatography-Mass Spectrometry Based Differential Analysis for Fast Determining Biotransformation of Therapeutic Biologics. *To be submitted to Drug Metab. Dispos.* ([#]Co-First authors)

4. **B. Chen,** R. Cheloha, N. Kumar, M. Xu, J. Checco, S. Nelson, R. Thorne, S. Gellman and L. Li, Stability Analysis of Parathyroid Hormone (1-34) and Its Bioactive Analog in Rat Kidney Homogenate by MALDI-MS and Multiplexed Parallel Reaction Monitoring LC-MS/MS. *To be submitted to ACS Chem. Bio.*

5. **B.Chen**, C.B. Lietz, L. Li, Coupling Matrix-Assisted Ionization with High Resolution Mass Spectrometer and Electron Transfer Dissociation for Characterizing Intact Protein and Post-Translational Modifications. *To be submitted to Anal. and Bioanal. Chem.*

6. **B.Chen**, C.B. Lietz, C.Ouyang, X. Zhong, M. Xu and L. Li (2016). Matrix-Assisted Ionization in Vaccum for Protein Detection, Fragmentation and PTM Analysis on a High Resolution Linear Ion Trap-Orbitrap Platform. *Analyt. Chim. Acta*., vol 916. p.52-59.

7. **B. Chen[#],** C. Ouyang[#] and L. Li (2015). High Throughput *In situ* DDA Analysis of Neuropeptides by Coupling Novel Multiplex Mass Spectrometric Imaging (MSI) with Gas-Phase Fractionation. *J. Am. Soc. Mass Spectrom.*, vol. 26 (12). p.1992-2001. Cover article ([#]Co-First authors)

8. **B.Chen,** C.B. Lietz, L. Li (2014). *In situ* Characterization of Multiply Charged Proteins Using a High-Performance MALDI-LTQ-Orbitrap Mass Spectrometer. *J. Am. Soc. Mass Spectrom.*, vol. 25 (12). *p. 2177-80.*

9. **B. Chen[#],** E. Gemperline[#], and L. Li (2014). Mass Spectrometric Imaging of Neurotransmitters: Challenges and Recent Advances. *Bioanalysis*, vol.6 (4). p. 525-40. ([#]Co-First authors)

10. R. Cheloha, **B. Chen**, N. Kumar, T. Watanabe, T. Dean, R. Thorne, L. Li, T. Gardella and S. Gellman, Identification of a Bioactive Analog of Parathyroid Hormone with Widely Distributed Backbone Modifications that Shows High Stability in Diverse Biological contexts. *Submitted to J. Am. Chem. Soc, under review.*

11. Z. L. Pratt, **B. Chen**, C. J. Czuprynski, A. C. Wong, and C. W. Kaspar. (2012). Characterization of Osmotically Induced Filaments of Salmonella enterica. *Appl. Environ. Microbiol*, vol. 78. p. 6704-13.

12. C. A. Turski, G. Turski, **B. Chen**, H. Wang, L. Li, K. Noguchi, C. Westmark, I. Duncan, C. Ikonomidou, Clemastine Effects in Rat Models of Pelizaeus Merzbacher Disease. *In preparation.*

13. C. OuYang, **B. Chen**, Y. Ji, L. Li; Enhance the MS/MS identification efficiency in matrix assisted laser desorption/ionization mass spectrometric imaging of biological tissue using hybrid multiplex-DDA-MSI methodology. *In preparation.*

14. C. OuYang, Q. Cao, **B. Chen**, L. Li; Comprehensive profiling of the complete neuropeptidome of *C. irroratus* via multifaceted mass spectrometric techniques: discovery and functional study of novel sulfakinin, WXXXnR and kinins. *In preparation.*

15. Y. Shi, B. Wang, **B. Chen**, X. Shi, K.C. Kent, L. Li; MALDI MS imaging reveals the temporal and spatial change of lipids in the progression of restenosis. *In preparation*

Presentations

1. **B. Chen,** X. Zhong, Y. Feng, S. Snovida, J. Rogers and L. Li, Relative Quantification of Glycan Using Multiplex Carbonyl-Reactive Tandem Mass Tags and MultiNotch MS3, oral presentation, 64th ASMS Annual Conference, June 5-9, 2016, San Antonio, TX;

2. **B. Chen,** X. Zhong, C.B. Lietz and L. Li, High Resolution and Accurate Mass (HRAM) Characterization of Multiply Charged Proteins by Newly Developed Ionization Techniques on CE-LSI/MAIV-LTQ-Orbitrap plateform, oral presentation, 63rd ASMS Annual Conference, May 31-June 4, 2015, St. Louis, MO;

3. **B. Chen,** C.B. Lietz, A. Van and L. Li, High Resolution and High Mass Accuracy Multiply Charged MALDI Technique for *In Situ* Protein Characterization – Sequencing, Identification and Visualization, poster presentation, 62nd ASMS Annual Conference, June 15-19, 2014, Baltimore, MD;

4. **B. Chen**, C.B. Lietz, C. Ouyang and L. Li. *In situ* Protein Identification and Visualization Using Multiply Charged MALDI Mass Spectrometric Imaging, oral presentation, 2014 Pittsburgh Conference on Analytical Chemistry and Allied Spectroscopy, March 2-4, 2014, Chicago, IL

5. **B. Chen,** N. Kumar, R.G. Thorne and L. Li. "Intranasal Delivery of Oxytocin and Its Analog to the Central Nervous System: Characterization of the Delivered Neuropeptide Distribution in the Brain Using Mass Spectrometry", poster presentation, 2014 WARF Discovery Challenge, May 21, 2014, Madison, WI;

6. **B. Chen**, H. Ye, M. Gautam, J. Wang, R.G. Thorne and L. Li. Mapping the Distribution of Intranasally Administered Oxytocin (OXT) in Rat Brain Using MADI Imaging Mass Spectrometry, poster presentation, 61th ASMS Annual Conference, June 10-13, 2013, Minneapolis, MN;

Appendix II
Challenges and Recent Advances in Mass Spectrometric Imaging of Neurotransmitters

Adapted from

B. Chen[#], E. Gemperline[#], and L. Li (2014). Mass Spectrometric Imaging of Neurotransmitters: Challenges and Recent Advances. *Bioanalysis*, vol.6 (4). p. 525-40. ([#]Co-First authors)

Defined key terms

MSI (mass spectrometric imaging): An analytical technique that allows for molecular analysis of tissue while retaining information about the spatial distribution of different analytes by collecting mass spectra in a predefined raster across a tissue sample, resulting in a two-dimensional distribution map for each mass measured.

Neurotransmitter: Neurotransmitters are endogenous substances released by synaptic terminals to transmit signals between nerve cells.

Neuropeptide: Neuropeptides are endogenous peptides synthesized in nerve cells or peripheral organs that are involved in cell-cell signaling. They are often considered as peptide neurotransmitters and peptide hormones with sizes ranging from 3 to 70 amino acids.

Matrix: Typically a small organic compound that is used to coat MALDI samples and assist in the ionization of analytes

Abstract

Mass spectrometric imaging (MSI) is a powerful tool that grants the ability to investigate a broad mass range of molecules, from small molecules to large proteins, by creating detailed distribution maps of selected compounds. To date, MSI has demonstrated its versatility in the study of neurotransmitters and neuropeptides of different classes toward investigation of neurobiological functions and diseases. These studies have provided significant insight in neurobiology over the years and current technical advances are further facilitating the improvement of this field. Herein, we briefly review new MSI studies of neurotransmitters focusing specifically on the challenges and recent advances of MSI of neurotransmitters.

Introduction

Mass spectrometric imaging (MSI) shows great promise for biological analyses because it allows for molecular analysis of tissue while retaining information about the spatial distribution of different analytes including proteins, peptides, lipids, and small molecules [1]. During an MSI experiment, a multitude of mass spectra are collected from a tissue slice in a predefined raster, resulting in a two-dimensional distribution map for each mass measured. One of the advantages of MSI is that it allows for the analysis of thousands of analytes at once, without the need of labels or prior knowledge of the analytes, and provides spatial information along with the mass analysis. MSI is often used in tandem with other techniques to obtain more molecular information, while using MSI to visualize the results [2-7]. Many excellent reviews have already been published on the subject of mass spectrometric imaging [8-17]. Herein we review current publications that highlight the critical role that MSI plays in the study of neurotransmitters and neuropeptides, focusing on the challenges and recent advances in the field.

Ionization Techniques- Advantages and Disadvantages

There are three main ionization methods used for MSI: matrix-assisted laser desorption/ionization (MALDI) [18, 19] , secondary ion mass spectrometry (SIMS) [20-22], and desorption electrospray ionization (DESI) [23, 24].

MALDI-MSI has proven to be a valuable technology with numerous applications for analyzing proteins [25, 26], lipids [27], neuropeptides [28, 29], and small molecules [2] at both organ and cellular levels. One advantage of using MALDI for MSI on biological samples is that it allows for the generation of larger ions, such as peptides and proteins, which is one of the reasons why MALDI is the most widely used method for MSI [1, 30-32]. Sample preparation is extremely important for this ionization technique. Immediately after the sacrifice of an animal specimen, rapid molecular degradation occurs. To limit the degradation of analytes, the tissue can be embedded in supporting media such as gelatin [28, 29] or sucrose [33] and snap-freezing in dry ice or liquid nitrogen. Polymer-containing material, such as optimal cutting temperature (OCT) compound, Tissue-tek, and carboxymethylcellulose (CMC), should be avoided as they often introduce polymer interferences into the mass spectrometer [34]. The embedded and frozen tissue should be stored at -80ºC until use [35]. Prior to long-term storage, the tissue sample can be stabilized using methods, such as microwave irradiation [36] or heat denaturation by Denator Stabilizor T1 (Gothenburg, Sweden) to deactivate proteolytic enzymes, preventing post mortem degradation of proteins or peptides of interest [37-39].

Next, the frozen tissue can be cut into thin sections with a cryostat. MSI experiments typically require 10-20 μm thick tissue sections [40]. The previous step of embedding tissue in supporting media allows for precise sectioning of tissue samples. Once sliced, tissue sections are then transferred and mounted onto a target plate or glass slide [41, 42] by thaw-mounting [34]. When

working with higher mass analytes, such as peptides and proteins, washing tissue sections with organic solvents is a recommended step to fix tissues and remove ion-suppressing salts and lipids, thus increasing the analyte signal [43-45].

The next step of the MALDI-MSI sample preparation process involves coating the tissue with a thin layer of matrix and irradiating the sample with a laser beam. The matrix is designed to absorb much of the incident laser, providing "soft" ionization for analyte compounds, which allows for the ionization of larger molecules (*m/z* over 100 kDa) [46]. Matrix selection and application is a critical step for MALDI-MSI, greatly impacting the sensitivity, spatial resolution, and selective analyte ionization of the experiment [43]. Conventional matrices include α-cyano-4-hydroxycinnamic acid (CHCA) and 2,5-dihydroxy benzoic acid (DHB) [28, 29, 34]. One disadvantage to using these conventional matrices is that they produce ions themselves which can interfere or mask analyte ions when looking at small molecules. High resolution instrumentation may negate some of the interference; however, less conventional matrices such as ionic matrices, made by mixing conventional matrices with organic bases [47-49], TiO_2 nanoparticles [50], 1,5-diaminonapthalene (DAN) [51], 2,3,4,5-Tetrakis(3′,4′-dihydroxylphenyl)thiophene (DHPT) [52], 1,8-bis(dimethyl-amino) naphthalene (DMAN) [53, 54] and ferulic acid [55] are being used more frequently and are reported to improve spectral quality, crystallization and vacuum stability. The matrix application technique plays a crucial role in the quality of mass spectral images, especially when obtaining high spatial resolution images [10, 51, 56].

Spatial resolution and reproducibility of results are limited by the matrix crystal size and application consistency, among other instrumental parameters such as raster step size and laser beam diameter [10]. Matrix application methods can be divided into two categories: solvent-based and solvent-free. Solvent-based methods apply matrix dissolved in solution and are typically

performed by manual airbrush or automated systems [56]. For solvent-free methods, dry matrix can be sublimated onto tissue under low pressure [57], filtered onto tissue through a small (~20 μm) sieve [58], or ground through fine mesh (~10-1 μm) above a tissue slice using a ball-mill [59]. These solvent-free methods were developed to limit spatial delocalization of soluble analytes that often occurs from excessive amounts of solvent during matrix application from solvent-based methods [60]. In comparison to the solvent-based matrix application methods, solvent-free methods yield very fine crystals amenable to high-spatial-resolution-MSI, but may also suffer from relatively low sensitivities due to the limited analyte-matrix interactions [51]. Several researchers have modified these dry matrix application techniques by rehydrating the sections following dry-coating to improve the detection sensitivity of analytes [25, 61].

SIMS is a long established technique in which a sample is put under high vacuum and bombarded with high energy primary ions which facilitates the ionization of analytes [62, 63]. The ionized analytes are referred to as secondary ions, and are sputtered from the sample surface and then drawn into the mass analyzer for analysis. The highly focused ion beam in SIMS provides excellent spatial resolution; however, the primary ion source is fairly limited to small molecules, under 1000 Da [2], due to its high energy that is prone to fragment large molecules in the ablation/ionization process. Recent advances in SIMS, such as using beams of gold trimers (Au_3^+) [64] or buckminsterfullerenes (C_{60}) [65], can provide significantly greater yields of higher mass ions. SIMS imaging does not require special preparation after sectioning and mounting the tissue, but there are some optional methods that improve the imaging results. The tissue can be coated with a thin layer of gold, silver, or matrix (such as 2,5-dihydroxybenzoic acid (DHB), α-cyano-4-hydroxycinnamic acid (CHCA), or sinapinic acid (SA)) to improve the ionization and reduce the fragmentation of larger molecules [66-68].

In contrast to traditional MALDI and SIMS, which require vacuum (although atmospheric pressure (AP)-MALDI has been developed), DESI is a simple, ambient ionization technique [69-72] that channels charged solvent droplets and ions from an electrospray source onto the sample surface [73]. The surface is impacted by the charged particles, yielding gaseous analyte ions. MSI had been mainly viewed as an invasive process until the development of ambient ionization techniques, such as DESI. DESI's ambient nature and softness allow for the examination of various natural surfaces with no need for matrix [74]. One advantage of DESI is its capability for high-throughput analysis with minimal tissue adulteration, again due to its ambient nature [13]. Since vacuum is not required for DESI, it has a greater advantage of being used for clinical or field application because the removal of the vacuum makes it more portable [75]. The ability to perform *in situ* analysis and the convenience of portable mass spectrometers suggests the potential role of DESI-MSI and other ambient ionization techniques in histology guided diagnoses and therapies in the clinical setting [75]. One disadvantage DESI has compared to vacuum MS methods, SIMS and MALDI, is that it has lower spatial resolution of approximately 180–200 μm [74]. Recently the nano-DESI probe has been developed which reported an increase in the spatial resolution to approximately 12 μm. With the nano-DESI probe, controlled desorption of analytes present in a restricted region of specimen is achieved using a minute amount of solvent between two capillaries [71]. **Table 1** summarizes the optimal analytes, mass range, and spatial resolutions of MALDI, SIMS, and DESI.

A fourth ionization technique worth mentioning is nanostructure-initiator mass spectrometry (NIMS) [76]. NIMS is a matrix-free ionization technique that shows promise for the analysis of small molecules. NIMS uses a liquid initiator to facilitate desorption instead of a crystalline MALDI matrix. NIMS initiators are different from MALDI matrices in that the

initiators do not absorb UV energy and most do not ionize, and thus do not produce interfering background ions. The advantages of the NIMS initiator are that the NIMS surface is stable in ambient air, has improved reproducibility, enables direct biofluid analysis and tissue imaging, and allows for a significantly expanded mass range [77]. In NIMS desorption/ ionization, the analyte is adsorbed on top of the NIMS surface and laser irradiation results in rapid surface heating the NIMS initiator to vaporize, triggering the desorption of adsorbed materials [76]. Several other MSI techniques have been developed more recently including infrared matrix-assisted laser desorption electrospray ionization (IR-MALDESI) [78-80], liquid extraction surface analysis (LESA) [81], and laser ablation electrospray ionization (LAESI) [82-86], but are beyond the scope of this review.

Neurotransmitters

Neurotransmitters are endogenous substances released by synaptic terminals upon depolarization to transmit signals between nerve cells [87, 88]. More than 100 substances have been identified as neurotransmitters since 1914, when the first neurotransmitter, acetylcholine, was discovered [89]. In the nervous system, neurotransmitters are the most common chemical messengers [90]. Neurotransmitters can be divided into six groups: acetylcholine, purines, amino acids, biogenic amines, peptides, and unconventional neurotransmitters. Except for peptides, all other neurotransmitters are considered to be small molecule neurotransmitters due to their smaller molecular weights (<1000 Da). Most small molecule neurotransmitters modulate activities requiring fast responses. Therefore, they are rapidly inactivated by highly specific transporter systems or enzymes in order to prevent continuous activation of the postsynaptic nerve cells [90]. Peptides and some small neurotransmitters tend to modulate slower and ongoing actions, and these neurotransmitters have slower turnover rates [87]. Due to differences in modes

of action, neuropeptides are sometimes considered to be neuromodulators or neurohormones. Neuropeptides with neurotransmitter functions are defined as putative neurotransmitters or co-transmitters [90].

Neurotransmitter MSI

Recently, many studies have successfully mapped the distributions of neurotransmitters using MSI by developing new sample preparation techniques, matrix application methods, ionization methods, and mass analyzers, which are summarized in **Table 2**. MSI studies of different classes of neurotransmitters are reviewed in the following sections.

MSI of Small Molecule Neurotransmitters

MSI of small molecule neurotransmitters is much more challenging than MSI of other biomolecules due to the following factors: 1) Conventional matrix compounds generate interference in the mass range of small molecules; 2) Small molecule neurotransmitters have rapid turnover rates, which introduces difficulties for MSI sample preparations; 3) Small molecule neurotransmitters have low *in vivo* concentrations, which requires a sensitive detection method. Despite the difficulties, several MSI studies have analyzed the distribution of small molecule neurotransmitters.

MSI of Acetylcholine

Acetylcholine acts as an excitatory transmitter to modulate motor systems in the CNS and PNS, except in the heart, where it acts as an inhibitory transmitter. Both DHB and CHCA, two common MALDI matrices used in small molecule profiling and imaging, produce strong interference for acetylcholine. Therefore, innovative MALDI matrices, high mass accuracy and

resolution mass analyzers or alternative data acquisition methods are needed to solve the matrix interference problem. Additionally, due to the rapid turnover rate of acetylcholine, a well-developed sample preparation procedure is needed to minimize postmortem degradation. Several recent studies have successfully detected endogenous acetylcholine in brain tissues [91-93].

Shariatgorji *et al.* developed a deuterated matrix, D^4-α-Cyano-4-hydroxycinnamic acid (D^4-CHCA), to solve the signal interference problem associated with small molecule MSI [93]. D^4-CHCA has mass shifts of +4, +8 and +12 Da. As shown in **Figure 1**, by switching between D^4-CHCA and CHCA, matrix peaks can be differentiated from acetylcholine as well as other small molecules. The distribution of acetylcholine was also confirmed by tandem MS with a characteristic fragmentation peak at *m/z* 87.0 [93]. Sugiura *et al.* developed a MSI method combining both tandem mass imaging and *in situ* freezing technique to visualize acetylcholine distribution in mouse brain [91]. In this study, acetylcholine transition signatures *m/z* 146 → 87 and *m/z* 146 → 92 were monitored to avoid matrix interference at the parent ion mass. The observed acetylcholine signal distribution at *m/z* 87 overlapped with the acetylcholinesterase *in situ* hybridization, proving the validity of this method. Furthermore, using *in situ* freezing technique, which freeze anesthetized mouse brain in liquid nitrogen during dissection, postmortem changes were minimized, dynamic range and sensitivity were improved [91].

The problem of matrix peaks interfering with the acetylcholine signal in MSI can also be solved by using high resolution and high accuracy mass analyzer. Ye *et al.* successfully mapped acetylcholine in rat brain tissue with standard DHB matrix with an LTQ Orbitrap mass analyzer [92]. The high resolving power of LTQ Orbitrap made it possible to separate acetylcholine peak from matrix peaks. Ye *et al.* have also mapped several other amino acid and biogenic amine neurotransmitters, such as histidine and AMP in rat and crab brain tissue using this method [92].

Figure 2 summarized the metabolites and neurotransmitters detected in rat brain tissue using MSI [92]. The successful detection of acetylcholine by MSI is very useful for biologists and neuroscientists to rapidly monitor the distribution and relative quantitation changes during various physiological states.

MSI of Purines

Purine neurotransmitters, including ATP, AMP, adenosine, and other purines, are small signaling molecules that contain purine rings. Most purines have similar molecular structures, similar molecular weights of 300-1000 Da, and similar *in situ* concentrations on the micromolar order of magnitude [94]. ATP was first thought to be a co-transmitter with an energy supply, but later found to have signal transmitting capability. It acts on spinal cord motor neurons and sensory and autonomic ganglia as an excitatory neurotransmitter. Adenosine, which is derived from ATP by enzymatic activities, is also widespread in the central nervous system as an excitatory neurotransmitter [87].

Similar to acetylcholine, MSI of purine neurotransmitters also faces the challenges of rapid turnover rates, low concentrations, and matrix interference. Nevertheless, several MSI studies have successfully mapped the distributions of purines, mainly ATP, ADP, and AMP, in brain tissues [7, 92, 94, 95].

Benabdellah *et al.* first reported the detection and identification of 13 primary metabolites including ADP, AMP, GTP, and UDP in rat brain sections using MALDI-TOF/TOF MSI [94]. Nine common MALDI matrices were tested on tissue surfaces in either positive or negative ion mode. Only 9-aminoacridine (9-AA) did not generate interfering matrix peaks on the target mass range (*m/z* 300-1000) under negative ion mode. A robotic sprayer was also used for matrix

application in order to generate a homogenous and thin layer of matrix, thus, improving reproducibility. However, the distribution of ATP was not detected in the tissue due to low abundance of ATP [94]. Hattori *et al.* developed a quantitative MSI technique for purines by combining *in situ* freezing, MALDI-MS, and quantitative capillary electrophoresis-electrospray ionization (CE-ESI)-MS on ischemic penumbra mouse brain samples [95]. In this study MSI results of samples prepared by *in situ* freezing and conventional postmortem freezing were compared. Both samples were coated with 9-AA and analyzed in negative ion mode. ATP could only be detected on *in situ* frozen samples as postmortem freezing reduced ATP autolysis. *In situ* metabolite concentrations were quantified in this study by parallel CE-ESI-MS experiments [95]. Sugiura *et al.* also utilized a similar quantitative MSI technique by combining MALDI-MSI with quantitative CE-ESI-MS for purines for monitoring spatiotemporal energy dynamics of hippocampal neurons in a kainite-induced seizure mouse model during the seizure process [7]. They reported the ATP depletion and recovery process, along with the changes in other metabolites in TCA cycle during the seizure using quantitative MSI. The successful detection and quantitation of purine neurotransmitters, especially ATP, not only allows researchers to monitor the changes of neurotransmitters, but also allows the observation of the energy consumption at different histological regions under different conditions.

MSI of Amino Acid Neurotransmitters

Amino acid neurotransmitters are individual amino acids that act as signaling molecules between neurons, including glutamate, γ-aminobutyric acid (GABA),glycine, D-serine and D-aspartate. Glutamate is the most common neurotransmitter in the CNS with an excitatory postsynaptic effect [96]. GABA is a common inhibitory neurotransmitter in the nervous system [97], although a recent study reported the existence of GABA excitatory synapses in the cerebellar

interneuron network [98]. Glycine is also a common, but more localized inhibitory neurotransmitter in the CNS, especially in the spinal cord. These amino acid neurotransmitters can be removed from the synaptic cleft via reuptake under the actions of various transporters [87]. For instance, GABA can be removed by the highly specific GABA transporters [90].

MSI of amino acid neurotransmitters also faces similar challenges as other small molecule neurotransmitters. Even though several studies have analyzed amino acid neurotransmitters in various nervous systems using gas chromatography [99], liquid chromatography [100], or microfluidic devices [101] coupled with ESI type mass spectrometers, few MSI studies have successfully visualized and quantified the distribution of amino acid neurotransmitters [92, 102-104].

Goto-Inoue *et al.* detected GABA (*m/z* 104.07) in eggplant by MALDI-MSI [102]. DHB was chosen as matrix and produced no interference at the target mass. No specific sample handling procedures or detection methods was used due to the higher concentration of GABA in eggplant when compared to the nervous system. Toue *et al.* visualized several amino acids in human colon cancer xenograft tissues using quantitative MSI, combining MALDI-MS with CE-ESI-MS [103]. Due to the low concentration of endogenous amino acids, *p*-*N*,*N*,*N*-trimethylammonioanilyl *N*'-hydroxysuccinimidyl carbamate iodide (TAHS) was applied on the surface of the tissue as a derivatization reagent to enhance ionization efficiency. Tandem MSI was used to solve the matrix interference problem. The rest of tissues were homogenized for quantitative CE-ESI-MS analysis. Several amino acids, including glutamate and glycine, were detected on the tissue surface by MALDI-MS and their concentrations were reported by CE-ESI-MS. Shariatgorji *et al*. has successfully quantified GABA brain concentrations by MALDI-MSI using their in-house imaging software [104]. In this study, a standard curve was established by

measuring GABA standard intensities with various concentrations on tissue surface; the GABA concentration on brain tissue could then be calculated from the standard curve. This method was also successfully applied to many other drugs and neurotransmitters such as acetylcholine and ATP.

MSI of Biogenic Amine Neurotransmitters

Biogenic amine neurotransmitters are small signaling molecules derived from amino acids [97]. Three catecholamine neurotransmitters: dopamine, epinephrine, and norepinephrine, are derived from tyrosine; histamine is derived from histidine and serotonin and 5-hydroxytryptamine (5-HT) are derived from tryptophan [87]. Dopamine plays an important role in modulation of arterial blood-flow, cognition, motor control and anxiety-related behavior [105]. Parkinson's disease is caused by a lack of dopamine in the brain [106]. Norepinephrine regulates sleep, attention, and feeding in both CNS and PNS, while epinephrine is mostly restricted to PNS [107]. Epinephrine and norepinephrine also act as hormones, regulating heart rate, respiratory rate, muscle contraction, and other actions. Histamine regulates attention and arousal and is also related to allergic reactions.. Serotonin works on CNS neurons that control circadian rhythm, emotions, and motor behaviors[87].

Similar to MSI of amino acid neurotransmitters, few studies have successfully performed MSI of biogenic amine neurotransmitters due to the previously mentioned challenges. Wu *et al.* detected epinephrine and norepinephrine in the adrenal gland of adult porcine by DESI-MSI, which is a matrix free method that avoids the matrix interference problem [108]. Recently, Shariatgorji *et al.* reported that dopamine was visualized and quantified by MALDI-MSI [104]. 2,4-diphenyl pyrylium (DPP) was used to derivatize dopamine, which could then be detected by

high sensitivity MALDI-MS using CHCA as matrix. The derivatized dopamine concentration on tissue could be determined by the in-house imaging software mentioned above.

MSI of Neuropeptides

Peptide neurotransmitters, or neuropeptides, such as substance P, endorphin and opioid peptides, are larger signaling molecules that are typically composed of 3-70 amino acids. They are derived from polypeptides, pre-propeptides and propeptides [87]. Substance P, the first discovered neuropeptide [58], is an excitatory neurotransmitter in pain perception. In contrast, endorphin is an inhibitory neurotransmitter in pain reduction and euphoria production [97]. Other neuropeptides are reported to be involved in anxiety, autism, and panic attacks [109-112]. Since the development of MSI for biological systems, MSI analysis of neuropeptides has been an intensive research topic and widely applied to various biological systems. MSI has been used to map the distribution of endogenous neuropeptides within the nervous systems of various organisms, including medicinal leech [113], terrestrial and fresh water snails [114, 115], sea slug *Aplysia californica* [116, 117], numerous species of crustaceans [29, 118-120] and rodents [121]. These MSI studies provide valuable information on the neuropeptide distributions and relative quantitation within various nervous systems, thus providing a new approach for neuroscience research in monitoring neuropeptidomic changes under different physiological conditions. Various ionization techniques have been used in neuropeptide MSI, such as MALDI, SIMS [121] and NIMS [122]; several advanced techniques have been developed for MSI , such as 3D MSI [123, 124] and quantitative MSI [125]. Additionally, MSI has been used for biomarker discovery studies in several disease models including Parkinson's disease [126], Alzheimer's disease [127], and cortical spreading depression [124]. Numerous excellent reviews and book chapters have summarized the MSI workflow, techniques, and applications to neuropeptides [47, 128-131]. Ye *et al.* used high-mass-resolution and high-mass-accuracy MALDI-

Fourier transform ion cyclotron resonance (FT-ICR) instrument to map neuropeptide distribution in the crustacean stomatogastric nervous system at cellular resolution [120]. Hanrieder *et al.* used MSI to study L-DOPA-induced dyskinesia in rat brain [126]. They noted elevated levels of neuropeptides including substance P and dynorphin B in the dorsolateral striatum of high-dyskinesia rats compared to control rats.

Challenges of Neurotransmitter MSI

Matrix Interference

Choosing an appropriate matrix and its application method is one of the main challenges in MALDI-MSI of small molecules, such as neurotransmitters, and there has been extensive method developments in this area. Conventional matrices produce matrix ions when the sample is ablated that potentially mask analyte ions in the low mass region (<500 Da). Some matrix application methods, such as manual airbrush, produce matrix crystals of varying sizes which leads to non-reproducible results. The use of solvent-based matrix application methods can also cause analyte diffusion when working with small molecules. As mentioned previously, Shariatgorji *et al.* developed a different strategy for reducing matrix interference by using a deuterated matrix [93]. The research group employed the traditional matrix, CHCA, but also synthesized a deuterated version, D^4-CHCA giving a 4, 8, or 12 Da mass shift of interfering matrix peaks between the two matrices. When these two matrices were used in conjunction, the mass shift characteristic of matrix interference allows analyte peaks in the lower mass range to be un-masked. In this work, the neurotransmitter, acetylcholine, was detected when employing D^4-CHCA, but was masked by matrix cluster peaks when employing traditional CHCA [93]; thus researchers were able to eliminate matrix interferences while still keeping the advantages of

CHCA ionization efficiency. Other strategies for eliminating matrix interference have been developed for small molecule MSI and could be applied to MSI of neurotransmitters in the future. For targeted analysis, Porta *et al.* demonstrated the use of MALDI-selected reaction monitoring (SRM)/MS [132]. Using this technique, the analyte was fragmented and several of the unique fragment ions were monitored; thus the matrix ions were no longer being detected and therefore did not interfere with the analyte signal. Recently, Tang *et al.* used solvent-free argon ion sputtering to apply gold nanoparticles to mouse brain tissue and were able to directly detect neurotransmitters and other small molecules via MALDI-MSI [133]. Argon ion sputtering is a solvent-free matrix application method that has been reported to produce a thin, even layer of matrix coating onto the sample surface [133]. The chemical interference from the gold nanoparticles was very minimal, thus alleviating the common problem of matrix ions masking analyte ions in the lower molecular weight region. Using this technique, the researchers were able to differentiate five unique regions of mouse tumor tissue based on the distributions of characteristic ions known to be metabolic markers of tumors. Water ice has been used as a matrix in infrared (IR)-MALDI-MS, but would be difficult to use on MS systems requiring high vacuum pressure, such as TOF instruments which are most commonly used for MALDI-MSI. Pirkl *et al.* employed a cooling stage to generate ions at high vacuum conditions using water ice as a matrix [134]. Ice is an ideal matrix for water-rich biological tissue because it produces matrix-ion-free spectra while still facilitating analyte ionization. Thus far, ice has been demonstrated as a suitable matrix for the detection of peptides, such as Substance P [134], from tissue sections with IR-MALDI-MS profiling. MSI has yet to be performed on tissue samples utilizing ice as the matrix. Another matrix-free imaging strategy was developed by Qian *et al.* [135]. In this research, a graphene paper was engineered using a pulse-laser process to form densely packed

nanospheres. This graphene paper was used as a substrate for matrix-free laser desorption/ionization (LDI)-MSI. This method is reported to enhance the detection of small molecules because the method used for engineering of this material creates a highly homogenous surface, eliminating the variability that is often seen when matrix is applied to the sample, producing more reliable and reproducible results.

Reproducibility in Sample Preparation

Aside from matrix selection and application, there are several other challenges of MALDI-MSI sample preparation that are being improved upon for enhanced MSI of small molecules (neurotransmitters) and neuropeptides. Consistency and reproducibility of techniques during sample preparation can be a challenge. Chang *et al.* developed a technique to obtain more reproducible sample preparations for SIMS-MSI of small molecules [136]. In this method, powerful magnets were used to fracture cells of interest. Typically cells are fractured via cryomicrotoming and freeze-fracture techniques that damage the cells and complicate SIMS-MSI results. By using powerful magnets to fracture the cells, the surface environment can be more controlled, which could provide more reproducible and reliable sample preparations. A comparison between the standard freeze-fracture technique and the powerful magnet method showing the differences in sample surface uniformity is shown in **Figure 3**. Another challenge in MSI of neurotransmitters is the low signal intensity cause by low abundance of analytes and/or signal suppression from other endogenous compounds in the tissue. Typically sample washing causes delocalization of small molecules and is therefore not part of the MSI workflow for neurotransmitters and small molecules. Shariatgorji *et al.* demonstrated a washing protocol with a pH-controlled buffer system for the enhanced detection of small molecules [137]. This approach can only be used for targeted analyses because the protocol employs an aqueous,

buffered wash solution with the pH adjusted to the point where the target analyte is insoluble. This washing step removes soluble, endogenous salts and other compounds that suppress signal, thus increasing the detection of small molecules. Goodwin *et al.* developed a method for stabilizing delicate tissue sections for MALDI-MSI [138]. Double-sided conductive carbon tape was used to collect, stabilize, and mount delicate, heat-treated rat brain tissue. Neuropeptides are rapidly modified post mortem; heat stabilization, as mentioned previously, can halt the post mortem degradation process, but can also result in more fragile tissues. Sectioning thin or delicate tissues using a cryostat can be challenging and may often result in tearing or folding of the tissue. The carbon tape did not interfere with the detection of small molecules or neuropeptides and could be used to reduce the variability in sample quality when attempting to section delicate tissues. The researchers used this method to detect and identify many endogenous compounds and show their unique distributions in a variety of rat tissues.

Quantitative MSI

The intensity of an MS signal related to the analyte's ionization efficiency as well as its concentration. With MALDI-MSI the smallest difference in matrix inhomogeneity can cause signal suppression and inaccurate quantitation. One technique that is being used for quantitative imaging is multi-isotope imaging mass spectrometry (MIMS) which has been reviewed previously [139]. Steinhauser *et al.* demonstrate this technique for the quantification of stem cell division and metabolism on the sub-micrometer scale [140]. MIMS is based on SIMS technology. The instrument can simultaneously measure data from multiple isotopes in the same region of the tissue. MIMS uses isotopic tags to localize and measure their incorporation into intracellular compartments and quantitative data is extracted based on the isotope ratios [141]. The research team used MIMS to test the "immortal strand hypothesis" which predicts that during stem cell

division, chromosomes containing older template DNA are segregated to the daughter cell destined to remain a stem cell. When the isotopic tag was introduced, if the hypothesis held true, there would be one completely unlabeled daughter cell after the first cell division. The results showed no unlabeled daughter cells and thus do not support the "immortal strand hypothesis". Reviews specifically focused on quantitative MSI have recently been published [13, 15, 139]. Another, more typical, approach to quantitative MSI employs an internal standard for quantification, which involves generating a standard curve by measuring standards spotted on the tissue surface, and calculating the concentration of the analyte in the tissue based on this standard curve [104]. Pirman *et al.* quantified cocaine from brain tissue using MALDI-MSI by employing deuterated cocaine as the internal standard [142]. In order to limit the background interference during the experiment, MS/MS MSI was performed with a wide isolation window to incorporate the analyte and the deuterated internal standard. A calibration curve was generated using control tissue and used to determine concentrations of the analyte. The quantitative MSI data were compared to quantitative LC-MS/MS and the results were comparable. Furthermore, several semi-quantitative studies have been successfully conducted [126, 143-150]. Recently new software tools have been developed to aid in quantitative MSI and will be discussed below.

Low Mass Resolution and Spatial Resolution of MSI Instruments

The main, on-going challenges for MSI instrumentation are obtaining faster acquisition speeds and higher spatial and chemical resolution. Spraggins and Caprioli report high-speed MALDI-MSI using a prototype time-of-flight (TOF) mass spectrometer [151]. This work incorporates a Nd:YLF solid state laser capable of repetition rates up to 5 kHz which reportedly produce more than a 10-fold increase in sample throughput when compared to commercially available instruments. This technique was applied to MSI of lipids, but should translate to MSI

of other chemical species including other small molecules or peptides. As mentioned previously, Ye *et al.* focused on increased mass resolution of MSI experiments [92]. High-resolution and high-accuracy mass spectrometry (HRMS) is able to distinguish analytes from interfering matrix ions. In this study, Ye *et al.* performed MALDI-MSI of neurotransmitters in rodent and crustacean nervous systems and were able to resolve peaks that were merged in lower resolution TOF/TOF instruments. Schober *et al.* tackled the problem of high-spatial resolution imaging, while still maintaining high mass accuracy and high mass resolution [152]. In this work, HeLa cells were imaged with optical fluorescence imaging and with a high resolution atmospheric-pressure (AP)-MALDI source attached to an Exactive Orbitrap mass spectrometer. A spatial resolution of 7 μm was achieved in this work as shown in **Figure 4**.

Data Processing

MSI data analysis software, such as BioMap (http://www.maldi-msi.org) and proprietary programs for MSI systems (e.g., FlexImaging from Bruker Daltonics, ImageQuest from Thermo Fisher Scientific and TissueView from Applied Biosystems/MDS), are primarily used to produce distribution maps for selected analytes. These software packages have different features but mostly allow the user to adjust color scales, overlay ion density maps, and integrate MS images with acquired histological pictures. MSI data typically requires manual extraction of ion images, which can be extremely time-consuming for large-scale analyses, such as untargeted studies. Paschke *et al.* have developed a free software package, called Mirion, for automatic processing of MS images [153]. With Mirion, the user selects an *m/z* range of interest and the software creates the ion images. Manual image generation is also available with Mirion, since no software algorithm is as good as the eye of the mass spectrometry expert. The capabilities of this software were demonstrated using peptide standards and tissue from mice. Another open-source MSI data

processing software has been developed, called MSiReader [154]. This software allows the user to select a region of interest and a reference region. The software can generate a mass list of compounds found in the region of interest, excluding peaks in the reference region. The created mass list, or a manually made mass list, can then be imported and an ion imaged will be extracted for every ion in the list. Software such as Mirion and MSiReader significantly improve MSI data processing in comparison to manual processing by drastically decreasing the amount of time it takes to work through a data set. Recently, software tools have been developed for quantitation of analytes from MSI data, such as Quantinetix from ImaBiotech. Källback *et al.* have developed a novel MSI software for labeled quantitation and normalization of endogenous neuropeptides [125] . Shariatgorji *et al*. have developed in-house software for MSI quantitation based on signal intensities. This software can be used to define region on interest, process spectra, normalize spectra and quantify analytes based on pre-established calibration curves. Several neurotransmitters, drugs and neuropeptides have been successfully quantified using this software [104].

Conclusions

Over the past decade, MSI has obtained increasing attention from biologists and become more routinely employed to map various classes of biomolecules from biological specimen. Its novel applications to the study of neurotransmitters and neuropeptides have provided valuable knowledge regarding disease mechanisms and related reparative processes. These studies offer significant insights into neurobiology and hold promise for our continuous search of effective treatment for diseases. We anticipate MSI for neurotransmitter mapping will lead to a better understanding of the biology of neurological diseases and improvements in clinical diagnostics.

Future Perspectives

Exciting technical advances are further improving the capabilities of MSI for biological applications from various aspects such as sample preparation and instrumentation. The development and use of novel matrices and matrix-free imaging techniques along with improvements in sample preparation are generating more reproducible, clean, and reliable results with improved analyte detection. The advancements in instrumentation for shorter acquisition times are increasing the throughput of MSI techniques, making MSI more applicable to large-scale study of complex biological systems. The improved mass accuracy, mass resolution, and spatial resolution are exciting developments that could greatly enhance the sensitivity of MSI and make this technique capable of studying biological problems on a cellular scale. Data processing and analysis is the current bottle-neck of MSI, but progress is certainly being made in this area. Again, once software becomes commercially available and used enough to inspire confident, reliable results, MSI has the potential to be a powerful analytical tool, expanding into many new areas of research and industries.

Executive Summary

- 6.1 Small Molecule Neurotransmitter MSI
    - MSI of small molecules is challenging due to matrix interference, rapid turnover rate and low in situ concentration. Innovative MSI techniques such as *in situ* freezing, novel matrices and matrix free techniques, high resolution and high mass accuracy mass analyzer have been used to overcome these difficulties.
- 6.2 Neuropeptide MSI

    - MSI of neuropeptides is well developed and widely applied to many species and disease states. Advanced MSI techniques such as 3D imaging and quantitative imaging have been developed to further improve neuropeptide detection and visualization.

- 6.3 Novel Matrices
    - Advancements in the use of novel matrices and matrix-free methods enhance signal detection and produce cleaner spectra in the low mass region which will allow for improved metabolomics and small molecule studies.
- 6.4 Sample Preparation
    - Challenges in sample preparation are being solved in novel ways, leading to more reproducible results that could even turn MSI into a quantitative technique.
- 6.5 Data Processing
    - There have been several recent advances for improved mass resolution, spatial resolution, acquisition time, and data processing. Making these advancements commercially available could produce significant progress in many different fields of study.

Acknowledgements

Preparation of this manuscript was supported in part by National Science Foundation (NSF CHE- 0957784) and National Institutes of Health through grant 1R01DK071801. E.G. acknowledges an NSF Graduate Research Fellowship (DGE-1256259). L.L. acknowledges an H. I. Romnes Faculty Fellowship.

References

[1] Balluff, B., Schone, C., Hofler, H., and Walch, A. (2011) MALDI imaging mass spectrometry for direct tissue analysis: technological advancements and recent applications, *Histochem Cell Biol 136*, 227-244.

[2] Ye, H., Gemperline, E., Venkateshwaran, M., Chen, R., Delaux, P. M., Howes-Podoll, M., Ane, J. M., and Li, L. (2013) MALDI mass spectrometry-assisted molecular imaging of metabolites during nitrogen fixation in the Medicago truncatula-Sinorhizobium meliloti symbiosis, *The Plant journal : for cell and molecular biology 75*, 130-145.

[3] Burnum, K. E., Cornett, D. S., Puolitaival, S. M., Milne, S. B., Myers, D. S., Tranguch, S., Brown, H. A., Dey, S. K., and Caprioli, R. M. (2009) Spatial and temporal alterations of phospholipids determined by mass spectrometry during mouse embryo implantation, *J Lipid Res 50*, 2290-2298.

[4] Yanagisawa, K., Shyr, Y., Xu, B. G. J., Massion, P. P., Larsen, P. H., White, B. C., Roberts, J. R., Edgerton, M., Gonzalez, A., Nadaf, S., Moore, J. H., Caprioli, R. M., and Carbone, D. P. (2003) Proteomic patterns of tumour subsets in non-small-cell lung cancer, *Lancet 362*, 433-439.

[5] Skold, K., Svensson, M., Nilsson, A., Zhang, X. Q., Nydahl, K., Caprioli, R. M., Svenningsson, P., and Andren, P. E. (2006) Decreased striatal levels of PEP-19 following MPTP lesion in the mouse, *Journal of proteome research 5*, 262-269.

[6] Stauber, J., Lemaire, R., Franck, J., Bonnel, D., Croix, D., Day, R., Wisztorski, M., Fournier, I., and Salzet, M. (2008) MALDI Imaging of formalin-fixed paraffin-embedded tissues: Application to model animals of Parkinson disease for biomarker hunting, *Journal of proteome research 7*, 969-978.

[7] Sugiura, Y., Taguchi, R., and Setou, M. (2011) Visualization of spatiotemporal energy dynamics of hippocampal neurons by mass spectrometry during a kainate-induced seizure, *PloS one 6*, e17952.

[8] Chatterji, B., and Pich, A. (2013) MALDI imaging mass spectrometry and analysis of endogenous peptides, *Expert Rev Proteomic 10*, 381-388.

[9] Hanrieder, J., Phan, N. T. N., Kurczy, M. E., and Ewing, A. G. (2013) Imaging Mass Spectrometry in Neuroscience, *Acs Chem Neurosci 4*, 666-679.

[10] Goodwin, R. J. A. (2012) Sample preparation for mass spectrometry imaging: Small mistakes can lead to big consequences, *J Proteomics 75*, 4893-4911.

[11] Jones, E. A., Deininger, S. O., Hogendoorn, P. C. W., Deelder, A. M., and McDonnell, L. A. (2012) Imaging mass spectrometry statistical analysis, *J Proteomics 75*, 4962-4989.

[12] Gilmore, I. S. (2013) SIMS of organics-Advances in 2D and 3D imaging and future outlook, *J Vac Sci Technol A 31*.

[13] Lietz, C. B., Gemperline, E., and Li, L. (2013) Qualitative and quantitative mass spectrometry imaging of drugs and metabolites, *Advanced drug delivery reviews 65*, 1074-1085.

[14] Nimesh, S., Mohottalage, S., Vincent, R., and Kumarathasan, P. (2013) Current Status and Future Perspectives of Mass Spectrometry Imaging, *Int J Mol Sci 14*, 11277-11301.

[15] Sun, N., and Walch, A. (2013) Qualitative and quantitative mass spectrometry imaging of drugs and metabolites in tissue at therapeutic levels, *Histochem Cell Biol 140*, 93-104.

[16] Weaver, E. M., and Hummon, A. B. (2013) Imaging mass spectrometry: From tissue sections to cell cultures, *Advanced drug delivery reviews 65*, 1039-1055.

[17] Norris, J. L., and Caprioli, R. M. (2013) Analysis of Tissue Specimens by Matrix-Assisted Laser Desorption/Ionization Imaging Mass Spectrometry in Biological and Clinical Research, *Chem Rev 113*, 2309-2342.

[18] Karas, M., and Hillenkamp, F. (1988) Laser Desorption Ionization of Proteins with Molecular Masses Exceeding 10000 Daltons, *Anal Chem 60*, 2299-2301.

[19] Caprioli, R. M., Farmer, T. B., and Gile, J. (1997) Molecular imaging of biological samples: Localization of peptides and proteins using MALDI-TOF MS, *Anal Chem 69*, 4751-4760.

[20] Liebl, H. (1967) Ion Microprobe Mass Analyzer, *Journal of Applied Physics 38*, 5277-5283.

[21] Brown, A., and Vickerman, J. C. (1984) Static Sims, Fabms and Sims Imaging in Applied Surface-Analysis, *Analyst 109*, 851-&.

[22] Cliff, B., Lockyer, N. P., Corlett, C., and Vickerman, J. C. (2003) Development of instrumentation for routine ToF-SIMS imaging analysis of biological material, *Appl Surf Sci 203*, 730-733.

[23] Wiseman, J. M., Ifa, D. R., Song, Q. Y., and Cooks, R. G. (2006) Tissue imaging at atmospheric pressure using desorption electrospray ionization (DESI) mass spectrometry, *Angew Chem Int Edit 45*, 7188-7192.

[24] Takats, Z., Wiseman, J. M., and Cooks, R. G. (2005) Ambient mass spectrometry using desorption electrospray ionization (DESI): instrumentation, mechanisms and applications in forensics, chemistry, and biology, *J Mass Spectrom 40*, 1261-1275.

[25] Cazares, L. H., Troyer, D., Mendrinos, S., Lance, R. A., Nyalwidhe, J. O., Beydoun, H. A., Clements, M. A., Drake, R. R., and Semmes, O. J. (2009) Imaging mass spectrometry of a specific fragment of mitogen-activated protein kinase/extracellular signal-regulated kinase kinase kinase 2 discriminates cancer from uninvolved prostate tissue, *Clin Cancer Res 15*, 5541-5551.

[26] Deininger, S. O., Ebert, M. P., Futterer, A., Gerhard, M., and Rocken, C. (2008) MALDI imaging combined with hierarchical clustering as a new tool for the interpretation of complex human cancers, *Journal of proteome research 7*, 5230-5236.

[27] Murphy, R. C., Hankin, J. A., and Barkley, R. M. (2009) Imaging of lipid species by MALDI mass spectrometry, *J Lipid Res 50*, S317-S322.

[28] Chen, R., Hui, L., Sturm, R. M., and Li, L. (2009) Three dimensional mapping of neuropeptides and lipids in crustacean brain by mass spectral imaging, *Journal of the American Society for Mass Spectrometry 20*, 1068-1077.

[29] DeKeyser, S. S., Kutz-Naber, K.K., Schmidt, J.J., Barrett-Wilt, G.A.and Li, L. (2007) Mass spectral imaging of neuropeptides in decapod crustacean neronal tissues, *Journal of proteome research 6*, 1782-1791.

[30] Chang, W. C., Huang, L. C. L., Wang, Y. S., Peng, W. P., Chang, H. C., Hsu, N. Y., Yang, W. B., and Chen, C. H. (2007) Matrix-assisted laser desorption/ionization (MALDI) mechanism revisited, *Analytica Chimica Acta 582*, 1-9.

[31] Karas, M., and Kruger, R. (2003) Ion formation in MALDI: The cluster ionization mechanism, *Chem Rev 103*, 427-439.

[32] Knochenmuss, R. (2003) A quantitative model of ultraviolet matrix-assisted laser desorption/ionization including analyte ion generation, *Anal Chem 75*, 2199-2207.

[33] Verhaert, P. D. E. M., Pinkse, M. W. H., Strupat, K., and Conaway, M. C. P. (2010) Imaging of similar mass neuropeptides in neuronal tissue by enhanced resolution MALDI MS with an ion trap-orbitrap$^{(TM)}$ hybrid instrument, *Methods Mol Biol 656*, 433-449.

[34] Schwartz, S. A., Reyzer, M. L., and Caprioli, R. M. (2003) Direct tissue analysis using matrix-assisted laser desorption/ionization mass spectrometry: practical aspects of sample preparation, *J Mass Spectrom 38*, 699-708.

[35] Jehl, B., Bauer, R., Dorge, A., and Rick, R. (1981) The use of propane-isopentane mixtures for rapid freezing of biological specimens, *Journal of Microscopy-Oxford 123*, 307-309.

[36] Che, F. Y., Lim, J., Pan, H., Biswas, R., and Fricker, L. D. (2005) Quantitative neuropeptidomics of microwave-irradiated mouse brain and pituitary, *Mol Cell Proteomics 4*, 1391-1405.

[37] Svensson, M., Boren, M., Skold, K., Falth, M., Sjogren, B., Andersson, M., Svenningsson, P., and Andren, P. E. (2009) Heat stabilization of the tissue proteome: a new technology for improved proteomics, *Journal of proteome research 8*, 974-981.

[38] Rountree, C. B., Van Kirk, C. A., You, H. N., Ding, W., Dang, H., VanGuilder, H. D., and Freeman, W. M. (2010) Clinical application for the preservation of phosphoproteins through in-situ tissue stabilization, *Proteome Sci 8*.

[39] Sturm, R. M., Greer, T., Woodards, N., Gemperline, E., and Li, L. J. (2013) Mass Spectrometric Evaluation of Neuropeptidomic Profiles upon Heat Stabilization Treatment of Neuroendocrine Tissues in Crustaceans, *Journal of proteome research 12*, 743-752.

[40] Crossman, L., McHugh, N. A., Hsieh, Y. S., Korfmacher, W. A., and Chen, J. W. (2006) Investigation of the profiling depth in matrix-assisted laser desorption/ionization imaging mass spectrometry, *Rapid Commun Mass Sp 20*, 284-290.

[41] Chaurand, P., Fouchecourt, S., DaGue, B. B., Xu, B. G. J., Reyzer, M. L., Orgebin-Crist, M. C., and Caprioli, R. M. (2003) Profiling and imaging proteins in the mouse epididymis by imaging mass spectrometry, *Proteomics 3*, 2221-2239.

[42] Chaurand, P., Schriver, K. E., and Caprioli, R. M. (2007) Instrument design and characterization for high resolution MALDI-MS imaging of tissue sections, *J Mass Spectrom 42*, 476-489.

[43] Kaletas, B. K., van der Wiel, I. M., Stauber, J., Dekker, L. J., Guzel, C., Kros, J. M., Luider, T. M., and Heeren, R. M. A. (2009) Sample preparation issues for tissue imaging by imaging MS, *Proteomics 9*, 2622-2633.

[44] Lemaire, R., Wisztorski, M., Desmons, A., Tabet, J. C., Day, R., Salzet, M., and Fournier, I. (2006) MALDI-MS direct tissue analysis of proteins: improving signal sensitivity using organic treatments, *Anal Chem 78*, 7145-7153.

[45] Seeley, E. H., Oppenheimer, S. R., Mi, D., Chaurand, P., and Caprioli, R. M. (2008) Enhancement of protein sensitivity for MALDI imaging mass spectrometry after chemical treatment of tissue sections, *Journal of the American Society for Mass Spectrometry 19*, 1069-1077.

[46] Tanaka, K., Waki, H., Ido, Y., Akita, S., Yoshida, Y., Yoshida, T., and Matsuo, T. (1988) Protein and polymer analyses up to m/z 100000 by laser ionization time-of-flight mass spectrometry, *Rapid Commun Mass Sp 2*, 151-153.

[47] Ye, H., Gemperline, E., and Li, L. (2013) A vision for better health: mass spectrometry imaging for clinical diagnostics, *Clinica chimica acta; international journal of clinical chemistry 420*, 11-22.

[48] Fitzgerald, J. J. D., Kunnath, P., and Walker, A. V. (2010) Matrix-enhanced secondary ion mass spectrometry (ME-SIMS) using room temperature ionic liquid matrices, *Anal Chem 82*, 4413-4419.

[49] Lemaire, R., Tabet, J. C., Ducoroy, P., Hendra, J. B., Salzet, M., and Fournier, I. (2006) Solid ionic matrixes for direct tissue analysis and MALDI Imaging, *Anal Chem 78*, 809-819.

[50] Shrivas, K., Hayasaka, T., Sugiura, Y., and Setou, M. (2011) Method for simultaneous imaging of endogenous low molecular weight metabolites in mouse brain using TiO2 nanoparticles in nanoparticle-assisted laser desorption/ionization-imaging mass spectrometry, *Anal Chem 83*, 7283-7289.

[51] Thomas, A., Charbonneau, J. L., Fournaise, E., and Chaurand, P. (2012) Sublimation of new matrix candidates for high spatial resolution imaging mass spectrometry of lipids:

enhanced information in both positive and negative polarities after 1,5-diaminonapthalene deposition, *Anal Chem 84*, 2048-2054.

[52] Chen, S., Chen, L., Wang, J., Hou, J., He, Q., Liu, J., Xiong, S., Yang, G., and Nie, Z. (2012) 2,3,4,5-Tetrakis(3',4'-dihydroxylphenyl)thiophene: a new matrix for the selective analysis of low molecular weight amines and direct determination of creatinine in urine by MALDI-TOF MS, *Anal Chem 84*, 10291-10297.

[53] Shroff, R., Rulisek, L., Doubsky, J., and Svatos, A. (2009) Acid-base-driven matrix-assisted mass spectrometry for targeted metabolomics, *Proc Natl Acad Sci U S A 106*, 10092-10096.

[54] Shroff, R., and Svatos, A. (2009) Proton sponge: a novel and versatile MALDI matrix for the analysis of metabolites using mass spectrometry, *Anal Chem 81*, 7954-7959.

[55] Mainini, V., Bovo, G., Chinello, C., Gianazza, E., Grasso, M., Cattoretti, G., and Magni, F. (2013) Detection of high molecular weight proteins by MALDI imaging mass spectrometry, *Molecular Biosystems 9*, 1101-1107.

[56] Baluya, D. L., Garrett, T. J., and Yost, R. A. (2007) Automated MALDI matrix deposition method with inkjet printing for imaging mass spectrometry, *Anal Chem 79*, 6862-6867.

[57] Hankin, J. A., Barkley, R. M., and Murphy, R. C. (2007) Sublimation as a method of matrix application for mass spectrometric imaging, *Journal of the American Society for Mass Spectrometry 18*, 1646-1652.

[58] Puolitaival, S. M., Burnum, K. E., Cornett, D. S., and Caprioli, R. M. (2008) Solvent-free matrix dry-coating for MALDI Imaging of phospholipids, *Journal of the American Society for Mass Spectrometry 19*, 882-886.

[59] Trimpin, S., Herath, T. N., Inutan, E. D., Wager-Miller, J., Kowalski, P., Claude, E., Walker, J. M., and Mackie, K. (2010) Automated Solvent-Free Matrix Deposition for Tissue Imaging by Mass Spectrometry, *Anal Chem 82*, 359-367.

[60] Troendle, F. J., Reddick, C. D., and Yost, R. A. (1999) Detection of pharmaceutical compounds in tissue by matrix-assisted laser desorption/ionization and laser desorption/chemical ionization tandem mass spectrometry with a quadrupole ion trap, *Journal of the American Society for Mass Spectrometry 10*, 1315-1321.

[61] Deutskens, F., Yang, J. H., and Caprioli, R. M. (2011) High spatial resolution imaging mass spectrometry and classical histology on a single tissue section, *J Mass Spectrom 46*, 568-571.

[62] Fletcher, J. S., Lockyer, N. P., and Vickerman, J. C. (2011) Developments in molecular SIMS depth profiling and 3D imaging of biological systems using polyatomic primary ions, *Mass Spectrometry Reviews 30*, 142-174.

[63] Liebl, H. (1980) Sims Instrumentation and Imaging Techniques, *Scanning 3*, 79-89.

[64] Touboul, D., Halgand, F., Brunelle, A., Kersting, R., Tallarek, E., Hagenhoff, B., and Laprevote, O. (2004) Tissue molecular ion imaging by gold cluster ion bombardment, *Anal Chem 76*, 1550-1559.

[65] Jones, E. A., Lockyer, N. P., and Vickerman, J. C. (2007) Mass spectral analysis and imaging of tissue by ToF-SIMS - The role of buckminsterfullerene, C-60(+), primary ions, *International Journal of Mass Spectrometry 260*, 146-157.

[66] Keune, K., and Boon, J. J. (2004) Enhancement of the static SIMS secondary ion yields of lipid moieties by ultrathin gold coating of aged oil paint surfaces, *Surface and Interface Analysis 36*, 1620-1628.

[67] Nygren, H., Malmberg, P., Kriegeskotte, C., and Arlinghaus, H. F. (2004) Bioimaging TOF-SIMS: localization of cholesterol in rat kidney sections, *Febs Letters 566*, 291-293.

[68] Adriaensen, L., Vangaever, F., Lenaerts, J., and Gijbels, R. (2005) Matrix-enhanced secondary ion mass spectrometry: the influence of MALDI matrices on molecular ion yields of thin organic films, *Rapid Commun Mass Sp 19*, 1017-1024.

[69] Dill, A. L., Eberlin, L. S., Costa, A. B., Zheng, C., Ifa, D. R., Cheng, L. A., Masterson, T. A., Koch, M. O., Vitek, O., and Cooks, R. G. (2011) Multivariate statistical identification of human bladder carcinomas using ambient ionization imaging mass spectrometry, *Chemistry-a European Journal 17*, 2897-2902.

[70] Gao, Y. H., Yang, C. H., Liu, X., Ma, R. J., Kong, D. L., and Shi, L. Q. (2012) A multifunctional nanocarrier based on nanogated mesoporous silica for enhanced tumor-specific uptake and intracellular delivery, *Macromolecular Bioscience 12*, 251-259.

[71] Laskin, J., Heath, B. S., Roach, P. J., Cazares, L., and Semmes, O. J. (2012) Tissue imaging using nanospray desorption electrospray ionization mass spectrometry, *Anal Chem 84*, 141-148.

[72] Vismeh, R., Waldon, D. J., Teffera, Y., and Zhao, Z. Y. (2012) Localization and quantification of drugs in animal tissues by use of desorption electrospray ionization mass spectrometry imaging, *Anal Chem 84*, 5439-5445.

[73] Takats, Z., Wiseman, J. M., Gologan, B., and Cooks, R. G. (2004) Mass spectrometry sampling under ambient conditions with desorption electrospray ionization, *Science 306*, 471-473.

[74] Ifa, D. R., Wu, C. P., Ouyang, Z., and Cooks, R. G. (2010) Desorption electrospray ionization and other ambient ionization methods: current progress and preview, *Analyst 135*, 669-681.

[75] Cooks, R. G., Manicke, N. E., Dill, A. L., Ifa, D. R., Eberlin, L. S., Costa, A. B., Wang, H., Huang, G. M., and Zheng, O. Y. (2011) New ionization methods and miniature mass spectrometers for biomedicine: DESI imaging for cancer diagnostics and paper spray ionization for therapeutic drug monitoring, *Faraday Discuss 149*, 247-267.

[76] Northen, T. R., Yanes, O., Northen, M. T., Marrinucci, D., Uritboonthai, W., Apon, J., Golledge, S. L., Nordstrom, A., and Siuzdak, G. (2007) Clathrate nanostructures for mass spectrometry, *Nature 449*, 1033-U1033.

[77] Greving, M. P., Patti, G. J., and Siuzdak, G. (2011) Nanostructure-Initiator Mass Spectrometry Metabolite Analysis and Imaging, *Anal Chem 83*, 2-7.

[78] Robichaud, G., Barry, J. A., Garrard, K. P., and Muddiman, D. C. (2013) Infrared Matrix-Assisted Laser Desorption Electrospray Ionization (IR-MALDESI) Imaging Source Coupled to a FT-ICR Mass Spectrometer, *Journal of the American Society for Mass Spectrometry 24*, 92-100.

[79] Sampson, J. S., Hawkridge, A. M., and Muddiman, D. C. (2006) Generation and detection of multiply-charged peptides and proteins by matrix-assisted laser desorption electrospray ionization (MALDESI) Fourier transform ion cyclotron resonance mass spectrometry, *Journal of the American Society for Mass Spectrometry 17*, 1712-1716.

[80] Sampson, J. S., Hawkridge, A. M., and Muddiman, D. C. (2008) Construction of a Versatile High Precision Ambient Ionization Source for Direct Analysis and Imaging, *Journal of the American Society for Mass Spectrometry 19*, 1527-1534.

[81] Eikel, D., Vavrek, M., Smith, S., Bason, C., Yeh, S., Korfmacher, W. A., and Henion, J. D. (2011) Liquid extraction surface analysis mass spectrometry (LESA-MS) as a novel profiling tool for drug distribution and metabolism analysis: the terfenadine example, *Rapid Commun Mass Sp 25*, 3587-3596.

[82] Nemes, P., Barton, A. A., Li, Y., and Vertes, A. (2008) Ambient molecular imaging and depth profiling of live tissue by infrared laser ablation electrospray ionization mass spectrometry, *Anal Chem 80*, 4575-4582.

[83] Nemes, P., Barton, A. A., and Vertes, A. (2009) Three-Dimensional Imaging of Metabolites in Tissues under Ambient Conditions by Laser Ablation Electrospray Ionization Mass Spectrometry, *Anal Chem 81*, 6668-6675.

[84] Nemes, P., and Vertes, A. (2007) Laser ablation electrospray ionization for atmospheric pressure, in vivo, and imaging mass spectrometry, *Anal Chem 79*, 8098-8106.

[85] Nemes, P., and Vertes, A. (2010) Laser Ablation Electrospray Ionization for Atmospheric Pressure Molecular Imaging Mass Spectrometry, *Methods Mol Biol 656*, 159-171.

[86] Nemes, P., Woods, A. S., and Vertes, A. (2010) Simultaneous Imaging of Small Metabolites and Lipids in Rat Brain Tissues at Atmospheric Pressure by Laser Ablation Electrospray Ionization Mass Spectrometry, *Anal Chem 82*, 982-988.

[87] Purves, D. (2012) *Neuroscience*, 5th ed., Sinauer Associates, Sunderland, Mass.

[88] Werman, R. (1966) Criteria for Identification of a Central Nervous System Transmitter, *Comp Biochem Physiol 18*, 745-&.

[89] Fishman, M. C. (1972) Sir Henry Hallett Dale and acetylcholine story, *Yale J Biol Med 45*, 104-118.

[90] von Bohlen und Halboch, O., and Dermietzel, R. (2006) *Neurotransmitters and Neuromodulators: Handbook of Receptors and Biological Effects*, 2 ed.

[91] Sugiura, Y., Zaima, N., Setou, M., Ito, S., and Yao, I. (2012) Visualization of acetylcholine distribution in central nervous system tissue sections by tandem imaging mass spectrometry, *Anal Bioanal Chem 403*, 1851-1861.

[92] Ye, H., Wang, J., Greer, T., Strupat, K., and Li, L. (2013) Visualizing Neurotransmitters and Metabolites in the Central Nervous System by High Resolution and High Accuracy Mass Spectrometric Imaging, *Acs Chem Neurosci 4*, 1049-1056.

[93] Shariatgorji, M., Nilsson, A., Goodwin, R. J., Svenningsson, P., Schintu, N., Banka, Z., Kladni, L., Hasko, T., Szabo, A., and Andren, P. E. (2012) Deuterated matrix-assisted laser desorption ionization matrix uncovers masked mass spectrometry imaging signals of small molecules, *Anal Chem 84*, 7152-7157.

[94] Benabdellah, F., Touboul, D., Brunelle, A., and Laprevote, O. (2009) In situ primary metabolites localization on a rat brain section by chemical mass spectrometry imaging, *Anal Chem 81*, 5557-5560.

[95] Hattori, K., Kajimura, M., Hishiki, T., Nakanishi, T., Kubo, A., Nagahata, Y., Ohmura, M., Yachie-Kinoshita, A., Matsuura, T., Morikawa, T., Nakamura, T., Setou, M., and Suematsu, M. (2010) Paradoxical ATP elevation in ischemic penumbra revealed by quantitative imaging mass spectrometry, *Antioxid Redox Signal 13*, 1157-1167.

[96] Curtis, D. R., Phillis, J. W., and Watkins, J. C. (1959) Chemical excitation of spinal neurones, *Nature 183*, 611-612.

[97] Reece, J. B., and Campbell, N. A. (2011) *Campbell biology / Jane B. Reece [et al.]*, 9th ed., Benjamin Cummings / Pearson, Boston.

[98] Chavas, J., and Marty, A. (2003) Coexistence of excitatory and inhibitory GABA synapses in the cerebellar interneuron network, *J Neurosci 23*, 2019-2031.

[99] Kondrat, R. W., Kanamori, K., and Ross, B. D. (2002) In vivo microdialysis and gas-chromatography/mass-spectrometry for 13C-enrichment measurement of extracellular glutamate in rat brain, *J Neurosci Methods 120*, 179-192.

[100] Buck, K., Voehringer, P., and Ferger, B. (2009) Rapid analysis of GABA and glutamate in microdialysis samples using high performance liquid chromatography and tandem mass spectrometry, *J Neurosci Methods 182*, 78-84.

[101] Wei, H., Li, H., Gao, D., and Lin, J. M. (2010) Multi-channel microfluidic devices combined with electrospray ionization quadrupole time-of-flight mass spectrometry applied to the monitoring of glutamate release from neuronal cells, *Analyst 135*, 2043-2050.

[102] Goto-Inoue, N., Setou, M., and Zaima, N. (2010) Visualization of spatial distribution of gamma-aminobutyric acid in eggplant (Solanum melongena) by matrix-assisted laser desorption/ionization imaging mass spectrometry, *Anal Sci 26*, 821-825.

[103] Toue, S., Sugiura, Y., Kubo, A., Ohmura, M., Karakawa, S., Mizukoshi, T., Yoneda, J., Miyano, H., Noguchi, Y., Kobayshi, T., Kabe, Y., and Suematsu, M. (2013) Microscopic imaging mass spectrometry assisted by on-tissue chemical derivatization for visualizing multiple amino acids in human colon cancer xenografts, *Proteomics*.

[104] Shariatgorji, M., Nilsson, A., Goodwin, R., Zhang, X., Schintu, N., Svenningsson, P., and Andren, P. E. (2013) MALDI-MS imaging and quantitation of primary amine neurotransmitters dopamine, GABA and glutamate directly in brain tissue sections, In *2013 American Society for Mass Spectrometry Annual Conference*, Minneapolis, MN.

[105] Bannon, M. J. (2005) The dopamine transporter: role in neurotoxicity and human disease, *Toxicol Appl Pharm 204*, 355-360.

[106] Greer, M., and Williams, C. M. (1963) Dopamine metabolism in Parkinson's disease, *Neurology 13*, 73-76.

[107] Berecek, K. H., and Brody, M. J. (1982) Evidence for a neurotransmitter role for epinephrine derived from the adrenal medulla, *Am J Physiol 242*, H593-601.

[108] Wu, C., Ifa, D. R., Manicke, N. E., and Cooks, R. G. (2010) Molecular imaging of adrenal gland by desorption electrospray ionization mass spectrometry, *Analyst 135*, 28-32.

[109] Mallimo, E. M., and Kusnecov, A. W. (2013) The role of orphanin FQ/nociceptin in neuroplasticity: relationship to stress, anxiety and neuroinflammation, *Front Cell Neurosci 7*.

[110] Bowers, M. E., Choi, D. C., and Ressler, K. J. (2012) Neuropeptide regulation of fear and anxiety: Implications of cholecystokinin, endogenous opioids, and neuropeptide Y, *Physiol Behav 107*, 699-710.

[111] Teng, B. L., Nonneman, R. J., Agster, K. L., Nikolova, V. D., Davis, T. T., Riddick, N. V., Baker, L. K., Pedersen, C. A., Jarstfer, M. B., and Moy, S. S. (2013) Prosocial effects of oxytocin in two mouse models of autism spectrum disorders, *Neuropharmacology 72*, 187-196.

[112] Zwanzger, P., Domschke, K., and Bradwejn, J. (2012) Neuronal Network of Panic Disorder: The Role of the Neuropeptide Cholecystokinin, *Depress Anxiety 29*, 762-774.

[113] Meriaux, C., Arafah, K., Tasiemski, A., Wisztorski, M., Bruand, J., Boidin-Wichlacz, C., Desmons, A., Debois, D., Laprevote, O., Brunelle, A., Gaasterland, T., Macagno, E., Fournier, I., and Salzet, M. (2011) Multiple changes in peptide and lipid expression associated with regeneration in the nervous system of the medicinal leech, *PloS one 6*, e18359.

[114] Mark, L., Maasz, G., and Pirger, Z. (2012) High Resolution Spatial Distribution of Neuropeptides by Maldi Imaging Mass Spectrometry in the Terrestrial Snail, Helix Pomatia, *Acta Biologica Hungarica 63*, 113-122.

[115] Altelaar, A. F., van Minnen, J., Jimenez, C. R., Heeren, R. M., and Piersma, S. R. (2005) Direct molecular imaging of Lymnaea stagnalis nervous tissue at subcellular spatial resolution by mass spectrometry, *Anal Chem 77*, 735-741.

[116] Zimmerman, T. A., Rubakhin, S. S., Romanova, E. V., Tucker, K. R., and Sweedler, J. V. (2009) MALDI mass spectrometric imaging using the stretched sample method to reveal neuropeptide distributions in aplysia nervous tissue, *Anal Chem 81*, 9402-9409.

[117] Rubakhin, S. S., Greenough, W. T., and Sweedler, J. V. (2003) Spatial profiling with MALDI MS: distribution of neuropeptides within single neurons, *Anal Chem 75*, 5374-5380.

[118] Chansela, P., Goto-Inoue, N., Zaima, N., Sroyraya, M., Sobhon, P., and Setou, M. (2012) Visualization of neuropeptides in paraffin-embedded tissue sections of the central nervous system in the decapod crustacean, Penaeus monodon, by imaging mass spectrometry, *Peptides 34*, 10-18.

[119] Chen, R., Hui, L., Cape, S. S., Wang, J., and Li, L. (2010) Comparative Neuropeptidomic Analysis of Food Intake via a Multi-faceted Mass Spectrometric Approach, *Acs Chem Neurosci 1*, 204-214.

[120] Ye, H., Hui, L., Kellersberger, K., and Li, L. (2013) Mapping of neuropeptides in the crustacean stomatogastric nervous system by imaging mass spectrometry, *J Am Soc Mass Spectrom 24*, 134-147.

[121] Monroe, E. B., Annangudi, S. P., Hatcher, N. G., Gutstein, H. B., Rubakhin, S. S., and Sweedler, J. V. (2008) SIMS and MALDI MS imaging of the spinal cord, *Proteomics 8*, 3746-3754.

[122] Sturm, R. M., Greer, T., Chen, R., Hensen, B., and Li, L. (2013) Comparison of NIMS and MALDI platforms for neuropeptide and lipid mass spectrometric imaging in brain tissue, *Anal Methods 5*, 1623-1628.

[123] Andersson, M., Groseclose, M. R., Deutch, A. Y., and Caprioli, R. M. (2008) Imaging mass spectrometry of proteins and peptides: 3D volume reconstruction, *Nat Methods 5*, 101-108.

[124] Jones, E. A., Shyti, R., van Zeijl, R. J., van Heiningen, S. H., Ferrari, M. D., Deelder, A. M., Tolner, E. A., van den Maagdenberg, A. M., and McDonnell, L. A. (2012) Imaging mass spectrometry to visualize biomolecule distributions in mouse brain tissue following hemispheric cortical spreading depression, *J Proteomics 75*, 5027-5035.

[125] Kallback, P., Shariatgorji, M., Nilsson, A., and Andren, P. E. (2012) Novel mass spectrometry imaging software assisting labeled normalization and quantitation of drugs and neuropeptides directly in tissue sections, *J Proteomics 75*, 4941-4951.

[126] Hanrieder, J., Ljungdahl, A., Falth, M., Mammo, S. E., Bergquist, J., and Andersson, M. (2011) L-DOPA-induced dyskinesia is associated with regional increase of striatal dynorphin peptides as elucidated by imaging mass spectrometry, *Mol Cell Proteomics 10*, M111 009308.

[127] Stoeckli, M., Knochenmuss, R., McCombie, G., Mueller, D., Rohner, T., Staab, D., and Wiederhold, K. H. (2006) MALDI MS imaging of amyloid, *Methods Enzymol 412*, 94-106.

[128] Ljungdahl, A., Hanrieder, J., Bergquist, J., and Andersson, M. (2013) Analysis of Neuropeptides by MALDI Imaging Mass Spectrometry, *Methods Mol Biol 1023*, 121-136.

[129] Andersson, M., Andren, P., and Caprioli, R. M. (2010) MALDI Imaging and Profiling Mass Spectrometry in Neuroproteomics, In *Neuroproteomics* (Alzate, O., Ed.) 2011/09/02 ed., CRC Press, Boca Raton, FL.

[130] Ye, H., Greer, T., and Li, L. (2012) Probing neuropeptide signaling at the organ and cellular domains via imaging mass spectrometry, *Journal of proteomics 75*, 5014-5026.

[131] Ye, H., Greer, T., and Li, L. (2011) From pixel to voxel: a deeper view of biological tissue by 3D mass spectral imaging, *Bioanalysis 3*, 313-332.

[132] Porta, T., Grivet, C., Kraemer, T., Varesio, E., and Hopfgartner, G. (2011) Single Hair Cocaine Consumption Monitoring by Mass Spectrometric Imaging, *Anal Chem 83*, 4266-4272.

[133] Tang, H. W., Wong, M. Y. M., Lam, W., Cheng, Y. C., Che, C. M., and Ng, K. M. (2011) Molecular histology analysis by matrix-assisted laser desorption/ionization imaging mass spectrometry using gold nanoparticles as matrix, *Rapid Commun Mass Sp 25*, 3690-3696.

[134] Pirkl, A., Soltwisch, J., Draude, F., and Dreisewerd, K. (2012) Infrared Matrix-Assisted Laser Desorption/Ionization Orthogonal-Time-of-Flight Mass Spectrometry Employing a Cooling Stage and Water Ice As a Matrix, *Anal Chem 84*, 5669-5676.

[135] Qian, K., Zhou, L., Liu, J., Yang, J., Xu, H. Y., Yu, M. H., Nouwens, A., Zou, J., Monteiro, M. J., and Yu, C. Z. (2013) Laser Engineered Graphene Paper for Mass Spectrometry Imaging, *Scientific Reports 3*.

[136] Chang, C. C., Chen, C. N., Lin, W. J., Lo, T. Y., Lei, S. L., and Mai, F. D. (2013) Novel method to prepare biological samples using powerful magnets on TOF-SIMS analysis, *Surface and Interface Analysis 45*, 248-250.

[137] Shariatgorji, M., Kallback, P., Gustavsson, L., Schintu, N., Svenningsson, P., Goodwin, R. J. A., and Andren, P. E. (2012) Controlled-pH Tissue Cleanup Protocol for Signal Enhancement of Small Molecule Drugs Analyzed by MALDI-MS Imaging, *Anal Chem 84*, 4603-4607.

[138] Goodwin, R. J. A., Nilsson, A., Borg, D., Langridge-Smith, P. R. R., Harrison, D. J., Mackay, C. L., Iverson, S. L., and Andren, P. E. (2012) Conductive carbon tape used for

support and mounting of both whole animal and fragile heat-treated tissue sections for MALDI MS imaging and quantitation, *J Proteomics 75*, 4912-4920.

[139] Steinhauser, M. L., and Lechene, C. P. (2013) Quantitative imaging of subcellular metabolism with stable isotopes and multi-isotope imaging mass spectrometry, *Seminars in cell & developmental biology*.

[140] Steinhauser, M. L., Bailey, A. P., Senyo, S. E., Guillermier, C., Perlstein, T. S., Gould, A. P., Lee, R. T., and Lechene, C. P. (2012) Multi-isotope imaging mass spectrometry quantifies stem cell division and metabolism, *Nature 481*, 516-519.

[141] McMahon, G., Glassner, B. J., and Lechene, C. P. (2006) Quantitative imaging of cells with multi-isotope imaging mass spectrometry (MIMS)-Nanoautography with stable isotope tracers, *Appl Surf Sci 252*, 6895-6906.

[142] Pirman, D. A., Reich, R. F., Kiss, A., Heeren, R. M. A., and Yost, R. A. (2013) Quantitative MALDI Tandem Mass Spectrometric Imaging of Cocaine from Brain Tissue with a Deuterated Internal Standard, *Anal Chem 85*, 1081-1089.

[143] Jones, E. A., van Remoortere, A., van Zeijl, R. J. M., Hogendoorn, P. C. W., Bovee, J. V. M. G., Deelder, A. M., and McDonnell, L. A. (2011) Multiple Statistical Analysis Techniques Corroborate Intratumor Heterogeneity in Imaging Mass Spectrometry Datasets of Myxofibrosarcoma, *PloS one 6*.

[144] Kriegsmann, M., Seeley, E. H., Schwarting, A., Kriegsmann, J., Otto, M., Thabe, H., Dierkes, B., Biehl, C., Sack, U., Wellmann, A., Kahaly, G. J., Schwamborn, K., and Caprioli, R. M. (2012) MALDI MS imaging as a powerful tool for investigating synovial tissue, *Scand J Rheumatol 41*, 305-309.

[145] Karlsson, O., Roman, E., Berg, A. L., and Brittebo, E. B. (2011) Early hippocampal cell death, and late learning and memory deficits in rats exposed to the environmental toxin BMAA (beta-N-methylamino-L-alanine) during the neonatal period, *Behav Brain Res 219*, 310-320.

[146] Ljungdahl, A., Hanrieder, J., Falth, M., Bergquist, J., and Andersson, M. (2011) Imaging Mass Spectrometry Reveals Elevated Nigral Levels of Dynorphin Neuropeptides in L-DOPA-Induced Dyskinesia in Rat Model of Parkinson's Disease, *PloS one 6*.

[147] Meistermann, H., Norris, J. L., Aerni, H. R., Cornett, D. S., Friedlein, A., Erskine, A. R., Augustin, A., Mudry, M. C. D., Ruepp, S., Suter, L., Langen, H., Caprioli, R. M., and Ducret, A. (2006) Biomarker discovery by imaging mass spectrometry - Transthyretin is a biomarker for gentamicin-induced nephrotoxicity in rat, *Mol Cell Proteomics 5*, 1876-1886.

[148] Onishi, S., Tatsumi, Y., Wada, K., Yang, H. J., Sugiura, Y., Setou, M., and Yoshikawa, H. (2013) Sulfatide accumulation in the dystrophic terminals of gracile axonal dystrophy mice: lipid analysis using matrix-assisted laser desorption/ionization imaging mass spectrometry, *Med Mol Morphol 46*, 160-165.

[149] Oppenheimer, S. R., Mi, D. M., Sanders, M. E., and Caprioli, R. M. (2010) Molecular Analysis of Tumor Margins by MALDI Mass Spectrometry in Renal Carcinoma, *Journal of proteome research 9*, 2182-2190.

[150] Willems, S. M., van Remoortere, A., van Zeijl, R., Deelder, A. M., McDonnell, L. A., and Hogendoorn, P. C. W. (2010) Imaging mass spectrometry of myxoid sarcomas identifies proteins and lipids specific to tumour type and grade, and reveals biochemical intratumour heterogeneity, *J Pathol 222*, 400-409.

[151] Spraggins, J. M., and Caprioli, R. (2011) High-Speed MALDI-TOF Imaging Mass Spectrometry: Rapid Ion Image Acquisition and Considerations for Next Generation Instrumentation, *Journal of the American Society for Mass Spectrometry 22*, 1022-1031.

[152] Schober, Y., Guenther, S., Spengler, B., and Rompp, A. (2012) Single Cell Matrix-Assisted Laser Desorption/Ionization Mass Spectrometry Imaging, *Anal Chem 84*, 6293-6297.

[153] Paschke, C., Leisner, A., Hester, A., Maass, K., Guenther, S., Bouschen, W., and Spengler, B. (2013) Mirion-A Software Package for Automatic Processing of Mass Spectrometric Images, *Journal of the American Society for Mass Spectrometry 24*, 1296-1306.

[154] Robichaud, G., Garrard, K. P., Barry, J. A., and Muddiman, D. C. (2013) MSiReader: an open-source interface to view and analyze high resolving power MS imaging files on Matlab platform, *Journal of the American Society for Mass Spectrometry 24*, 718-721.

Figure legends

Figure 1. D^4-α-Cyano-4-hydroxycinnamic acid (D^4-CHCA) has been synthesized for use as a matrix for MALDI-MS and MALDI-MS imaging (MSI) of small molecule drugs and endogenous compounds. MALDI-MS analysis of small molecules has historically been hindered by interference from matrix ion cluster and fragment peaks that mask signals of low molecular weight compounds of interest. By using D^4-CHCA, the cluster and fragment peaks of CHCA, the most common matrix for analysis of small molecules, are shifted by +4, +8, and +12 Da, which expose signals across areas of the previously concealed low mass range. Here, obscured MALDI-MS signals of a synthetic small molecule pharmaceutical, a naturally occurring isoquinoline alkaloid, and endogenous compounds including the neurotransmitter acetylcholine have been unmasked and imaged directly from biological tissue sections. Reprinted with permission from ref. [93]. Copyright 2012 American Chemical Society.

Figure 2. MS images of metabolites and neurotransmitters (NTs) identified from rat central nervous system (CNS). (a) Optical image of a rat brain section subjected to MSI sample preparation. (b-h) MS images of metabolites and NTs, including (b) choline at *m/z* 104.1070, (c) acetylcholine at *m/z* 146.1175, (d) AMP at *m/z* 348.0706, (e) GMP at *m/z* 364.0655, (f) cholesterol with neutral loss at *m/z* 369.3519, (g) potassiated PC(32:0) at *m/z* 772.5258, and (h) nicotinamide adenine dinucleotide at *m/z* 644.1177. Other than low MW molecules, (i) MS image of the acetylated peptide ASQKRPSQRHGSKYLATA at *m/z* 2028.076 was also shown. (j) Overlaid image of a NT, acetylcholine, as in (c) and cholesterol-derived ion as in (f). Reprinted with permission from ref. [92]. Copyright 2013 American Chemical Society.

Figure 3. Image of TOF-SIMS (A)(B)(C)(D) are of the same image using the freeze-fracture method; (E)(F)(G)(H) are the same image with the powerful magnet method; (A)(E) are bright field; (B)(F) are Ca, *m/z* 40; (C)(G) are Cd, *m/z* 48; (D)(H) are total ions. Reprinted with permission from ref. [136].

Figure 4. HeLa cells on ITO slide (A) optical fluorescence of $DIOC_6(3)$ stained HeLa cells, λ = 501 nm. (B-D) MALDI imaging (28 x 21 pixels, pixel size 7 µm): (B) selected ion image of staining agent $DIOC_6(3)$ ($[M^+]$), (C) selected ion image of PC(32:1) ($[M + Na]^+$), and (D) selected ion image of PC(34:1) ($[M + Na]^+$). Reprinted with permission from ref. [152].

Table 1. Comparison of MSI approaches detailing ionization methods, mass analyzers, optimal analytes, mass range, and spatial resolution. Reprinted from ref.[16] Copyright © 2013 with permission from Elsevier.

Type of MSI	Ionization Source	Common Mass Analyzer	Optimal Analytes	Mass Range (Da)	Spatial Resolution (μm)
MALDI	UV/IR laser Soft ionization	TOF	Lipids, peptides, proteins, small molecules	0–50,000	30–50
SIMS	Ion gun Hard ionization	TOF Magnetic sector Orbitrap	Lipids, small peptides, small molecules	0–2000	0.5–1
DESI	Solvent spray Soft ionization	Orbitrap	Lipids, peptides, small molecules	0–2000	100

Table 2. Summary of neurotransmitter groups, sample preparation, suitable matrices, MSI acquisition methods, and related studies.

Neurotransmitter Groups		**Examples**	**Sample Preparation**	**Matrices**	**MSI Methods**	**Related Studies**
Small Molecule NTs	Acetylcholine	Acetylcholine	In situ freezing	deuterated matrix (D4-CHCA)	MALDI Tandem mass MSI; High resolution and mass accuracy MSI	*91-93*
	Purines	ATP, AMP, adenosine	In situ freezing	9-AA	MALDI High resolution and mass accuracy MSI	*7, 92, 94, 95*
	Amino acids	Glutamate, GABA, Glycine	N/A	DHB	MALDI High resolution and mass accuracy MSI	*92, 102-104*
	Biogenic amines	Dopamine, Epinephrine, Serotonin	DPP derivatization	CHCA	DESI MALDI	*104, 108*
Peptide NTs	Neuropeptides	Substance P, Somatostatin	N/A	CHCA, DHB, etc.	MALDI, SIMS, NIMS	*26, 113, 127, 128, 131*

Figures

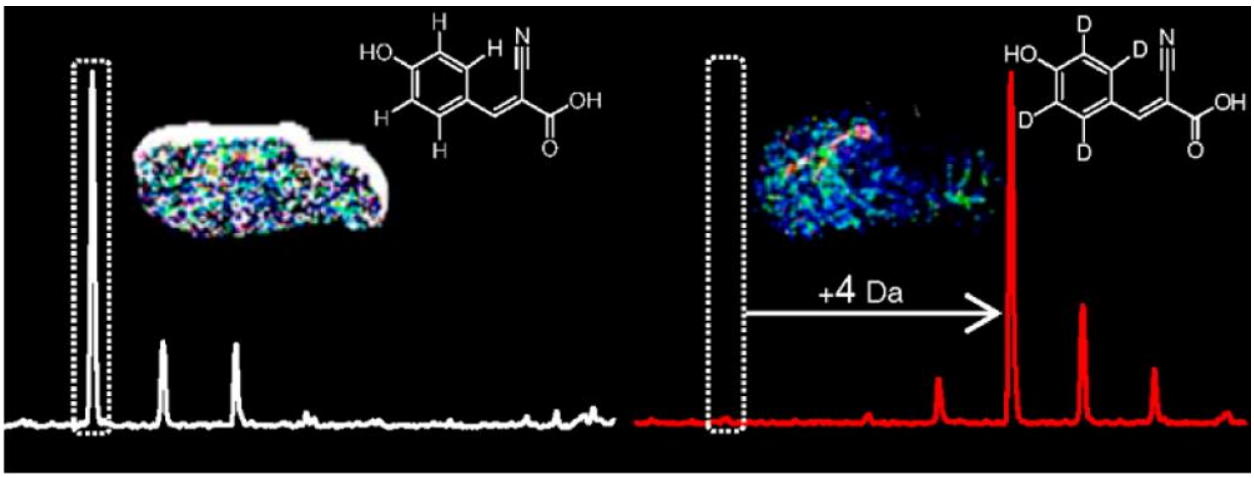

Figure 1

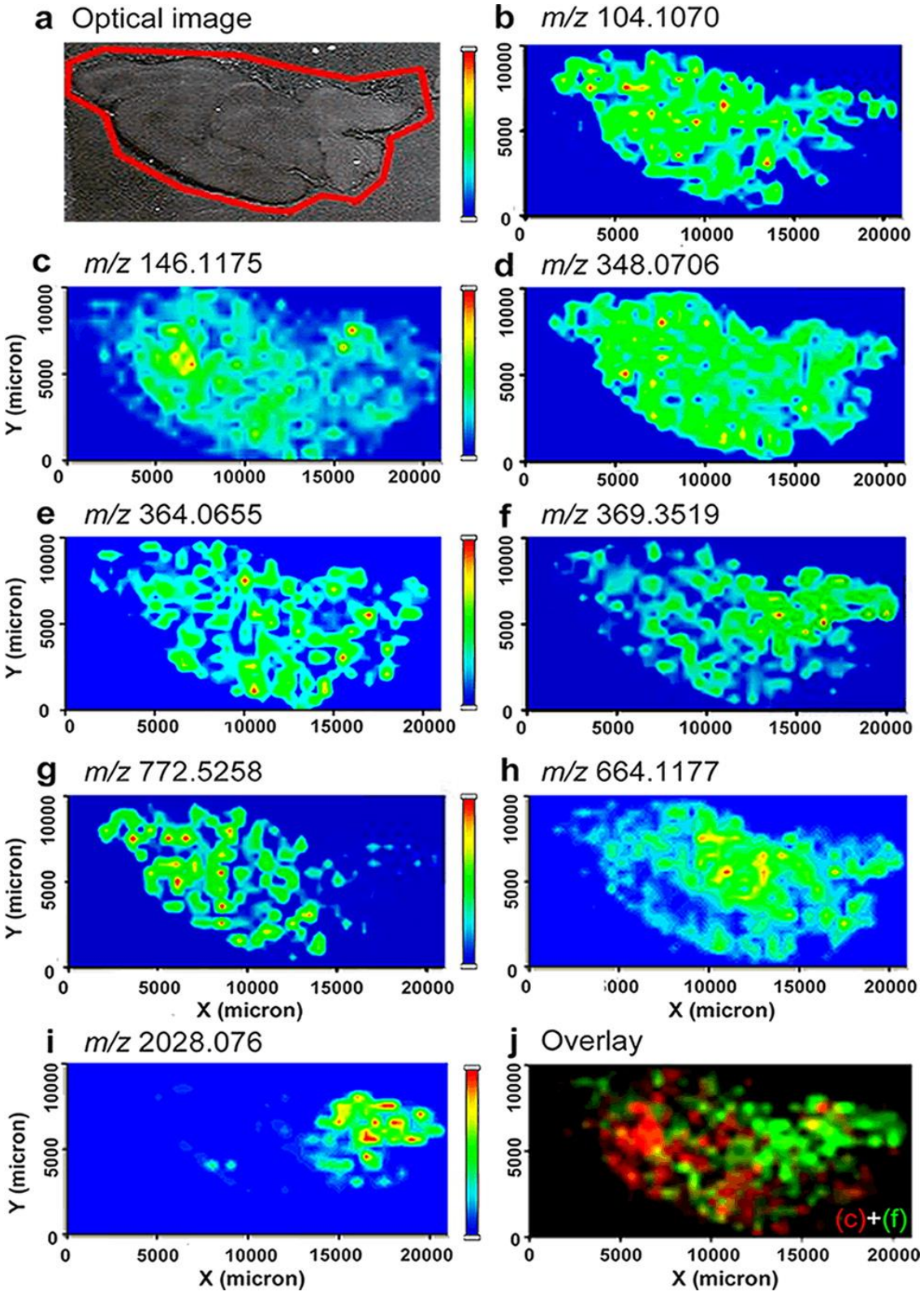
a Optical image
b m/z 104.1070
c m/z 146.1175
d m/z 348.0706
e m/z 364.0655
f m/z 369.3519
g m/z 772.5258
h m/z 664.1177
i m/z 2028.076
j Overlay
Y (micron)
X (micron)
0
5000
10000
15000
20000
(c)+(f)

Figure 2

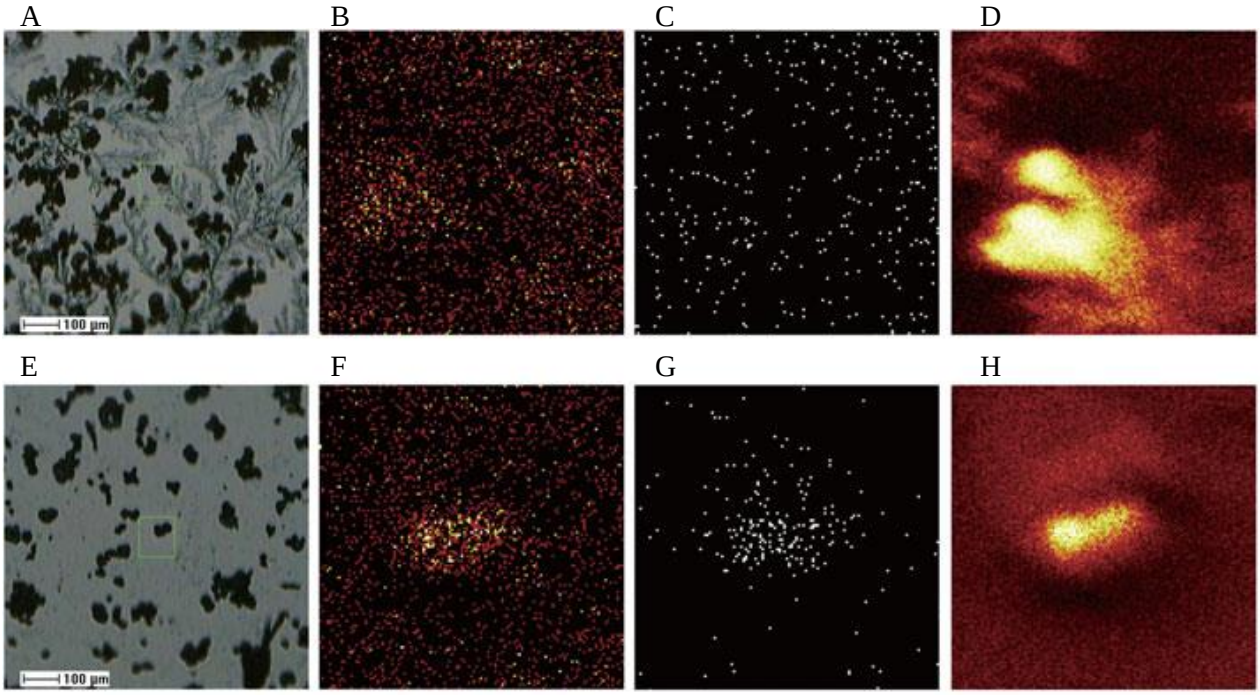

Figure 3

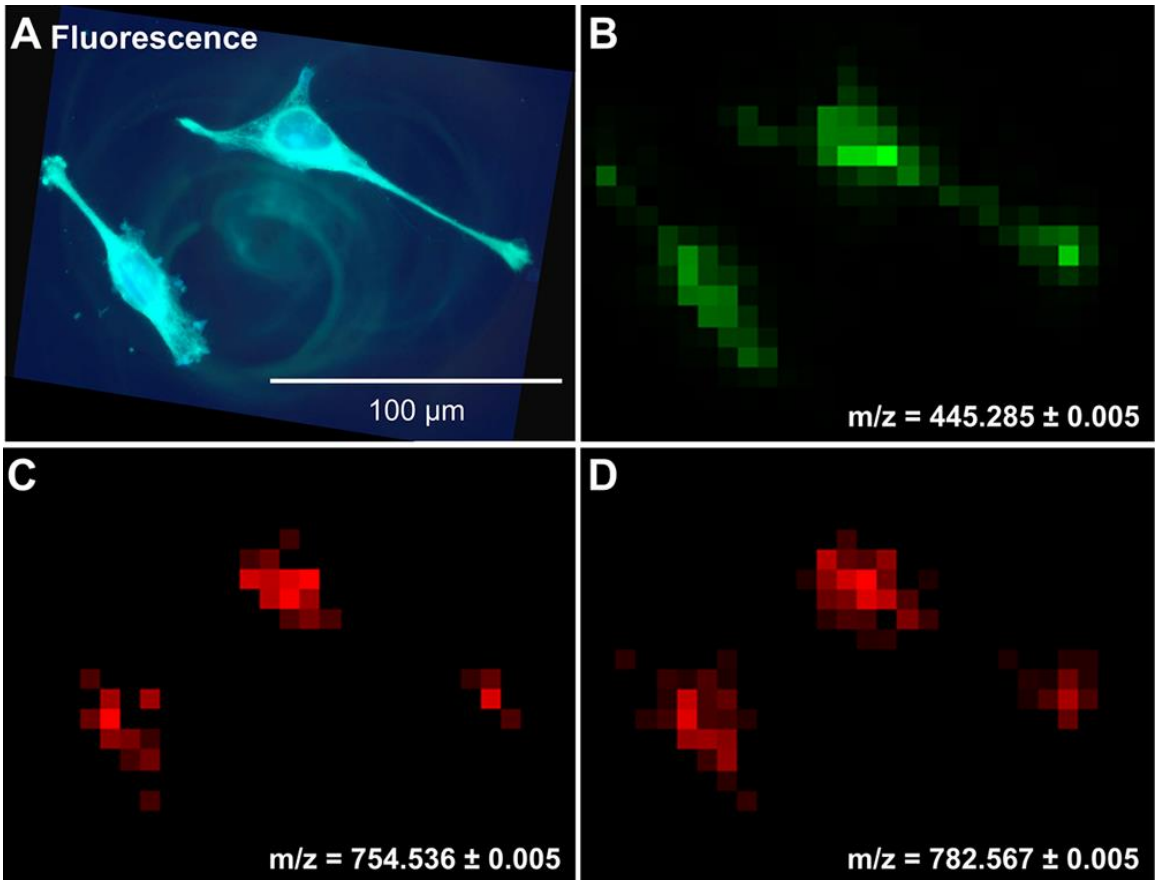
A Fluorescence
100 µm
B
m/z = 445.285 ± 0.005
C
m/z = 754.536 ± 0.005
D
m/z = 782.567 ± 0.005

Figure 4

Appendix III
LC-MS Differential Analysis for Fast and Sensitive Determination of Biotransformation of Therapeutic Proteins

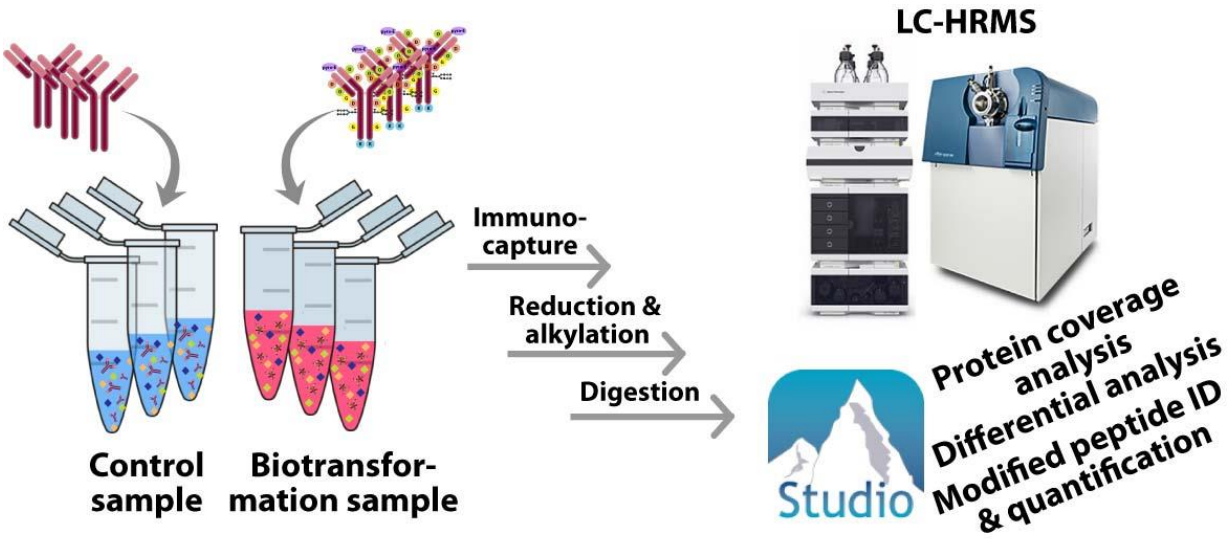

Adapted from: **B. Chen[#],** M. Yao[#], W. Zhao, J. Mehl, L. Li and M. Zhu, Liquid Chromatography-Mass Spectrometry Based Differential Analysis for Fast Determining Biotransformation of Therapeutic Biologics. *To be submitted* ([#]Co-First authors)

Author controbution: study was designed by M. Yao and M. Zhu; experiment was performed by M. Yao and W. Zhao; data was analyzed by B. Chen, M. Yao, J. Mehl and M. Zhu; manuscript was written by B. Chen and edited by M. Yao, M. Zhu and L. Li.

Abstract

Therapeutic biologics has become a fast-growing segment of pharmaceutical industry in the past three decades. Although the metabolism of biologics is much more predictable than small molecule drugs, the biotransformation process can significantly affect the activity of biologics. Unfortunately, there are only very limited number of published studies on the biotransformation process of biologics, most of which focused on one or a few types of modification. In this study, an untargeted LC-MS based differential analysis approach was developed to rapidly and precisely determine the universal biotransformation profile of biologics with the assistance of bioinformatics tool. A human monoclonal antibody (mAb) was treated with t-butyl hydroperoxide and compared with control mAb by bottom-up proteomics approach. Thirty-seven types of post-translational modifications were identified and thirty-eight peptides were significantly changed. Moreover, while all modifications were screened and detected, only the ones related to the treatment process were revealed by differential analysis. Other modifications that were co-existing in both groups were filtered away. This novel analytical strategy can be effectively applied to study biotransformation mediated protein modifications, which will streamline the process of biologics drug discovery and development.

Keywords: therapeutic biologics, biotransformation, mass spectrometry, differential analysis, monoclonal antibody

Introduction

Since the approval and commercialization of the first mAb in 1986, the development of therapeutic biologics has captured significant attentions in the pharmaceutical industry in the past three decades [1, 2]. In general, therapeutic biologics refers to substance derived from living organisms that is applicable to prevent, treat or cure a disease or a condition of human beings [3, 4]. In addition to mAb that represents the majority of marketed biologics, other biologics modalities, such as therapeutic peptide, bi-functional biologics and ADC, have emerged rapidly in the drug discovery processes [2]. Some therapeutic proteins contain artificial amino acids, unique peptide sequences or linkage structures or small molecule drug moieties [2, 3, 5].

Like endogenous proteins, antibody therapeutics undergo catabolism such as oxidation, deamination, glycosylation, phosphorylation and isomerization in a biological system to form catabolites (peptides and amino acids). Here we define biotransformation of a therapeutic protein as a chemical and enzymatic process occurred in a biological system, which changes the structure of a therapeutic protein and leads to its clearance in vitro and in vivo. Biotransformation of a therapeutic protein can follow either predictable catabolism pathways similar to the disposition and elimination processes of endogenous proteins or pathways different from protein catabolism due to the presence of an artificial amino acid, peptide sequence, linkage structure of amino acids and conjugated drug [6-8]. Biotransformation-derived protein modifications may have profound impacts on the biologics' activity or disposition behavior, as they could potentially lead to reduced target binding efficiency, shorter half-life, higher clearance, poor bioavailability, increased off-target binding/toxicity, increased immunogenicity and changed assay detection [9-13]. For example, the Methionine oxidation in human IgG1 causes significant reduction in the binding affinity and reduced serum half-life [13]; the isomerization of a

single Asp residue leads to completely lost of the target-binding ability in a model mAb (mAb X) [14].

Usually, drug metabolism and pharmacokinetics research of therapeutic proteins focus on protein quantitative analysis in drug development using ligand-binding assays (LBA) such as enzyme-linked immunesorbent assay. LBAs are highly sensitive, easy to operate and capable of high throughput analysis. Recently, LC-MS based methods that quantitatively monitor a few signature peptide(s) hydrolyzed from a therapeutic protein using triple quadrupole and high resolution mass spectrometers (HRMS) have been increased employed to support pharmacokinetics characterization in drug discovery and preclinical development [15]. However, there is no effective methodology available to study the global changes in biologics upon biotransformation process, and most of the published biotransformation studies only focus on one type of modifications [11, 13, 16]. For example, Bults *et al.* reported a LC-MS approach to analyze trastuzumab and its deamidation product *in vivo*, in which a selected reaction monitoring approach was used to monitor five molecular species from tryptic digested trastuzumab from human plasma without enrichment [16]. This method is highly specific to monitor the deamidation at N55 and it is not a means to monitor the global biotransformation of a therapeutic protein. Thus, investigation of therapeutic protein biotransformation has to relay on HRMS-based proteomics workflows, such as top-down or bottom-up approaches [17].

Intact protein or protein assemblies are directly analyzed in a top-down proteomics workflow, which requires ultrahigh resolving powers and usually has limited protein sequence coverage and sensitivity. In a typical bottom-up proteomics workflow, protein samples are enzymatically digested into peptides, which are then subjected to LC-MS experiments. The resulting MS/MS spectra are compared with the protein sequence database to find the best

matched peptide. To search for modified peptides, MS/MS spectra are compared with a list of pre-defined modifications on peptides in traditional database software. Some software packages, such as PEAKS, used improved algorithm for PTM search, which are capable of screening more than 650 known PTM types in one run. [18]. Compared to the top-down workflow, bottom-up approach offers several advantages, including improved sequence coverage, superior analytical specificity, sensitivity, precision and accuracy [2, 19].

A key analytical challenge in determining global biotransformation of therapeutic proteins via a bottom-up workflow is the large number of low levels of protein modifications. These modifications either present in a dosing solution or formed in sample preparations, such as enzymatic hydrolysis, isolation and enrichment processes, which are not associated with biotransformation process. It would take a lot of effort and time to detect and characterize these modified proteins and distinguish them from biotransformation-derived protein modifications. Herein, we developed and validated an untargeted LC-HRMS based differential analysis method for quick detection and identification of modified peptides derived from biotransformation of therapeutic mAb. A human mAb was forced oxidized and compared with control mAb by a bottom-up proteomics workflow. Generated LC-MS datasets were processed by bioinformatic tools for differential analysis. Modified peptides which have significantly higher levels in the biotransformation sample were highlighted and structurally characterized. Moreover, relative quantification of biotransformation-related modified peptide was performed. To our knowledge, this is the first study that analyzes the global biotransformation of mAb using LC-HRMS and differential analysis. With relatively easy sample preparation and rapid data acquisition, this method provides a template for the drug discovery and development industry to characterize therapeutic biologics in a high throughput manner.

Materials and methods

Materials and Chemicals

All reagents were used without additional purifications. Mouse anti-human IgG R10Z8E9 was available in house (Arctic Database) and Denabeads (M-280 tosylativated) was purchased from Invitrogen (Carlsbad, CA). Male rat serum was purchased from Bioreclamation IVT (New York, NY). Trypsin used for mAb digestion was purchased from Promega (Madison, WI). The phosphate buffered saline (PBS) and all solvents used in LC mobile phases (water, acetonitrile and formic acid (FA) were purchased from GE healthcare Bio-sciences (Malborough, MA). tBHP, dithiothreitol (DTT) iodoacetamide (IAA) and ammonium bicarbonate (AMBIC) were purchased from Sigma Aldrich (St. Louis, MO) and the Zwittergent 3-12 detergent (Zwitt) was purchased from Calbiochem (EMD Millipore, Billerica, MA).

Preparation of immunocapture beads

Mouse anti-human IgG antibodies were used in preparing tosylactivated beads. Denabeads M-280 tosylativated (24 mg or 800 µL) were prepared by washing with buffer A (0.1 M borate buffer pH 9.5) twice. The total of 480 µg antibody was mixed with the beads in buffer A followed by adding 488 µL buffer C (3 M ammonium sulphate in buffer A). The mixture was incubated on a rotator in 37 °C overnight. The supernatant was removed after the incubation and the mixture was incubated in 1 mL buffer D (PBS pH 7.4 with 0.5% (w/v) BSA) on a rotator at 37 °C for 1 hr. The mixture was then washed with 1 mL buffer E (PBS pH 7.4 with 0.1% (w/v) BSA) twice and stored in 800 µL buffer E at 4 °C until use (within 10 weeks). The resulting tosylactivated beads had a concentration of 0.6 µg/µL of captured antibody.

Generation of biotransformation and control samples of biologics

A human mAb with 145.0 kDa a model therapeutic biologics. (20 µg/µL, 10 µL) was treated with 40 µL 0.1% tBHP at 25 °C overnight to introduce various protein modifications. The biotransformed and control mAb solutions (25 µL each with 100 µg mAb) were spiked into 75 µL rat serum to generate a biotransformation sample and control sample, respectively. The resulting serum sample each had 100 µg mAb with a concentration of 1 µg/µL.

Sample preparations

mAb in rat serum was enriched by immunocapture using the tosylactivated beads, which were prepared according to the procedure described in the previous section. For each sample, 170 µL beads were loaded into a well of 96-deepwell plate followed by 200 µL buffer E and 100 µL of the rat serum sample. The mixture was incubated at room temperature for 1 hr on a shaker and washed with 200 µL PBS with 0.05% Zwitt. The beads were then transferred to a fresh well using 200 µL PBS with 0.5 M NaCl and 0.05% Zwitt and washed with 200 µL 500 mM AMBIC/0.05% Zwitt, 200 µL of 2 mM AMBIC and eluted with 50 µL of 12 mM HCl. The eluted fraction was transferred to a well containing 25 µL of 100 mM AMBIC and 20 µL water. Five µL DTT (100 mM) was added to the mixture and incubated at 60 °C for 60 min. Then 11 µL of IAA (100 mM) was added to the mixture and incubated in dark for 30-45 min. Trypsin was added to each sample with a 1:25 trypsin:protein ratio (for samples with 100 µg mAb, 4 µg trypsin was added) and incubated at 37 °C overnight. Finally, 10% formic acid (1.2 µL) was added to make a final concentration of 0.1% FA to quench the reaction.

LC-MS analysis

An Agilent 1290 Infinity II LC system (Agilent Technologies, Santa Clara, US) was connected to a TripleTOF 5600 mass spectrometer (AB Sciex, Framinghan, MA) for all LC-MS analysis. 10 µL of sample was injected onto a C_{18} column (Waters Acquity UPLC BEH C_{18}, 1.7 µm) for each run. Mobile phase A was H_2O with 0.1% FA and mobile phase B was ACN with 0.1% FA. The following gradient with a flow rate of 400 ng/mL was used (time/minute, % mobile phase B): (0, 2), (2, 2), (45, 45), (47, 90), (50, 90), (51, 2) (55, 2).

To maximize the information acquired on the mass spectrometer for each sample, a full MS scan (*m/z* 300-2000) was acquired followed by top 20 information dependent acquisition (IDA) MS/MS scans (*m/z* 100-1600) at positive ion mode. The parameters for CUR, DP, CE; Gas1, Gas2 in full MS scan mode was 30, 10, 55, and 55. The mass tolerance was 50 mDa. Source temperature was set to 450 °C and tray temperature was set to 22 °C. The criteria for the IDA scans were as follows: top 20 most intensive peaks with charge states from 2 to 5 and intensities greater than 50 were selected. Dynamic background subtraction was set for exclusion. Dynamic collision energy was enable for multiply charge peptides.

Data processing

A customized version of PEAKS 7.5 (Bioinformatics Solution Inc., Waterloo, ON, Canada) was used for peptide mapping, PTM searching and differential analysis (label free quantification). The following parameters were used for peptide mapping against the tocilizumab database: parent mass error tolerance of 50 ppm, fragment mass error tolerance of 1.0 Da and up to 3 missed cleavages were allowed. Deamidation (NQ), and oxidation (M) were set as variable modifications, carbamidomethylation was set as fix modification. All 53 common and 420 uncommon PTMs were included for PTM searching. Up to 3 PTMs were allowed for each

peptide. False discovery rate was set as 1%. Each data file was normalized to total ion count before differential analysis. One of the control samples was used as reference sample for normalization in order to compare the ratio for each peptide in different samples. After searching, the labeled peak search for PTM and spider search for mutation were attached for labeled free quantification, which is for differential analysis. The resulting heat map represents the $\log_2$ ratio to the average area across different samples. Different filtering criteria were used for data interpretation.

Results

A bottom-up proteomics-based differential analysis workflow

In the current study, a bottom-up proteomics-based differential analysis strategy was developed and evaluated for untargeted detection and characterization of global biotransformation products on a therapeutic mAb (Figure 1). In this analysis, a biotransformation sample and a corresponding control sample are obtained. The biotransformation sample was either from an in vitro incubation of a therapeutic protein or collected from an animal or human subject after dosing a therapeutic protein. The control sample was either pre-incubation or pre-dosing sample. Immunocapture and/or other methods were employed to recover and enrich the therapeutic protein and its modification products from the biological matrix. The recover proteins were further reduced, alkylated and digested by trypsin, followed by peptide analyses by LC-HRMS. Resulting full scan MS and MS/MS datasets of the biotransformation and control samples, which could be acquired by a data-dependent or data-independent method, were subjected for peptide mapping, modification analysis and differential analysis using a customized proteomics data-processing software. Peptide mapping was achieved by comparing the acquired MS^2 spectra with theoretically calculated fragment ion *m/z* values from the mAb amino acid

residue sequence. Peptide modification analysis was achieved by searching the mass differences of known modifications and compared with the acquired MS^2 spectrum. Differential analysis was performed by comparing the peak area of extracted ion chromatogram of detected features between the biotransformation and control samples in triplets. Coverage of the peptide mapping was determined to ensure the quality of protein hydrolysis and peptide mapping processes. Modified peptides via biotransformation, which were either absent in the control sample or had significantly higher levels in the test sample than in the control sample, were determined using differential analysis. Furthermore, structures of the detected modified peptides were elucidated using the software of common modifications of mAb and/or manual interpretation for uncommon peptide modifications. In the current study, simplified biotransformation and control samples of a human mAb were generated to test the effectiveness of the workflow (Figure 1).

The coverage of peptide mapping and identification of protein modifications

The sequence coverage and peptide modifications detected in the light chain and heavy chain of the control mAb sample were presented in Supplemental Figure 1. The sequence coverage was calculated by the number of amino acid residues detected divided by the total number of amino acid residues presented. By using the untargeted LC-HRMS approach, 93% of the light chain and 92% of the heavy chain were covered when the force discovery rate was set to be 1%. The result indicated that the quality of protein processes and LC/HRMS analysis was good. Sixty and 129 unique peptides were detected for the light chain and heavy chain of the mAb, respectively, recovered from the biotransformation sample. Common modifications, such as carbamidomethylation, deamidation and oxidation, were labeled in the figures. Additionally, less common protein modifications such as sulfation and pyro-glu from E (Table 1 and Supplemental Figure 1) could be found via the data-processing using the customized software. In

total, 37 types of modifications were determined and characterized by the PEAKS PTM search algorithm. Twenty-nine types of modifications were observed in the control samples (511 modified peptides) and twenty-nine types of modifications were observed in the biotransformed samples (489 modified peptides). The corresponding peptide spectrum match (#PSM), delta mass of each modification (ΔMass), position and -10logP values were listed on Table 1. Carbamidomethyl, deamidation, oxidation and dihydroxy were among the most popular modifications; other less common ones, such as point mutation of single amino acid, sulfation and carboxylation were also detected (Supplemental Figure 1).

Identification of modified peptides derived by biotransformation

Modified peptides derived from biotransformation were determined by the differential analysis (Figure 2). These peptides were either only present or had a significantly higher level in the biotransformation sample. Table 2 summarized a partial list of these peptides with significance values (-10logP) above 5. Most of these peptides were associated with Methionine oxidation. In the sample profile and group profile columns, the left panel represented the biotransformed samples while the right panel represented the control samples. All the unoxidized peptides (row 1, 3, 5 & 7) had much higher intensities in the control samples while all the oxidized peptides (row 2, 4, 6 & 8) had much higher intensities in the biotransformed samples. Some data points were not shown in the sample profile due to the corresponding peptide intensity was too low to be detected.

As an example, the extracted ion chromatogram of the doubly charged unmodified and oxidized forms of a peptide (TTAMDYWGQGSLVTVSSASTK) were shown in Figure 2. High abundance of the unchanged peptide was observed in all three of the control samples with intensities above 1E4, while the signals could be barely seen in the biotransformation samples

(Figure 2a). On the other hand, high abundance of the oxidized form of this peptide was observed in the biotransformation sample, but barely any signal was detected in the control sample (Figure 2b). A 2-minute shift in retention time was observed between these peptide forms, which was associated to the oxidation of Methionine that enhances the hydrophilicity of the peptide.

The corresponding MS^2 spectra of these peptides (Figure 3) were acquired by the IDA scans during the elution of the corresponding peptides. For both peptides, y_2 to y_{15} ions (except for y_{11} ion for the oxidized form) and some of the b ions were detected with high abundance. Based on the fragment ion information, the sequence of these peptides could be confidently assigned by the database searching algorithm of PEAKS. By comparing the spectra of unchanged (Figure 3a) and oxidized (Figure 3b) forms, the mass difference between Methionine and oxidized Methionine (+15.99) was observed in the b_7 ions (shown in dotted blue lines) as well as some other b ions. The mass difference in the MS^2 spectra allow the database searching algorithm as well as the PTM analysis algorithm to detect the type and location of potential modifications existing in each peptide.

Quantitative estimation of modified peptides derived by biotransformation

Percentage of modified peptides presented in each sample was calculated and summarized in Figure 4 (common modifications of heavy chain) and Table 3 (other modifications). By examining the oxidation profiles, a large percentage of Methionine residues in the biotransformed samples have been oxidized (Figure 4a). The highly oxidized (> 95%) residues include M70o, M254o and M430o of the heavy chain. About 50% of the M106o had also been oxidized. On the other hand, most of the Methionine residues in the control samples remained unmodified (Figure 4b). Only 5%-10% of the M106 were oxidized in the control

sample, which could be modified during the storage or sample preparation process. Additionally, the disappearances of unmodified peptides in the biotransformation and control samples were quantitively estimated by the data-processing. As shown in Figure 4, some of unmodified peptides completely disappeared such as M106o and M254o, and some remained a small % after biotransformation, such as M70o. Furthermore, some unmodified peptides were absent in both biotransformation and control samples, such as C228c and C263c due to sample process rather than biotransformation.

Summary of biotransformation-derived protein modifications

The modified percentages of other types of modifications including deamidation, carbamidomethylation and dimethylation, were consistent in both sample groups (Figure 4 c&d, Table 3). The sources of these modifications were mostly from production, storage or sample preparation, which were not directly related to tBHP treatment.

Figure 5 summarized the results of differential analysis with a significance (-10logP) of at least 15 and fold changes at least 2 folds. Total number of peptide identified (red), number of modified peptide (green), modified peptides which were up-modified in biotransformation samples (dark blue) and un-modified peptide down-modified in biotransformation samples (light blue) were listed according to their fold changes (x-axis: 2, 5, 10, 20, 50 and 100 folds). Peptides confidently detected in at least 3 samples (Figure 5a) and peptides confidently detected in all 6 samples (Figure 5b) were listed. Figure 5c represents the relationship amongst these datasets. As some peptides were undetectable in the control or biotransformed group, features detected in both 3 samples (in control group or biotransformed group) and all 6 samples were monitored.

Discussion

A rapid and sensitive LC-HRMS based strategy was developed in this study to characterize the biotransformation-mediated modifications in an artificially oxidized mAb model system. Due to the similarity in property and sample handling procedures, this approach is also suitable on other classes of therapeutic biologics, such as therapeutic peptide, ADC and bi-functional biologics.

Most of the previous studies on biotransformation focus on one particular class of modification, such as oxidation [13] or N-term glutamate to pyroglutamate conversion [11]. While these studies allow in depth structure elucidation and *in vivo* studies, they were not as informative as a high throughput study to screen all modifications in one run. By using the untargeted LC-HRMS based approach, different modifications could be detected in a high throughput fashion to generate valuable information, while the sources of modifications (storage, sample preparation or treatment) could be potentially unveiled by differential analysis. The uniqueness of this workflow is mainly presented in the following two aspects: 1. Instead of focusing on one modification, all modifications can be examined in one time with the help of bioinformatics tool; 2. By comparing with control samples, the shared modifications were filtered away and only the modifications of interest were reported.

The conserved Methionine residues (M254 and M430) located in the FnRn binding site and play important roles in FcRn binding were found to be oxidized in the biotransformed samples. This result matches previous reports. According to Wang *et al.*, oxidizing these two Methionine residues at high content could significantly reduce the serum circulation half-life of mAb.

Due to the large size of therapeutic biologics and large number of potential modification sites, there exists a large amount of low level modifications that are universally presented in all

samples. Most of them were introduced during production, storage and sample preparations, which are not directly related to the biotransformation process. By performing database search and PTM analysis by bioinformatics tool, we observed a relatively high level of basal modifications in the control samples. Moreover, most of the modification types and modified peptides were shared by the control and biotransformed samples. Some random modifications were only observed in one replicates of either control or biotransformed samples. Therefore, it is difficult to pick out the specific modifications that were induced by the tBHP treatment without differential analysis. Furthermore, if conventional LBAs were used, these modifications were usually detected and combined with the actual biotransformation-mediated modifications results, which overestimates the degree of biotransformation within biologics. In contrast, LC-HRMS based differential analysis assures direct analysis on the biotransformation-mediated modifications without including unspecific modifications, which generates more accurate results and saves time and effort from analyzing irrelevant results.

Moreover, the possible source of modifications can be determined by this approach. If the modifications were induced by certain treatment, significant differences could be observed between biotransformed and control samples; if the modifications were related to storage, differences could be observed between old and fresh samples; if the modifications were associated with sample preparation, it could be universally presented in all sample groups.

In summary, a novel approach was developed to systematically study the universal biotransformation of therapeutic biologics with LC-HRMS based untargeted differential analysis. With this approach, sequence coverage of the human mAb was above 92% and 37 types of modifications were identified (all point mutations were treated as one type of modification). As many as 38 peptides were significantly changed, up to 21 of them have modifications and up to

18 of peptide with modifications were up-modified in biotransformed samples. In this method, different modifications could be rapidly detected, while the sources of modifications could be potentially unveiled by differential analysis as the co-existing modifications in both samples were filtered away.

Due to the similarity in property and sample handling procedures, this approach is also suitable on other classes of therapeutic biologics, such as therapeutic peptide, ADC and bi-functional biologics. This new analytical strategy can be effectively applied to study biotransformation-mediated protein modifications in the process of drug discovery and development.

Acknowledgments

The authors would like to thank Bioinformatics Solution Inc. (Waterloo, ON, Canada) for the technical support on the PEAKS software. L.L. acknowledges an H.I. Romnes Faculty Research Fellowship and a Vilas Distinguished Achievement Professorship with funding provided by the Wisconsin Alumni Research Foundation and University of Wisconsin-Madison School of Pharmacy. The authors declare that they have no conflict of interest.

References

[1] Waldmann, T. A. (2003) Immunotherapy: past, present and future, *Nature medicine 9*, 269-277.

[2] Xu, X., and Vugmeyster, Y. (2012) Challenges and Opportunities in Absorption, Distribution, Metabolism, and Excretion Studies of Therapeutic Biologics, *Aaps Journal 14*, 781-791.

[3] Hamuro, L. L., and Kishnani, N. S. (2012) Metabolism of biologics: biotherapeutic proteins, *Bioanalysis 4*, 189-195.

[4] Zhao, L., Ren, T. H., and Wang, D. D. (2012) Clinical pharmacology considerations in biologics development, *Acta pharmacologica Sinica 33*, 1339-1347.

[5] Katsila, T., Siskos, A. P., and Tamvakopoulos, C. (2012) Peptide and protein drugs: the study of their metabolism and catabolism by mass spectrometry, *Mass spectrometry reviews 31*, 110-133.

[6] Cheloha, R. W., Maeda, A., Dean, T., Gardella, T. J., and Gellman, S. H. (2014) Backbone modification of a polypeptide drug alters duration of action in vivo, *Nature biotechnology 32*, 653-655.

[7] Walles, M., Rudolph, B., Wolf, T., Bourgailh, J., Suetterlin, M., Moenius, T., Peraus, G., Heudi, O., Elbast, W., Lanshoeft, C., and Bilic, S. (2016) New Insights in Tissue Distribution, Metabolism, and Excretion of [3H]-Labeled Antibody Maytansinoid Conjugates in Female Tumor-Bearing Nude Rats, *Drug metabolism and disposition: the biological fate of chemicals 44*, 897-910.

[8] Zhang, D., Yu, S. F., Ma, Y., Xu, K., Dragovich, P. S., Pillow, T. H., Liu, L., Del Rosario, G., He, J., Pei, Z., Sadowsky, J. D., Erickson, H. K., Hop, C. E., and Khojasteh, S. C. (2016) Chemical Structure and Concentration of Intratumor Catabolites Determine Efficacy of Antibody Drug Conjugates, *Drug metabolism and disposition: the biological fate of chemicals 44*, 1517-1523.

[9] Cai, B., Pan, H., and Flynn, G. C. (2011) C-terminal lysine processing of human immunoglobulin G2 heavy chain in vivo, *Biotechnology and bioengineering 108*, 404-412.

[10] Hall, M. P. (2014) Biotransformation and in vivo stability of protein biotherapeutics: impact on candidate selection and pharmacokinetic profiling, *Drug metabolism and disposition: the biological fate of chemicals 42*, 1873-1880.

[11] Liu, Y. D., Goetze, A. M., Bass, R. B., and Flynn, G. C. (2011) N-terminal glutamate to pyroglutamate conversion in vivo for human IgG2 antibodies, *The Journal of biological chemistry 286*, 11211-11217.

[12] Liu, Y. D., van Enk, J. Z., and Flynn, G. C. (2009) Human antibody Fc deamidation in vivo, *Biologicals : journal of the International Association of Biological Standardization 37*, 313-322.

[13] Wang, W., Vlasak, J., Li, Y., Pristatsky, P., Fang, Y., Pittman, T., Roman, J., Wang, Y., Prueksaritanont, T., and Ionescu, R. (2011) Impact of methionine oxidation in human IgG1 Fc on serum half-life of monoclonal antibodies, *Molecular immunology 48*, 860-866.

[14] Prueksaritanont, T., and Tang, C. Y. (2012) ADME of Biologics-What Have We Learned from Small Molecules?, *Aaps Journal 14*, 410-419.

[15] An, B., Zhang, M., and Qu, J. (2014) Toward sensitive and accurate analysis of antibody biotherapeutics by liquid chromatography coupled with mass spectrometry, *Drug metabolism and disposition: the biological fate of chemicals 42*, 1858-1866.

[16] Bults, P., Bischoff, R., Bakker, H., Gietema, J. A., and van de Merbel, N. C. (2016) LC-MS/MS-Based Monitoring of In Vivo Protein Biotransformation: Quantitative Determination of Trastuzumab and Its Deamidation Products in Human Plasma, *Analytical chemistry 88*, 1871-1877.

[17] Domon, B., and Aebersold, R. (2006) Mass spectrometry and protein analysis, *Science 312*, 212-217.

[18] Han, X., He, L., Xin, L., Shan, B. Z., and Ma, B. (2011) PeaksPTM: Mass Spectrometry-Based Identification of Peptides with Unspecified Modifications, *J Proteome Res 10*, 2930-2936.

[19] Ewles, M., and Goodwin, L. (2011) Bioanalytical approaches to analyzing peptides and proteins by LC--MS/MS, *Bioanalysis 3*, 1379-1397.

Figure Legends

Figure 1. Workflow of LC-HRMS based differential analysis for detecting biotransformation-mediated modifications.

Figure 2. Representative chromatograms that show significantly differences between biotransformed and control group.

Figure 3. Representative MS/MS spectra of *m/z* 1095.530 (a) and *m/z* 1103.523 (b), z=2 for both ions. Peptide sequences and fragment ions were annotated on the spectra.

Figure 4. Partial PTM profiles of biotransformation (a,c) and control (b,d) samples. Figure a and b compared the oxidation profiles and figure c and d compared all modifications. The column in red represented the modified peptide and the column in blue represented unmodified peptide. In the x-axis, the capital letter represented corresponding amino acid residues, the number represented the positions of these modifications and the last letter represented the type of modifications: d=deamination; c=carbamidomethylation; o=oxidation.

Figure 5. Features detected by differential analysis with significance (-10logP) of 15 in at least 3 samples (a) and all 6 samples (b) and a Venn diagram (c) representing the relationships among these datasets. The X-axis represents the fold changes of 2, 5, 10, 20, 50 and 100.

Figures

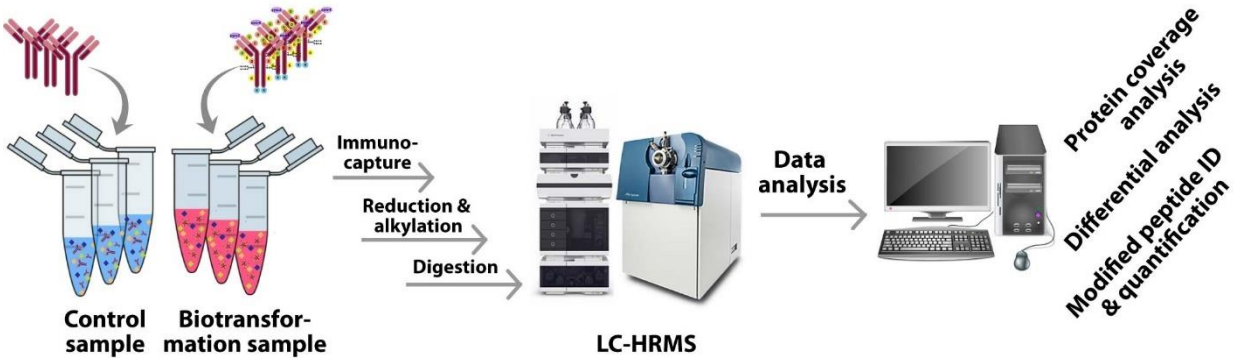

Figure 1

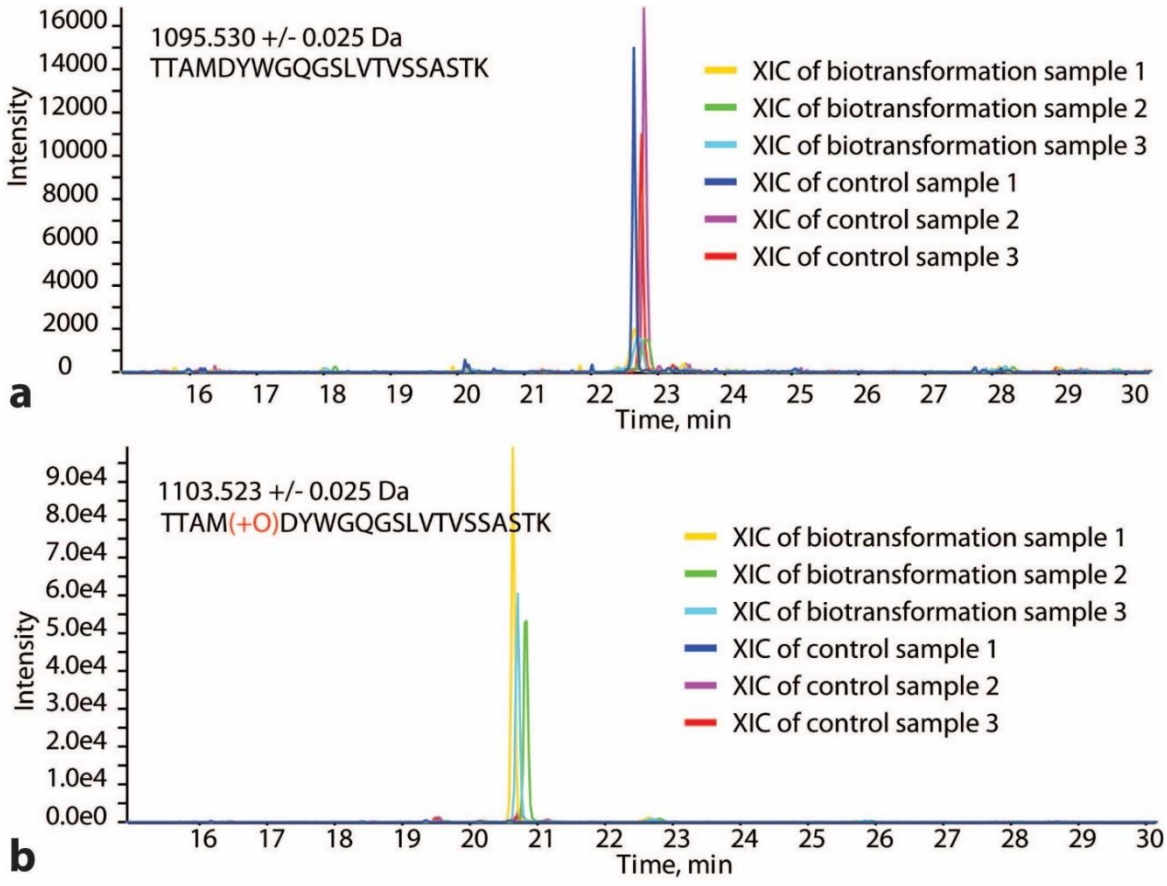

Figure 2

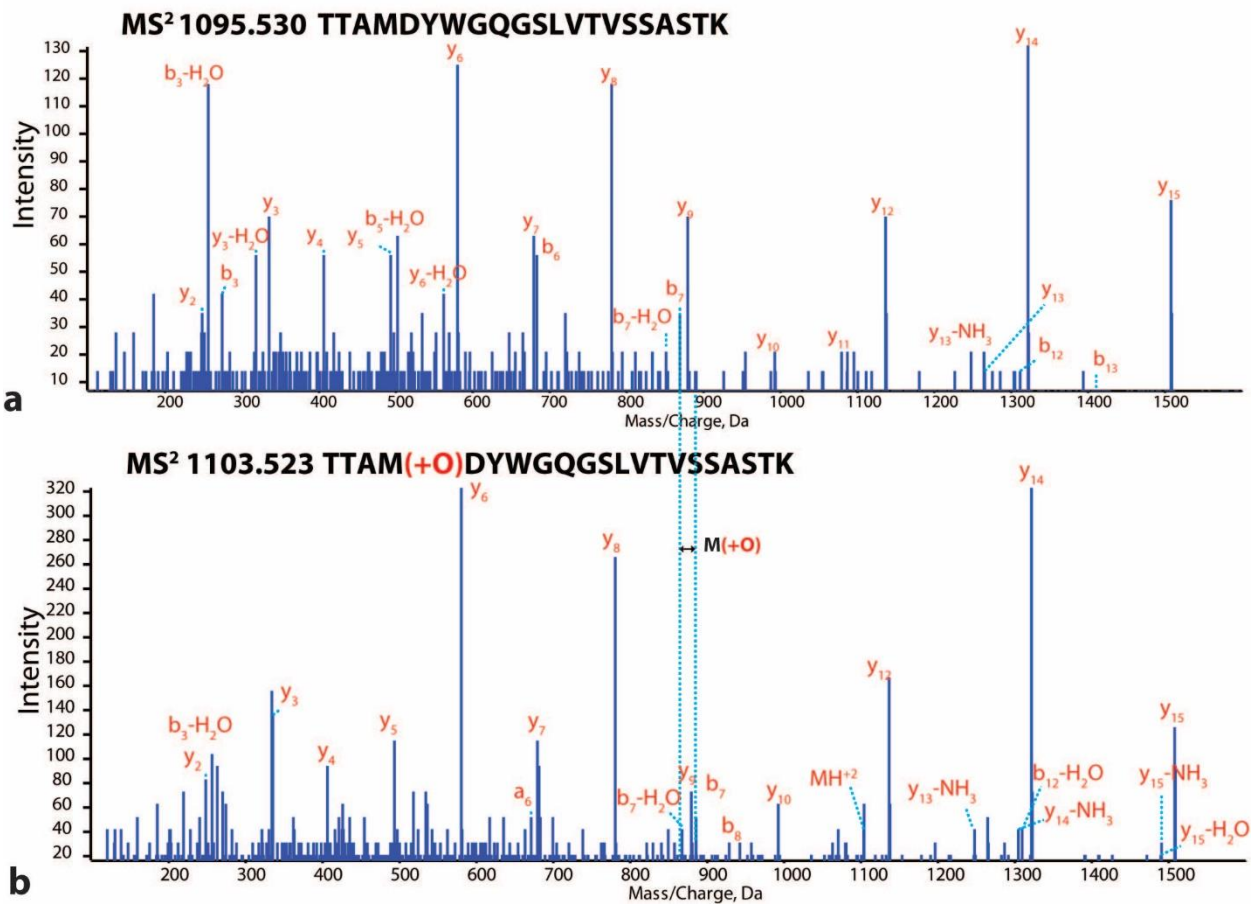
MS² 1095.530 TTAMDYWGQGSLVTVSSASTK
Intensity
Mass/Charge, Da
a
MS² 1103.523 TTAM(+O)DYWGQGSLVTVSSASTK
M(+O)
Intensity
Mass/Charge, Da
b

Figure 3

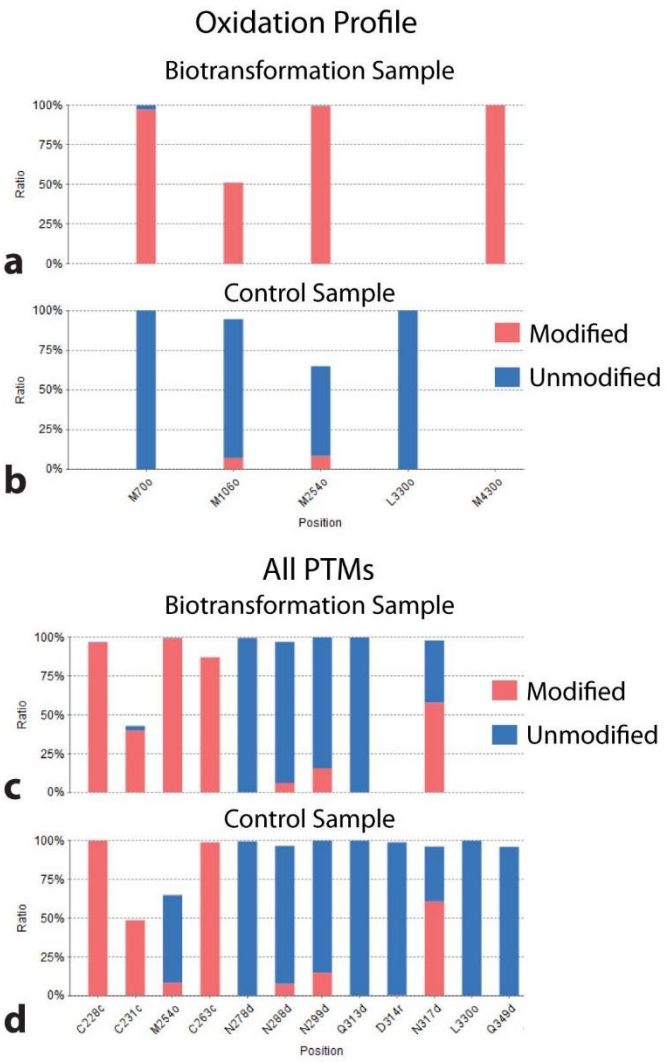
Oxidation Profile
Biotransformation Sample
Ratio
100%
75%
50%
25%
0%
a
Control Sample
Modified
Unmodified
b
M70o
M106o
M254o
L330o
M430o
Position
All PTMs
Biotransformation Sample
c
Control Sample
d
C228c
C231c
M254o
C263c
N278d
N286d
N298d
Q313d
D314r
N317d
L330o
Q349d

Figure 4

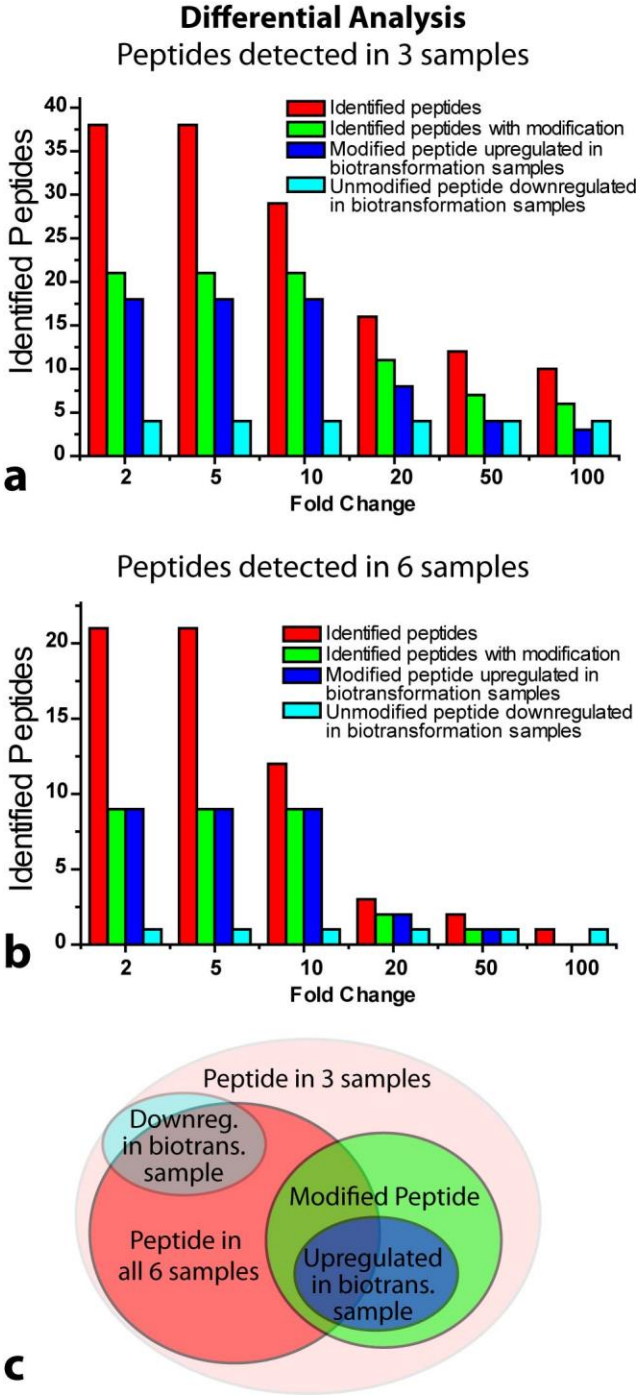
Differential Analysis
Peptides detected in 3 samples
Identified Peptides
Identified peptides
Identified peptides with modification
Modified peptide upregulated in biotransformation samples
Unmodified peptide downregulated in biotransformation samples
Fold Change
a
Peptides detected in 6 samples
Identified Peptides
Identified peptides
Identified peptides with modification
Modified peptide upregulated in biotransformation samples
Unmodified peptide downregulated in biotransformation samples
Fold Change
b
Peptide in 3 samples
Downreg. in biotrans. sample
Modified Peptide
Peptide in all 6 samples
Upregulated in biotrans. sample
c

Figure 5

Tables

Table 1. Partial List of PTMs detected by PEAKS PTM algorithm.

Name	**#PSM**	**∆Mass**	**Position**	**-10lgP**
Carbamidomethyl	1638	57.02	C	200
Carbamidomethyl	1407	57.02	DEHK,N-term	132.5
Deamidation	964	0.98	NQ	200
Oxidation	223	15.99	M	155.8
Dihydroxy	143	31.99	CFKPRW	126.5
Oxidation	129	15.99	HW	122.7
Ubiquitin	80	114	CKST	84.31
Ammonia loss	59	-17.03	N	130.8
Ammonium	56	17.03	DE,C-term	53.12
Hydroxylation	39	15.99	DKNPY	72.49
Pyro-glu from Q	34	-17.03	N-term	105.1
Dehydration	33	-18.01	DSTY,C-term	87.02
DehydroalaC	26	-33.99	C	104.9
Trifluoro	23	53.97	L	43.29
Cysteic acid	22	47.98	C	83.85
Amidation	19	-0.98	C-term	56.34
Dethiomethyl	18	-48	M	43.77
Methyl ester	15	14.02	DE,C-term	38.11
Methylation	14	14.02	S	42.68
Carbamylation	13	43.01	N-term	35.57
Sulfation	13	79.96	ST	133.3
Carboxylation	12	43.99	DK	55.7
Pyro-cmC	10	39.99	N-term	87.79
Carbamidomethyl DTT	10	209	C	62.44

353

Table 2. Partial list of significantly changed peptides by differential analysis. In the sample profile and group profile columns, the left panel represented the biotransformed samples and the right panel represented the control samples.

Peptide	Significance (-10lgP)	m/z	z	Avg. Area	Sample Profile	Group Profile	PTM
DTLMISR	29.63	418.2209	2	1.40E+04			
DTLM(+15.99)ISR	18.98	426.2198	2	2.70E+04			Oxidation (M)
SVMHEALHNHYTQK	16.39	565.6129	3	660.4			
SVM(+15.99)HEALHNHYTQK	7.72	428.4561	4	180.6			Oxidation (M)
SC(+57.02)SVMHEALHNHYTQK	17.57	486.2236	4	513.1			Carbamidomethylation
SC(+57.02)SVM(+15.99)HEALHNHYTQK	12.71	490.2209	4	238.2			Carbamidomethylation; Oxidation (M)
TTAMDYWGQGSLVTVSSASTK	12.94	730.6826	3	666.4			
TTAM(+15.99)DYWGQGSLVTVSSASTK	17.17	1103.523	2	6.20E+03			Oxidation (M)

354

Table 3. Summary of peptides that underwent other significant biotransformation. The mass difference of each PTM was shown in the peptide sequence: deamidation (+0.98), carbamidomethylation (+57.02) and dimethylation (+28.03).

Native peptides	Modified peptides	% Modified (Biotransformed)	
		Biotransformed	Control
TVLHQDWLNGK	TVLHQDWLN(+0.98)GK	45.5	36.6
VVSVLTVLHQDWLNGK	VVSVLTVLHQDWLN(+0.98)GK	76.3	39.6
C(+57.02)PAPELLGGPSVFLFPPKPK	C(+57.02)(+28.03)PAPELLGGPSVFLFPPKPK	55.5	44.3
EEQYNSTYR	EEQYN(+0.98)STYR	42	10.5
FNWYVDGVEVHNAK	FNWYVDGVEVHN(+0.98)AK	3.3	4.8
HQDWLNGK	HQDWLN(+0.98)GK	64	51
IC(+57.02)NVNHKPSNTK	IC(+57.02)NVN(+0.98)HKPSNTK	6.4	0

Supporting information

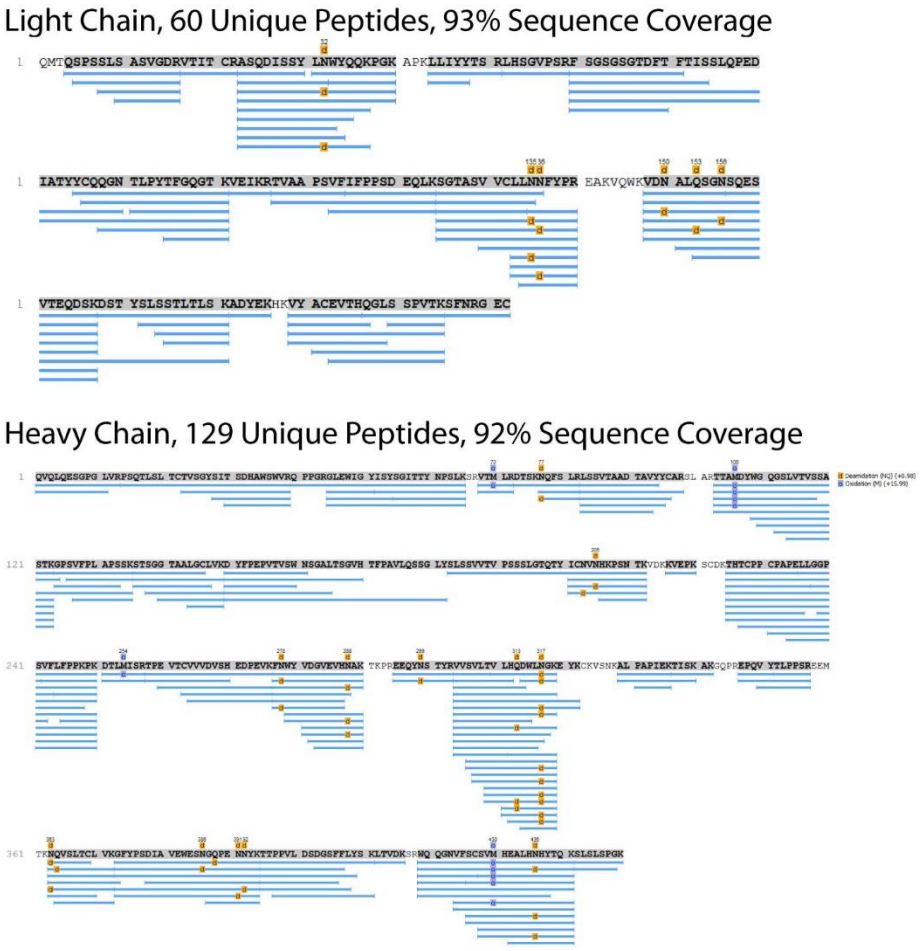

Supplemental Figure 1. Sequence coverage and modifications detected in the heavy and light chains.

Supplemental Table 1. Full list of PTMs detected by PEAKS PTM algorithm. All point mutations were counted as one type of PTMs during data analysis

Name	#PSM	ΔMass	Position	-10lgP	Area	AScore
Carbamidomethyl	1638	57.02	C	200	1.24E+05	1000
Carbamidomethyl	1407	57.02	DEHK,N-term	132.5	4.57E+03	65.71
Deamidation	964	0.98	NQ	200	1.62E+05	0
Oxidation	223	15.99	M	155.8	1.82E+04	1000
Sodium	197	21.98	DE,C-term	119.8	4.84E+03	33.58
Dihydroxy	143	31.99	CFKPRW	126.5	1.36E+03	58.99
Oxidation	129	15.99	HW	122.7	3.35E+02	20.75
Ubiquitin	80	114	CKST	84.31		7.65
Ammonia loss	59	-17.03	N	130.8	1.02E+04	1000
Ammonium	56	17.03	DE,C-term	53.12	5.61E+02	21.68
Met->Val	50	-31.97	V	67.07	2.77E+02	1000
Leu->His	44	23.97	H	59.73	4.53E+03	1000
Hydroxylation	39	15.99	DKNPY	72.49	2.88E+02	17.01
Leu->Met	37	17.96	M	62.2	1.88E+03	1000
Pyro-glu from Q	34	-17.03	N-term	105.1	3.70E+04	1000
Dehydration	33	-18.01	DSTY,C-term	87.02	1.30E+02	14.84
DehydroalaC	26	-33.99	C	104.9	4.10E+02	1000
Gly->Cys	24	45.99	C	34.2	3.78E+02	1000
Trifluoro	23	53.97	L	43.29	2.63E+04	0
Cysteic_acid	22	47.98	C	83.85	7.10E+02	1000
Amidation	19	-0.98	C-term	56.34	1.96E+03	1000
Pro->Thr	19	3.99	T	54.84	4.79E+03	1000
Dethiomethyl	18	-48	M	43.77	3.48E+04	1000
Cation:K	18	37.96	DE,C-term	75.31	1.25E+03	48.45
Methyl ester	15	14.02	DE,C-term	38.11	9.61E+02	68.81
Methylation	14	14.02	S	42.68	1.75E+03	14.02
Carbamylation	13	43.01	N-term	35.57	1.01E+04	79.05
Sulfation	13	79.96	ST	133.3	1.05E+02	0
Arg->Lys	13	-28.01	K	28.57	3.61E+03	1000
Cation:Ca[II]	12	37.95	DE	62.21	1.16E+03	59.1
Carboxylation	12	43.99	DK	55.7	2.77E+02	63.64
Pyro-cmC	10	39.99	N-term	87.79	1.78E+03	1000
Leu->Val	10	-14.02	V	35.41	5.88E+02	1000

CarbamidomethylDTT	10	209	C	62.44	2.60E+02	1000
Bromobimane	8	190.1	C	50.35	3.14E+02	1000
Acetylation	8	42.01	N-term	93.51	1.17E+02	1000
Phosphorylation	8	79.97	ST	96.28	8.82E+01	15.39
Sulphone	8	31.99	M	93.51	1.17E+02	1000
O-Diethylphosphate	7	136	CS	61.64		0
Cys->ethylaminoAla	6	11.07	C	43.65	3.64E+02	0
Ala->Pro	6	26.02	P	43.13	2.81E+02	1000
Tyr->Asn	6	-49.02	N	35.51	1.64E+03	1000
Lys->Asn	5	-14.05	N	55.95	1.38E+03	1000
Ser->Leu	5	26.05	L	94.19	2.24E+02	1000
Thr->Arg	5	55.05	R	47.18	2.88E+01	1000
Met->Thr	5	-29.99	T	39.61	2.63E+02	1000
Carboxymethyl	5	58.01	N-term	59.27	4.89E+03	58.79
Propionald+40	5	40.03	HK	77.59	1.78E+02	69.9
Cation:Fe[II]	4	53.92	DE	32.17	4.50E+03	77.53
Lysaminoadipicsealde	4	-1.03	K	32.72		62.5
Ala->Ser	4	15.99	S	39.66	7.48E+02	1000

.

Appendix IV Development of Potent, Protease-Resistant Agonists of the Parathyroid Hormone Receptor with Broad β Residue Distribution

Adapted from:
R. Cheloha, **B. Chen**, N. Kumar, T. Watanabe, T. Dean, R. Thorne, L. Li, T. Gardella and S. Gellman, Development of Potent, Protease-Resistant Agonists of the Parathyroid Hormone Receptor with Broad β Residue Distribution. *Submitted to JACS, manuscript under review.*

Abstract

The parathyroid hormone receptor-1 (PTHR1) is a member of the B-family of GPCRs; these receptors are activated by long polypeptide hormones and constitute targets of drug development efforts. Parathyroid hormone (PTH; 84 residues) and PTH-related protein (PTHrP) are natural agonists of PTHR1, and an N-terminal fragment of PTH, PTH(1−34), is used clinically to treat osteoporosis. Conventional peptides in the 20-40-mer length range, such as PTH(1-34), are rapidly degraded by proteases, which may limit their biomedical utility. We have used the PTHR1-ligand system to explore the impact of broadly distributed replacement of α-amino acid residues with β-amino acid residues, based on the expectation that $\alpha \rightarrow \beta$ replacements will diminish susceptibility to proteolysis. This effort led us to identify new PTHR1 agonists that contain $\alpha \rightarrow \beta$ replacements throughout their sequences, maintain potent agonist activity, and display remarkable resistance to proteolysis. One highly stabilized analogue is shown to be active in mice. These findings suggest a path toward identifying protease-resistant agonists of other B-family GPCRs.

Introduction

Individual cells in multicellular organisms must receive and respond to a wide array of molecular messages from other cells.[1] Much of this information is conveyed by polypeptides, such as growth factors, cytokines or peptide hormones. Aberrant polypeptide-mediated signaling is associated with many human diseases, and therapeutic benefits can be achieved through use of synthetic polypeptides to block excessive signaling (e.g., engineered antibodies or receptor fragments) or to augment insufficient signaling (e.g., peptide hormone analogues).[2] Although drug molecules based on the poly-α-amino acid backbone frequently display high potency and selectivity, this molecular class manifests intrinsic limitations. Poly-α-peptides that do not adopt a stable tertiary structure, such as peptide hormones and their analogues, tend to be degraded rapidly by proteases.[3-5]

Concerns about poly-α-peptides as drugs have led to exploration of oligomers with unnatural backbones as a source of molecules that can strongly and specifically engage natural target proteins but

resist biodegradation.[6] This pursuit offers many opportunities for chemical innovation,[7] but progress to date has been limited, particularly in terms of establishing efficacy *in vivo*[8-14]and characterizing immune responses.[15,16] Our own efforts have focused on peptidic oligomers that contain both α- and β-amino acid residues (α/β-peptides).[17-21] We recently demonstrated that α/β analogues of two hormones, glucagon-like peptide-1 (GLP-1) and parathyroid hormone (PTH), can serve as potent agonists of the cognate receptors, the GLP-1R and the PTHR1, respectively, in cell-based assays,[12,13,22] and these compounds manifest the predicted activity in mice.[12,13,22] The sites of α→β replacement in these bioactive analogues were limited to the C-terminal portions of PTH(1-34) or GLP-1(7-37), regions that are known to be α-helical in the receptor-bound state.[23,24] Related studies have been reported with α/β analogues of vasoactive intestinal peptide, a hormone for which no structural information is available.[14] It is noteworthy that the introduction of as few as one or two α→β replacements can substantially diminish PTHR1 agonist activity,[25,26] which shows that proper selection of substitution sites is crucial.[27]

This report discloses new α/β-peptide analogues of PTH(1-34), which is the active ingredient in the osteoporosis drug teriparatide.[28] Our previous examination[12] of analogues containing C-terminal α→β replacements culminated in evaluation of compounds **B5** and **D6** *in vivo* (the latter is renamed **6β** below). Both of these α/β-peptides were potent agonists of the PTHR1 as judged by cell-based assays; each matched PTH(1-34) in terms of promoting production of the second messenger cyclic adenosine monophosphate (cAMP).[12] Upon subcutaneous injection of **B5** or **D6**, mice displayed a "calcemic effect" that is characteristic of PTH(1-34) itself, i.e., both α/β-peptides caused a short-term rise in Ca^{2+} in the bloodstream.[12] This outcome provides an easily and rapidly detected indication that the PTHR1 has been engaged in the animal; however, from a clinical perspective**,** an excessive increase in blood calcium ion concentration can be a deleterious side effect of pharmacological PTHR1 activation in the context of osteoporosis therapy.[29] PTHR1 agonists are of particular interest, clinically, if they promote bone growth, but this outcome requires weeks to months of treatment to assess, and is therefore less useful as a read-out of bioactivity in vivo than is the calcemic effect, which occurs within minutes of administration.[30,31]

α/β-Peptide **D6** displayed a calcemic effect of prolonged duration relative to that induced by PTH(1-34), but the calcemic effect induced by **B5** was more transient than that of PTH(1-34).[12] Both α/β-peptides persisted longer in the mouse bloodstream than did PTH(1-34), with **D6** persisting longer than **B5**. The fact that PTH(1-34) analogues containing five or six α→β replacements retained high agonist activity was significant, given that earlier reports had shown that a single α→β replacement could substantially disrupt PTHR1 agonist activity.[25,26] The lack of correlation between persistence in the bloodstream (**D6** > **B5** > PTH(1-34)) and duration of calcemic response (**D6** > PTH(1-34) > **B5**) observed for this pair of analogues relative to PTH(1-34) was noteworthy.

The studies described here were motivated by three related questions. First, is it possible to place β residues near the N-terminus of a PTH(1-34) analogue while retaining agonist activity? This question is important because long stretches of α residues, such as the 13 N-terminal residues of **D6**, are highly susceptible to proteolysis. Our previous exploration of PTH(1-34) analogues[11,12] was limited to compounds containing α→β replacements in the portion known to be α-helical in the receptor-bound state, as demonstrated by the co-crystal structure of PTH(15-34) bound to the extracellular domain of the PTHR1.[23] The design of these initial PTH(1-34) analogues was based on our previous studies of α-helix mimicry with α/β-peptides.[21] In contrast to the structural information available describing the C-terminal portion of PTH(1-34) bound to the PTHR1, the receptor-bound conformation of the N-terminal portion of PTH is unknown.[31] This segment engages the core of the membrane-embedded heptahelical domain of the PTHR1 to initiate signal transduction.[32,33] Therefore, incorporation of β residues into this portion with retention of agonist activity represents a fundamental design challenge. Previous exploration of α→β replacements in a non-helical α-peptide[34] revealed the difficulty of making backbone modifications without loss of affinity for a target protein. Incorporation of non-natural α-residues into the N-terminal portion of PTHR1 agonists frequently causes substantial losses in biological activity[35,36]

Our second motivating question: is it possible to generate potent PTHR1 agonists that contain ring-constrained β residues rather than the flexible β^3 residues employed in α/β-peptides such as **B5** and

D6. This question arises because prior α-helix mimicry efforts have shown that β residues with a five-membered ring constraint, such as ACPC or APC (Figure 1), tend to enhance the stability of the α-helix-like conformation relative to β^3 residues (i.e., β residues bearing a side chain next to the nitrogen).[37,38] In addition, these cyclic β residues enhance resistance to proteolysis relative to β^3 residues.[39,40] We expected that cyclic β residues would be tolerated in the C-terminal portion of PTH(1-34) analogues,[13] because this region must adopt an α-helix-like conformation,[23] but it was necessary to test this prediction. Since the receptor-bound conformation of the N-terminal portion of PTH(1-34) is unknown, the effect on agonist activity of placing cyclic β residues in this region could not be predicted.

The third motivating question: is it possible to identify highly active PTH(1-34) analogues that contain β residues throughout the entire sequence? This question is important because of interest in oral delivery of peptide hormone analogues.[41-43] Patients generally prefer orally delivered drug regimens over parenteral administration, and oral delivery may therefore enhance dosing compliance.[44,45] However, poly-α-peptides face two large barriers to oral delivery. First, these molecules must survive the harsh proteolytic environments of the stomach and small intestine, which have been evolutionarily optimized for degradation of poly-α-peptides into amino acids and short peptides that can be absorbed as nutrients.[46] Second, these molecules must be able to move from the lumen of the intestine into the bloodstream.[47] Many compounds with MW < 500 and appropriate lipophilicity can move passively from the gut into the blood, but these routes are not generally available to long peptides and proteins.[42] Previous *in vitro* studies have shown that α/β-peptides containing at least 25% β residues distributed across the sequence can display substantial resistance to cleavage by aggressive proteases.[17,19,37] We therefore wondered whether it would be possible to achieve the necessary β residue density in a potent PTHR1 agonist to slow degradation under conditions encountered in the digestive tract, since such an α/β-peptide could circumvent the first barrier to oral polypeptide delivery and therefore provide a basis for future efforts to circumvent the second.

Materials and methods

Peptide synthesis and purification.

Peptides were synthesized as C-terminal amides on NovaPEG rink amide resin (EMD) using previously reported microwave-assisted solid-phase conditions, based on Fmoc protection of main chain amino groups[38]. Protected β^3-homoamino acids were purchased from PepTech or ChemImpex. See supporting information for detailed methods, HPLC chromatographs, and mass spectrometry data.

Binding and cAMP assays.

Binding to the R0 conformation of the human PTHR1 was assessed by competition assays by using membranes with ^{125}I-PTH(1–34) as tracer radio ligand as previously described.[11] cAMP signaling was assessed using HEK-293-derived cell lines that stably express the Glosensor cAMP reporter (Promega Corp.)[48] along with wild-type human PTHR1 (GP-2.3 cells) or human PTHR1 lacking the extracellular domain (GD5 cells). See supporting information for further details regarding methodology and data processing.

Simulated gastric and intestinal fluid stability studies.

Simulated gastric and intestinal fluids (SGF and SIF) were prepared according to instructions provided in the United States Pharmacopeia test solutions section. Experimental details regarding preparation of SGF and SIF, corresponding peptide degradation studies, and subsequent analysis are found in the supporting information.

Rat kidney homogenate studies.

All experimental protocols were approved by the Institutional Animal Care and Use Committee at the University of Wisconsin-Madison and performed in accordance with the National Institutes of Health Guide for the Care and Use of Laboratory Animals (8th edition; 2011). Kidney tissues were harvested, washed with ice-cold saline solution and adhering tissues

were trimmed. 4 mL of incubation buffer (50 mM Tris-HCl, pH 7.4) was added per gram of tissue, which was homogenized using a Teflon homogenizer. PTH standards (PTH(1-34) and **M-Cyc-9β**) were spiked in rat kidney homogenates to achieve a final concentration of 50 µg/mL (~12 µM). Samples were incubated, processed, and analyzed using either mass spectrometry or bioassay according to the supporting information.

In vivo pharmacology: calcemic response and pharmacokinetics.

Mice (CD1, female, age 9–12 weeks) were treated in accordance with the ethical guidelines adopted by Massachusetts General Hospital. Mice were injected subcutaneously with vehicle (10 mM citric acid/150 mM NaCl/0.05% Tween-80, pH 5.0) containing PTH(1-34) or α/β-peptide at a dose of 20 nmol/kg body weight. Further details are available in the supporting information.

Data Calculations.

Data were processed by using the Microsoft Excel and GraphPad Prism 4.0 software packages. Data from binding and cAMP dose–response assays were analyzed using a sigmoidal dose–response model with variable slope. Paired data sets were statistically compared by using Student's t test (two-tailed) assuming unequal variances for the two sets.

Results

α→β Scan of the N-terminal region of PTH(1-34)

In order to determine whether the N-terminal portion of PTH(1-34) can tolerate $\alpha \rightarrow \beta^3$ replacements, we synthesized analogues of this peptide in which each of the first eight residues was individually replaced by the homologous β^3 residue, i.e., by the β^3 residue bearing the same side chain as the original α residue (**1-8**, Figure 1). As with other α/β^3-peptides described previously, including **B5** and **D6**, α/β^3-peptides **1-8** were straightforward to prepare via conventional solid-phase methods; the necessary Fmoc-protected β^3-amino acid building blocks are commercially available. α/β-Peptides **1-8**

were evaluated as agonists of the PTHR1 expressed in HEK293 cells (GP2.3 cell line),[12] which have been stably transfected to express this receptor and a modified luciferase that is activated by the second messenger cAMP.[48] Thus, agonist efficacy can be assessed in terms of the degree to which a peptide induces intracellular production of cAMP via luminescence measurements.

The data (Figure 1, Supporting Figure 1) indicate that $\alpha \rightarrow \beta^3$ replacement is well tolerated at position 1 or 2, because analogues **1** and **2** display cAMP-inducing potencies comparable to that of PTH(1-34). Substitutions at the remaining six N-terminal positions, however, cause a 10- to 200-fold loss of efficacy (increased EC_{50} values). The sensitivity of PTH(1-34) to single-site modifications at residues 3-8 is noteworthy, because we previously observed that incorporation of five or six $\alpha \rightarrow \beta^3$ modifications in the C-terminal portion (as in **B5** or **D6**) had little or no effect on efficacy as measured by cAMP production.

A second set of analogues (**1^c-9^c**) was prepared in which individual N-terminal residues were replaced by a β residue containing a five-membered ring constraint, ACPC or APC (Figure 1). The nonpolar cyclopentane-based ACPC residue[49] was used at the first eight positions, but APC[50] was used to replace His-9. These choices were dictated by the fact that APC bears a basic side chain nitrogen, which might mirror the basic imidazole ring in the His-9 side chain, while none of the preceding eight residues has a basic side chain. We did not prepare the PTH(1-34) analogue containing a β^3 substitution at position 9 because Fmoc-protected β^3-hHis is not commercially available, and the reported synthetic route to this molecule is cumbersome.[51]

Extensive structural precedent has established that β residues with a five-membered ring constraint and *trans* disposition of the amino and carboxyl groups support the adoption of an α-helix-like conformation by α/β-peptides.[17,21,37,38] ACPC and APC stabilize helical conformations relative to the more flexible β^3 residues. Since the conformation of the N-terminal portion of PTH bound to PTHR1 is unknown, one could not predict whether the cyclic β residues would be tolerated near the N-terminus. It is therefore noteworthy that several of the analogues containing a cyclic β residue matched PTH(1-34) in

terms of potency and efficacy at promoting cAMP production. Particularly striking were the results of ACPC substitution at position 5, 6 or 7, because in each case the resulting analogue was very similar in agonist activity to PTH(1-34), while the analogous β^3 substitutions caused a 12- to 160-fold decline in efficacy. These trends were mirrored in analogous experiments using a cell line (GD5)[52] that stably expresses a truncated version of the PTHR1 that lacks the extracellular domain (Supporting Figure 2). In these experiments, the introduction of ACPC at positions 1, 5, or 7 resulted in relatively minor losses in biological activity, whereas nearly all other β-substitutions caused moderate to complete losses in bioactivity (Supporting Figure 2). This finding is consistent with previous observations that the biological activities of PTHR1 agonists are more sensitive to N-terminal modifications in assays using cells that express a truncated PTHR1 lacking the extracellular domain in comparison to assays using the full-length PTHR1.[35,53]

Based on the results of single cyclic β substitutions, we examined two PTH(1-34) analogues with multiple cyclic β residues in the N-terminal region (Figure 2, Table 1, and Supporting Figure 3). Placing ACPC residues at positions 1 and 7 generated an α/β-peptide (**2β**) with efficacy indistinguishable from that of the analogues containing only one of the substitutions or from PTH(1-34) itself. However, introduction of a third ACPC residue, at position 5 (**3β**), caused a substantial decline in agonist activity.

α/β-Peptide analogues of PTH(1-34) containing multiple cyclic β residues and broad β distribution.

We prepared α/β-peptide **Cyc-6β** (Figure 2) to determine whether replacement of the six β^3 residues in **6β** (previously designated **D6**)[12] with cyclic β residues would affect agonist activity. At four positions we used the hydrophobic cyclic β residue ACPC, and at the remaining two sites we used the basic cyclic β residue APC. It is straightforward to mimic the natural side chain upon $\alpha \rightarrow \beta^3$ replacement, but side chain mimicry becomes more ambiguous when cyclic β residues are employed, particularly since only a few such residues are currently available. Since β^3-hTrp, β^3-hMet and β^3-hPhe all bear hydrophobic side chains, it is logical to replace these β^3 residues with ACPC. APC is a logical replacement for β^3-hLys because both residues have a basic side chain. The remaining two residues bear

acidic side chains. We replaced β^3-hGlu with APC and β^3-hAsp with ACPC in an effort to balance concern about creating an α/β-peptide that might be excessively hydrophobic with concern about deviating too far from the natural pattern of charged side chains in PTH(1-34). **Cyc-6β** was indistinguishable from **6β** as a PTHR1 agonist, based on cAMP production, and both were very similar to PTH(1-34) itself (Table 1).

We then prepared two α/β-peptide analogues of PTH(1-34) containing α→β replacement at nine sites, **9β** and **Cyc-9β**, in the hope of identifying a potent PTHR1 agonist with β residues distributed along the entire length (Figure 2). Analogue **9β**, which combines the three α→cyclic β replacements of **3β** with the six α→β^3 replacements of **6β**, displayed ~50-fold lower potency relative to the analogue containing only the three N-terminal cyclic β residues (**3β**) (Table 1). Since PTH(1-34) and **6β** are very similar in efficacy, the difference between **3β** and **9β** suggests some sort of anti-cooperativity, in terms of activating the PTHR1, between the sets of α→β replacements in the N- and C-terminal regions of **9β**. Replacing the six β^3 residues of **9β** with cyclic β residues, to generate **Cyc-9β**, provided a nearly 10-fold improvement in potency, but **Cyc-9β** nevertheless displays > 200-fold lower potency relative to PTH(1-34), as monitored by stimulation of cAMP production (Table 1).

α/β-Peptide analogues of M-PTH(1-34) containing multiple cyclic β residues and broad β distribution.

A new series of α/β-peptides was prepared based on previously reported potent synthetic analogues of PTH(1-34), designated M-PTH(1-34), that display a modified signaling profile *in vivo* relative to PTH(1-34) (Figure 2).[54] Two versions of M-PTH(1-34) have been described, one containing the Ser3→Ala modification and the other with the Ser3→aminoisobutyric acid (Aib) modification. The Ser3→Ala substitution was shown to substantially improve the bioactivity of PTH(1-14) analogues in an early structure-activity relationship study,[55] while a later study showed that incorporation of Aib at position 3 further enhanced PTHR1 activation potency, at least in PTH(1-14) derivatives.[35] Our PTHR1 activation assays showed the Ser3→Ala version of M-PTH(1-34) to have slightly reduced cAMP-inducing potency relative to PTH(1-34), which is consistent with previous reports on the properties of the

Ser3→Aib version of M-PTH(1-34) (Table 1, Supporting Figure 4).[54] Analogues of the Ser3→Ala version of M-PTH(1-34) bearing only C-terminal α→β replacements, **M-6β** and **M-Cyc-6β**, were very similar in efficacy to M-PTH(1-34) (Table 1). Thus, the M-PTH(1-34) scaffold parallels the PTH(1-34) scaffold in response to C-terminal α→β replacements (Figure 2, Supporting Figure 4). The Ser3→Aib version of M-PTH(1-34) was used as the basis for analogues containing N-terminal α→β replacements (Figure 2). In the M-PTH(1-34) context, these replacements evoked responses quite different from those caused by analogous replacements in the PTH(1-34) context. Thus, α/β-peptides **M-3β**, **M-9β** and **M-Cyc-9β** were all quite similar to the α-peptide prototype, M-PTH(1-34), in terms of cAMP-inducing potency (Table 1), which contrasts with the substantial declines in potency observed for the corresponding α/β analogues of PTH(1-34) (Table 2). Particularly striking is the observation that the cAMP potencies of **M-Cyc-9β** and M-PTH(1-34) differ by < 3-fold, while the efficacies of **Cyc-9β** and PTH(1-34) differ by > 200-fold (Table 2).

The agonist activity of **M-Cyc-9β** represents an affirmative answer to all three of the questions that motivated these studies. This α/β-peptide contains multiple α→β replacements near the N-terminus, all of the replacements are derived from cyclic β-amino acids, the sites of α→β replacement are distributed along the entire length, and this analogue approaches PTH(1-34) in efficacy and potency as an agonist of the PTHR1. Subsequent studies focused on a more extensive characterization of **M-Cyc-9β**, *in vitro* and *in vivo*.

*Susceptibility of **M-Cyc-9β** to proteolysis.*

PTH(1-34) disappears rapidly from the bloodstream following subcutaneous injection.[56] This disappearance is due in part to removal via filtration and/or proteolysis by the kidneys.[57] Proteases in homogenized rat kidney preparations rapidly degrade PTH(1-34), causing cleavage at multiple sites.[58] We therefore sought to determine whether the backbone modifications in **M-Cyc-9β** would enhance stability relative to PTH(1-34) in rat kidney tissue homogenate.

HPLC analysis was not feasible for these assays because kidney homogenate contains high levels of diverse biomolecules that complicate chromatographic resolution and interpretation. We therefore developed a mass spectrometry-based method for quantifying the concentration of intact PTH(1-34) or **M-Cyc-9β** within samples of kidney homogenate as a function of time. This approach indicated that the half-life of **M-Cyc-9β** is about 15 times longer than that of PTH(1-34) in rat kidney homogenate (Figure 3a). Sites of hydrolysis in each peptide were identified using matrix-assisted laser desorption/ionization-time of flight (MALDI-TOF) mass spectrometry (Figure 3b-c). Many degradation fragments were observed for PTH(1-34) within 5 min of exposure to rat kidney homogenate, and cleavage was so rapid and broadly distributed that few large fragments could be detected after 15 min (Figure 3b). Intact PTH(1-34) could not be detected by MALDI-TOF MS after the first 5 min. In contrast, only a few fragments of **M-Cyc-9β** could be detected upon incubation with rat kidney homogenate, and intact α/β-peptide was clearly evident even after 4 hr (Figure 3c).

Mass spectrometric analysis was complemented by the application of a bioassay method for assessing the persistence of agonist activity (Figure 3d). This method measures the capacity of a preparation of peptide exposed to kidney homogenate, or other degradative conditions, to induce cAMP responses in GP2.3 cells as a function of duration of exposure to the degradative agent. This approach was thus used to monitor the loss of peptide bioactivity in kidney homogenate over time (Figure 3d). After 30 min exposure to kidney homogenate, the activity of PTH(1-34) had declined approximately 1,000-fold, as indicated by a rightward shift in the dose-response plot. In contrast, the activity of **M-Cyc-9β** in this assay was not significantly altered after 60 min exposure to kidney homogenate. Collectively, these studies revealed that α/β-peptide **M-Cyc-9β**, containing nine cyclic β residues distributed throughout the backbone, displays substantial resistance to destruction in the presence of rat kidney homogenate relative to α-peptide PTH(1-34).

We turned to simulated gastric fluid (SGF) and simulated intestinal fluid (SIF) for further evaluation of the proteolytic susceptibility of **M-Cyc-9β**. The stomach environment promotes very rapid

breakdown of proteins into short peptides and amino acids.[42] SGF, an acidic solution of pepsin, enables one to estimate the lifetime of a peptide or protein in the stomach.[46] We used SGF to compare **M-Cyc-9β**, PTH(1-34), and **6β** in terms of the likelihood of degradation after oral ingestion. Two assays were employed to assess persistence as a function of time of exposure to SGF. One assay measured the amount of full-length peptide present at various times via HPLC.[17] The second relied on the bioassay described above for kidney homogenate studies to evaluate the capacity of material generated by SGF treatment to activate the PTHR1 as a function of time of exposure to SGF. These assays provide complementary insights. Results from the latter will reflect net activity based on all species present. Some degradation products, e.g., peptides lacking only a few C-terminal residues, may retain PTHR1 agonist activity, while other degradation products, e.g., those lacking only a few N-terminal residues, may display antagonist activity.[31]

The HPLC assay (Supporting Figure 5) showed that neither PTH(1-34) nor the α/β-peptide **6β** could be detected after 5 sec in SGF. In striking contrast, **M-Cyc-9β** displayed a half-life of 4 hr in SGF. These observations show that the profoundly destructive nature of the stomach environment toward conventional peptides such as PTH(1-34) is manifested as well toward α/β-peptides that still retain long stretches of α-amino acid residues, such as **6β**, but is largely ineffective against peptides with β-residues regularly spaced along nearly the entire peptide chain. The markedly improved stability of **M-Cyc-9β** in SGF thus supports our hypothesis that distribution of cyclic β residues along the entire length of an α/β-peptide will confer substantial resistance to proteolysis.

The PTHR1 activation assay results (Figure 4) further highlight the remarkable resistance of **M-Cyc-9β** to proteolytic degradation. After 5 sec exposure to SGF, the PTH(1-34) sample displayed no detectable agonist activity; however, very weak PTHR1 agonist activity was observed for the **6β** sample after 5 sec in SGF. In contrast, even after 4 hr in SGF the **M-Cyc-9β** sample displayed very strong agonist activity. Characterization of the peptide fragments produced following incubation in SGF using MALDI-TOF MS (Figure 4e) provides insight into the mechanism by which biological activity is

destroyed by SGF. Protease-catalyzed hydrolysis of **6β** following residue 7 produces two fragments that, based on previous structure-activity studies,[31] are likely to be devoid of biological activity.

Simulated intestinal fluid (SIF) contains a mixture of pancreatic enzymes (pancreatin), including trypsin, in pH-neutral buffer.[46] Even if a peptide survives passage through the stomach, this molecule must persist in the small intestine in order to have an opportunity to move out of the GI tract.[41,42] Because of the complex composition of SIF, an HPLC-based assay could not be established. Therefore, only the PTHR1 activation bioassay was employed to assess susceptibility to proteolysis in SIF. **M-Cyc-9β** and PTH(1-34) were compared (Figure 4f). After 10 min exposure, very little agonist activity was retained in the PTH(1-34) sample. In contrast, the **M-Cyc-9β** sample retained considerable activity at this time point.

*Activity of **M-Cyc-9β** in vivo.*

The potent PTHR1 agonist activity observed for **M-Cyc-9β** in cell-based assays (Figure 2) and the remarkable resistance to proteolysis demonstrated by studies with kidney homogenates, SGF and SIF (Figures 3 and 4) prompted us to ask whether this α/β-peptide would activate the PTHR1 *in vivo*. This question was addressed by monitoring the calcemic effect induced by **M-Cyc-9β** in mice after subcutaneous injection (Figure 5). This assessment included **Cyc-6β**, a PTH(1-34) analogue that represents an intermediate stage in the evolution of **M-Cyc-9β** from **6β**; α/β-peptide **6β** itself was previously evaluated *in vivo*.[12]

New α/β-peptides **M-Cyc-9β** and **Cyc-6β** are indistinguishable from one another and very similar to PTH(1-34) in terms of the temporal profile of changes in bloodstream Ca^{2+} concentration they induce (Figure 5a). These data indicate that both of the new α/β-peptides are competent to engage the PTHR1 *in vivo*. It is curious, however, that neither **M-Cyc-9β** nor **Cyc-6β** generates the long-lasting calcemic effect previously observed for **6β**[20] and for the α-peptide M-PTH(1-34).[12,54] As noted above, an excessive calcemic effect is generally regarded as undesirable from a therapeutic perspective in treating osteoporosis.[29]

An activity-based bioassay was used to monitor the level of **M-Cyc-9β** or **Cyc-6β** in the mouse bloodstream after injection (Figure 5b). This assay is based on the ability of serum from mice injected with peptide to activate the PTHR1 in our cell-based assay. Results from the cell-based assay were converted to serum peptide concentrations using a standard curve (supporting Figure 6); a control study was performed with PTH(1-34). As previously observed,[12,54] after injection of PTH(1-34) the level of excess PTHR1-stimulating activity in the mouse bloodstream rises almost immediately and then rapidly subsides, nearly returning to the baseline level after 2 hr. New α/β-peptides **M-Cyc-9β** and **Cyc-6β** display divergent behavior in terms of bloodstream bioavailability, despite their similarity in terms of calcemic effect profile (Figure 5a). **Cyc-6β** attains a concentration in the bloodstream that is modestly higher than that of PTH(1-34), and **Cyc-6β** seems to persist slightly longer than does PTH(1-34). In contrast, **M-Cyc-9β** is barely detectable in the mouse bloodstream at any point after injection. The contrast between the robust but indistinguishable calcemic responses induced by **M-Cyc-9β** and **Cyc-6β** and the substantial difference between the bloodstream bioavailability profiles of these two α/β-peptides may indicate that **M-Cyc-9β** rapidly and tightly binds to cell-surface PTHR1, while the binding of **Cyc-6β** is slower and/or weaker, such that **Cyc-6β** is detectable in the blood for longer periods than is M-Cyc-9β.

We compared affinities of these α/β-peptides and of PTH(1-34) for the PTHR1 in the absence of G protein (the R0 state of the receptor) via an established competition assay.[59] **M-Cyc-9β** binds two-fold more strongly to the receptor than does PTH(1-34), while **Cyc-6β** binds two-fold *less* strongly than does PTH(1-34) (Supporting Figure 7). This trend is consistent with the hypothesis that the low level of **M-Cyc-9β** detected in the mouse bloodstream after injection reflects peptide sequestration via receptor binding; however, it is not clear whether the four-fold affinity difference between **M-Cyc-9β** and **Cyc-6β** is sufficiently large to explain our observations. Another possible source of variation between these two α/β-peptides, which is not captured in the binding assay and was not tested, would involve the rate at which the agonist-PTHR1 complex is removed from the cell surface; the PTH(1-34)-PTHR1 complex is

known to be rapidly internalized and to continue signaling from endosomes.[60] Overall, it appears that strong and rapid binding of **M-Cyc-9β** to the PTHR1, possibly augmented by unusually rapid receptor internalization, could explain how this α/β-peptide can exert a strong effect on Ca^{2+} levels despite the fact that **M-Cyc-9β** is largely absent from the bloodstream.

There is a parallel between the *in vivo* behavior documented here for **M-Cyc-9β** and that reported previously for M-PTH(1-34).[54] Both of these molecules induce a robust calcemic effect upon injection in mice, but neither peptide achieves the bloodstream levels detected for PTH(1-34) after injection. This parallel suggests that differences in the M-PTH sequence relative to the PTH sequence impart both strong calcium-mobilization activity and rapid clearance from the bloodstream. Collectively, our observations and previous data for PTHR1-agonist peptides show that there is no correlation between the strength of the calcemic effect induced by a PTHR1 agonist peptide and the duration of that peptide's persistence in the mouse bloodstream.

Extension of the optimal α/β substitution pattern to PTHrP(1-34) and abaloparatide. There are two known natural agonists of PTHR1, parathyroid hormone and parathyroid hormone-related protein (PTHrP).[31] As is the case with PTH(1-34), N-terminal segments of PTHrP, such as PTHrP(1-34) or PTHrP(1-36), retain full agonist activity.[61] However, PTH(1-34) and PTHrP(1-36) differ considerably in their receptor-activating properties.[62] PTH(1-34) induces long-lasting receptor activation in which cAMP generation continues after PTHR1 has been internalized; PTH(1-34) remains bound to the internalized receptor.[54,60] In contrast, cAMP generation induced by PTHrP(1-36) is short-lived and mostly limited to receptor molecules on the cell surface.[59,60] PTHR1 activated by PTHrP(1-36) is only weakly active after internalization, at which point PTHrP(1-36) has dissociated from the receptor.[62] Differences in the cAMP signaling profiles for PTH and PTHrP are attributed to a divergence in the capacity of these peptides to bind to the R0 state of PTHR1.[54,59,60,62,63] PTH(1-34) binds more tightly than does PTHrP(1-36) to the R0 state of PTHR1, and M-PTH(1-34) binds even more tightly than does PTH(1-34).[54,59,63] This rank order coincides with the duration of PTHR1-mediated cAMP responses induced by these α-peptides in cell-

based assays.[54,59,63-65] The mechanistic underpinnings of this correlation are an active area of investigation.[60,62,66-70]

The distinctive signaling profile of PTHrP makes analogues of this peptide potentially advantageous as a basis for osteoporosis therapy, relative to PTH(1-34), because some PTHrP-analogues can promote bone growth but are less prone to causing an undesirable rise in blood calcium ion levels (decreased calcemic effect).[71-73] The decreased calcium mobilization activity of PTHrP analogues relative to PTH(1-34) may be related to the weaker R0 affinity of such peptides.[60,74] The enhanced calcium mobilization activities of M-PTH(1-34)[54], and a newly described PTHR1 agonist LA-PTH[65,75], relative to PTH(1-34), along with the higher affinity of these peptides for the PTHR1 R0 state relative to PTH(1-34), support this hypothesis. Abaloparatide is a synthetic peptide based on the sequence of PTHrP(1-34), containing multiple modifications in the segment spanning residues 22 to 31, that has recently completed a clinical trial for osteoporosis treatment with favorable results.[64,76,77] Abaloparatide binds even more weakly than does PTHrP(1-36) to the PTHR1 R0 state and also exhibits significantly reduced calcium mobilization activity relative to PTH(1-34) in the clinic.[64,76] As is the case with teriparatide, abaloparatide is delivered via subcutaneous injection.

Because the sequences of PTHrP(1-34) and abaloparatide differ significantly from those of PTH(1-34) and M-PTH(1-34), we used the former two to evaluate the generality of the pattern of nine cyclic β residues in **M-Cyc-9β**. This substitution pattern enabled retention of PTHR1 agonist activity in the context of the M-PTH(1-34) sequence, but these nine α→cyclic β substitutions (to generate **Cyc-9β**) caused a substantial drop in potency in the context of the PTH(1-34) sequence. Therefore, the outcome of these substitutions in the context of PTHrP(1-34) and abaloparatide could not be predicted (Figure 6).

Results of cell-based assays indicate that PTHrP(1-34) is very similar to PTH(1-34) in terms of stimulating cAMP production via engagement of the PTHR1 (Table 2, Supporting Figure 8), which is consistent with previous reports.[61] Imposing the nine α→cyclic β replacements found in **M-Cyc-9β** on the PTHrP(1-34) sequence, to generate **PTHrP-9β**, caused a small decline in agonist potency (~6-fold),

which is very similar to the effect of these replacements in the M-PTH(1-34) sequence (Table 2). The nine α→ cyclic β replacements in the abaloparatide sequence caused a slightly larger decline in agonist potency (~18-fold), but the resulting α/β-peptide, **Abl-9β**, was nevertheless quite potent in terms of stimulating cAMP production (Table 2). Making only six α→ cyclic β replacements in the C-terminal regions of PTHrP(1-34) and abaloparatide sequences at positions analogous to those of the replacements in **Cyc-6β** provided analogues (**PTHrP-6β** and **Abl-6β**) that also exhibited potent agonist activity (Supporting Figure 9).

Variation in affinity for different PTHR1 conformational states among the PTH(1-34), PTHrP(1-34), abaloparatide and α/β-peptide analogues offers another potential metric, beyond agonist activity (stimulation of cAMP production), by which peptides containing α→β replacements might be compared to prototype α-peptides and to one another. Use of previously developed binding assays using membrane preparations containing embedded receptor[59] demonstrated that PTHrP(1-34) and abaloparatide bound to the PTHR1 R0 conformational state 3- and 22-fold less tightly than does PTH(1-34), respectively, in accord with past findings (Supporting Figure 10).[59,64] The analogues of these peptides with a full set of α→cyclic β replacements, **PTHrP-9β** and **Abl-9β**, bound PTHR1 R0 4- and 3-fold less tightly than does PTH(1-34), respectively. Thus, the incorporation of nine α→cyclic β replacements into the PTHrP scaffold provides an analogue (**PTHrP-9β**) that maintains the weak PTHR1 R0 affinity characteristic of the prototype α-peptide, PTHrP(1-34), whereas the introduction of these same replacements in the abaloparatide scaffold (**Abl-9β)** modestly increases PTHR1 R0 affinity relative to the prototype. The origin of the different responses of the PTHrP(1-34) and abaloparatide sequences to the imposition of full sets of α→cyclic β replacements, with respect to R0 affinity, is unknown, but could plausibly be based on altered modes of interaction with the conformationally pliable ligand-binding surface of the receptor.

The PTHR1 bioactivity assay described above was used to evaluate the susceptibilities of PTHrP(1-34), abaloparatide, **PTHrP-9β** and **Abl-9β** to degradation in SGF and SIF (Figure 7, Supporting Figure 11). Both of the α-peptides were very rapidly degraded in SGF, as expected, with no agonist

activity detected for the PTHrP(1-34) sample after 3 min exposure, and very little activity detected for the abaloparatide sample at this time point (Figure 7). In contrast, no significant decline in agonist activity was detected for either α/β-peptide after 45 min exposure to SGF.

In SIF, the PTHrP(1-34) sample displayed very low agonist activity after 10 min exposure, and the abaloparatide sample displayed very low agonist activity after 20 min exposure (Supporting Figure 11). In each case, however, the analogous α/β-peptide manifested only a small decline in activity at the same time point. Thus, the pattern of α→cyclic β replacements that generated an M-PTH(1-34) analogue with both potent agonist activity toward PTHR1 and substantial resistance to proteolysis seems to deliver the same favorable combination of properties when extended to the PTHrP(1-34) and abaloparatide sequences.

Discussion

The results described here represent a substantial advance in the development of backbone-modified polypeptide hormone analogues because we have shown that a systematic "β-residue scan" can identify sites in the N-terminal region of PTH(1-34) that tolerate α→β replacements. Cyclic β residues prove to be superior to β^3 residues for maintaining potent agonist activity toward the PTHR1. In addition, we find that combining substitutions in the N-terminal region with an α→β substitution pattern previously identified in the C-terminal region of PTH(1-34) is most effective if cyclic β residues are employed throughout. Our approach ultimately identified nine sites of α→cyclic β substitution that deliver a modestly potent PTHR1 agonist in the context of PTH(1-34) and highly potent agonists in the context of three other sequences known to activate PTHR1: M-PTH(1-34), PTHrP(1-34) and abaloparatide. One of these potent α/β-peptide agonists, **M-Cyc-9β**, was active *in vivo*, inducing a calcemic effect in mice after injection. **M-Cyc-9β** is remarkably stable in environments that instantaneously destroy conventional peptides, such as kidney homogenate and simulated gastric fluid. These properties should support future efforts to achieve oral delivery of a bioactive α/β-peptide.

The observation that the analogues of M-PTH(1-34), PTHrP(1-34) and abaloparatide containing nine α→β substitutions (**M-Cyc-9β, PTHrP-9β** and **Abl-9β**) possessed potent agonist activity, whereas the corresponding analogue of PTH(1-34) (**Cyc-9β**) exhibited only moderate potency, indicates that different PTHR1 agonists may interact with this receptor in subtly different ways. Since the six C-terminal α→cyclic β substitutions used in this study are uniformly well-tolerated, with respect to retention of signaling activity, for all the PTHR1 agonist sequences tested (Table 1, Supporting Figure 9), it is likely that the divergence in the impact of α→β replacements on biological activity stems from modifications in the N-terminal portions of these peptides. The incorporation of an Ile5→ACPC substitution in the PTH(1-34) sequence or related α/β-peptide analogues causes a substantial loss in agonist potency (Table 1), which is consistent with previous observations that modifications at position 5 of PTH(1-34) usually cause substantially reduced agonist activity.[55] In this context, it is noteworthy that introduction of the Ile5→ACPC substitution into the M-PTH(1-34) sequence does not impair agonist activity (Table 1). This finding is consistent with the previously documented capacity of the receptor affinity-enhancing α residue substitutions found in the M-PTH sequence to mask the detrimental effects of unfavorable modifications, such as C-terminal truncation.[54] Histidine is found instead of isoleucine at position 5 of the PTHrP and abaloparatide sequences. Past work has shown that His5→Ile replacement in the PTHrP(1-36) scaffold enhances PTHR1 affinity.[59] The hydrophobicity of the ACPC residue found at position 5 of **PTHrP-9β** and **Abl-9β** may enable this β residue to mimic the impact of isoleucine at this position of the PTHrP/abaloparatide scaffold. It seems likely that characteristics of the residue at position 5 play a key role in controlling the activities of PTHR1 agonists.[31]

The identification of several potent PTHR1 agonists with varied β residue content enables an exploration of the relationship between variations in susceptibility to proteolysis and variations in bloodstream bioavailability. Our results indicate that these two characteristics are not directly correlated. For example, **M-Cyc-9β** is far less susceptible to proteolysis than is PTH(1-34) in all conditions evaluated, yet **M-Cyc-9β** was only weakly detectable in the mouse bloodstream following injection,

whereas PTH(1-34) was robustly detected (Fig. 5). We speculate that the low levels of **M-Cyc-9β** in the bloodstream may reflect rapid and essentially irreversible sequestration of this α/β-peptide by the PTHR1 in target tissues. Past work has shown that PTHR1 agonists with high affinity for the R0 state of the PTHR1 induce more enduring biological responses than does PTH(1-34), but that these high-R0-affinity agonists are less evident in the bloodstream following injection than is PTH(1-34).[54,75] This behavior may be related to the capacity of PTHR1 agonists with high R0 affinity to bind pseudo-irreversibly to the receptor, which is mostly located on bone and kidney cells, thereby removing peptide from circulation. The high R0 affinity of **M-Cyc-9β** might therefore contribute to its low bloodstream bioavailability.

The relatively modest extension in the duration of bloodstream bioavailability for **Cyc-6β** relative to PTH(1-34) was unexpected given the substantially prolonged bioavailability exhibited by **6β** relative to PTH(1-34) in past work.[12] The source of this *in vivo* difference between **6β** and **Cyc-6β** is not clear, given the similar properties of these α/β-peptides in cell-based assays (Table 1). One possible factor is that **6β** differs from **Cyc-6β** in physicochemical properties: **6β** shows a prolonged retention time on C18 reversed-phase HPLC relative to **Cyc-6β**, which itself shows a prolonged retention time relative to PTH(1-34), indicating that the rank order of hydrophobicity for these peptides is **6β** > **Cyc-6β** > **PTH(1-34)** (Supporting Figure 12). Enhanced peptide hydrophobicity can promote association with serum proteins, which can increase effective molecular weight and thereby slow filtration of the peptide from the bloodstream by kidney.[78] Since kidney filtration represents a major route of PTH elimination from the bloodstream,[57] differences between the bioavailability profiles of **6β** and **Cyc-6β** may be connected to differences in the hydrophobicity of these peptides.

The successful introduction of α→β replacements throughout the sequences of PTHR1 agonists with retention of potent bioactivity raises the possibility that these agonists might ultimately prove to be orally deliverable. The oral route is generally regarded as superior to all others in terms of patient preference, but this delivery strategy is problematic for peptides for at least two reasons. First, peptides are usually degraded rapidly in the stomach or small intestine. Second, peptides are too large to cross the

wall of the small intestine passively and enter the bloodstream.[42] Results reported here show that the peptides **M-Cyc-9β**, **PTHrP-9β**, and **Abl-9β** overcome the first problem, and they lay the groundwork for future efforts to address the challenge of enabling large peptides to move from the gastrointestinal tract into the bloodstream. Most current attempts to solve this problem rely on formulation of a peptide with small molecules that promote the passive peptide diffusion through epithelial cells that line the intestinal lumen.[41] Favorable results have been reported for medium-size peptide drugs such as PTH derivatives,[79-82] salmon calcitonin and glucagon-like peptide-1.[41] These efforts have relied on empirical screening efforts with large libraries of small molecule permeation enhancers and different dosing conditions using large populations of animals to identify optimal approaches.[81,83]

The results presented here strengthen the prospect that α/β-peptides will emerge as useful tools for analyzing biological phenomena at the molecular level, and perhaps even as therapeutic agents. Large-scale manufacture of α-peptides containing 20-40 residues for clinical use is feasible,[84] and the solid-phase synthesis of α/β-peptides is qualitatively similar to α-peptide synthesis. Ultimately, it would be attractive to produce α/β-peptides via the biosynthetic machinery, and recent reports encourage the hope that this goal could be achieved. Initial explorations suggested that the ribosomal biosynthesis of polypeptides containing β residues was inefficient or impossible.[85-87] Subsequent findings, however, show that β-amino acids can be incorporated by the ribosome into polypeptides.[88-91] These findings raise the prospect that evolutionary approaches could be harnessed for discovery of new bioactive α/β-peptides, and for the production of optimized compounds.

Acknowledgements

Research support was provided by the Wisconsin Alumni Research Foundation Discovery Challenge (R.W.C., B.C., N.K.). Additional support was provided by the University of Wisconsin-Madison Institute for Clinical and Translational Research and the Clinical and Translational Science Award program administered through the NIH National Center for Advancing Translational Sciences (NIH UL1TR000427 and KL2TR00428; R.G.T) and the

University of Wisconsin-Madison School of Pharmacy (N.K, R.G.T). The LC/MS instrument was purchased through funding support from NIH S10 RR029531. LL acknowledges a Vilas Distinguished Achievement Professorship with funding provided by the WARF and University of Wisconsin-Madison School of Pharmacy. This work was also supported by the National Institute of Health grants GM-056414 (R01; S.H.G.), DK11794 (PO1; T.J.G.) and AR066261 (P30; T.J.G.). R.W.C. was supported in part by a Biotechnology Training Grant from NIGMS (T32 GM008349). We thank the Analytical Instrumentation Center (School of Pharmacy, University of Wisconsin-Madison) for instrumentation support.

NOTES: The authors declare the following competing financial interest(s): S.H.G. is a co-founder of Longevity Biotech, Inc., which is pursuing biomedical applications of α/β-peptides. S.H.G., R.W.C., and T.J.G. are co-inventors on a patent application covering the PTH analogues described here. T.W. is an employee of Chugai Pharmaceutical Co. Ltd. and contributed to this work as an appointee at Massachusetts General Hospital.

Supporting Information Available: Supplementary methods and supplementary figures 1-14 and supporting table 1 are available free of charge at pubs.acs.org.

References

[1] Hunter, T., Signaling - 2000 and beyond. *Cell* **2000,** *100* (1), 113-127.

[2] Leader, B.; Baca, Q. J.; Golan, D. E., Protein therapeutics: A summary and pharmacological classification. *Nature Reviews Drug Discovery* **2008,** *7* (1), 21-39.

[3] Diao, L.; Meibohm, B., Pharmacokinetics and Pharmacokinetic-Pharmacodynamic Correlations of Therapeutic Peptides. *Clinical Pharmacokinetics* **2013,** *52* (10), 855-868.

[4] Vlieghe, P.; Lisowski, V.; Martinez, J.; Khrestchatisky, M., Synthetic therapeutic peptides: science and market. *Drug Discovery Today* **2010,** *15* (1-2), 40-56.

[5] Fosgerau, K.; Hoffmann, T., Peptide therapeutics: current status and future directions. *Drug Discovery Today* **2015,** *20* (1), 122-128.

[6] Checco, J. W.; Gellman, S. H., Targeting recognition surfaces on natural proteins with peptidic foldamers. *Current Opinion in Structural Biology* **2016,** *39*, 96-105.

[7] Pelay-Gimeno, M.; Glas, A.; Koch, O.; Grossmann, T. N., Structure-Based Design of Inhibitors of Protein-Protein Interactions: Mimicking Peptide Binding Epitopes. *Angewandte Chemie-International Edition* **2015,** *54* (31), 8896-8927.

[8] Kushal, S.; Lao, B. B.; Henchey, L. K.; Dubey, R.; Mesallati, H.; Traaseth, N. J.; Olenyuk, B. Z.; Arora, P. S., Protein domain mimetics as in vivo modulators of hypoxia-inducible factor signaling. *Proceedings of the National Academy of Sciences of the United States of America* **2013,** *110* (39), 15602-15607.

[9] Takada, K.; Zhu, D.; Bird, G. H.; Sukhdeo, K.; Zhao, J. J.; Mani, M.; Lemieux, M.; Carrasco, D. E.; Ryan, J.; Horst, D.; Fulciniti, M.; Munshi, N. C.; Xu, W. Q.; Kung, A. L.; Shivdasani, R. A.; Walensky, L. D.; Carrasco, D. R., Targeted Disruption of the BCL9/beta-Catenin Complex Inhibits Oncogenic Wnt Signaling. *Science Translational Medicine* **2012,** *4* (148).

[10] Lao, B. B.; Grishagin, I.; Mesallati, H.; Brewer, T. F.; Olenyuk, B. Z.; Arora, P. S., In vivo modulation of hypoxia-inducible signaling by topographical helix mimetics. *Proceedings of the National Academy of Sciences of the United States of America* **2014,** *111* (21), 7531-7536.

[11] Cheloha, R. W.; Watanabe, T.; Dean, T.; Gellman, S. H.; Gardella, T. J., Backbone Modification of a Parathyroid Hormone Receptor-1 Antagonist/Inverse Agonist. *ACS Chemical Biology* **2016,** *11* (10), 2752-2762.

[12] Cheloha, R. W.; Maeda, A.; Dean, T.; Gardella, T. J.; Gellman, S. H., Backbone modification of a polypeptide drug alters duration of action in vivo. *Nature Biotechnology* **2014,** *32* (7), 653-655.

[13] Johnson, L. M.; Barrick, S.; Hager, M. V.; McFedries, A.; Homan, E. A.; Rabaglia, M. E.; Keller, M. P.; Attie, A. D.; Saghatelian, A.; Bisello, A.; Gellman, S. H., A Potent alpha/beta-Peptide Analogue of GLP-1 with Prolonged Action in Vivo. *Journal of the American Chemical Society* **2014,** *136* (37), 12848-12851.

[14] Olson, K. E.; Kosloski-Bilek, L. M.; Anderson, K. M.; Diggs, B. J.; Clark, B. E.; Gledhill, J. M.; Shandler, S. J.; Mosley, R. L.; Gendelman, H. E., Selective VIP Receptor Agonists Facilitate Immune Transformation for Dopaminergic Neuroprotection in MPTP-Intoxicated Mice. *Journal of Neuroscience* **2015,** *35* (50), 16463-16478.

[15] Cheloha, R. W.; Sullivan, J. A.; Wang, T.; Sand, J. M.; Sidney, J.; Sette, A.; Cook, M. E.; Suresh, M.; Gellman, S. H., Consequences of Periodic alpha-to-beta(3) Residue Replacement for Immunological Recognition of Peptide Epitopes. *Acs Chemical Biology* **2015,** *10* (3), 844-854.

[16] Uppalapati, M.; Lee, D. J.; Mandal, K.; Li, H. Y.; Miranda, L. P.; Lowitz, J.; Kenney, J.; Adams, J. J.; Ault-Riche, D.; Kent, S. B. H.; Sidhu, S. S., A Potent D-Protein Antagonist of VEGF-A is Nonimmunogenic, Metabolically Stable, and Longer-Circulating in Vivo. *Acs Chemical Biology* **2016,** *11* (4), 1058-1065.

[17] Horne, W. S.; Johnson, L. M.; Ketas, T. J.; Klasse, P. J.; Lu, M.; Moore, J. P.; Gellman, S. H., Structural and biological mimicry of protein surface recognition by alpha/beta-peptide foldamers. *Proceedings of the National Academy of Sciences of the United States of America* **2009,** *106* (35), 14751-14756.

[18] Horne, W. S.; Boersma, M. D.; Windsor, M. A.; Gellman, S. H., Sequence-based design of alpha/beta-peptide foldamers that mimic BH3 domains. *Angewandte Chemie-International Edition* **2008,** *47* (15), 2853-2856.

[19] Checco, J. W.; Kreitler, D. F.; Thomas, N. C.; Belair, D. G.; Rettko, N. J.; Murphy, W. L.; Forest, K. T.; Gellman, S. H., Targeting diverse protein-protein interaction interfaces with alpha/beta-peptides derived from the Z-domain scaffold. *Proceedings of the National Academy of Sciences of the United States of America* **2015,** (1091-6490 (Electronic)).

[20] Checco, J. W.; Lee, E. F.; Evangelista, M.; Sleebs, N. J.; Rogers, K.; Pettikiriarachchi, A.; Kershaw, N. J.; Eddinger, G. A.; Belair, D. G.; Wilson, J. L.; Eller, C. H.; Raines, R. T.; Murphy, W. L.; Smith, B. J.; Gellman, S. H.; Fairlie, W. D., alpha/beta-Peptide Foldamers Targeting Intracellular Protein-Protein Interactions with Activity in Living Cells. *Journal of the American Chemical Society* **2015,** *137* (35), 11365-11375.

[21] Johnson, L. M.; Gellman, S. H., alpha-Helix Mimicry with alpha/beta-Peptides. *Methods in Enzymology* **2013,** *523*, 407-429.

[22] Hager, M. V.; Johnson, L. M.; Wootten, D.; Sexton, P. M.; Gellman, S. H., β-Arrestin-Biased Agonists of the GLP-1 Receptor from β-Amino Acid Residue Incorporation into GLP-1 Analogues. *Journal of the American Chemical Society* **2016**.

[23] Pioszak, A. A.; Xu, H. E., Molecular recognition of parathyroid hormone by its G protein-coupled receptor. *Proceedings of the National Academy of Sciences of the United States of America* **2008,** *105* (13), 5034-5039.

[24] Underwood, C. R.; Garibay, P.; Knudsen, L. B.; Hastrup, S.; Peters, G. H.; Rudolph, R.; Reedtz-Runge, S., Crystal Structure of Glucagon-like Peptide-1 in Complex with the Extracellular Domain of the Glucagon-like Peptide-1 Receptor. *Journal of Biological Chemistry* **2010,** *285* (1), 723-730.

[25] Schievano, E.; Mammi, S.; Carretta, E.; Fiori, N.; Corich, M.; Bisello, A.; Rosenblatt, M.; Chorev, M.; Peggion, E., Conformational and biological characterization of human parathyroid hormone hPTH(1-34) analogues containing beta-amino acid residues in positions 17-19. *Biopolymers* **2003,** *70* (4), 534-547.

[26] Peggion, E.; Mammi, S.; Schievano, E.; Silvestri, L.; Schiebler, L.; Bisello, A.; Rosenblatt, M.; Chorev, M., Structure-function studies of analogues of parathyroid hormone (PTH)-1-34 containing beta-amino acid residues in positions 11-13. *Biochemistry* **2002,** *41* (25), 8162-8175.

[27] Denton, E. V.; Craig, C. J.; Pongratz, R. L.; Appelbaum, J. S.; Doerner, A. E.; Narayanan, A.; Shulman, G. I.; Cline, G. W.; Schepartz, A., A beta-Peptide Agonist of the GLP-1 Receptor, a Class B GPCR. *Organic Letters* **2013,** *15* (20), 5318-5321.

[28] Neer, R. M.; Arnaud, C. D.; Zanchetta, J. R.; Prince, R.; Gaich, G. A.; Reginster, J. Y.; Hodsman, A. B.; Eriksen, E. F.; Ish-Shalom, S.; Genant, H. K.; Wang, O. H.; Mitlak, B. H., Effect of parathyroid hormone (1-34) on fractures and bone mineral density in postmenopausal women with osteoporosis. *New England Journal of Medicine* **2001,** *344* (19), 1434-1441.

[29] Qin, L.; Raggatt, L. J.; Partridge, N. C., Parathyroid hormone: a double-edged sword for bone metabolism. *Trends in Endocrinology and Metabolism* **2004,** *15* (2), 60-65.

[30] Cheloha, R. W.; Gellman, S. H.; Vilardaga, J.-P.; Gardella, T. J., PTH receptor-1 signalling[mdash]mechanistic insights and therapeutic prospects. *Nat Rev Endocrinol* **2015,** *11*, 712-724.

[31] Gardella, T. J.; Vilardaga, J.-P., International Union of Basic and Clinical Pharmacology. XCIII. The Parathyroid Hormone Receptors-Family B G Protein-Coupled Receptors. *Pharmacological Reviews* **2015,** *67* (2), 310-337.

[32] Hollenstein, K.; de Graaf, C.; Bortolato, A.; Wang, M. W.; Marshall, F. H.; Stevens, R. C., Insights into the structure of class B GPCRs. *Trends in Pharmacological Sciences* **2014,** *35* (1), 12-22.

[33] Bortolato, A.; Dore, A. S.; Hollenstein, K.; Tehan, B. G.; Mason, J. S.; Marshall, F. H., Structure of Class B GPCRs: new horizons for drug discovery. *British Journal of Pharmacology* **2014,** *171* (13), 3132-3145.

[34] Haase, H. S.; Peterson-Kaufman, K. J.; Levengood, S. K. L.; Checco, J. W.; Murphy, W. L.; Gellman, S. H., Extending Foldamer Design beyond alpha-Helix Mimicry: alpha/beta-Peptide Inhibitors of Vascular Endothelial Growth Factor Signaling. *Journal of the American Chemical Society* **2012,** *134* (18), 7652-7655.

[35] Shimizu, N.; Guo, J.; Gardella, T. J., Parathyroid hormone (PTH)-(1-14) and -(1-11) analogs conformationally constrained by alpha-aminoisobutyric acid mediate full agonist responses via the juxtamembrane region of the PTH-1 receptor. *Journal of Biological Chemistry* **2001,** *276* (52), 49003-49012.

[36] Caporale, A.; Biondi, B.; Schievano, E.; Wittelsberger, A.; Mammi, S.; Peggion, E., Structure-function relationship studies of PTH(1-11) analogues containing D-amino acids. *European Journal of Pharmacology* **2009,** *611* (1-3), 1-7.

[37] Peterson-Kaufman, K. J.; Haase, H. S.; Boersma, M. D.; Lee, E. F.; Fairlie, W. D.; Gellman, S. H., Residue-Based Preorganization of BH3-Derived alpha/beta-Peptides: Modulating Affinity, Selectivity and Proteolytic Susceptibility in alpha-Helix Mimics. *ACS Chemical Biology* **2015,** (1554-8937 (Electronic)).

[38] Horne, W. S.; Price, J. L.; Gellman, S. H., Interplay among side chain sequence, backbone composition, and residue rigidification in polypeptide folding and assembly. *Proceedings of the National Academy of Sciences of the United States of America* **2008,** *105* (27), 9151-9156.

[39] Johnson, L. M.; Mortenson, D. E.; Yun, H. G.; Horne, W. S.; Ketas, T. J.; Lu, M.; Moore, J. P.; Gellman, S. H., Enhancement of alpha-Helix Mimicry by an alpha/beta-Peptide Foldamer via Incorporation of a Dense Ionic Side-Chain Array. *Journal of the American Chemical Society* **2012,** *134* (17), 7317-7320.

[40] Werner, H. M.; Cabalteja, C. C.; Horne, W. S., Peptide Backbone Composition and Protease Susceptibility: Impact of Modification Type, Position, and Tandem Substitution. *ChemBioChem* **2016,** *17* (8), 712-718.

[41] Karsdal, M. A.; Riis, B. J.; Mehta, N.; Stern, W.; Arbit, E.; Christiansen, C.; Henriksen, K., Lessons learned from the clinical development of oral peptides. *British Journal of Clinical Pharmacology* **2015,** *79* (5), 720-732.

[42] Smart, A. L.; Gaisford, S.; Basit, A. W., Oral peptide and protein delivery: intestinal obstacles and commercial prospects. *Expert Opinion on Drug Delivery* **2014,** *11* (8), 1323-1335.

[43] Henriksen, K.; Andersen, J. R.; Riis, B. J.; Mehta, N.; Tavakkol, R.; Alexandersen, P.; Byrjalsen, I.; Valter, I.; Nedergaard, B. S.; Teglbjaerg, C. S.; Stern, W.; Sturmer, A.; Mitta, S.; Nino, A. J.; Fitzpatrick, L. A.; Christiansen, C.; Karsdal, M. A., Evaluation of the efficacy, safety and pharmacokinetic profile of oral recombinant human parathyroid hormone rhPTH(1-31)NH2 in postmenopausal women with osteoporosis. *Bone* **2013,** *53* (1), 160-166.

[44] DiBonaventura, M. D.; Wagner, J. S.; Girman, C. J.; Brodovicz, K.; Zhang, Q. Y.; Qiu, Y.; Pentakota, S. R.; Radican, L., Multinational Internet-based survey of patient preference for newer oral or injectable Type 2 diabetes medication. *Patient Preference and Adherence* **2010,** *4*, 397-406.

[45] Fallowfield, L.; Atkins, L.; Catt, S.; Cox, A.; Coxon, C.; Langridge, C.; Morris, R.; Price, M., Patients' preference for administration of endocrine treatments by injection or tablets: results from a study of women with breast cancer. *Annals of Oncology* **2006,** *17* (2), 205-210.

[46] Wang, J.; Yadav, V.; Smart, A. L.; Tajiri, S.; Basit, A. W., Toward Oral Delivery of Biopharmaceuticals: An Assessment of the Gastrointestinal Stability of 17 Peptide Drugs. *Molecular Pharmaceutics* **2015,** *12* (3), 966-973.

[47] Pawar, V. K.; Meher, J. G.; Singh, Y.; Chaurasia, M.; Reddy, B. S.; Chourasia, M. K., Targeting of gastrointestinal tract for amended delivery of protein/peptide therapeutics: Strategies and industrial perspectives. *Journal of Controlled Release* **2014,** *196*, 168-183.

[48] Binkowski, B. F.; Butler, B. L.; Stecha, P. F.; Eggers, C. T.; Otto, P.; Zimmerman, K.; Vidugiris, G.; Wood, M. G.; Encell, L. P.; Fan, F.; Wood, K. V., A Luminescent Biosensor with Increased Dynamic Range for Intracellular cAMP. *Acs Chemical Biology* **2011,** *6* (11), 1193-1197.

[49] LePlae, P. R.; Umezawa, N.; Lee, H. S.; Gellman, S. H., An efficient route to either enantiomer of trans-2-aminocyclopentanecarboxylic acid. *Journal of Organic Chemistry* **2001,** *66* (16), 5629-5632.

[50] Lee, H. S.; LePlae, P. R.; Porter, E. A.; Gellman, S. H., An efficient route to either enantiomer of orthogonally protected trans-3-aminopyrrolidine-4-carboxylic acid. *Journal of Organic Chemistry* **2001,** *66* (10), 3597-3599.

[51] Lelais, G.; Micuch, P.; Josien-Lefebvre, D.; Rossi, F.; Seebach, D., Preparation of protected beta(2)- and beta(3)-homocysteine, beta(2)- and beta(3)-homohistidine, and beta(2)-homoserine for solid-phase syntheses. *Helvetica Chimica Acta* **2004,** *87* (12), 3131-3159.

[52] Carter, P. H.; Dean, T.; Bhayana, B.; Khatri, A.; Rajur, R.; Gardella, T. J., Actions of the Small Molecule Ligands SW106 and AH-3960 on the Type-1 Parathyroid Hormone Receptor. *Molecular Endocrinology* **2015,** *29* (2), 307-321.

[53] Hoare, S. R. J.; Gardella, T. J.; Usdin, T. B., Evaluating the signal transduction mechanism of the parathyroid hormone 1 receptor - Effect of receptor-G-protein interaction on the ligand binding mechanism and receptor conformation. *Journal of Biological Chemistry* **2001,** *276* (11), 7741-7753.

[54] Okazaki, M.; Ferrandon, S.; Vilardaga, J. P.; Bouxsein, M. L.; Potts, J. T.; Gardella, T. J., Prolonged signaling at the parathyroid hormone receptor by peptide ligands targeted to a specific receptor conformation. *Proceedings of the National Academy of Sciences of the United States of America* **2008,** *105* (43), 16525-16530.

[55] Shimizu, M.; Potts, J. T.; Gardella, T. J., Minimization of parathyroid hormone - Novel amino-terminal parathyroid hormone fragments with enhanced potency in activating the type-1 parathyroid hormone receptor. *Journal of Biological Chemistry* **2000,** *275* (29), 21836-21843.

[56] Kent, G. N.; Loveridge, N.; Reeve, J.; Zanelli, J. M., PHARMACOKINETICS OF SYNTHETIC HUMAN PARATHYROID-HORMONE 1-34 IN MAN MEASURED BY CYTOCHEMICAL BIOASSAY AND RADIOIMMUNOASSAY. *Clinical Science* **1985,** *68* (2), 171-177.

[57] Serada, M.; Sakurai-Tanikawa, A.; Igarashi, M.; Mitsugi, K.; Takano, T.; Shibusawa, K.; Kohira, T., The role of the liver and kidneys in the pharmacokinetics of subcutaneously administered teriparatide acetate in rats. *Xenobiotica* **2012,** *42* (4), 398-407.

[58] Liao, S.; Qie, J. K.; Xue, M.; Zhang, Z. Q.; Liu, K. L.; Ruan, J. X., Metabolic stability of human parathyroid hormone peptide hPTH (1-34) in rat tissue homogenates: kinetics and products of proteolytic degradation. *Amino Acids* **2010,** *38* (5), 1595-1605.

[59] Dean, T.; Vilardaga, J. P.; Potts, J. T.; Gardella, T. J., Altered selectivity of parathyroid hormone (PTH) and PTH-Related protein (PTHrP) for distinct conformations of the PTH/PTHrP receptor. *Molecular Endocrinology* **2008,** *22* (1), 156-166.

[60] Ferrandon, S.; Feinstein, T. N.; Castro, M.; Wang, B.; Bouley, R.; Potts, J. T.; Gardella, T. J.; Vilardaga, J.-P., Sustained cyclic AMP production by parathyroid hormone receptor endocytosis. *Nature Chemical Biology* **2009,** *5* (10), 734-742.

[61] Cupp, M. E.; Nayak, S. K.; Adem, A. S.; Thomsen, W. J., Parathyroid hormone (PTH) and PTH-related peptide domains contributing to activation of different PTH receptor-mediated signaling pathways. *J Pharmacol Exp Ther* **2013,** *345* (3), 404-18.

[62] Vilardaga, J. P.; Jean-Alphonse, F. G.; Gardella, T. J., Endosomal generation of cAMP in GPCR signaling. *Nat Chem Biol* **2014,** *10* (9), 700-6.

[63] Dean, T.; Linglart, A.; Mahon, M. J.; Bastepe, M.; Juppner, H.; Potts, J. T.; Gardella, T. J., Mechanisms of ligand binding to the parathyroid hormone (PTH)/PTH-related protein receptor: Selectivity of a modified PTH(1-15) Radioligand for G alpha(S)-coupled receptor conformations. *Molecular Endocrinology* **2006,** *20* (4), 931-943.

[64] Hattersley, G.; Dean, T.; Corbin, B. A.; Bahar, H.; Gardella, T. J., Binding Selectivity of Abaloparatide for PTH-Type-1-Receptor Conformations and Effects on Downstream Signaling. *Endocrinology* **2016,** *157* (1), 141-149.

[65] Maeda, A.; Okazaki, M.; Baron, D. M.; Dean, T.; Khatri, A.; Mahon, M.; Segawa, H.; Abou-Samra, A. B.; Jueppner, H.; Bloch, K. D.; Potts, J. T., Jr.; Gardella, T. J., Critical role of parathyroid hormone (PTH) receptor-1 phosphorylation in regulating acute responses to PTH. *Proceedings of the National Academy of Sciences of the United States of America* **2013,** *110* (15), 5864-5869.

[66] Castro, M.; Nikolaev, V. O.; Palm, D.; Lohse, M. J.; Vilardaga, J. P., Turn-on switch in parathyroid hormone receptor by a two-step parathyroid hormone binding mechanism. *Proceedings of the National Academy of Sciences of the United States of America* **2005,** *102* (44), 16084-16089.

[67] Feinstein, T. N.; Wehbi, V. L.; Ardura, J. A.; Wheeler, D. S.; Ferrandon, S.; Gardella, T. J.; Vilardaga, J. P., Retromer terminates the generation of cAMP by internalized PTH receptors. *Nature Chemical Biology* **2011,** *7* (5), 278-284.

[68] Feinstein, T. N.; Yui, N.; Webber, M. J.; Wehbi, V. L.; Stevenson, H. P.; King, J. D., Jr.; Hallows, K. R.; Brown, D.; Bouley, R.; Vilardaga, J. P., Noncanonical control of vasopressin receptor type 2 signaling by retromer and arrestin. *J Biol Chem* **2013,** *288* (39), 27849-60.

[69] Gidon, A.; Al-Bataineh, M. M.; Jean-Alphonse, F. G.; Stevenson, H. P.; Watanabe, T.; Louet, C.; Khatri, A.; Calero, G.; Pastor-Soler, N. M.; Gardella, T. J.; Vilardaga, J. P., Endosomal GPCR signaling turned off by negative feedback actions of PKA and v-ATPase. *Nat Chem Biol* **2014,** *10* (9), 707-9.

[70] Gidon, A.; Feinstein, T. N.; Xiao, K. H.; Vilardaga, J. P., Studying the regulation of endosomal cAMP production in GPCR signaling. *G Protein-Coupled Receptors: Signaling, Trafficking and Regulation* **2016,** *132*, 109-126.

[71] Horwitz, M. J.; Tedesco, M. B.; Gundberg, C.; Garcia-Ocana, A.; Stewart, A. F., Short-term, high-dose parathyroid hormone-related protein as a skeletal anabolic agent for the treatment of postmenopausal osteoporosis. *Journal of Clinical Endocrinology & Metabolism* **2003,** *88* (2), 569-575.

[72] Horwitz, M. J.; Tedesco, M. B.; Garcia-Ocana, A.; Sereika, S. M.; Prebehala, L.; Bisello, A.; Hollis, B. W.; Gundberg, C. M.; Stewart, A. F., Parathyroid Hormone-Related Protein for the Treatment of Postmenopausal Osteoporosis: Defining the Maximal Tolerable Dose. *Journal of Clinical Endocrinology & Metabolism* **2010,** *95* (3), 1279-1287.

[73] Horwitz, M. J.; Augustine, M.; Kahn, L.; Martin, E.; Oakley, C. C.; Carneiro, R. M.; Tedesco, M. B.; Laslavic, A.; Sereika, S. M.; Bisello, A.; Garcia-Ocana, A.; Gundberg, C. M.; Cauley, J. A.; Stewart, A. F., A Comparison of Parathyroid Hormone-Related Protein (1-36) and Parathyroid Hormone (1-34) on Markers of Bone Turnover and Bone Density in Postmenopausal Women: The PrOP Study. *Journal of Bone and Mineral Research* **2013,** *28* (11), 2266-2276.

[74] Pioszak, A. A.; Parker, N. R.; Gardella, T. J.; Xu, H. E., Structural Basis for Parathyroid Hormone-related Protein Binding to the Parathyroid Hormone Receptor and Design of Conformation-selective Peptides. *Journal of Biological Chemistry* **2009,** *284* (41), 28382-28391.

[75] Shimizu, M.; Joyashiki, E.; Noda, H.; Watanabe, T.; Okazaki, M.; Nagayasu, M.; Adachi, K.; Tamura, T.; Potts, J. T.; Gardella, T. J.; Kawabe, Y., Pharmacodynamic Actions of a Long-Acting PTH Analog (LA-PTH) in Thyroparathyroidectomized (TPTX) Rats and Normal Monkeys. *Journal of Bone and Mineral Research* **2016,** (7), 1405-1412.

[76] Varela, A.; Chouinard, L.; Lesage, E.; Smith, S. Y.; Hattersley, G., One Year of Abaloparatide, a Selective Activator of the PTH1 Receptor, Increased Bone Formation and Bone Mass in Osteopenic Ovariectomized Rats Without Increasing Bone Resorption. *Journal of Bone and Mineral Research* **2016**, n/a-n/a.

[77] Leder, B. Z.; O'Dea, L. S. L.; Zanchetta, J. R.; Kumar, P.; Banks, K.; McKay, K.; Lyttle, C. R.; Hattersley, G., Effects of abaloparatide, a human parathyroid hormone-related peptide analog, on bone mineral density in postmenopausal women with osteoporosis. *The Journal of clinical endocrinology and metabolism* **2015,** *100* (2), 697-706.

[78] Plum, A.; Jensen, L. B.; Kristensen, J. B., In vitro protein binding of liraglutide in human plasma determined by reiterated stepwise equilibrium dialysis. *Journal of Pharmaceutical Sciences* **2013,** *102* (8), 2882-2888.

[79] Sturmer, A.; Mehta, N.; Giacchi, J.; Cagatay, T.; Tavakkol, R.; Mitta, S.; Fitzpatrick, L.; Wald, J.; Trang, J.; Stern, W., Pharmacokinetics of Oral Recombinant Human Parathyroid Hormone rhPTH(1-31)NH2 in Postmenopausal Women with Osteoporosis. *Clinical Pharmacokinetics* **2013,** *52* (11), 995-1004.

[80] Guo, L. T.; Ma, E. L.; Zhao, H. W.; Long, Y. F.; Zheng, C. X.; Duan, M. X., Preliminary evaluation of a novel oral delivery system for rhPTH1-34: In vitro and in vivo. *International Journal of Pharmaceutics* **2011,** *420* (1), 172-179.

[81] Leone-Bay, A.; Sato, M.; Paton, D.; Hunt, A. H.; Sarubbi, D.; Carozza, M.; Chou, J.; McDonough, J.; Baughman, R. A., Oral delivery of biologically active parathyroid hormone. *Pharmaceutical Research* **2001,** *18* (7), 964-970.

[82] Hammerle, S. P.; Mindeholm, L.; Launonen, A.; Kiese, B.; Loeffler, R.; Harfst, E.; Azria, M.; Arnold, M.; John, M. R., The single dose pharmacokinetic profile of a novel oral human parathyroid hormone formulation in healthy postmenopausal women. *Bone* **2012,** *50* (4), 965-973.

[83] Leone-Bay, A.; Paton, D. R.; Freeman, J.; Lercara, C.; O'Toole, D.; Gschneidner, D.; Wang, E.; Harris, E.; Rosado, C.; Rivera, T.; DeVincent, A.; Tai, M.; Mercogliano, F.; Agarwal, R.; Leipold, H.; Baughman, R. A., Synthesis and evaluation of compounds that facilitate the gastrointestinal absorption of heparin. *Journal of Medicinal Chemistry* **1998,** *41* (7), 1163-1171.

[84] Bray, B. L., Large-scale manufacture of peptide therapeutics by chemical synthesis. *Nature Reviews Drug Discovery* **2003,** *2* (7), 587-593.

[85] Hartman, M. C. T.; Josephson, K.; Szostak, J. W., Enzymatic aminoacylation of tRNA with unnatural amino acids. *Proceedings of the National Academy of Sciences of the United States of America* **2006,** *103* (12), 4356-4361.

[86] Ellman, J. A.; Mendel, D.; Schultz, P. G., SITE-SPECIFIC INCORPORATION OF NOVEL BACKBONE STRUCTURES INTO PROTEINS. *Science* **1992,** *255* (5041).

[87] Tan, Z. P.; Forster, A. C.; Blacklow, S. C.; Cornish, V. W., Amino acid backbone specificity of the Escherichia coli translation machinery. *Journal of the American Chemical Society* **2004,** *126* (40).

[88] Dedkova, L. M.; Fahmi, N. E.; Paul, R.; del Rosario, M.; Zhang, L.; Chen, S.; Feder, G.; Hecht, S. M., beta-Puromycin Selection of Modified Ribosomes for in Vitro Incorporation of beta-Amino Acids. *Biochemistry* **2012,** *51* (1).

[89] Maini, R.; Nguyen, D. T.; Chen, S. X.; Dedkova, L. M.; Chowdhury, S. R.; Alcala-Torano, R.; Hecht, S. M., Incorporation of beta-amino acids into dihydrofolate reductase by ribosomes

having modifications in the peptidyltransferase center. *Bioorganic & Medicinal Chemistry* **2013,** *21* (5), 1088-1096.

[90] Fujino, T.; Goto, Y.; Suga, H.; Murakami, H., Ribosomal Synthesis of Peptides with Multiple beta-Amino Acids. *Journal of the American Chemical Society* **2016,** *138* (6), 1962-1969.

[91] Czekster, C. M.; Robertson, W. E.; Walker, A. S.; Soll, D.; Schepartz, A., In Vivo Biosynthesis of a beta-Amino Acid-Containing Protein. *Journal of the American Chemical Society* **2016,** *138* (16), 5194-5197.

Figure legends

Figure 1. Sequences of PTH(1-34) analogues in the N-terminal β-scan library and cAMP stimulating potency. Each peptide is comprised of the native sequence for α-residues for positions 10-34 (see figure 2 for full sequence). The single letter code is used to indicate conventional proteinogenic amino acids. Colored dots indicate sites at which α-to-β replacements have been introduced. β^3-Residues display an identical sidechain to that displayed by the corresponding α-residue. cAMP inducing potencies (EC_{50}) for are shown for analogues with cells expressing hPTHR1. Average EC_{50} values are from values obtained in three independent experiments for all α/β-peptides or six independent experiments for PTH(1-34). Analogues with "no activity" have too weak of activity to be characterized using this method. Full dose-response curves and tabulated data are found in supporting figure and supporting table 1.

Figure 2. Sequences of a peptides containing α-to-β replacements in the N-terminal segment, C-terminal segment or both. Differences between the PTH(1-34) and M-PTH(1-34) scaffolds are highlighted in bold in the M-PTH(1-34) sequence. The single letter code is used to indicate conventional proteinogenic amino acids. Colored dots indicate sites at which α-to-β replacements have been introduced. β^3-Residues display an identical sidechain to that displayed by the corresponding α-residue. Note that selected derivatives contain an α-amino isobutyric acid residue (Aib) at position 3.

Figure 3. Stability of PTH(1-34) or M-Cyc-9β in rat kidney homogenate. Peptides were incubated in kidney homogenates for the indicated durations, and intact peptide concentration was evaluated using a liquid chromatography/mass spectrometry (LC/MS) approach or a bioassay readout as described in the methods section. Sites of protease-catalyzed hydrolysis were evaluated using MALDI-TOF mass spectrometry. (**a**) The concentration of intact peptide from LC/MS analysis as a function of duration of incubation. Data points represent mean ± standard deviation. The curve results from fitting of the data to an exponential decay function, with half-lives listed. (**b-c**) Identification of peptide fragments derived from PTH(1-34) (**b**) or **M-Cyc-9β** (**c**) by MALDI-TOF mass spectrometry as a function of time. Peptide-derived fragments may give rise to observed signals are inserted above the peak of interest (**d**) Peptide bioactivity following exposure to kidney homogenate was assessed using a biological assay. Data points represent mean ± SEM. Times listed after peptide names represent the duration of time that the peptide was incubated with in kidney homogenate before quenching of protease activity. Curves result from fitting of a sigmoidal dose-response model with variable slope.

Figure 4. Degradation of PTH(1-34) derivatives in SGF and SIF. Peptide bioactivity following exposure to SGF was assessed using a biological assay (panels a-d). Data points represent mean ± SEM. Curves result from fitting of a sigmoidal dose response model with variable slope to the data. Note that the times listed after peptide names represent the duration of time that the peptide was incubated with in SGF before quenching of protease activity. (**e**) Sites of proteolysis in PTH(1-34) and derivatives SGF. Sites of protease action were identified by analyzing crude proteolysis mixtures using MALDI-TOF mass spectrometry as described in the methods section. Arrows point to major sites of proteolytic cleavage See figure 2 for structures. (**f-g**) Bioassay to assess degradation of PTH(1-34) or **M-Cyc-9β** in simulated intestinal fluid

(SIF). See the methods section of this chapter for additional methodological details. Data points represent mean ± SEM

Figure 5. Properties of PTH(1-34) and α/β-peptide derivatives in mice. Peptides were injected at a dose of 20 nmol/kg by subcutaneous injection in CD1 mice, n = 5, female, 8-12 weeks of age. * $p < 0.05$ vs. vehicle. Vehicle is 0.05% Tween-80, 10 mM citrate, 150 mM NaCl (pH5.0). Data points represent mean ± SEM. (**a**) PTH(1-34) and derivatives induce a calcemic response following subcutaneous injection into mice (**b**) Bloodstream bioavailability time course for PTH(1-34) or selected α/β-peptide derivatives. A luminescence response was induced in GP2.3 cells following addition of 2 µL of serum (mixed with CO_2 independent medium) taken from mice at different time points after injection (x-axis). This raw luminescence response was converted to the concentration of peptide in the bloodstream through use of a standard curve relating peptide concentrations to luminescence responses. See supporting figure 9 for the raw luminescence responses induced by serum and standard curves.

Figure 6. A comparison of the structures of highly substituted analogues of PTH, PTHrP and Abalopartide. The segment in which Abalopratide differs from PTHrP(1-34) is highlighted in red lettering.

Figures

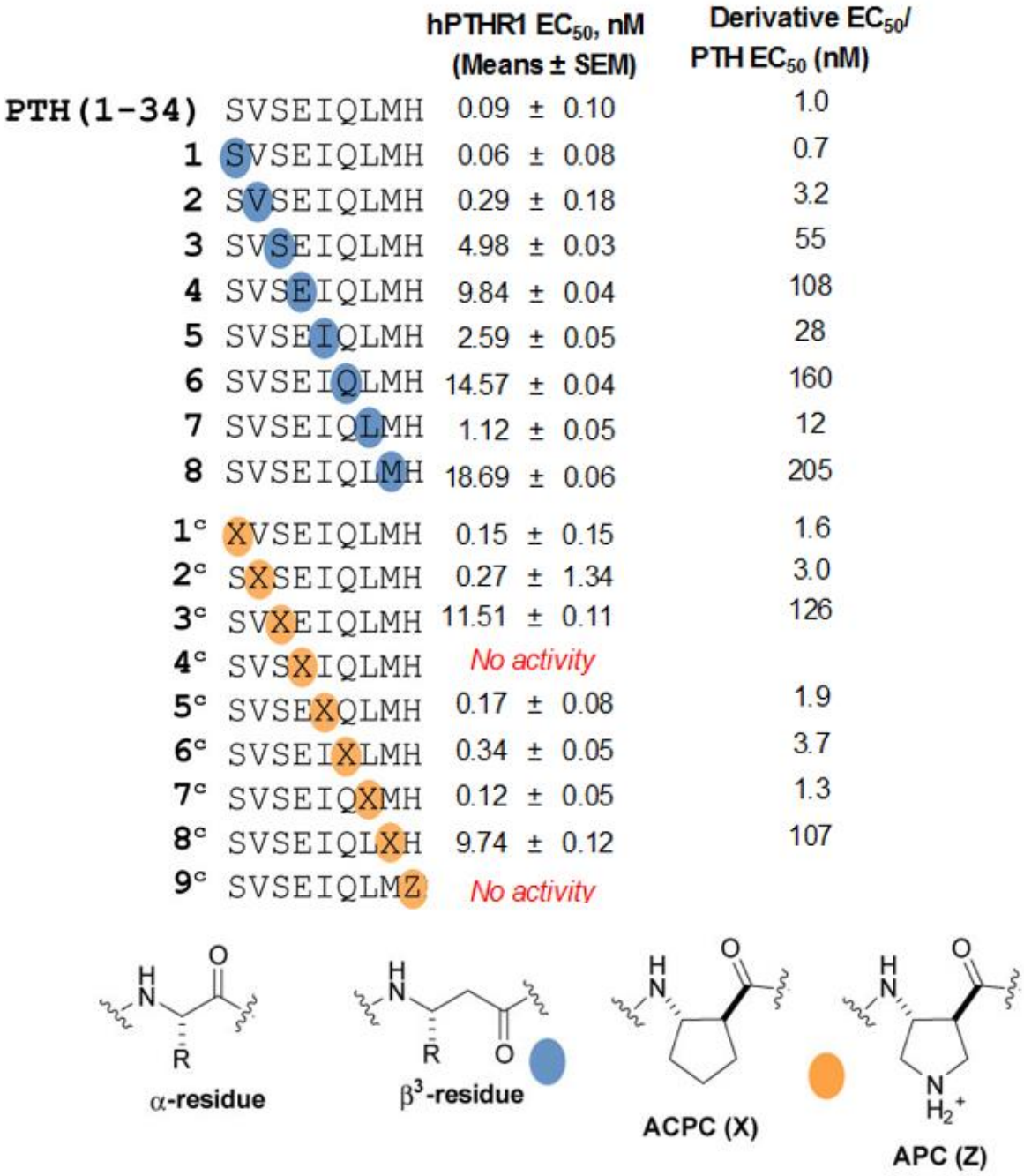

Figure 1

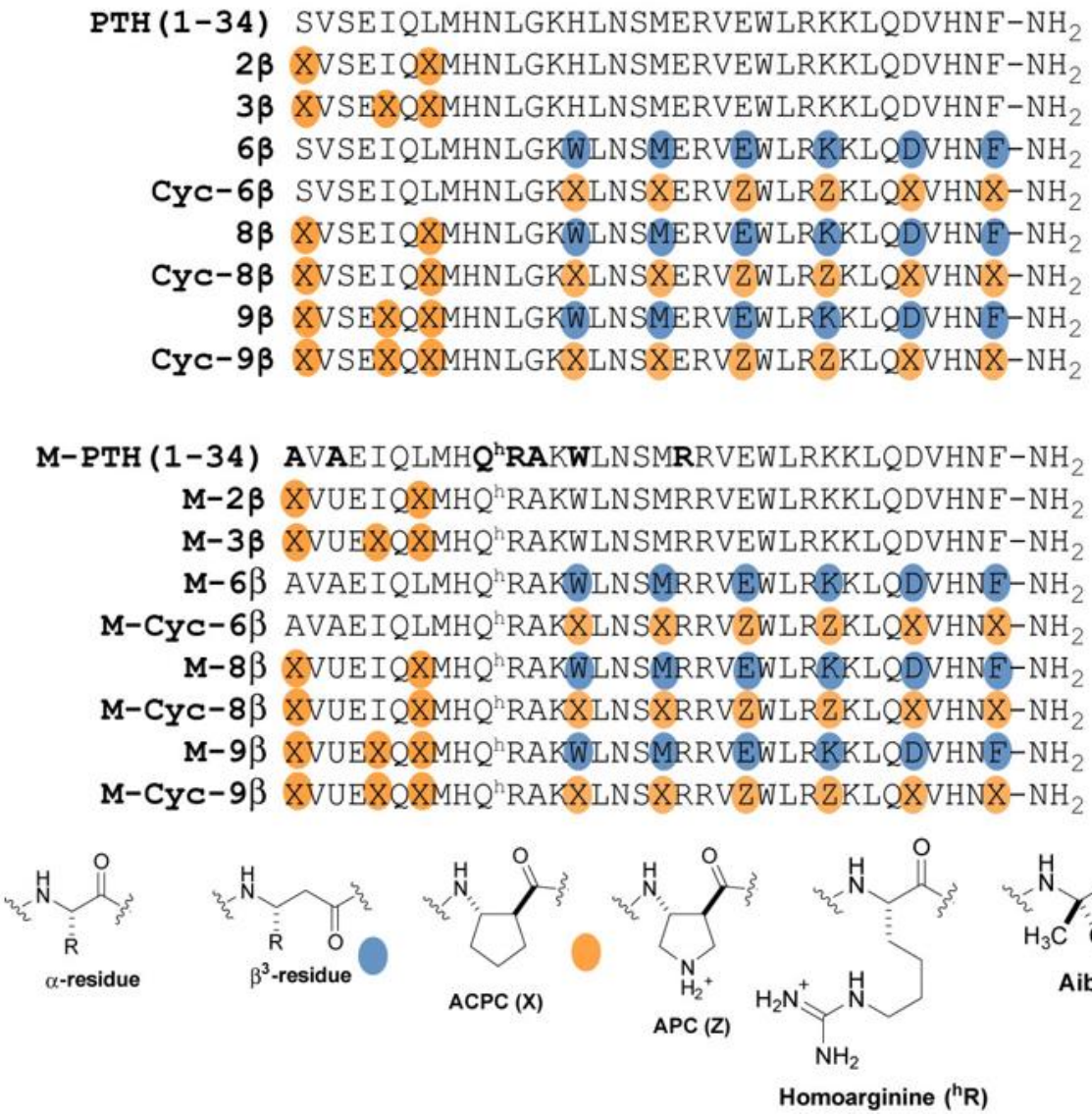
PTH(1-34) SVSEIQLMHNLGKHLNSMERVEWLRKKLQDVHNF-NH2
2β XVSEIQXMHNLGKHLNSMERVEWLRKKLQDVHNF-NH2
3β XVSEXQXMHNLGKHLNSMERVEWLRKKLQDVHNF-NH2
6β SVSEIQLMHNLGKWLNSMERVEWLRKKLQDVHNF-NH2
Cyc-6β SVSEIQLMHNLGKXLNSXERVZWLRZKLQXVHNX-NH2
8β XVSEIQXMHNLGKWLNSMERVEWLRKKLQDVHNF-NH2
Cyc-8β XVSEIQXMHNLGKXLNSXERVZWLRZKLQXVHNX-NH2
9β XVSEXQXMHNLGKWLNSMERVEWLRKKLQDVHNF-NH2
Cyc-9β XVSEXQXMHNLGKXLNSXERVZWLRZKLQXVHNX-NH2
M-PTH(1-34) AVAEIQLMHQhRAKWLNSMRRVEWLRKKLQDVHNF-NH2
M-2β XVUEIQXMHQhRAKWLNSMRRVEWLRKKLQDVHNF-NH2
M-3β XVUEXQXMHQhRAKWLNSMRRVEWLRKKLQDVHNF-NH2
M-6β AVAEIQLMHQhRAKWLNSMRRVEWLRKKLQDVHNF-NH2
M-Cyc-6β AVAEIQLMHQhRAKXLNSXRRVZWLRZKLQXVHNX-NH2
M-8β XVUEIQXMHQhRAKWLNSMRRVEWLRKKLQDVHNF-NH2
M-Cyc-8β XVUEIQXMHQhRAKXLNSXRRVZWLRZKLQXVHNX-NH2
M-9β XVUEXQXMHQhRAKWLNSMRRVEWLRKKLQDVHNF-NH2
M-Cyc-9β XVUEXQXMHQhRAKXLNSXRRVZWLRZKLQXVHNX-NH2
α-residue
β3-residue
ACPC (X)
APC (Z)
Homoarginine (hR)
Aib (U)

Figure 2

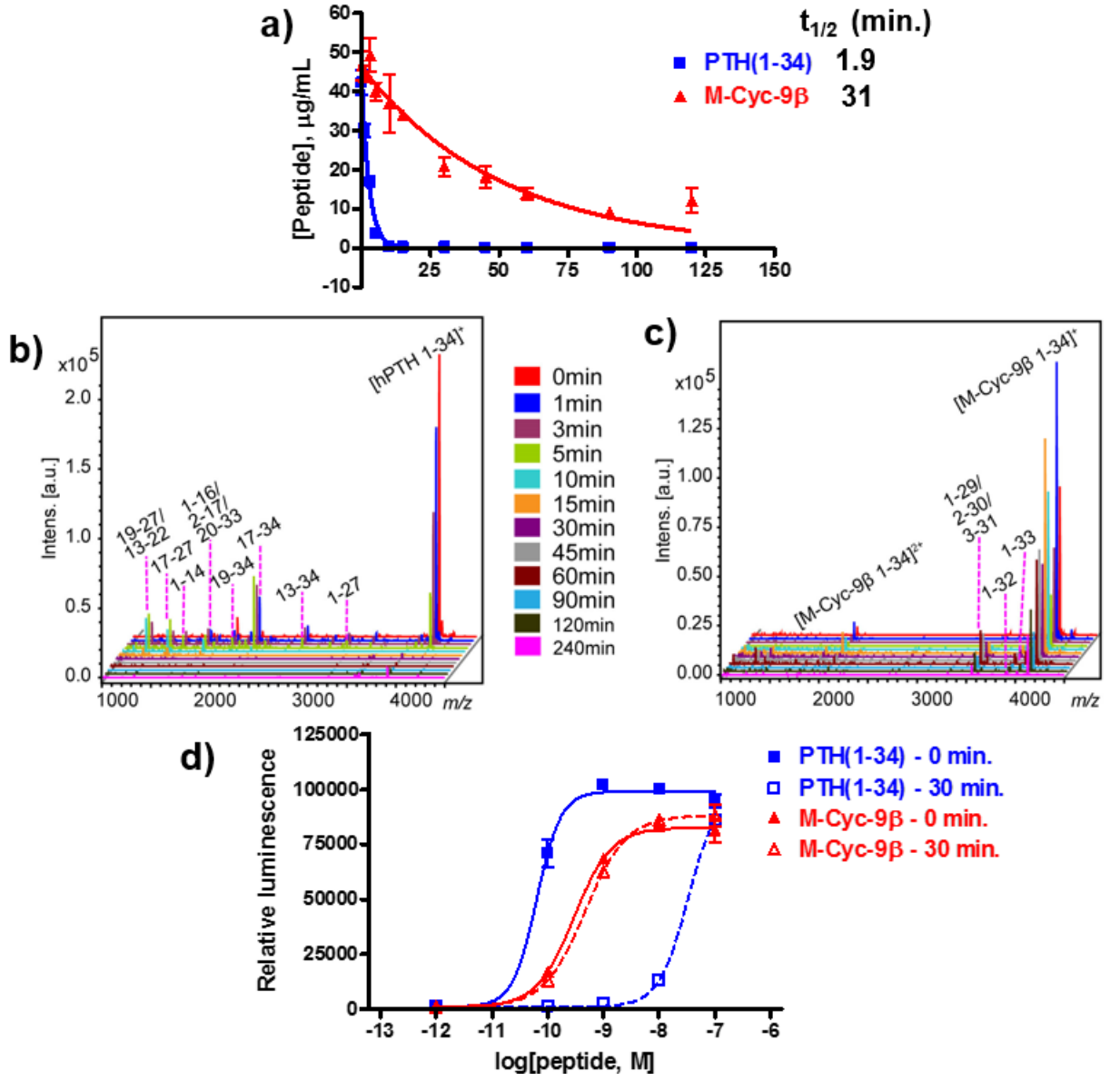
a)
[Peptide], µg/mL
t1/2 (min.)
PTH(1-34) 1.9
M-Cyc-9β 31
b)
x10^5
Intens. [a.u.]
[hPTH 1-34]+
19-27/ 13-22
17-27
1-16/ 2-17/ 20-33
1-14
19-34
17-34
13-34
1-27
m/z
0min
1min
3min
5min
10min
15min
30min
45min
60min
90min
120min
240min
c)
[M-Cyc-9β 1-34]+
[M-Cyc-9β 1-34]2+
1-29/ 2-30/ 3-31
1-32
1-33
d)
Relative luminescence
log[peptide, M]
PTH(1-34) - 0 min.
PTH(1-34) - 30 min.
M-Cyc-9β - 0 min.
M-Cyc-9β - 30 min.

Figure 3

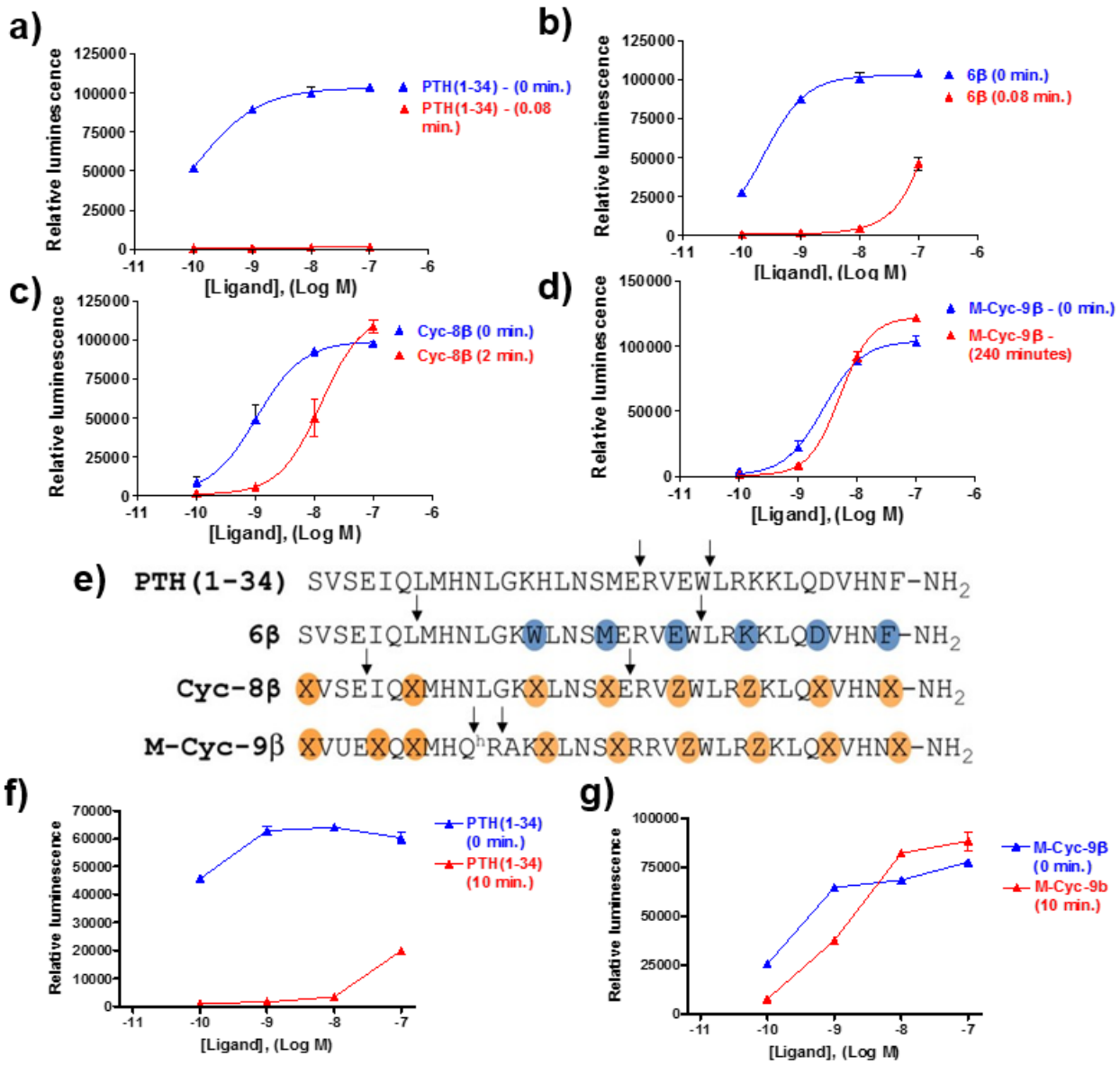
a)
Relative luminescence
125000
100000
75000
50000
25000
0
-11
-10
-9
-8
-7
-6
[Ligand], (Log M)
PTH(1-34) - (0 min.)
PTH(1-34) - (0.08 min.)
b)
Relative luminescence
[Ligand], (Log M)
6β (0 min.)
6β (0.08 min.)
c)
Relative luminescence
[Ligand], (Log M)
Cyc-8β (0 min.)
Cyc-8β (2 min.)
d)
Relative luminescence
150000
100000
50000
[Ligand], (Log M)
M-Cyc-9β - (0 min.)
M-Cyc-9β - (240 minutes)
e)
PTH(1-34) SVSEIQLMHNLGKHLNSMERVEWLRKKLQDVHNF-NH2
6β SVSEIQLMHNLGKWLNSMERVEWLRKKLQDVHNF-NH2
Cyc-8β XVSEIQXMHNLGKXLNSXERVZWLRZKLQXVHNX-NH2
M-Cyc-9β XVUEXQXMHQnRAKXLNSXRRVZWLRZKLQXVHNX-NH2
f)
Relative luminescence
70000
60000
50000
40000
30000
20000
10000
0
-11
-10
-9
-8
-7
[Ligand], (Log M)
PTH(1-34) (0 min.)
PTH(1-34) (10 min.)
g)
Relative luminescence
100000
75000
50000
25000
0
-11
-10
-9
-8
-7
[Ligand], (Log M)
M-Cyc-9β (0 min.)
M-Cyc-9b (10 min.)

Figure 4

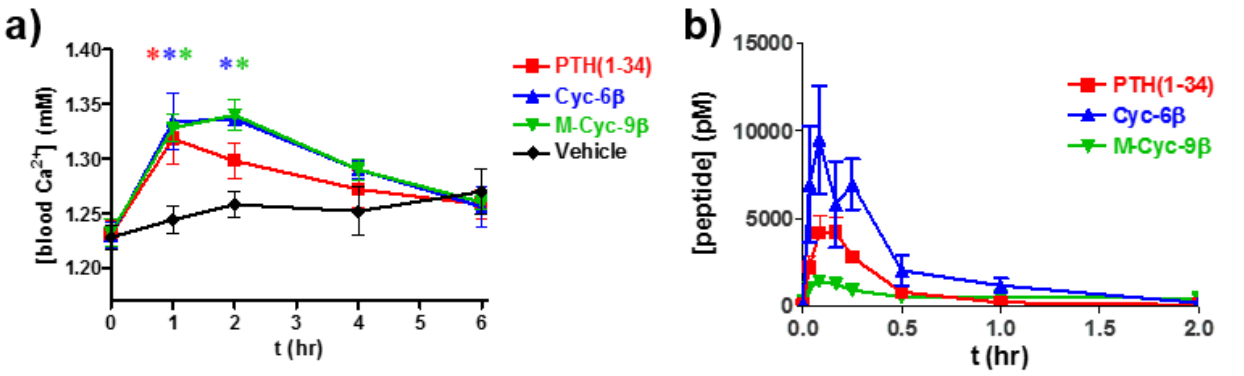
a)
1.40
1.35
1.30
1.25
1.20
[blood Ca2+] (mM)
***
**
0
1
2
3
4
5
6
t (hr)
PTH(1-34)
Cyc-6β
M-Cyc-9β
Vehicle
b)
15000
10000
5000
0
[peptide] (pM)
0.0
0.5
1.0
1.5
2.0
t (hr)
PTH(1-34)
Cyc-6β
M-Cyc-9β

Figure 5

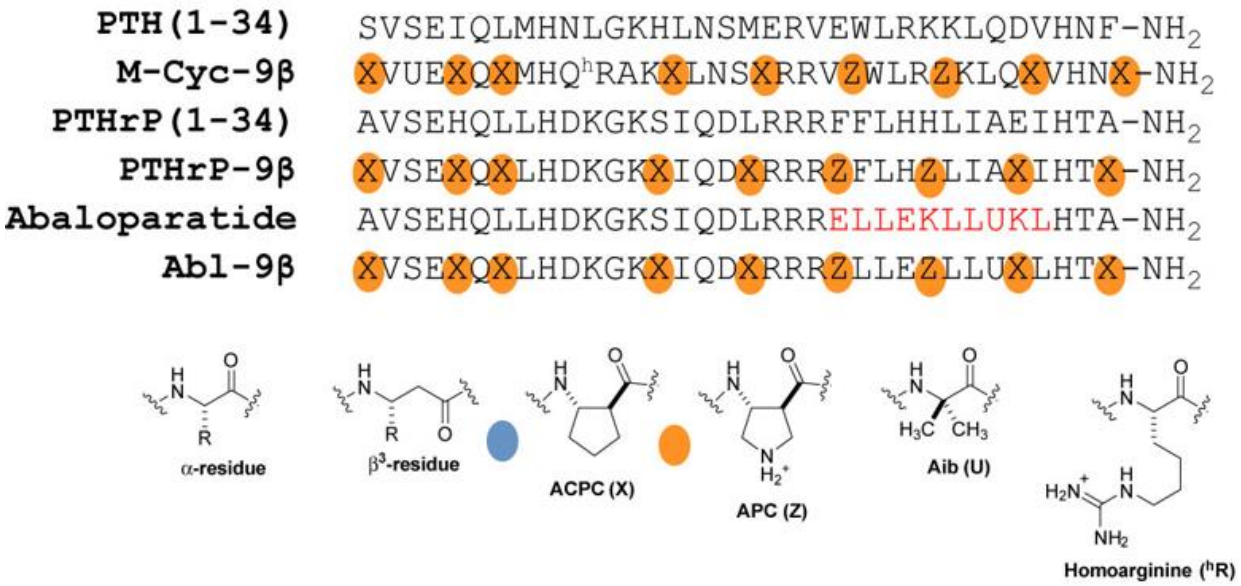
PTH(1-34) SVSEIQLMHNLGKHLNSMERVEWLRKKLQDVHNF-NH2
M-Cyc-9β XVUEXQXMHQhRAKXLNSXRRVZWLRZKLQXVHNX-NH2
PTHrP(1-34) AVSEHQLLHDKGKSIQDLRRRFFLHHLIAEIHTA-NH2
PTHrP-9β XVSEXQXLHDKGKXIQDXRRRZFLHZLIAXIHTX-NH2
Abaloparatide AVSEHQLLHDKGKSIQDLRRRELLEKLLUKLHTA-NH2
Abl-9β XVSEXQXLHDKGKXIQDXRRRZLLEZLLUXLHTX-NH2
α-residue
β3-residue
ACPC (X)
APC (Z)
Aib (U)
Homoarginine (hR)

Figure 6

Tables

Table 1. Summary of the cAMP inducing properties of α/β-peptide analogues of PTH(1-34). Tabulation of receptor activation and binding properties for the derivatives in figure 2 with hPTHR1. Mean EC_{50} values are averaged from EC_{50} values obtained in three independent experiments for all α/β-peptides or six independent experiments for PTH(1-34). See supporting figure 3 for cAMP dose-response curves and supporting figure 4 for composite binding curves. See methods section for experimental details.

Peptide	hPTHR1 EC_{50}, nM (Means ± SEM)	Derivative EC_{50}/ PTH EC_{50} (nM)
PTH(1-34)	0.08 ± 0.01	1.0
2β	0.14 ± 0.03	1.7
3β	3.0 ± 0.56	36.7
6β	0.17 ± 0.05	2.1
Cyc-6β	0.26 ± 0.05	3.2
8β	1.84 ± 0.11	22.6
Cyc-8β	0.71 ± 0.04	8.7
9β	167 ± 6.3	2,050
Cyc-9β	19 ± 1.3	234
M-PTH(1-34)	0.34 ± 0.04	4.2
M-2β	0.52 ± 0.19	6.3
M-3β	0.40 ± 0.11	4.9
M-6β	0.44 ± 0.10	5.4
M-Cyc-6β	0.51 ± 0.15	6.3
M-8β	0.83 ± 0.07	10
M-Cyc-8β	1.8 ± 0.23	22
M-9β	0.79 ± 0.25	9.7
M-Cyc-9β	0.78 ± 0.12	9.5

Table 2. Summary of the cAMP inducing properties of α/β-peptide analogues of PTHrP and Abaloparatide. Tabulation of receptor activation and binding properties for the derivatives in figure 6 with hPTHR1. Mean EC_{50} values are averaged from EC_{50} values obtained in three independent experiments. See supporting figure 7 for composite binding curves. See methods section for experimental details. The data found in this figure are derived from experiments distinct from those that provide data for table 1.

Derivative	hPTHR1 cAMP EC_{50}, nM (mean ± SEM)	Derivative EC_{50}/ PTH EC_{50} (nM)
PTH(1-34)	0.07 ± 0.01	1.0
M-Cyc-9β	0.48 ± 0.12	7.1
PTHrP(1-34)	0.08 ± 0.02	1.2
PTHrP-9β	0.51 ± 0.16	7.4
Abaloparatide	0.02 ± 0.005	0.3
Abl-9β	0.36 ± 0.09	5.3

Supporting information

Methods

Peptide synthesis and purification.

Peptides were synthesized as C-terminal amides on NovaPEG rink amide resin (EMD) using previously reported microwave-assisted solid-phase conditions, based on Fmoc protection of main chain amino groups.[38] Protected β^3-homoamino acids were purchased from PepTech or ChemImpex. Fmoc-ACPC was purchased from ChemImpex. Fmoc-APC was synthesized as previously described.[50]

After synthesis, the peptides were cleaved from the resin, and side chains were deprotected using reagent K (82.5% TFA, 5% phenol, 5% H_2O, 5% thioanisole, 2.5% ethanedithiol) for two hours. The TFA solution was dripped into cold diethyl ether to precipitate the deprotected peptide. Peptides were purified on a prep-C18 column using reverse phase-HPLC. Purity was assessed by analytical RP-HPLC (solvent A: 0.1% TFA in water, solvent B: 0.1% TFA in acetonitrile, C18 analytical column (4.6 X 250 mm), flow rate 1 mL/min, gradient 10-60% B solvent over 50 minutes). Masses were measured by MALDI-TOF-MS. See Supporting Figure 13 for analytical HPLC retention times, purity data and a list of observed masses from MALDI-TOF-MS (either monoisotopic $[M+H]^+$, *m/z* or average $[M+H]^+$, *m/z*, listed on the table). See Supporting Figure 14 for HPLC traces and MALDI-TOF mass spectra.

Binding and cAMP assays.

Reported IC_{50} and EC_{50} values are the average of ≥ 3 independent measurements. Data were fitted to a sigmoidal dose-response model with variable slope. Each assay consists of ≥ 4 data points (different concentrations) per peptide. Binding to the R0 conformation of the human PTHR1 was assessed by competition assays performed in 96-well plates by using membranes from either GP2.3 cells or Cos-7 cells transiently transfected to express human

PTHR1. In brief, binding was assessed by using ^{125}I-PTH(1–34) as tracer radio ligand and including GTPγS in the reaction (1 x 10^{-5} M) as previously described.[11]

cAMP signaling was assessed using HEK-293-derived cell lines that stably express the Glosensor cAMP reporter (Promega Corp.)[48] along with wild-type human PTHR1 (GP-2.3 cells) or human PTHR1 lacking the extracellular domain (GD5 cells). For cAMP dose–response assays, monolayers of confluent HEK 293 cells were pre-incubated with CO_2 independent media (Life Sciences) containing d-luciferin (0.5 mM) in 96 well plates at room temperature until a stable baseline level of luminescence was established (30 min). Varying concentrations of agonist were then added, and the time course of luminescence response was recorded using a Perkin Elmer plate reader following α/β-peptide addition. The maximal luminescence response (observed 12-20 min after ligand addition) was used for generating dose response curves.

In cases where peptides failed to induce cAMP responses near to the maximal response induced by PTH(1-34), a constraint was introduced when fitting of a sigmoidal dose response curve that specified that the maximal response for each peptide was above a threshold specified in the corresponding figure caption. This constraint enables an estimation of cAMP EC_{50} values based on the assumption that these peptides are full agonists. Peptides that possess partial agonism properties are not identified using this experimental approach.

Results from cAMP assays using derivatives from the N-terminal β-scan library are tabulated in Figure 1 and Supporting Figures 1 and 2. The categorization of derivatives (Supporting Figure 1) is based on the parameters listed below. Composite curves are shown in Supporting Figures 1 and 2.

For hPTHR1 assays (GP2.3 cells, Supporting Figure 1)

Potent: EC_{50} within 5-fold PTH(1-34)

Moderately potent: Average response at 10 nM > 90% PTH max

Moderately weak: 90% PTH max > Average response at 10 nM > 15% PTH max

Weak: Average response at 10 nM < 15% PTH max

For PTHR1ΔNT assays (GD5 cells, Supporting Figure 2)

Potent: EC_{50} within 10-fold PTH(1-34)

Moderately potent: Average response at 10 nM > 90% PTH max

Moderately weak: 90% PTH max > Average response at 10 nM > 15% PTH max

Weak: Average response at 10 nM < 15% PTH max

Simulated gastric fluid stability studies

Simulated gastric fluid was prepared according to instructions provided for test solutions in the United States Pharmacopeia. NaCl (20 mg) and pepsin from porcine mucosa (32 mg of >2500 U/mg pepsin, Sigma Aldrich P7012) were dissolved in 9.93 mL of deionized H_2O. Concentrated HCl (~37%) (700 µL) was then added to the solution to provide simulated gastric fluid (SGF). The resulting solution had a pH of ~1.2. SGF was prepared fresh for each assay and was incubated at 37° C before and during use.

All solutions used in the protocol, except peptide stocks, were first submitted to sonication to remove excess gas from the solution. Solutions of peptides (1 mM) dissolved in 10 mM acetic acid were used as stocks for these experiments. Aliquots of peptide stock were added to SGF (20 µL of peptide in 100 µL total solution, for a [peptide] of 200 µM) at t=0. Proteolysis was quenched at the indicated time by transferring 40 µL of the proteolysis solution into 80 µL of 10x PBS (1.37 M NaCl, 27 mM KCl, 80 mM Na_2HPO_4, 20 mM KH_2PO_4 at pH 7.4), as pepsin

is inactive at neutral pH. An additional 80 µL of deionized H_2O were added to the quenched solution to bring the total volume of the quenched solution to 200 µL ([peptide] in quenched solution was 40 µM). Each proteolysis experiment was run concurrently in duplicate to provide estimated variation (standard deviation) in the analyses described below. Control samples, in which proteolysis is prevented from occurring, were prepared by *first* mixing 32 µL of SGF with 80 µL of 10x PBS to quench protease activity, followed by addition of 8 µL of peptide stock and 80 µL of deionized H_2O.

From these quenched solutions (either control or proteolysis groups), a portion (180 µL) was transferred to an HPLC vial for injection (injected 150 µL) onto an analytical RP-HPLC (see peptide synthesis and purification section above), and peaks were analyzed. The time course of peptide degradation was experimentally determined by integrating the area of the peak corresponding to the non-hydrolyzed peptide in a series of HPLC traces, with duplicate proteolysis reactions being used to generate error bars corresponding to the standard deviation. A small portion of the reaction solution (1 µL) was used to acquire MALDI-TOF mass spectrometry data for identification of peptide fragments resulting from proteolysis.

A portion of these quenched reaction solutions (or control solutions) was diluted 1:40 in CO_2 independent medium to provide 1 µM solutions of peptide for application in an assay that uses activation of PTHR1 in live GP2.3 cells to measure residual peptide bioactivity. These solutions were then serially diluted (1:10) using CO_2 independent medium in a 96-well polypropylene dilution plate (concentration range 1000 nM to 1 nM on dilution plate). Aliquots from these serially diluted solutions (10 µL) were then transferred onto a different 96-well plate containing confluent monolayers of GP2.3 cells that had been preincubated with 90 µL of CO_2 independent media with 0.5 mM d-luciferin. Luminescence responses were recorded using a

BioTek plate reader. The final peptide concentrations used in this assay ranged from 100 nM to 0.1 nM. Control experiments showed that quenched solutions of SGF without peptide did not induce luminescent responses in GP2.3 cells. Incubation of peptide in solutions of SGF, in which protease activity had been quenched prior to addition of peptide, for up to four hours, did not result in diminished peptide bioactivity relative to freshly prepared peptide stocks in CO_2 independent medium (data not shown). The luminescent responses observed 20 minutes following peptide addition, which corresponds to a time at which maximal luminescence responses were observed in other assays using GP2.3 cells, were used to construct the dose response curves found in Figure 4. Note that concentrations on the x-axis of Figure 4 represent the estimated concentrations of the intact peptide before proteolysis. The concentration of intact peptide after proteolysis is not known for this assay.

Simulated intestinal fluid stability studies.

Simulated intestinal fluid (SIF) was prepared according to instructions provided in the United States Pharmacopeia. KH_2PO_4 (68 mg) was dissolved in 2.5 mL of H_2O followed by the addition of 0.77 mL of 0.2 M NaOH. An additional 5 mL of H_2O was added to this solution followed by addition of 100 mg of porcine pancreatin (US Pharmacopeia grade, MP Bio #102557). The pH of the solution was adjusted to pH 6.8 through addition of 0.2 M NaOH. Deionized water was added to a final volume of 10 mL. This solution was prepared immediately before each assay and was incubated at 37° C before and during use.

Assessment of peptide stability was carried out as described for simulated gastric fluid with the following exceptions. Simulated intestinal fluid was used instead of simulated gastric fluid for all steps. Protease action was quenched through a 1:1 dilution of the proteolysis solution with a 50% solution (volume/volume) of CH_3CN in H_2O solution containing 1% (by

volume) trifluoroacetic acid (SIF quenching solution). Control solutions, in which the activity of SIF is quenched before addition of peptide, had the following composition: 40 µL SIF, 50 µL SIF quenching solution (mixed first), and 10 µL 1 mM peptide stock (100 µM [peptide] after quenching). HPLC and MALDI-TOF mass spectra analyses were not performed. Quenched solutions were diluted 1:100 into CO_2 independent medium on a polypropylene dilution plate, which was further diluted with three sequential 1:10 dilutions in CO_2 independent medium (concentrations of peptide on the dilution plate range from 1000 nM to 1 nM), as for experiments using SGF. Solutions from the dilution plate were diluted 1:10 onto the plate with GP2.3 cells to provide peptide concentrations ranging from 100 nM to 0.1 nM in the assay. Control experiments showed that quenched diluted solutions of SIF without peptide did not induce luminescence responses from GP2.3 cells and that solutions of SIF that were quenched before addition did not cause erosion of peptide bioactivity (data not shown). Note that concentrations on the x-axis of Figure 4 represent the estimated concentrations of the intact peptide before proteolysis. The concentration of intact peptide after proteolysis is not known for this assay.

Rat kidney homogenate studies: Kidney preparation.

All experimental protocols were approved by the Institutional Animal Care and Use Committee at the University of Wisconsin-Madison and performed in accordance with the National Institutes of Health Guide

for the Care and Use of Laboratory Animals (8th edition; 2011). Adult female Sprague-Dawley rats (180–200 g; Harlan/Envigo, Indianapolis, IN, USA) were housed individually or in groups of two at room temperature under a 12-h light/dark cycle. Food and water were provided ad libitum. Animals were anesthetized with 1.5 g/kg urethane administered via intraperitoneal injections to effect. Body temperature of anesthetized animals was maintained at 37 °C using a

homeothermic blanket (Harvard Apparatus). Anesthetized rats were perfused transcardially with 50 ml cold 0.01 M PBS (pH 7.4) and then decapitated. Kidney tissues were harvested, washed with ice-cold saline solution and adhering tissues were trimmed. 4 mL of incubation buffer (50 mM Tris-HCl, pH 7.4) was added per gram of tissue, which was homogenized using a Teflon homogenizer. The homogenates were centrifuged at 2000 g for 10 min at 4 °C and the supernatants were stored at -80°C for future analysis. The homogenate samples were used for the stability assay within 8 days of tissue collection. Bicinchonic acid (BCA) assay was used to determine the total protein concentration in the tissue homogenates, which were then diluted to 2.5 mg protein/mL with incubation buffer.

PTH standards (PTH(1-34) and **M-Cyc-9β**) were spiked in rat kidney homogenates to achieve a final concentration of 50 µg/mL (~12 µM). Three replicates were prepared for each peptide. The spiked homogenates were incubated at 37 °C water bath and samples were collected at different time intervals (0, 1, 3, 5, 10, 15, 30, 45, 60, 90, 120 min). Two sets of samples were collected at each time point: a 50 µL sample was collected for liquid chromatography (LC) – mass spectrometry (MS) quantification study and a 10 µL sample was collected for matrix-assisted laser desorption/ionization (MALDI)-MS analysis. 5 µL internal standard (IS, 10 µg/mL rat PTH) was spiked in each LC-MS sample as quality control and normalization factor. The collected samples were immediately mixed with equal volumes of 1% trifluoroacetic acid (TFA) to terminate protease activity. The sample mixtures were centrifuged at 10,000 g for 10 minutes at 4 ºC. The supernatants were dried in a speed vacuum concentrator and stored in -20 ºC until further analysis.

Rat kidney homogenate studies: MALDI-MS analysis.

A sample from each time point was reconstituted in 10 µL H_2O with 0.1% formic acid (FA). 1 µL reconstituted sample was mixed with 1 µL 2,5-dihydroxybenzoic acid matrix (DHB, 150 mg/mL dissolved in 49.95% methanol, 49.95% H_2O and 0.1% FA) and spotted onto a MALDI target plate. An ultrafleXtreme MALDI-TOF/TOF mass spectrometer (Bruker Daltonics, Bremen, Germany) with reflectron positive mode was used for all MALDI MS analysis. 5000 laser shots were accumulated for each sample at *m/z* 700-5000. The acquired data was analyzed with flexAnalysis 3.4 (Bruker Daltonics, Bremen, Germany).

Rat kidney homogenate studies: Liquid chromatography/mass spectrometry analysis.

Sample from each time point was reconstituted in 50 µL H_2O with 0.1% formic acid (FA). Calibration standards (0, 0.05, 0.1, 0.5, 1, 5, 10, 25, 50 and 75 µg/mL) were prepared by dissolving peptide standards in the same sample matrix (1:1 tissue homogenate:1% TFA in H_2O with 1 µg/mL rat PTH(1-34) as an internal standard).

A Dionex UltiMate 3000 UHPLC system (Thermo Scientific, Bremen, Germany) coupled to a Q Exactive hybrid quadrupole-Orbitrap mass spectrometer (Thermo Scientific, Bremen, Germany) were used for all LC/MS analysis. The analyte and IS were separated on a Phenomenex Kinetex C18 column (100 x 2.1 mm ID, 1.7 µm). Mobile phase A was H_2O with 0.1% FA and mobile phase B was acetonitrile with 0.1% FA. The following gradient was used to separate the analyte and IS (time/minute, % mobile phase B): (0, 15), (3.8, 50), (4, 98), (5.3, 98), (5.4, 15), (6, 15). The flow rate was set at 0.30 mL/min with column temperature at 30 ºC and sampler temperature at 10 ºC. Three injections were performed for each sample.

A multiplexed parallel reaction monitoring (PRM) method was set up on the mass spectrometer. Briefly, two scan events were defined. Scan event 1 was a full MS scan to monitor

all ions from *m/z* 133.4 to 2000 with resolution of 70,000 (*m/z* 200). Scan event 2 was a targeted MS^2 event that multiplexed twice: +5 charged analyte and IS were fragmented together with normalized collisional energy (NCE) of 26 and +6 charged ions were fragmented together with NCE of 20.

Xcalibur (Thermo Scientific, Bremen, Germany) and Microsoft Excel were used for all data analysis. The y_{32} ion peak area ratio of analyte to IS was calculated for each sample. A linear equation between concentrations and peak area ratios was established from calibration standards. The concentrations from unknown samples were calculated based on the peak area ratios and the linear equation.

Rat kidney homogenate studies: Bioassay analysis.

The stability of peptides in kidney homogenate preparations was performed using a bioassay based readout as described above for simulated gastric fluid and simulated intestinal fluids, with the following exceptions. 1 mM stock solutions of peptide were diluted 1:85 into kidney homogenate at t = 0 (~12 µM). The concentration of peptide in kidney homogenate following dilution approximates the concentration used in the LC/MS-based approach described above. Protease activity was quenched through a 1:1 dilution of the proteolysis reaction with SIF quenching solution at the indicated times (see above for the composition of this solution for the composition of SIF quenching solution). 10 µL of quenched protease solution was then mixed with 53 µL of CO_2 independent medium on the dilution plate. The concentration of peptide in the solutions provided after dilution into CO_2 independent medium is 1000 nM. This solution was serially diluted (three 1:10 dilutions) on the dilution plate (1000 nM to 1 nM), and 10 µL of solutions from the dilatation plate were transferred to a plate with confluent monolayers of GP2.3 cells that had been preincubated in CO_2 independent medium containing 0.5 mM d-

luciferin for 30 minutes. Maximal luminescence responses were recorded approximately 20 minutes after addition of solutions containing peptides subjected to incubation in kidney homogenate. Note that concentrations on the x-axis of Figure 3d represent the estimated concentrations of the intact peptide before proteolysis. The concentration of intact peptide after proteolysis is not known for this assay. Control solutions containing kidney homogenate without added PTHR1 agonist did not induce detectable luminescence in these assays (data not shown).

In vivo pharmacology: calcemic response.

Mice (CD1, female, age 9–12 weeks) were treated in accordance with the ethical guidelines adopted by Massachusetts General Hospital. Mice (n = 5 per compound) were injected subcutaneously with vehicle (10 mM citric acid/150 mM NaCl/0.05% Tween-80, pH 5.0) containing PTH(1-34) or α/β-peptide at a dose of 20 nmol/kg body weight. Blood was withdrawn just prior to injection (t = 0) or at times thereafter. Tail vein blood was collected and immediately used for analysis. Blood Ca^{2+} concentration was measured with a Siemens RapidLab 348 Ca^{2+}/pH analyzer.

In vivo pharmacology: pharmacokinetics.

Blood content of PTH(1-34) or α/β-peptide derivatives was assessed in plasma from mice (n = 5) injected with vehicle containing PTH(1-34) or an α/β-peptide at a dose of 20 nmol/kg body weight in an experiment performed separately from the calcemic response assays described above. Blood was withdrawn just prior to injection (t=0) or at times thereafter. Tail vein blood was collected and treated with protease inhibitors (aprotinin, leupeptin, EDTA), centrifuged to remove blood cells, mixed with cAMP response assay buffer, and administered to GP2.3 cells. The raw luminescence readouts recorded in this assay were converted to blood peptide concentrations through use of a standard curve relating luminescence response to known peptide

concentrations under identical assay conditions (Supporting Figure 6). Previous work has demonstrated this cAMP response-based method for quantifying the blood concentrations of PTHR1 agonists yields results similar to those from an ELISA-based method[54]. Previous experiments showed GP2.3 cells exposed to plasma from mice injected with vehicle showed weak luminescence responses, indicating that observed cAMP responses were dependent on exogenous administration of a PTHR1 agonist.

Reversed-phase analytical HPLC retention time study.

Peptides were injected onto a reversed phase analytical HPLC column using a 10-60% gradient of solvent B in solvent A, as described above (Supporting Figure 12). The retention time indicated corresponds to the time at which the maximal signal corresponding to the peptide of interest was observed. All peptides were injected consecutively on the same day using identical conditions. PTH(1-34) was injected at the beginning and end of the studies to provide an estimation for variation in retention time resulting from alterations in instrument function. This variation is estimated to be less than 2 minutes.

Data Calculations.

Data were processed by using the Microsoft Excel and GraphPad Prism 4.0 software packages. Data from binding and cAMP dose–response assays were analyzed using a sigmoidal dose–response model with variable slope. Paired data sets were statistically compared by using Student's t test (two-tailed) assuming unequal variances for the two sets.

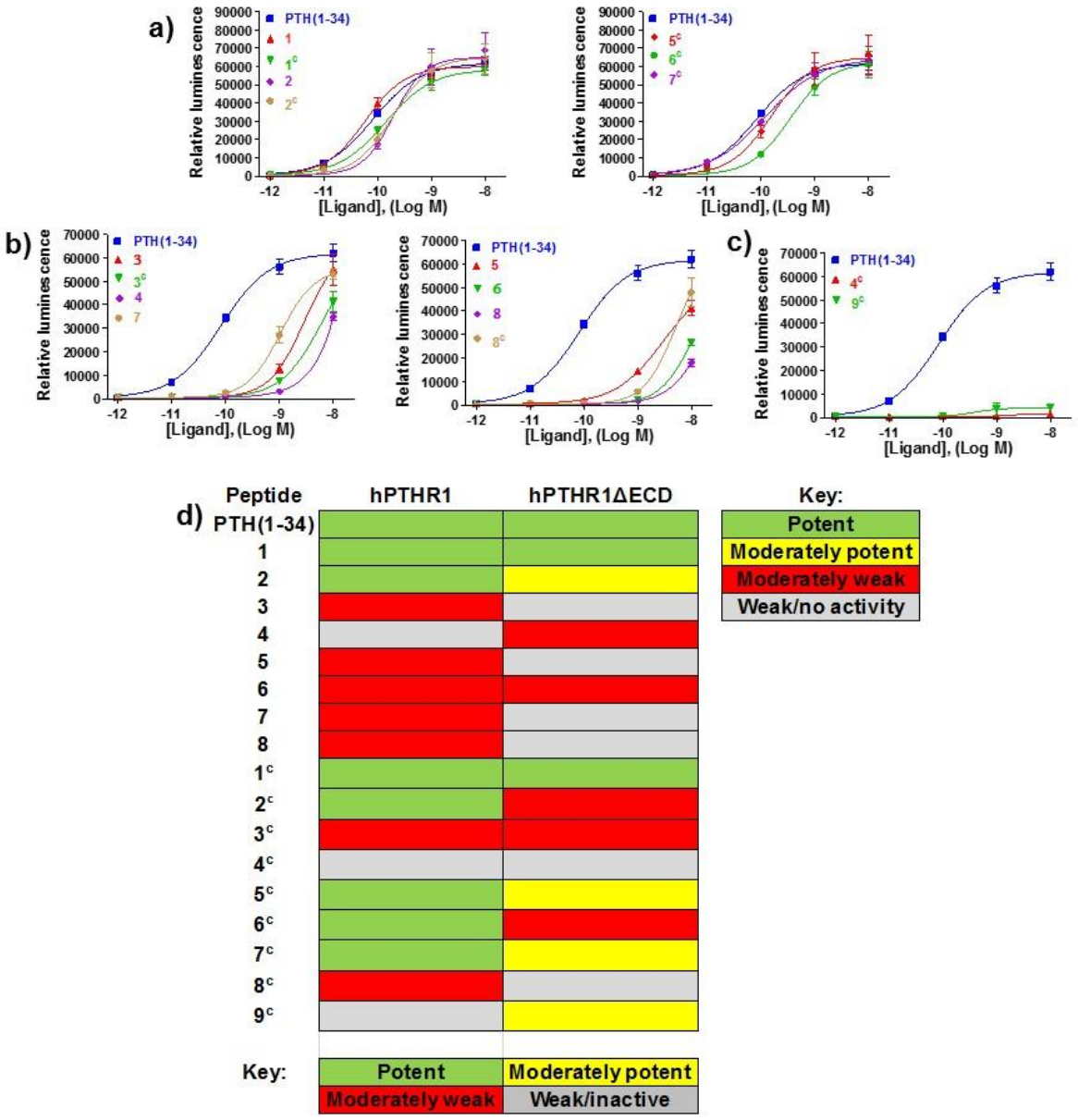

Supporting Figure 1: Summary cellular cAMP responses for human PTHR1. Parameters used to classify peptide bioactivity are found in the methods section. Composite dose response curves for (**a**) "potent", (**b**) "moderately weak", (**c**) or "weak" derivatives. See supporting methods for categorization criteria. Data points represent mean ± SEM from n = 3 experiments for α/β-peptides or n = 6 for PTH(1-34). Curves represent fitting of a sigmoidal dose response model with variable slope to the data points. Curves were constrained to plateau at a maximal value over 55,000 relative luminescence units. (**d**) Summary table of peptide cAMP inducing bioactivities in cells expressing either full-length PTHR1 or PTHR1 lacking extracellular domain (hPTHR1ΔECD). See Figure 1 for EC_{50} values. See Supporting Figure 2 for data for hPTHR ΔECD.

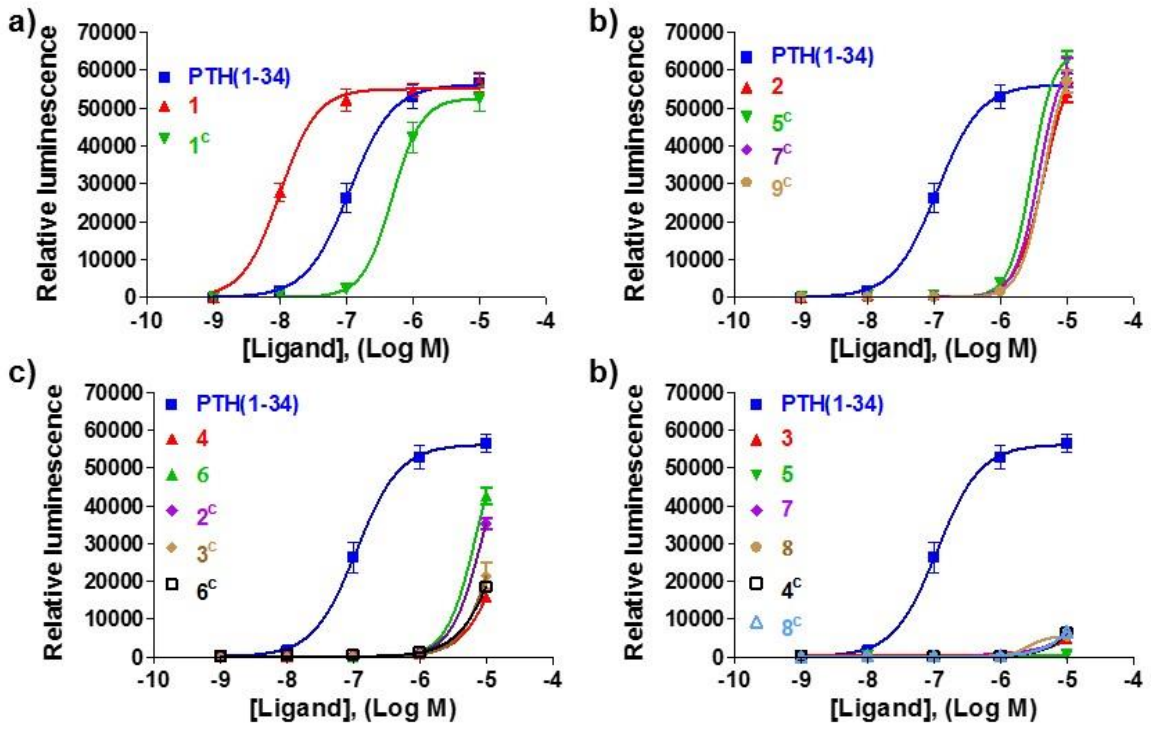

e)

Peptide	PTHR1ΔECD EC_{50}, nM (Means ± SEM)	Derivative EC_{50}/ PTH EC_{50} (nM)
PTH(1-34)	62 ± 37	1
1	10 ± 6	0.2
2	5,200 ± 3,000	84
3	*No activity*	
4	15,000 ± 8,800	250
5	*No activity*	
6	6,700 ± 3,900	110
7	*No activity*	
8	*No activity*	
1c	500 ± 290	8
2c	11,000 ± 6,200	170
3c	7,800 ± 4,500	130
4c	*No activity*	
5c	4,100 ± 2,300	65
6c	22,000 ± 13,000	360
7c	4,600 ± 2,700	74
8c	*No activity*	
9c	5,400 ± 3,100	87

Supporting Figure 2: Summary cellular cAMP responses for human PTHR1 lacking extracellular domain (hPTHR1ΔECD). Composite dose response curves for (**a**) "potent", (**b**) "moderately potent", (**c**) or "moderately weak" and (**d**) weak peptides. Data points represent mean ± SEM from n = 3 experiments for α/β-peptides or n = 6 for PTH(1-34). Curves represent fitting of a sigmoidal dose response model with variable slope to the data points. Curves were constrained to plateau at a maximal value over 65,000 relative luminescence units. (**e**) Data table for cAMP inducing bioactivities in cells expressing hPTHR1ΔECD. "*No activity"* denote peptides that induce maximal responses of <10% the maximal possible cAMP response.

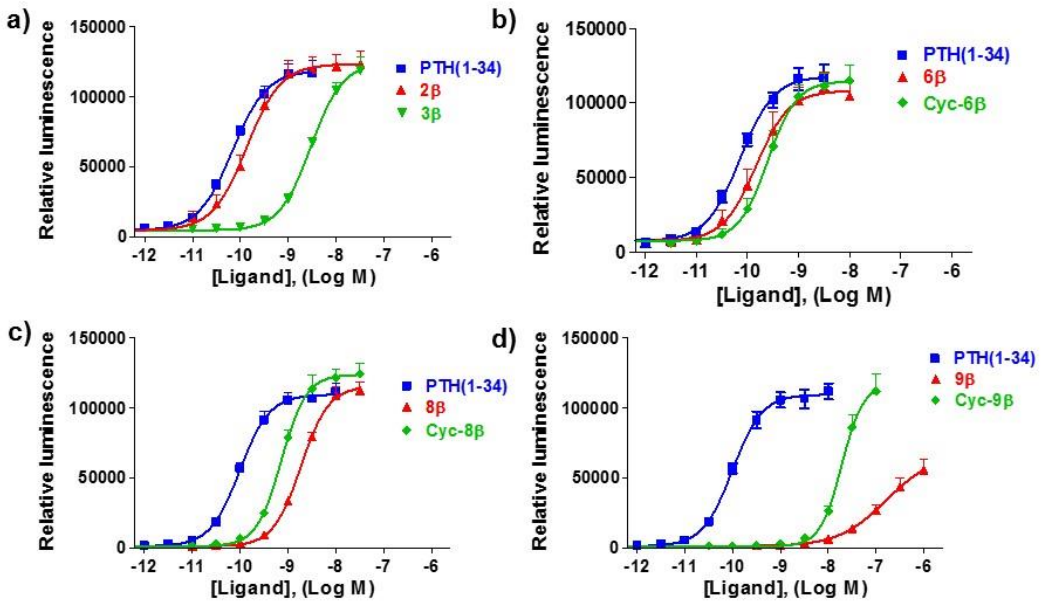

Supporting Figure 3: Composite curves for cAMP induction assays in cells expressing hPTHR1 using analogues of PTH(1-34). See methods section in the main text for a description of binding assays. Data points represent mean ± SEM from n = 3 experiments for α/β-peptides or n = 6 for PTH(1-34). See table 1 for tabulated EC_{50} values. Composite dose response curves for derivatives (**a**) **2β** and **3β** (**b**) **6β** and **Cyc-6β** (**c**) **8β** and **Cyc-8β** (**d**) or **9β** and **Cyc-9β.**

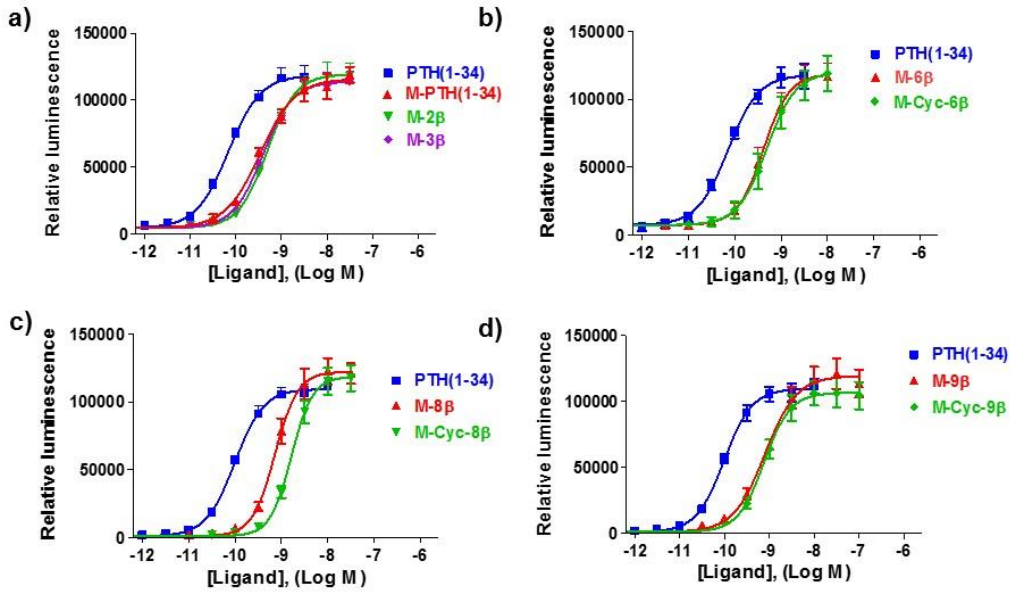

Supporting Figure 4: Composite curves for cAMP induction assays in cells expressing hPTHR1 using analogues of PTH(1-34). See methods section in the main text for a description of binding assays. Data points represent mean ± SEM from n = 3 experiments for M-PTH(1-34) and α/β-peptides or n = 6 for PTH(1-34). See table 1 for tabulated EC_{50} values. Composite dose response curves for derivatives (**a**) **M-2β** and **M-3β** (**b**) **M-6β** and **M-Cyc-6β** (**c**) **M-8β** and **M-Cyc-8β** (**d**) or **M-9β** and **M-Cyc-9β.**

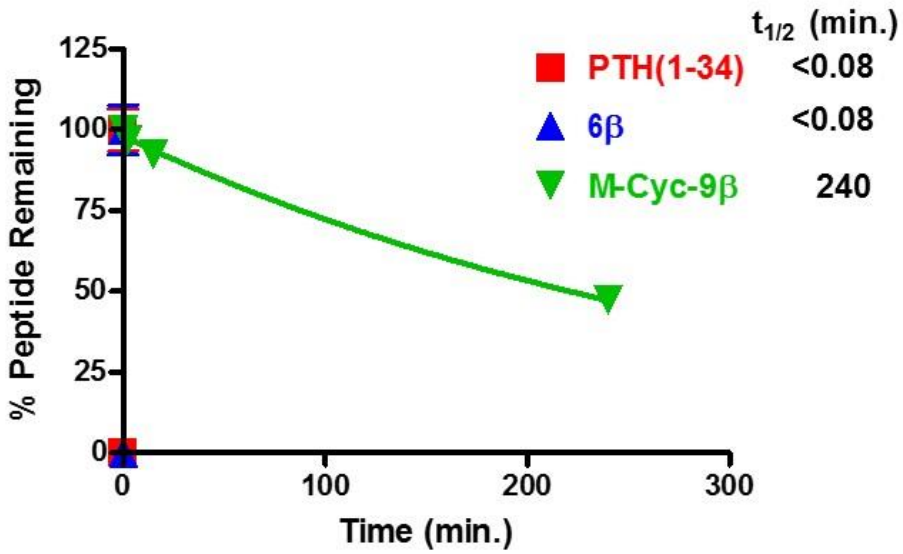

Supporting Figure 5: HPLC assay of PTH(1-34) analogue degradation in simulated gastric fluid (SGF). Peptide concentration or bioactivity following exposure to SGF was assessed using an HPLC-based assay. Data points represent mean ± standard deviation. Curves result from fitting of an exponential decay model to the data, with half-lives shown here. See Figure 2 for structures.

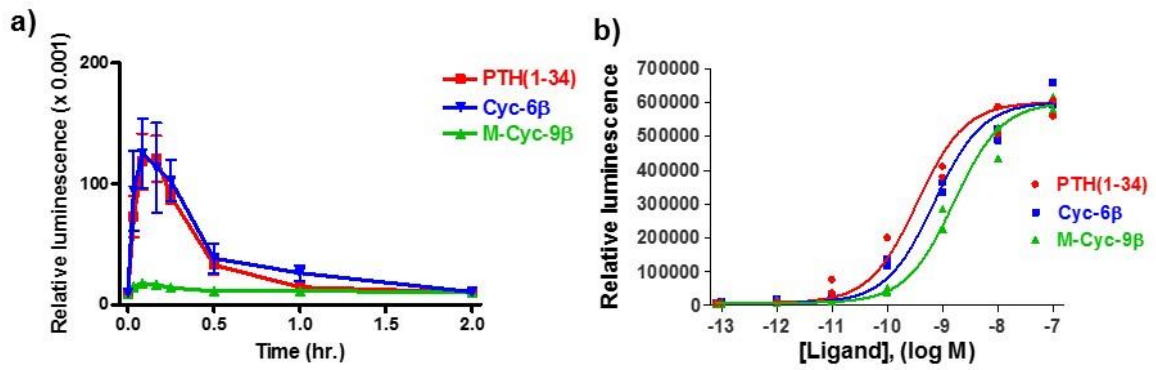

Supporting Figure 6: Bloodstream bioavailability of PTH(1-34) and α/β-peptide analogues. CD1 mice (n = 5 per compound), were injected subcutaneously with peptide at a dose of 20 nmol/kg body weight. Blood was withdrawn just prior to injection (t=0) or at times thereafter. Blood was centrifuged and plasma was mixed with medium and added to GP2.3 cells stably expressing PTHR1, as described in the methods section in the main text. (**a**) The raw luminescence response induced in GP2.3 cells resulting from addition of 2 µL of serum (mixed with CO_2 independent medium) taken from mice at different time points after injection (x-axis). This raw luminescence response was converted to the concentration of peptide in the bloodstream through use of a standard curve relating peptide concentrations to luminescence responses. (**b**) The standard curve relating peptide concentration (in CO_2 independent medium) to observed luminescence responses in GP2.3 cells, which was used to convert raw luminescence readings in panel **a** to the peptide concentrations shown in Figure 5 of the main text. The data in panel **b** results from a single dose-response assay, distinct from all other data, performed concurrently with the assay that provided the data in panel **a**.

a)

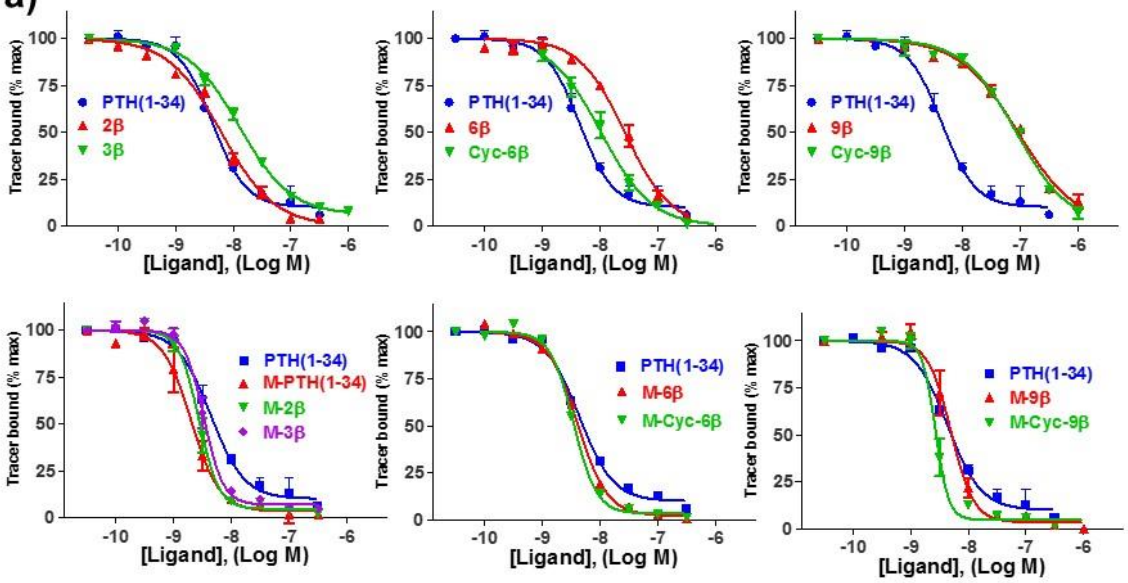

b)

Peptide	R^0 hPTHR1 IC_{50}, nM (Means ± SEM)	Derivative IC_{50}/ PTH IC_{50} (nM)
PTH(1-34)	5.2 ± 0.8	1.0
2β	6.0 ± 11.0	1.2
3β	13 ± 19	2.5
6β	72 ± 2.9	5.2
Cyc-6β	11 ± 2	2.2
9β	84 ± 11	16.2
Cyc-9β	83 ± 15	16.1
M-PTH(1-34)	2.0 ± 0.3	0.4
M-2β	2.8 ± 0.7	0.5
M-3β	3.7 ± 0.8	0.7
M-6β	4.6 ± 1.0	0.9
M-Cyc-6β	3.5 ± 0.5	0.7
M-9β	5.4 ± 0.9	1.1
M-Cyc-9β	2.8 ± 2.2	0.5

Supporting Figure 7: PTHR1 R0 binding assays. Membranes from Cos-7 cells transfected with human PTHR1 were used according to the methods section. (**a**) Composite dose response curves for analogues of PTH(1-34) and M-PTH(1-34). Data points represent mean ± SEM from n = 4 experiments. Curves represent fitting of a sigmoidal dose response model with variable slope to the data points. (**b)** Summary of average data from n =4 binding experiments. Note that this data is distinct from the data found in Supporting Figure 10 and differs in the source of the membranes used for binding experiments.

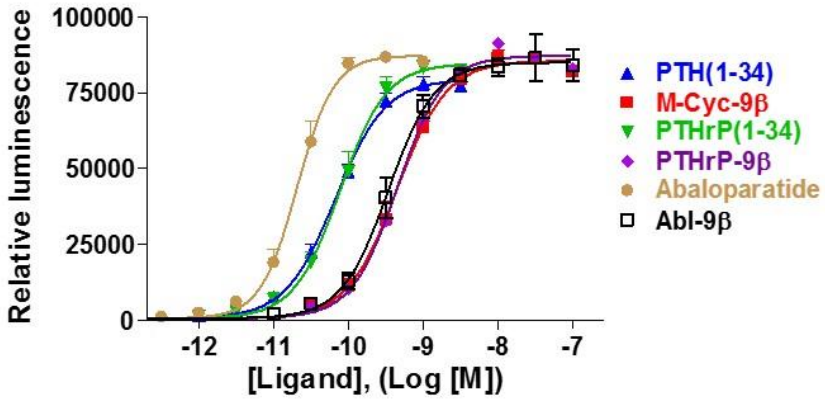

Supporting Figure 8: Composite curves for cAMP induction assays in cells expressing hPTHR1 with analogues containing nine β residues. See methods section in the main text for a description of cAMP assays. Data points represent mean ± SEM from n = 3 experiments. See table 2 for tabulated EC_{50} values.

a)

hPTH(1-34)	SVSEIQLMHNLGKHLNSMERVEWLRKKLQDVHNF-NH_2
hPTHrP(1-34)	AVSEHQLLHDKGKSIQDLRRRFFLHHLIAEIHTA-NH_2
PTHrP-6β	AVSEHQLLHDKGKSIQDLRRRFFLHKLIAEIHTA-NH_2
PTHrP-Cyc-6β	AVSEHQLLHDKGKXIQDXRRRZFLHZLIAXIHTX-NH_2
Abaloparatide	AVSEHQLLHDKGKSIQDLRRRELLEKLLUKLHTA-NH_2
Abl-6β	AVSEHQLLHDKGKSIQDLRRRELLEKLLUKLHTA-NH_2
Abl-Cyc-6β	AVSEHQLLHDKGKXIQDXRRRZLLEZLLUXLHTX-NH_2

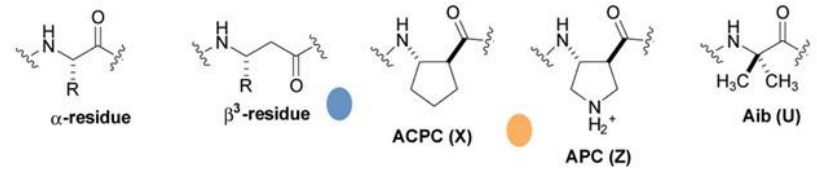

b)

Derivative	hPTHR1 cAMP EC_{50}, nM (mean ± SEM)	Derivative EC_{50}/ PTH EC_{50} (nM)	n
PTH(1-34)	0.10 ± 0.01	1.0	4
PTHrP(1-34)	0.10	1.0	1
PTHrP-6β	0.32 ± 0.15	3.1	2
PTHrP-Cyc-6β	0.65 ± 0.19	6.3	2
Abaloparatide	0.034 ± 0.02	0.3	4
Abl-6β	4.1 ± 0.27	40.3	2
Abl-Cyc-6β	0.18 ± 0.01	1.8	2

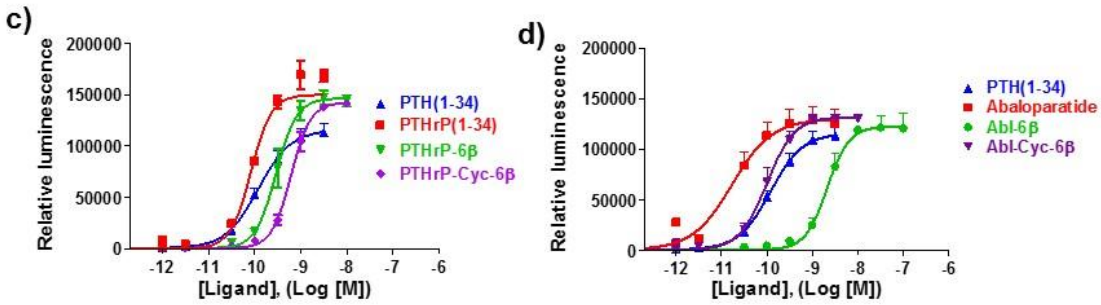

Supporting Figure 9: Properties of analogues of PTHrP and Abaloparatide containing α-to-β replacements in the C-terminal segment. (**a**) Sequences of peptides studied. (**b**) Data table for cAMP inducing bioactivities in cells expressing hPTHR1. Data is from the number of experiments indicated in the rightmost column. These data are distinct from data, but consistent with, shown in tables 1 and 2 in the main text. **(c-d**) Composite dose-response curves for cAMP induction in cells expressing human PTHR1. Data points represent mean ± SEM from the number of experiments indicated in panel **b**.

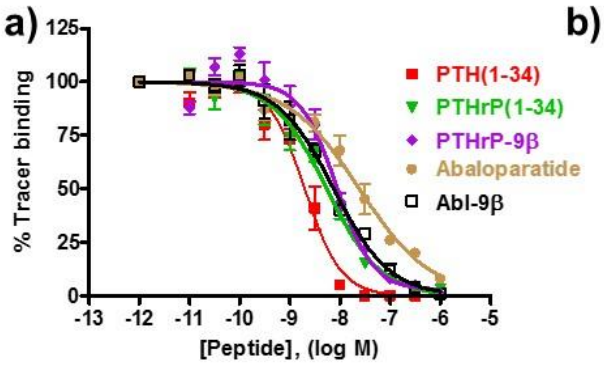

b)

Peptide	Binding (IC_{50}, nM) mean ± SEM
PTH(1-34)	2.0 ± 0.4
PTHrP(1-34)	6.1 ± 1.3
PTHrP-9β	8.6 ± 0.9
Abaloparatide	25 ± 6.8
Abl-9β	6.9 ± 1.0

Supporting Figure 10: Assessment of peptide binding to PTHR1 R0 state. (**a**) Composite dose-response curves for the displacement of radiolabeled tracer peptide using membrane preparations from the GP2.3 cell line with GTPγS. Binding assays were run according to the methods described in the supporting methods. (**b**) Data table for PTHR1 binding from n = 4 experiments. Note that this data is distinct from the data found in Supporting Figure 7 and differs in the source of the membranes used for binding experiments.

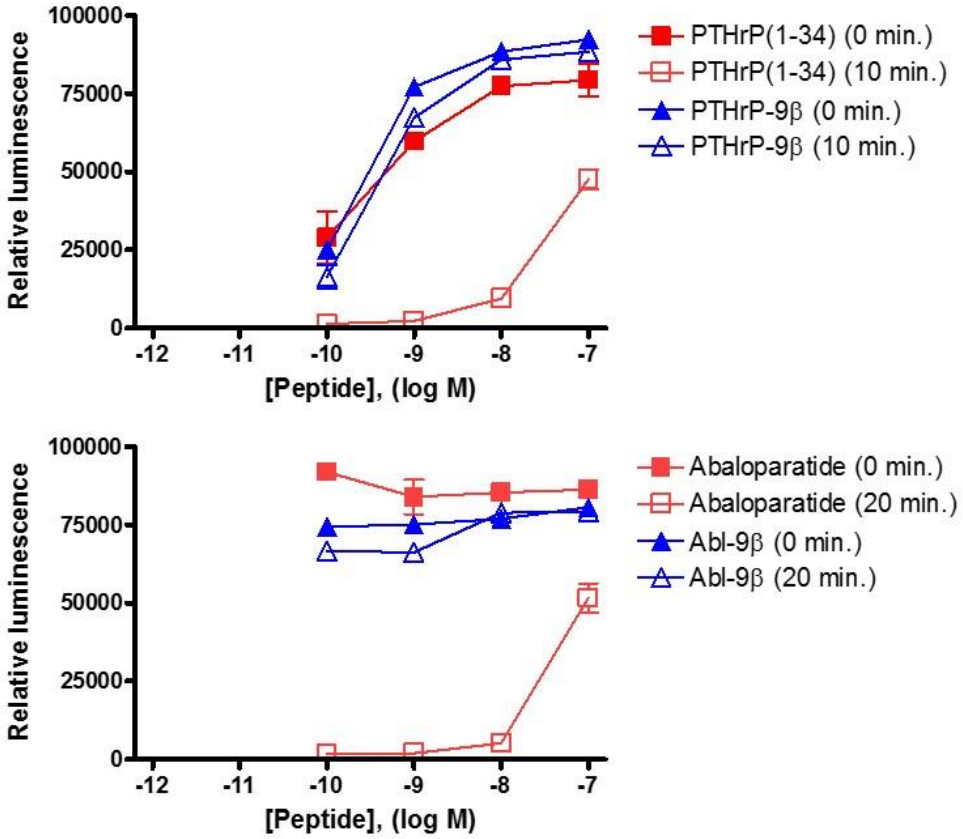

Supporting Figure 11: Degradation of PTHrP and Abaloparatide analogues in SIF. Peptide bioactivity following exposure to SIF was assessed using a biological assay. Data points represent mean ± SEM. Note that the times listed after peptide names represent the duration of time that the peptide was incubated with in SIF before quenching of protease activity.

Peptide	Analytical HPLC retention time (min.)
PTH(1-34)	34.3
6β	40.2
Cyc-6β	37.7
M-Cyc-9β	34.5

Supporting Figure 12: Comparison of HPLC retention times for selected derivatives of PTH(1-34). Analytical HPLC runs were performed using the methodology described in the supporting methods section, with peptides run consecutively on the same day to minimize day-to-day variability.

Peptide	Retention time	Purity	[M+H] calc (avg)	[M+H] calc (exact)	[M+H] observed	Average (AVG) or exact (EX) for observed
1	29.6	>97%	4132.7	4130.2	4130.7	EX
2	36.2	>97%	4132.7	4130.2	4129.1	EX
3	35.5	>97%	4132.7	4130.2	4130.1	EX
4	30.6	>97%	4132.7	4130.2	4130.1	EX
5	31.4	>97%	4132.7	4130.2	4129.1	EX
6	30.5	>97%	4132.7	4130.2	4131.2	EX
7	29.9	>97%	4132.7	4130.2	4130.7	EX
8	30.1	>97%	4132.7	4130.2	4130.3	EX
1[c]	30.6	>97%	4141.9	4138.2	4139.6	EX
2[c]	29.1	96.2%	4129.8	4127.2	4129.4	AVG
3[c]	30.7	95.3%	4141.9	4138.2	4141.1	AVG
4[c]	32.4	95.4%	4099.8	4097.2	4099.8	AVG
5[c]	28.7	96.8%	4115.8	4113.1	4115.2	AVG
6[c]	29	>97%	4100.8	4098.2	4099.9	AVG
7[c]	30.2	97.2%	4115.8	4113.1	4114.3	AVG
8[c]	29.7	>97%	4097.7	4095.2	4095.4	AVG
9[c]	30.7	>97%	4092.8	4090.2	4091.8	AVG
2β	40	>97%	4139.8	4137.2	4137.1	AVG
3β	40.5	>97%	4137.8	4135.2	4137	AVG
6β	37.6	>97%	4251	4248.3	4250.6	AVG
Cyc-6β	37.7	>97%	3998.7	3996.2	3997.2	AVG
8β	45.2	>97%	4273	4270.3	4274	AVG
Cyc-8β	43.3	>97%	4020.7	4018.2	4019.4	AVG
9β	43.1	>97%	4271	4268.3	4268.7	AVG
Cyc-9β	40.1	>97%	4018.7	4016.2	4019.5	AVG
M-2β	40.6	>97%	4299.1	4296.3	4299	AVG
M-3β	40.7	>97%	4297	4294.3	4295.9	AVG
M-6β	30.4	>97%	4331.1	4238.4	4330.7	AVG
M-Cyc-6β	39.7	>97%	4078.9	4076.4	4077.9	AVG
M-8β	41.3	>97%	4383.2	4380.4	4381.5	AVG
M-Cyc-8β	39.4	>97%	4130.9	4128.4	4129.5	AVG
M-9β	42.6	>97%	4381.3	4378.4	4381.7	AVG
M-Cyc-9β	42.6	>97%	4128.9	4126.4	4130.4	AVG
M-PTH(1-34)	39.9	>97%	4247	4244.3	4248	AVG
PTHrP(1-34)	Sigma aldrich (#H9148)					
PTHrP-6β	28.8	>97%	4092.8	4090.3	4092.9	AVG
PTHrP-Cyc-6β	31.5	>97%	4001.7	3999.3	4000.9	AVG
PTHrP-9β	32.1	>97%	4013.8	4011.3	4014.1	AVG
Abl-6β	26.8	>97%	4045.8	4043.4	4045.8	AVG
Abl-Cyc-6β	26.3	>97%	3973.7	3791.3	3972.7	AVG
Abl-9β	32.3	>97%	3985.8	3983.3	3985.6	AVG
Abaloparatide	24.4	>97%	3961.7	3959.3	3962.5	AVG

Supporting Figure 13: Summary of analytical HPLC and MALDI-TOF data. Analytical HPLC runs were performed using the methodology described in the supporting methods. Exact masses correspond to the singly protonated monoisotopic mass. Average masses correspond to the average isotopic molecular weight plus one mass unit to account for the singly protonated ion.

Supporting Figure 14: HPLC and MALDI-TOF mass spectra data

Peptide #

1

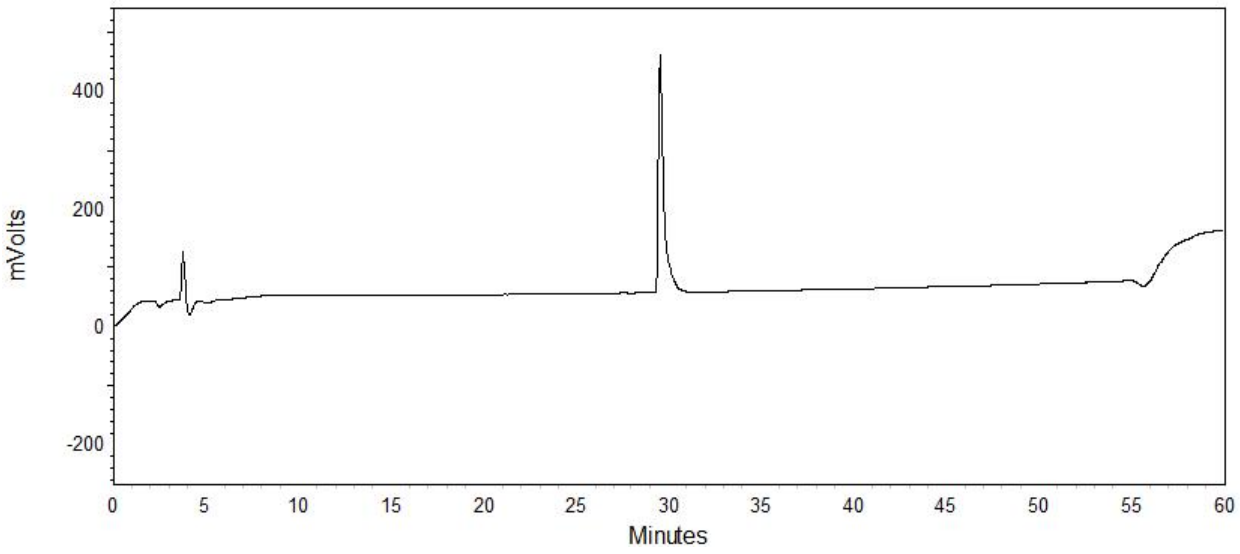

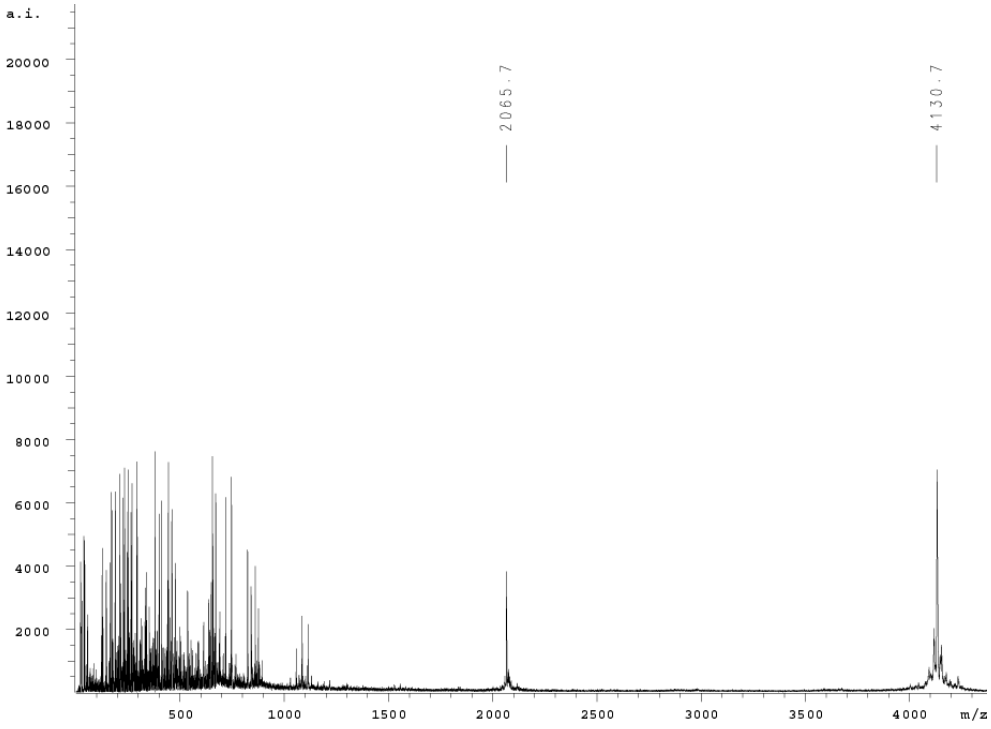

2

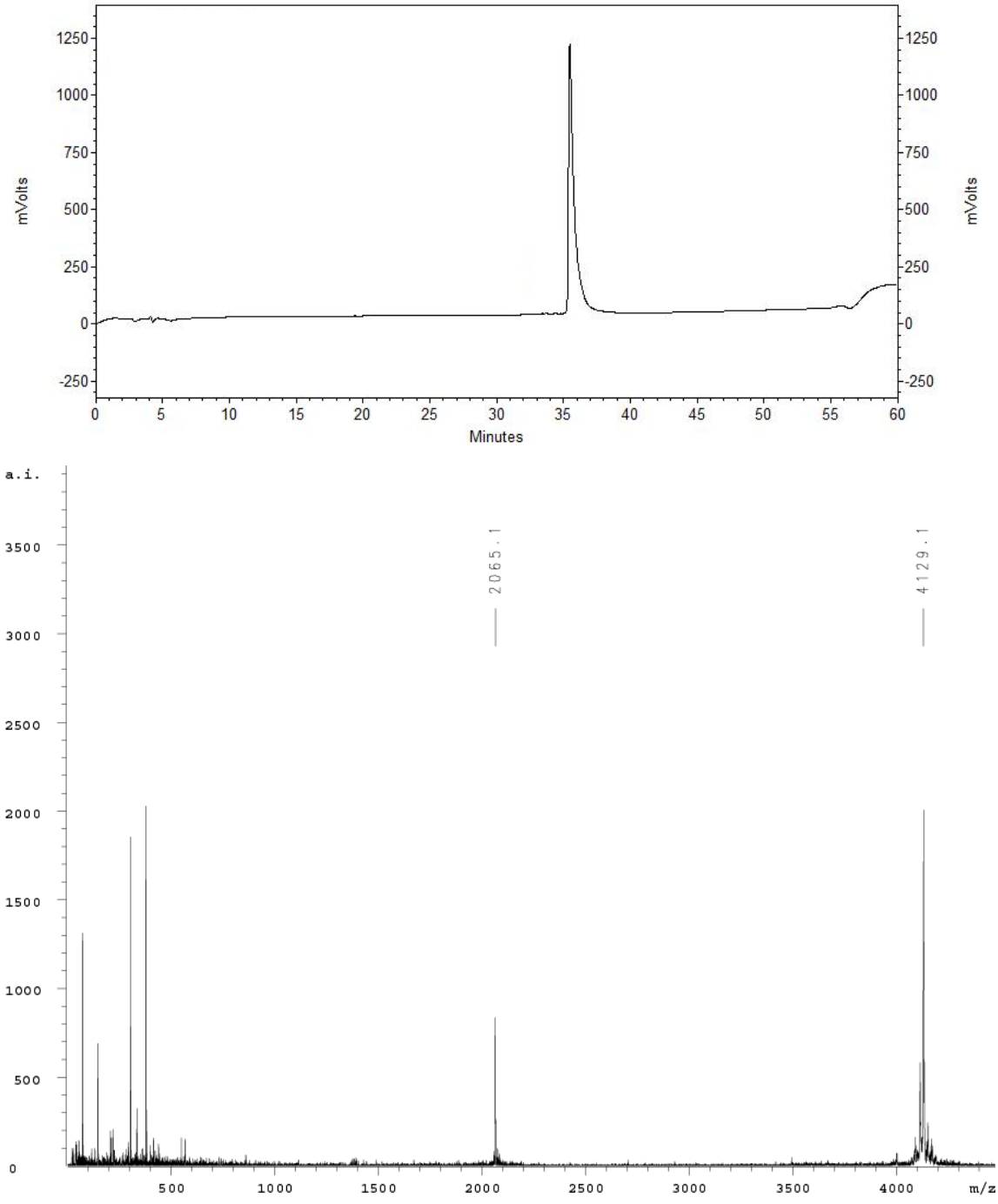

3

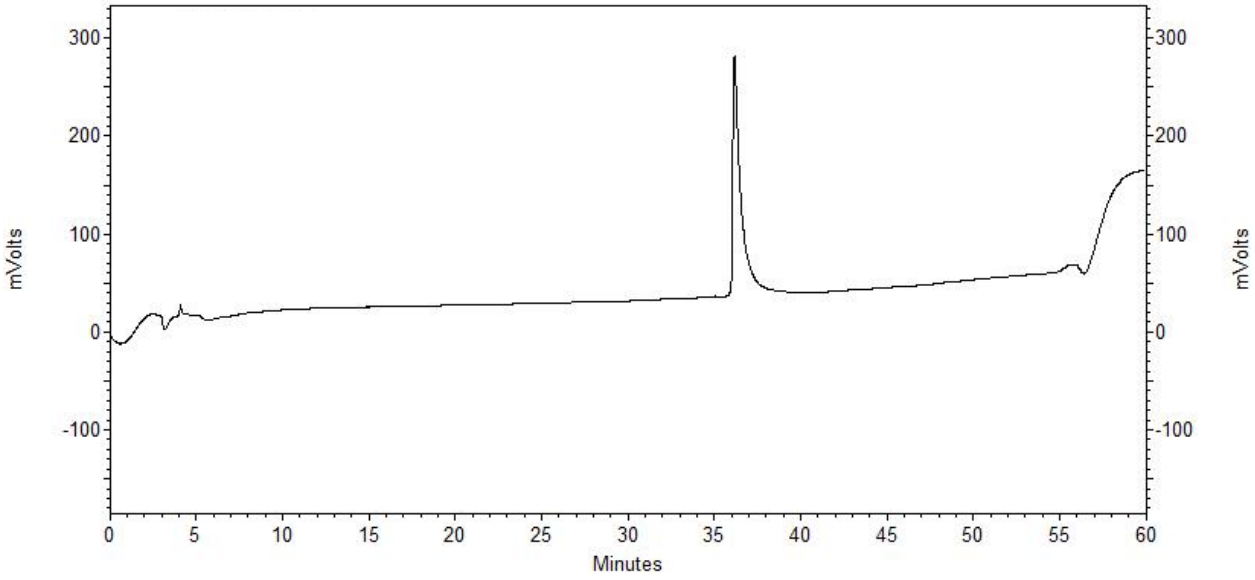
mVolts
300
200
100
0
-100
0
5
10
15
20
25
30
35
40
45
50
55
60
Minutes

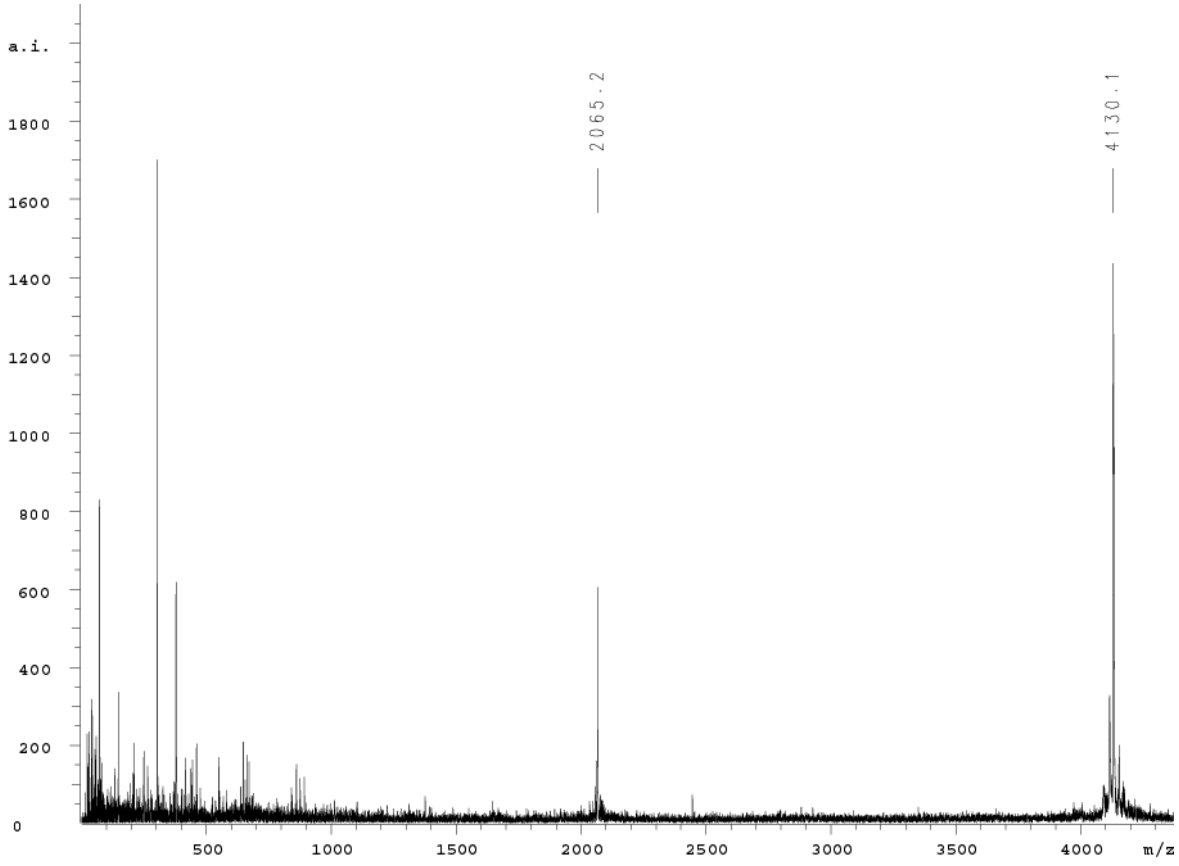
a.i.
1800
1600
1400
1200
1000
800
600
400
200
0
2065.2
4130.1
500
1000
1500
2000
2500
3000
3500
4000
m/z

4

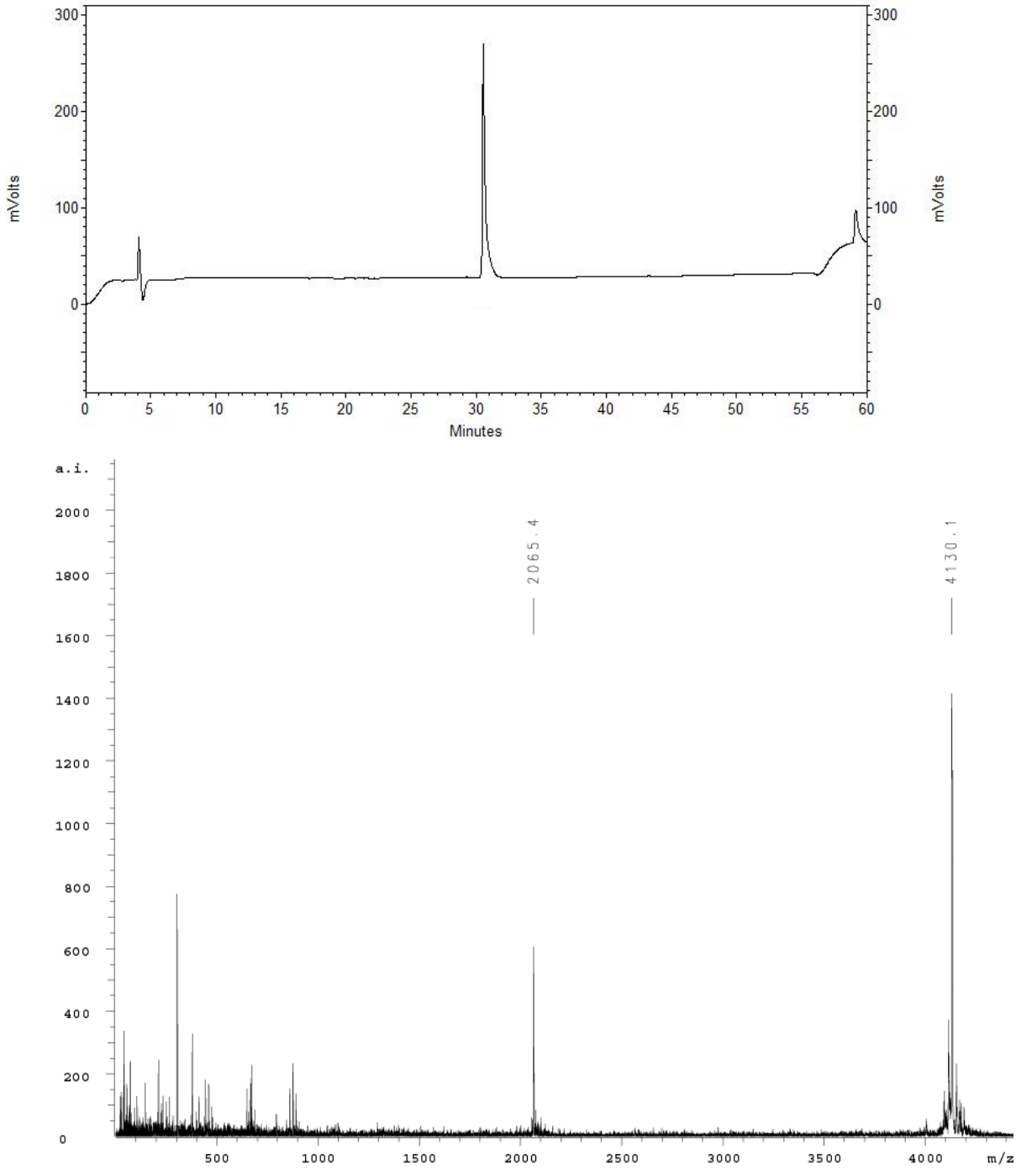

5

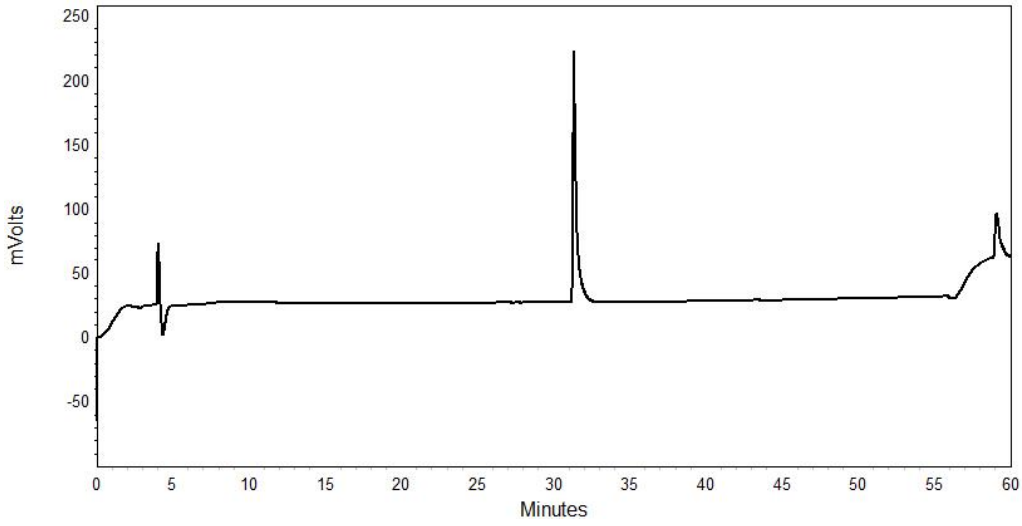
mVolts
250
200
150
100
50
0
-50
0
5
10
15
20
25
30
35
40
45
50
55
60
Minutes

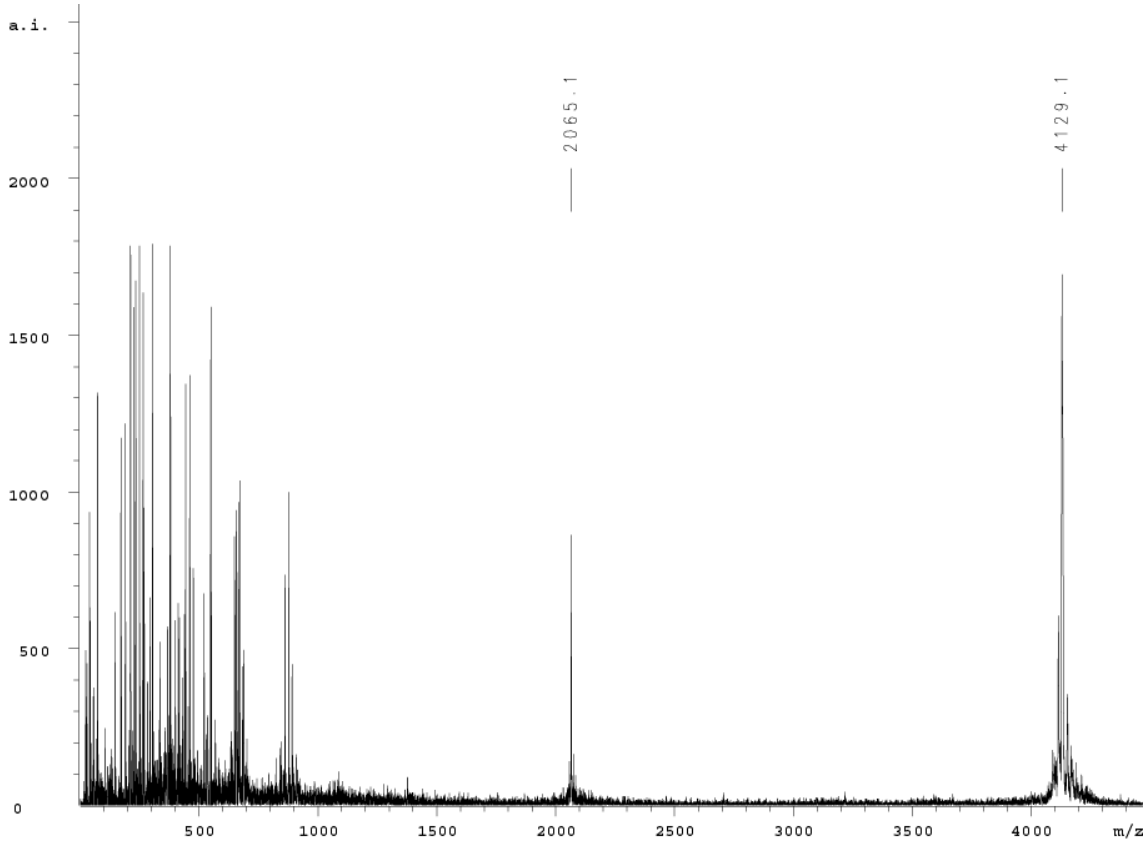
a.i.
2065.1
4129.1
2000
1500
1000
500
0
500
1000
1500
2000
2500
3000
3500
4000
m/z

6

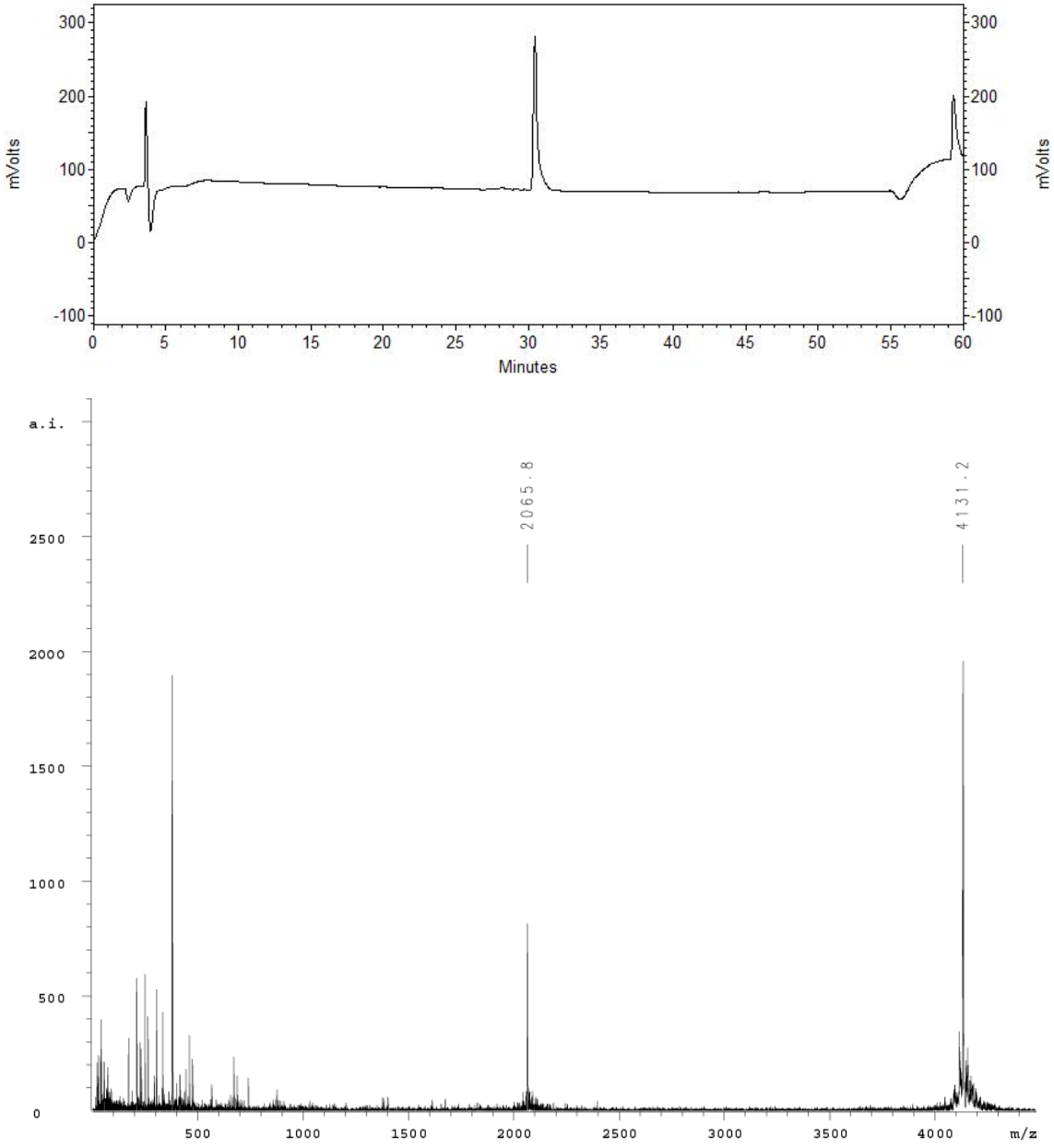

7

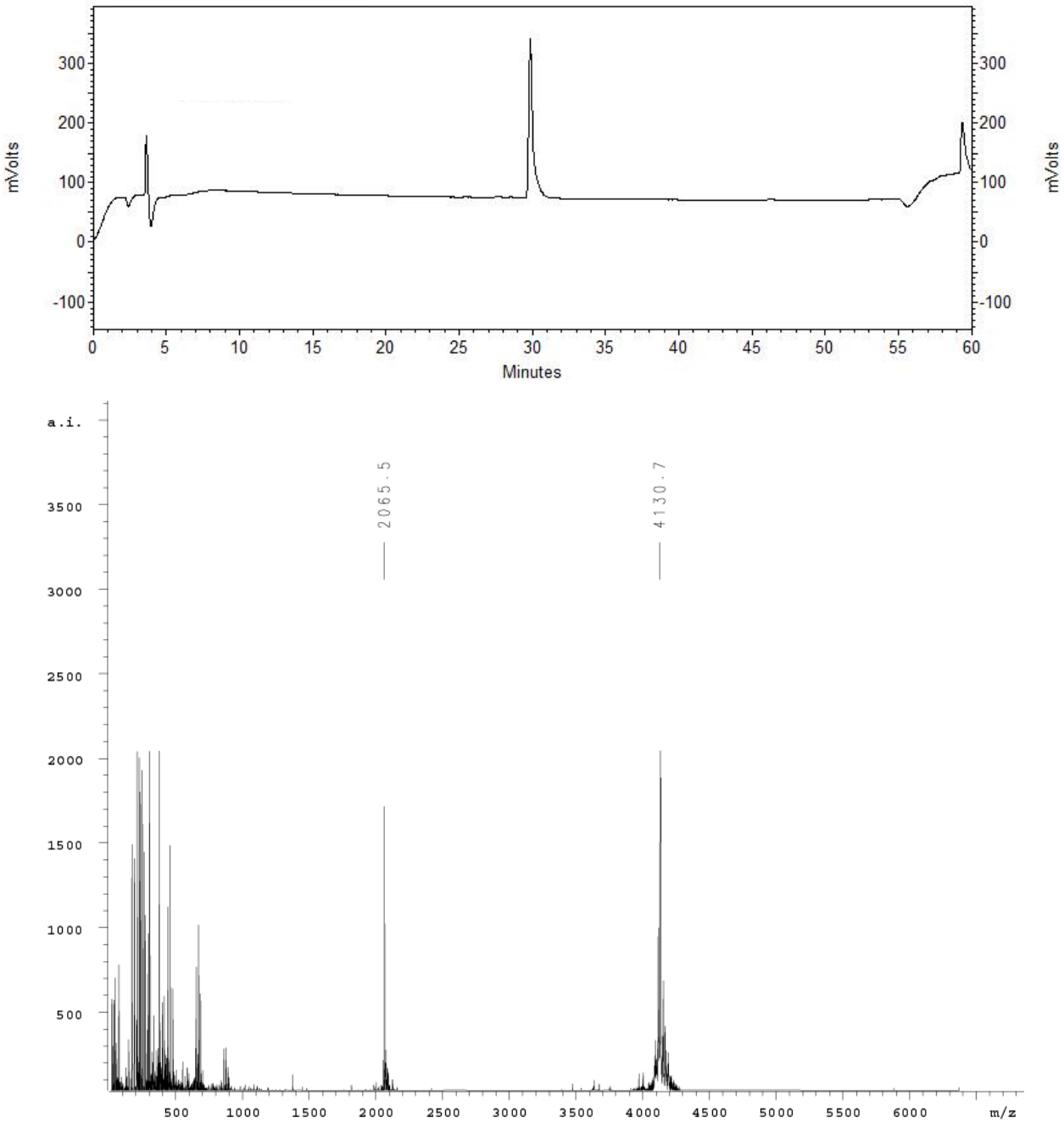
mVolts
300
200
100
0
-100
0
5
10
15
20
25
30
35
40
45
50
55
60
Minutes
a.i.
2065.5
4130.7
3500
3000
2500
2000
1500
1000
500
500
1000
1500
2000
2500
3000
3500
4000
4500
5000
5500
6000
m/z

8

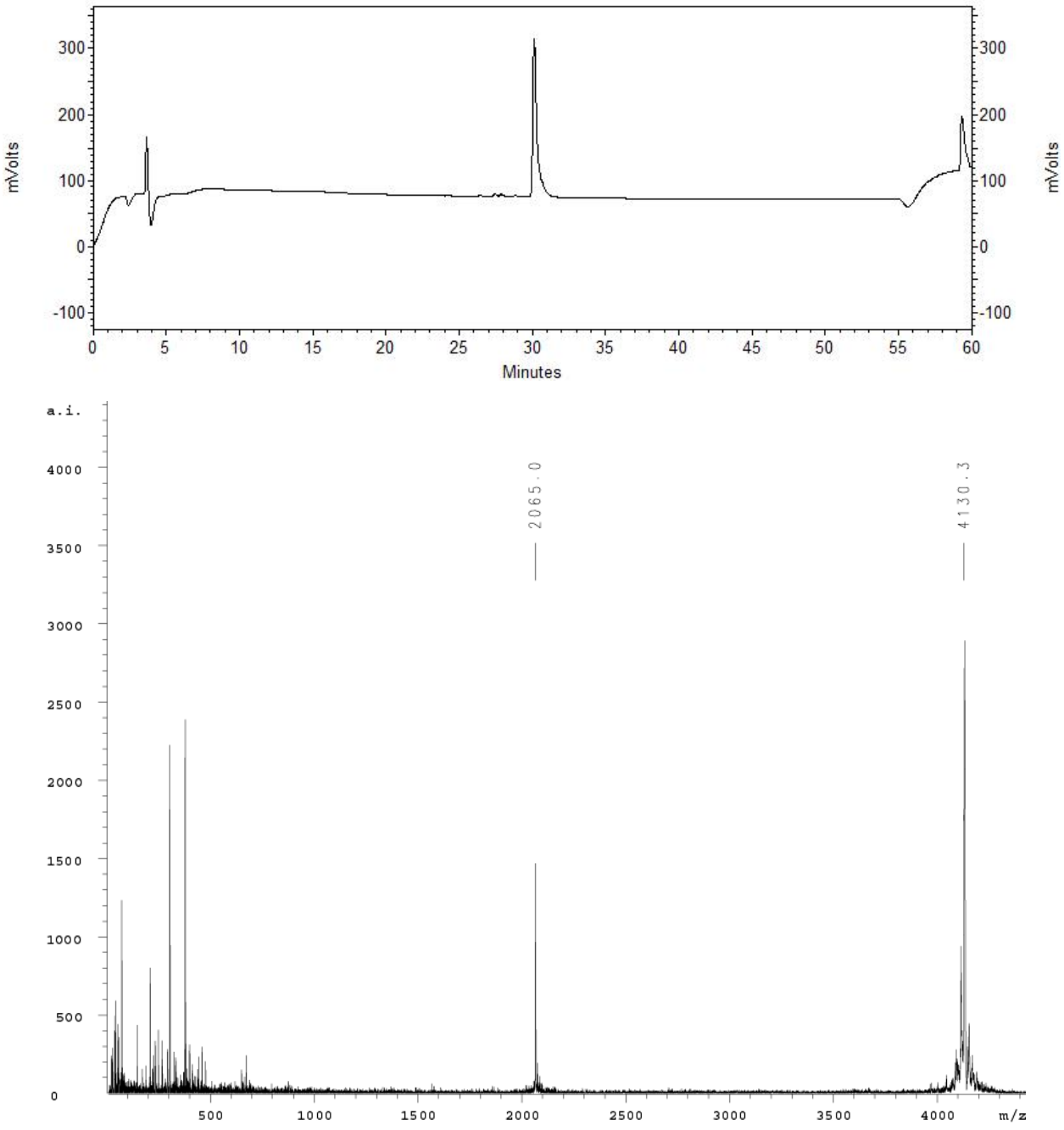

1[c]

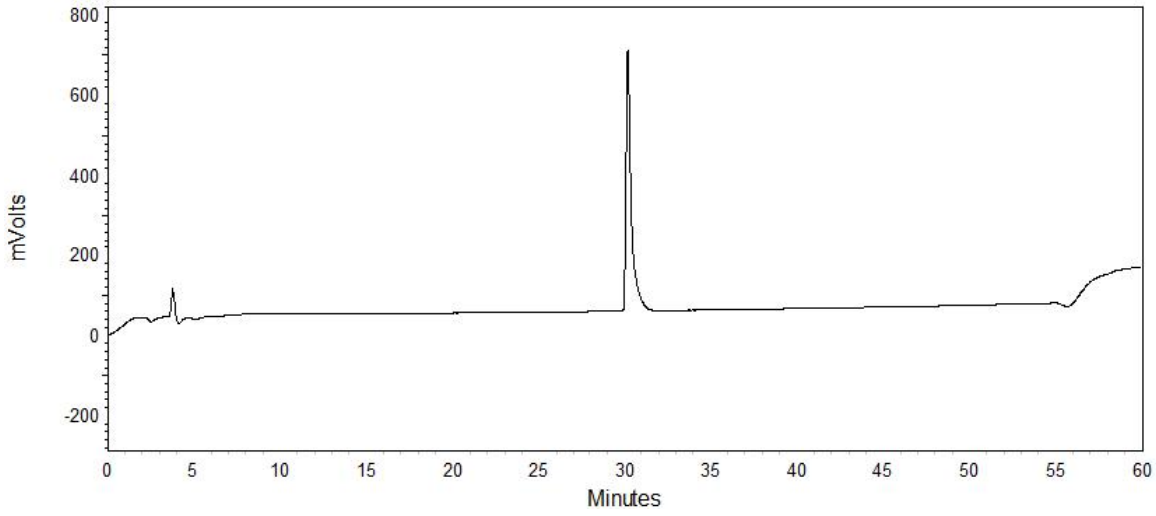
800
600
400
200
0
-200
mVolts
0
5
10
15
20
25
30
35
40
45
50
55
60
Minutes

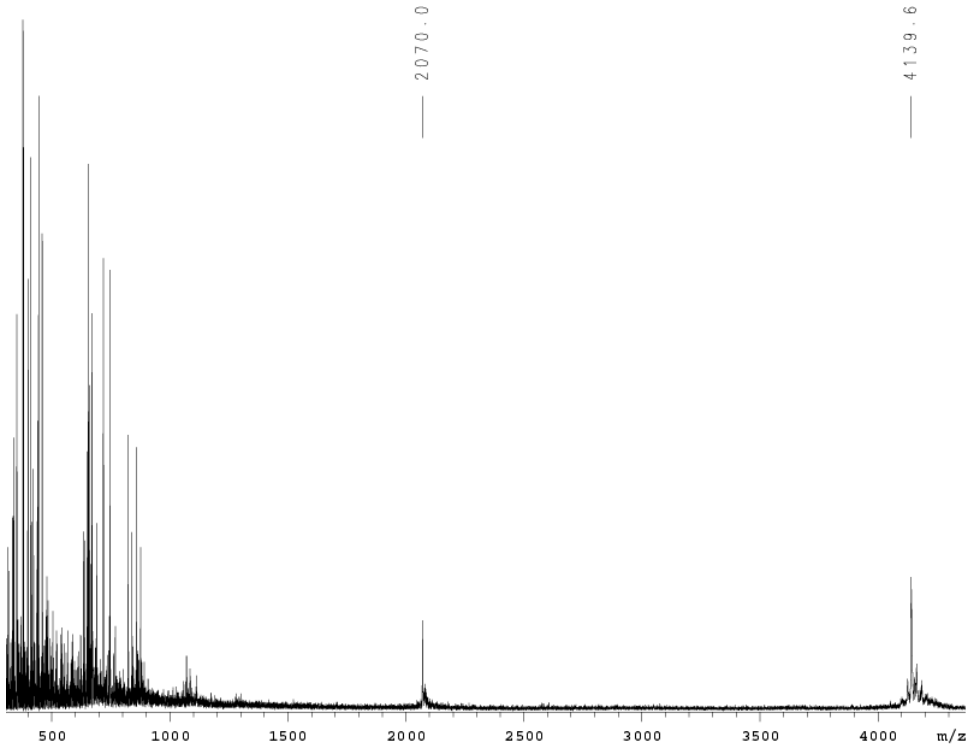
2070.0
4139.6
500
1000
1500
2000
2500
3000
3500
4000
m/z

2[c]

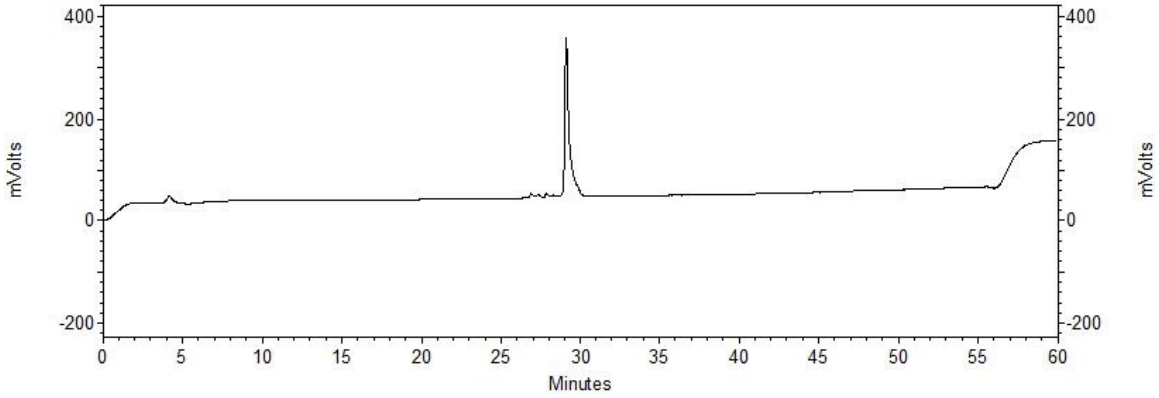

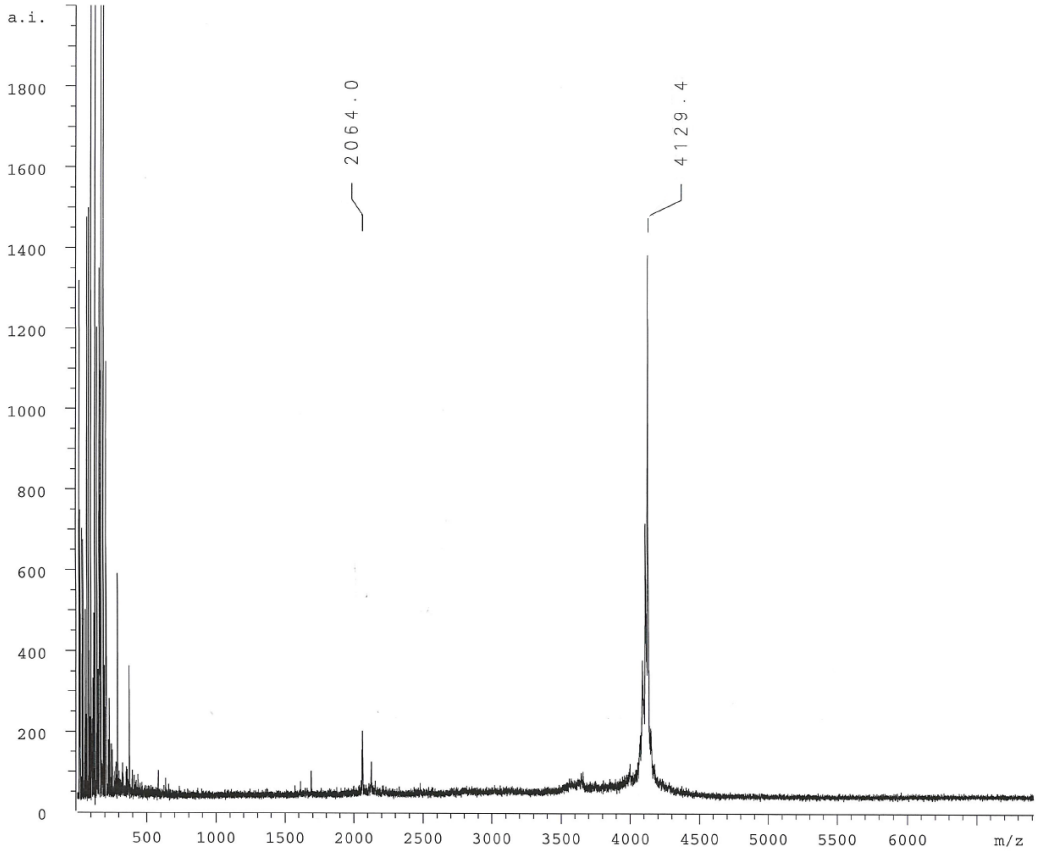

3[c]

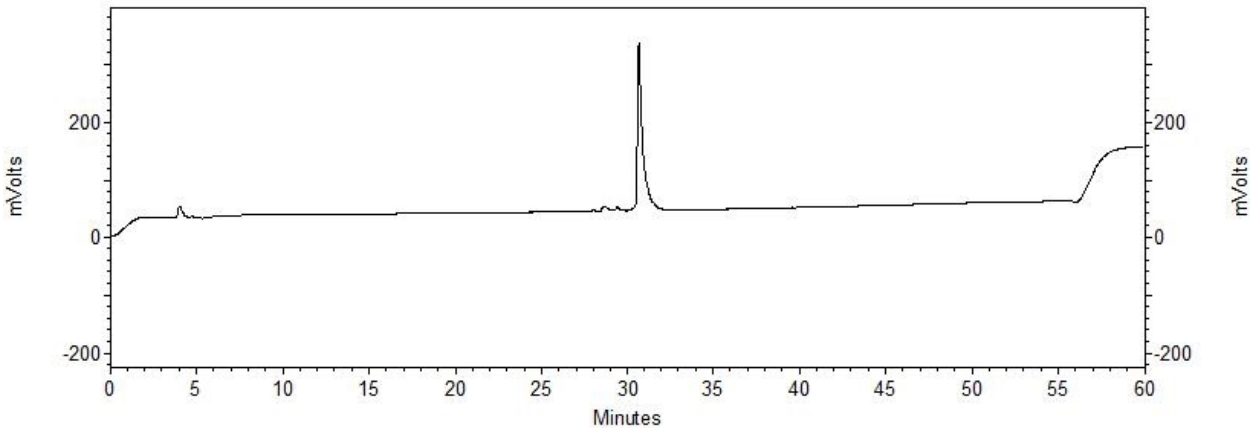
mVolts
200
0
-200
0
5
10
15
20
25
30
35
40
45
50
55
60
Minutes

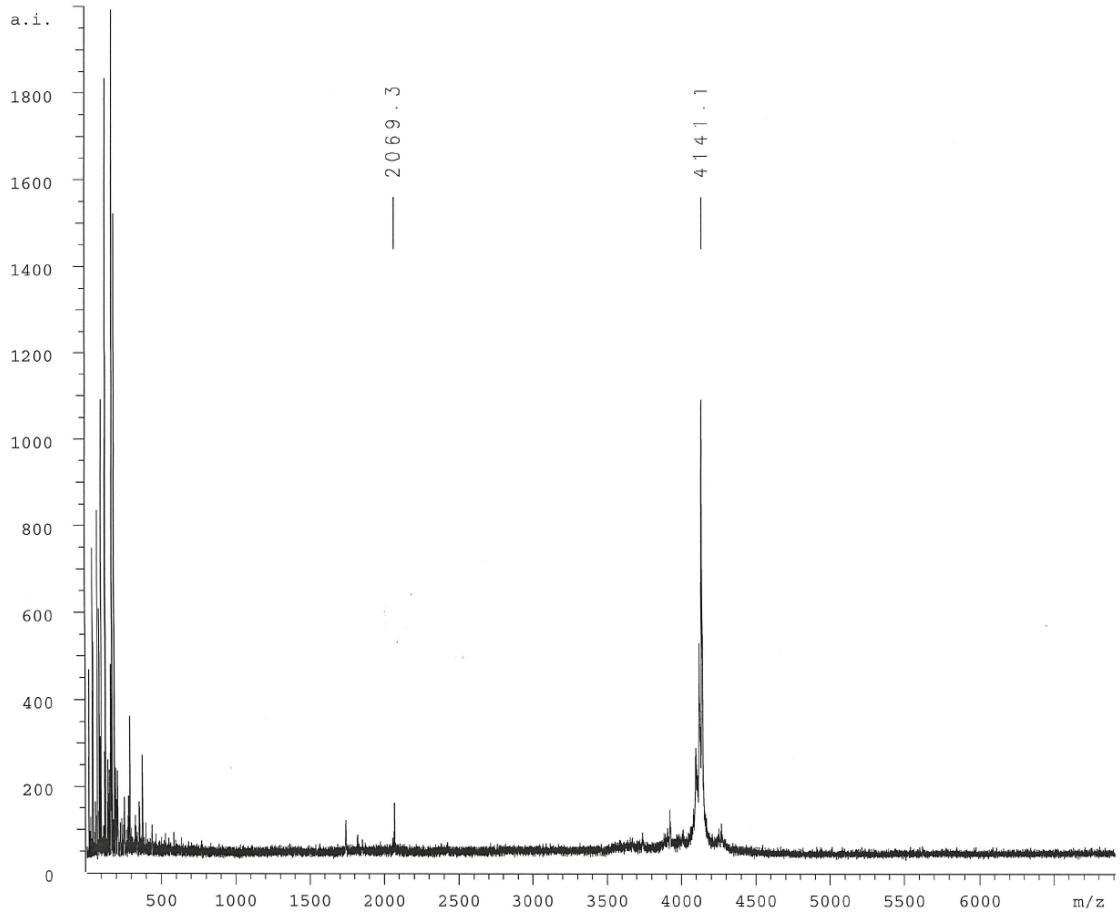
a.i.
1800
1600
1400
1200
1000
800
600
400
200
0
2069.3
4141.1
500
1000
1500
2000
2500
3000
3500
4000
4500
5000
5500
6000
m/z

4[c]

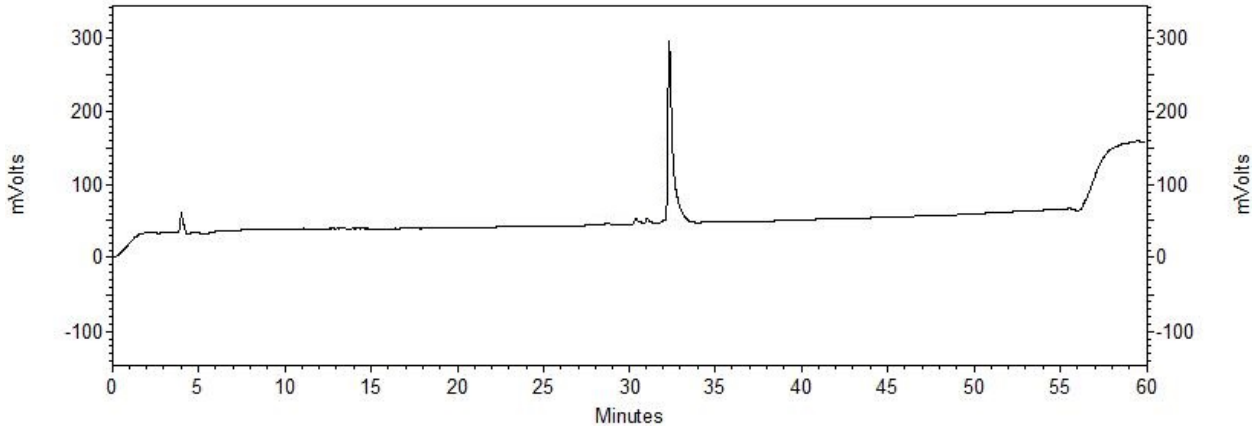
mVolts
Minutes
300
200
100
0
-100
0
5
10
15
20
25
30
35
40
45
50
55
60

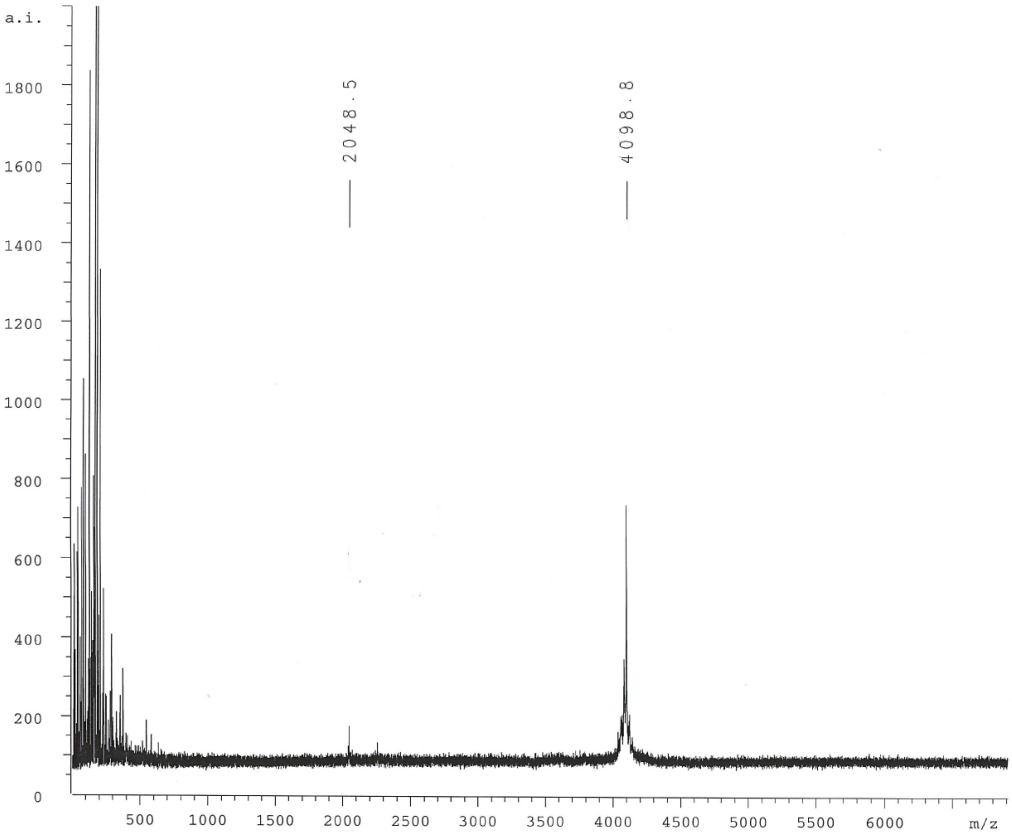
a.i.
2048.5
4098.8
1800
1600
1400
1200
1000
800
600
400
200
0
500
1000
1500
2000
2500
3000
3500
4000
4500
5000
5500
6000
m/z

5[c]

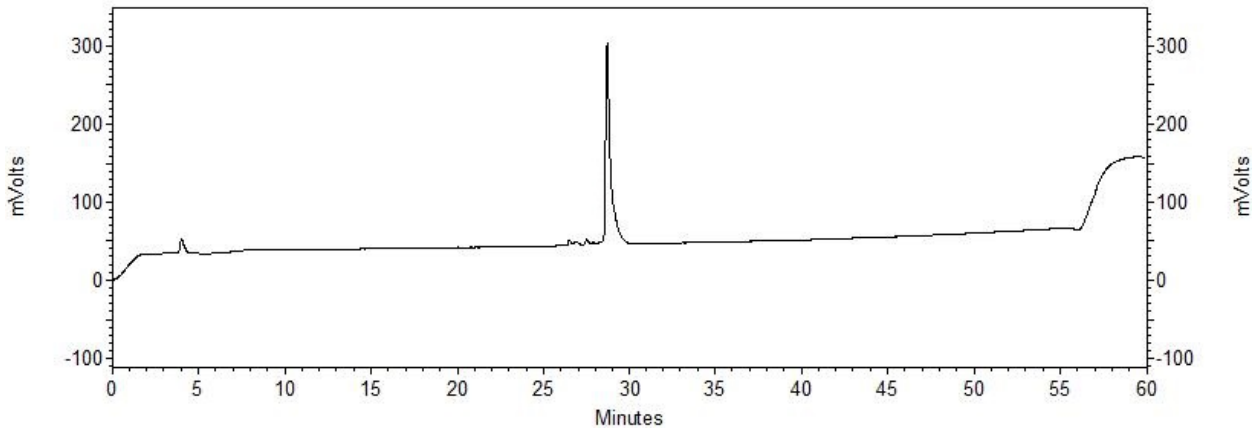
mVolts
300
200
100
0
-100
0
5
10
15
20
25
30
35
40
45
50
55
60
Minutes

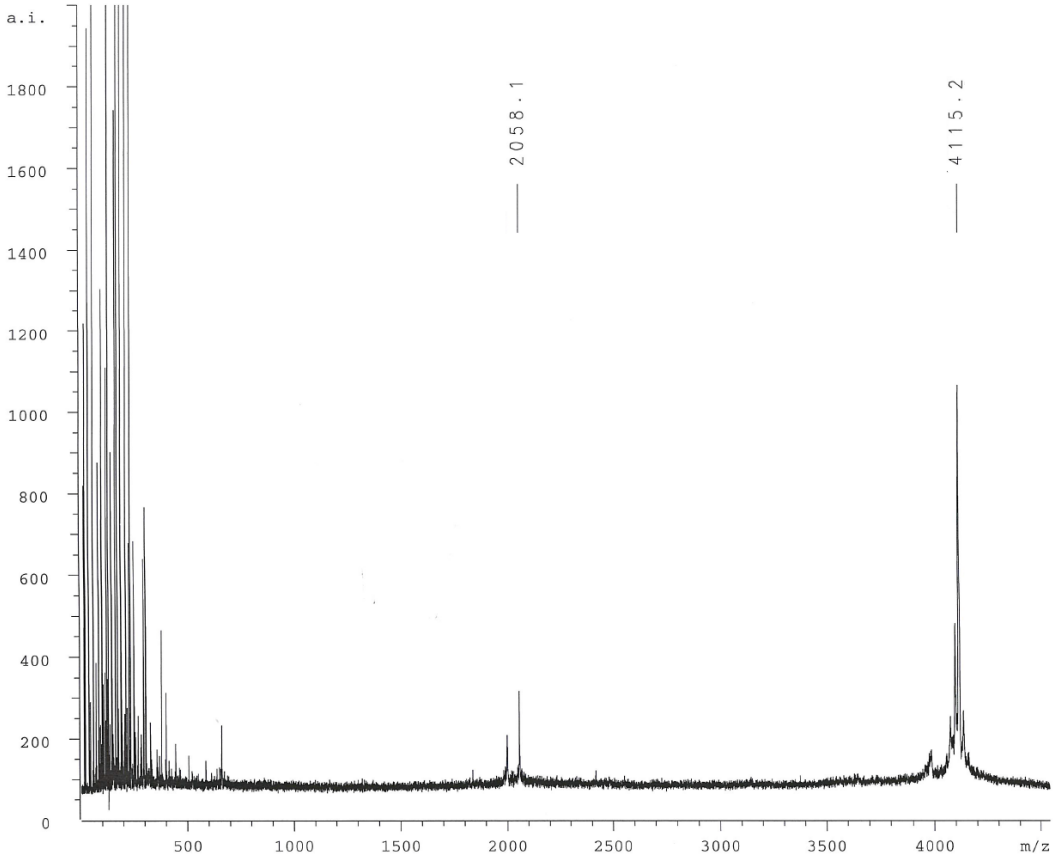
a.i.
1800
1600
1400
1200
1000
800
600
400
200
0
2058.1
4115.2
500
1000
1500
2000
2500
3000
3500
4000
m/z

6[c]

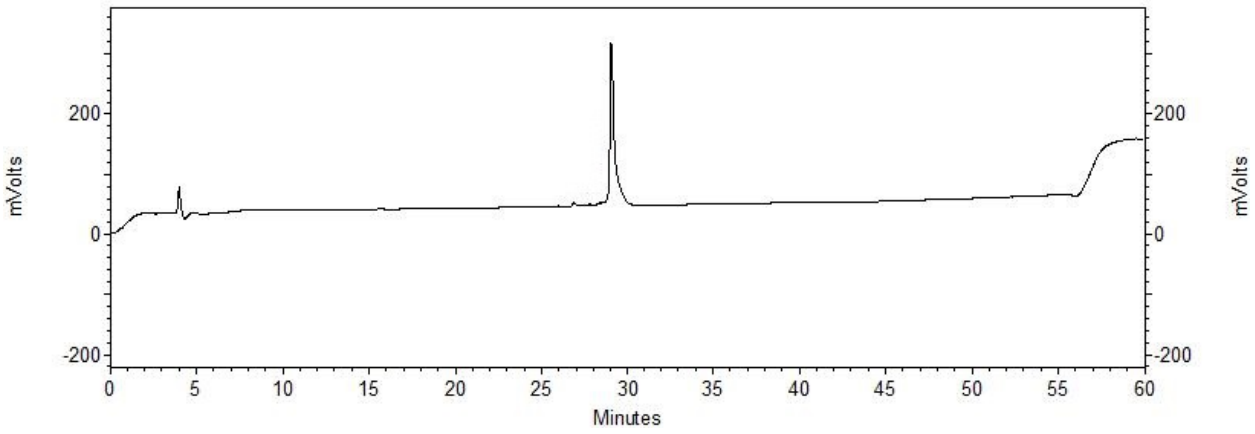
mVolts
200
0
-200
0
5
10
15
20
25
30
35
40
45
50
55
60
Minutes

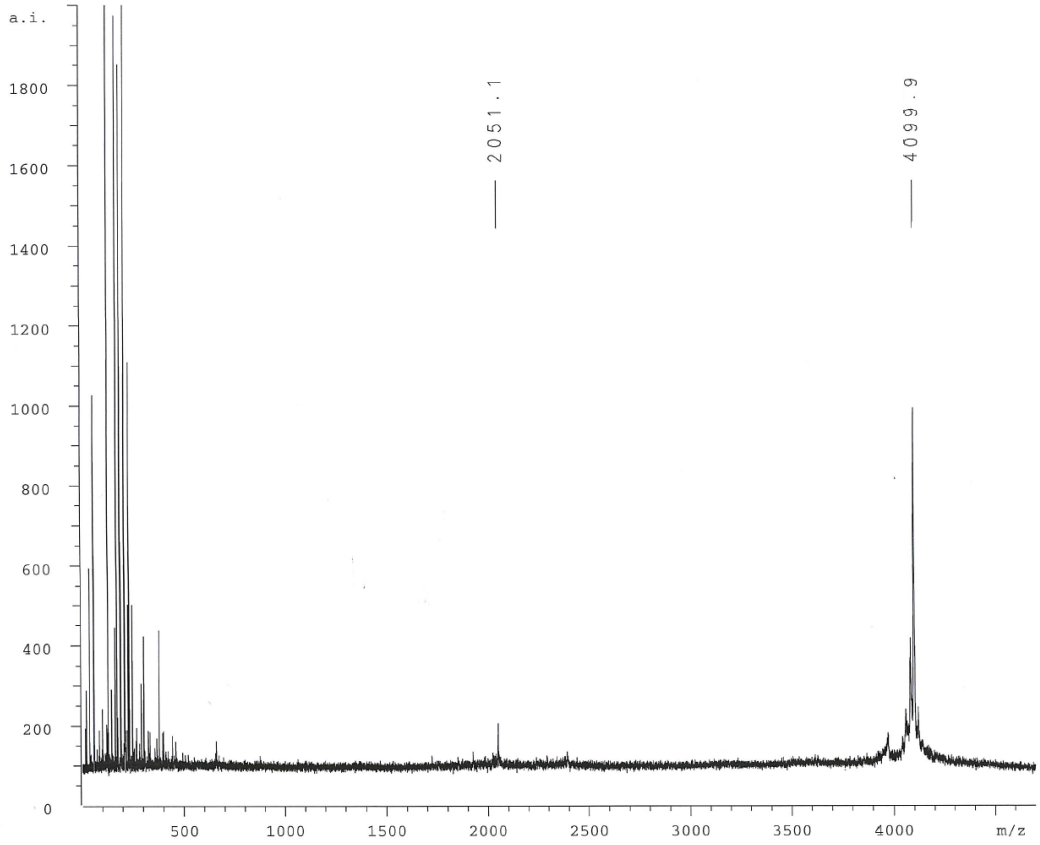
a.i.
1800
1600
1400
1200
1000
800
600
400
200
0
2051.1
4099.9
500
1000
1500
2000
2500
3000
3500
4000
m/z

7[c]

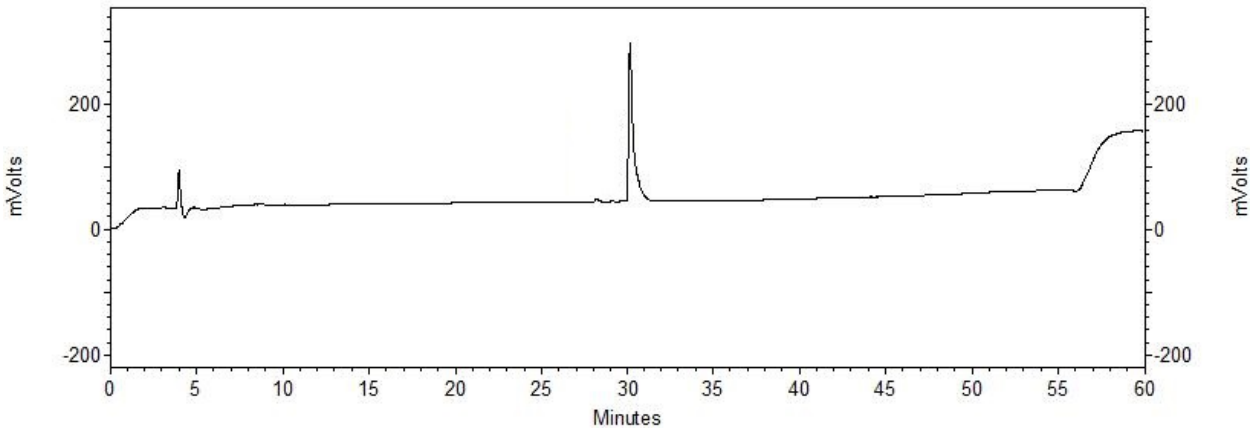
mVolts
200
0
-200
0
5
10
15
20
25
30
35
40
45
50
55
60
Minutes

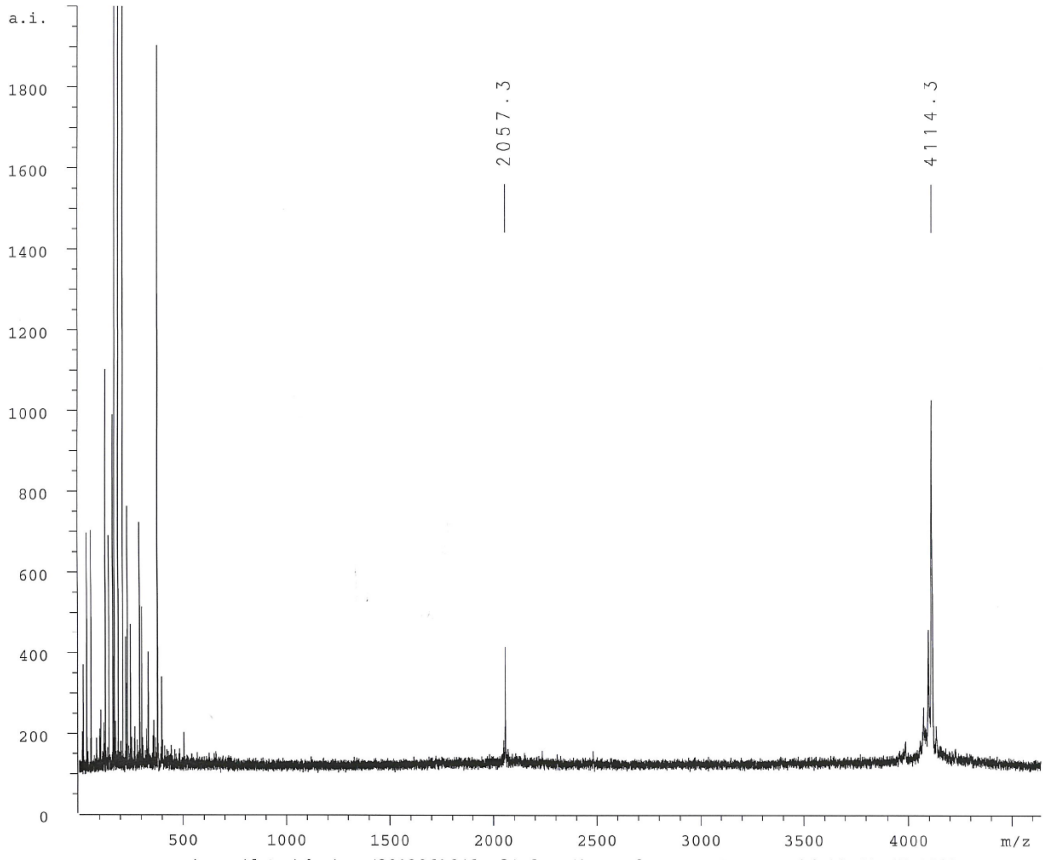
a.i.
1800
1600
1400
1200
1000
800
600
400
200
0
2057.3
4114.3
500
1000
1500
2000
2500
3000
3500
4000
m/z

8[c]

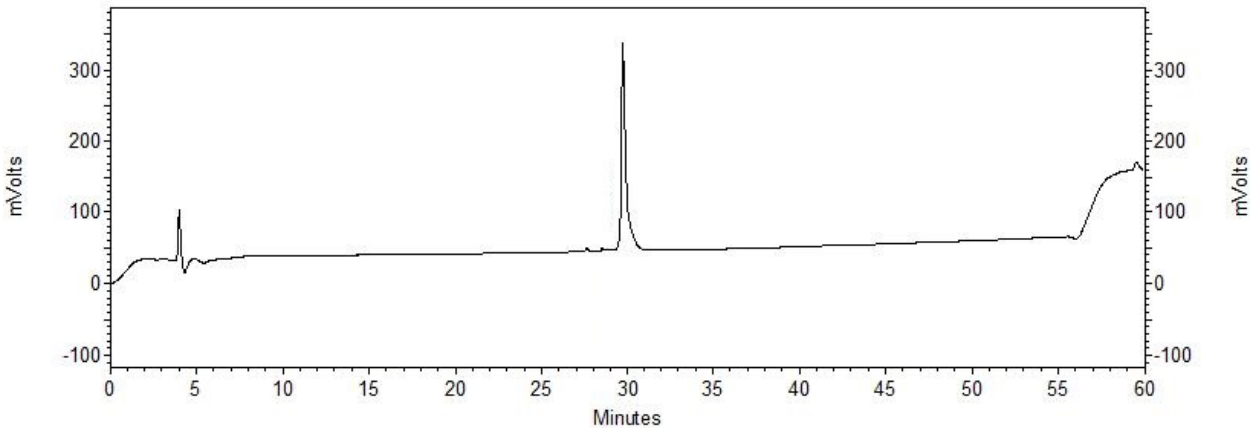
mVolts
300
200
100
0
-100
0
5
10
15
20
25
30
35
40
45
50
55
60
Minutes

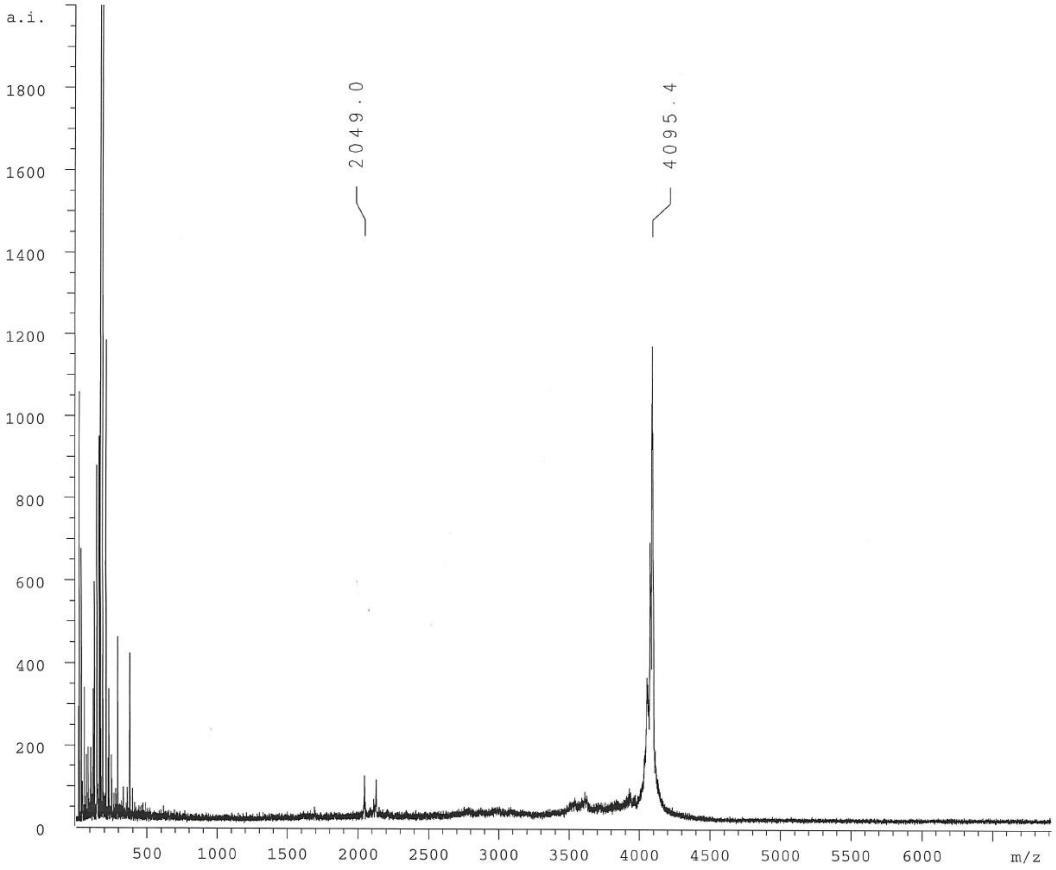
a.i.
1800
1600
1400
1200
1000
800
600
400
200
0
2049.0
4095.4
500
1000
1500
2000
2500
3000
3500
4000
4500
5000
5500
6000
m/z

9[c]

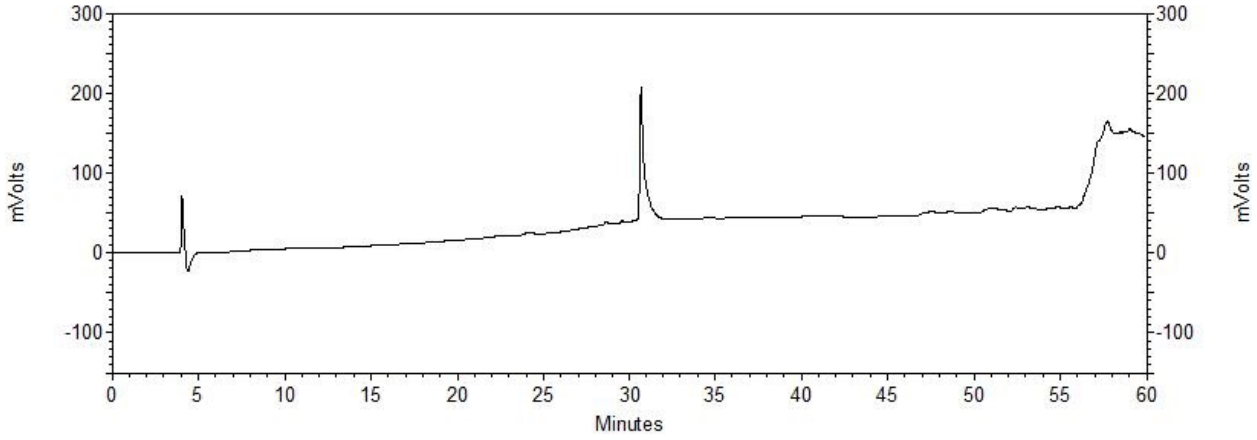

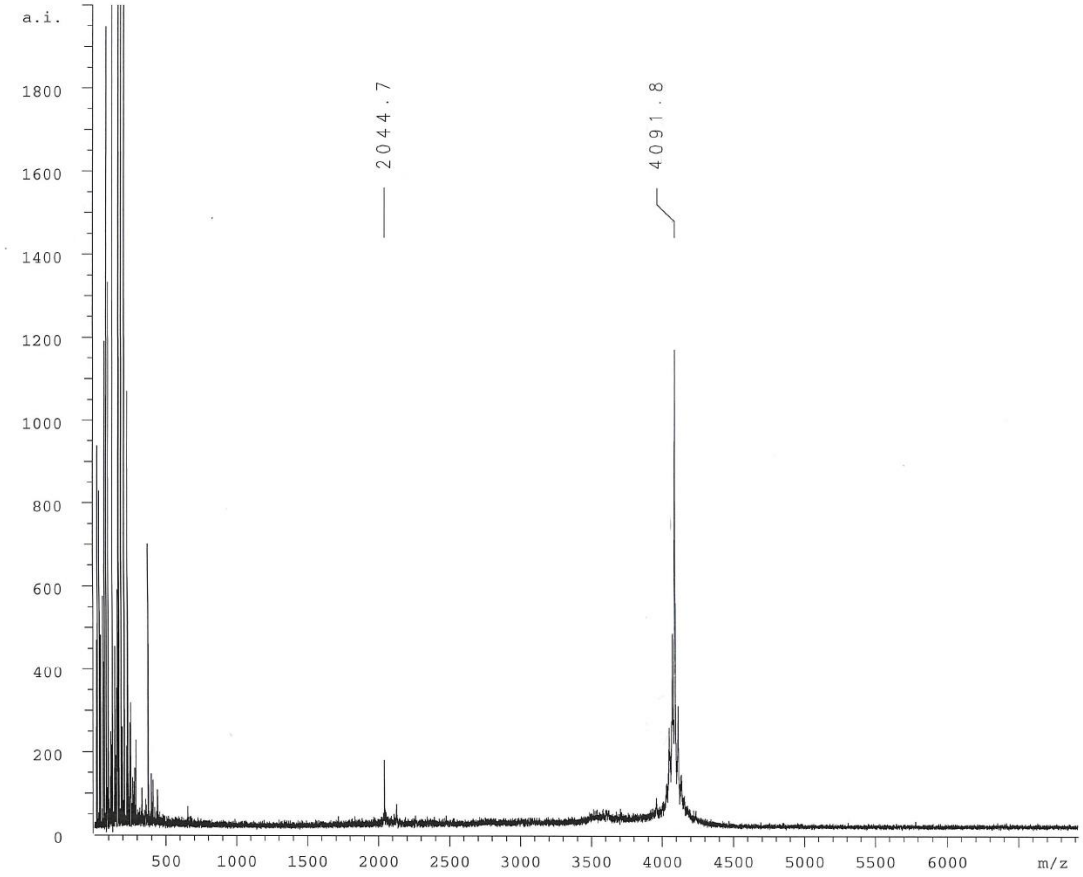

2β

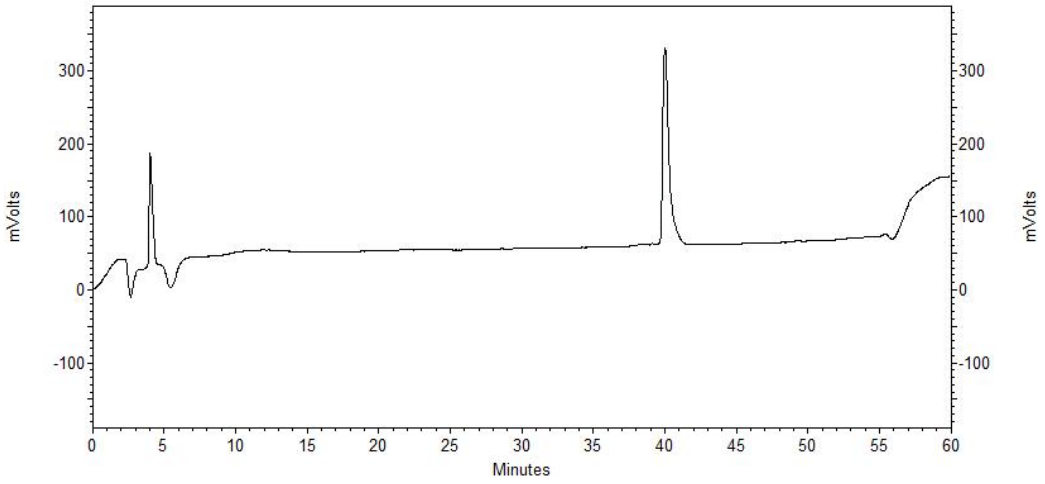
mVolts
300
200
100
0
-100
0
5
10
15
20
25
30
35
40
45
50
55
60
Minutes

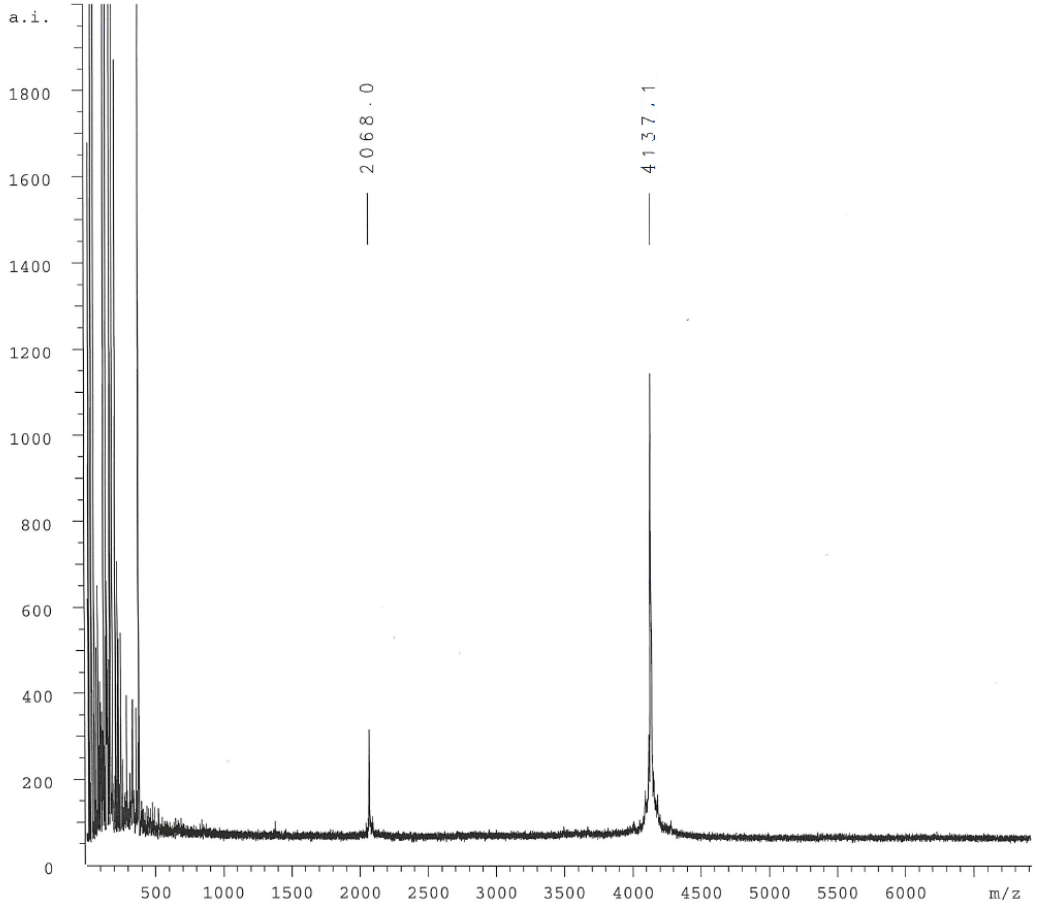
a.i.
1800
1600
1400
1200
1000
800
600
400
200
0
2068.0
4137.1
500
1000
1500
2000
2500
3000
3500
4000
4500
5000
5500
6000
m/z

3β

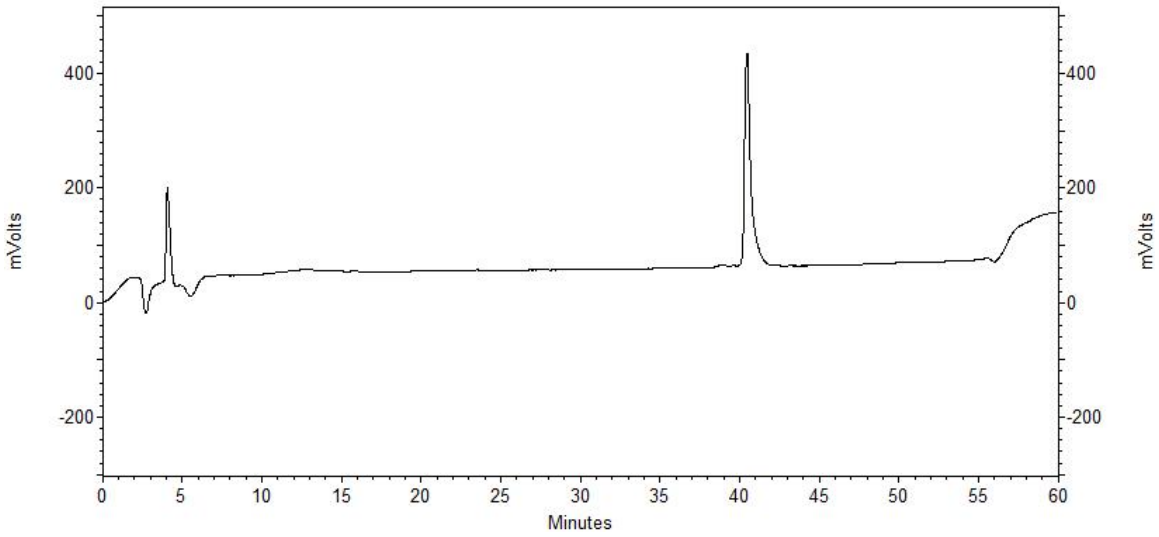
mVolts
400
200
0
-200
0
5
10
15
20
25
30
35
40
45
50
55
60
Minutes

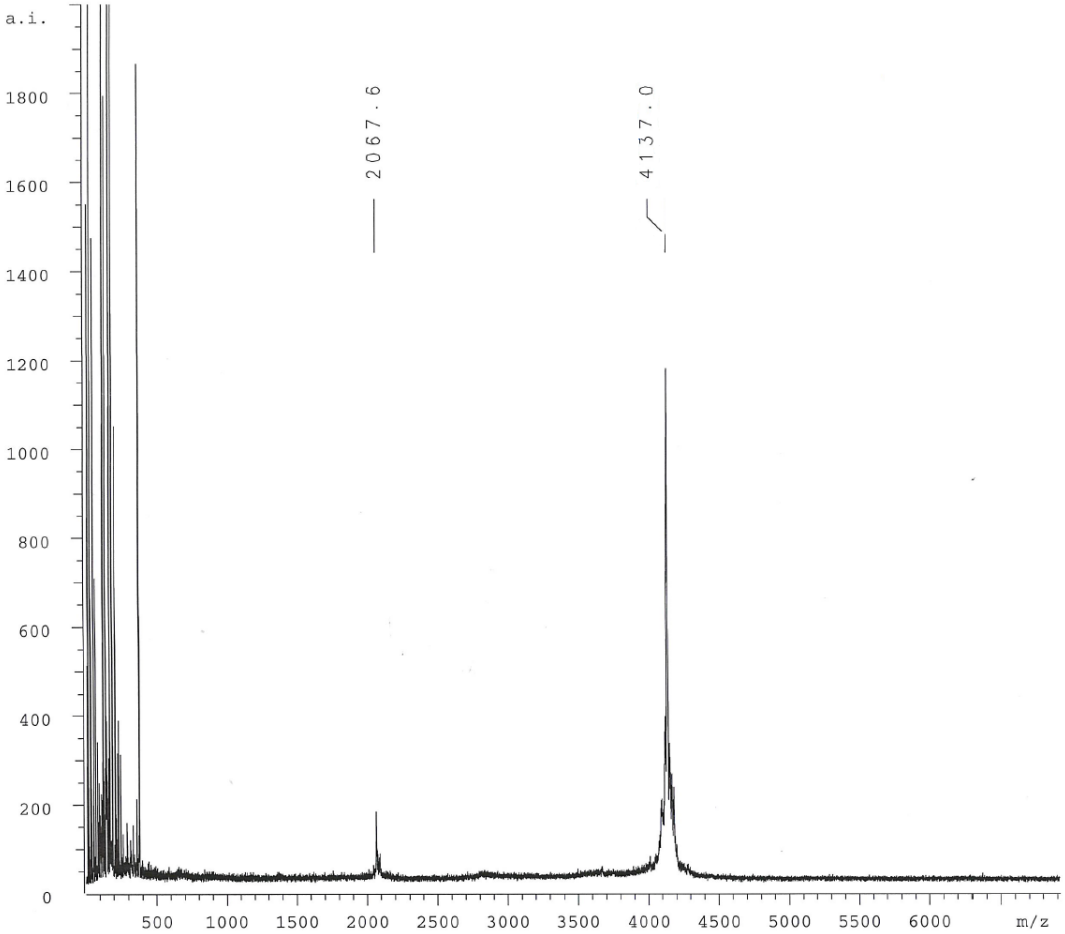
a.i.
1800
1600
1400
1200
1000
800
600
400
200
0
2067.6
4137.0
500
1000
1500
2000
2500
3000
3500
4000
4500
5000
5500
6000
m/z

6β

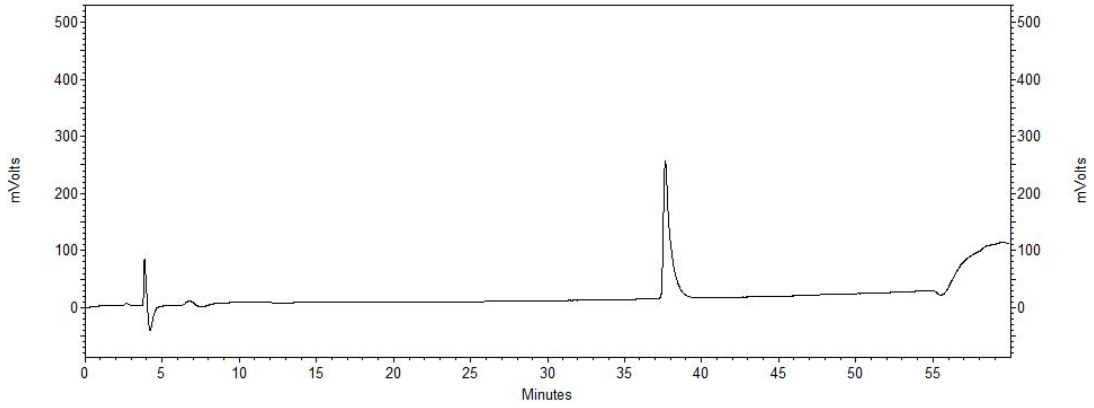
mVolts
Minutes
0
5
10
15
20
25
30
35
40
45
50
55
100
200
300
400
500

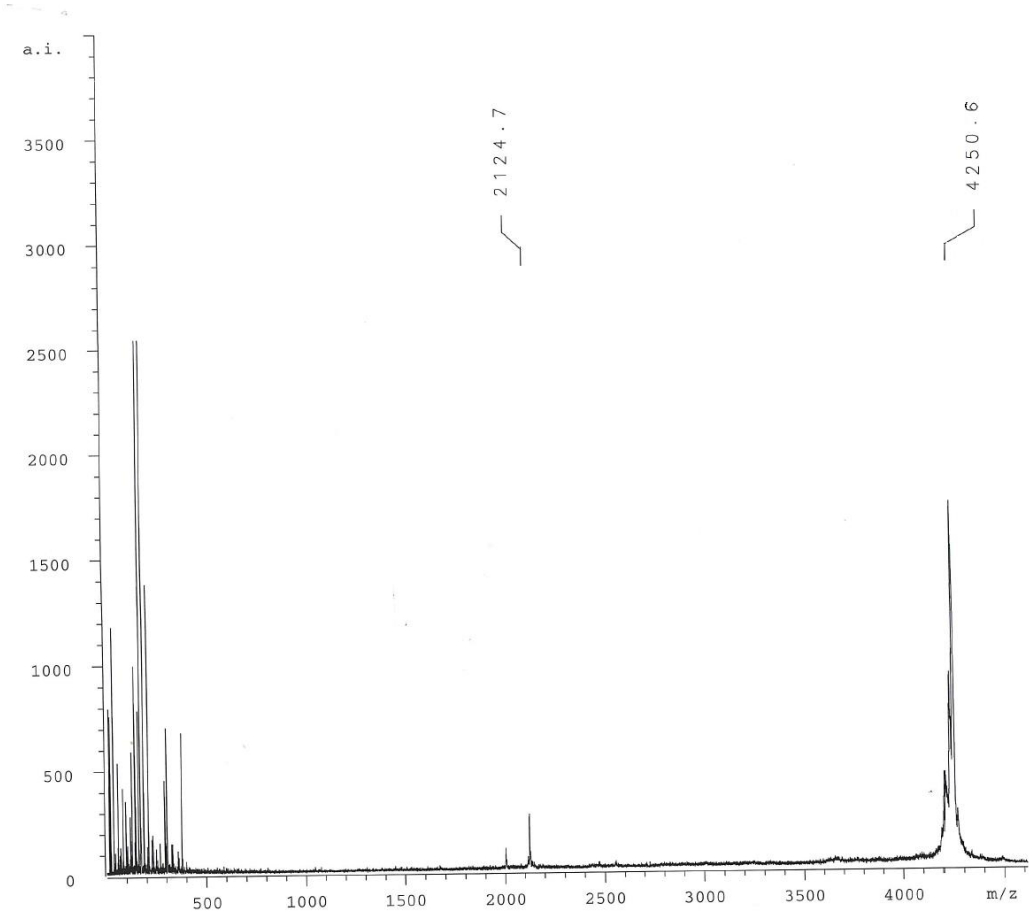
a.i.
2124.7
4250.6
m/z
0
500
1000
1500
2000
2500
3000
3500
4000

Cyc-6β

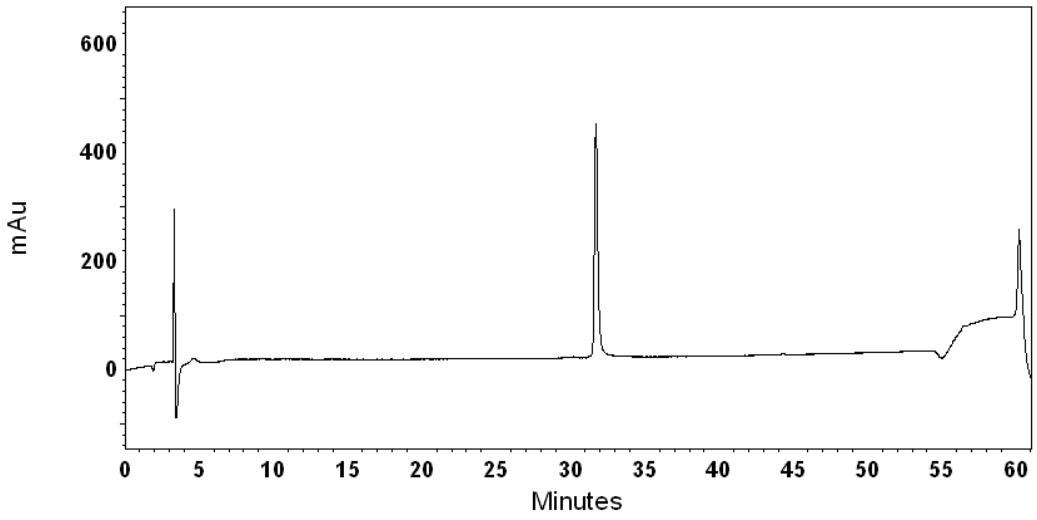
600
400
200
0
mAu
0 5 10 15 20 25 30 35 40 45 50 55 60
Minutes

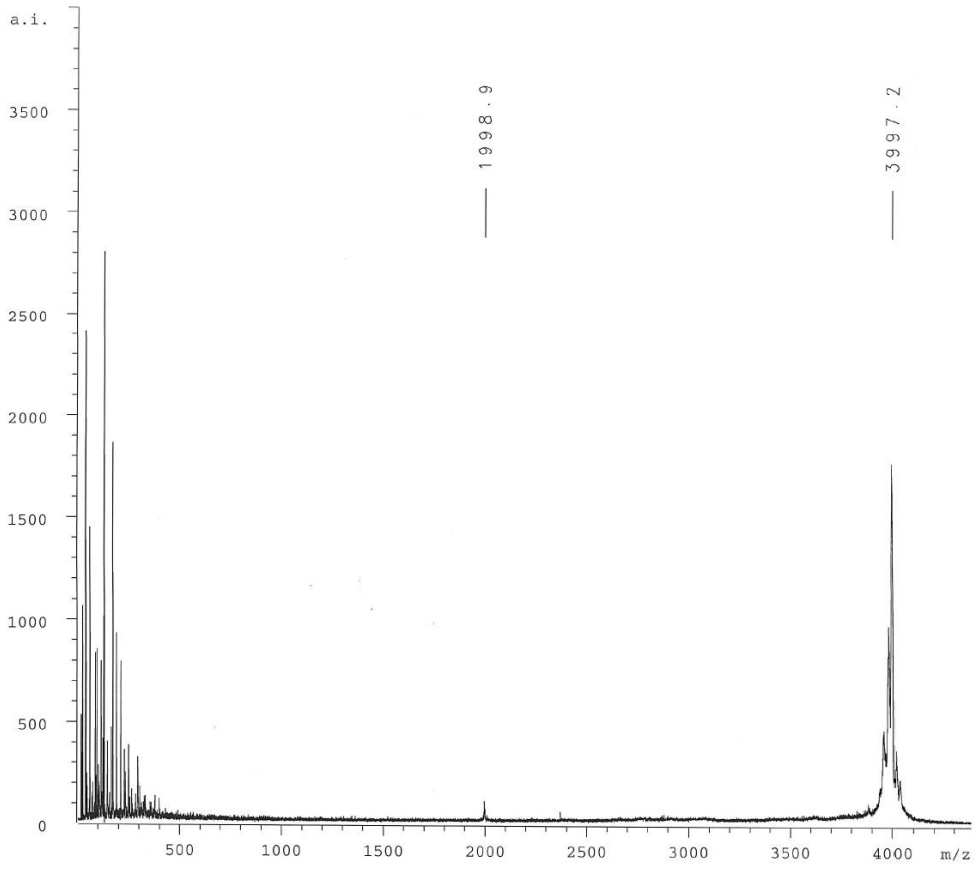
a.i.
3500
3000
2500
2000
1500
1000
500
0
1998.9
3997.2
500 1000 1500 2000 2500 3000 3500 4000 m/z

8β

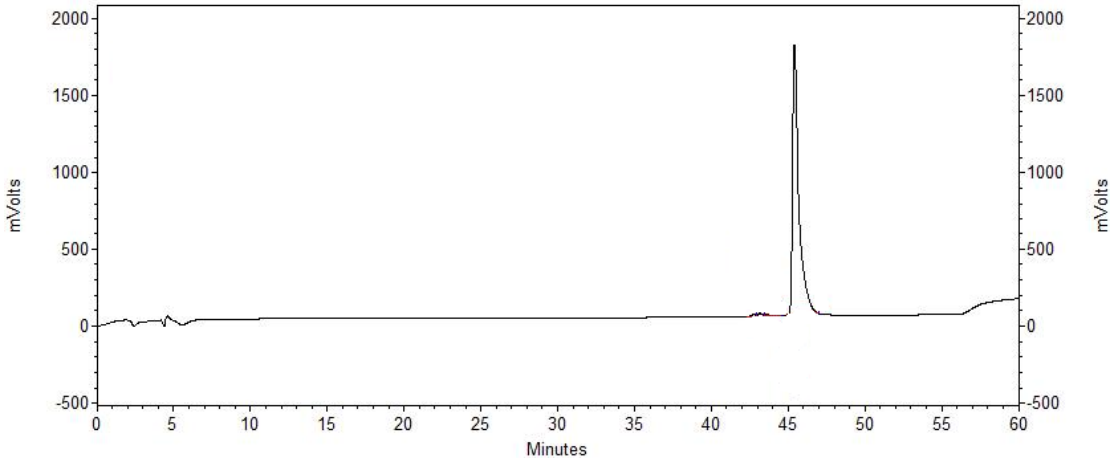

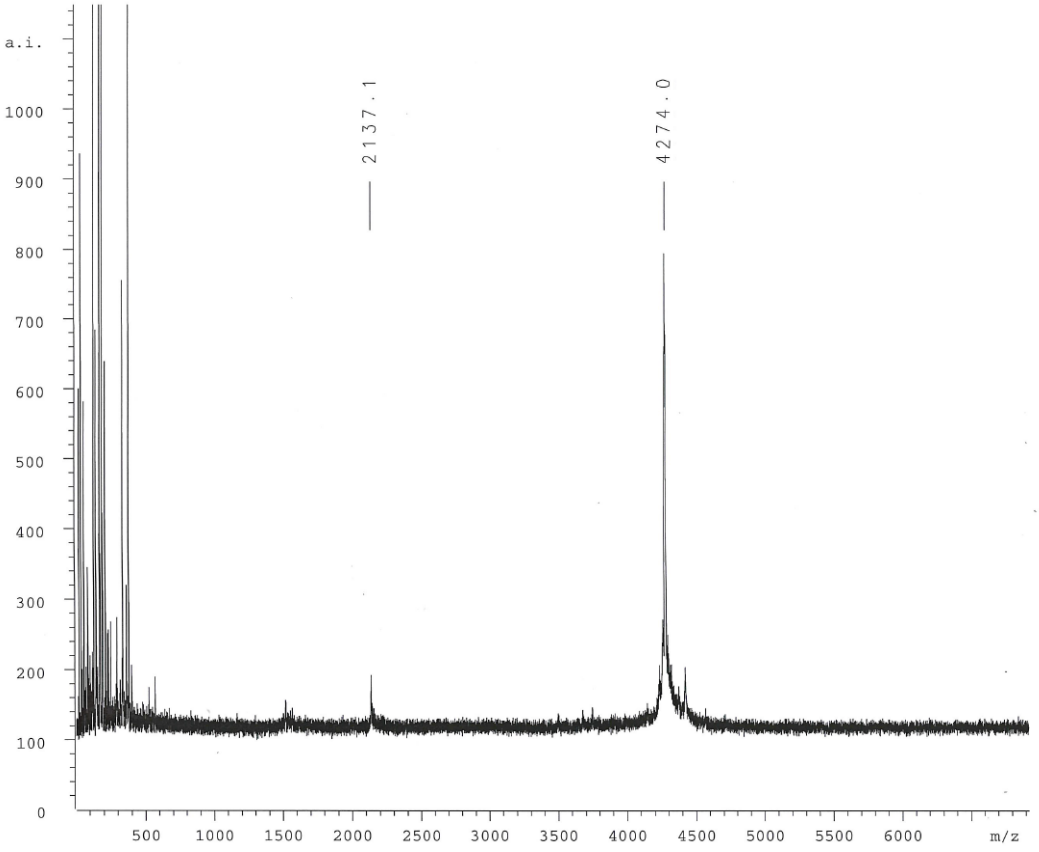

Cyc-8β

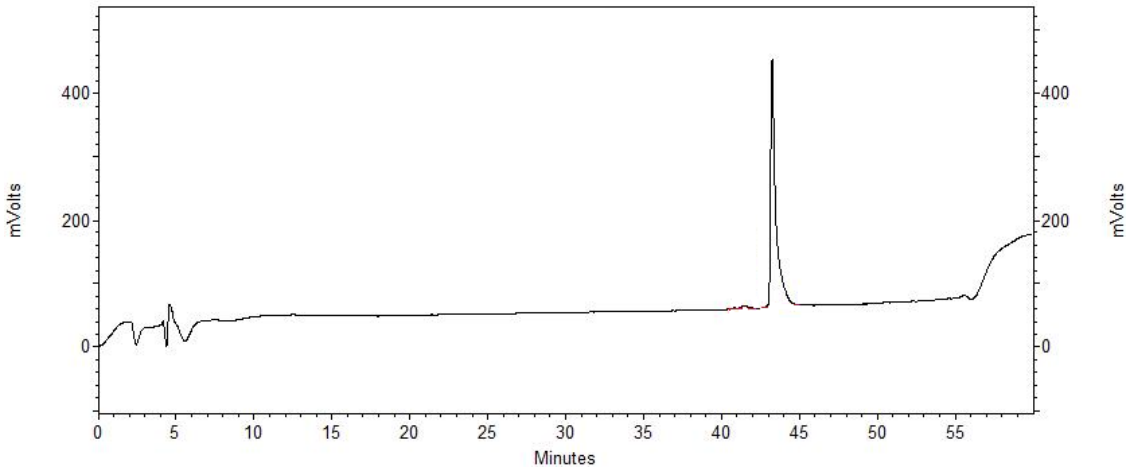
mVolts
400
200
0
0
5
10
15
20
25
30
35
40
45
50
55
Minutes

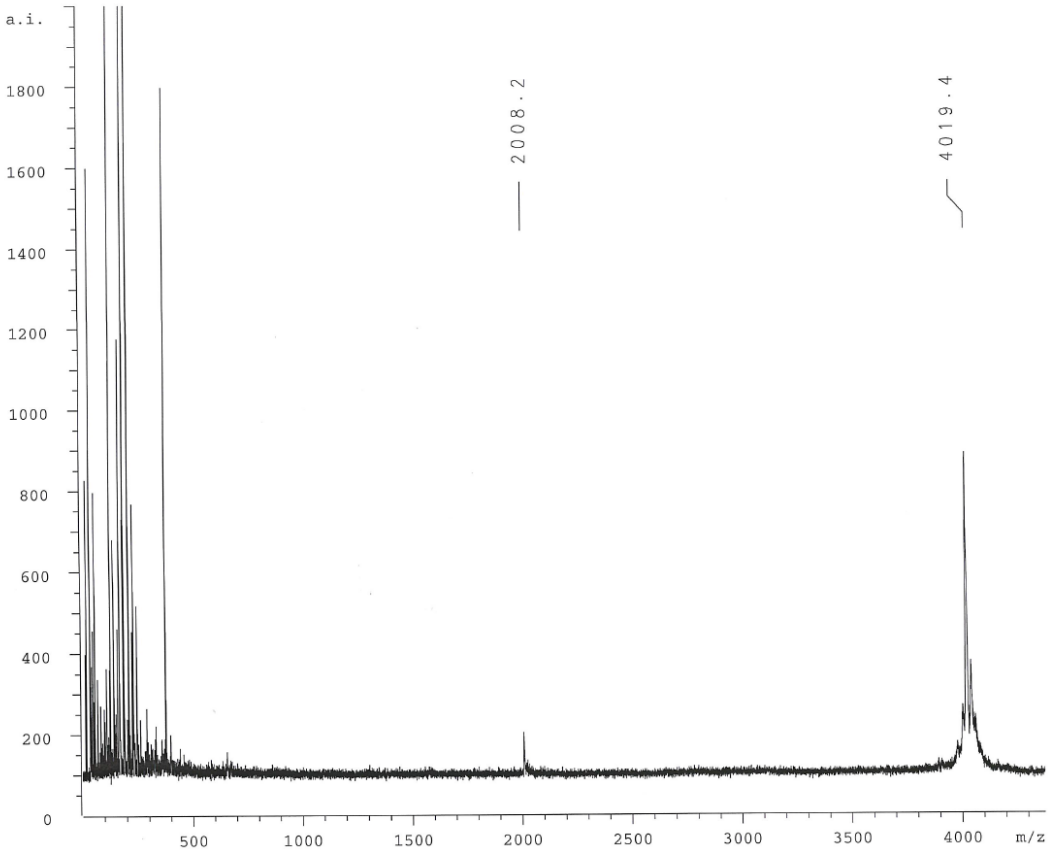
a.i.
1800
1600
1400
1200
1000
800
600
400
200
0
2008.2
4019.4
500
1000
1500
2000
2500
3000
3500
4000
m/z

9β

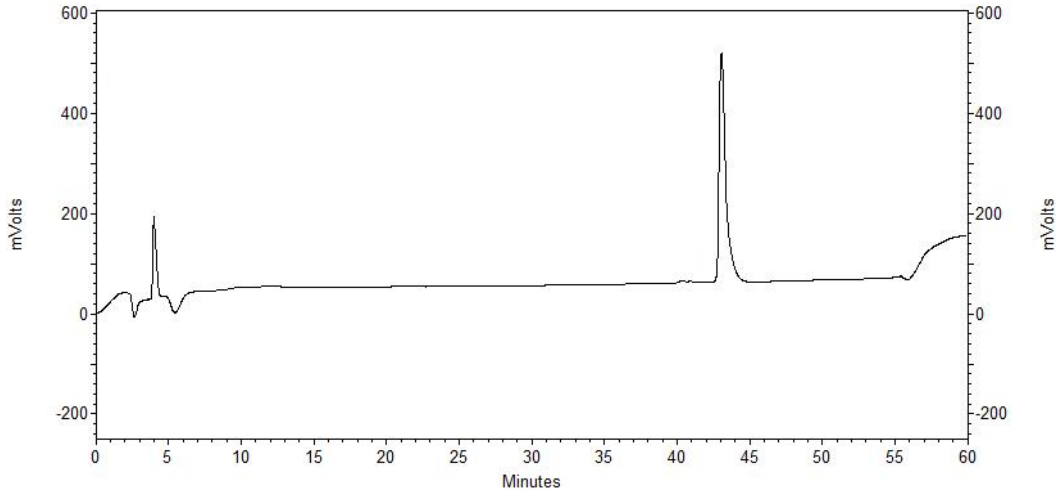
600
400
200
0
-200
mVolts
0 5 10 15 20 25 30 35 40 45 50 55 60
Minutes

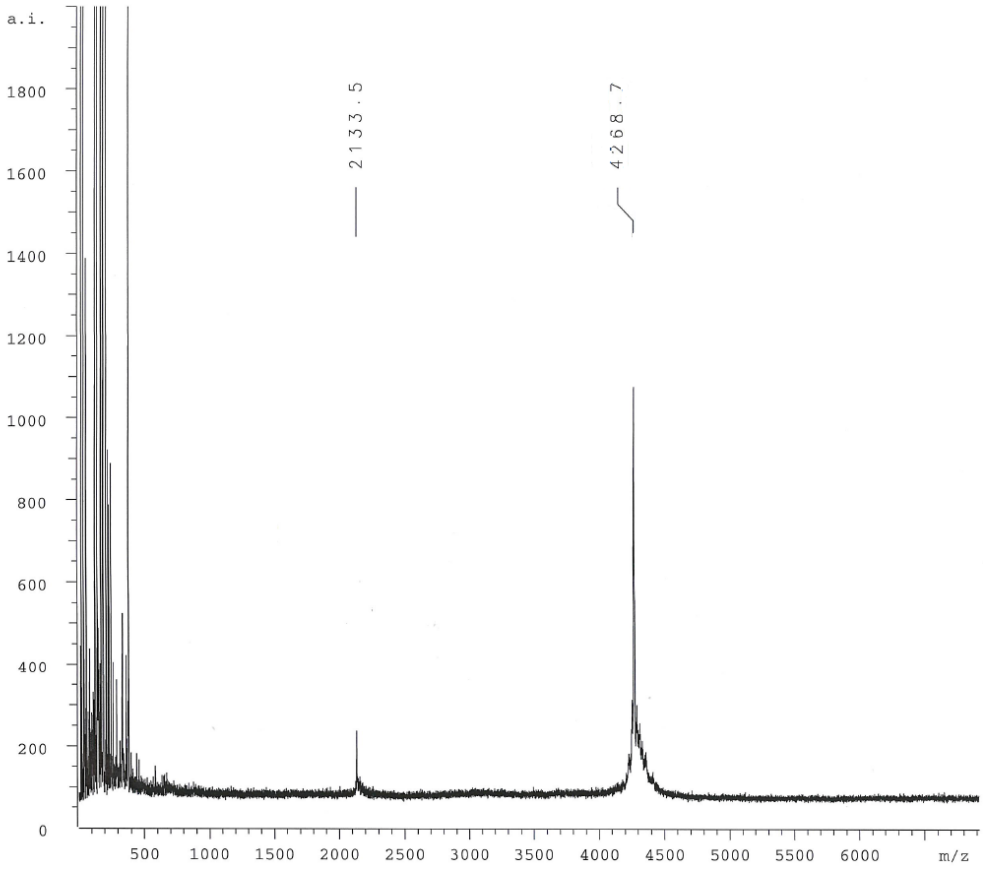
a.i.
1800
1600
1400
1200
1000
800
600
400
200
0
2133.5
4268.7
500 1000 1500 2000 2500 3000 3500 4000 4500 5000 5500 6000
m/z

Cyc-9β

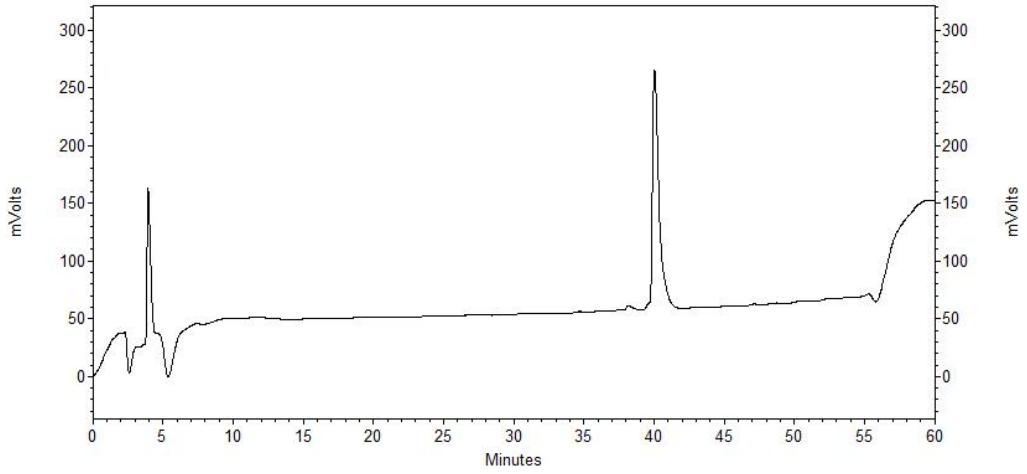
mVolts
Minutes
0
5
10
15
20
25
30
35
40
45
50
55
60
0
50
100
150
200
250
300

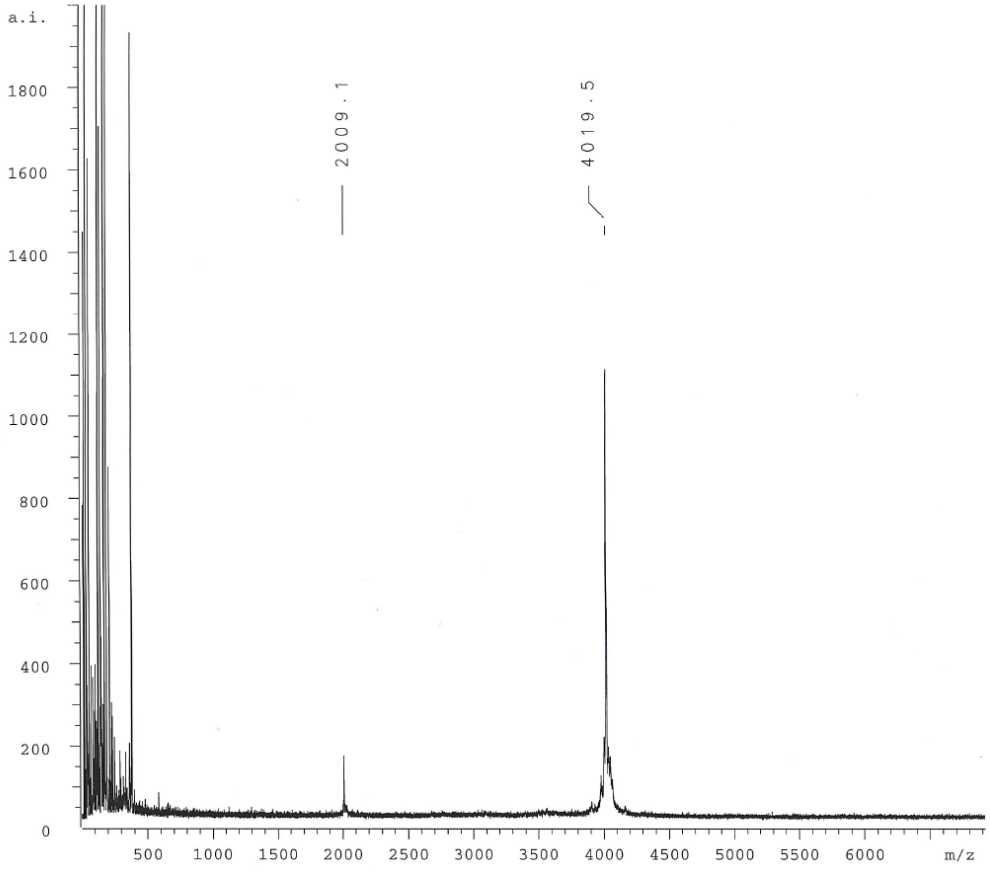
a.i.
2009.1
4019.5
m/z
0
200
400
600
800
1000
1200
1400
1600
1800
500
1000
1500
2000
2500
3000
3500
4000
4500
5000
5500
6000

M-2β

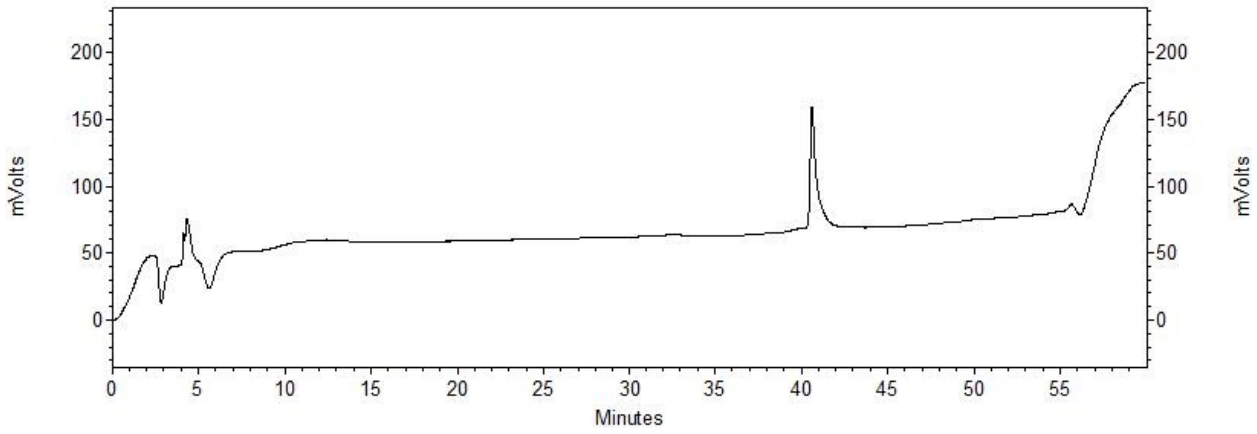
mVolts
200
150
100
50
0
0
5
10
15
20
25
30
35
40
45
50
55
Minutes

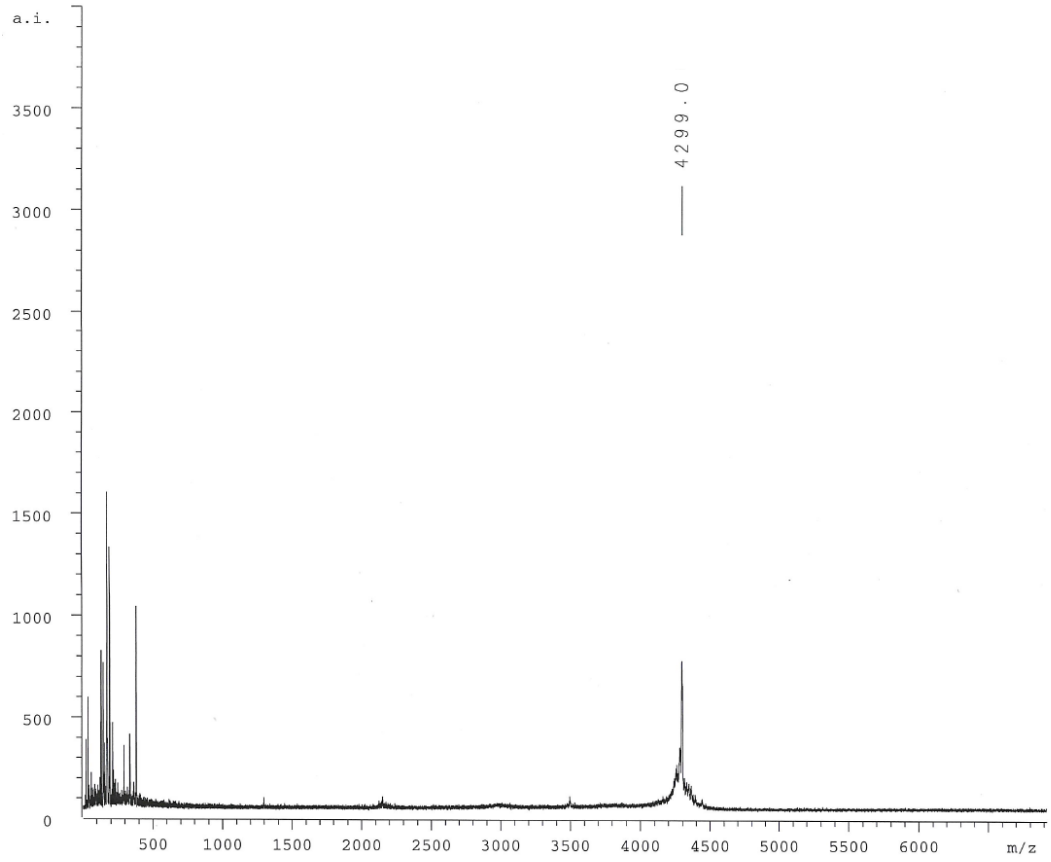
a.i.
4299.0
3500
3000
2500
2000
1500
1000
500
0
500
1000
1500
2000
2500
3000
3500
4000
4500
5000
5500
6000
m/z

M-3β

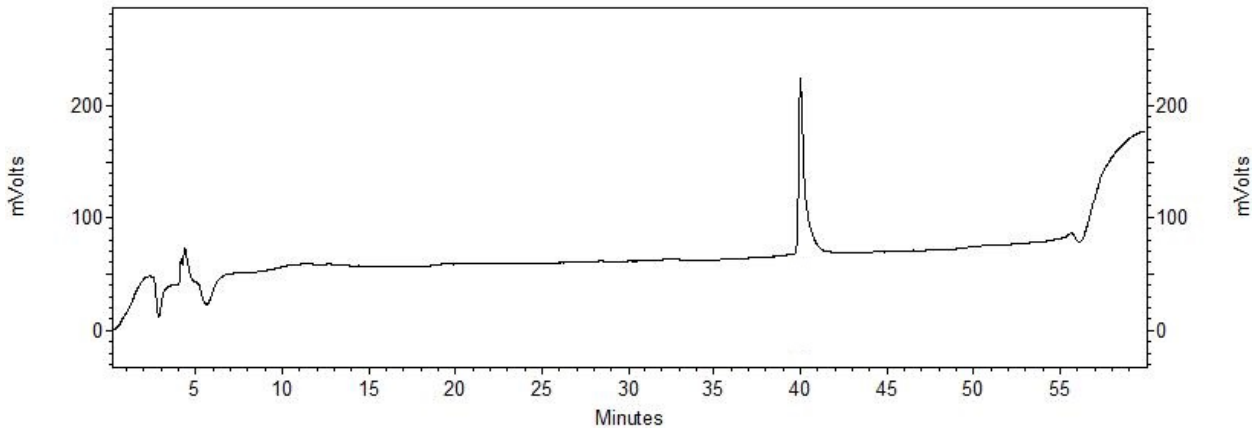
mVolts
200
100
0
5
10
15
20
25
30
35
40
45
50
55
Minutes

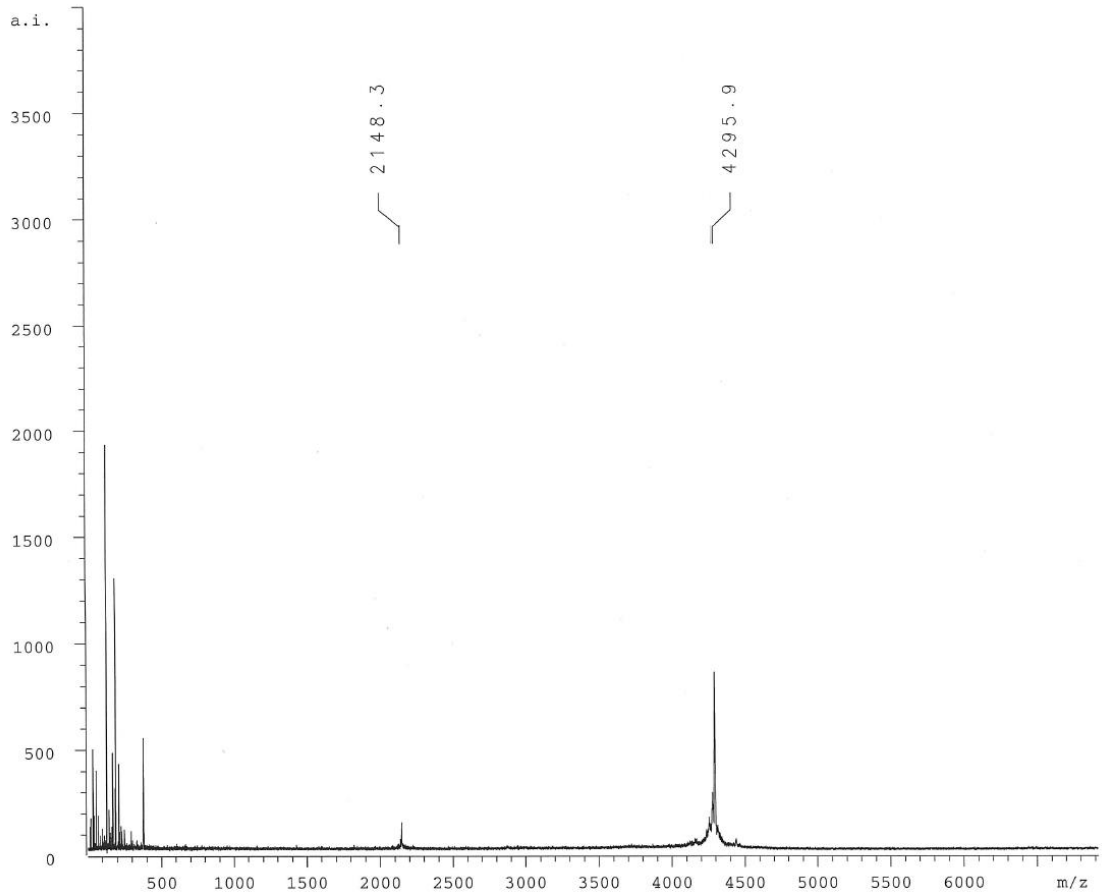
a.i.
3500
3000
2500
2000
1500
1000
500
0
2148.3
4295.9
500
1000
1500
2000
2500
3000
3500
4000
4500
5000
5500
6000
m/z

M-6β

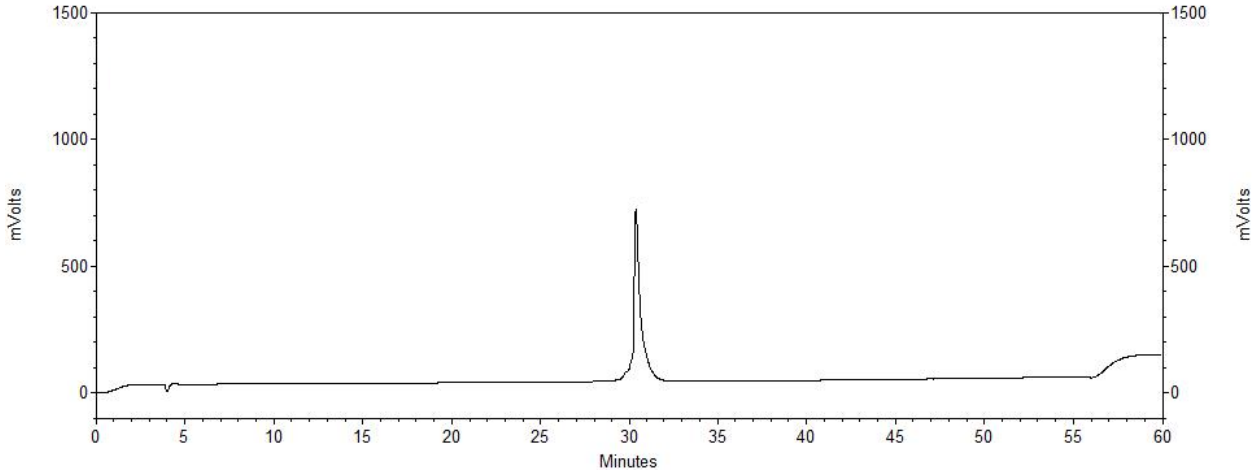
1500
1000
500
0
mVolts
0
5
10
15
20
25
30
35
40
45
50
55
60
Minutes

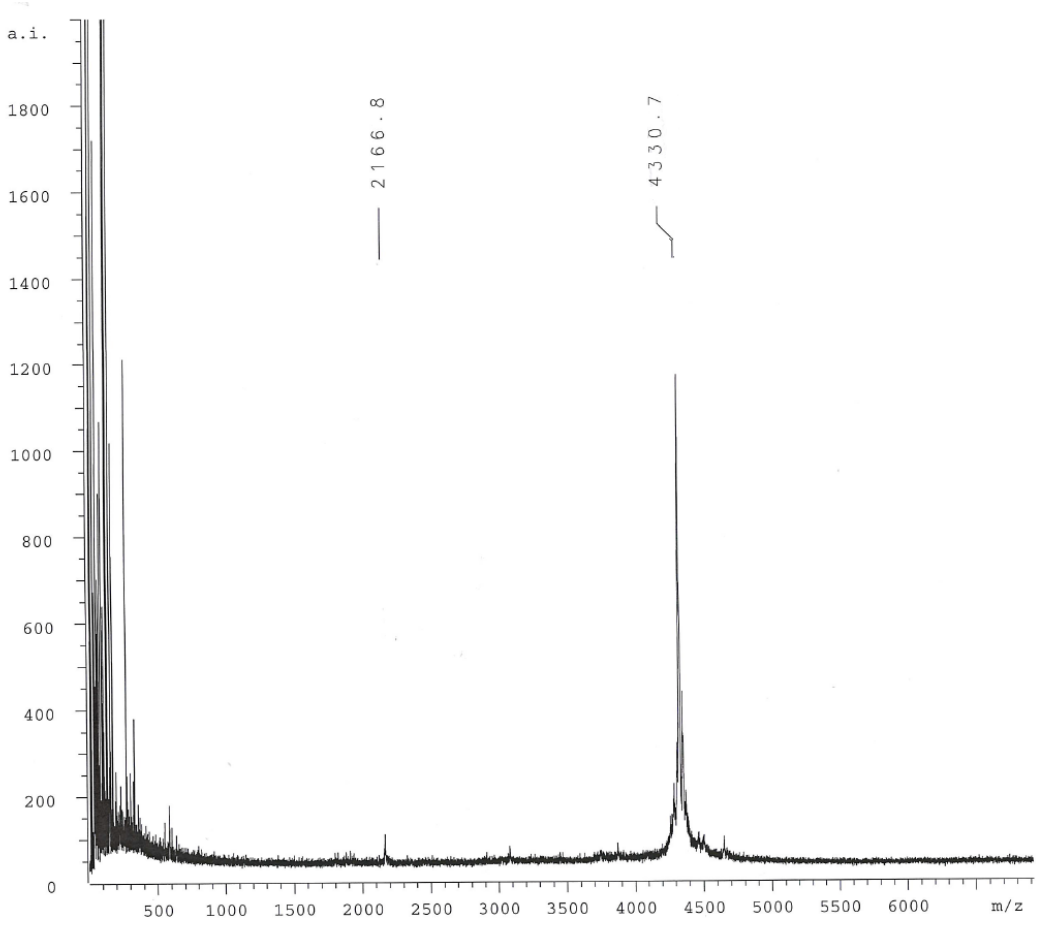
a.i.
1800
1600
1400
1200
1000
800
600
400
200
0
2166.8
4330.7
500
1000
1500
2000
2500
3000
3500
4000
4500
5000
5500
6000
m/z

M-Cyc-6β

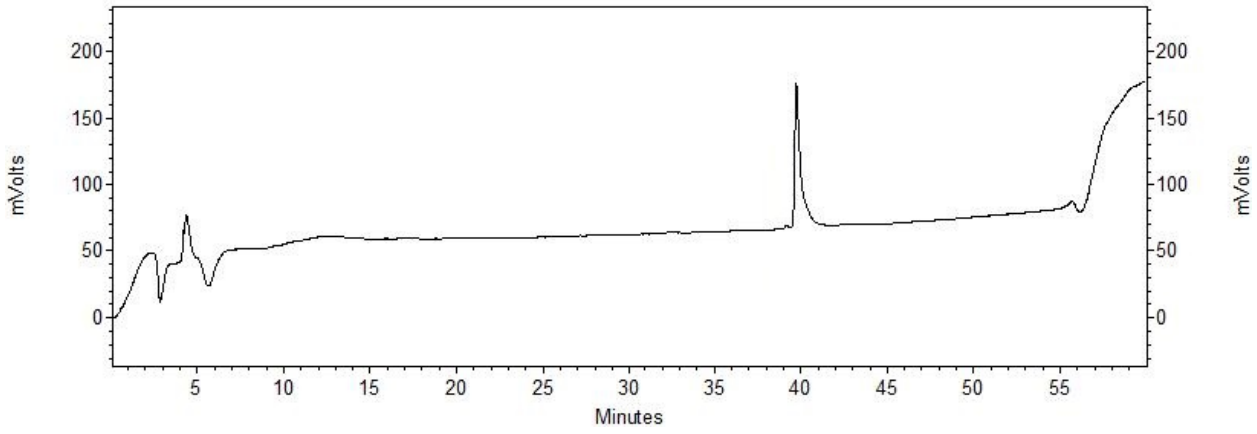
mVolts
200
150
100
50
0
5
10
15
20
25
30
35
40
45
50
55
Minutes

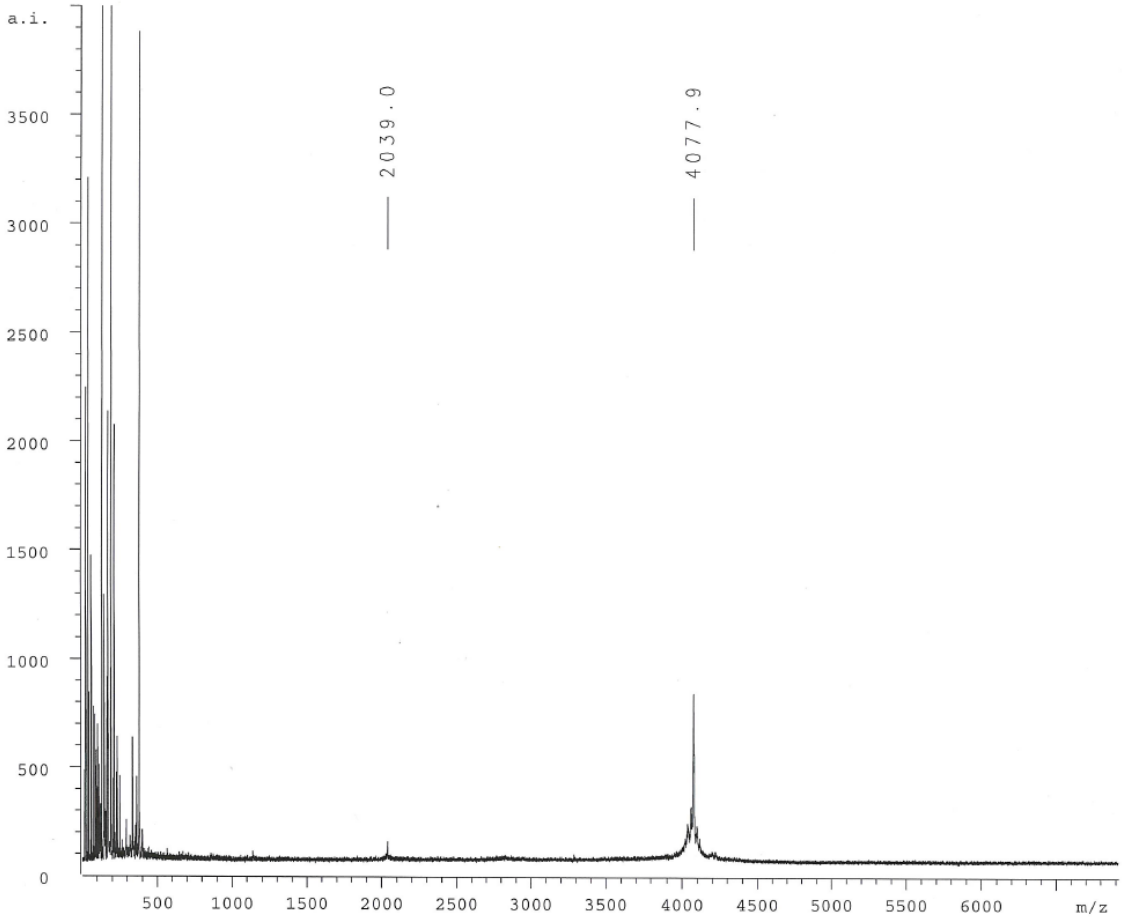
a.i.
3500
3000
2500
2000
1500
1000
500
0
2039.0
4077.9
500
1000
1500
2000
2500
3000
3500
4000
4500
5000
5500
6000
m/z

M-8β

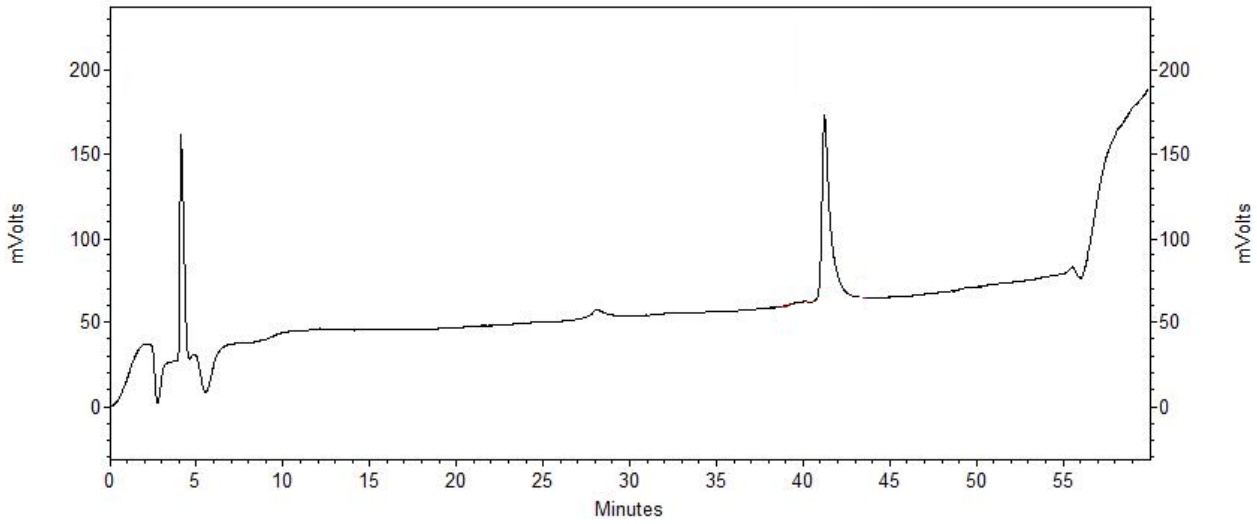
mVolts
200
150
100
50
0
0
5
10
15
20
25
30
35
40
45
50
55
Minutes

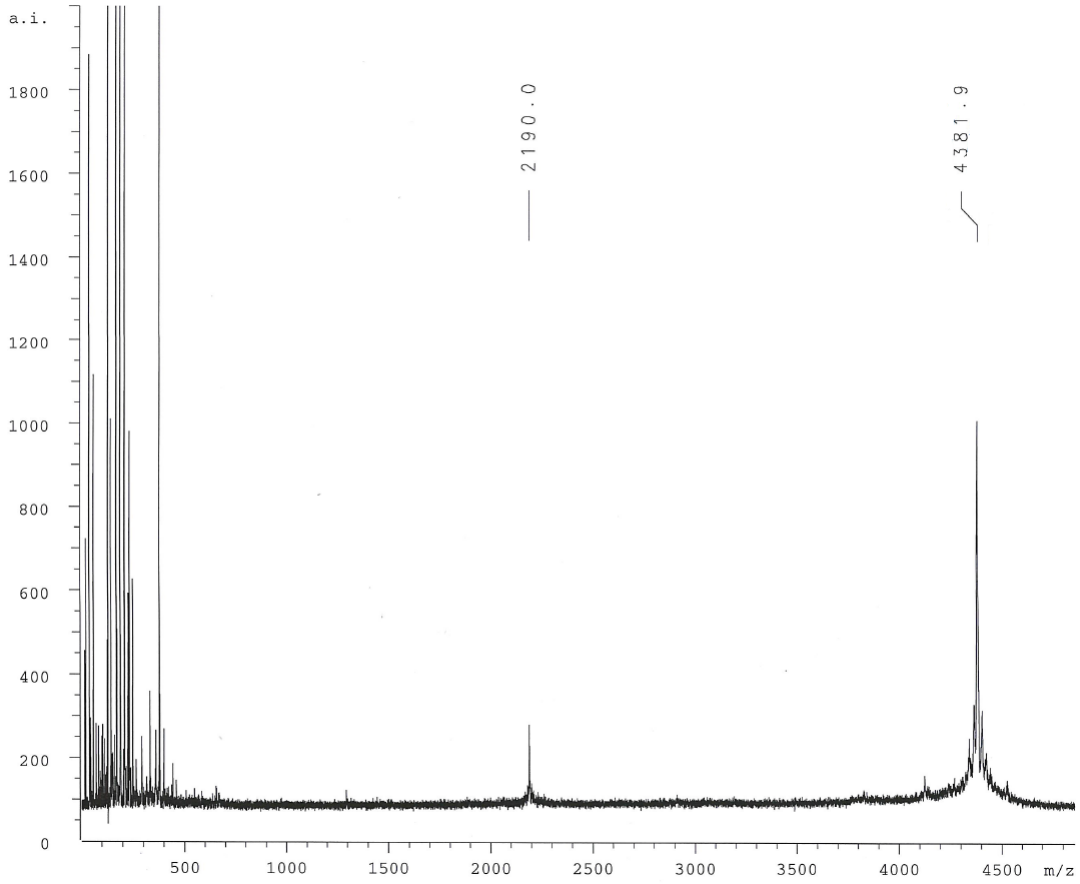
a.i.
1800
1600
1400
1200
1000
800
600
400
200
0
2190.0
4381.9
500
1000
1500
2000
2500
3000
3500
4000
4500
m/z

M-Cyc-8β

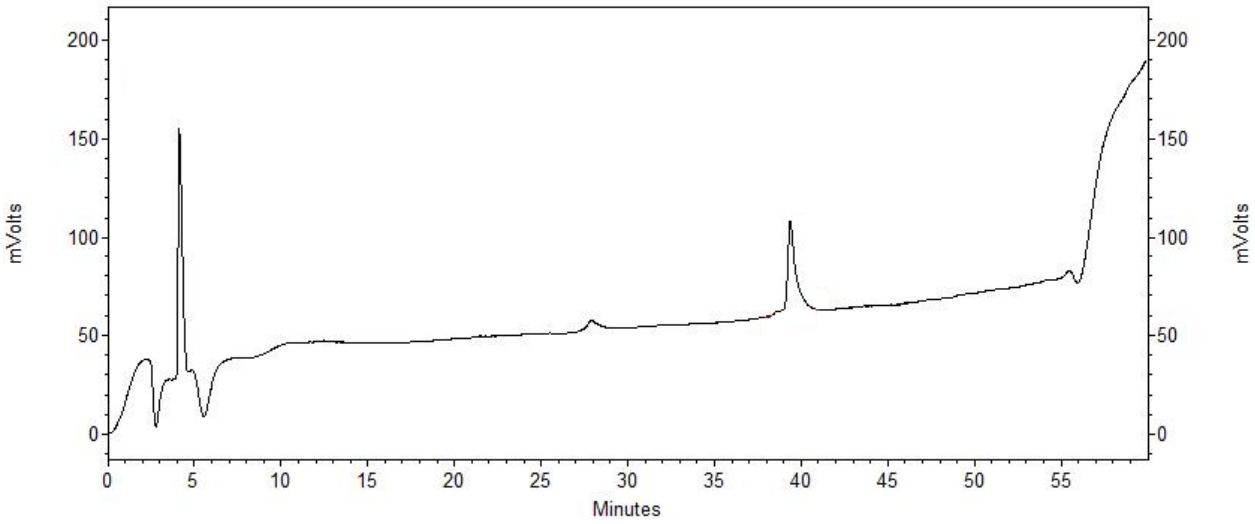
mVolts
Minutes
0
50
100
150
200
0
5
10
15
20
25
30
35
40
45
50
55

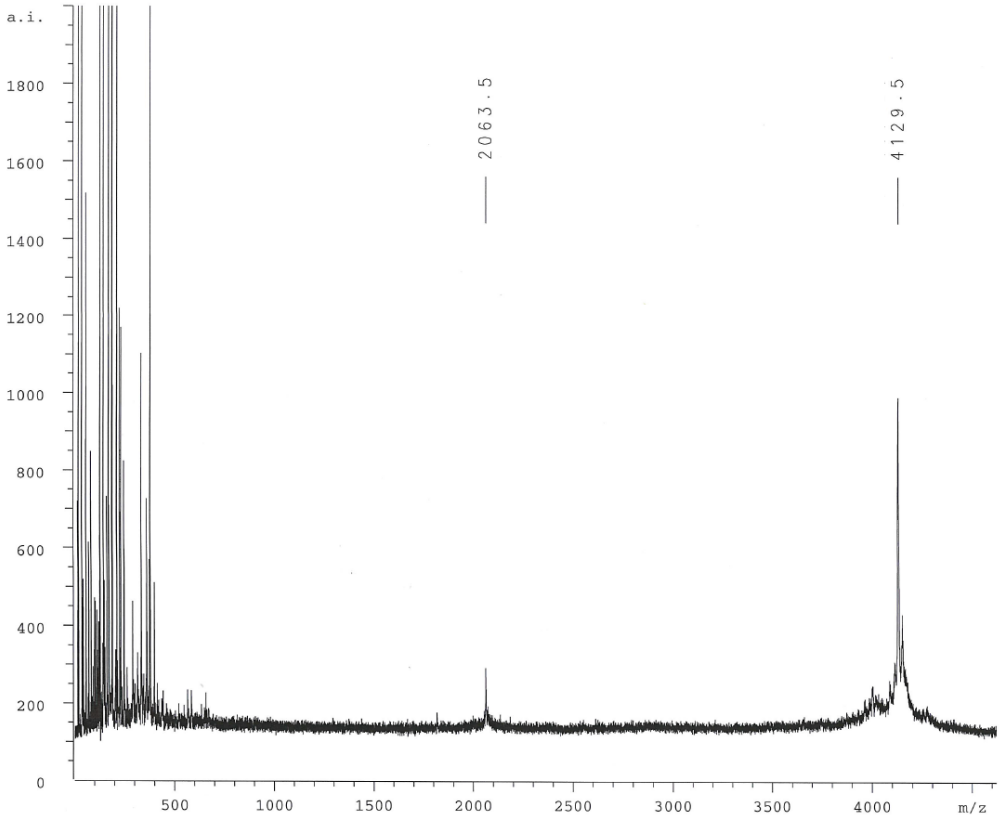
a.i.
2063.5
4129.5
m/z
0
200
400
600
800
1000
1200
1400
1600
1800
500
1000
1500
2000
2500
3000
3500
4000

M-9β

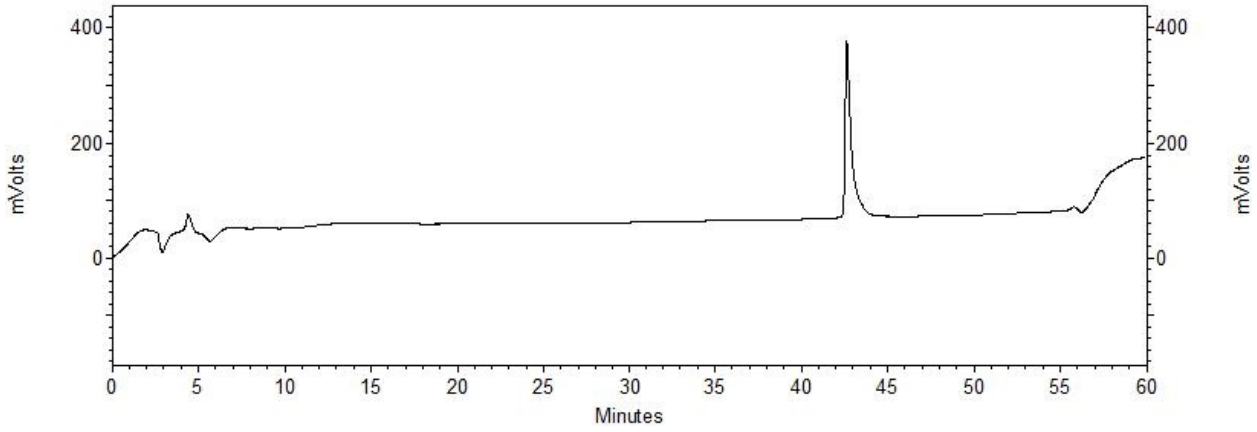
400
200
0
mVolts
0
5
10
15
20
25
30
35
40
45
50
55
60
Minutes

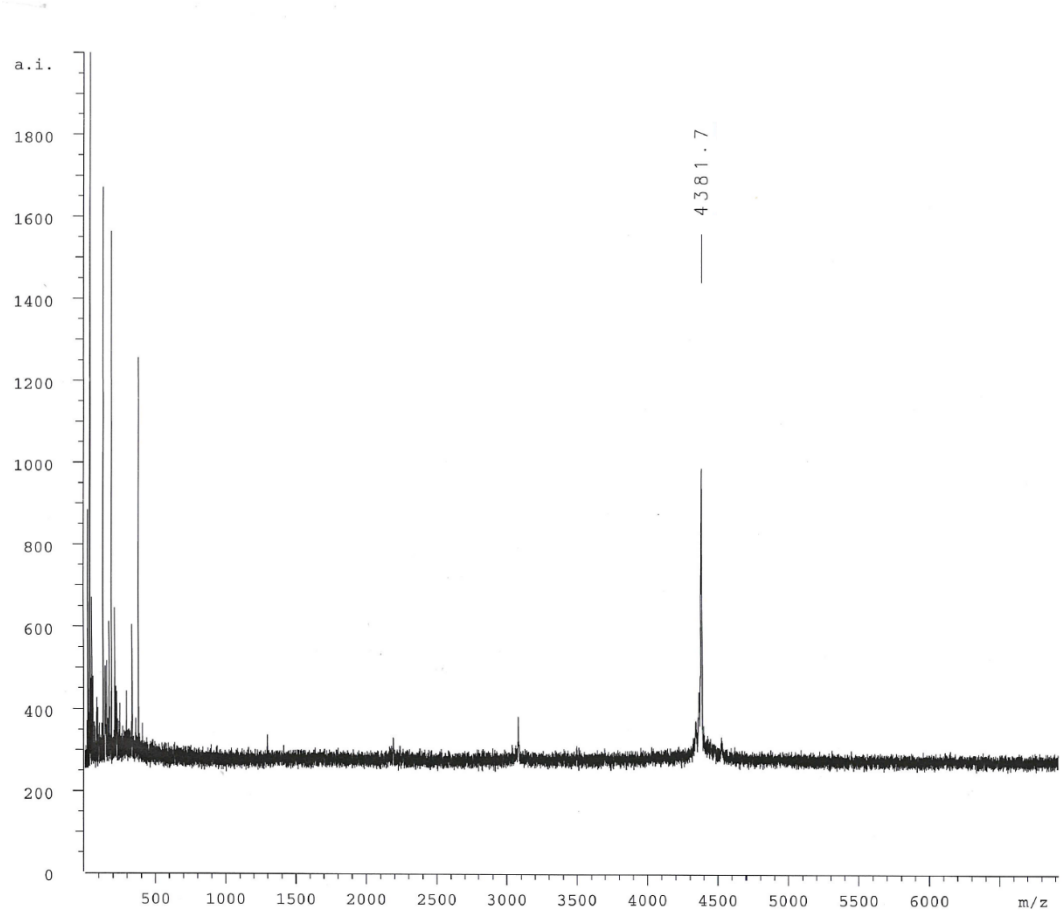
a.i.
1800
1600
1400
1200
1000
800
600
400
200
0
4381.7
500
1000
1500
2000
2500
3000
3500
4000
4500
5000
5500
6000
m/z

M-Cyc-9β

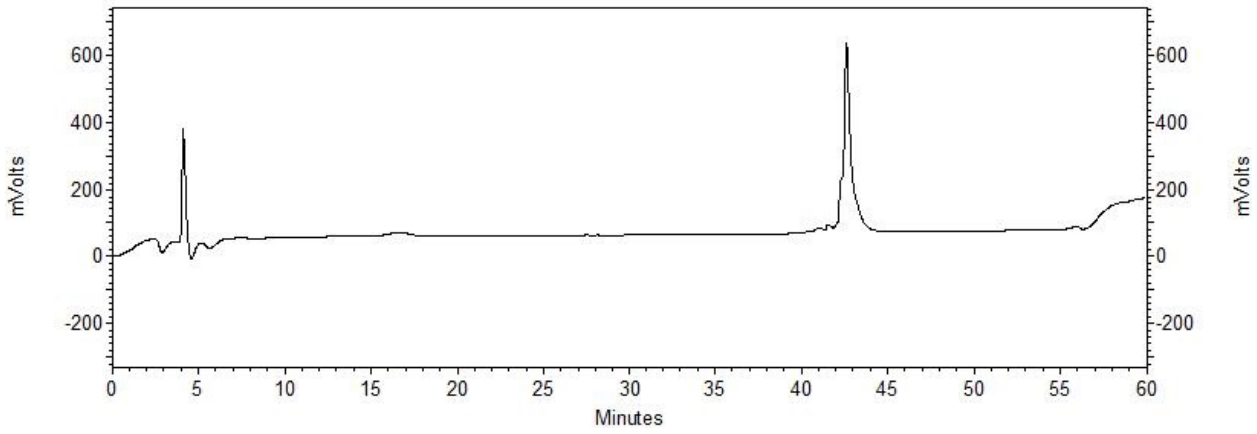
mVolts
600
400
200
0
-200
0
5
10
15
20
25
30
35
40
45
50
55
60
Minutes

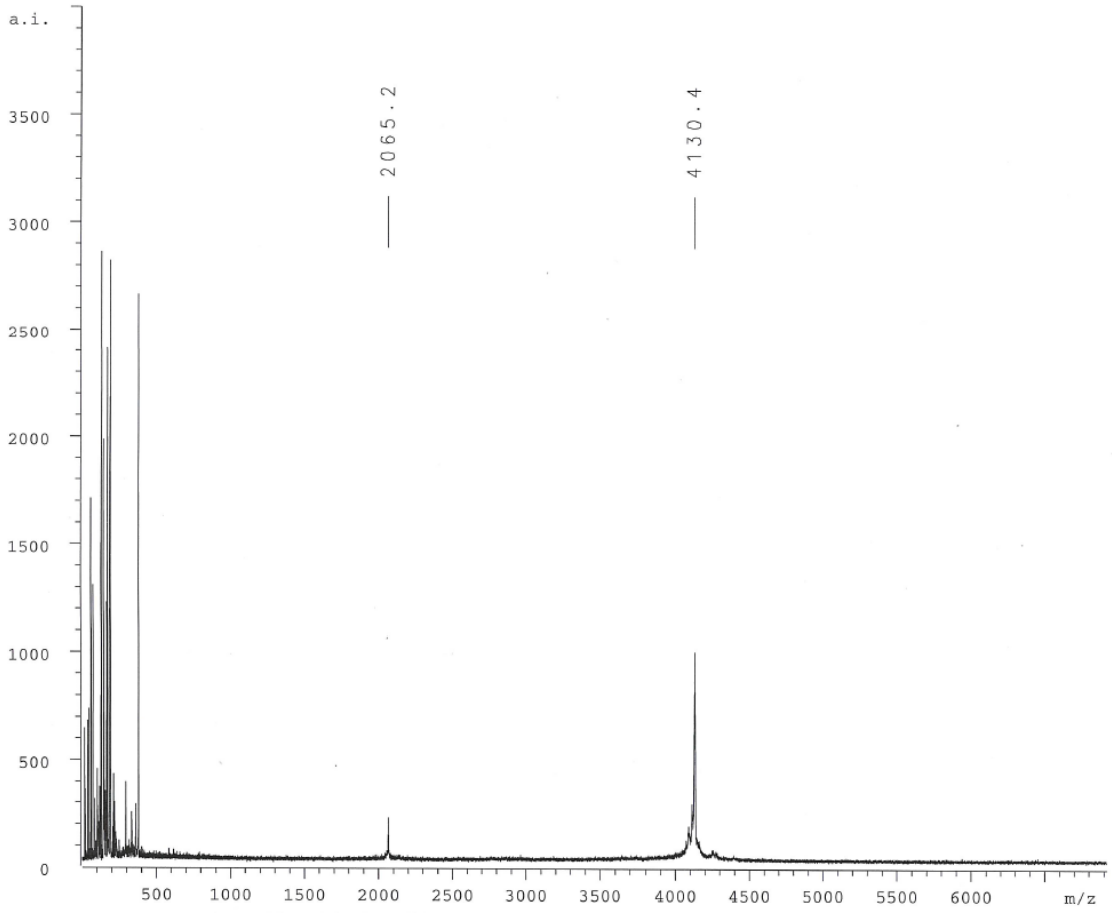
a.i.
3500
3000
2500
2000
1500
1000
500
0
2065.2
4130.4
500
1000
1500
2000
2500
3000
3500
4000
4500
5000
5500
6000
m/z

M-PTH(1-34)

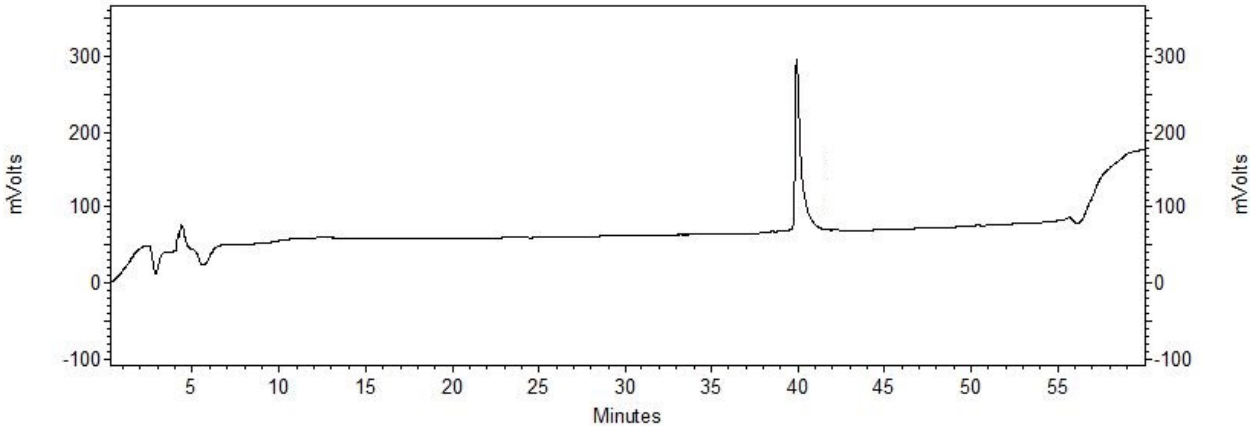
mVolts
300
200
100
0
-100
5
10
15
20
25
30
35
40
45
50
55
Minutes

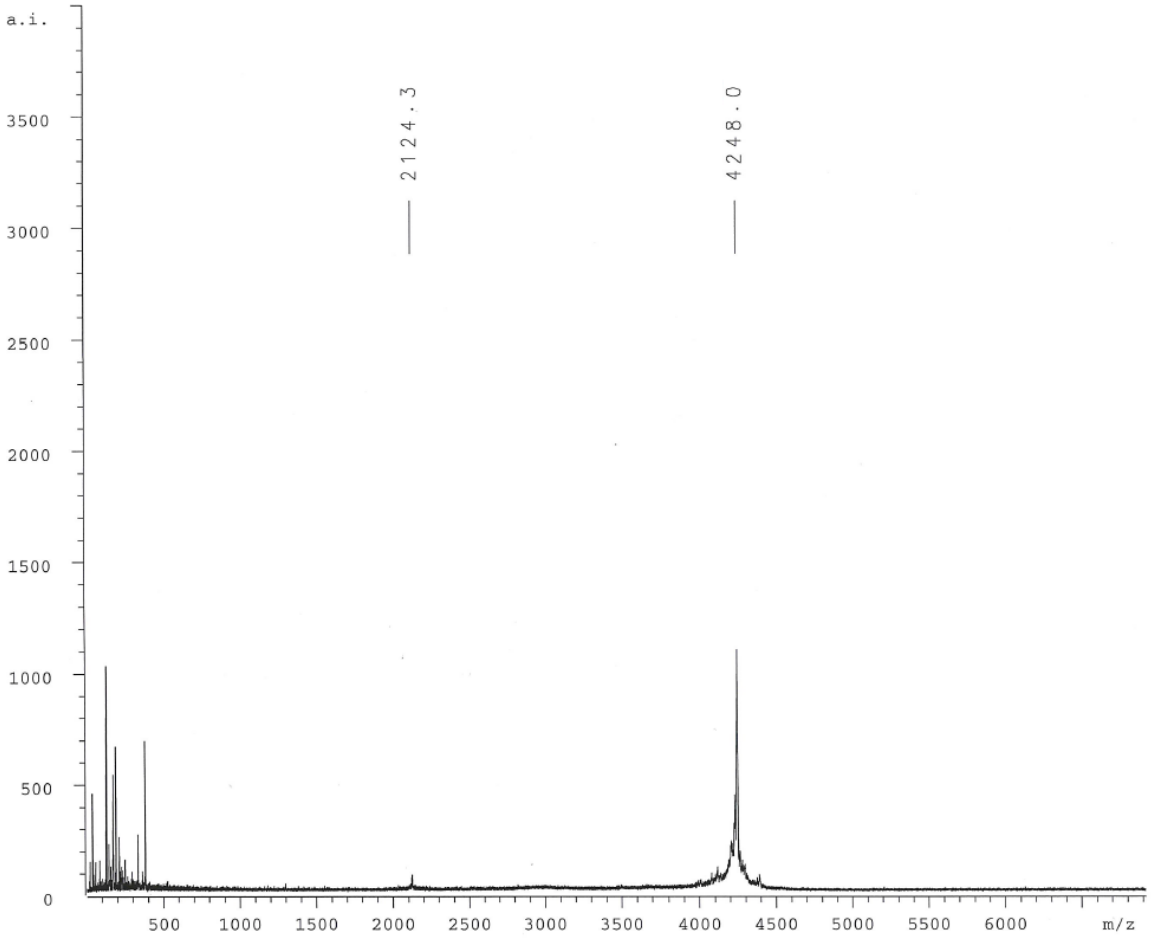
a.i.
3500
3000
2500
2000
1500
1000
500
0
2124.3
4248.0
500
1000
1500
2000
2500
3000
3500
4000
4500
5000
5500
6000
m/z

PTHrP-6β

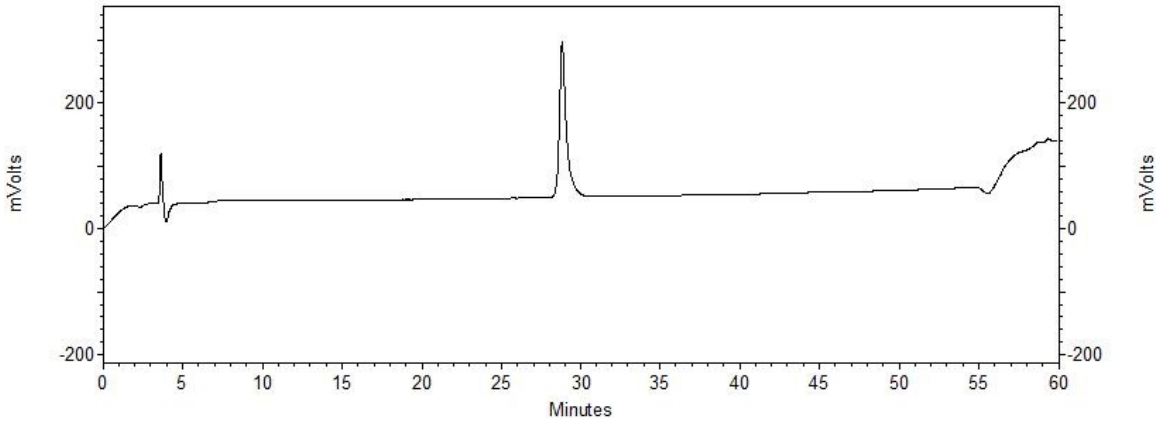
mVolts
200
0
-200
0
5
10
15
20
25
30
35
40
45
50
55
60
Minutes

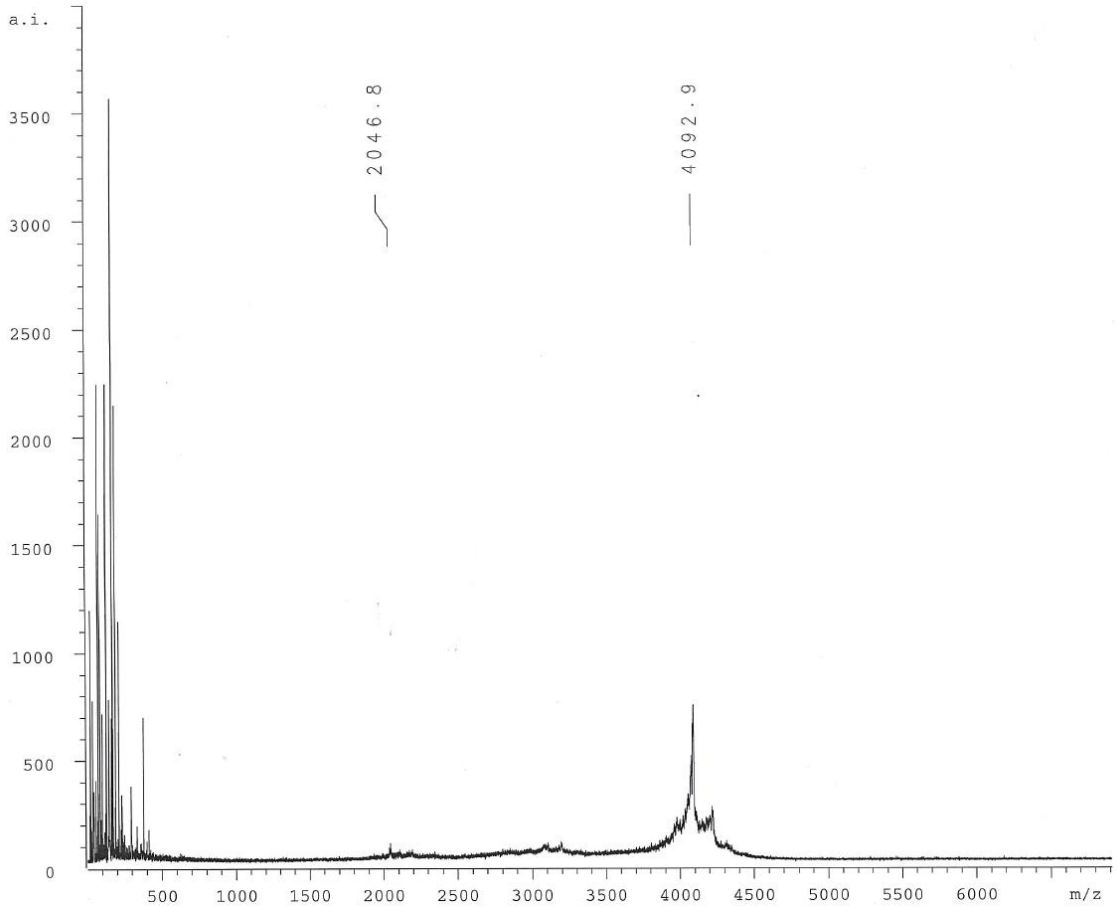
a.i.
2046.8
4092.9
3500
3000
2500
2000
1500
1000
500
0
500
1000
1500
2000
2500
3000
3500
4000
4500
5000
5500
6000
m/z

PTHrP-Cyc-6β

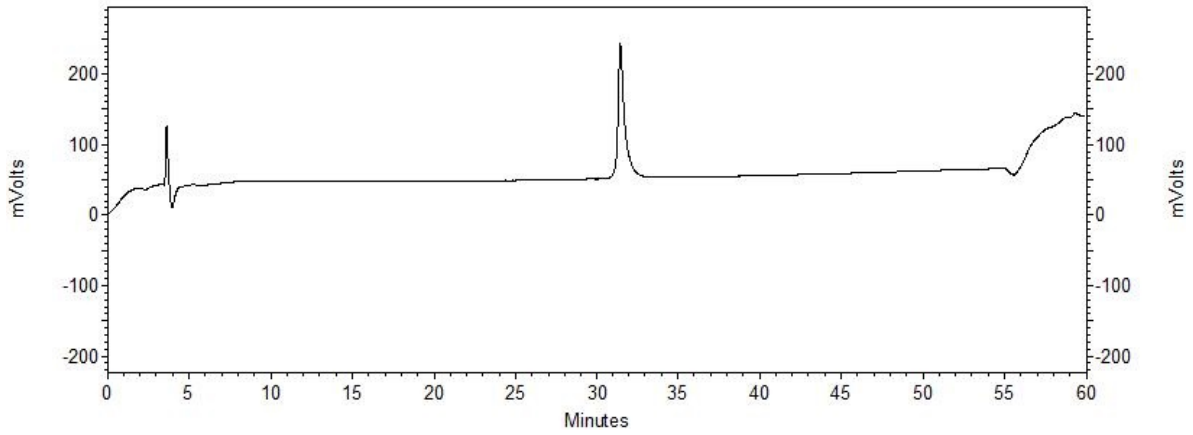
mVolts
200
100
0
-100
-200
0
5
10
15
20
25
30
35
40
45
50
55
60
Minutes

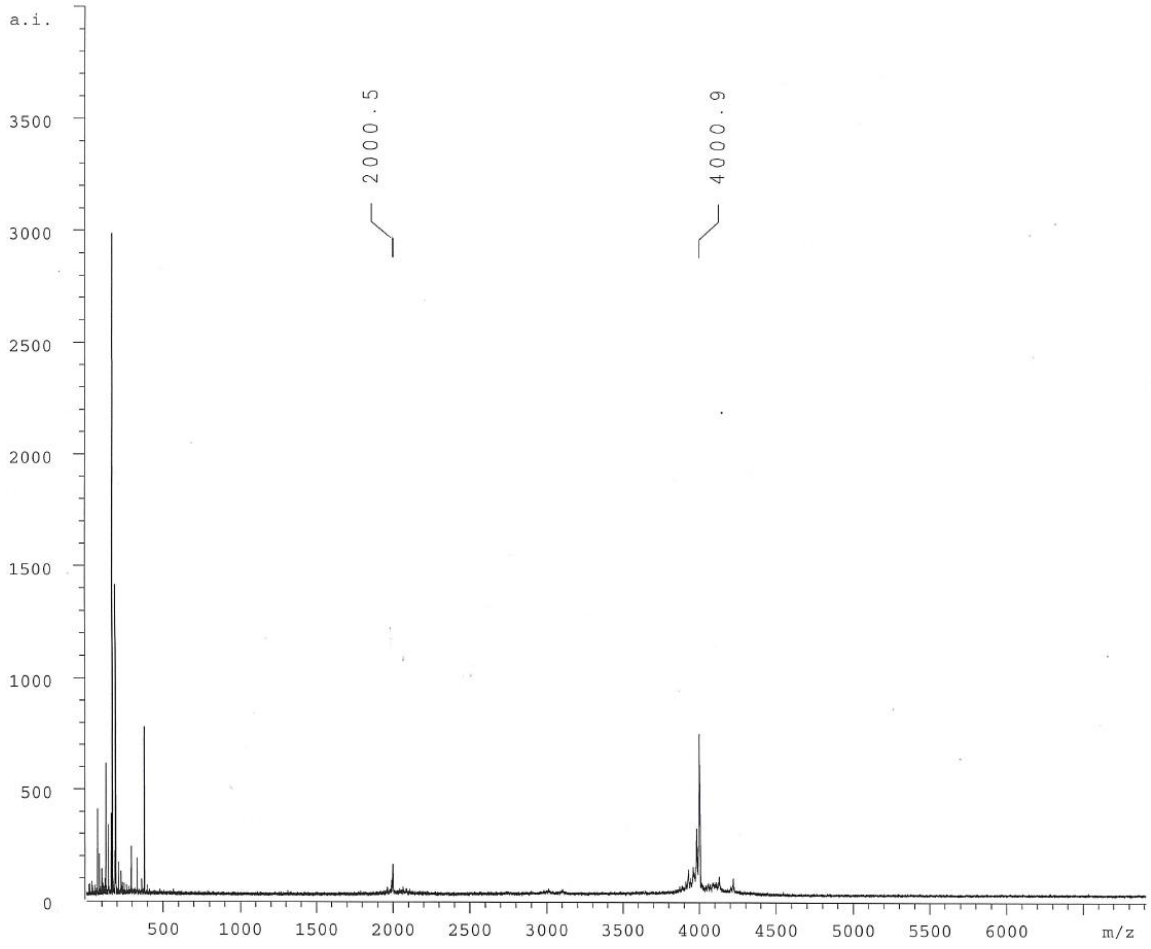
a.i.
3500
3000
2500
2000
1500
1000
500
0
2000.5
4000.9
500
1000
1500
2000
2500
3000
3500
4000
4500
5000
5500
6000
m/z

PTHrP-Cyc-9β

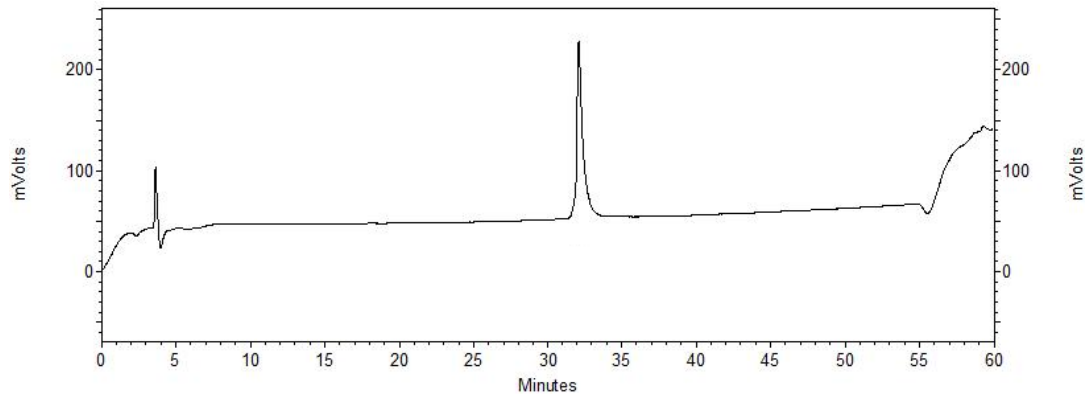
mVolts
200
100
0
0
5
10
15
20
25
30
35
40
45
50
55
60
Minutes

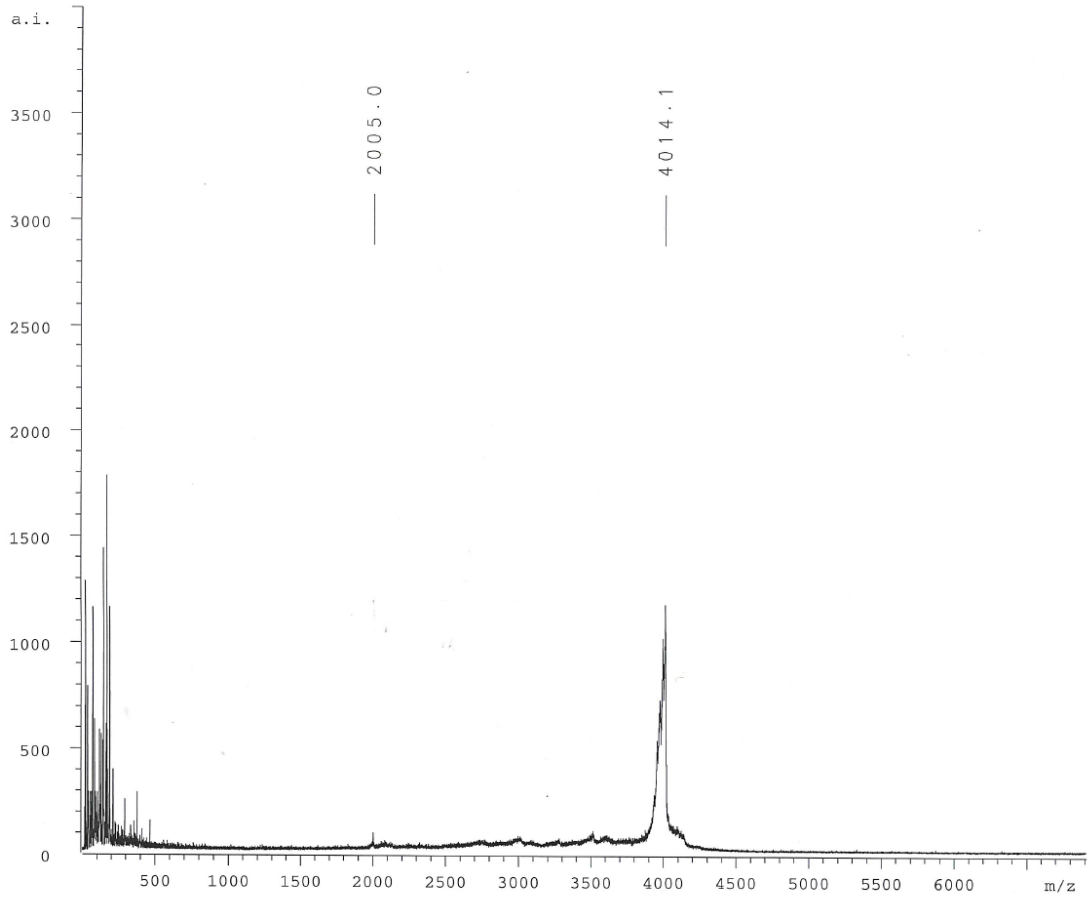
a.i.
3500
3000
2500
2000
1500
1000
500
0
2005.0
4014.1
500
1000
1500
2000
2500
3000
3500
4000
4500
5000
5500
6000
m/z

Abl-6β

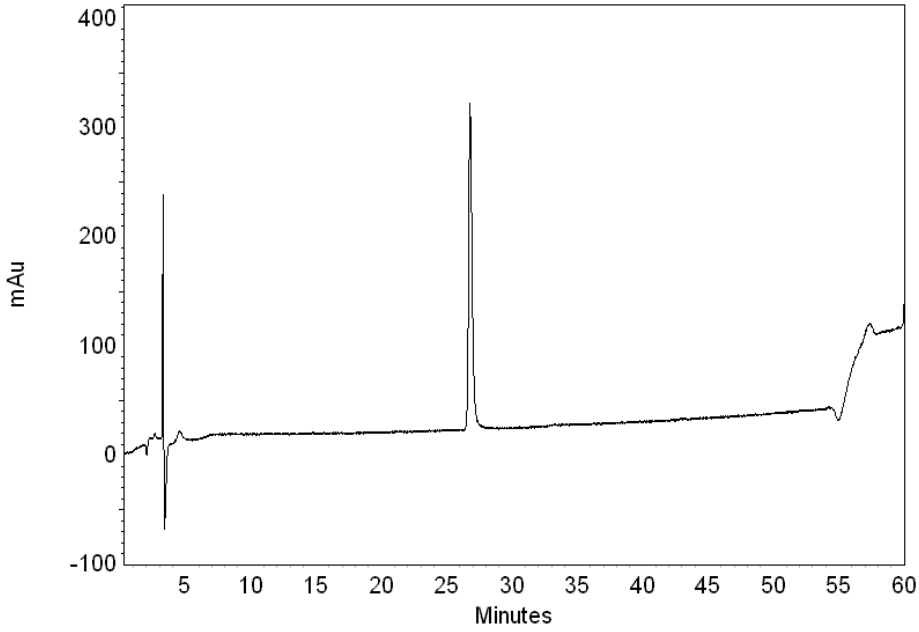
400
300
200
100
0
-100
mAu
5
10
15
20
25
30
35
40
45
50
55
60
Minutes

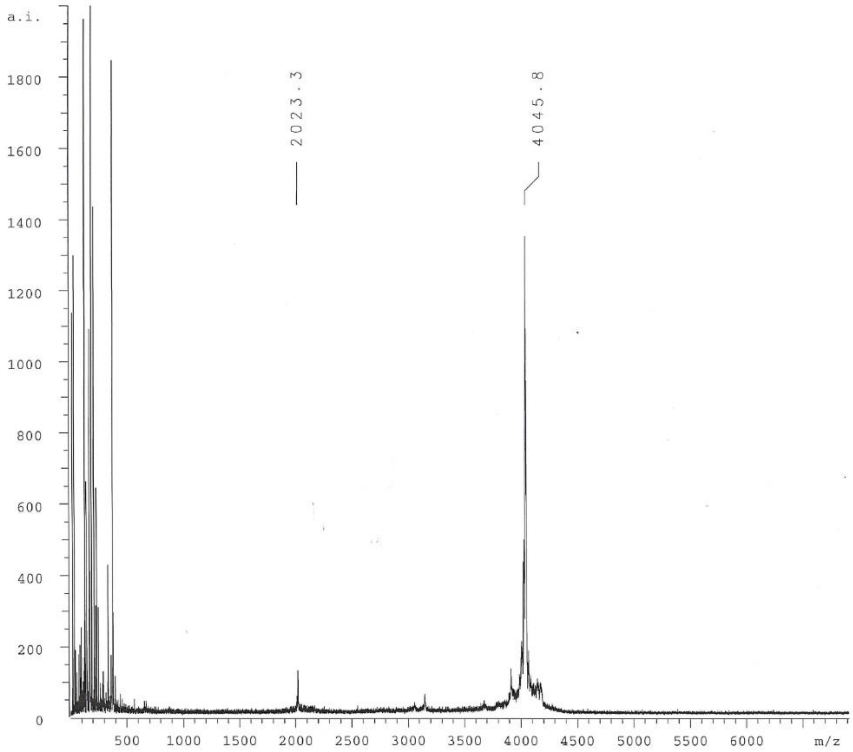
a.i.
1800
1600
1400
1200
1000
800
600
400
200
0
2023.3
4045.8
500
1000
1500
2000
2500
3000
3500
4000
4500
5000
5500
6000
m/z

Abl-Cyc-6β

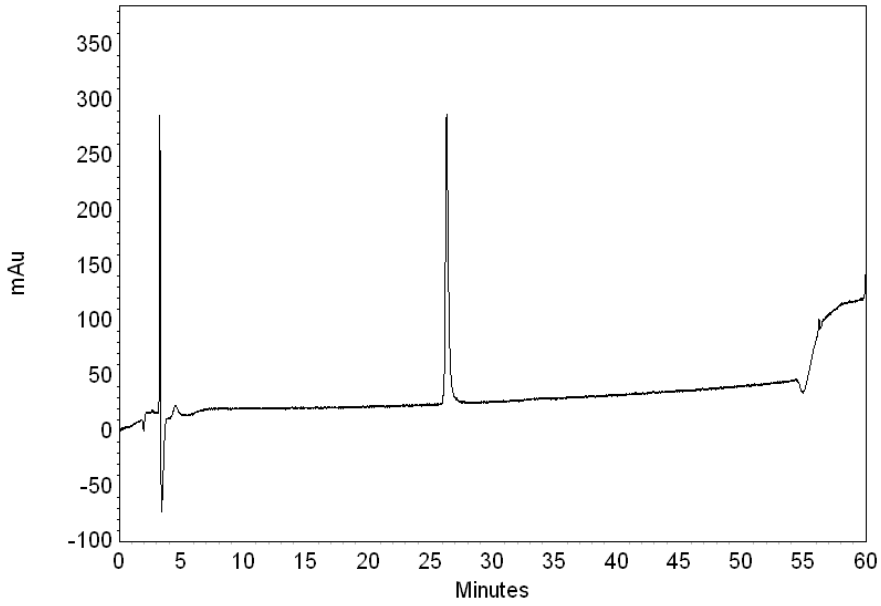
mAu
350
300
250
200
150
100
50
0
-50
-100
0
5
10
15
20
25
30
35
40
45
50
55
60
Minutes

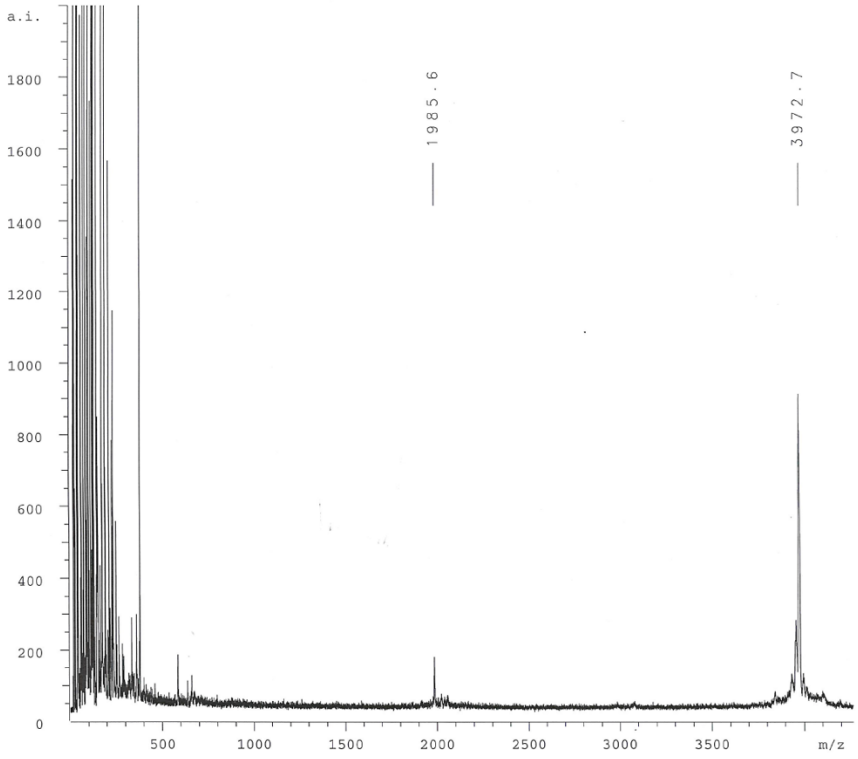
a.i.
1800
1600
1400
1200
1000
800
600
400
200
0
1985.6
3972.7
500
1000
1500
2000
2500
3000
3500
m/z

Abl-9β

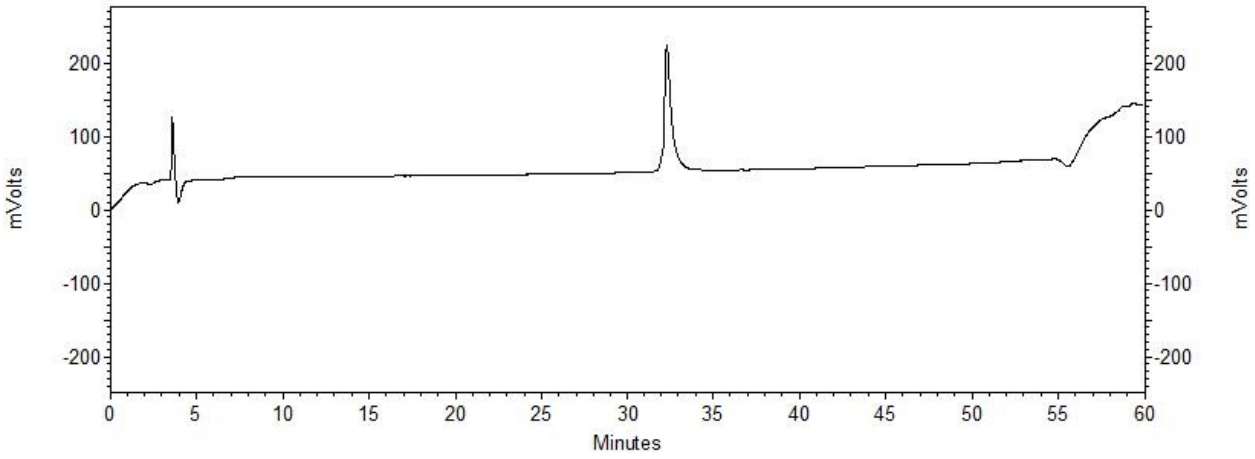
mVolts
200
100
0
-100
-200
0
5
10
15
20
25
30
35
40
45
50
55
60
Minutes

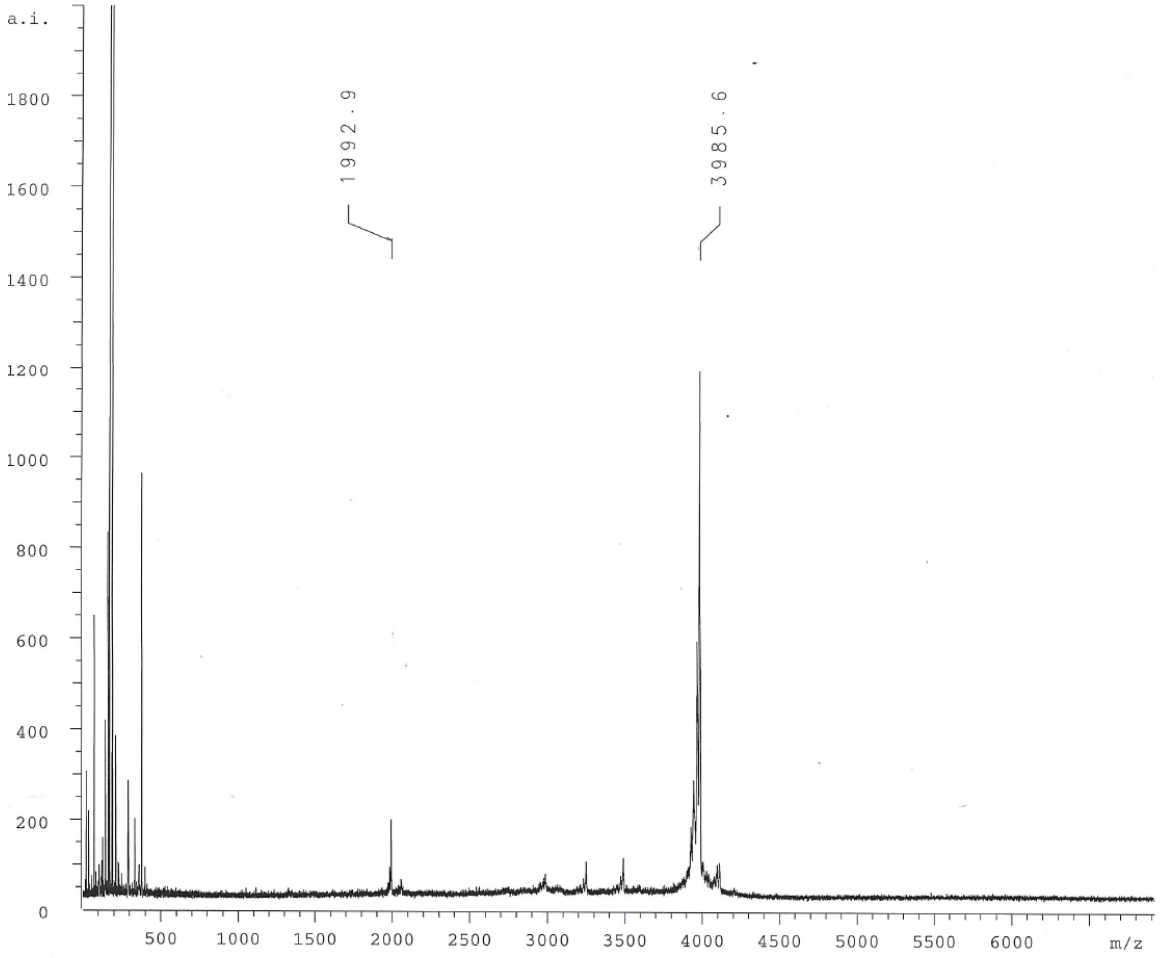
a.i.
1992.9
3985.6
1800
1600
1400
1200
1000
800
600
400
200
0
500
1000
1500
2000
2500
3000
3500
4000
4500
5000
5500
6000
m/z

Abaloparatide

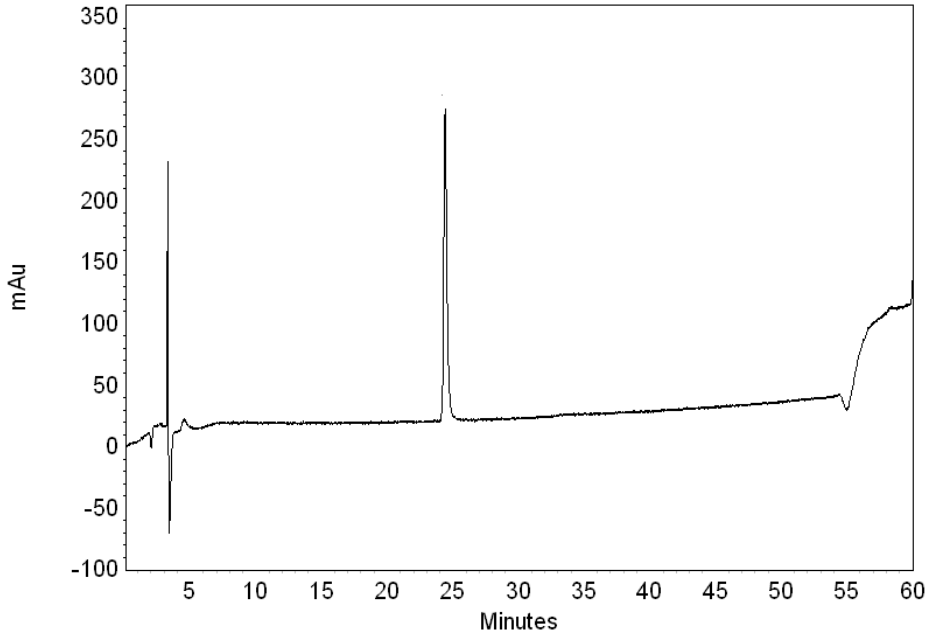

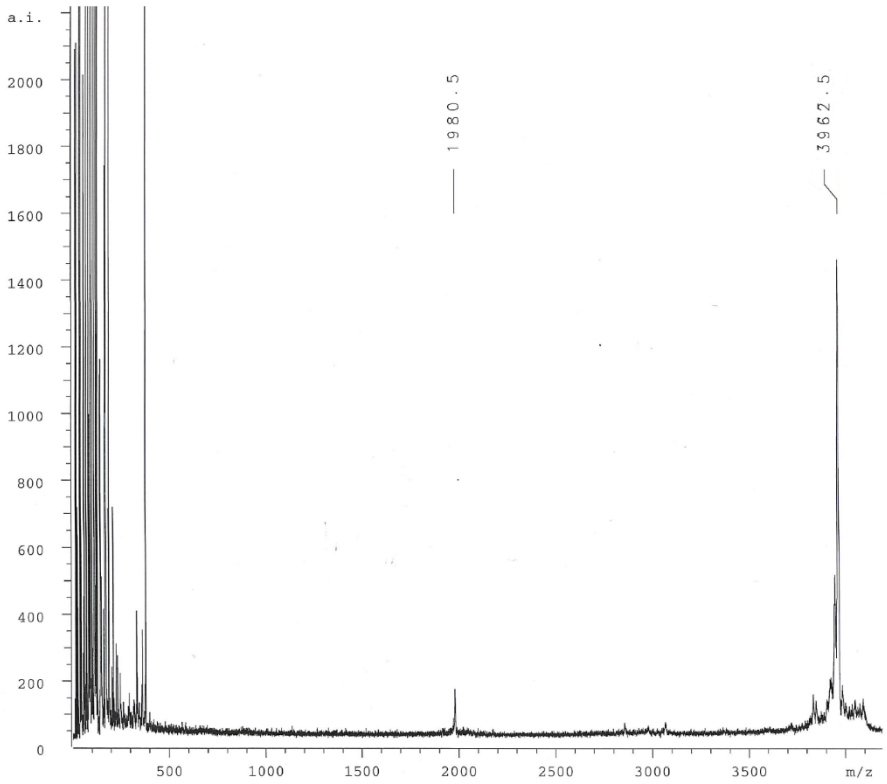

Supporting references

[1] Horne, W. S.; Price, J. L.; Gellman, S. H., Interplay among side chain sequence, backbone composition, and residue rigidification in polypeptide folding and assembly. *Proceedings of the National Academy of Sciences of the United States of America* **2008,** *105* (27), 9151-9156.

[2] Lee, H. S.; LePlae, P. R.; Porter, E. A.; Gellman, S. H., An efficient route to either enantiomer of orthogonally protected trans-3-aminopyrrolidine-4-carboxylic acid. *Journal of Organic Chemistry* **2001,** *66* (10), 3597-3599.

[3] Cheloha, R. W.; Watanabe, T.; Dean, T.; Gellman, S. H.; Gardella, T. J., Backbone Modification of a Parathyroid Hormone Receptor-1 Antagonist/Inverse Agonist. *ACS Chemical Biology* **2016,** *11* (10), 2752-2762.

[4] Binkowski, B. F.; Butler, B. L.; Stecha, P. F.; Eggers, C. T.; Otto, P.; Zimmerman, K.; Vidugiris, G.; Wood, M. G.; Encell, L. P.; Fan, F.; Wood, K. V., A Luminescent Biosensor with Increased Dynamic Range for Intracellular cAMP. *Acs Chemical Biology* **2011,** *6* (11), 1193-1197.

[5] Okazaki, M.; Ferrandon, S.; Vilardaga, J. P.; Bouxsein, M. L.; Potts, J. T.; Gardella, T. J., Prolonged signaling at the parathyroid hormone receptor by peptide ligands targeted to a specific receptor conformation. *Proceedings of the National Academy of Sciences of the United States of America* **2008,** *105* (43), 16525-16530.